Nanotechnology for corrosion control

Silsesquioxane based nanofillers
for iron carbonate film enhancement

Wassim Taleb

Submitted in accordance with the requirements for the degree of
Doctor of Philosophy

The University of Leeds
Institute of Functional Surfaces (iFS)
School of Mechanical Engineering

December 2016

The candidate confirms that the work submitted is his own and that appropriate credit has been given where reference has been made to the work of others.

This copy has been supplied on the understanding that it is copyright material and that no quotation from the thesis may be published without proper acknowledgement.

The right of Wassim Taleb to be identified as Author of this work has been asserted by him in accordance with the Copyright, Designs and Patents Act 1988.

© 2016 The University of Leeds and Wassim Taleb

Papers contributing to this thesis

Taleb, W., Pessu, F., Wang, C., Charpentier, T., Barker, R. and Neville, A. Siderite micro-modification for enhanced corrosion protection. *Materials Degradation*. 2017, **In Press.**

Acknowledgments

Professor Anne Neville, thank you for your support and professionalism during my research period; You supervised me during my master degree and now for this PhD and I am all hopes that we will carry on doing research together for years to come. I really appreciate the buffer zone that you so elegantly create, allowing you to be at the same time a supervisor but also a friend which all research students appreciate.

Richard Barker: Best co-supervisor; many thanks for your daily advice and support. I still remember how difficult it was for me to approach you during my MSc professional project period to get some help on using the potentiostats because no one ever saw you smiling in the lab but as we say, appearances could be deceiving and you turned out to be a very nice guy and a highly professional and dedicated colleague.

Thibaut Charpentier: I would never forget all the discussions we had evolving around chemistry and nanotechnology. My sincere thanks for your continual feedback and availability during my PhD but also for keeping my French speaking abilities alive and kicking. A big thanks to Doris too for helping me split then combine my chapters back.

Chun Wang, Stuart Micklethwaite, Michael Ward, Adrian Eagles, Andrew O'Brian, Jordan Thomas, Michael Huggan, Ron Cellier; your technical help and support in the labs and the use of the available analysis instrumentations have made this thesis what it is and I greatly appreciate your patience and commitment.

Finally, I would like to acknowledge the huge sentimental backup provided by my wife Lin, my father, mother and sister without whom I won't be the person I am.

I would like to end this part with my everlasting favourite quote:

"Imagination is more important than knowledge. For knowledge is limited to all we now know and understand, while imagination embraces the entire world, and all there ever will be to know and understand."

Abstract

Carbon dioxide internal corrosion is one of the most common degradation mechanisms occurring in oil and gas exploration and production environments when carbon steel is the material of construction. Both general and localized attack can lead to severe production cuts and safety incidents and these are commonly mitigated via the use of corrosion inhibitors, the deployment of which significantly increases the operational expenditure.

When environmental conditions are favourable, a naturally growing corrosion product known as iron carbonate precipitates onto the internal pipe wall providing protection from degradation but only when it is well adherent to the surface and compact. To date, research trying to take advantage of the protective abilities of these naturally growing films is limited.

The aim of this research is to encourage the iron carbonate kinetics of formation but also its mechanical properties via the addition of a hybrid organic-inorganic molecule to mimic the formation of a nanocomposite. This should allow for the modified iron carbonate to better resist mechanical removal in order to sustain its naturally inherent steel protection properties over a wider range of environmental conditions.

Electrochemical results show how the addition of a silsesquioxane-based nanofiller acts as nucleating agent and accelerates the build-up of the iron carbonate corrosion products. Mechanical properties such as hardness and modulus extracted from nanoindentation tests ascertain that the modified corrosion products are more robust.

This thesis describes a novel approach relying on the protectiveness of the corrosion layer growing *in situ* in oil and gas transport systems to mitigate carbon steel dissolution in specific environmental conditions. It is anticipated that the benefits of such a batch treatment of the nanofiller would be greater than for conventional film-forming inhibitors.

Thesis in a nutshell

Concept

Nanofiller (OA-POSS)	**+**	Porous structure (FeCO$_3$)	**=**	Hybrid corrosion film (improved properties)
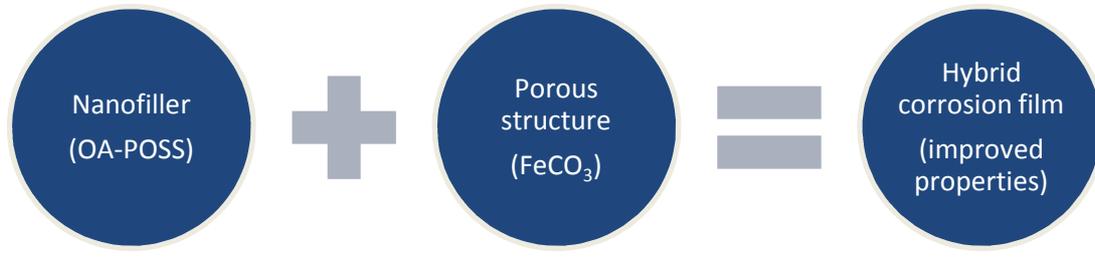
Findings

OA-POSS
(a nanofiller)

- Enhanced modulus
- Enhanced hardness
- More compact corrosion film
- Based on nanoindentation results

OA-POSS
(a nucleating agent)

- Faster FeCO$_3$ crystal growth
- Proven kinetic effect
- Potential thermodynamic alteration
- Based on electrohemical results

Table of contents

List of Figures

xxiii

List of Tables

List of Equations

xxxv

List of units

A	ampere
Å	angstrom
°C	degrees Celsius
cm	centimetre
$	American dollars
g	gram
gm	gram molecular
J	joule
°K	degrees kelvin
x K	1000 magnification
mbar	millibar
mmpy	millimetre per year
MPa	megapascal
mpy	milli-inch or mils per year
m/s	meters per second
nm	nanometre
pm	picometer
ppm	parts per million
psi	pounds per square inch
µm	micrometre
V	volt
wt %	weight percentage

List of chemicals

C, Ca	Carbon, calcium
CaCO$_3$	Calcium carbonate
CO$_2$, CO_3^{2-}	Carbon Dioxide, carbonates
Cu	Copper
Fe, Fe^{2+} , Fe^{3+}	Iron, ferrous Iron, ferric Iron
Fe$_3$C	Iron Carbide
Fe$_x$Ca$_y$CO$_3$	Iron calcium carbonate
FeCO$_3$, $Fe(HCO_3)_2$	Iron Carbonate, iron bicarbonate
HCO_3^- , H$_2$CO$_3$	Bicarbonates, carbonic acid
H$^+$, H$_2$S	Hydrogen ion, hydrogen sulfide
MDEA	Methyldiethanolamine
Mg, Mn	Magnesium, manganese
N$_2$	Nitrogen
NaCl, NaOH	Sodium chloride, sodium hydroxide
NaHCO$_3$	Sodium bicarbonate
Nb, Ni	Niobium, Nickel
O$_2$	Oxygen
P	Phosphorus
PDMS	Polydimethylsiloxane
S	Sulphur
Sb$_2$O$_3$	Antimony trioxide
Si, SiC	Silicon, silicon carbide
SnCl$_2$	Stannous chloride
V	Vanadium

List of abbreviations

AC	Alternate Current
AFM	Atomic Force Microscopy
API	American Petroleum Institute
ASTM	American Society for Testing and Materials
BET	Brunauer–Emmett–Teller
BOL	Bottom of Line
CE	Counter Electrode
CI	Corrosion Inhibitor
CNT	Carbon Nanotubes
CPE	Constant Phase Element
CR	Corrosion Rate
CS	Carbon Steel
DC	Direct Current
ε	Volumetric porosity
EDL	Electrical Double Layer
EDX	Energy-Dispersive X-Ray
EIS	Electrochemical Impedance Spectroscopy
EOR	Enhanced Oil Recovery
E_r	Young's Modulus
FILC	Flow Induced Localised Corrosion
FTIR	Fourier Transform Infrared Spectroscopy
GDP	Gross Domestic Product
ICP	Inductively Coupled Plasma
IEP	Iso Electric Point
ISO	International Organization for Standardization
MBOE	Millions of Barrels of Oil Equivalent
MTOE	Million Tons of Oil Equivalent

NACE	National Association of Corrosion Engineers
OA-POSS	OctaAmmonium POSS
OCP	Open Circuit Potential
OES	Optical Emission Spectroscopy
pH	potential Hydrogen
POSS	Polyhedral Oligomeric Silsesquioxane
R_p	Polarisation Resistance
R_s	Solution Resistance
R_{CT}	Resistance Charge Transfer
RE	Reference Electrode
RPM	Rounds Per Minutes
SCC	Stress Cracking Corrosion
SEM	Scanning Electron Microscopy
SHE	Standard Hydrogen Electrode
TEM	Transmission Electron Microscopy
TGA	Thermogravimetric Analysis
TOL	Top of Line
USA	United States of America
VSI	Vertical Scanning Interferometry
WE	Working Electrode
XPS	X-ray Photoelectron Spectroscopy
XRD	X-ray Diffraction

Preface

This dissertation is ultimately based on the experimental apparatus and data collected at the iFS corrosion labs at the school of mechanical engineering. None of the text of the dissertation is taken directly from previously published or collaborative articles.

The Inductively Coupled Plasma Optical Emission Spectrometry (ICP-OES) analysis results in section 8.5.2 were collected at the School of Earth and Environment of the University of Leeds by the aqueous analytical chemical experimental officer Stephen Reid.

The synchrotron X-Ray Diffraction (XRD) results in sections 8.2.2 and 10.4.1.3 were collected with the joint help of my colleague Danny Burkle at the I13 imaging branchline in Manchester.

All micrographs from the Scanning Electron Microscope (SEM) and the Transmission Electron Microscope (TEM) were carried out at the Leeds Electron Microscopy and Spectroscopy Centre which is part of the Institute of materials research at the university of Leeds.

The ferrite and pearlite percentages in Figure 5-2 were analysed jointly with the assistance of my colleague Rehan De Motte using Matlab programming.

Interferometry data acquisition and analysis was done under the supervision of Dr Frederick Pessu from the iFS at the University of Leeds measurement lab.

The thesis is divided in four parts; Part I, Chapter 1 sets up the background by describing the oil and gas industry, the energy demands, the various types of oilfield corrosion and corresponding corrosion costs. It explains why carbon dioxide corrosion is an issue and how this research can help mitigate such a degradation (section 3.1). The rationale that led to carry out this research is described in section 1.7 which sets up the aim and objectives. First, it describes how adding an adequate nanofiller can help create a less brittle iron carbonate ($FeCO_3$) film while showing better mechanical properties such as hardness and Young's modulus. Moreover, it is also advises how such a nanofiller is thought to alter the crystal nucleation and growth of the $FeCO_3$ crystals. These hybrid corrosion films are ultimately supposed to behave better with relation to both localised and general corrosion.

Part I, 1.8 details the theory of aqueous corrosion by defining what corrosion is, then explains the thermodynamics and kinetics of this degradation

mechanism along with the electrochemical techniques used to study it. As such, the Butler-Volmer equation around which most assumptions used in all electrochemical techniques is outlined in section 2.4.3.

Part II corresponds to the literature review and is divided in three separate chapters detailing the current advances in understanding carbon dioxide corrosion (Chapter 3), iron carbonate corrosion products (Chapter 4) and nanocomposite implications in the oil and gas industry (4.9). Section 3.8 highlights the potential role of $FeCO_3$ in corrosion control while enumerating the various reasons that lead to its disruption. The fact that $FeCO_3$ provides a corrosion protection ten times higher than frequently used corrosion inhibitors (CI) has led to some recent initiatives to take advantage of such properties and this is described in section 4.8. A summary of the literature review and a recapitulation of the research aims is found in section 4.9.

Part III details all the materials used in this research (Chapter 5) and the environmental conditions and methods used to carry out the electrochemical, morphological and mechanical investigations (Chapter 6).

Part IV constitutes the bulk of the thesis and presents the results gathered through this research; it starts with the tests carried out in order to clarify the choice of running conditions in Chapter 7. The early stages of interaction between the nanofiller of choice and the working electrode is set forth in section 7.2. Findings describing the nanofiller as a chemical compound which accelerates the $FeCO_3$ crystal nucleation and growth but also acts as a mechanical enhancer are described in Chapter 8. Varying the Potential Hydrogen (pH) and following up the nanofiller behaviour and its effect on the precipitation of $FeCO_3$ is specified in 8.5.6 with section 9.5 focusing on the nanofiller interaction with various ionic species.

Chapter 10 is reserved for the discussion and future work. The mechanism suspected in allowing the nanofiller to create a hybrid iron carbonate corrosion film is pointed out while trying to provide a model postulating the relationship between the mechanical enhancement, the general and localised corrosion mitigation and the nanofiller addition. Section 10.6 summarises some gaps in the current work and gives recommendations for additional experiments and research ideas that could complement it.

Part I.   Background

Chapter 1 Introduction

1.1   A metal based society

Iron is the fourth most abundant metal on Earth occurring in a variety of rock and soil minerals and has allowed mass production of designs and systems that will progressively revolutionize the development of human civilisation since the start of the Iron age.[1]

Metals are known to react with their environment and to degrade to a certain extent with time in a natural phenomenon known as corrosion; a thermodynamic process favoured by nature. Thus, every natural system is known to stabilise at its lowest potential energy level under a certain set of constraints also known as chemical stability.[2] Therefore, the electrons added into the metal during the extractive metallurgy processes will be rejected so the metal shift from a state of instability to a more stable state with the lowest energy possible.

Corrosion can take many forms and is thereby classified by the cause of the chemical deterioration of a metal such as general, localized or galvanic corrosion. It is also dependent on the atmosphere the degrading material is in contact with or the fluid composition; hence in the oil and gas industry, atmospheric, sweet or sour corrosion are induced when oxygen (O_2), carbon dioxide (CO_2) or hydrogen sulphide (H_2S) is the major phase in contact with the steel respectively.[3]

A better understanding of this corrosive behaviour could limit the adverse implications of such material deterioration allowing the reduction of the risks linked with events that could lead to human life loss and other related safety issues. For example, in 1967, the collapse in of the Ohio Silver bridge (Figure 1-1) due to corrosion fatigue led to the loss of 46 lives and its repercussions were valued at millions of dollars.[4]

Figure 1-1 Silver Bridge after collapse showing the Ohio side of river[5]

Another beneficial aspect of corrosion mitigation is decreasing the cost involved and better conserving the materials used. In fact, metallic equipment in service in the refining and petrochemical industries which are exposed to long periods of environmental stresses are known to age and have their mechanical and corrosion resistance properties diminished which could lead to severe safety risks on site.[6]

Section 1.2 describes how societies are expected to rely on oil and gas as a primary source of energy for decades to come. It also depicts corrosion as one of the major risks that the structures involved in the exploration and production of hydrocarbons are subjected to.

1.2 Energy demands

The need for energy keeps on growing worldwide, and in 2009, China has even exceeded consumption of the United States of America (USA) for the first time in history. Unfortunately, readily available resources to cover these demands are limited and renewable alternatives, while evolving, still have a long gap to close before replacing the more classical hydrocarbon pathways. This has accelerated interdisciplinary energy research with the aim of reducing energy needs and increasing energy efficiency.[7]

Currently it is estimated that there exist twenty four metric tons oil reserve for every man, woman and child alive on Earth but this world reserve of oil is scheduled to run out in just 42 years at the current known production rates.[8]

While renewables are slowly developing, an associated surge in supply for petroleum and oil products is inevitable. Although it looks like humanity will run out of its oil and gas reserves, new technologies for more enhanced oilwell exploitation keep arising and lately nanotechnology implementations have revived hopes that a new age of fossil fuels is ahead. With only 5 to 20% of the oilfield reserves being extracted via primary recovery methods, developing Enhanced Oil Recovery (EOR) techniques that could allow the recovery of the other 70% from the petroleum reservoirs looks appealing and could prove vital.[9]

Luckily, relevant technological advances have allowed for alternative sources of oil and natural gas to be produced as is the case with Brazil's pre-salt reserves and shale gas in the United States.[10] As such, Figure 1-2 highlights the big expansion in dry gas production in various USA wells which was almost increased tenfold between 2000 and 2013. Alternate energy resources such tar sands and geothermal power supply have also proven to be very beneficial and could help fill the gap in the future.[11]
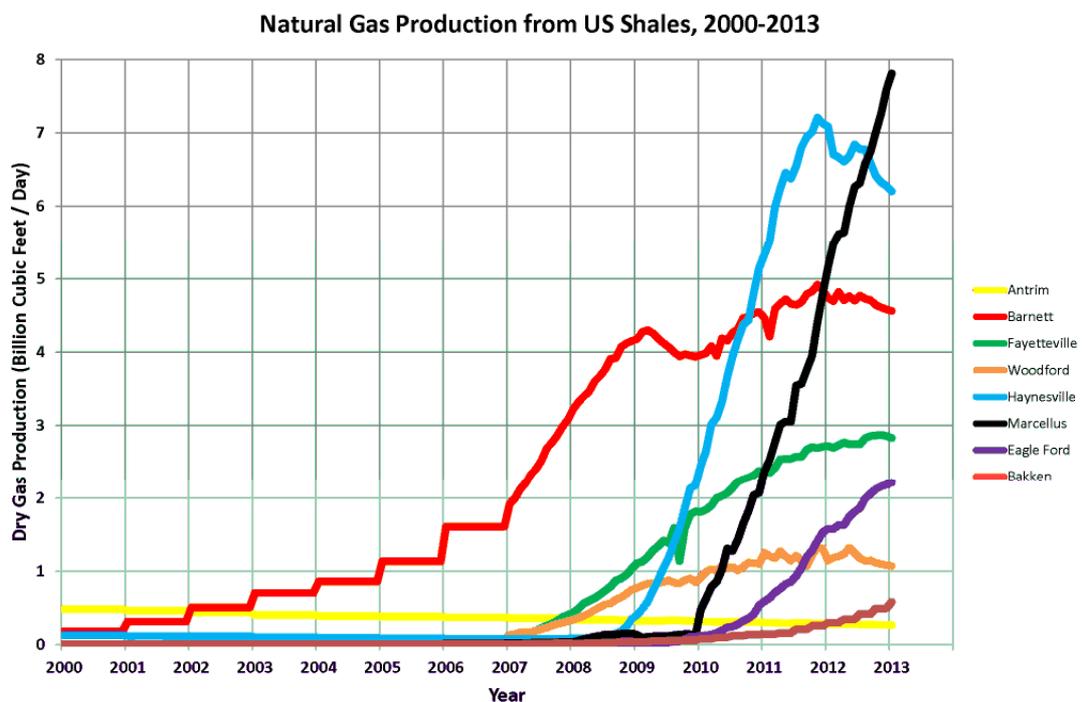
Figure 1-2 Natural gas production from US shale from various sites[12]

Since hydrocarbons are thought to remain the primary source of energy, it is important to understand how they are processed and be able to develop techniques that will maintain an operational network so the energy needs are sustained. Recent field manipulations suggest that the required excess energy will be mostly achieved via the implementation of the horizontal drilling and associated hydrofracturing processes which enable the production of natural gas from shale gas, tight gas and coalbed methane.[13]

The oil and gas network is the main structure that allows for the extraction and processing of the oil and gas in order to produce the required energy and is described in section 1.3.

1.3 Oil and gas network

The oil and gas industry is one of the largest and most complex and important global industries. Its first phase began in Pennsylvania in 1859 when Colonel Edwin Drake drilled successfully for oil. The first step in producing oil and gas is the completion of the oil and gas field development, after which the recovery of oil and gas can start. This upstream management requires the monitoring of both pre-production costs but also the lifting costs.[14]

In order to be used as an energy source, the hydrocarbons should be extracted from the underground, separated from the non-energy containing products and further purified as shown in Figure 1-3 and adapted from Papavinasam et al.[15] In fact, crude oil has little value if not refined into products such as gasoline and diesel which means that producers of crude oil must sell and transport their products to refineries.

Crude oil has become an important source of energy mainly due to its ease of transportation as a liquid which is normally accomplished through production and transmission pipelines. Thus countries such as Alaska and Russia have erected hundreds of kilometres long of carbon steel pipelines that allowed the transportation of hydrocarbons from very remote locations to the markets.[16]

The API divides the petroleum industry into three categories; upstream, downstream and pipelines. The vast oil network schematised in Figure 1-3 comprises various materials which are exposed to a multitude of operating conditions such as temperature, flow and pressure and these can function under changing boundary conditions over time.[17] Seventeen different corrosive environments can be distinguished in this petroleum chain from the oil well to the refining utilities and these are detailed in section 1.4.
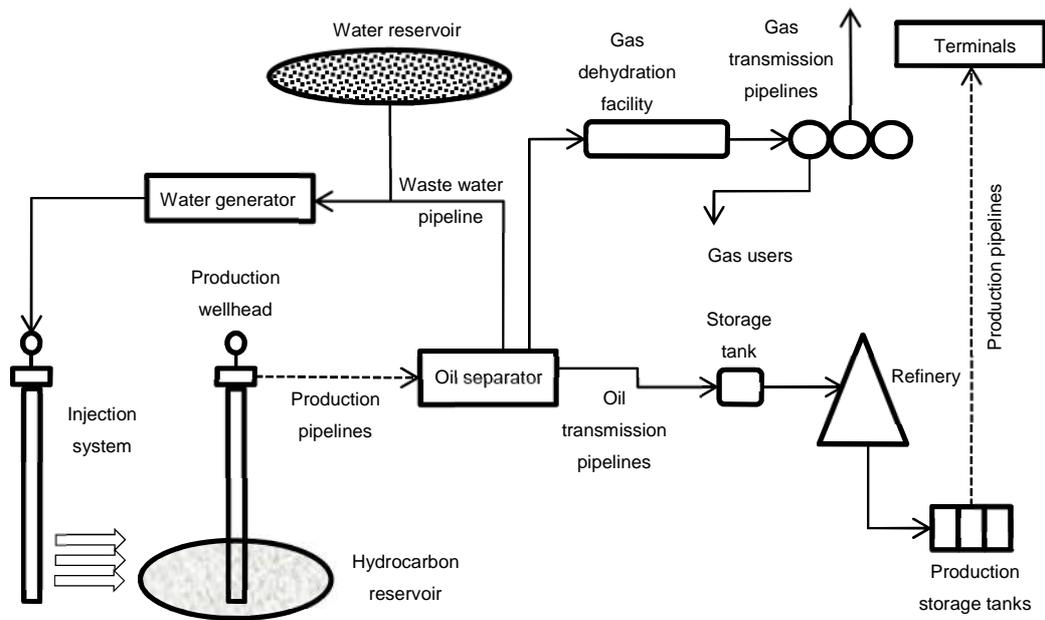
Figure 1-3 Paths of conventional crude oils from well to consumer[15]

Hydrocarbon sources which provide more than 80% of the energy demands are divided into two groups known as conventional and unconventional and Figure 1-4 summarises the gas counterpart of these resources; these are not distinguished because of their chemical compositions but rather due to the geological characteristics of their reservoir rock.[18]
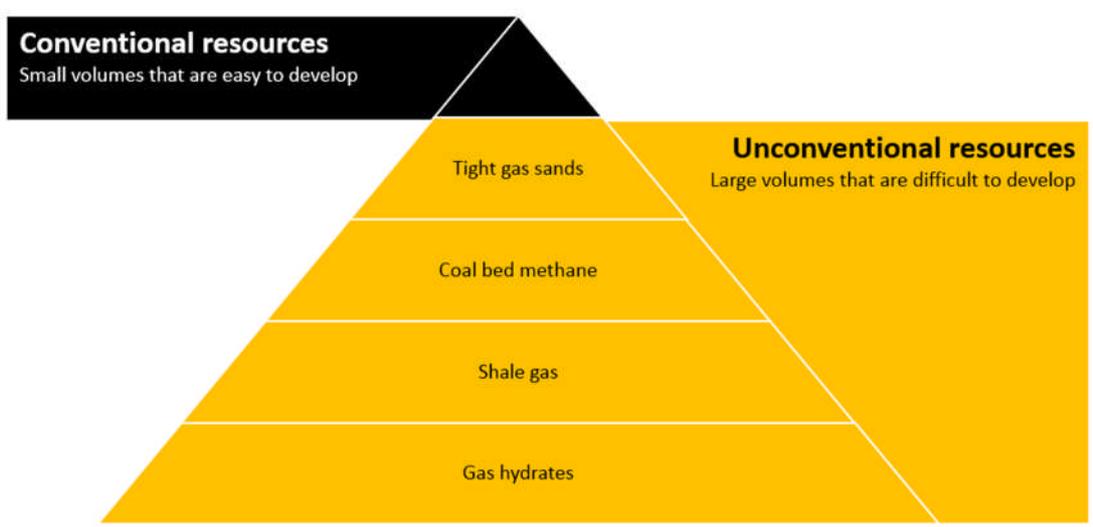
Figure 1-4 Conventional and unconventional gas sources[19]

The conventional oil and gas sources are defined as those where the fluid contains more than 40% of hydrocarbons. These are known to flow easily which means that their extraction is readily processed via conventional

methods. The unconventional sources are defined as those that cannot produce hydrocarbons at economic flow rates unless a stimulation process is implemented such as heat treatment, hydraulic fractures or the installation of multilateral welbores. They are nonetheless in continuous expansion especially in the United States where oil extraction from shale resources is believed to lead the country for its energy auto sufficiency in the next few years.[20]

These non-conventional supplies are the ones that the industry is trying to extract because the known conventional reservoirs are coming to age and being more and more exhausted. Recent estimates show that unconventional resources such as oilsands, oil shales, gas shales, tight gas, coal bed methane and gas hydrates range between 13 to 15 trillion barrels of crude oil and 32,000 trillion cubic feet of natural gas.[21] In such a complex megastructure, corrosion degradation mechanisms are numerous and are known to take place in many segments; the mechanisms vary depending on the structure materials used and the environmental conditions and these are described in section 1.4.

1.4 Types of oilfield corrosion

Depending on the chemical environment, seventeen corrosive environments can be described throughout the petroleum chain. The environmental parameters which greatly influence the degradation processes are mainly CO_2 and H_2S partial pressures, fluid temperature, water salinity and the pH.[22]

Table 1-1 List of oilfield corrosive environments in oil and gas production[23]

Corrosive environment	Oil and gas production	Acid gas treatment	Refining petrochemistry
Liquid water + CO_2	x	x	x
Liquid water + H_2S	x	x	x
Mercury and liquid metals	x		
Water + bacteria	x		x
Water + chlorides	x	x	x
Concentrated acids	x		x
Alcohols	x		x

6

Table 1-1 displays seven of these corrosive chemical environments known to occur in the oil and gas production with sour, sweet and bacteriological corrosion environments being the most common when hydrogen sulfide, carbon dioxide and various microorganisms are the dominant fluid phase respectively.[23]

Water containing dissolved carbonic acid is corrosive to carbon and low alloy steel and this type of corrosion is termed sweet corrosion or carbon dioxide corrosion. Sweet corrosion is becoming more and more common with the extensive use of CO_2 flooding as an oil recovery technique as depicted in two recent case studies undertaken by Laumb et al.[24] (Figure 1-5)
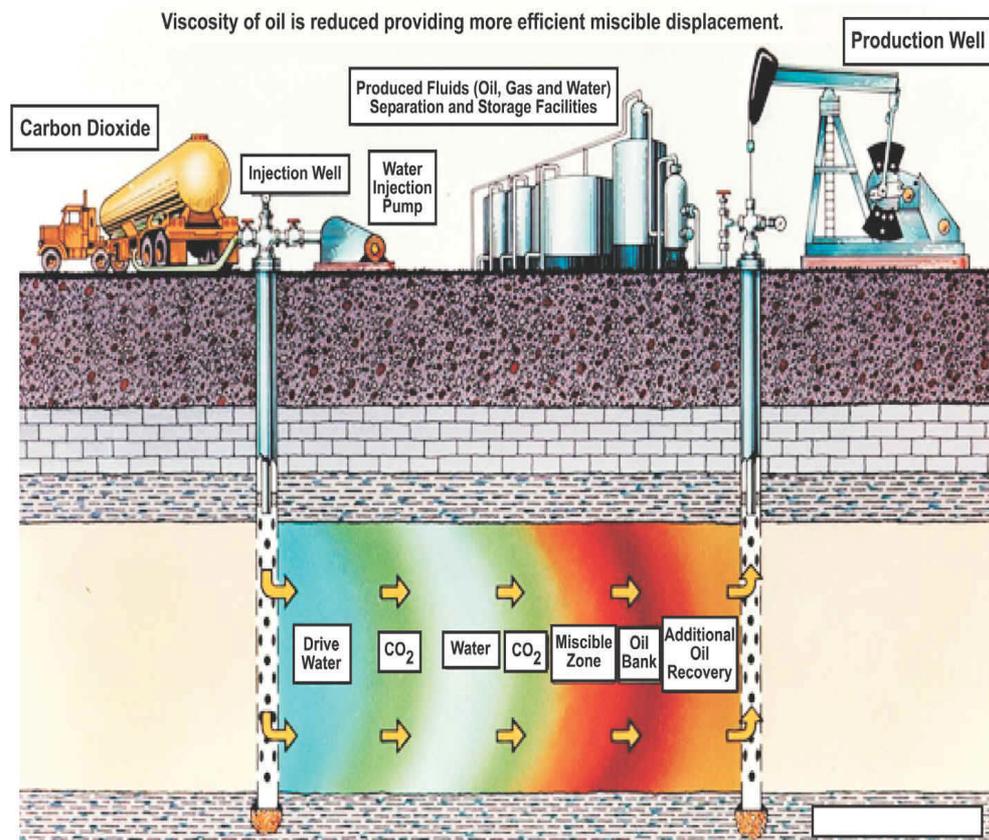
Figure 1-5 CO_2 flooding as an enhanced oil recovery technique[25]

Corrosion can also be classified depending on the attack mechanism leading to various corrosion modes known as uniform, galvanic, pitting, crevice, intergranular and stress corrosion. Erosion-corrosion and bacterial corrosion can also occur when sand and biofilms are present respectively.[26]

The degradation mechanism can initiate both inside (internal corrosion) or outside of the material (external corrosion) and specific mitigation strategies

are to be implemented depending on the degradation location. Only internal corrosion processes are of interest for this research and are therefore detailed in section 1.5.2.

1.5 Corrosion mitigation techniques

1.5.1 External corrosion mitigation

When external corrosion is to be treated, common mitigation techniques such as lining the structures with coatings or the installation of a cathodic protection system are used. Coatings act as a physical barrier which isolates the metal from the corrosive medium and are mostly applied on aluminium and zinc alloys while some organic coatings have been used on iron structures.[27] Cathodic protection aims to nullify the flow of current between the anode and cathode by transforming the material that should be protected to a cathode. The two most commonly used cathodic protection techniques are the galvanic sacrificial anodes and the impressed current anodes.[28]

1.5.2 Internal corrosion mitigation

To protect the materials most frequently used in the petroleum industry, many techniques can be implemented. Pigging, drying, internal linings, process optimization by controlling the pH, oxygen and bacterial growth are often used as mitigating techniques to hinder the progress of internal corrosion.

1.5.2.1 Approaches relying on design stage and operational conditions

At the design stage, considerations can be taken so that corrosion can be mitigated by choosing the appropriate materials suitable for the operational field environment. This is part of the capital expenditure of a project which if judged to be too high will be supplemented by an operational expenditure alternative such as the use of coatings, corrosion inhibitors and cathodic protection. Meanwhile, corrosion management and fault-tree structure and other computerized prediction models for corrosion failure keep developing.[29]

When the operational conditions such as flow rate, concentration, temperature, pressure, corrosive agents, and mechanical stresses are known, materials can be designed to withstand various stresses for the desired lifetime with a certain allowance. This is usually computed by considering the corrosion as uniform and the materials' corrosion allowance thickness in mm is always engineered higher or equal to the predicted corrosion rate in mmpy

multiplied by the desired lifetime which should remain above a certain thickness in years of service.[30]

Another approach to mitigate the corrosion aims at controlling the field parameters by themselves. These can include, but are not limited to, the temperature of the corrosive fluids, the concentration and partial pressure of the corrosive agents, the mechanical stresses the materials are subjected to, the hydrodynamic flow conditions and the monitoring of the solid particles availability which could cause erosion-corrosion depending on the water chemistry.[31]

The design and engineering step could also play a primordial role in reducing the risks of particular corrosion mechanisms such as crevice corrosion which can be limited by suitable geometrical alterations prior to servicing. Another example is the reduction of galvanic corrosion via a suitable assembly of the metallic alloys. Erosion-corrosion could also be reduced by designing surfaces with reduced bottlenecks especially in pipelines.[32]

1.5.2.2 Corrosion inhibitors as the mitigation technique of choice

Most flow assurance problems are treated with their respective inhibitors such as biocides, hydrate inhibitors, wax and asphaltene inhibitors, scale inhibitors and the most widely used corrosion inhibitors.[33] A corrosion inhibitor is any chemical additive that once added in low quantity within an aggressive or corrosive environment is known to either decrease or forestall the corrosion progress between the metal surface and the media.[34]

Up-to-date, corrosion inhibitors are still the method of choice for reducing internal corrosion. These are compounds that are known to alter the nature of the electrochemical reactions without taking part themselves in the process. Depending on their mode of action, they can be classified as cathodic and anodic, inorganic and organic, or filming and non-filming corrosion inhibitors.[35] When they eliminate the corrosive agents such as oxygen, they are termed scavengers. In the specific case of oil wells, it is established that the corrosion inhibitors incorporate into the thin layer of corrosion product such as is iron carbonates and iron sulfides.[36]

One commonly used corrosion inhibitor in CO_2 corrosion mitigation is Bis-imidazoline which structure is shown in Figure 1-6; the positive ammonium group adsorbs on the negatively charged steel while the long carbon chain creates a barrier to the water molecules hindering their access to the steel surface. Using pigs for corrosion inhibitor applications has proved its worth

when gas and gas-condensate transmission pipelines are considered, especially in multiphase flow service. Selecting a pig for inhibitor batching is based on its ability to create a good seal between the pig cups and the pipe wall.[37]

In acidic conditions on the other hand, the corrosion inhibitor plays a vital role in reducing the hydrogen evolution reaction via an adsorption phenomenon that subsequently inhibits corrosion and protects the metal surface.[38]

Recently a review paper published by Raja et al.[39] concluded that a variety of corrosion inhibitors (inorganic, organic, polymeric, green, and vapour phase) were successfully identified and serious research to better understand the mechanisms is under progress. Moreover, the importance of identifying environmental friendly corrosion inhibitors is warranted and the current research seems to be more focused toward greener alternatives which renders this research aim and objectives as described in section 1.7 promising.
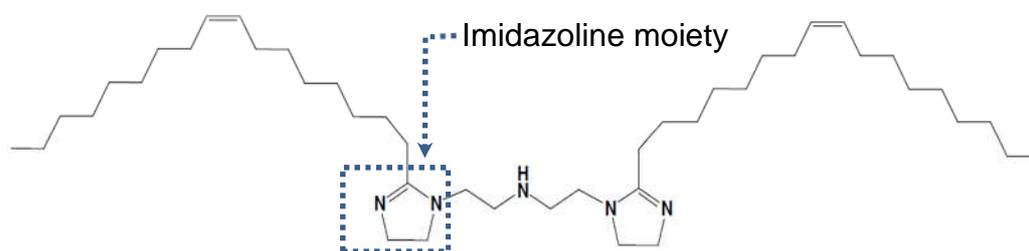
Figure 1-6 Bis-Imidazoline corrosion inhibitor[40]

With so many degradation processes being present in the petrochemical environment, it is predicted that the cost of protecting the oilfield structures is enormous and weight with major implications on a country's economy.

1.6 Cost of corrosion

With the magnitude of the oilfield installations and the currently available mitigation techniques, the cost of corrosion remains excessively high. As such, the study of corrosion has been intensifying mainly due to the cost implications or capital-expenditures related to corrosion issues but also due to the need to minimize accidents. Nonetheless, a recent study has shown,

that even in the USA, engineers still graduate with little grasp of corrosion although its financial and strategic importance are obvious.[41]

Figure 1-7 summarises some of the major sectors affecting the cost of corrosion in American oilfields. The transmission pipeline related corrosion costs alone are as high as 7,000 million American dollars and it is well known that 3 to 5% of developed countries Gross Domestic Product (GDP) is invested to mitigate such problems. The cost of corrosion control could be also summarized per sector as in Figure 1-8 and is mostly related to operational rather than capital expenditure. It is always higher for offshore installations as compared to onshore infrastructures and this trend has not changed for the past few decades.[42]
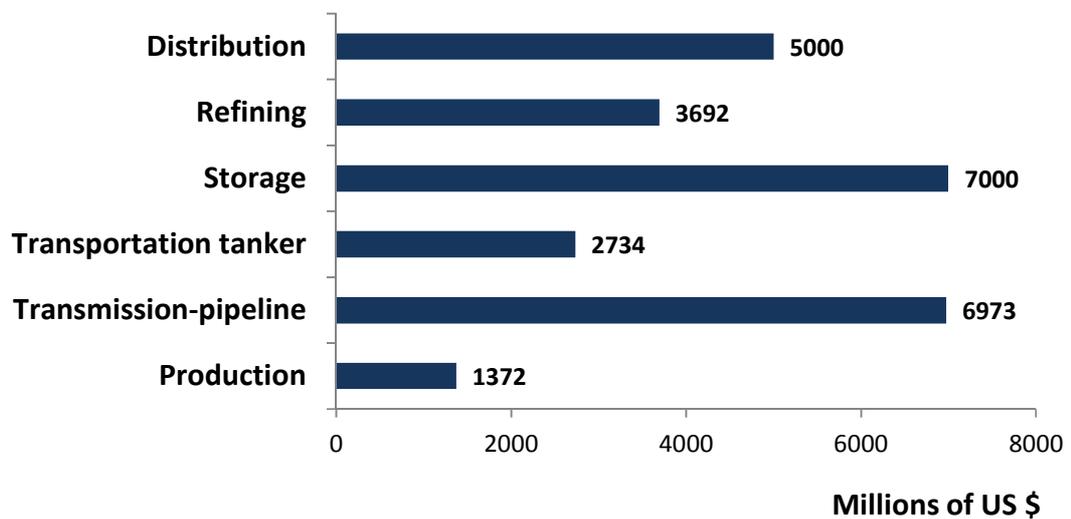
Figure 1-7 Annual corrosion cost in major sectors of USA oil and gas industry[43]
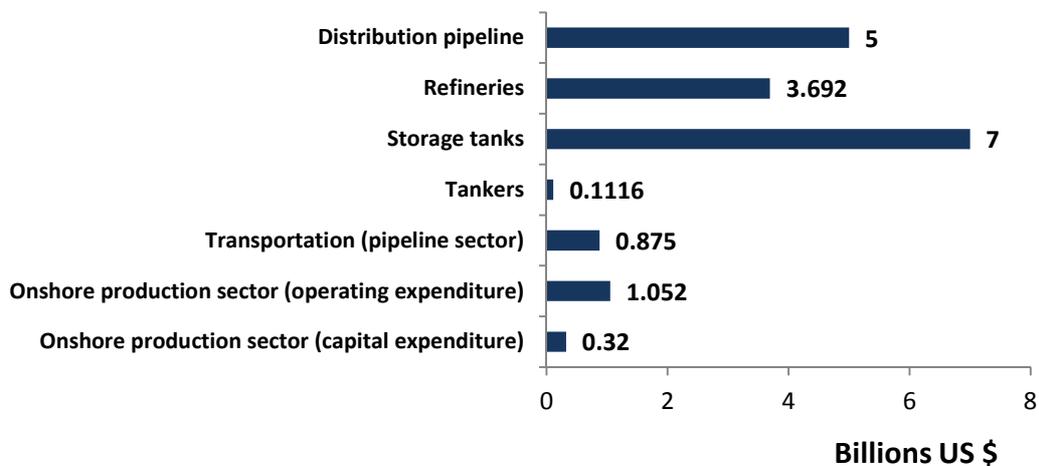
Figure 1-8 Corrosion control and maintenance yearly costs in USA[42]

The cost of corrosion control could be also summarized per sector as in Figure 1-8 and is mostly related to operational rather than capital expenditure. It is always higher for offshore installations as compared to onshore infrastructures and this trend has not changed for the past few decades.[42]

As a consequence of various interactions, failures often occur when the integrity of the downhole and aboveground oilfield infrastructure is compromised in its vast network. Internal corrosion accounts for more than half of these failures whether appearing at the production sector or the transportation manifold. For example, 40% of the failures in production pipelines in Canadian Alberta were due to various internal corrosion processes up to 2005.[44]

This is mostly applicable for smaller diameter pipelines, whereas external corrosion is responsible for most of the failures in larger diameter pipelines. Recently, on the 26th of November 2013, Chinese authorities have detained seven employees from China Petroleum and Chemical Corporation, or Sinopec after a pipeline blast has been responsible for the death of 55 people at least; it all started with reports of major crude oil leaks which were caused by a serious corrosion protection failure.[45]

The values presented in Figure 1-8 are an adaptation of estimated figures extrapolated from studies and investigations undertaken during the last 40 years of operation in the United States oil and gas sector. It shows how staggering both direct and indirect losses incurred from corrosion are. As such, research and development in areas such as materials development and selection, innovative surface protection systems, and condition based monitoring using sensors and remote data collection methods could constitute promising investment. When such strategies are implemented globally by governments and corporations, it is forecasted that it could significantly reduce the corrosion cost by a factor as high as 25 to 30% of the total annual cost of corrosion and that is in the case in the American economy alone.[46]

1.7 Rationale overview, aims and objectives of this research

The main objective of this research is to evaluate a novel CO_2 corrosion mitigation technique other than the ones that are commonly implemented as discussed in section 1.5.1. In fact, corrosion inhibitors behave well but these film-forming chemicals create layers that are easily washed away thus forcing a frequent and recurrent dosage of the desired product. The work described

in this thesis exploits some of the nanocomposite technology advances and provides a proof of concept for the general and localised corrosion mitigation of a hybrid iron carbonate corrosion layer. In fact, it provides a corrosion mitigating option focusing on the enhancement of a naturally growing corrosion layer in the oil and gas environment under specific conditions.

Recently, advances in nanostructured materials in various research areas have been transposed to the oil and gas industry with the hope of providing optimised solutions for production and transport installations.[47] Advances in polymer research for that matter could be adapted to the oilfield especially when dealing with thermo-mechanical enhancements that has proven to be successful on both thermoplastic and thermosetting products.[48]

The main idea in such approaches is to incorporate an inorganic-based nanofiller in a polymer transforming it to a nanocomposite which will manifest some enhanced properties. Sinan et al.[49] have for instance shown how the addition of octavinylisobutyl based Polyhedral Oligomeric SilSesquioxane (POSS) on poly-lactic acid biodegradable polymer matrix can increase the value of the maximum specific work of fracture when an optimum loading of 7% by weight of the POSS nanofiller was applied. The thermo-oxidative stability of another nanocomposite obtained when blending amine functionalized POSS derivatives to polypropylene polymers was greatly improved as seen by the work of Grala et al.[50]

El Achaby et al.[51] prepared biopolymer nanocomposite films by adding exfoliated graphene oxide nanosheets into carboxymethyl cellulose at various graphene oxide loadings (0.4 to 7 wt %). They found that these graphene oxide form a three-dimensional network throughout strong interfacial interactions with carboxymethyl cellulose, and gradually increase numerous properties of nanocomposite films. In fact, by adding 7 wt % of graphene oxide, 18% increases of thermal stability, 17% of glass transition temperature, 623% of Young's modulus, and 268% of tensile strength were achieved. The high performances of these films can be expected to have potential applications in biomaterials or packaging materials.

TEM characterizations are commonly employed to investigate the dispersion quality and the morphology of nanocomposite films. The TEM micrographs of ultrathin films containing 0.4, and 7 wt % of graphene oxide are shown in Figure 1-9 and a fine dispersion of graphene oxide in the carboxymethyl cellulose matrix can be clearly observed.

13

In these micrographs, the isolated nanosheets appear as distinct dark lines homogeneously dispersed within the matrix (Figure 1-9a), with a few agglomerates observed at high graphene oxide content (Figure 1-9b).

(a)   (b)
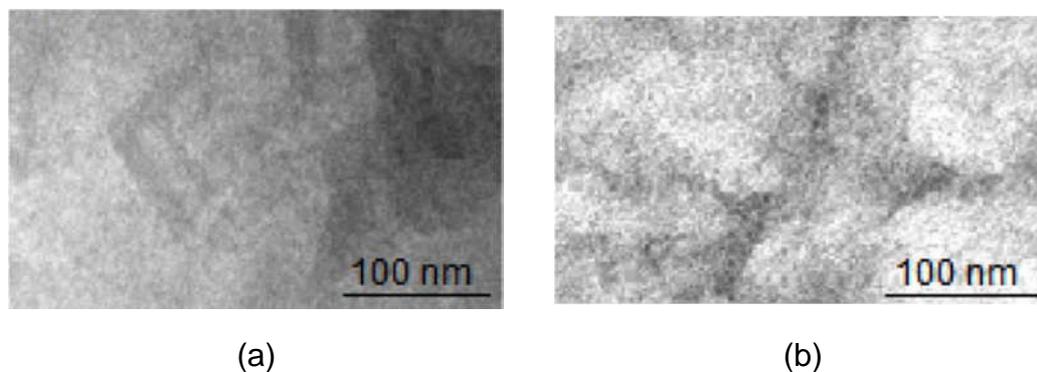
Figure 1-9 TEM images of carboxymethyl cellulose/graphene oxide nanocomposite films with (a) 0.4 wt % of graphene oxide, (b) 7 wt % of graphene oxide samples[51]

The research aim presented in this thesis is schematised in Figure 1-10 and Figure 1-11 and relies on the modification of the naturally grown iron carbonate film with a hybrid polyhedral oligomeric silsesquioxane based moiety which contains an inorganic silicon core and an organic sidechain. The choice of the exact chemistry and the reasons that led to such a compound are detailed in section 5.2.1.

The first explored enhancement is the creation of a less brittle $FeCO_3$ film by relying on the nanofiller organic sidechains. The choice of a hybrid nanofiller is explained by the fact that corrosion scales in general are brittle; thus in order to limit the strain effects, a molecule that contains organic chemistry alongside an inorganic is optimal.

Inorganics such as nanoclays are known to introduce hardness, strength and fragility and are used for their good barrier properties such as the polystyrene nanocomposites using nanoclay as a filler and described by Panwar et al.[52] Organics on the other hand introduce elasticity, plasticity and rubbery such as the cellulose nanocrystals used for their tensile strength properties thus reinforcing thermoplastic elastomers.[53]
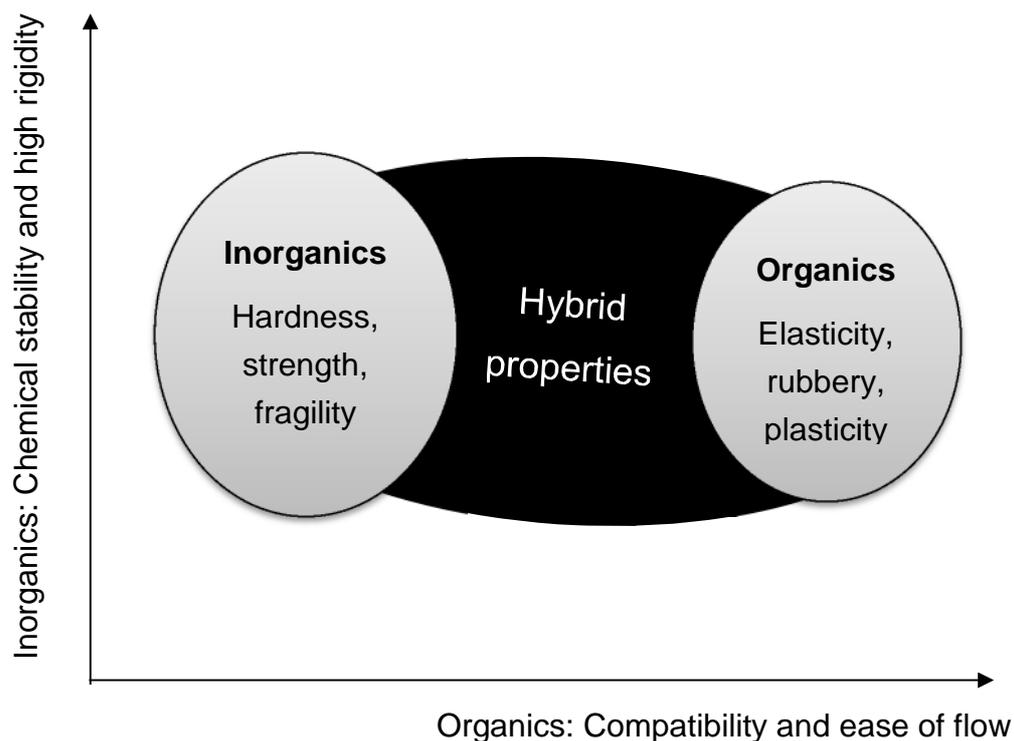
Figure 1-10 Schematic representation of thesis hypothesis I: A less brittle iron carbonate

Moreover, it is anticipated that such nanofillers will allow the $FeCO_3$ crystals to nucleate faster and to develop a corrosion layer that has better mechanical properties. As such, Figure 1-11 presents a schematic of the hypothesis where a polished carbon steel X65 steel sample is supposed to allow the growth of iron carbonate layers with higher densities depending on the nanofiller loading whereas no iron carbonate should form at the same conditions in the nanofiller absence.

These sought modifications are shown to help the hybrid iron carbonate films better protect the underlying steel for long exposure periods by reducing both the general and localised corrosion attack. This is considered as a new approach in the corrosion mitigation industry since a thorough literature review only shows pH stabilisation techniques being used to this regard.[54]

Most of these pH stabilisation approaches are only applicable at a pH as high as 7 and a temperatures higher than 70°C and they require the addition of hydrate preventers. The advantage of using the currently researched nanofiller is its proven ability to modify the precipitation kinetics of the iron carbonate corrosion layer without altering the *in situ* pH thus without the need for any additional flow assurance chemical addition.

15
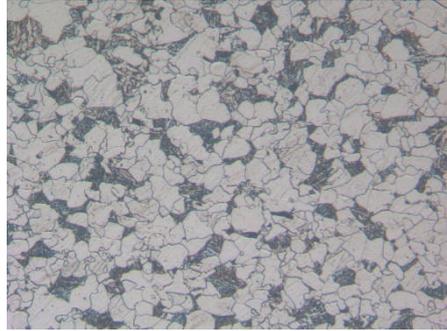
Pre-corroded X65 carbon steel

+

POSS

Cl⁻ H₃N⁺

Cl⁻ H₃N⁺

Cl⁻ H₃N⁺

Cl⁻ H₃N⁺

Organic side-chains

Inorganic core

NH₃⁺ Cl⁻

NH₃⁺ Cl⁻

NH₃⁺ Cl⁻

NH₃⁺ Cl⁻

(a)

(b)
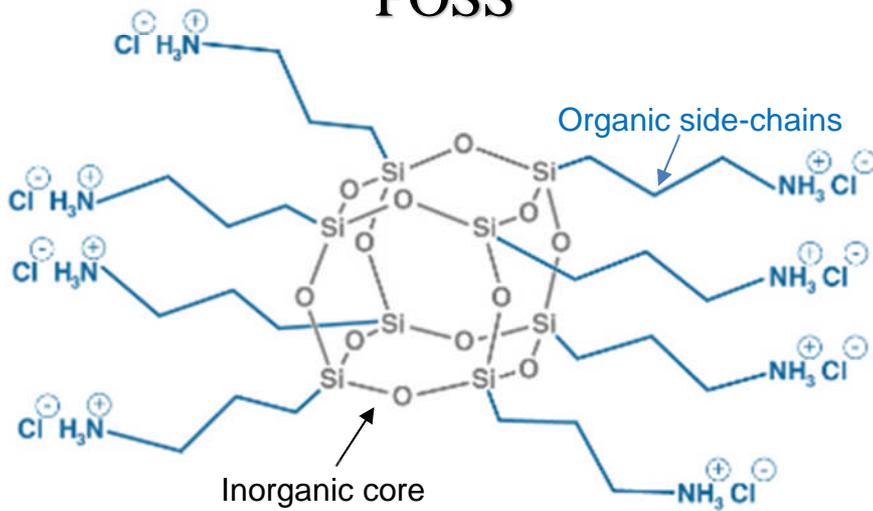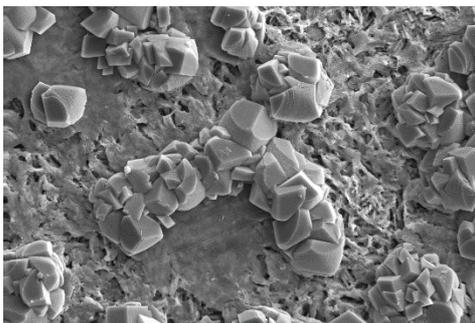
Iron carbonate nucleation
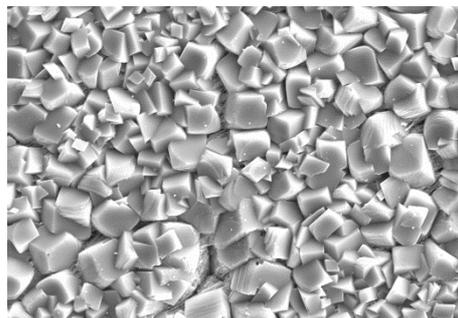
Compact iron carbonate

Figure 1-11 Schematic representation of thesis hypothesis II: nucleating agent potential (a) and nanofiller activity (b)

16

1.8 Choice of silsesquioxanes as hybrid nanofillers

Most of the time, it is difficult to enhance materials' properties without avoiding additional shortcomings such as increasing the brittleness when the hardness is enhanced.[55] Materials with single element are no longer able to meet the industry demand and it was shown that combining two or more materials can create composites that retain the advantages of the original components. One constituent is called the reinforcing phase and the other is termed the matrix.[56]

Recently, research has focused on some organic-inorganic hybrid materials known as the polyhedral oligomeric silsesquioxanes.[57] Silsesquioxanes are classified depending on the number of silicon atoms within their core (T_6, T_8, T_{10}, T_{12}, T_n) where T_n represents the number of silicon atoms linked to three oxygens each. They can also be divided into groups according to their geometry and terminologies such as octahedral or decahedral are commonly referenced. They are known to form ladder, cage, partial-cage and polymer structures among others with the cage structure being the most stable, T_8 more specifically. They enable better control of the distribution of inorganic phase in the host polymer when compared to the classic organosilanes alternative.[58]

POSS molecules are part of the silica glass family[59] and have found use in material science as nanocomposites but also in photonics and biotechnology where they play the catalyst role.[60, 61] Since they are of low toxicity and soluble when hydrophilic organic substituents are used, a major application for drug delivery, tumour diagnostics and therapy has emerged.[62] Polyhedral oligomeric silsesquioxanes have already proven their worth as nanofillers due to their high degree of interaction with a multitude of polymer matrices.[63] Other studies have shown how the addition of POSS improves some of the mechanical parameters but also increases the wear resistance of some rubber blends that are used for the production of tyres.[64]

Chemistry wise, the POSS are derivatives of silica compounds which when connected to 3 instead of 4 oxygen moieties is termed silsesquioxane. A typical POSS molecule is generally a rigid cubic structure as shown in Figure 1-12.[65] This cubic cage architecture is thermodynamically the most stable in organo-silsesquioxanes due to steric effects.[66]

T_8 POSS or octahedral POSS where n=8 are the most attractive since they have proved their efficiency in improving mechanical, thermal and dielectric properties of a multitude of polymers.[67] The polyhedral architecture is

favoured when silsesquioxanes are branched with small organic residues as is the case for n=10, 12, 14 and 16.
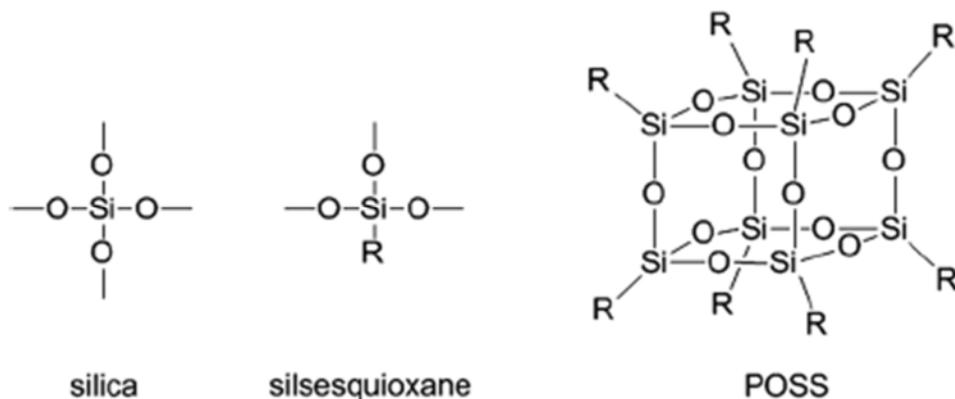
Figure 1-12 Ramifications of the silica branching chemistries

The empirical formula of silsesquioxane is $(RSiO_{1.5})_{2n}$ where n is an integer and R is an organic compound. POSS are a special type of silsesquioxane that are termed cube-octameric and which formula could be written as $(RSiO_{1.5})_8$. The inorganic part or Si_8O_{12} is the inorganic entity and usually provides hardness and strength thus functioning as a molecular reinforcement mainly due to the rigid Si-O bonds.[68]

The organic chains (R) can span a whole range of chemistries such as alkyl, phenyl, alcohols, thiols, and amines.[69] Those can make POSS molecules compatible with both polymers and monomers and should provide compatibility with the latter and enhance some of its properties such as elasticity, plasticity and rubbery.[70] This duality allows for an excellent polymer-POSS compatibility where the POSS molecules act as well-dispersed nanofillers.[71] Usually, it was shown that POSS molecules enhance the polymer when added to a certain weight percentage limit (3 to 5% wt) then the improvement drops with higher loadings.[72, 73]

When it comes to their size, POSS molecules vary between 1.5 to 3 nm in diameter depending on the branching group; 1.5 nm being the nominal dimension of the inorganic cage with an Si-Si diameter equal to 0.53 nm.[74] For example, when compared to the Buckminsterfullerene which is around 1 nm wide, octamethyl POSS has almost the same dimensions as depicted in

Figure 1-13 where the blue corresponds to the carbon atoms, silicon atoms are in green, oxygen atoms in red and the silver is for hydrogen.[75]
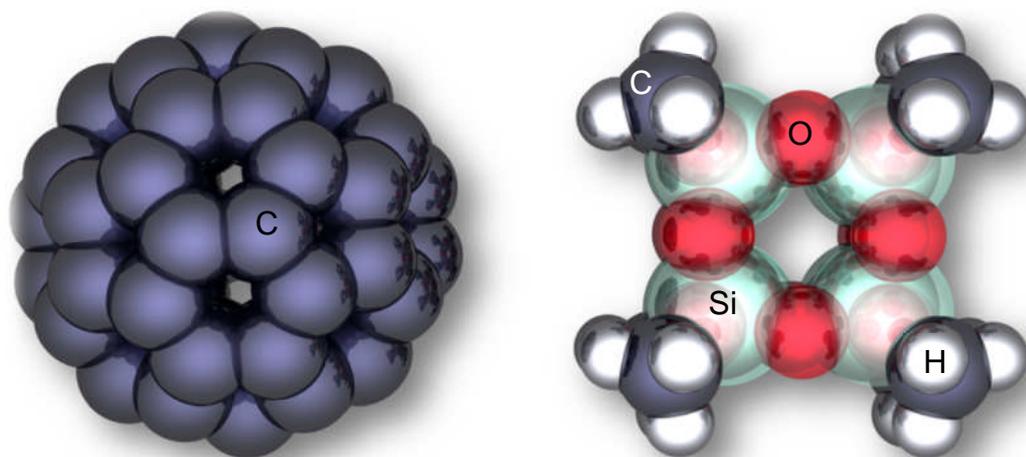
Figure 1-13 Buckminsterfullerene (left) and octamethyl POSS (right)

POSS are not nanoparticles but could be classified as supramolecular structures with nanoscale dimensions since they can be analysed by techniques that apply only to molecules such as ^{1}H or ^{29}Si solution NMR spectroscopy.[76] They have been used to modify both thermosetting and thermoplastic polymers such as polyethylene, polypropylene, phenolic resin, polysilicone, polyurethane, epoxy and polycarbonate.[77]

Furthermore, POSS was shown to improve the mechanical properties of the studied polymer with[78] or without[79] the need of establishing covalent bonds. The POSS filler effects could be explained by the fact that they lead to some molecular motions suppression within the polymer chains and this is mainly caused by the rigid silica cube.[80]

A more in-depth description of the various reasons that led to the choice of OA-POSS as the specific molecule to be studied is given later on in section 5.2.1.

Chapter 2 Theory of aqueous corrosion

According to the International Organization for Standardization (ISO) 8044 standard, corrosion is defined as "the physical-chemical interaction between a metal and its environment, leading to modifications of metal properties and to significant alteration of the metal function, its environment or the technical system involved".

Normally, the degradation of any material by its environment should be termed corrosion even though the definition focuses on the destructive attack of a metal when it reacts with its environment. As such, materials like plastics, concrete or even wood, all undergo a sort of environmental deterioration but this study relates to the degradation of metals which are employed in oil and gas environments due to their mechanical properties.

When engineering materials are categorised as metals, polymers and ceramics then the transport of mass across the interface to the environment may be broadly considered as electrochemical, chemical, or physical respectively. Thus polymeric and ceramic materials generally do not support electron conduction and hence corrode by either direct chemical or physical mechanisms.

When corrosion is sustained by a current flow, it is referred to as electrochemical corrosion and this type of corrosion is the basis for many corrosion mechanisms such as the CO_2 induced corrosion described in section 3.4. When electrochemical corrosion is occurring, mechanisms may be inferred from measurements of electrical potential and current.

2.1 The electrochemical nature of corrosion

Corrosion is an electrochemical process that will only occur when four elements are present: These correspond to the acronym ACME and are an Anode, a Cathode, a Metal and Electrolyte; they constitute together what is termed a corrosion cell. The metal behaves as the conductor and creates a path of contact between the anode and cathode as schematized in Figure 2-1. These two electrodes are thus connected externally by the metallic conductor providing a path for the flow of conventional current or passage of electrons from the anode to the cathode.[81]
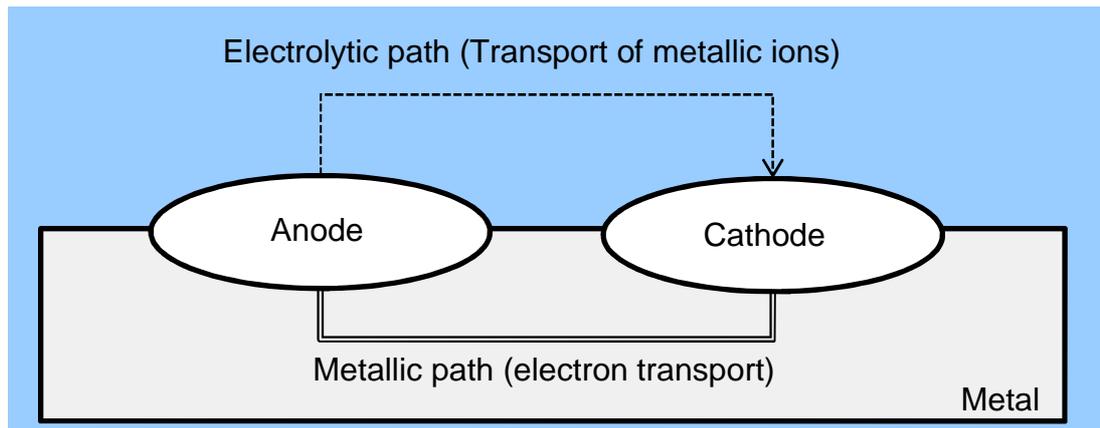
Figure 2-1 The basic four components in a corrosion cell[81]

The electrochemical nature of this process denotes the fact that the corrosion mechanism does not initiate through a direct reaction between the studied specimen and its environment but rather through electrochemical half cells. Equation 2-1 to Equation 2-6 describe such half cells which are defined as one where electrons appear on one side or another of the reaction as written. It is stated that the loss of metal takes place as an anodic process while cathodic reactions are the ones where species are being reduced via the consumption of the electrons produced at the anode.[82]

The fact that two or more electrochemical half-cell reactions can propagate on the same metal surface is explained mainly by the heterogeneous nature of the metal surface.[83] The corrosion is often described chemically as the dissolution of the anode due to an oxidation process by which a metallic ion leaves the metal surface into the solution or what is known as the ionically conductive electrolyte shown as the electrolytic path in Figure 2-1. The excess electrons produced inevitably charge the metal surface. Equation 2-1 shows a typical anodic reaction with M being a generic metal and n the charge number.[84]

When carbon steel is studied, M corresponds to the iron element Fe which is divalent and thus its oxidation releases two electrons as per Equation 2-2. The electrolytic path enables the transportation of the metal ions from the anode to the cathode. When this occurs, a reduction reaction takes place as per Equation 2-3. The electrons required for this reaction are provided via the metallic path.

Equation 2-1 General anodic oxidation

$$M \rightarrow M^{n+} + n.e^-$$
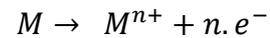
Equation 2-2 Iron anodic oxidation

$$Fe \rightarrow Fe^{2+} + 2.e^-$$
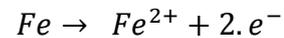
Equation 2-3 General cathodic reduction

$$M^{n+} + n.e^- \rightarrow M$$
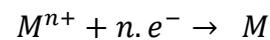
Equation 2-4 Hydrogen reduction

$$2H^+ + 2.e^- \rightarrow H_2$$
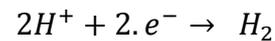
Equation 2-5 Oxygen reduction in neutral or basic environment

$$O_2 + 2 H_2O + 4e^- \rightarrow 4OH^-$$
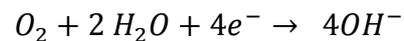
Equation 2-6 Oxygen reduction in acid environment

$$O_2 + 4H^+ + 4e^- \rightarrow 2H_2O$$
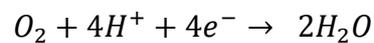
Usually as shown in Equation 2-4 to Equation 2-6, the solution contains other species that could undergo the reduction process instead of the created metal ion on the anode. The pH is what dictates the likelihood of a specific reduction reaction to occur such as the hydrogen-evolution in acidic conditions or the hydroxide creation in basic environments. It should be noted that in practice, both anode and cathode can exist on the same metal.[85]

2.2 Thermodynamics of the corrosion process

As all natural phenomena, corrosion only occurs if the reaction is energetically favourable; this is described by the thermodynamics of the corrosion reaction in which every element tries to minimize its energy state. Figure 2-2 shows how energy is supplied to the iron ore in order to convert it to the iron metal which naturally loses that energy when it transforms to rust.[86]
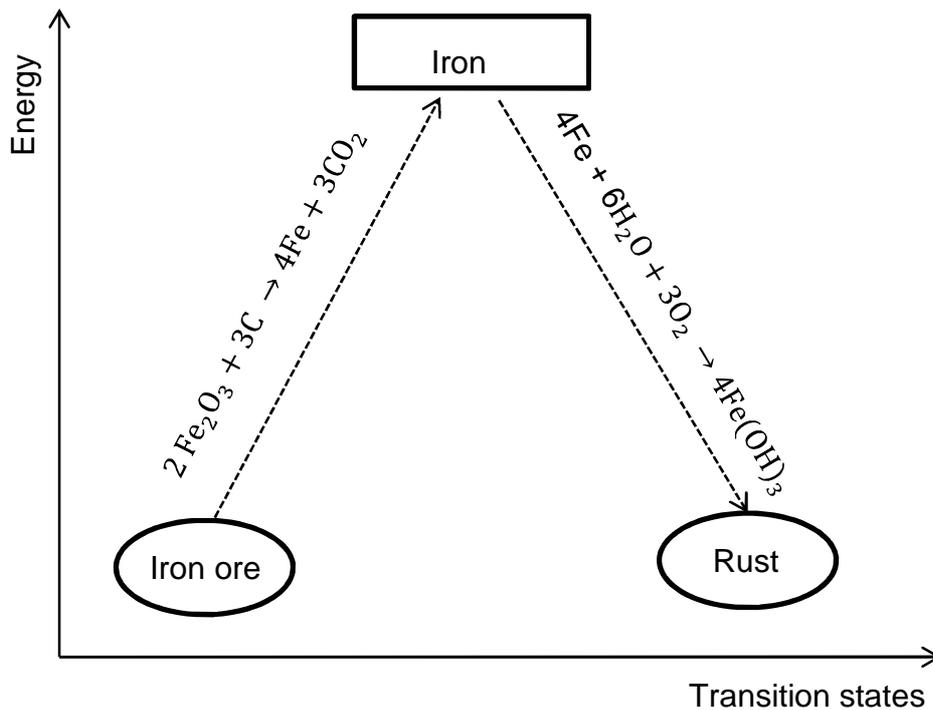
Figure 2-2 Illustration of corrosion associated energy[86]

Metals listed in Table 2-1 adapted from Papavinasam et al.[26] have a natural tendency to corrode or revert back to their original lower energy state. In fact, all metals exist in nature as ores such as metal oxides and they are produced via several processes including smelting, refining, casting, rolling and shaping which add to the energy of the system.

Table 2-1 Energy required to convert ore to metal and average standard electrode potential versus Standard Hydrogen Electrode (SHE)[26]

Energy level	Metal	Oxidation number	E_0 (Volts) at 25°C
Higher	Magnesium	II	-2.370
	Zinc	II	-0.763
	Iron	II	-0.440
	Nickel	II	-0.250
	Copper	II	+0.337
	Platinum	II	+1.200
Lower	Gold	III	+1.500

When all four elements described with the ACME acronym are present, the developed measured electrode potential is called the free corrosion potential or E_{corr} also known as the Open Circuit Potential (OCP). This potential can be linked to the material energy level E_0 with some common values listed in Table 2-1. The magnesium for instance with the oxidation number II has the highest tendency to corrode or revert back to the most stable state and is defined as an active material while gold which requires the less energy to be extracted is known as a noble material.[87]

Numerically, Table 2-2 shows the standard free energy change in Joule (J) when the chemical reactions are evolving in an oxygen environment for both copper and zinc with zinc being more prone to corrosion.[88] The temperature T is in degrees kelvin (°K).

Table 2-2 Thermodynamic data for reactions involving oxygen[88]

Oxidation reaction	Standard free energy change (J)
$Cu_2O + \frac{1}{2}O_2 \rightarrow 2CuO$	-130,930 + 94.5 T
$Zn + \frac{1}{2}O_2 \rightarrow ZnO$	-335,890 + 107.5 T

The thermodynamic of this phenomenon is described in Equation 2-7 where ΔG is the change in Gibbs free energy, n the number of electrons participating in the transfer reaction, F the Faraday constant and E^* the electrode potential as described in the Nernst-Latimer convention.[89]

This approach relies on the electrode potential values depicted in the electromotive series which were generated under highly idealised conditions; nonetheless they indicate the relative reactivity of metals and the Gibbs free energy can be used to assess the spontaneity of the chemical system.[90]

Equation 2-7 Thermodynamic relationship

$$\Delta G = -n.F.E^* = R.T.ln\frac{c_1}{c_2}$$

When this convention is used both E^* for Equation 2-1 and Equation 2-3 have the same absolute values but are of opposite signs depending on the way the reaction is written; anodic direction or cathodic direction. In the Gibbs-Stockholm convention, the standard redox potential E_0 replaces E^* and is defined as the potential of a metal in contact with its own ions at a

concentration equal to unit activity at 25°C as shown for some metals in Table 2-1.

The same change in Gibbs free energy in Equation 2-7 can be expressed with relation to two different portions of a metal that are exposed to two different concentrations of a solution (c_1 and c_2) of one of its salts; Since the current will tend to flow in the direction that will decrease the concentration difference, the metal exposed to the low concentration will behave as an anode and corrode. Here, R represents the ideal gas constant (R= 8.314 x 10^{-3}) and T is the temperature in units of kelvins.

Galvanic series exist and list metals and alloys standard potential E_0 at 25°C which could be used in order to compute the Nernst potential E as shown in Equation 2-8 where R is the gas constant and T is the absolute temperature in degree Kelvin. The entity being oxidized is denoted as [OX] while the one being reduced is labelled [RED]. The number of electrons involved in the process is denoted as n. The Nernst equation was first published in 1888 by the German chemist who later won the 1920 Nobel prize in chemistry and is used to determine the potential of a metal in a solution in which its ions are not at unit activity.[91]

Equation 2-8 Nernst equation

$$E = E_0 + 2.3 \frac{R.T}{n.F} log \frac{[OX]}{[RED]}$$

When the activity of oxidized species increases, the electrode potential becomes more positive and the opposite applies when the reduced species activity is higher. This explains the value difference between E_{corr} and E_0. Thus, the Nernst equation describes the dependence of any chemical reaction on the concentrations of the species involved as well as the temperature. The influence of the solution composition is shown by the logarithmic term.[92] It is not possible to measure the potential of a single element such as iron or copper and this is done usually by comparing two electrodes' potentials via the use of reference electrodes such as the silver-silver-chloride or saturated calomel electrodes.[93]

The use of the galvanic series allows the distinction of the electrode which acts as a cathode and the one which behaves as the anode. The metal with the more positive electrode potential in a couple will always act as the

cathode; for example copper is the cathode when in presence of the element iron as shown in Table 2-1 since $E_{0\ copper} = +0.337$ and $E_{0\ iron} = -0.440$.

Pourbaix diagrams which are derived from electrochemical measurements and thermodynamic data are often used in order to assess the relative stabilities of metals with respect to their respective ions, hydrous and anhydrous oxides. They are represented as potential-pH diagrams and show the conditions under which a metal either react or not and these are termed respectively corrosion or immunity regions.[94]

Such a diagram is shown in Figure 2-3 when iron is the corroding material and was computed using the vector graphic editor Inkscape available from Western Oregon University. The plot indicates that below -0.6 volts (V) iron is stable and this is known as the immunity region. When the potential is shifted toward more active domains, ferrous Fe^{2+} and ferric Fe^{3+} iron are created. At higher pH values, the passive region is dominant.
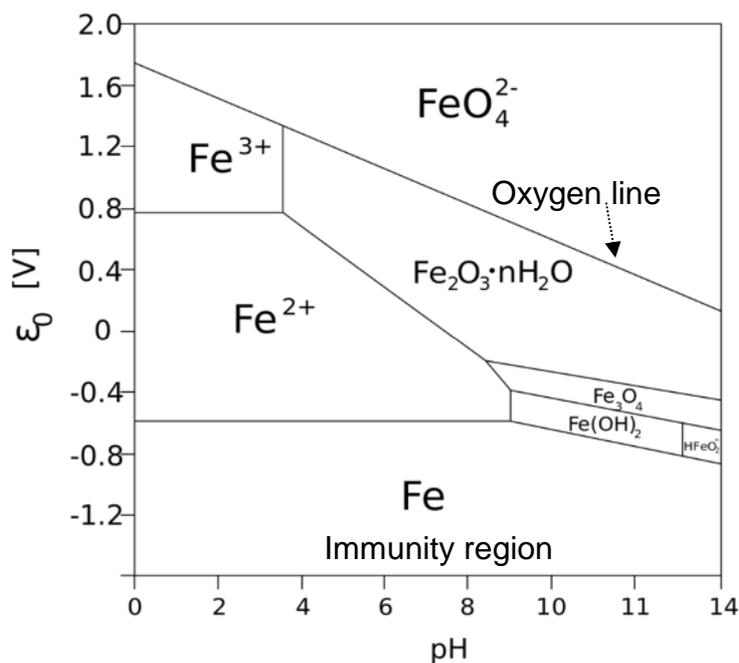
Figure 2-3 Pourbaix diagram for iron at 25°C[95]

The thermodynamic study of the corrosion process such as the use of the previously described Pourbaix diagrams only describes the feasibility of the process and has many limitations; the main misconception is that equilibrium is assumed while actual conditions may be far from equilibrium in practice. Moreover, the Pourbaix diagrams do not give any information on actual corrosion rates. Thus, once it has been determined if the corrosion reaction takes place or not and in which direction, one should compute how fast this

degradation process happens or otherwise at which rate the degradation process evolves. This is described by the kinetics of the corrosion reaction with Wagner-Traud paper being the first published in such studies.[96]

2.3 Corrosion kinetics

The corrosion rate is usually described as a penetration rate in millimetres per year but no standard unit exists. They can be expressed by the corresponding weight loss, penetration or corrosion current densities. These could be determined via various techniques such as direct weight loss, thickness measurements or the commonly implemented electrochemical techniques which will be detailed in section 2.4.

The corrosion rate is directly proportional to the rate of electron transfer thus to the correspondent current flow which is usually described as a corrosion current density where the surface of the corroding element is taken into account. Both the mixed potential theory and the Butler-Volmer equation are used to this regard[97] and these are described in detail in section 2.4.3. These theories evolve around polarisation curves which are the basic kinetic law for any electrochemical reaction.[98]
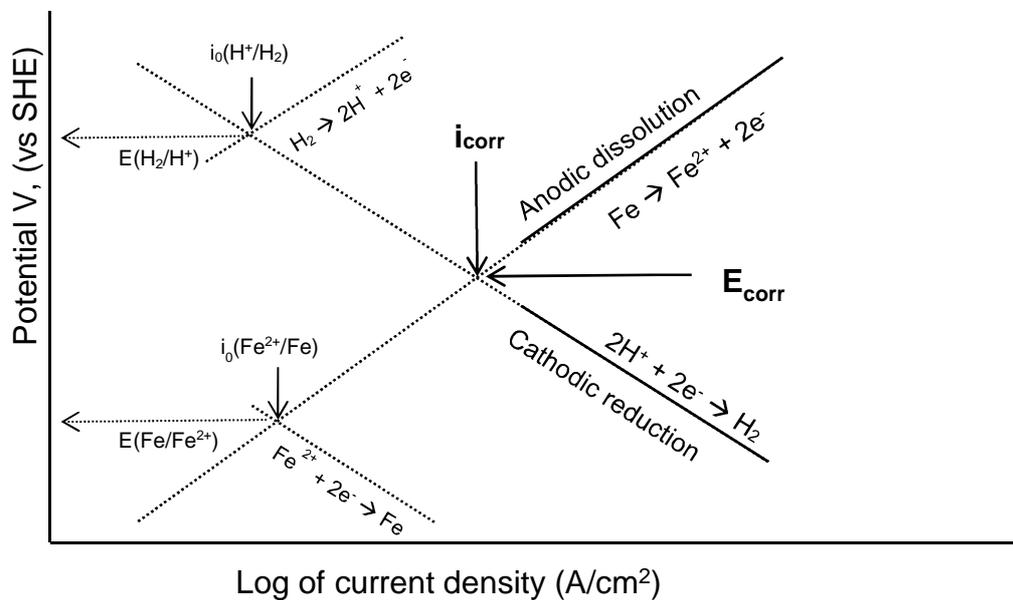
Figure 2-4 Schematic of Evans' diagram for iron in acid solution[99]

The current flowing in a single electrode at E_0 is known as the exchange current density i_0 and Figure 2-4 shows those for both the hydrogen and iron

electrode systems when combined in what's known as the Evans' diagram. In fact, when two elements are in solution, the potential of the metal will not be at the redox potential of either of them but rather around a value which is known as the corrosion potential of the system or E_{corr}.

Only two reactions are of interest in that case since it is known that iron is the corroding specimen; the iron dissolution at the anode and the hydrogen-evolution at the cathode are known to both intersect at the free corrosion potential. At this point, the charge conservation is maintained and the measured current is called the corrosion current i_{corr} and is directly proportional to the rate of dissolution of the metal iron, in other words to the corrosion rate of this element.[100]

The Evans' diagram confirms that most of the factors affecting the rate of corrosion can be understood from a superposition of the current and potential curves. They allow to easily follow changes that occur when exchange currents are modified.[101] Many environmental factors are also known to influence the corrosion rate such as flow, pressure, temperature, or the oil-gas-aqueous phase composition. These will also dictate the various corrosion types as described in section 1.4.

To corrode, an ion in the metallic lattice must pass through the Electrical Double Layer (EDL) and enter free solution. The double layer presents a potential barrier to the passage of ions and so has an acute effect on corrosion kinetics. The EDL is a denomination used whenever a region exists between two phases and charge is separated across the interface between them; this corresponds to the zone between a corroding material and the bulk solution in the case of aqueous corrosion.

The kinetics involved in corrosion obey the Arrhenius relationship as all chemical processes do. Equation 2-9 depicts such relation where k is the reaction rate, k_0 a fundamental rate constant and ΔG the activation energy. R and T correspond to the ideal gas constant and temperature expressed in Kelvin respectively.

Equation 2-9 Simplified Arrhenius equation

$$k = k_0 e^{\frac{-\Delta G}{R.T}}$$

The chemical nature of corrosion suggests that it is driven by a change in ΔG, the Gibbs free energy, but the electrical nature of corrosion suggests that a voltage drives the reaction as well. Both quantities are equivalent since they can be considered as the driving force and are related through the expression ΔG = −n.F.E, where n is the stoichiometric number of electrons in the reaction, F is Faraday's constant and E is the voltage driving the reaction. The minus sign is used to correct for the conventions where a chemical reaction only proceeds if ΔG is negative but an electrical reaction only occurs if E is positive. The detailed corrosion kinetics equations are elaborated in section 2.4.3.

2.4 Study of corrosion: Electrochemical methods

Metallic corrosion in aqueous systems is electrochemical in nature; for this reason studying such phenomena using electrochemistry techniques makes sense. The applications of electrochemistry are broad and could be described as the reduction of metal ions into atoms on an electrode surface by both chemical and electrochemical routes. Only the latter involves a flow of current and ultimately metal reduction initiates at the nanoscale and leads to atom agglomerates or nanoparticles.[102] This could be followed by the formation of films at the microscale level or even at the macroscale in the case of electrowinning technology.

2.4.1 Three electrode cell setup

Since the potential of any common metal immersed in a solution cannot be measured directly, techniques such as the three electrode setup have been introduced to overcome such drawback. In fact, the available measuring devices such as a potentiostat can only measure a difference in potential and a reference electrode should be added to the system in order to provide a reference point to measure the desired potential of the corroding specimen. An electrode is defined as a system where the oxidation state of species can be changed by the intervention of an electrically conducting surface at which electrons can be transferred.

Both Alternating Current (AC) and Direct Current (DC) electrochemical techniques rely on the use of the three electrode cell setup drawn in Figure 2-5. After applying an electrical signal to the specimen or working electrode, the response of the electrode to that signal is measured using a potentiostat connected to additional components; the reference electrode and counter electrode sometimes referred to as the auxiliary electrode. The additional

interface is created to complete the electrical circuit and connect the metal-solution interface to the potential-measuring device.
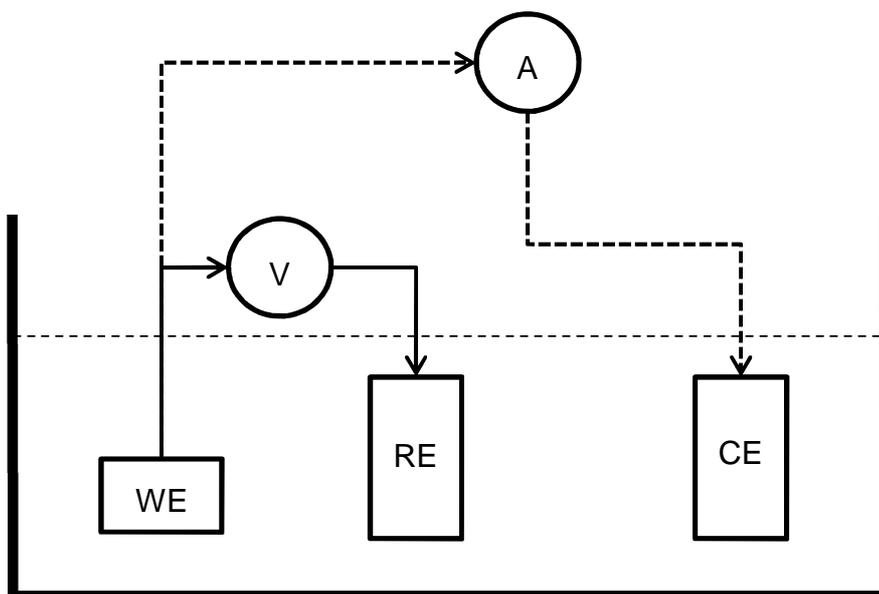
Figure 2-5 Schematic diagram of a 3 electrodes cell setup with (A) Ammeter, (V) Voltmeter, (WE) Working Electrode, (RE) Reference Electrode and (CE) Counter Electrode

The working electrode is the primary electrode which corrosion rate is being measured and is described in section 5.1. Nowadays, both RE and CE are included in the same glass compartment and commercialised as readily available silver-silver chloride or saturated calomel electrodes with built-in platinum wires as the counter electrode entity.

In Figure 2-5, the potentiostat allows the measurement of the voltage between the WE and the RE through a high-impedance voltmeter and the ammeter computes the current flowing between the CE and WE. This setup tends to minimize the current that passes through the RE while the CE allows the application of the desired current or potential through the WE. The CE is usually made of an inert material and will always be polarised in the opposite direction in regards to the WE. The reference electrode is present to monitor the potential of the WE and all these electrodes are connected through the conducting electrolyte.

2.4.2 Polarisation techniques

When the electrode equilibrium is disturbed, a net current i flows across its surface and displaces its potential anodically or cathodically depending on the

30

current direction while the potential shifting value is dictated by the same current magnitude.

Whenever an electrode potential is shifted, it is termed as polarisation and the value of this potential shift is known as the overpotential symbolised with the Greek letter η. Three main polarisation phenomenon can occur simultaneously; these are known as activation, concentration and resistance polarisation.

2.4.2.1 Activation polarisation

While always part of the total polarisation effect, activation polarisation results from the relative changes in the activation energies with relation to material dissolution or deposition whenever the electrode equilibrium potential is disturbed. If the current is of a dissolution nature than the polarisation is termed as anodic or positive while being negative or cathodic when the deposition currents are of order.

Thus, for a polarised electrode, the activation energy for dissolution is decreased while the activation energy for deposition is increased; this leads to a net current which is the difference between the two partial currents and build the basics of the Butler-Volmer equation detailed in section 2.4.3.

If it is assumed that if the electrode is anodically polarised then the applied polarisation should raise the metal energy by a factor of n.F.η and the activated complex energy by α.n.F.η. This is explained by the fact that the Gibbs activation free energy ΔG* is linked to the transferred charges n, the Faraday constant or one faraday of charge per mole F and the potential E as detailed in Equation 2-7.

The energy landscape for a corrosion reaction evolving conditions is schematised as a bold line in Figure 2-6. The term α is a symmetry factor usually equal to 0.5; this value applies when the position of the maximum in any electrode energy profile for activation polarisation is equidistant from the two minima. It is also described as the fraction of the width of the EDL that must be crossed to reach the excited state.

Under equilibrium conditions, the energy landscape is symmetrical when free energy is plotted against distance from the metallic surface; but when an overpotential is applied, the energy is changed on the free solution side of the plot by an amount equal to –n.F.η. The overpotential is distributed so that a

fraction, α lies across the barrier in the forward direction and (1 − α) lies across the barrier in the backward direction as schematised in Figure 2-6.
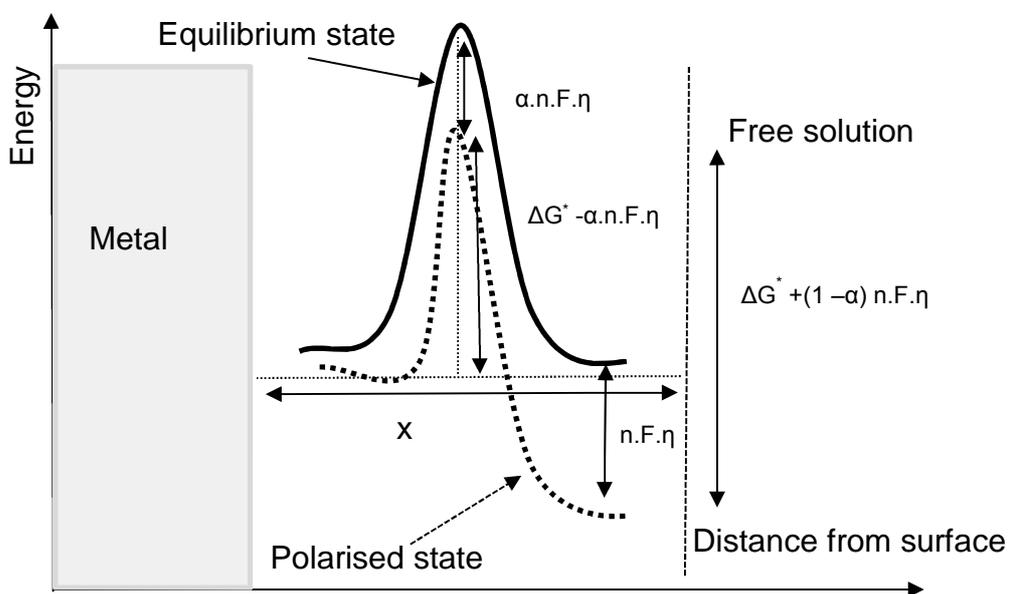
Figure 2-6 Energy landscape when an overpotential is applied[103]

In simple words, it's like the overall effect of the overpotential is to lower the required activation energy for the forward reaction by a value equal to α.n.F.η. Activation polarisation is of order when both linear polarisation resistance and Tafel extrapolation techniques are implemented as described in sections 2.4.4 and 2.4.5 respectively.

2.4.2.2 Concentration polarisation

When the electrode potential is altered far beyond its equilibrium potential, the net current flowing increases at first according to the Tafel equation (Equation 2-19). Nevertheless, this current cannot be increased ad infinitum because there are limits to the rate at which ions can carry charges through the solution to and from the working electrode. Examples of that could be hydrogen-evolution or reduction of oxygen where in both cases, an excess potential over that predicted by the basic Tafel equation is present.

Since ions are produced or consumed at the electrode surface faster than they can diffuse to or from the bulk of the solution, concentration polarisation arises. If the reaction is of anodic nature, the concentration of ions in the immediate vicinity of the dissolving specimen is raised above that in the bulk solution. In opposition, in a cathodic reaction, the local concentration is depressed and as a consequence, the polarisation for a given current is

greater than that predicted by the Tafel equation. The excess potential is called the concentration polarisation η_C and the magnitude of the effect can be examined by applying the Nernst Equation.

2.4.2.3 Resistance polarisation

Normally, the total polarisation at an electrode η_T is the sum of three components which are the activation polarisation η_A, the concentration polarisation η_C and the resistance polarisation η_R as per Equation 2-10.

Equation 2-10 Electrode polarisation

$$\eta_T = \eta_A + \eta_C + \eta_R$$

But usually, ohmic resistances are not taken into account unless the reaction itself or a complementary reaction produces films on the electrode surface.

2.4.3 Butler-Volmer Equation

The Butler-Volmer relation draws a theoretical model of the current and overvoltage reaction as shown in Equation 2-11 and can be related to the absolute reaction rate theory. When a clean and pure metal is immersed in a solution of one of its salts, it reaches a state of dynamic equilibrium in which the rates of cathodic and anodic reactions are equal and flowing currents correspond to the exchange currents i_{ex}. The oxidation reaction at the anode will be exactly balanced by a reduction reaction at the cathode.

When even a small disturbance from this equilibrium potential is introduced then the anodic and cathodic currents will no longer be equal and the net current will follow the applied disturbance in potential. If the value of the exchange current is large, there will be a large change in the net current for a given change in potential. On the contrary, large differences in potential from equilibrium will only create small net restoring currents if the exchange current is small.

Equation 2-11 Butler-Volmer equation under steady-state conditions

$$i = i_{ex} \left[e^{\frac{(1-\alpha).F.\eta}{R.T}} - e^{\frac{-\alpha.F.\eta}{R.T}} \right]$$

When activation polarisation is the polarisation technique, the overvoltage or overpotential η refers to the polarisation effects at the studied electrode as

described earlier in section 2.4.2.1. This is the difference between the equilibrium potential and the actual working corrosion cell potential. The net current originates when there is either a shift in potential in the cathodic or anodic direction as per Equation 2-13 and Equation 2-14 respectively. The exchange current i_{ex} is equal to the cathodic and anodic currents at equilibrium (i_{cath} and i_{an} respectively) as per Equation 2-12. i_{ex} is just the reversible reaction rate at equilibrium and it is thus a kinetic parameter. While the exchange current is not measurable, the net current can be quantified.

Equation 2-12 Exchange current at equilibrium conditions

$$i_{ex} = i_{an} = i_{cath}$$

Equation 2-13 Net current in a cathodic potential shift

$$i = i_{cath} - i_{an}$$

Equation 2-14 Net current in an anodic potential shift

$$i = i_{an} - i_{cath}$$

From the geometry of the energy profile described in Figure 2-6, these two partial currents are no longer equal due to the fact that the activation energy for dissolution is decreased to [$\Delta G^* - (1-\alpha)n.F.\eta$] while the deposition activation energy is increased to [$\Delta G^* + \alpha.n.F.\eta$]. These currents are extracted from the Gibbs activation free energy as per Equation 2-15 and Equation 2-16 where k is the rate constant related to the Arrhenius theory for the studied dissolution reaction.

Equation 2-15 Dissolution or anodic current i_{an}

$$i_{an} = k.e^{\frac{\Delta G^* - (1-\alpha)n.F.\eta}{R.T}} = k.e^{\frac{-\Delta G^*}{R.T}}.e^{\frac{(1-\alpha)n.F.\eta}{R.T}} = i_{ex}e^{\frac{(1-\alpha)n.F.\eta}{R.T}}$$

Equation 2-16 Cathodic current i_{cath}

$$i_{cath} = i_{ex}.e^{\frac{-\alpha.n.F.\eta}{R.T}}$$

There exist two limiting cases for the Butler-Volmer equation explaining the approximations used in the polarisation techniques when the overvoltage is

very high or very low as described in sections 2.4.4 and 2.4.5 for the Tafel polarisation and linear polarisation technique respectively.

2.4.4 Tafel Polarisation

The Tafel relation shown in Equation 2-19 depicts a linear relationship between the overvoltage and the logarithm of the established current. In fact, for very large values of overvoltage with η>100 mV, the second term from the Butler-Volmer relation in Equation 2-11 can be neglected as shown hereafter for both large positive or negative values of applied overpotentials.

Equation 2-17 Butler-Volmer for η > 100mV

$$i = i_{ex}.e^{\frac{-\alpha.F.\eta}{R.T}}$$

Equation 2-18 Butler-Volmer for η < -100mV

$$\ln i = \ln i_{ex} + \frac{(1-\alpha)F.\eta}{R.T}$$

Equation 2-19 Tafel equation

$$\eta = -\frac{R.T}{(1-\alpha)F}\ln i_{ex} + \frac{R.T}{(1-\alpha)F}\ln i$$

Equation 2-20 Simplified Tafel Equation

$$\eta = a + b.\ln i$$

The simplified Tafel equation is obtained by considering that only η and i are variables for a given electrode system where a and b are constants.

If the exchange current is to be kept in the equations then both the anodic and cathodic overpotentials are expressed as per Equation 2-21 and Equation 2-22 respectively.

Equation 2-21 Simplified Tafel anodic overpotential

$$\eta_{anodic} = b.\log(i_{ex}) + b.\log(i_{anodic})$$

Equation 2-22 Simplified Tafel cathodic overpotential

$$\eta_{cathodic} = b.\log(i_{ex}) - b.\log(i_{cathodic})$$

Tafel extrapolation relies on the fact that the slope of the potential (Y-axis) versus the logarithm of the current density (X-axis) plot around the OCP is linear as shown in Figure 2-7 if sufficiently large potentials are applied in both anodic and cathodic directions. This graph was plotted from laboratory results in order to better explain how the representative electrochemical data is extracted from such a technique.
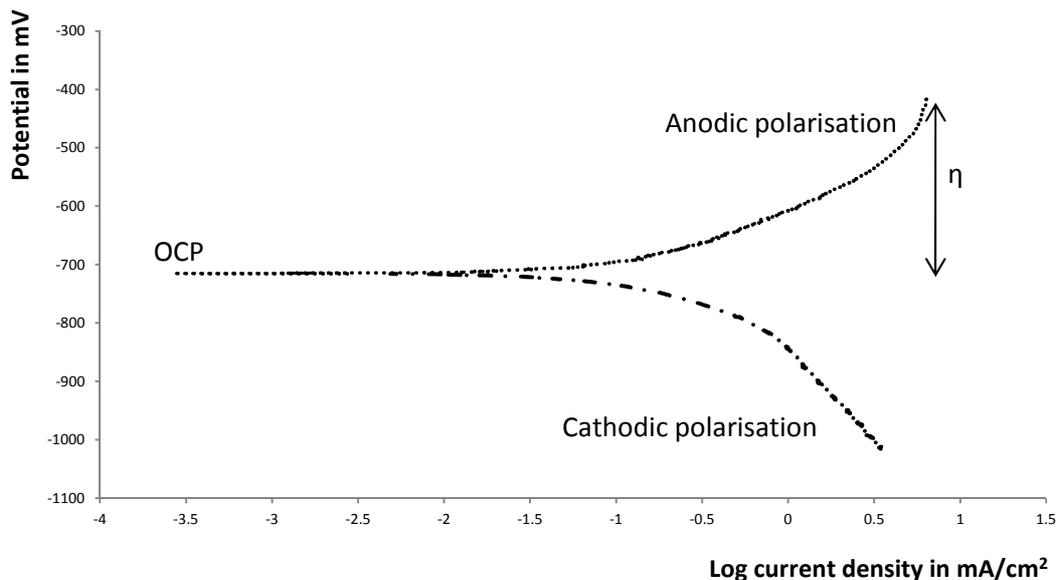
Figure 2-7 Tafel log current to potential relationship

If α is attributed the value of 0.5, Equation 2-11 becomes a hyperbolic sine function and the graph shape is in agreement with such a function. The Tafel slope is given as per Equation 2-23. This will be assimilated to β_a and β_c when applied to the anodic and cathodic counterparts respectively with α_a and α_c being the symmetry factors for anodic and cathodic reaction as defined by Bockris et al.[104]

Equation 2-23 **Tafel slopes of the anodic and cathodic reactions**

$$\beta_a = \frac{2.303.R.T}{\alpha_a.n.F} \ and \ \beta_c = \frac{2.303.R.T}{\alpha_c.n.F}$$

The test shown in Figure 2-8 was run on X65 carbon steel with a 600 SiC finish in 3.5% NaCl, at 70°C, a pH of 6.6, in a CO_2 saturated environment and a LPR sweep of ±300mV at a sweep rate of 10 mV/min which give 300 data points per polarisation curve. The cathodic and anodic polarisation curves join

at an OCP value of -715 mV. The Tafel lines extrapolation are identified as linear portions of the graphs usually between ± 50 to 100 mV from OCP as described by Badea et al.[105] while errors in the relevant manipulation are said to amount to less than 2% at 100mV.[106] These regions are described as near-linear and the tangent slope drawn in net anodic and cathodic regions will correspond to the anodic Tafel slope β_a and the cathodic Tafel slope β_c.
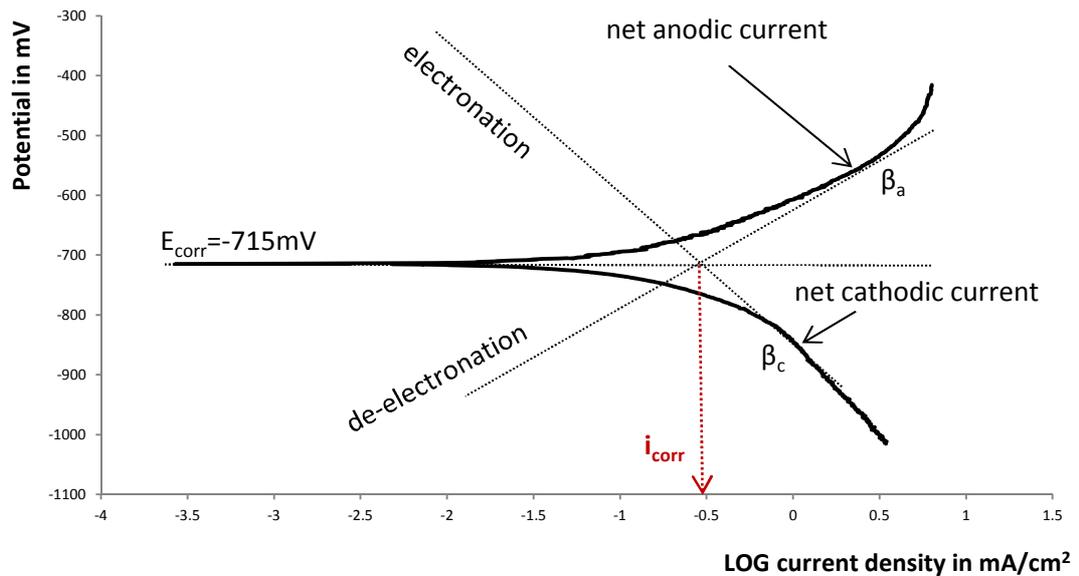
Figure 2-8 Extrapolation of the corrosion current I_{corr} using Stern diagram

From Figure 2-8, the corrosion current or I_{corr} can also be extrapolated by either the anodic or cathodic Tafel regions or both at the intersection point with E_{corr} at -715mV.

Technically, this test is run via a potentiodynamic polarisation method following the set of experiments in this described order; E_{corr} is measured until it stabilizes then the cathodic polarisation is conducted first. Another cell resting time is introducing before the final anodic polarisation is undertaken. Depending on the environmental conditions and material used, the OCP settle time is usually less than an hour. Mathematically, this linear relation is detailed in Equation 2-24 where E_{appl} is the applied potential in both anodic and cathodic direction, E_{corr} is the free corrosion potential and β_a and β_c are the anodic and cathodic Tafel constants respectively.

Equation 2-24 Tafel region correlation

$$I = I_{corr} \cdot e^{\frac{2.303\,(E_{appl} - E_{corr})}{\beta_a}} - e^{\frac{2.303\,(E_{appl} - E_{corr})}{\beta_c}}$$

Equation 2-25 Anodic Tafel slope

$$\eta_a = \beta_a \log \frac{I}{I_{corr}}$$

Equation 2-26 Cathodic Tafel slope

$$\eta_c = -\beta_c \log \frac{I}{I_{corr}}$$

Both Equation 2-25 and Equation 2-26 explain the linearity correlation between potential and the logarithm of the current density and that was proved experimentally by McCafferty et al.[107] The drawback of this technique is the required high overpotentials which renders it destructive and this is why for long term experiments linear polarisation tests are preferred.

2.4.5 Linear polarisation resistance

When the absolute values of the overpotential are lower than 5 mV, the Butler-Volmer equation can be rewritten as per Equation 2-27 where the exponential terms in Equation 2-11 were replaced by the first two terms in the McLaurin series expansion of e^x. In fact, for small values of the independent variable, the hyperbolic sine function approximates to a linear function.[108]

Equation 2-27 Linear polarisation resistance relationship

$$i = i_{ex}[1 + \frac{(1-\beta).F.\eta}{R.T} - 1 + \frac{\beta.F.\eta}{R.T}]$$

This approach allows to carry non-destructive low overvoltage laboratory studies of reactions with the assumption that activation control is the dominant process. As such two simplified relations involving the net current can be extrapolated as per Equation 2-28.

Equation 2-28 Simplified net and exchange current linear relation

$$i = 2i_{ex}.sinh\frac{n.F.\eta}{2.R.T} \approx \frac{i_{ex}}{R.T} F.\eta$$

In the LPR experiment, the slope is termed the polarisation resistance or R_p. This slope is inversely proportional to the corrosion current I_{corr} as shown in the Stern-Geary relation as per Equation 2-29.

Equation 2-29 Stern-Geary relation

$$I_{corr} = \frac{B}{R_p}$$

The constant B is composed of the anodic and cathodic Tafel constants as shown in Equation 2-30 and these are determined by running the Tafel or polarisation resistance method also called Tafel extrapolation method described in section 2.4.4.

Equation 2-30 Stern-Geary proportionality constant

$$B = \frac{\beta_a \cdot \beta_c}{2.303\,(\beta_a + \beta_c)}$$

Most electrochemical software assume the Tafel constants β_a and β_c for mild steel to be equal to 120 mV per decade. This is true for a reaction where the number of electrons exchanged equals 1 and the transfer coefficient is 0.5 at 25°C.[109] The better option is to start otherwise with a destructive Tafel extrapolation methodology and determine the real Tafel slopes values. This technique can be used as a potential step method where the potential is applied in increments as low as ± 5 mV or it can be scanned at a constant rate in the potentiodynamic method.

Figure 2-9 shows how the test is started at a potential 20mV negative in relation to E_{corr} (due to the cathodic polarisation) than it is moved 20mV to the positive direction (by applying an anodic polarisation). The data in this test were extracted from an laboratory test ran on an X65 carbon steel finished to 600 grit with SiC paper grit, at a pH of 6.8, a temperature of 60°C, a solution with a salt concentration of 3.5% sodium chloride in a carbon dioxide saturated environment.

The slope R_p can be computed from Figure 2-9 and if it is assumed that the current distribution is uniform across the working electrode than the corrosion rate in mmpy can be related to the current density i_{corr} in mA/cm^2 as per Equation 2-31.

Equation 2-31 Faradaic corrosion rate

$$CR = K_{corr} \left(\frac{i_{corr}}{\rho_{metal}} \right) EW$$
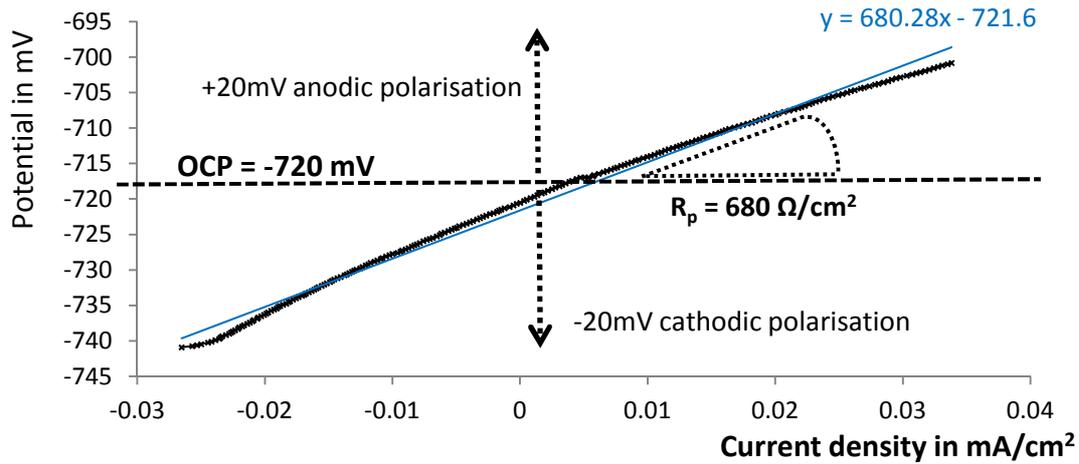
Figure 2-9 Example of an linear polarisation resistance curve

The corrosion process usually involves charge transfer and mass transfer processes simultaneously across the metal/solution interface. The link between charge and mass transfer is the Faraday (F). In the above relation, ρ_{metal} is the metal density, K_{corr} is a constant equal to 3.27×10^{-3} mm.g/µA/cm/year and EW is the material's equivalent weight described as the atomic weight divided by the number of transported charges for pure elements.

The advantage of this technique relies on the use of small voltage amplitudes, usually below 30 mV which allows for test repeatedly without affecting the corrosion rate evolution because the metal surface is barely altered by the applied overpotential. One major drawback of this technique is that the measured total resistance incorporates at the same time the solution resistance R_s and polarisation resistance R_p whereas R_s is assumed to be negligible. The AC techniques described in section 2.4.6 overcomes this problem and in most cases both AC and DC tests are implemented concomitantly.

2.4.6 Electrochemical Impedance Spectroscopy (EIS)

One of the most common alternating current techniques, AC impedance is a steady state technique that can access phenomena with a broad range of relaxation times while enabling the separation of different rate processes. It applies an AC signal (voltage or current) and registers the electrode response and the wide range of frequencies used allow the determination of a wide spectrum of interfacial processes. The relations applicable in AC conditions are shown in Equation 2-32 and Equation 2-33.

Equation 2-32 Relationship between current and potential

$$E = I.Z$$

Equation 2-33 The definition of impedance

$$Z = \frac{\Delta E}{\Delta I}$$

The impedance Z is defined as the alternating potential divided by the alternating current. This voltage is dependent on the AC frequency and time while the current depends on the phase angle shift in addition. Usually EIS is run in a potentiostatic manner where a small potential ranging between 5 and 10 mV is applied over a large frequency range e.g. 10^{-2} to 10^6 Hz and the common three electrode cell potentiostat setup described in section 2.4.1 allows the monitoring of the working electrode AC current response.

Three different forms of presenting the potential and current values registered during an EIS experiment are in use; one Nyquist plot relating the imaginary versus the real impedance values as shown in Figure 2-10 and two Bode plots relating the impedance module and the phase shift to the frequency as per Figure 2-11 and Figure 2-12 respectively.
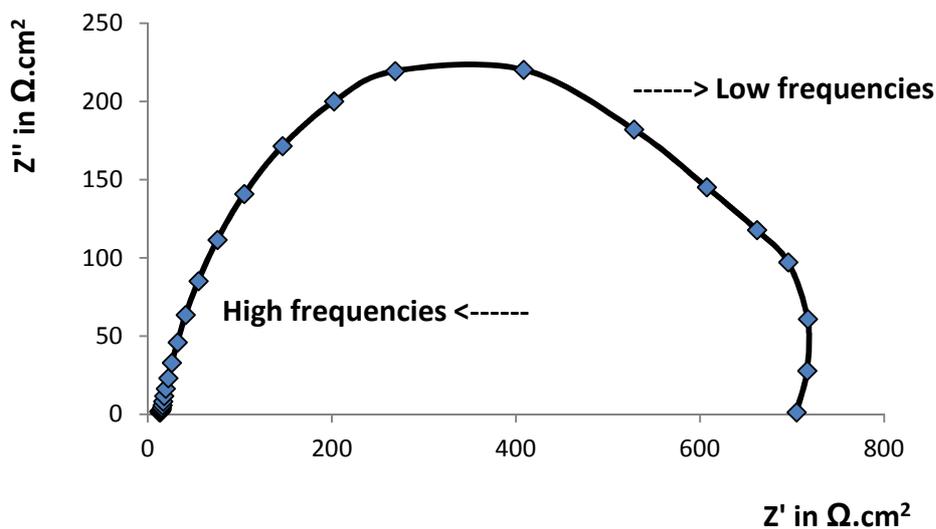
Figure 2-10 Nyquist plot for carbon steel in CO_2 environment after 15 hours, pH 6.8, 50°C

The Nyquist graph in Figure 2-10 is adapted from experimental data extracted from an EIS experiment ran with an AC sinusoidal excitation of 10 mV for a frequency range starting at 10kHz and ending at 10mHz while registering 40 points per decade. It shows the imaginary part of the impedance on the Y-axis with regard to the real part of that impedance on the X-axis. The unit is the one of a resistance in ohms but these values have incorporated the sample exposed surface for the corrosion reaction and are thus plotted as resistance densities. On this type of plot, the high frequencies are to the left while the low frequency range is to the right of the X-axis.

Contrary to the Nyquist graph, on the Bode plot, the frequencies decrease from right to left hand side and both axes are drawn with a logarithmic scale because of their magnitude. The impedance module variation in Figure 2-11 shows a resistive behaviour at the high and low frequencies and a capacitive one in the middle frequencies; the reason behind such trends can be explained by simplifying Equation 2-34.

Equation 2-34 Expression of the impedance module

$$Z(w) = Z' + Z'' = R_s + \frac{R_p}{1 + j.w.R_p.C_d}$$

At high frequencies, the frequency dependant term vanishes, resulting in the following relation: $Z(w) = R_s$. At very low frequencies, it simplifies to $Z(w) = R_s + R_p$. At other frequencies, the capacitance interference (C_d) which is the double layer capacitance effect cannot be ignored as shown on Figure 2-12.
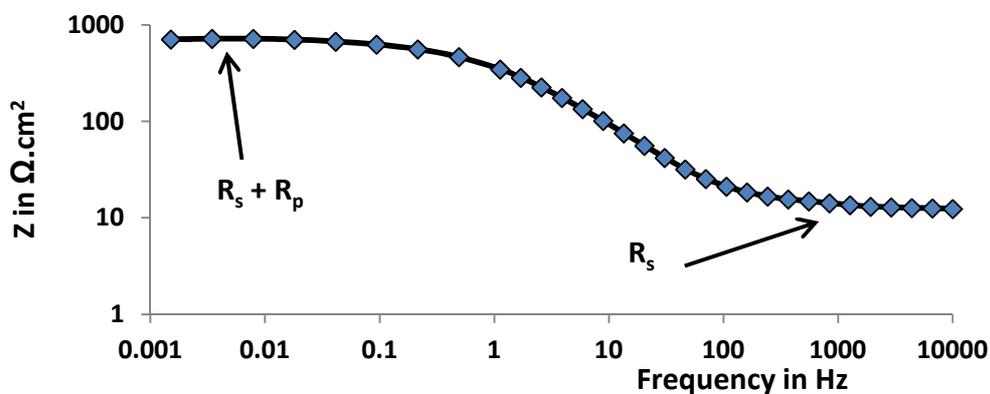
Figure 2-11 Bode plot: Impedance magnitude versus frequency

The second Bode plot displays the phase angle shift between the applied AC potential and the registered AC current as shown in Figure 2-12. The capacitive behaviour or time-constants can be easily deduced from such a Bode plot since a totally capacitive behaviour is recognized with a phase angle equal to -90° while a resistor is known to have a phase angle equal to zero.
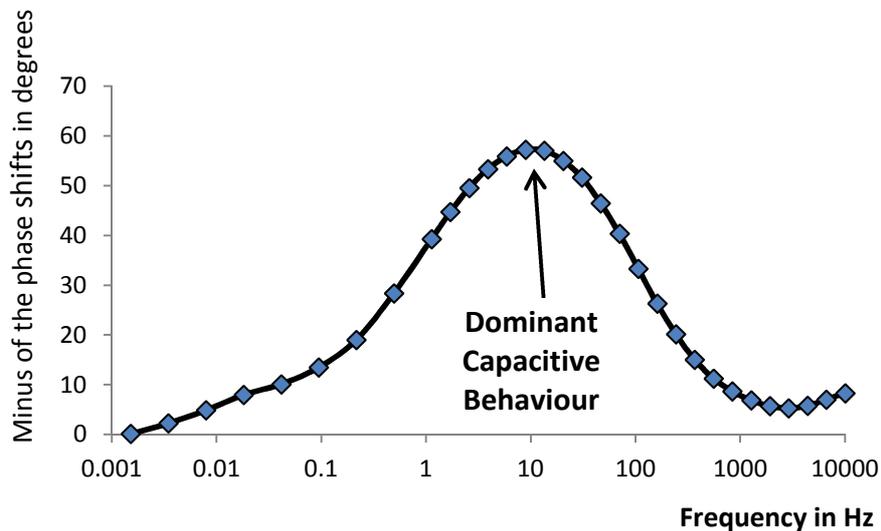
Figure 2-12 Bode plot: Phase angle shift versus applied frequency

The literature review presented in Part II focuses on three main topics which are divided in three chapters. Since corrosion can differ in its mechanisms with regard to the major gas present and this thesis focuses on corrosion when carbon dioxide is the dominant gas phase thus Chapter 3 aims at detailing the mechanisms of CO_2 corrosion, the various categories and factors influencing CO_2 corrosion along with the prediction and prevention from such degradation mechanism.

Iron carbonate, the major corrosion layer formed under such conditions, and responsible in some cases for providing a natural corrosion mitigation by acting as a diffusion barrier and blocking active sites is discussed in Chapter 4. Characterising such corrosion products is vital since this thesis main aim is to modify them via the addition of a specifically chosen hybrid nanofiller and similar approaches where nanofillers are intermixed within specific polymer matrices are highlighted in 4.9. Although iron carbonate is not a polymer, these techniques guided this research in trying to incorporate silicon-based nanofillers in the on-growing iron carbonate in order to follow the kinetics of formation and mechanical properties enhancement in these corrosion layers.

Part II. Literature review

Chapter 3 Carbon dioxide corrosion

Depending on the gas which is abundantly present in the liquid phase, three types of degradation mechanism are described within the oilfield structures; sweet corrosion initiates when carbonic acid is dissolved in the water, sour corrosion develops when hydrogen sulfide is present while oxygen corrosion is only found in water injection systems and some traces present in aging assets.[110]

Figure 3-1 compares the general corrosion rate values at different gas pressures; for example, in order to achieve a corrosion rate equal to 5 milli-inch per year, around 1.7 ppm of O_2 should be present in the aqueous phase as compared to 100 ppm of CO_2 in the case of sweet corrosion and 400 ppm of H_2S in the case of sour corrosion. In other words, oxygen is almost 80 times more corrosive than CO_2 and 400 times more corrosive than H_2S.
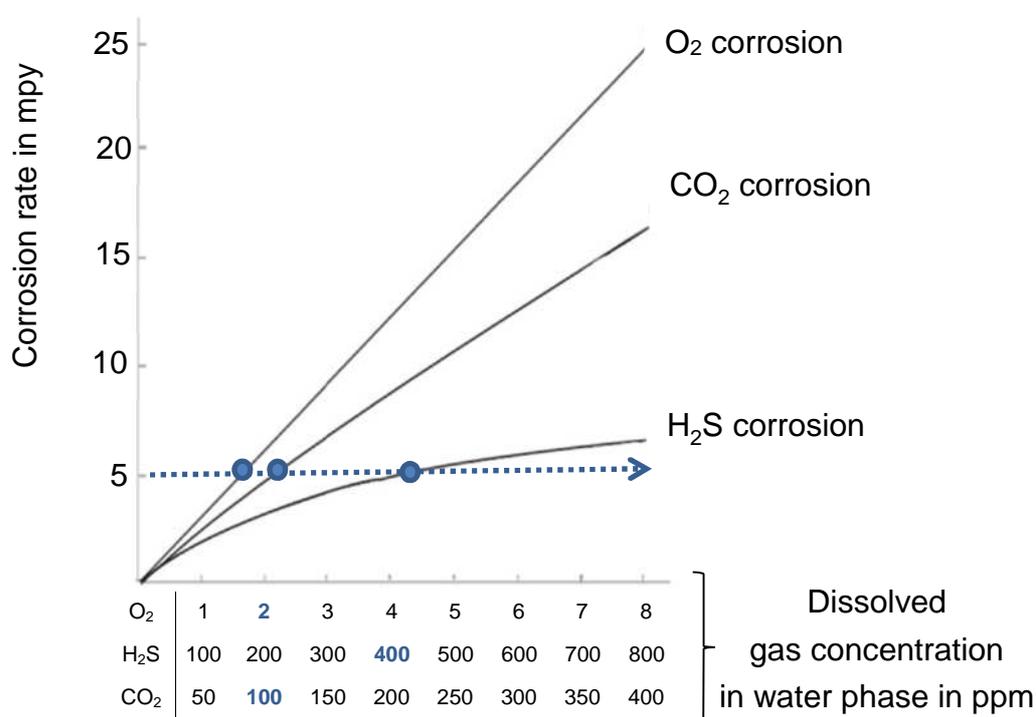
Figure 3-1 Comparison of general corrosion rates of carbon steel in oxygen, carbon dioxide and hydrogen sulfide environments[43]

In the oil and gas industry, hydrocarbons are transported through structures where high concentrations of CO_2 and significant amounts of liquid water are common thus providing the electrolyte for the corrosion of mild steel to initiate. Usually both H_2S and CO_2 coexist but the field is defined as suffering from carbon dioxide corrosion when the H_2S partial pressure is lower than 0.3kPa as described in the material standard issued by the National Association of Corrosion Engineers (NACE) entitled "NACE MR0175 / ISO 15156".[111]

In aqueous solution, both CO_2 and H_2S have similar corrosivity when carbon steel is the studied material but hydrogen sulfide corrosion is known to induce hydrogen embrittlement and cracking problems because it promotes the absorption of hydrogen.[112] It should also be noted, that at same pH, the CO_2 corrosion rate is even higher than values expected when strong acids are present which renders carbon dioxide corrosion a big threat for the oilfield structures.[113]

3.1 Why is carbon dioxide corrosion problematic?

Corrosion is worth investigating in oilfield applications, because corrosion problems represent a large portion of the total costs for oil and gas producing companies every year worldwide. The total overall corrosion cost could be averaged to almost 3% of the GDP and this includes the capital, control and design costs related to all types of metallic corrosion.[114]

Carbon dioxide corrosion is the predominant form of attack and the major cause of incidents in the oil and gas industry.[115] It affects the turnover and tangible assets, increases the capital expenditures, the lifting costs while causing lost or deferred production. Studying carbon dioxide corrosion could prove crucial in order to control direct costs associated with the loss of production and the replacement or repair to the damaged equipment but also life and environmental safety could be better protected if the fundamental mechanisms of such corrosion attack is better understood.[116] Moreover, it has been estimated that 25% of all safety incidents were related to this specific corrosion type while the corresponding field cost was averaged to be as high as 0.3$ per produced barrel.[117]

This scenario is predicted to endure in the near future since the carbon steel is supposed to remain the material of choice even when it is known to be prone to severe corrosion attack. In fact, carbon steels are often used as a construction material in oil producing and gathering facilities due to their

mechanical, structural and cost requirements thus being the best candidates for long distance transportation pipelines of unprocessed well-stream for example.[118] Transport of carbon dioxide for carbon capture and storage also uses low-cost carbon steel pipelines owing to their negligible corrosion rates in dry CO_2 and a recent publication by Barker et al.[119] presents a detailed review of the integrity risks posed to dense-phase CO_2 pipelines in the form of internal corrosion. The damage can be accentuated when other mechanical stresses are present such as the coupled effect of CO_2 attack and tensile stress on well cement under CO_2 storage conditions studied by Gu et al.[120]

Site developments have allowed for the reduction of such attack in the CO_2 gas injection process by actively separating water from the dry CO_2. But such techniques are not applicable when oil production, gathering and transportation processes are in order.[121] From the previously described economic effects of corrosion, it seems obvious that an optimum control and management of this drawback is a necessity in order to implement a cost-effective design of the oilfield facilities. Corrosion inhibitors along with the manipulation of surface deposits are two commonly used approaches for lowering the corrosion rates on site.[122] More recently, thermally sprayed coatings such as thermally sprayed aluminium was assessed in order to mitigate corrosion of carbon steel in carbon capture and storage environments as described by Paul et al.[123]

Carbon dioxide corrosion often occurs in oil and gas operational conditions where the maximum temperature and pressure are limited to 150°C and 50 bars respectively. With a pH fluctuating between 3.5 and 7, it has been observed that the corrosion rate increases with temperature until a certain threshold where a protective scale layer known as iron carbonate covers the steel surface and provides protection from electrochemical degradation to a certain extent.[124]

Other corrosion products can grow in these conditions such as magnetite (Fe_3O_4), hematite(Fe_2O_3), and cementite (Fe_3C) showing various electrical resistances and mechanical properties that explain why iron carbonate is the only protective compound among these films.[125] The exists many limitations for relying on corrosion products such as $FeCO_3$ to mitigate corrosion mainly due to their susceptibility to dissolve as detailed in section 4.6.4 and an example of such breakdown is shown in Figure 3-2.
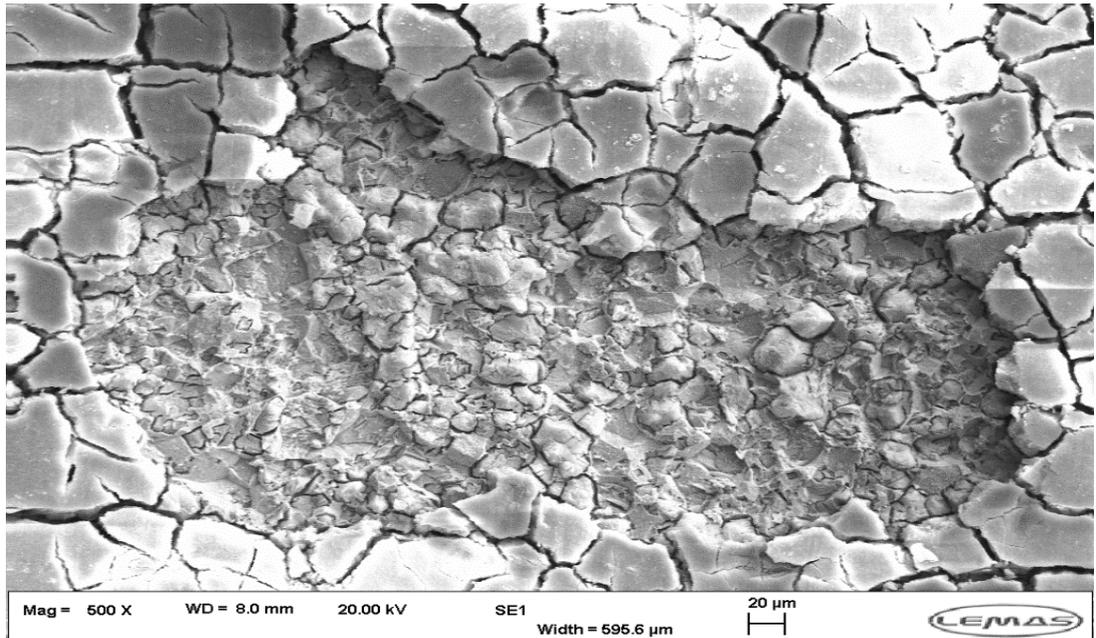
Figure 3-2 SEM micrographs showing a cohesive failure of developed corrosion layer over X65 samples [pH=5, 60°C, 3.5% NaCl, 118 hours]

3.2 Equipment subjected to CO_2 corrosion

Carbon dioxide corrosion first occurrence goes back to the 1940s when faced with gas-condensate fields in the USA.[126] It is widespread in all oilfields alongside sour corrosion but with various ratios since CO_2 as an acid gas can be naturally present or physically added to these systems.

This is shown in Table 3-1 which summarizes some of the components that could be affected by such combined corrosion attack in the production sector. It is shown that, whenever carbonic acid comes into contact with carbon or low alloy steels, such as well tubing, wellheads, separators, pumps or pipelines, both sweet (CO_2) and sour (H_2S) corrosion can develop. CO_2 degradation mechanism is mostly of pitting nature and it also occurs in the boiler feedwater and condensate systems present in most refining units.

Major areas where CO_2 corrosion takes place naturally are gas condensate wells, high pressure sweet oil wells, flowing wells and any zones where water condenses such as pipelines transporting wet natural gas containing carbon dioxide. Both carbon dioxide and water are a prerequisite for sweet corrosion to take place while the presence of additional gases or a more complex phase in the brine, such as presence of oil, would only affect its kinetics and intensity. In fact it is known that CO_2 is three times more soluble in hydrocarbons than water itself.[127]

Table 3-1 Major oilfield components subjected to CO_2 corrosion[23]

Component	Flow	Oil	Water	CO₂	H₂S	O₂
Drill pipe			x	x	x	
Casing pipe			x	x	x	
Downhole tubular	x	x	x	x	x	
In situ production	x	x	x	x	x	
Wellhead		x	x	x	x	
Production pipelines	x	x	x	x	x	
Separators		x	x	x	x	
Gas dehydration facilities			x	x	x	

Human intervention affecting the available quantities of CO_2 in the field are mainly due to enhanced oil recovery techniques which have been recently implemented. When CO_2 is injected as part of EOR techniques, it contributes to sweet corrosion propagation and this is usually achieved via the addition of carbon dioxide saturated water into wells.[128] Recently, the use of water alternating gas is becoming very common and it was shown that simultaneous water and gas injection with CO_2 could increase the original oil in place production by almost 75%.[129]

3.3 Mechanisms of CO₂ corrosion

According to Dugstad et al.[130] the "CO₂ corrosion" terminology and the CO_2 effect is not solely related to one mechanism. In fact, a wide range of electrochemical, chemical and mass transport processes are occurring simultaneously at the corroding steel and the electrolyte interface.

Equation 3-1 Dissolution of CO_2

$$CO_{2\ (gas)} \leftrightarrow CO_{2\ (aq)}$$
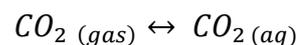
Equation 3-2 Formation of carbonic acid

$$CO_{2(aq)} + H_2O_{(l)} \leftrightarrow H_2CO_{3(aq)}$$
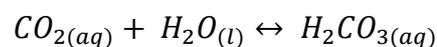
Equation 3-3 CO_2 hydration dissociation constant

$$K = \frac{H_2CO_{3(aq)}}{CO_{2(aq)}} = 1.3 \times 10^{-3}$$

Equation 3-4 First dissociation of carbonic acid

$$H_2CO_{3(aq)} \leftrightarrow HCO_{3(aq)}^- + H_{(aq)}^+$$

Equation 3-5 Second dissociation of carbonic acid

$$HCO_{3(aq)}^- \leftrightarrow CO_{3(aq)}^{2-} + H_{(aq)}^+$$

Equation 3-6 Iron corrosion reaction

$$H_2CO_3 + Fe \rightarrow Fe^{2+} + CO_3^{2-} + H_2$$
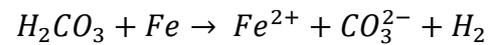
Equation 3-7 Formation of iron bicarbonate

$$Fe^{2+} + 2(HCO_3^-) \rightarrow Fe(HCO_3)_2$$
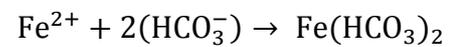
Equation 3-8 Formation of iron carbonate

$$Fe^{2+} + CO_3^{2-} \rightarrow FeCO_3$$
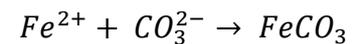
Equation 3-9 Iron bicarbonate decomposition

$$Fe(HCO_3)_2 \leftrightarrow FeCO_3 + H_2CO_3$$
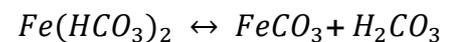
Dry carbon dioxide gas is not corrosive by itself at the temperatures encountered within the oil and gas production systems. Sweet corrosion initiation requires the dissolution of the dry CO_2 gas in any aqueous medium, such as water hydrates, which relates the effect of CO_2 corrosion on its partial pressure (Equation 3-1) and promotes an electrochemical reaction between the steel and the contacting aqueous phase.

The hydration reaction is slow[131] and only a small fraction of CO_2 will be present as dissolved carbonic acid which is corrosive to both carbon and low allow steel (Equation 3-2).[132] This is explained by the value of the dissociation constant related to this reaction which is equal to 1.3x10^{-3} as described in Equation 3-3.[133] H_2CO_3 is diprotic and dissociates into two ions which are bicarbonates (Equation 3-4) and carbonates (Equation 3-5) depending on the pH.[134] The steps of the initiated corrosion electrochemical reaction are summarised in Equation 3-6 to Equation 3-8.[135]

Theoretically, both iron bicarbonate $Fe(HCO_3)_2$ and iron carbonate $FeCO_3$ are produced from the carbon steel corrosion at pH below 10 (Equation 3-7) and

above 10 respectively (Equation 3-8). But what we observe in real oil and gas service is the latter or iron carbonate film.[136] In fact, when iron bicarbonate has not even been observed in experimental studies and it is suggested that it decomposes into iron carbonate and carbonic acid at higher temperatures as per Equation 3-9.[137]

As described in section 2.1, every corrosion mechanism is divided into both anodic and cathodic counterparts and carbon dioxide corrosion is no exception.[138] As such, the main anodic reaction of CO_2 corrosion of mild steel is the iron oxidation or dissolution (Equation 3-10) while the main cathodic reactions are the hydrogen-evolution from H_2CO_3, HCO_3^- and H^+ as per Equation 3-11, Equation 3-12 and Equation 3-13 respectively leading to the overall simplified iron dissolution in carbon dioxide where iron carbonate corrosion films are formed as per Equation 3-14. This only occurs when the carbonate and ferrous iron concentrations exceed the solubility limit as described in section 4.3.

It should be noted that the anodic reaction as per Equation 3-10 is actually a multi-step process as detailed by Nešić et al.[113] and the two electrons involved in this reaction are not released in a single step by rather through a sequence of intermediate phases.

Carbon dioxide cathodic reactions are reported to be more intense than what is expected at a specific pH mainly due to the buffering properties of the carbonic acid.[139] The term "buffer" relates to the fact that carbonic acid acts as a "reservoir" of hydrogen ions and is able to replenish them when they get depleted by the reduction reaction at the metal surface as in Equation 3-13. The anodic reaction induces the creation of the iron carbonate scale due to its low solubility.

In terms of the heterogeneous reactions at the steel surface, hydrogen-evolution (Equation 3-13) remains the main cathodic reaction under oil and gas transportation conditions. This reaction strongly depends on the solution pH and is often limited by the rate at which the protons can be transported to the steel surface by mass-transfer thus making this reaction very flow-dependant.[131] When the pH is lower than 4, the dominant process is the cathodic reduction of H^+ due to its higher concentration. At intermediate proton concentrations or when $4<pH<6$, the limiting diffusion rate of H^+ is smaller due to its lower concentration.

Hydrogen-evolution only occurs at a much faster rate when CO_2 is hydrated to form H_2CO_3 due to the excess protons provided by the further dissociation of the formed carbonic acid.[131] The direct reduction of H_2CO_3 where the protons are directly reduced from the carbonic acid adsorbed at the surface (Equation 3-11) constitutes a second cathodic reaction alternative and is strongly affected by the CO_2 partial pressure in the system.[140]

Equation 3-10 Iron oxidation or the anodic reaction

$$Fe \rightarrow Fe^{+}_{(aq)} + 2e^{-}$$
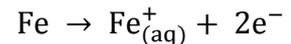
Equation 3-11 Hydrogen-evolution from bicarbonates

$$2H_2CO_{3(aq)} + 2e^{-} \rightarrow H_{2(aq)} + 2HCO^{-}_{3(aq)}$$
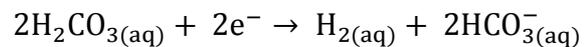
Equation 3-12 Hydrogen-evolution from carbonates

$$2HCO^{-}_3 + 2e^{-} \rightarrow H_2 + 2CO^{2-}_3$$
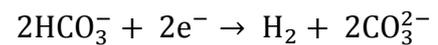
Equation 3-13 Hydrogen-evolution from hydrogen ion

$$2H^{+}_{(aq)} + 2e^{-} \rightarrow H_{2(aq)}$$
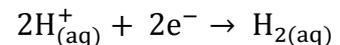
Equation 3-14 Overall CO_2 corrosion reaction

$$Fe + H_2O + CO_2 \rightarrow FeCO_3 + H_2$$
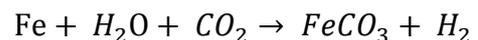
The kinetics and rate-determining step of the corrosion process are still debated but recent studies have suggested the presence of a nanoporous and compact interfacial nanometric corrosion layer between the metal and the covering corrosion products. It is postulated that this configuration should help explain the kinetic control of the sweet corrosion mechanism.[141] Previous concepts highlight the sole presence of iron carbide and iron carbonate in the scale or corrosion film; the cementite being the remains of the original steel microstructure left behind after dissolution of the metal matrix as described by Kermani et al.[117]

The effect of corrosion product layers on the anodic and cathodic reactions of carbon steel in CO_2-saturated methyldiethanolamine solutions at 99°C has

been researched and results showed that the rate-determining step of the anodic dissolution changed from a diffusion process to an electrochemical reaction with an increase in MDEA concentration while the rate-determining step of the cathodic reduction changed from an electrochemical reaction to a diffusion process with an increase in MDEA concentration.[142] Whilst there exists a debate about the sweet corrosion mechanism with regard to which entities are involved in the corrosion reaction in itself, it remains evident that the extent of corrosion is directly dependent on the CO_2 partial pressure since it directly influences the pH of the solution and the dissolved species concentration as detailed in section 3.5.

Recently, the corrosion mechanism originally proposed by de Waard and Milliams[143] and involving the direct reduction of carbonic acid as the dominant cathodic mechanism (Equation 3-11) was challenged by Nešić et al.[144] who stipulated a pH buffering effect as the dominant cathodic reaction. This alternative possibility suggests that carbonic acid dissociates and provides an additional source of hydrogen ions near the steel surface, while the only cathodic reaction is reduction of hydrogen ions (Equation 3-13). If such a buffering effect mechanism is in place, carbonic acid, formed from the hydration of CO_2, partially dissociates to provide most of the $H^+_{(aq)}$ and $HCO^-_{3(aq)}$ as per Equation 3-4.

3.4 Types of corrosion observed in sweet environments

3.4.1 Uniform corrosion

Sweet corrosion can manifest primarily as a general corrosion process where an iron carbonate layer is formed and can help protect the metal in specific conditions (Figure 3-3). Uniform CO_2 corrosion of mild steel can be considered as one of the most studied and well understood corrosion systems. In addition to numerous studies covering specific aspects of this corrosion system, several holistic reviews of the underlying physicochemical processes[145] as well as reviews of uniform corrosion rate prediction models[146] are available in the literature.

It could also appear as a localized attack and three variations of such degradation have been detailed in the literature; pitting, mesa attack and Flow Induced Localized Corrosion (FILC).[117] This results in a loss of surface metal at discrete areas while the surrounding parts remain essentially unaffected or in the worst case scenario subjected to general corrosion.[147]

In fact, the experience of the oil industry with deep gas wells for example shows that corrosion is not so severe at the bottom of the well mainly because the environmental conditions of temperature and pressure allow for a uniform scale mainly composed of iron carbonate to cover the surface of the tubing.[148]

| Mag = 2.00 K X | WD = 8.5 mm | 20.00 kV | SE1 | 10 µm | LEMAS |

Width = 148.5 µm
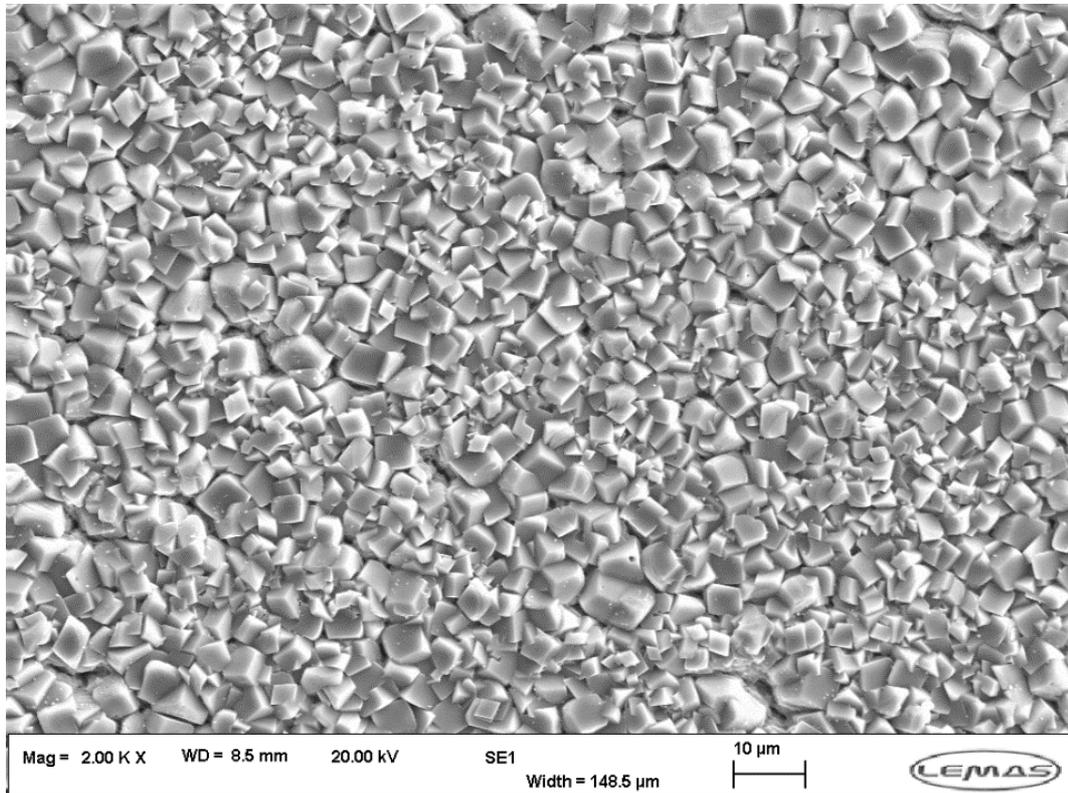
Figure 3-3 SEM micrograph showing the iron carbonate film developing in general corrosion conditions over a carbon steel sample (pH6.6, 60°C, 3.5% NaCl, 0.8bar CO_2 partial pressure after 98 hours of exposure)

3.4.2 Pitting corrosion

Pitting corrosion is a stochastic process which is difficult to predict; it occurs preferentially at certain depths and can initiate in almost the full range of operating temperatures when the flow conditions are stagnant or moderate. It has been referenced since the beginning of CO_2 corrosion research as discussed by Baylis.[149]

It was shown from previous studies that the susceptibility to pitting corrosion is higher and the time for pitting to occur is lower when both the temperature and the carbon dioxide partial pressure are increased. It was also postulated that there exists a range of temperatures for which pitting occurs on different alloys.[150]

Hence, when carbon steel is in the presence of CO_2 at temperatures between 80°C and 90°C, pitting degradation mechanisms are abundant. These usually show as circular depressions with tapered and smooth sides constituting the pits. Such pits can be as deep as 50µm once the covering iron carbonate layer has been removed for surface analysis as seen in Figure 3-4.[151]

(a)

(b)
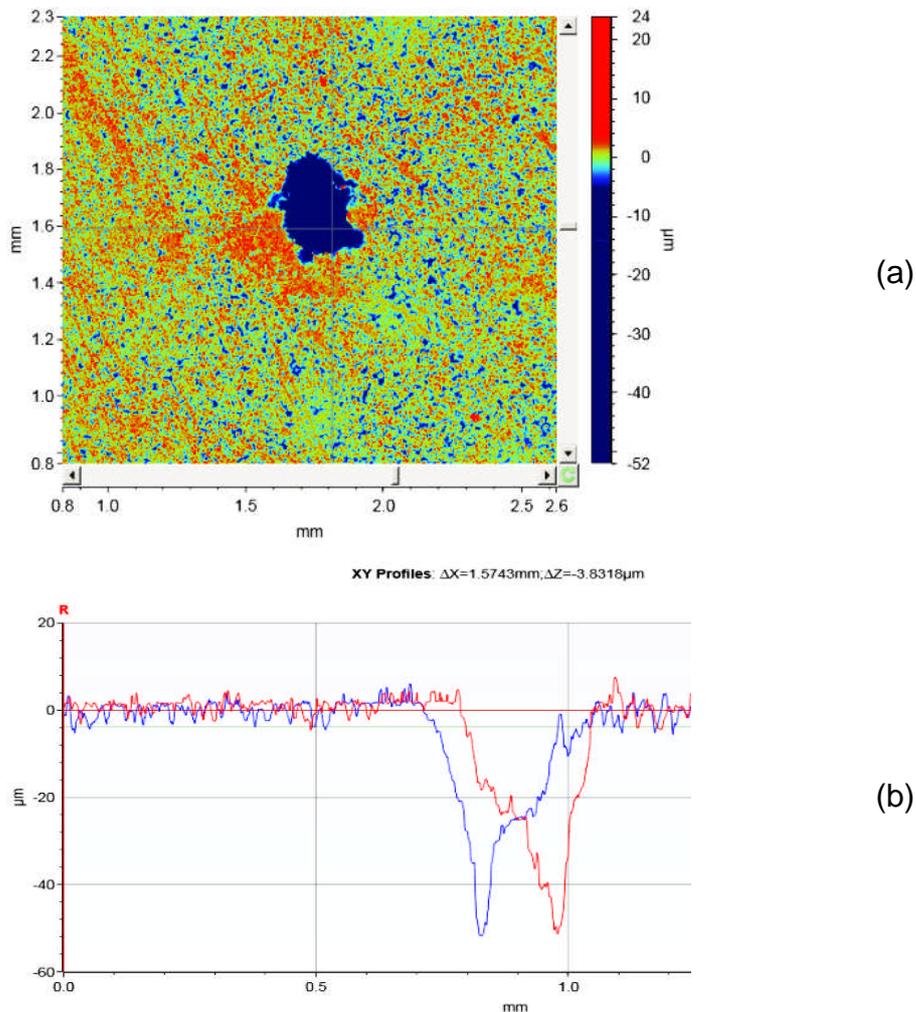
Figure 3-4 Examples of 3D and 2D profiles of measurable maximum pits on the surface of X-65 carbon steel; (a) 3D and (b) 2D at 50°C after 168 hours exposed to a 10 wt. % NaCl solution saturated with CO_2 at a pH of 7.5 adapted from Pessu et al.[152]

The oil and gas industry often use the empirical ASME B31G method to evaluate the remaining lifetime of pipelines attacked by pitting which provides guidance in the evaluation of metal loss in pressurized pipelines and piping systems.[153]

3.4.3 Mesa attack

Another very common localized sweet corrosion process is termed mesa attack and is also stochastic in nature. It occurs at average flow rates which are responsible for the removal of some parts of the protective iron carbonate film leading to the initiation of such degradation phenomena.[154] Such a failure is shown in Figure 3-5 and its causes has been routed to the internally formed galvanic coupling between the steel ferrite phase and the cementite layer.[155] Usually, when a critical iron carbonate film thickness have been reached, it is followed by a spalling of those scales which is explained by the increasing intrinsic growth stresses, thus leading to the galvanic area which corrodes very heavily.[156]

Adherent
FeCO$_3$ layer

Delaminated
FeCO$_3$ area
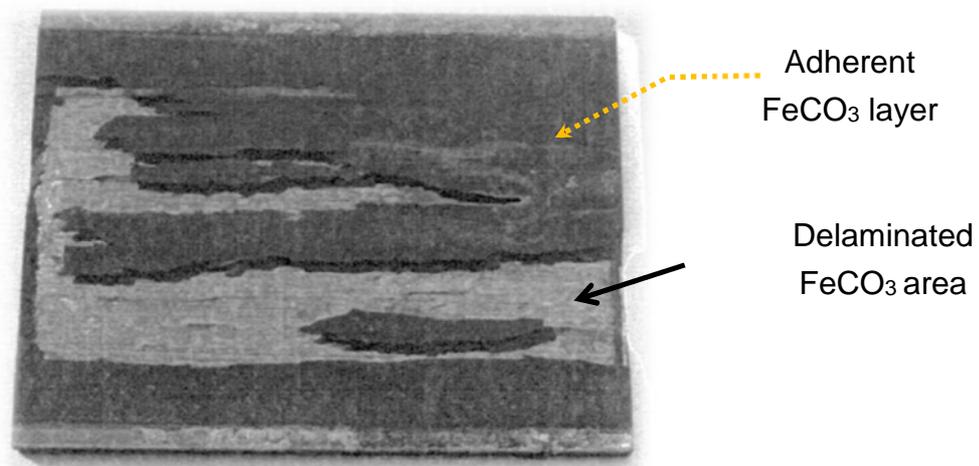
Figure 3-5 Overview of carbon steel specimen with mesa attack[157]

The form of mesa attack observed in field pipelines is typically characterised by flat, film-free regions, separated by sharp steps from neighbouring areas which show significantly less damage. The understanding of the exact conditions and causes of the mesa corrosion degradation mechanism requires advanced systematic studies in order to better assess and prevent it.

A scheme explaining the galvanic mechanism occurring in CO_2 corrosion is shown in Figure 3-6; this only occurs when the iron carbonate film is not fully covering the surface of the steel and it could be simplified to a galvanic coupling between the ferrite in the steel and the cementite trapped in the deposit of $FeCO_3$.[158]
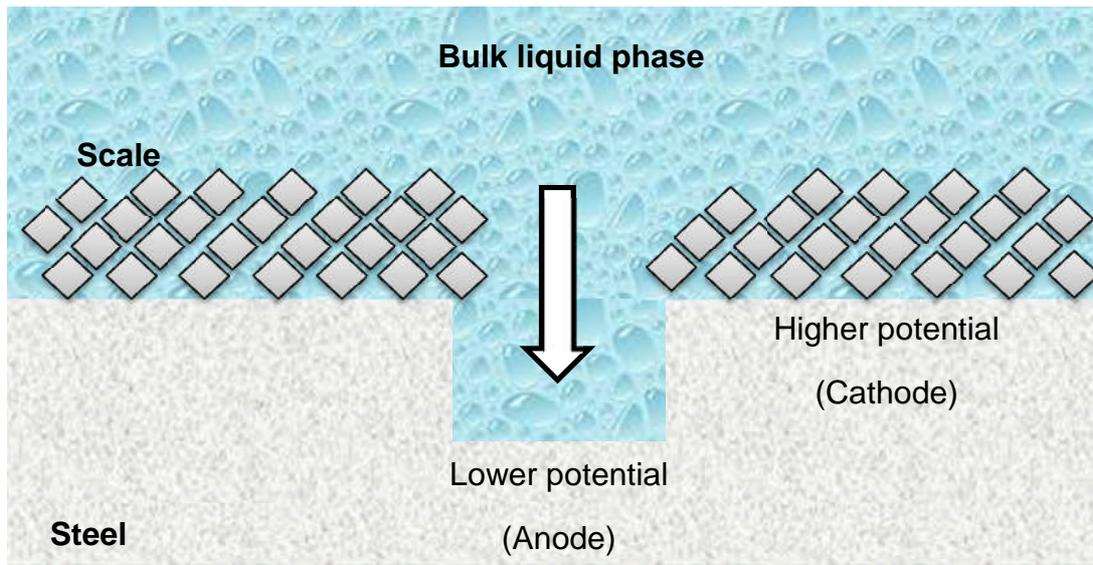
Figure 3-6 One dimensional galvanic mechanism for localized CO_2 corrosion

The scale breakdown can happen for a variety of reasons but mainly due to fluid flow or intrinsic stresses.[159] After that, a galvanic effect is established between the scale-covered surface or cathode and the scale-free surface or anode leading to propagation of the localized attack. Thus the galvanic cell is established between the pit area created under a bare steel region exposed to the corrosive entities present in the bulk medium and the surface covered with the scale products.

The terms higher and lower potentials are related to the measured free corrosion potentials of each area and it was shown that the OCP of the scale-covered surface was higher than the OCP of the bare surface which explains the used terminology of cathodic and anodic regions. In such cases, the cathode contribution is usually dominant due to the large area ratio of the cathode as compared to the anode which is found to be a thousand fold in artificial pits and this greatly increases the metal dissolution in the localized pit area.[157]

It was shown that the magnitude of the galvanic attack is dependent on the ratio of the anodic and cathodic regions; therefore, when the ratio is more unfavourable to the anode, the galvanic current density is greater and the pits can grow faster and deeper.[160] A model which describes how to avoid mesa attack, is available but none can predict it so far.[161]

3.4.4 Flow Induced Localised Corrosion

The third type of localized corrosion that develops in sweet conditions is flow induced localized corrosion which normally spreads from pre-existing pits or mesa sites due to increased fluid flow. Because of the high local flow conditions and the resultant stresses or internal strain caused by the iron carbonate film growth in itself, the corrosion film is delaminated and a well adherent and protective siderite layer is unable to reform. Figure 3-7 depicts such a process in a mixture of CO_2 and H_2S at a superficial liquid velocity of 1m/s and a superficial gas velocity of 3m/s.[162] Although, FILC is seen in more cases involving partial pressures of CO_2 and not H_2S, the degradation type was observed to interchange from FILC to pitting corrosion whenever the H_2S partial pressure was higher than 10 mbar.
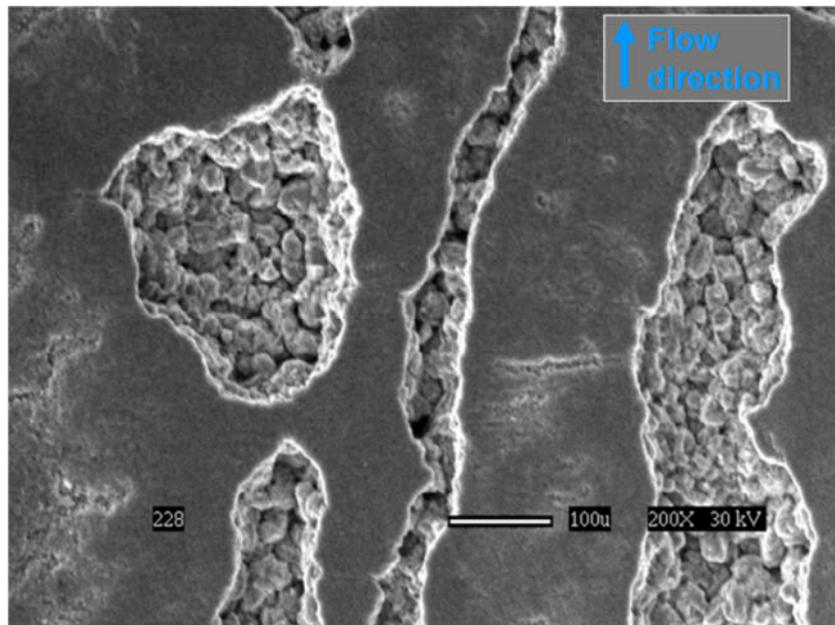
Figure 3-7 Observation of FILC in mild steel coupon after 20 days exposure showing the corrosion film disruption (60°C, 7.7 bar pCO_2, 0.25 mbar pH_2S, pH 6, V_{SG} = 3m/s, V_{SL} = 1m/s)[162]

For many years, such degradation mechanism has rendered corrosion personnel pondering how to determine a criterion for selecting pipelines that should operate in low velocity and a high water cut oil emulsion system in which corrosion mitigation measures need to be implemented. The challenge resides in combining both water cut and velocity parameters into a practical corrosion mitigation model in order to prioritize field pipelines with similar fluid properties.[163]

Flow induced corrosion usually contributes to mesa attack at high flow rates by wearing off the corrosion scales due to liquid vortices and a theoretical model was elaborated in 2000 by Schmitt et al.[164]

3.5 Factors influencing carbon dioxide corrosion

The factors that influence CO_2 corrosion are numerous and known to act interdependently; these can be classified as environmental, physical and metallurgical as shown in Figure 3-8.[165]

Acid gases
- Co_2
- H_2S

Others
- pH buffering
- Initial production conditions
- Trend of water cut
- Corrosion layer
- Scale inhibitor
- Other additives

Operating conditions
- Temperture
- Pressure
- Phase ratios
- Water cut
- Water wetting

Steel
- Composition
- Microstructure

CO$_2$ corrosion

Fluid chemistry
- Water chemistry
- Local/bulk analyses
- In situ-pH
- Organic acids

Hydrodynamics
- Local / bulk flow
- TOLC / BOLC

Inhibition
- Inhibitor efficiency
- Glycol and methanol effect

Hydrocarbon
- Crude oil
- Wax
- Gas condensate

Figure 3-8 Key parameters influencing carbon dioxide corrosion adapted from Kermani et al.[117]

Carbon dioxide source wells may produce from a few percent to almost pure CO_2 both in liquid or vapour phase; for example hot gas well water analysis showed the presence of 223mg/L of dissolved CO_2.[166] When water is present both hydrate formations and corrosion emerge as flow assurance issues but the focus here is on the CO_2 corrosion process.

Due to the large temperature gradient in many gas wells, corrosion mechanisms can change, resulting in different types of corrosion in the same well, whereas oil wells do not exhibit this behaviour. For example, the bottom

temperature of gas wells in Holland was reported to vary between 97°C and 124°C while the minimum and maximum observed pressures were registered at 0.9 and 3 bar respectively.[167]

3.5.1 Water wetting and chemistry

Water is the most common impurity in oil and gas and its contact with the corroding surface is a prerequisite for the degradation process to initiate and as such, the water cut can be detrimental with regard to the corrosion attack initiation and severity. If a water-in-oil emulsion is present, no corrosion will take place while oil-in-water emulsions significantly increase the degradation rate. The transition between these two regimes was shown to occur roughly between a 30 to 40 weight percent of water in oil ratio.[168]

If hydrocarbons associated with water are allowed to be in direct contact between the water and the steel surface via the adsorption of a continuous hydrocarbon film then the corrosion process is greatly reduced. It should be noted that this parameter is directly related to the liquid velocity and the flow regime established in the system but also to the surface area affected especially when Top Of the Line (TOL) or Bottom Of the Line (BOL) corrosion are compared.[169] It was shown that some CO_2 corrosion inhibitors increased the oil wettability of surfaces with ferric corrosion products acting in synergy.[170]

Water chemistry which dictates the brine acidity is also a key influencing factor on carbon dioxide corrosion severity since it directly affects the supersaturation ratios of Fe^{2+}, HCO_3^{2-} and calcium carbonate ($CaCO_3$) which may or may not coexist and affect the stability of iron carbonate films.[171]

Oilfield produced water is usually characterised by a high amount of dissolved salts such as the dissolved chloride ions. These can adversely affect the pH value and controversial effects on the extent of degradation generated in sweet corrosion conditions can be described by either accelerating corrosion reactions or reducing them.[172, 173] Another approach to describe these trends relies on the solution ionic strength and it was shown that localised corrosion only occurs for high concentrations of chlorides ions.[174]

Other divalent ions such as calcium were shown to increase the corrosion rate when abundantly present as seen in Figure 3-9 due to the displacement of ferrous iron required to the precipitation of the protective iron carbonate layer.[175] This is expected since both calcium carbonate and iron carbonate are isostructural and each cation can incorporate into any of the two crystal entities. In fact a mixed metal carbonate crystal $Fe_xCa_yCO_3$ (x+y=1) was

identified on the steel surface when the calcium concentration was above a certain threshold.
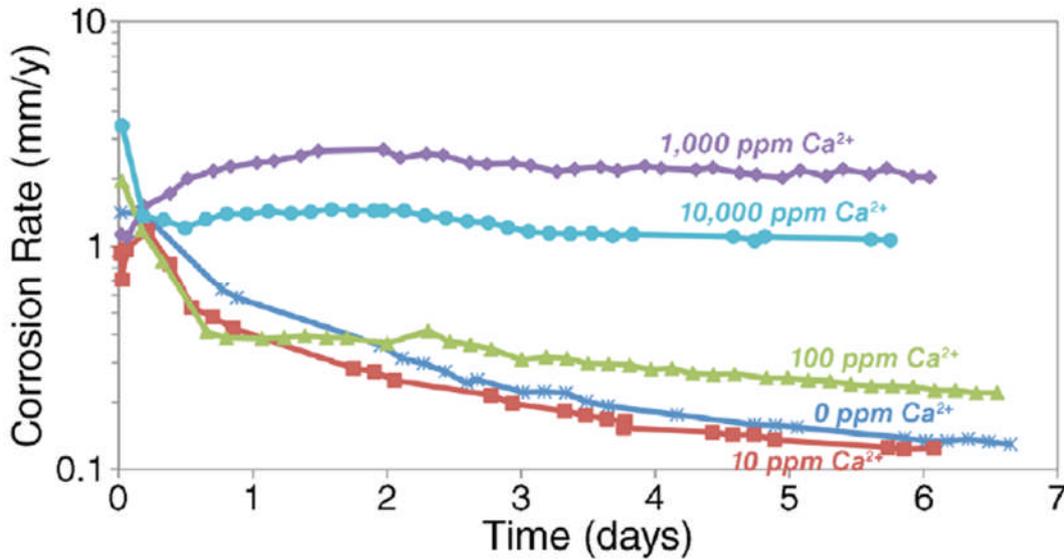
Figure 3-9 Variations of corrosion rate for mild steel exposed to a simulated brine with different initial concentrations of Ca^{2+} at 80°C and pCO_2 of 0.05 MPa with 10 ppm Fe^{2+}.[175]

3.5.2 Carbon dioxide partial pressure

The corrosion reaction is directly dependent on the concentration of carbon dioxide in the aqueous phase and this is linked to the CO_2 partial pressure in the gas that is in equilibrium with this solution. In fact, it is the thermodynamic activity of CO_2 that should be taken into account and not its concentration since this will vary depending on the solution chemistry which is very complex in most scenarios.

The CO_2 activity is directly related to the gas fugacity which, depending on the servicing pressure in the studied structure, can be quite different from the partial pressure and this is especially the case when the operational conditions are exceeding 100 bar and the gas will stop behaving as ideal. CO_2 partial pressure is also of major significance when affecting both the solution pH and the activity of the dissolved species at a predefined temperature.[176]

Under film forming conditions, if the partial pressure of CO_2 is increased than the rate of degradation will also rise and this is explained by the solution pH drop and an increase in the concentration of carbonic acid which is believed to favour the reaction described in Equation 3-11.

On the other hand, when scales have the potential to form, increasing the CO_2 partial pressure will enhance the growth of films with better protective properties mainly due to the increase in the carbonate concentration which is known to be in direct correlation with the partial pressure of carbon dioxide.[177] iron carbonate crystals grown in higher CO_2 partial pressure appeared to have smaller grain sizes with the scale film being more compact as per Figure 3-10.[178]

(a)   (b)   (c)
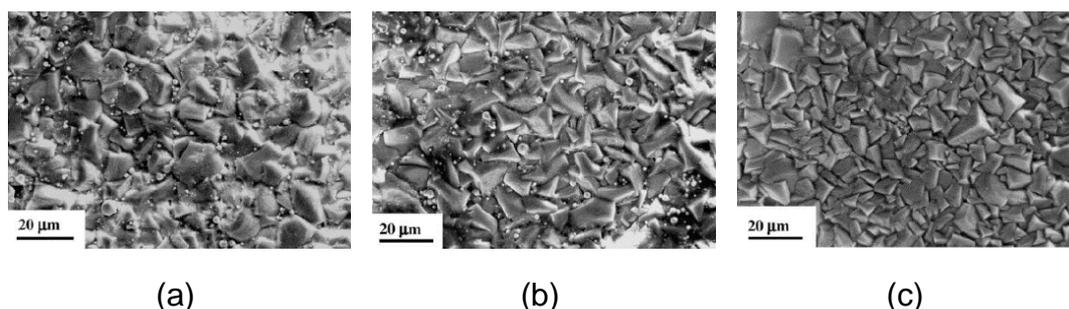
Figure 3-10 Surface morphologies of scale formed at T = 65°C, v = 0 and various CO_2 pressures (a) 0.1 MPa, (b) 0.3 MPa and (c) 1.0 MPa[178]

3.5.3 Effect of temperature

Like its effect on any other chemical reaction, temperature is known to accelerate the kinetics of most chemical and electrochemical processes and affects both the nature and morphology of the corrosion films. In fact, the general corrosion rate has been shown to increase up to temperatures in the 70°C - 90°C range and then starts dropping and this behaviour is directly linked to the build-up of a protective iron carbonate layer.[179]

The temperature is actually responsible for the reduction in the iron carbonate solubility which increases the kinetics of the corrosion film formation as shown in Figure 3-11. Thus, the system interchanges from one where the mass and charge transfer are increasing prior to the scale build-up to one where the rate determining step is controlled by a diffusion process due to the thick barrier introduced by the addition of the $FeCO_3$ layer.[180] With relation to their morphology, the iron carbonate crystals grown at higher temperatures are smaller in size and the film is more compact. For example crystals grown at 90°C are 1 to 2 μm wide while crystals grown at 80°C are 5 to 10μm as seen in Figure 3-12. Similarly, the scale thickness reduces with temperature and films grown at 80°C are around 20μm thick while the ones grown at 90°C are just 8μm in thickness.[181]
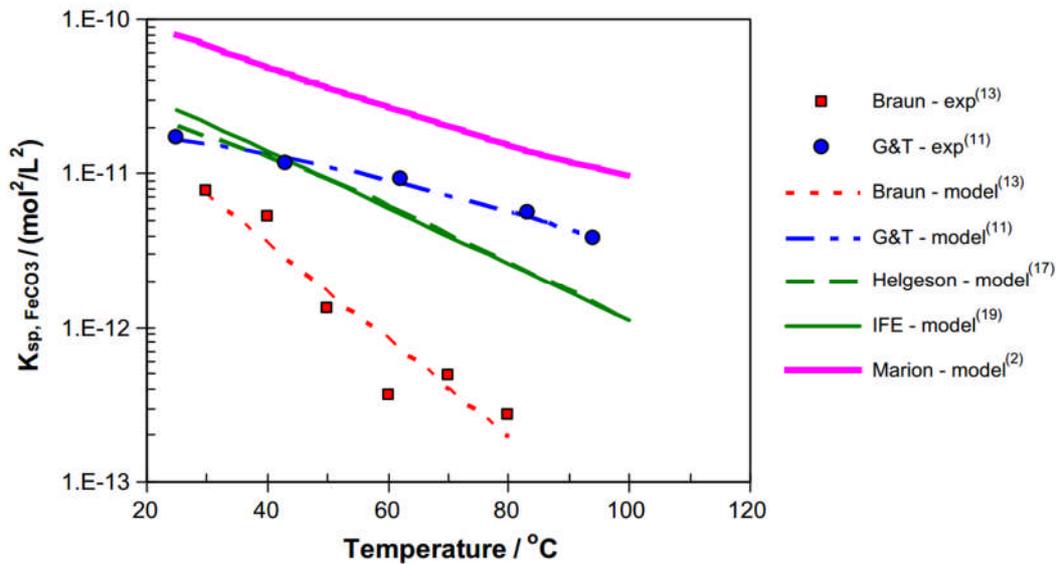
Figure 3-11 The experimental and calculated solubility data of iron carbonate vs. temperatures at an ionic strength equal to zero[182]
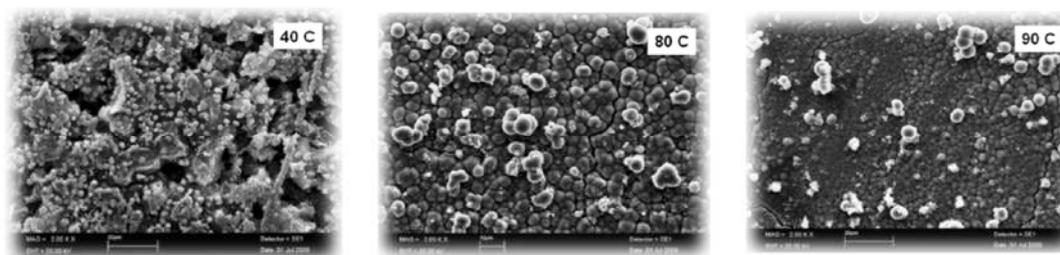
Figure 3-12 Electron microscopy images of the top surface of the final films formed at increasing temperatures from left to right (40°C, 80°C, 90°C and scale bars of 20, 10 and 20 μm respectively) and 0.5 M NaCl[183]

At higher pressures, research in carbon capture and storage have shown that the temperature directly affects the critical water content and thus the general and localized corrosion rates in such transport systems.[184] Moreover, a joint temperature and pH matrix test showed that the optimum conditions for the formation of a dense and thick layer of iron carbonate on an X70 grade steel were 85°C and a pH of 6.5 at which the corrosion rates were seen to be a their minimum.[185]

3.5.4 Effect of pH

The pH can directly affect the corrosion reaction electrochemistry by enhancing some types of cathodic behaviours; as such, at a pH lower than 4 and with the excess of hydrogen ions, the H^+ reduction is shown to dominate

the cathodic part of the reaction but also to be sensitive to flow. When the solution is shifted to a more basic environment with a pH higher than 5 units then the dissolved carbon dioxide dictates the cathodic reactions evolution which means that the reduction of the carbonic acid dominates the cathodic reaction.[186]

The main effect of the pH is linked to its modification of the $FeCO_3$ solubility which is seen to drop by a factor of one hundred when the pH is shifted by just one unit between 5 and 6. This allows a faster growth of more protective scales that safeguards the underlying steel as shown in Figure 3-13.[187] As a result, the formation of a very protective pseudo-passive layer, which is just 1 micrometre thick, have been referenced by Li et al.[188] These effects occurred at relatively lower bulk pH than expected and were correlated to commonly accepted higher local acidity values in the near vicinity of the steel surface. These conditions were made possible by the outer and thicker iron carbonate film which was not directly responsible for the extent of corrosion protection.
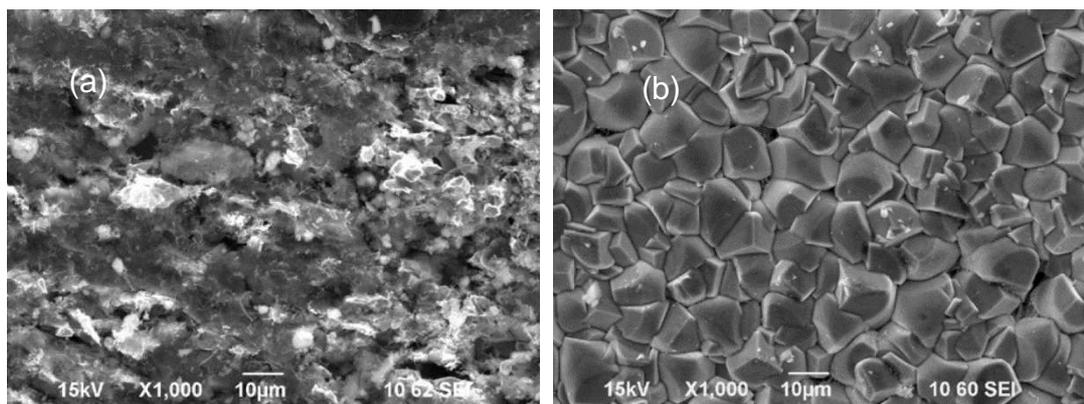
Figure 3-13 SEM Images (a) pH=4 and (b) pH=6 at 80°C, after 20 hours immersion in 1 wt% NaCl[189]

Pessu et al.[152] have described the formation of three different corrosion layers when the pH value was varied between 3.8 to 6.6 then 7.5 at 50°C. At the lower pH, a non-protective and porous iron carbide develops within an amorphous iron carbonate scale. At 6.6, a commonly growing and protective iron carbonate corrosion layer was distinguished while a pseudo-passivating effect was depicted at higher pH.

Such effects had led previously to a corrosion mitigation method termed pH stabilisation and there are several fields currently under operation relying on a full or partial pH stabilisation technique. Such approach can be

complemented with the addition of film forming corrosion inhibitors but only in the case of reduced presence of formation water to limit calcium scaling. These fields have reported no corrosion problems when ferrous iron corrosion was closely monitored.[190]

3.5.5 Effect of the microstructure

The chemical composition, heat treatments and microstructural state can all affect the severity of the sweet corrosion attack; as such, it was shown that adding 3% chromium to the carbon steel can reduce the corrosion rate by ten-fold.[191] If the chromium is further increased to a value as high as 11% then a thin oxide layer, which is highly resistant to sweet corrosion, is formed and passivates the metal surface.

An annealed, quenched and tempered, normalized and banded API 5L X42 carbon steel in 0.5 M NaCl had all their corrosion resistance reducing in the cited order. These variations were attributed to a modification in the cathodic polarisations curves with the quenched and tempered and annealed showing the highest percentage of iron carbonate scale formation as seen in Figure 3-14.[192]
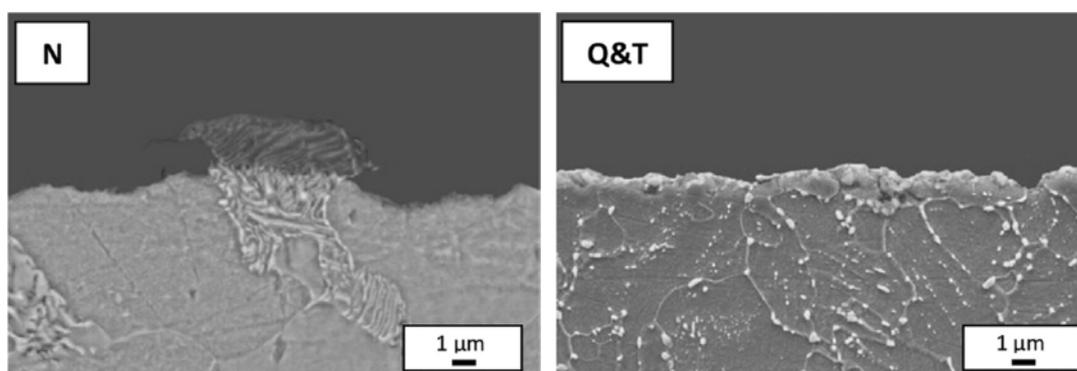
Figure 3-14 SEM observations of the cross-sectional views of the corroded steel surfaces after 6 h of immersion in a 0.5 M NaCl solution saturated with CO_2: Normalized (N) and quenched and tempered (Q&T) samples.[192]

Iron carbide was shown to accelerate the nucleation sites for iron carbonate growth and thus reducing the corrosion rate in a second stage after initial dissolution; this has been studied by comparing a tempered martensite to a ferrite-pearlite microstructure.[193] Similar results were found when normalised carbon steels showed lower ratios of pitting corrosion if compared to quenched and tempered steels and again this was attributed to the fact that

the carbide layers in the more homogeneous normalised steel allow better anchoring for $FeCO_3$ film growth and better protection.[194]

When two influencing effects were combined such as microstructural and water wetting, the competition between the formation of iron carbonate films or chromium rich counterparts have been described when 3Cr alloy steel was used.[195] Hence, higher water content enhanced the formation of the chromium enriched layer which provided better general corrosion mitigation.

Most of the techniques used to study the microstructural effect relied on the description of corrosion inhibitor efficiency for various metallographic steel structures and tried to correlate those to a modification of the corrosion rate.[196] Numerous experiments carried out at higher pressure in autoclaves helped establish a relationship between the distribution of pearlitic bands and localised corrosion but the effects of minor elemental concentrations such as chromium, nickel and molybdenum were more difficult to validate.[197]

Other effects such as hydrodynamics can also impact the degradation process and limiting flowstream velocities have been computed from mini-loop tests where general and localised corrosion or scale formation barriers can be separated.[198]

3.6 CO_2 corrosion: prediction and prevention

Corrosion predictive models are developed for three main reasons: First, they have proven to be a very useful tool that can be used to determine corrosion allowances in order to engineer structures with the minimal but safe design thickness. Secondly, they predict the remaining life of facilities which is generally two to three decades. Finally, they also provide guidance in daily corrosion management such as the amount of corrosion inhibitor to be administered. The prediction models can be classified as both mechanistic and empirical; while a mechanistic model takes the chemical, electrochemical and transport processes into account, an empirical model only starts with some simple empirical correlations. However, both models use data retrieved from laboratory testing and field data for calibration and refinement.[199]

3.6.1 Prediction models for CO_2 corrosion

An industry standard approach has not been published yet in order to compute the internal CO_2 corrosion. Multiple models exist and differ in terms of parameters considered (temperature, flow rate), the type of approach

(mechanistic, empirical) but also the computed influencing factors (corrosion product layers formed such as $FeCO_3$ or Fe_3C).[200]

Empirical models are correlation of measured corrosion rate in mmpy to a number of input variables. The models have empirical parameters which are regressed to corrosion rate data. The principles of the model have no physical meaning. Some of the models are known by name such as the COPRA correlation.[201]

Semi-empirical models are similar to the empirical models since they are fitted to corrosion rate data. They are set up to resemble some of the physical principles of the real system and are not pure correlation. The NORSOK M-506 model is an example and was developed by the Norwegian institute of standards together with the oil company Statoil.[202]

Mechanistic models are chemically mechanistic in the sense that they rely only on chemical relations and the model has not been fitted to experimental corrosion rate measurements. The core of all mechanistic corrosion models is the electrochemical kinetic model and FREECORP is one such example.[203]

A list of those models starting from the basic De Waard et al.[204] system developed in 1975 then revised in 1995 up till Cassandra model in 2001 is detailed by Wang et al.[205] These models were screened for their efficiency and a comparative study established that the computed values started deviating when the temperature exceeds 75°C.[206]

Most models rely on the computation of the acidity in the system which is the key element in assessing the severity of the corrosion damage. The input parameters are the various factors that affect corrosion and those have been described in section 2.4; mainly the water composition, the temperature, the CO_2 partial pressure, $FeCO_3$ and other scale saturation conditions when applicable. Recently, flow regimes have been also incorporated within these prediction models.[207]

The de Waard-Milliams model is the oldest building block for the prediction of CO_2 corrosion, and is represented in Figure 3-15. This monogram has gained wide acceptance and is a good starting point to predict the carbon steel sweet corrosion rate. For example the real corrosion rate with a scale factor of 0.3, a temperature of 120°C and a CO_2 gas pressure of 0.2 bar is equal to the corrosion rate that is read (10mmpy) multiplied by the scale factor (0.3) which corresponds to 3 mmpy.[143]
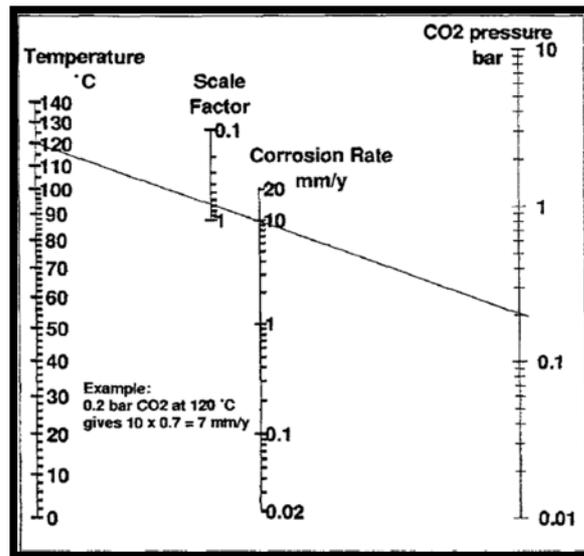
Figure 3-15 Nomogram for CO_2 corrosion rate estimation[204]

This model takes into account the effect of the total pressure, surface layer, temperature, velocity, hydrocarbon presence and glycol additions. Later the model was improved to account for both the effects of flow regimes and the microstructure of the tested specimen. Other models have been published such as Dugstad model[208] (1994), Srinivasan model[209] (1996), Nešić model[210] (1996) and Masamura model[211] (1999). Nyborg review paper published in 2002 discuss the performance of most of these CO_2 corrosion models[212] while a more recent paper details the industry based predictive software for CO_2 corrosion and they have very different approaches in accounting for oil wetting and the effect of protective corrosion films.[199]

Most of these prediction software compute the general corrosion and further research is required in order to adapt those to more localised corrosive events; These are based mostly on mechanistic models that are supplemented by some parametrical studies.[213] With the advances in flow effects calculations and the expanding parametric matrices being validated, many of the CO_2 corrosion models associated with electrolyte flow are no longer empirical and are described by computational methods.[214]

For instance, Nešić's model systematically incorporates most of physical and electrochemical phenomena involved in CO_2 corrosion process. It has considered electrochemical reactions occurring in CO_2-water system while ignoring the impact of diffusion process and formation of preventive scale on the corrosion process.

67

Figure 3-16 shows how this compares with two other models as in the case of the effect of CO_2 partial pressure on the corrosion rate for example.
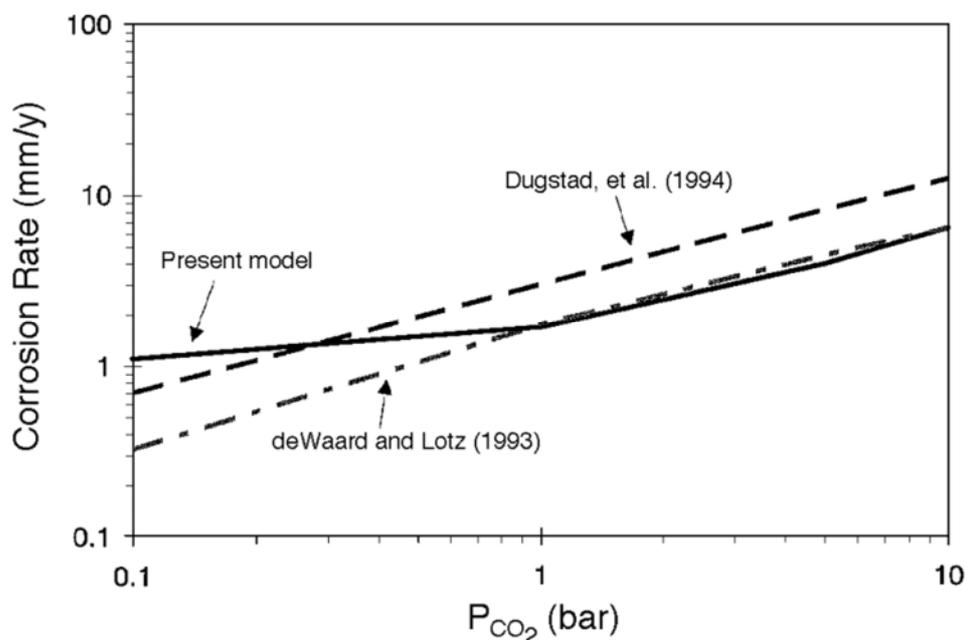
Figure 3-16 Comparison of predicted P_{CO_2} effect on the corrosion rate for the case of a solution at pH 4, T = 20°C, v = 1 m/s, shear stress (т) = 3.1 Pa, diameter pipe = 25 mm , and Reynolds number (Re) = 25,000.[210]

By extending their 1995 corrosion model[215] to account for the formation of iron carbonate layer on steel surface, Dayalan et al.[216] devised a model that incorporates various processes involved in CO_2 corrosion such as electrochemical reactions, chemical reactions, and mass transfer effects.

Nordsveen et al.[133] emphasised the need to incorporate the mass transfer and formation of $FeCO_3$ layer during the model formulation in order to enhance the model accuracy. Thus, the mass transfer mechanism consists of the diffusion of species through the electrolyte and the porous surface film in addition to the migration process due to the electrochemical potential gradients.

Recently, a mechanistic transient model of uniform CO_2/H_2S corrosion of carbon steel has been developed, which accounts for the key processes underlying corrosion. It does not only predict the corrosion rate, but also the surface concentration of all key species involved in the corrosion process.[217]

3.6.2 CO$_2$ corrosion prevention

There exist four main methods commonly implemented in order to mitigate the damages incurred by the sweet corrosion phenomenon. As in most oil and gas production and processing industries, corrosion inhibitors have always been considered the first line of defence against internal corrosion; in CO$_2$ corrosion, the administration of amine, amide or mostly imidazoline-based corrosion inhibitors via batch treatments remains the method of choice but biodegradable additives such as polyamino acids, poly-succinates and polyaspartates have taken their part of the market recently too.[218, 219] Most of the CO$_2$ corrosion inhibitors consist of amphiphilic, surface active molecules with hydrocarbons chains amounting between twelve to eighteen carbons.[220]

Zheludkevich et al.[221] researched anticorrosion coatings with a self-healing effect based on nano-containers impregnated with the adequate corrosion inhibitor and a scheme of such an approach is given in Figure 3-17. Other than mitigating corrosion, some research focuses on monitoring the progress of the corrosion mechanism by itself; as such Palumbo et al.[222] have proposed an anelastic spectroscopy study of iron carbonate scales from CO$_2$ corrosion of steel in order to follow up the protective film build-up and degree of protection via the apparition of corresponding anelastic relaxation peaks.
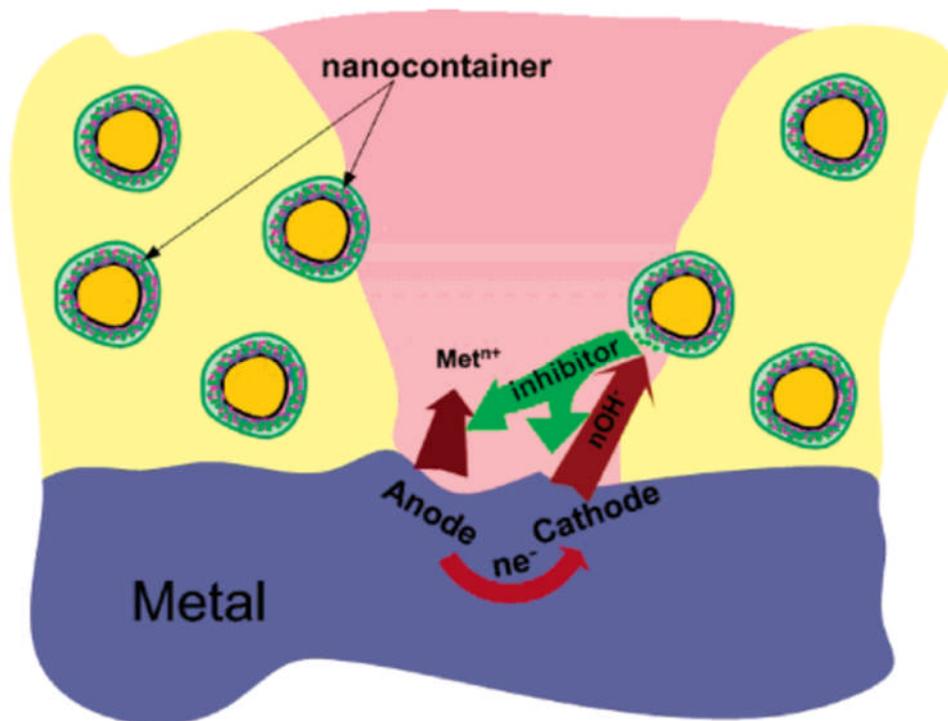
Figure 3-17 Scheme of the controllable release of the inhibitor from the nano-containers and the "smart self-healing" process.[221]

In the specific case of heat condensers and hot wet acid gas pipelines, glycol is added in order to control the hydrates formation and other neutralizing agents aim to raise the pH to a value as high as 6.[223] The use of stainless steel instead of carbon steel can be economical in special cases for well tubing, pipes and pipelines and their composition is selected according to the water salinity and temperature and not the CO_2 partial pressure.[224] Corrosion resistant coatings or claddings are a viable option where organic coatings can be used in pressure vessels in areas where water accumulates.[225]

3.7 Summary of carbon dioxide corrosion

CO_2 corrosion is dominant in various oilfield environments and generally occurs in conjunction with H_2S corrosion in many structures such as production pipelines and drill pipes especially with the implementation of EOR techniques. Whether CO_2 corrosion occurs as a uniform, pitting, mesa or FILC attack, the extent of material degradation is shown to be strongly linked to the formation of iron carbonate films.

As shown in Equation 3-6, the corrosion reaction of carbon steel in the presence of CO_2 leads to the production of the carbonate CO_3^{2-} and ferrous iron Fe^{2+} ionic species in the bulk solution. The availability of these ions strongly determines both the thermodynamics and kinetics of the iron carbonate film formation on the surface of the corroding steel.

The factors affecting CO_2 corrosion detailed in section 3.5 emphasise that the nature, protectiveness, stability, adherence, coverage and chemistry of the deposited iron carbonate films are dependent mainly on the CO_2 partial pressure, the solution pH and the temperature. Depending on the local pH and the ferrous iron concentration, section 3.5.2 has shown that increasing the partial pressure of CO_2 gas is likely to increase the tendency for protective iron carbonate film to form during corrosion of carbon steel. CO_2 partial pressure also influences the threshold for such corrosion films to be formed in terms of affecting the scaling temperature.

Temperatures in excess of 70-90ºC were found to promote iron carbonate films that mitigate CO_2 corrosion, other environmental variables like pH, solution chemistry, and ionic strength may also have some significant influence on the integrity of iron carbonate layers, especially at lower temperatures where the corrosion product is likely to be non-protective.

Beside its effects on formation of $FeCO_3$ corrosion products, the pH is modelled around its influence on H^+ reduction too. Higher pH suppresses the H^+ reduction reaction and thus its contribution to the limiting cathodic current density. Higher pH was also found to reduce the corrosion rate of steel in these conditions. Solution pH between 6 and 7 was revealed to enhance the formation of protective $FeCO_3$ films with corrosion rate lower than 0.1mmpy. At pH values lower than 4, the H^+ reduction reaction contribution to the limiting cathodic current density increases and subsequently increases the corrosion rate. Non-crystalline form or amorphous form of $FeCO_3$ is favoured in these conditions and may become the precursor for pitting corrosion in carbon steel materials.

3.8 Iron carbonate importance in corrosion mitigation

Most of the factors that influence carbon dioxide corrosion, do so with regard to the quality of the corrosion scale product that is covering the steel surface. In fact, during oil and gas transportation via carbon steel pipelines, it is not uncommon for a $FeCO_3$ corrosion product to form on the internal surface of the pipework.

Since the $FeCO_3$ formation process is one of the most important factors governing the corrosion rate, understanding the factors governing the rate of $FeCO_3$ precipitation is an important step in understanding the overall CO_2 corrosion process and this is detailed in the next chapter. Moreover, the present research aims of taking advantage of this naturally forming film and rely on it in order to better protect the steel structure as depicted in Figure 1-11 previously.

The fact that iron carbonate layers have been shown to reduce corrosion rates at increasing temperatures even in top of the line corrosion renders this approach even more interesting. The $FeCO_3$ was shown to fully cover the underlying steel when the surface temperature reaches 45°C as per Figure 3-18. As such, based on the water chemistry calculation and their experimental data, Islam et al.[226] have shown that low supersaturation with long retention times would be able to provide adequate protection on the TOL by forming iron carbonate protective layers.
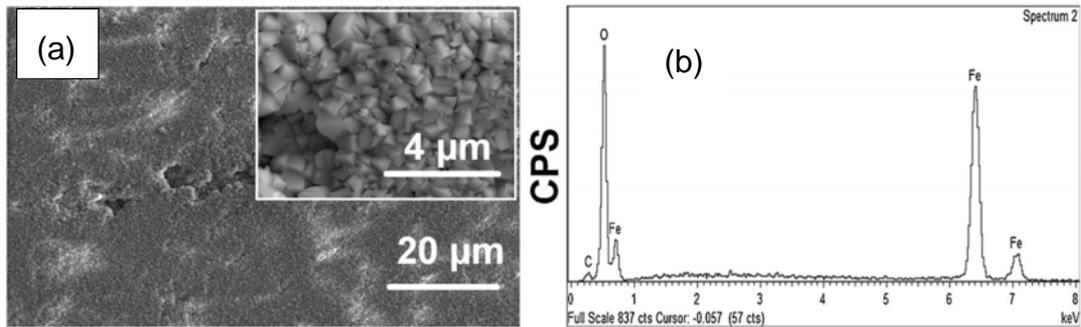
Figure 3-18 SEM images (a) and EDS spectra (b) of 1030 carbon steel samples, with 1200 grit surface finish, after 240 h of exposure at 55°C gas temperature and 45°C surface temperature[226]

Even though the kinetic behaviour of iron carbonate formation at top of the line is different from that at the bottom of the line, both iron carbonate types will be subjected to the same physical, chemical and mechanical disruptive events that renders the reliance of iron carbonate as a corrosion mitigation strategy scarcely researched. These effects are summarised in Figure 3-19 and are discussed in more details in the subsequent chapter in order to better formulate an iron carbonate enhancing strategy.
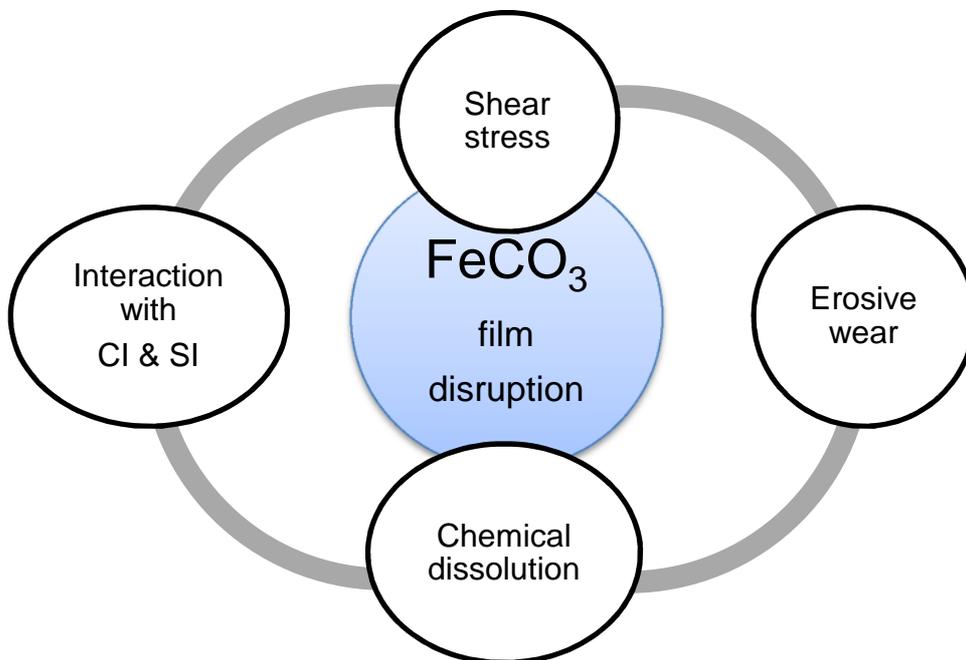
Figure 3-19 Mechanisms known to facilitate FeCO₃ films' removal: shear stress,[227] erosive wear,[228] chemical dissolution,[229] interaction with scale inhibitors (SI),[230] and interactions with corrosion inhibitors (CI).[231]

72

Chapter 4 Iron carbonate

Iron carbonate also known as ferrous carbonate, siderite or chalybite has been referenced in many research fields. It is often encountered in nature as a solid solution containing varying amounts of foreign divalent cations.[232] Siderite is commonly found in hydrothermal veins associated with fluorite, galena and barite and as concretions in shales and sandstones.[233] Environments such as carbonate rich springs, rice fields, marine rocks and the bottom of lakes where volcanic CO_2 is released are known to overgrow with such mineral.[234]

Recently, new discoveries on the microbially-mediated synthesis of iron carbonates in anaerobic conditions have been published in many journals such as Scientific Reports;[235] the described $FeCO_3$ appear to be very similar in their crystal structure to the scale films formed in carbon dioxide corrosion which is described in this chapter.[236] In fact, siderite formation is known to be facilitated by both mesophilic and thermophilic iron reducing bacteria[237] and has been interpreted to be microbially-mediated in many natural environments.[238]

Another iron carbonate derivative, chukanovite, with formula $FeCO_3(OH)_2$ has been recently identified on an iron meteorite as a corrosion product but no similar compound has ever been referenced in nature as shown in Figure 4-1.[239] Siderite has also been identified in other extra-terrestrial materials, such as interplanetary dust particles.[240]

(a)   (b)
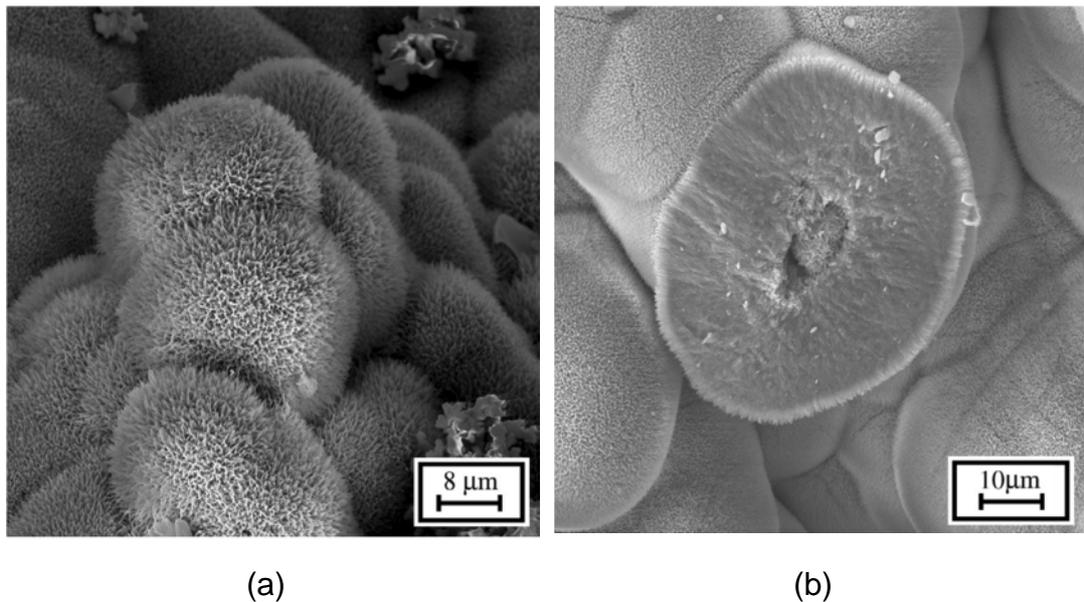
Figure 4-1 SEM images of aggregates of chukanovite shown as (a) a spherulitic crust and (b) as a section of a spherulite.[239]

4.1 Mechanisms: Iron carbonate as a protective film

Ferrous carbonate is a stable compound and the predominant corrosion product layer in steel-CO_2 systems. The precipitation of iron carbonate is one of the most important factors governing the corrosion rate of the underlying steel. The formed film is actually capable of reducing the corrosion kinetics by over an order of magnitude; this is accomplished because $FeCO_3$ acts as a diffusion barrier to the known electrochemically active species but also by blocking the potentially active sites on the steel surface.[241]

The barrier properties augment when the iron carbonate layer thickens and becomes more compact with time (Figure 4-2). Usually a few micrometres of a well compact and adherent layer are sufficient to drastically reduce the CR up to one hundredfold. $FeCO_3$ itself can be soluble and the conditions favouring its formation are elevated temperature and increased pH as is the case in bicarbonate-bearing waters. Turbulence is often the critical factor in the production or retention of the protective iron carbonate film. Corrosion will therefore occur where the protective $FeCO_3$ film has detached or did not grow and it occurs usually in a uniform fashion over the exposed metal surface.
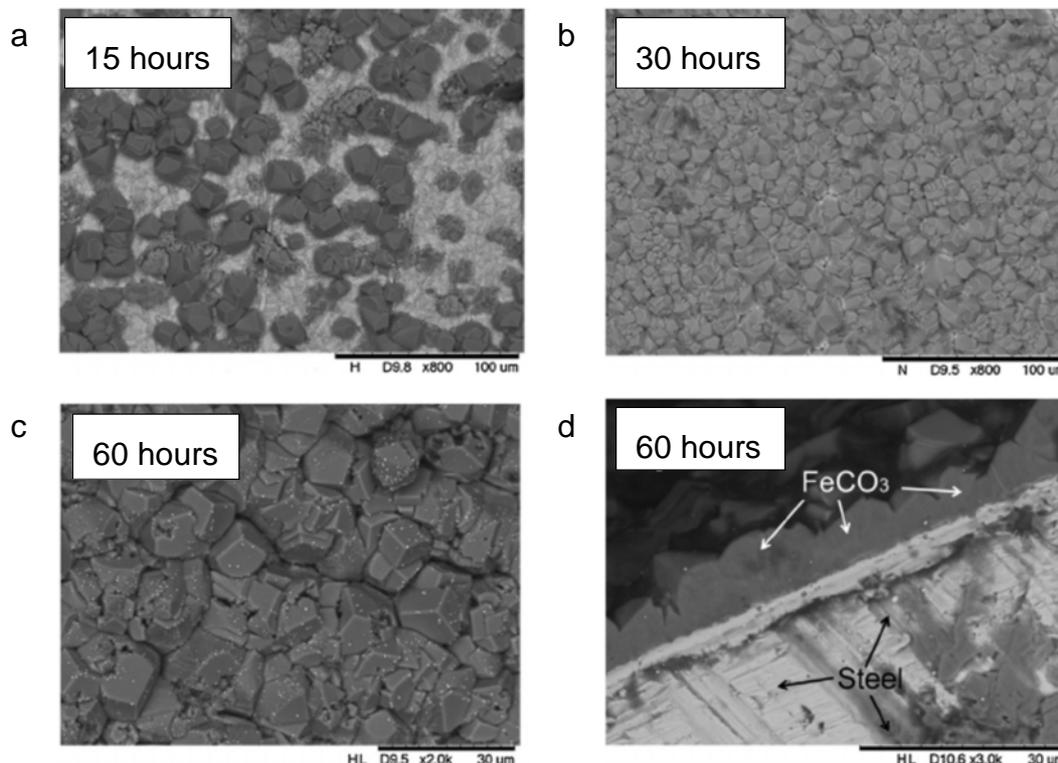
Figure 4-2 SEM photos of the $FeCO_3$ layer formed on API 5L X52 surface at different immersion times: 15 h (a), 30 h (b), 60 h (c) and 60 h (d, shown in cross-section).[242]

Typically, both Fe_3C and $FeCO_3$ scales form concomitantly and only when $FeCO_3$ is the major phase in contact with the underlying steel that it is shown to be protective.[117] Moreover, Sun et al.[231] showed that a higher supersaturation of ferrous iron and bicarbonate ions is required for the $FeCO_3$ scale to form faster (20 to 40 hours) and for the CR to decrease more rapidly.

This was also discussed by Hua et al.[243] who showed that the precipitation of compact $FeCO_3$ stacked platelets appear to be responsible for reducing the susceptibility of the surface to localised corrosion as depicted by the 2 µm thick film in region B which is more protective with regard to localised corrosion than the 6µm thick film developing within 48 hours in region A (Figure 4-3).

(a)

(b)   (c)
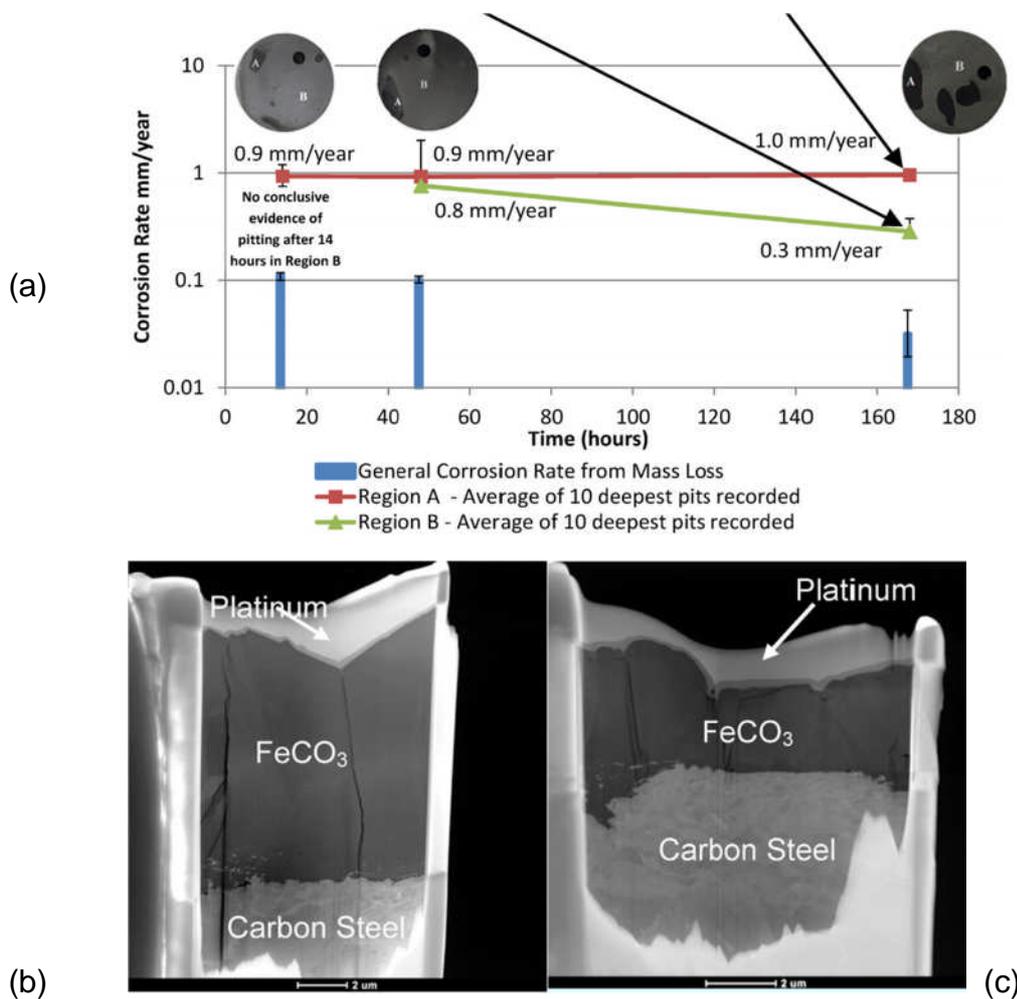
Figure 4-3 Average corrosion rates of carbon steel from water-saturated CO_2 conditions at 35°C and 80 bar for different time periods presented in conjunction with the average pitting ratesalong with the a high-angle annular dark-field TEM image of region A (b) and the high-angle annular dark-field TEM image of region B (c).[243]

Usually iron carbonate develops as a duplex or double layer structure over the underlying carbon steel surface especially for tests carried out for periods of time exceeding 7 days as shown in Figure 4-4.[244] The inner layer is known to be predominantly responsible for the corrosion protection due to its lower porosity when compared to the outer layer. The major role of the protective layer is to hinder the access of the water and the chloride ions to the underlying metal surface thus reducing the corrosion degradation mechanism and this is usually followed by a shift of the potential to higher anodic values.[245]
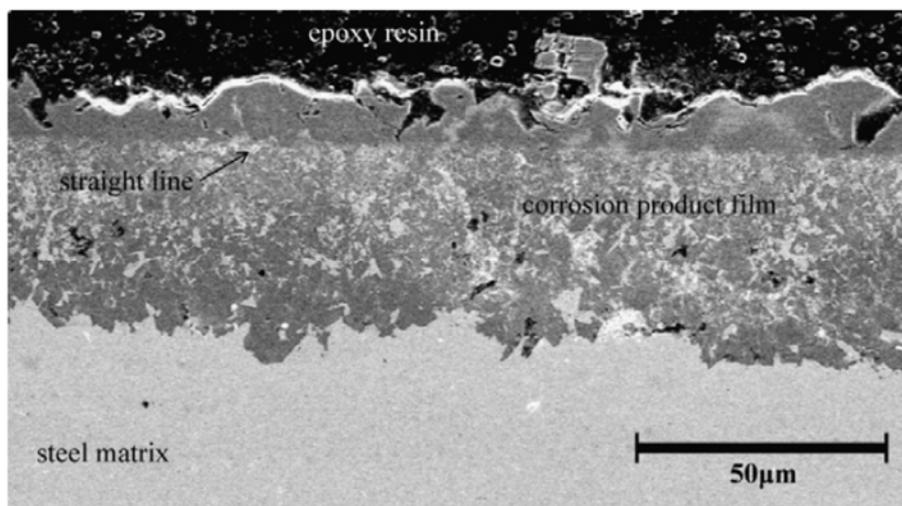
Figure 4-4 Cross-sectional morphology of the corrosion product films (Temperature=75°C, test duration=240 hours, 10 bar CO_2, pH 6.5).[244]

It has also been reported that there is another very thin "passive" layer formed together with the $FeCO_3$ layer, which can provide further protection form corrosion.[246]

4.2 Iron carbonate structure and morphology

4.2.1 FeCO$_3$ structure

Iron carbonate is often considered as the scale counterpart of calcium carbonate ($CaCO_3$) where the iron atom replaces the calcium. It has an empirical formula of $FeCO_3$ and a molecular weight of 115.86 gram molecular. One possible presentation of the crystal form of iron carbonate, which is classified as trigonal hexagonal scalenohedral, is shown in Figure 4-5a.[247] The hexagonal spacing or repeating unit is around half a nanometre (nm) in diameter since 1nm is equal to 10 angstroms (A°) thus siderite and calcite form both rhombohedral crystals at room temperature.[248]
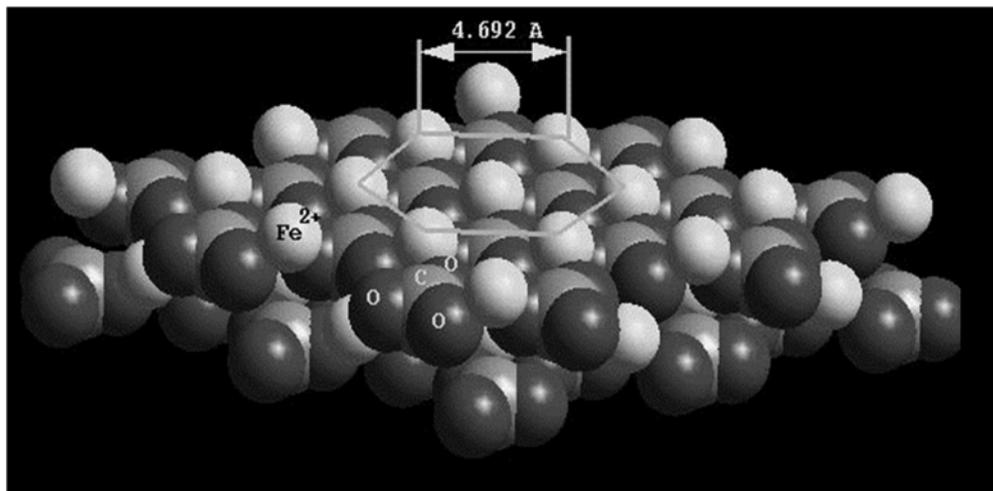
(a)
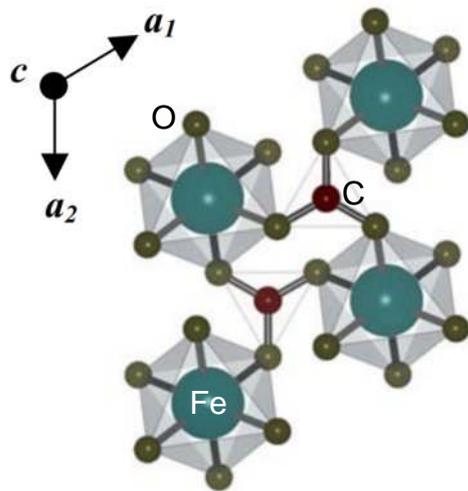
(b)
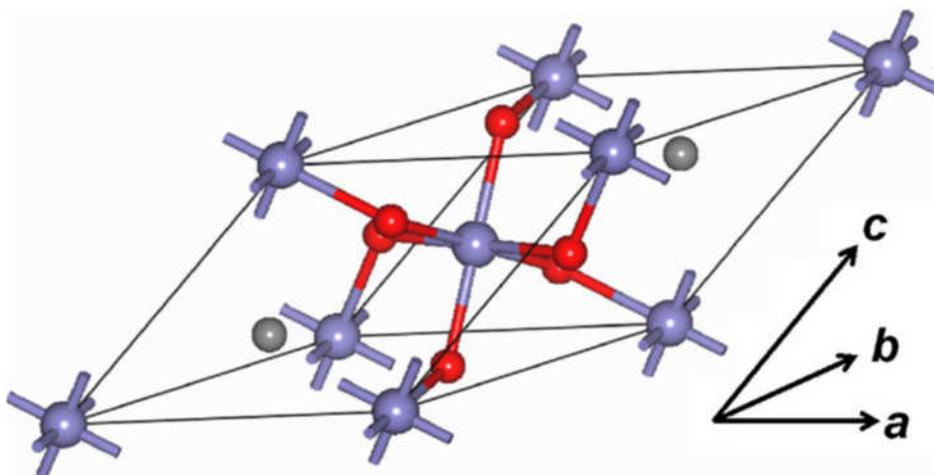
(c)

Figure 4-5 Iron carbonate [001] possible Miller plane (a) and a part of the crystal structure on $FeCO_3$ viewed parallel to the c axis (b) with the primitive unit cell of $FeCO_3$ consisting of two formula units. Blue, grey, and red spheres represent Fe, C, and O atoms, respectively in (c)

77

Crystalline iron carbonate embraces the calcite structure R$\bar{3}$c with crystals of known forms and Miller planes [110], [$\bar{1}\bar{1}$1] or [001] while amorphous iron carbonate can also evolve depending on the environmental conditions.[249] The [001] Miller plane is known to be the most stable for the $FeCO_3$ crystalline structure which involves the breaking of the weakest bonds by definition.

The [011] Miller plane was drawn originally for the purpose of modelling the interaction of the $FeCO_3$ crystal with different types of corrosion inhibitors and to compute both their adsorption and binding energy. It is important to get hold of the crystal structure of $FeCO_3$ in order to better understand the steric effects that will be created once the siderite film will be in contact with other added chemicals that are commonly used as flow assurance additives in the oil and gas industry.

Corner-sharing FeO_6 octahedra and CO_3 trigonal units build the crystal structure of $FeCO_3$-siderite. The ferrous iron is in 6-coordination with oxygen atoms of the carbonate group. The carbon atoms lie in the plane surrounded by its three neighbouring oxygen atoms, that is normal to the c axis (Figure 4-5 b).[250] With u designating the atomic internal structural parameter, the $FeCO_3$ crystallographic unit cell consists of two molecular formula units with two iron atoms. As shown in Figure 4-5c, Fe, C and O atoms are located at the cell origin (0 0 0), the position of (0 0 1/4) and (u 0 1/4) in a hexagonal setting, respectively.[251]

Using dual copper Cu $K_{\alpha1+2}$ radiation, Figure 4-6 shows the diffraction pattern of a synthetic iron carbonate powder; these XRD diffraction peaks were indexed to the R-3c [167] space group, and the lattice parameters are given by a=4.6916 Å, b=4.6916 Å, and c=15.3796 Å with accordance to the ICSD reference code: 01–083–1764[252] and coinciding with iron carbonate crystals grown in corrosion tests.

Iron carbonate could also develop as a non-crystalline phase and recent publications allude to the identification of amorphous or nanocrystalline siderite, which could form initially, and offer a degree of protection to the underlying substrate.[253] From the broad spectral response under Raman and knowledge from the literature, it was speculated that the dark nanoaggregates observed in regions devoid of μm-sized iron carbonate crystals are likely amorphous $FeCO_3$, albeit oxidised. Such nanocrystalline aggregates of $FeCO_3$ are believed to be precursor sites, onto which incoming growth units of $FeCO_3$ become attached, during the development of crystalline siderite.[254]
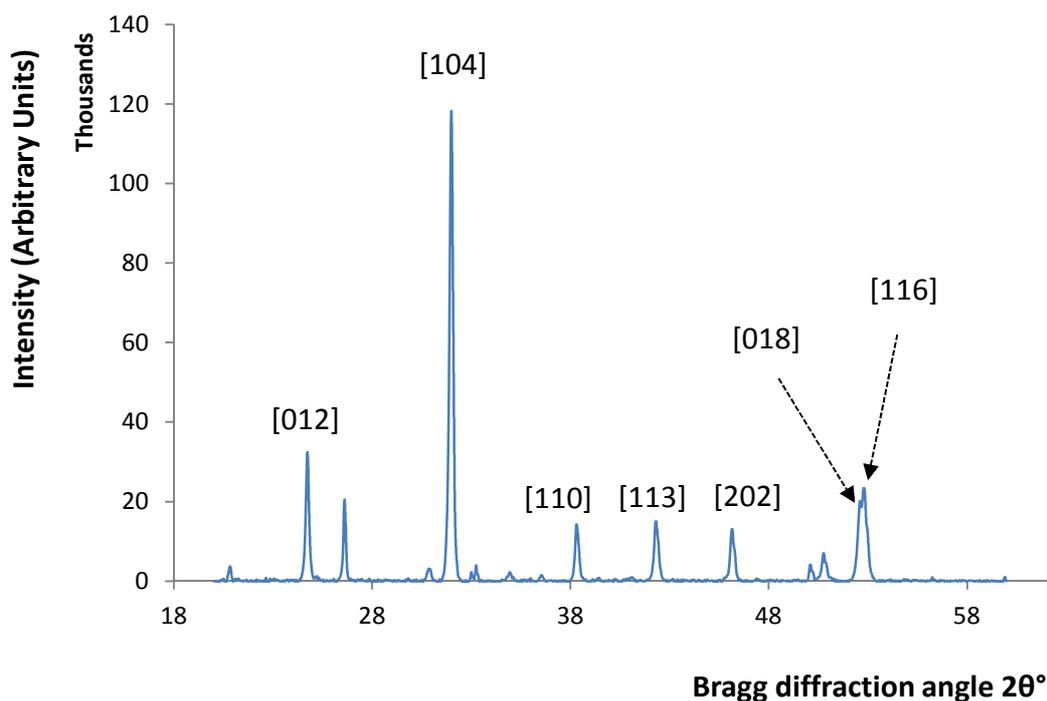
Figure 4-6 XRD pattern for synthetic siderite showing the respective Miller indices

The above described structure leads to a molecule which a volume equal to 293.53 $Å^3$ and the details of the peak list showing highest intensities and respective Miller indices are given in Table 4-1.

Table 4-1 Peak list for $FeCO_3$ (λ= 1.540598 Å, temperature= 25±1°C)

Layer spacing d (Å)	Relative intensity (I) %	Miller indices (hkl)	Diffraction angle 2θ (°)
3.593	25	012	24.76
2.795	100	104	32.00
2.346	20	110	38.34
2.134	20	113	42.32
1.9650	20	202	46.16
1.7382	30	018	52.61
1.7315	35	116	52.83

4.2.2 FeCO$_3$ morphology

Many papers have discussed the formation of iron carbonate as a multi-layer system. For example Li et al.[255] have discovered a three layer corrosion film validated via EIS data. Others have characterised a two layer system at temperatures as high as 160°C as compared to the one-layered system obtained at 100°C on low alloy API P110 carbon steel; the inner layer being thin and compact while the external layer is thick and loose.[256] Figure 4-7 shows a cross-section of such corrosion products separated by the resin and steel with a non-uniform thickness ranging from 50 to 100 microns.
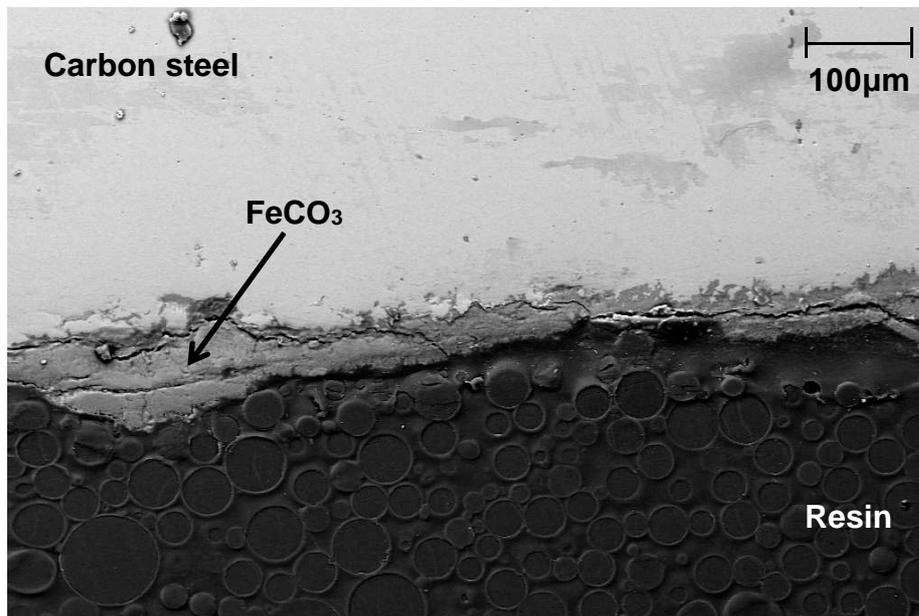
Figure 4-7 SEM micrograph of FeCO$_3$ cross-sections grown at 60°C, 3.5% NaCl, pH6.6, 0.8 bar CO$_{2\,pp}$, 50ppm Fe^{2+} for 98 hours.

Iron carbonate films are known to reduce corrosion kinetics by acting as diffusion barriers to electrochemically-active species and by blocking active sites on the steel surface and their morphology plays the most important role when determining the efficiency of such a process.[257] The magnitude of the corrosion rate and the occurrence or not of localized corrosion is determined by the nucleation, growth, morphology and stability of this scale layer. The morphology of the developed FeCO$_3$ corrosion product is known to be detrimental in corrosion protection efficiency. As such, a compact, tight film usually protects the steel while a loose, poorly adherent film does not.[258]

When studying the oxygen effect on CO_2 corrosion, localized corrosion was observed although the general corrosion rates were relatively low. This was explained by the degradation of the iron carbonate crystals and formation of iron oxides such as magnetite, hematite and goethite along with $FeCO_3$ within the corrosion products.[259]

More recently, a Mott-Schottky electrochemical analysis has established a link between protective and non-protective iron carbonate films which behave as n-type or p-type semi-conductor respectively and these semiconducting properties of the $FeCO_3$ film are determined by the anion species in the formation solution.[260]

4.3 Thermodynamics of iron carbonate film precipitation

Ferrous carbonate precipitation kinetics affect the iron and carbonate concentrations of many natural and industrial systems. In fact, iron carbonate scaling tendency is defined as the ratio between the precipitation and corrosion flux; the precipitation kinetics of $FeCO_3$ film depends on the concentration of both iron and carbonate ions. The formation and growth of these scales are accelerated at higher pH and temperature values. Mathematical models have been developed for the simulation of scale formation of iron carbonate by thermodynamic and electrochemical means.[261]

4.3.1 General features

Siderite precipitation process follows in principle two steps of nucleation and particle growth in a similar way to $CaCO_3$.[262] The dominant step will therefore determine the final film morphology and ultimate protection level. It was shown however that the nucleation rate is only important when homogeneous crystallisation processes are present and this does not correspond to iron carbonate growing on carbon steel. $FeCO_3$ scale precipitation on mild steel is known to be a heterogeneous in nature and the crystal growth largely dominates the overall kinetic process.[263]

Equation 4-1 Iron carbonate relative supersaturation

$$S_R = \frac{Q - Q_{eq}}{K_{sp}} = S - 1$$

81

In fact, the precipitation process starts with heterogeneous nucleation due to the numerous imperfections on the steel surface which generate the required nucleation sites. This is followed by the crystal growth step which essentially limits the precipitation rate. These two processes are related to the relative supersaturation (S_R) expressed as per Equation 4-1 where Q is the concentration of the solute, Q_{eq} is the equilibrium solubility and S is the iron carbonate supersaturation.

As such, nucleation rate is supposed to increase exponentially with the relative supersaturation whilst the particle growth varies linearly with S_R. Therefore, particle growth should be dominant at low relative supersaturation and nucleation mechanisms prevail when high relative supersaturation values are of order leading to nanocrystalline and sometimes even amorphous films.[253]

Lasaga[264] identified four key regions for the crystal nucleation and growth adapted to a generic salt AB as a function of the concentrations of its ionic components [A+] and [B-] as per Figure 4-8. Yang[265] adapted these components to the case of iron carbonate crystal growth.
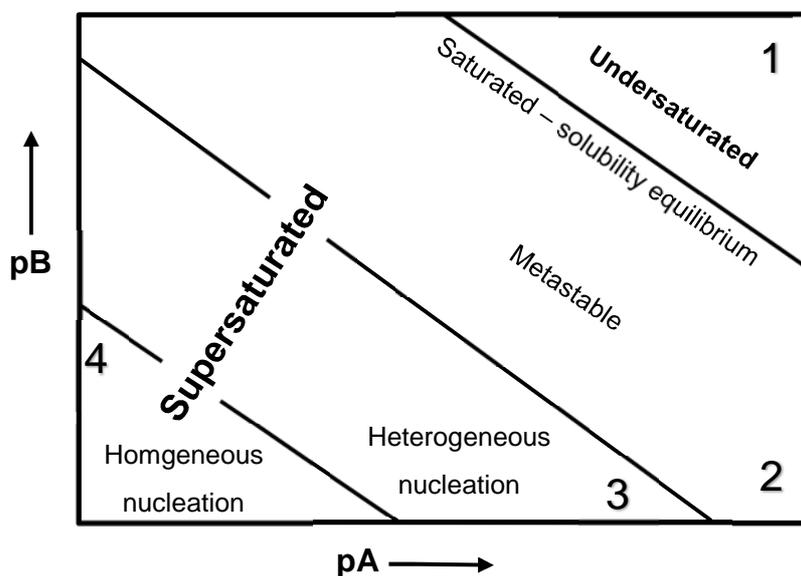
Figure 4-8 Different stability areas for the electrolyte $A_\alpha B_\beta$ in a pA-pB diagram; the areas being separated by straight lines corresponding to constant values of the ionic product $[A]^\alpha[B]^\beta$ and having slope = α/β while the coordinate pA=-log[A] (moles/liter) and pH is analogous.[264]

In region 1, dissolution is of order as the system is undersaturated or S<1; consequently, no crystal growth occurs. Region 2 is characterised by a metastable or seeded growth; the system is supersaturated but the growth only progresses on seed crystals and the system remains supersaturated for a considerable period of time in the absence of seed crystals.[266] In region 3, heterogeneous nucleation dominates, which is a nucleation process induced by the presence of foreign particles which is followed by the crystal growth step. Region 4 is dominated by homogeneous nucleation and growth with saturation being further increased allowing a spontaneous and homogeneous nucleation and growth to initiate.

The standard enthalpy of formation of $FeCO_3$ ($\Delta_f H°$) is given at 298.15 °K and 1 bar by Equation 4-2 relating it to the standard state Gibbs energy ($\Delta_f G°$) and the standard state entropy (S°). The indication of temperature and pressure are a must since there exist a defined standard state for every temperature and pressure in the system. Generally, a compound forms when the free enthalpy is negative.[267]

Equation 4-2 Siderite standard enthalpy of formation

$$\Delta_f H^{\circ}_{FeCO_3} = \Delta_f G^{\circ}_{FeCO_3} + T.\Delta_f S^{\circ}_{FeCO_3}$$

Table 4-2 Standard state thermodynamic properties of siderite

Authors	Year	$\Delta_f H°$, kJ.mol^{-1}	$\Delta_f G°$, kJ.mol^{-1}	S°, J.mol^{-1}.K^{-1}	C°$_p$, J.mol^{-1}.K^{-1}
Anderson	1934			92.9	82.35
Kelley & Anderson	1935	-747.60	-673.75	92.9	82.09
Holland	1990	-761.18	-688.04	95.50	82.27
Robie & Hemingway	1995	-755.9	-682.8	95.47	82.27
Preis & Gamsjäger	2002	-752.0	-678.9	95.47	

Since the values used for the Fe^{2+} properties vary greatly between the different study groups, it is difficult to specify a standard enthalpy recommended value. Standard state properties of siderite from known study

groups are summarized in Table 4-2.[268] They vary between as high as -747.6 to as low as -761.18 kJ.mol^{-1} as detailed by the study carried out by Holland et al.[269]

There are two equations that govern the determination of the solubility constant of siderite which are termed solubility product (sp) and pressure solubility product (psp) as seen from Equation 4-3 and Equation 4-4 respectively.

Equation 4-3 Solubility product determination

$$FeCO_3(s) \leftrightharpoons Fe^{2+} + CO_3^{2-}$$
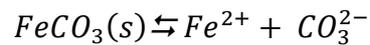
Equation 4-4 Pressure solubility product determination

$$FeCO_3(s) + 2H^+ \leftrightharpoons Fe^{2+} + CO_2(g) + H_2O\ (l)$$
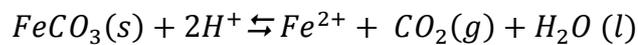
It should be noted that these equilibrium constants have not been computed very accurately until recently due to a multitude of controversies; mainly the choice of the most appropriate speciation scheme. The inclusion of new unusual compounds was undertaken with the aim of explaining the supersaturation phenomena which should not be confused or used in the calculations of equilibrium data. It is important to highlight the fact that, once the siderite film is established, the superstation is of no more importance and the scale can persist and protect in such conditions.

4.3.2 Iron carbonate precipitation

The precipitation kinetics plays a determinant role in the growth of the siderite scale. Iron carbonate is believed to precipitate via a one stage reaction with carbonates or a two stage reaction with bicarbonates.

Equation 4-5 One-stage FeCO₃ precipitation pathway

$$Fe^{2+} + CO_3^{2-} \rightarrow FeCO_3$$
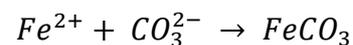
Equation 4-6 Two-stage FeCO₃ precipitation pathway

$$Fe^{2+} + 2HCO_3^- \rightarrow Fe(HCO_3)_2$$

$$Fe(HCO_3)_2 \rightarrow FeCO_3 + CO_2 + H_2O$$
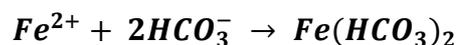
The iron-carbonate precipitation rate depends on many factors as the supersaturation (S), the thermodynamic solubility product (K_{sp}) in mol²/dm⁶ as per Equation 4-9 where $[Fe^{2+}]_{eq}$ and $[CO_3^{2-}]_{eq}$ are the concentrations of the species at equilibria expressed in mol/dm³, the temperature (T) and the surface to volume ratio (Surf/V) as shown in the Equation 4-7.[270] A direct assumption from such relation is that iron carbonate dissolves at lower temperatures while thicker scales build up when the temperature is increased.

Equation 4-7 FeCO₃ precipitation rate

$$R_{FeCO_3} = \frac{Surf}{V} e^{28.2 - \frac{64851}{R.T}} K_{sp}(S-1)$$

Thus, the precipitation rate is a function of temperature as well as species concentration. The supersaturation of iron carbonate is defined as per Equation 4-8 where K_{sp} is evaluated in pure water and is only temperature dependant. Otherwise the solution ionic strength (I) should be taken into account as per Equation 4-9.

Equation 4-8 FeCO₃ Supersaturation

$$S = \frac{[Fe^{2+}][CO_3^{2-}]}{K_{sp}}$$

Equation 4-9 Solubility product constant for iron carbonate[271]

$$K_{sp} = 10^{-59.3498 - 0.041377xT - \frac{2.1963}{T} + 24.5724xlog(T) + 2.518xI^{0.5} - 0.067xI}$$

$$K_{sp} = [Fe^{2+}]_{eq}[CO_3^{2-}]_{eq}$$

The driving force for iron carbonate precipitation is the supersaturation (S) of FeCO₃.[272] Theoretically, iron carbonate film will dissolve for supersaturation values lower than unity which occurs often in the oil and gas with the pH varying between values of 4 to 6. Equilibrium is achieved between precipitation and dissolution for supersaturation value of 1 while the film starts building up for values above unity. In practice, it was shown that only when iron carbonate supersaturation is higher than 10 to 30 units that the corrosion films were proven to activate their protective nature.[273]

Recent studies have shown that the iron carbonate supersaturation corresponding to a given ferrous iron concentration increases by a factor of one hundred every one unit of pH thus increasing the FeCO₃ growth rate.[274]

Furthermore, mass transport conditions appear to greatly increase the growth rate for tests carried out in cylinder and jet impingement apparatus while mass transport effects were shown not to affect the dissolution in the reverse reaction.[275] A schematic of the mass transfer region and mass transfer process at the steel interface is summarized in Figure 4-9 and Figure 4-10 adapted from J. Hernandez et al.[245]
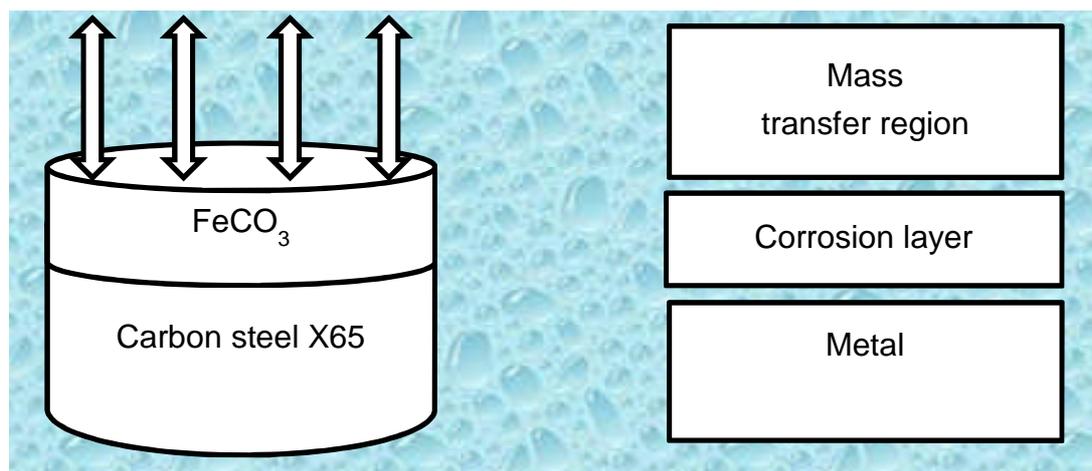
Figure 4-9 Mass transfer region above iron carbonate corrosion layer[245]
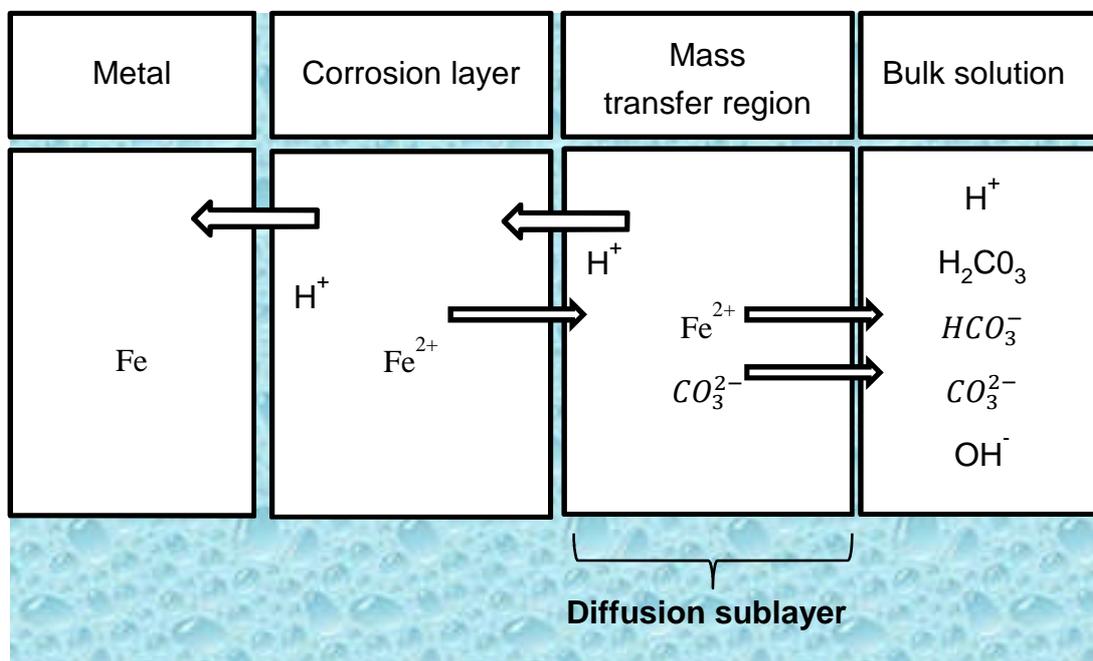
Figure 4-10 Mass transfer process between $FeCO_3$ and electrolytic solution[245]

The unified iron carbonate solubility limit or product in based on literature data and expressed in mol^2/L^2.[182] Some common values of iron carbonate solubility

product have been summarised in Table 4-3 by chronological order and these were determined at temperatures below 90 °C, various ionic strengths and carbon dioxide pressure ranging from 0.01 to 0.93 bars.[276]

It can be seen that the values are scattered especially for the ones computed below 30°C. The solubility product of siderite is known to be around 11.03 ±0.10 for dried crystals and 10.43 ±0.15 for wet crystals thus the reported values varies by a factor of 5.[277]

Table 4-3 Literature values for siderite solubility product

Temperature in °C	$\log_{10} K_{sp^0-FeCO_3}$	Year	References
30	-10.46	1918	Smith et al.[278]
17	-10.12	1970	Singer et al.[279]
20	-10.40	1976	Bardy et al.[280]
50	-11.20	1981	Reiterer et al.[281]
25	-10.60	1984	Robie et al.[282]
30	-11.11	1991	Braun et al.[283]
25	-10.80	1992	Bruno et al.[284]
25	-10.90	2002	Silva et al.[285]

Another important parameter commonly used in the characterisation of the iron carbonate film growth is the scaling tendency defined as the ratio between $FeCO_3$ precipitation rate and the corrosion rate when both are expressed in the same units as per Equation 4-10. $FeCO_3$ films are only viable if the scaling tendency is high enough.[286]

Equation 4-10 Scaling tendency (ST) relationship

$$ST = \frac{R_{FeCO_3}}{CR}$$

The corrosion layer can vary in thickness depending on the environmental conditions between few micrometres to tens of micrometres. This is mainly affected by the temperature and CO_2 partial pressure variations. The reactants such as H_2CO_3, HCO_3^- and H^+ are consumed in the corrosion process at the metal surface while Fe^{2+} and CO_3^{2-} are produced. It was stated that the diffusion of these species throughout the boundary layer cannot take place independently of each other but rather conditionally; local

electroneutrality and equilibrium laws should be satisfied at all times and locations.[287]

A modelling equilibrium relationship commonly used states that the sum of the rates of cathodic reactions should be equal to the rate of mass transfer of reactants which in term is equal to the rate of anodic reaction but also to the rate of mass transfer of products. Both ferrous iron and carbonate concentrations or activities can be computed by using the ion interaction model of Pitzer.[288] Sometimes, the iron carbonate scale will not form until the Fe^{2+} and CO_3^{2-} are 5 to 10 times higher than what is expected from the previously described thermodynamic equations.[289] This supersaturation state before the film formation depends actually on the pH, the surface volume ratio and the temperature.

In water, the iron carbonate kinetics of precipitation were studied using the temperature ramping approach by linearly increasing the temperature to promote nucleation of the scale. For temperatures below 110°C, it was shown that the precipitation rate constants were around 3.5×10^{-12} m/s and 3.5×10^{-11} m/s at 50°C and 75°C respectively.[290]

Iron carbonate dissolution is controlled by both a diffusion and a kinetic mechanism; thus the chemical reaction rate determines the transfer of carbonate ions into solution and diffusion processes determine the removal of ions into the depth of solution. In a recent publication, the $FeCO_3$ specific dissolution rate, in the absence of oxygen, dropped from values around 10^{-6} mol/m^2/sec up to 10^{-8} when the pH was buffered from acidic conditions to a value of 6 then stabilised around 10^{-9} mol/m^2/sec for higher pH values.[291]

The influence of the laminar and turbulent flow transition zone on dissolution kinetics and on the formation of the iron carbonate layer was studied by using a rotating cylinder electrode (RCE) and establishing the velocity boundary layer associated with the electrode rotation velocity. It was found that the maximum CO_2 corrosion rate value is established when the structure of the hydrodynamic boundary layer is between the turbulent and laminar regions. This effect could be associated with the transition region in which micro vortices, where high agitation of the species near the surface are expected to develop, and inhibit the $FeCO_3$ layer precipitation process.[292]

A recent work published in the royal society of chemistry using small and wide angle X-ray scattering beamline of the Australian synchrotron elaborated a

model for CO_2 corrosion of pipeline steels in which corrosion-protective siderite scales nucleate within a thin surface gel of amorphous iron carbonate.

This *in situ* study described a transition layer termed "amorphous ferrous carbonate gel layer" from which the $FeCO_3$ was shown to crystallise in a further step.[293] This correlates the results of another work group that used reduced pair distribution function measurements to establish the formation and transformation of a short range ordered iron carbonate precursor. This precursor was shown to transform to siderite or siderite/chukanovite mixtures within hours and the rate of such transformation was highly dependent on pH.[294]

4.4 Factors influencing the kinetics of iron carbonate

Since the precipitation of $FeCO_3$ is strongly related to the saturation ratio, it's logical to assume that any factor that could influence the solubility product will also affect the nucleation and growth of iron carbonate.[295] Two main factors are discussed hereafter which greatly affect the solubility of iron carbonate and these correspond to the temperature and the solution ionic strength.

4.4.1 Temperature

Several studies have focused on the effect that temperature could have on the iron carbonate solubility product and some of these models are listed in Table 4-4 with T_K and T_C the temperature in degree Kelvin and degree Celsius respectively.

Table 4-4 Summary of $FeCO_3$ solubility product prediction models

Author	Mathematical model
Greenberg and Thomson[296]	$\log(K_{sp}) = -59.2385 - 0.041377\,(T_k)$ $- \dfrac{2.1963}{T_k} + 24.5724\log(T_k)$
Marion et al.[297]	$\log(K_{sp}) = -14.66 + \dfrac{1365.17}{T_k}$
Sun and Nešić[182]	$\log(K_{sp}) = -10.13 - 0.0182\,(T_C)$
Braun[283]	$\log(K_{sp}) = -10.13 - 0.0314\,(T_C)$
Benezeth et al.[298]	$\log(K_{sp}) = 175.568 + 0.0139\,(T_k)$ $- \dfrac{6738.483}{T_k} - 67.898\log(T_k)$

The model by Greenberg and Thomson remains the most common as they conducted numerous tests in order to determine the iron carbonate solubility for temperatures ranging from 25 to 94°C.[295]

4.4.2 Ionic strength

While this parameter is known to affect the solubility parameter, information related to the influence of the ionic strength on $FeCO_3$ solubility remains scarce. Nonetheless, Silva et al.[285] have experimentally investigated the iron carbonate solubility in NaCl solution for ionic strengths ranging from 0.1 to 5.5. This allowed them to propose an equation relating the $FeCO_3$ solubility product (K_{sp}) to the ionic strength (I) expressed in mol/L and being a measure of the dissolved chemical constituents.

Sun[271] adapted the Greenberg and Thomson model by introducing the effect of an ionic strength equal to 0.02 due to the presence of the following ions: $H^+, HCO_3^-, CO_3^{2-}, OH^-$ and Fe^{2+}. The proposed unified equation satisfies both the temperature and ionic strength fluctuations and the variation of the iron carbonate solubility at various temperatures for different ionic strengths is shown in Figure 4-11 and the corresponding relation in Equation 4-11.
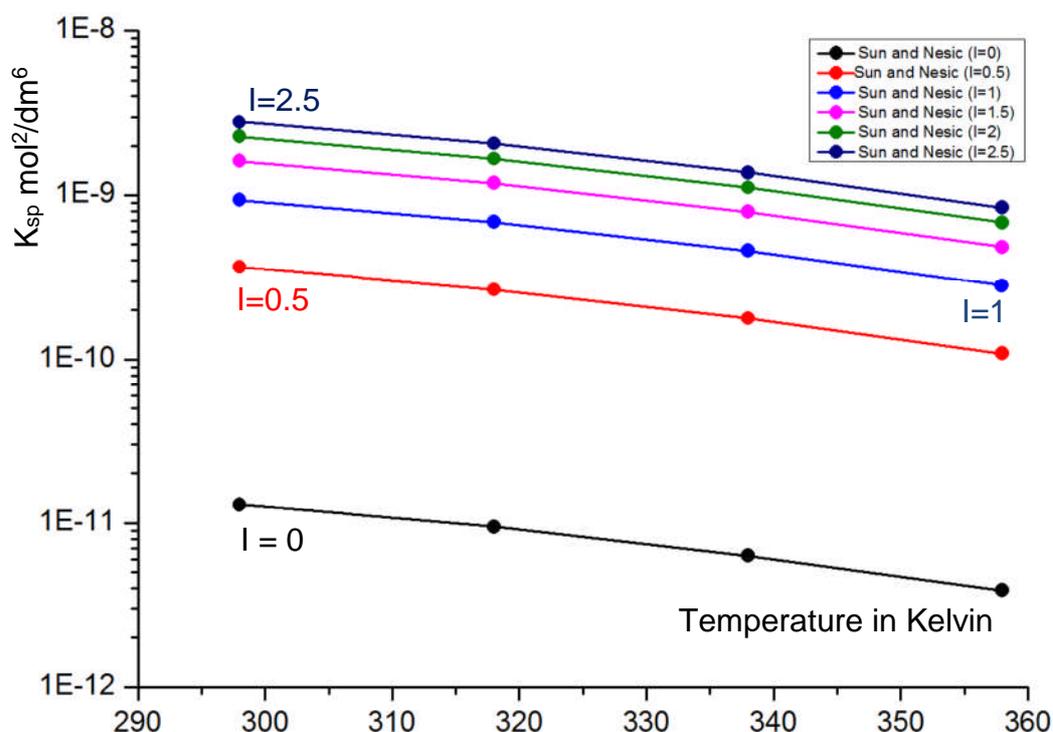
Figure 4-11 Plots of FeCO₃ solubility as a function of temperature for ionic strengths ranging between 0 and 2.5 using the unified equation as defined in the Sun and Nešić model

Equation 4-11 Solubility product as a function of ionic strength

$$log(K_{sp}) = -10.9 + 2.518(I^{0.5}) - 0.657\ (I)$$

4.4.3 Effect of pH and CO₂ partial pressure

Similarly to the parameters affecting CO_2 corrosion in general as described in section 3.5, both the pH and the carbon dioxide partial pressure have an effect on the formation of iron carbonate corrosion scale films. When the pH increases, the iron carbonate solubility is reduced due to the fact that fewer ferrous iron ions are required to exceed the solubility limit thus generating substantial levels of precipitation as shown in Figure 4-12.
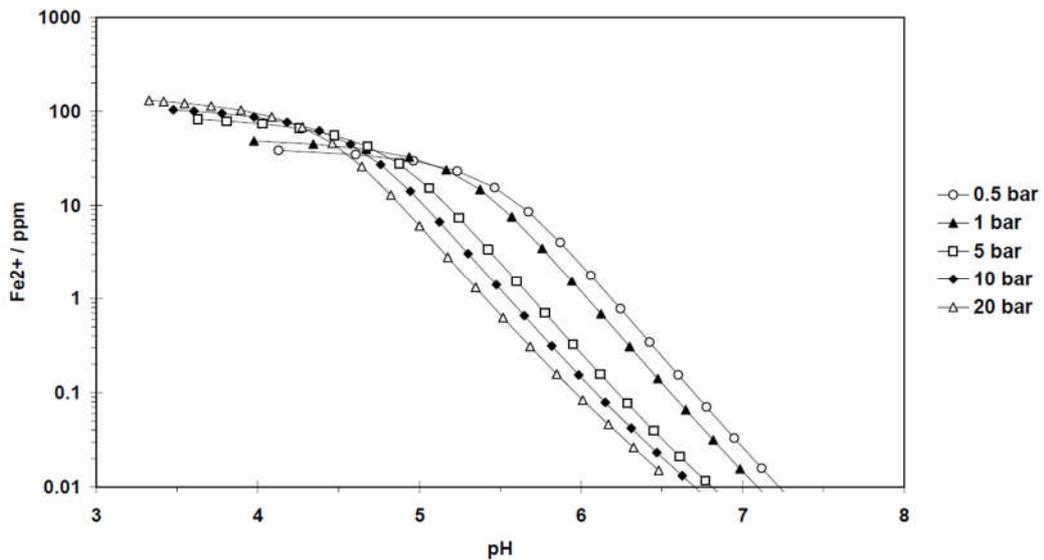
Figure 4-12 Amounts of ferrous iron required to reach FeCO₃ saturation in a 1 wt% NaCl solution as a function of pH for various CO₂ partial pressure adapted from Dugstad et al.[130]

With regard to the gas partial pressure effect, it was shown that an increase in CO_2 partial pressure at a constant pH value will lead to an increase in the bicarbonate concentration which inevitably favours the supersaturation state thus accelerating the iron carbonate precipitation process if the pH value is high enough. The effect of the CO_2 partial pressure on the ferrous iron concentration is rather complex and evolve as per Figure 4-13.
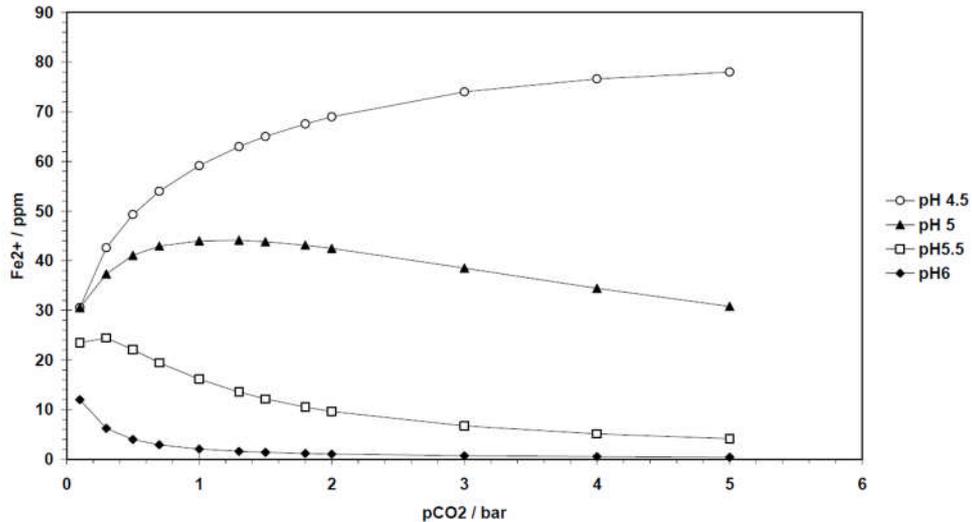
Figure 4-13 The required ferrous ion concentration required to reach iron carbonate saturation plotted as a function of pCO_2 at various pH values in a 3.5% NaCl solution at 60°C adapted from Dugstad et al.[130]

4.5 Iron carbonate physico-chemical properties

4.5.1 Magnetic properties

Iron carbonate was shown to behave as an antiferromagnetic compound; magnetic susceptibility and neutron-diffraction experiments have established such classification along with a low Néel temperature of 38K. All the magnetic moments (Fe^{2+} ion) are ferromagnetically coupled inside a (0001) iron plane, whereas neighbouring planes along the c axis are antiferromagnetically coupled. $FeCO_3$ shows the metamagnetic transition from the antiferromagnetism towards ferromagnetism.[299]

4.5.2 Zeta potential

Zeta potential altering systems can be used in hydraulic fracturing treatments by minimizing proppant flow back, controlling fines migration, enhancing fluid load recovery and inhibiting scale formation such as calcium carbonate.[300]

Zeta potential measurement is a widely used technique to characterize surface charge of solids and adsorption onto them. It is defined as the potential at the shear surface between the stagnant and the mobile part of the electrolyte surrounding a charged particle moving in an electric field.[301] It can be used for the determination of the surface charge of oilfield systems which is useful for the understanding of interactions between various chemicals and formations in the oil industry. As such, the determination of the charge of iron

carbonate layer at various pH can be a first step for understanding or predicting how it would interact with other flow assurance added chemicals such as corrosion and scale inhibitors for instance.

Figure 4-14 shows the variation of the iron carbonate charge as a function of pH in 0.1% NaCl brine solution, at 22°C and at 1 bar carbon dioxide partial pressure.[302] The system IsoElectric Point (IEP) where the zeta potential is equal to zero occurs around a pH of 6 and it coincides with the point of $FeCO_3$ saturation at equilibrium.
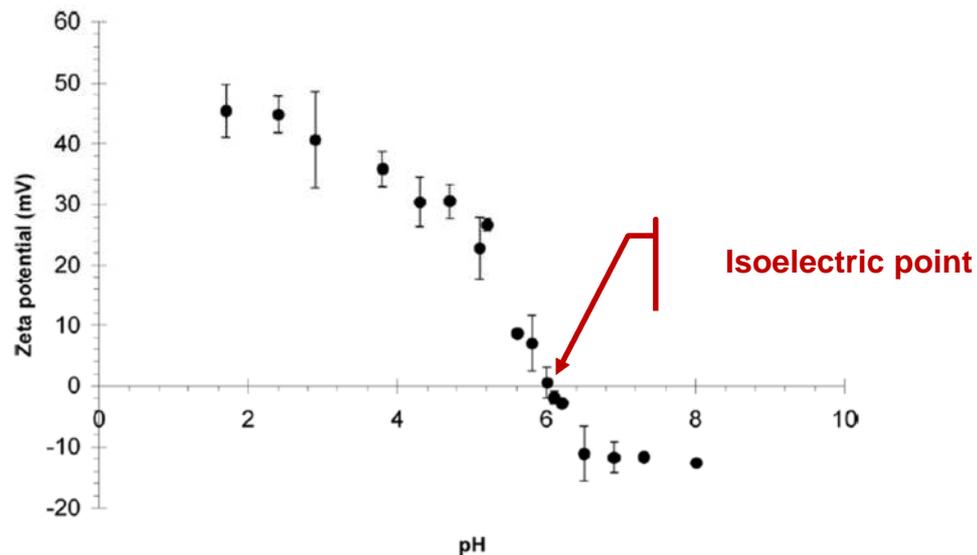
Figure 4-14 Zeta potential (ζ) of iron carbonate[302]

For values of pH higher than 6, the $FeCO_3$ charge is negative and its stability is considered to be insipient due to the low absolute value which is stabilised at 10 mV for pH higher than 6.5. For pH values below the IEP, the zeta potential is positive and shows a moderate colloid stability behaviour with absolute zeta potential values fixed at 45mV for pH values lower than 3.

It is important to note that zeta potential measurements can only be carried out on materials that are mixed in suspensions beforehand; as such iron carbonate suspensions are equilibrated in the presence of an inert electrolyte having a constant ionic strength and under a constant partial pressure.[303]

Novel research in high performance lithium-ion battery anodes have developed $FeCO_3$ via hydrothermal reactions and these were proven to exhibit high reversible capacity and good cycling stability which make them a material

of choice as anodes. This was explained by the outstanding electrochemical performance of the uniform nanosized cube-like $FeCO_3$ structure.[304]

4.5.3 Porosity parameter

Iron carbonate affects the corrosion rate by reducing and virtually sealing its porosity since it reduces greatly the diffusion fluxes of the species which dominate the electrochemical reaction. This was further validated by Glyn F. Kennell et al.[305] while developing a model of carbon dioxide corrosion based on a new electrode kinetic model, along with a full mass transport model that considers electromigration, diffusion, and convection. The proposed model highlights the fact that the porosity of the film is the major factor controlling the corrosion rate after film formation.

But even though the corrosion layers can be few micrometres thick, they do not act as an impermeable barrier if they remain porous. Water and other oxidative species can thus penetrate and interact with the metal surface through micropores and nanopores.[306] The corrosion reaction inevitably induces numerous voids under the precipitated $FeCO_3$ film which inevitably leads to an increased porosity followed by an even higher corrosion rate.

It is convenient to express the morphology of iron carbonate films by the distribution of volumetric porosity (ε) since it is used as the principal parameter affecting transport of species through the $FeCO_3$ layers. The specific porosity of $FeCO_3$ as defined in Equation 4-12 can be measured by gas adsorption; V_{void} is the volume of voids in the iron carbonate film, V_{total} is the total volume of the corrosion product layer which includes the dispersed voids volume and $V_{FeCO_{3(s)}}$ is the volume of the iron carbonate film when it is of crystalline nature.[244]

Equation 4-12 Volumetric porosity of $FeCO_3$

$$\varepsilon = \frac{V_{void}}{V_{total}} = \frac{V_{total} - V_{FeCO_{3(s)}}}{V_{total}} = 1 - \frac{V_{FeCO_3}}{V_{total}}$$

The porosity values shown in Table 4-5 were obtained by running a standard nitrogen adsorption device, using the standard volumetric method by nitrogen adsorption at 77 °K. The environmental conditions were a temperature of 90°C, a pH of 6.5 and a CO_2 partial pressure of 10bar.

Table 4-5 Porosity of $FeCO_3$ and corrosion rate at different times in days[244]

Time (days)	0.6	4	6	8	10
ε (10^{-3})	2.29	1.45	0.809	0.820	1
CR (mmpy)	0.101	0.0382	0.00910	0.00655	0.0123

This data shows clearly a linear relationship between the computed volumetric porosity and corrosion rate thus validating the tight link between the pore distribution in the iron carbonate corrosion layer and its protectiveness with relation to electrochemical corrosion attack.

In another study, the effect of temperature and test duration on the porosity of the $FeCO_3$ corrosion layers was shown; the thickness and porosity of some $FeCO_3$ films grown via the addition of 50ppm of ferrous iron are summarised in Table 4-6 at different reaction times. The environmental conditions were set at temperatures ranging from 60°C to 80°C and a pH of 6.6.[307]

Table 4-6 Thickness and porosity of iron carbonate corrosion products[307]

Temperature (°C)	Reaction time (Hours)	Thickness (µm)	Porosity
60	2.5	1	0.71
	5	2	0.59
70	2.5	2	0.81
	5	4	0.73
	7.5	8	0.78
	10	10	0.78
80	2.5	4	0.79
	5	6	0.79
	7.5	8	0.84
	10	8	0.82
90	2.5	4	0.79
	5	6	0.76

The calculated porosity of the iron carbonate scale under the different test conditions is between 0.6 and 0.85. While the film thickness does not appear to have a direct correlation with regard to the degree of protectiveness, the $FeCO_3$ film density or porosity is essential to accomplish a high mitigation of the corrosion reaction; this is explained by the fact that the diffusion of dissolved CO_2 through the film is the main mechanism providing the reactants to the steel surface in the presence of dense $FeCO_3$ layers.

4.6 Iron carbonate mechanical properties

Under flow conditions and during sweet corrosion process, the morphology and mechanical properties of the iron carbonate film should be investigated in order to determine its protection level. The determination of Young's modulus; adhesion strength and interfacial fracture toughness should lead to such conclusions. Recently, both instrumented indentation and molecular dynamic simulations are used concomitantly in order to better assess and understand the viscoelastic properties of such corrosion products.[308]

4.6.1 Qualitative studies

It is still unclear whether iron carbonate grown in laboratory conditions has the same mechanical properties as the ones developing in real oilfield site conditions and the relevant published research remain scarce.[286] The first attempt to quantify deformation mechanisms for such corrosion products was actually undertaken on iron oxide layers that formed during the same process by Schütze in 1997.[309] These studies were mainly focusing on the scale chemical and mechanical resistance when subjected to high temperature regimes and gave an exhaustive list of all authors who attempted to estimate the magnitude of the stresses arising from the oxide growth as well as those arising from temperature changes.

The effect of both the support material surface roughness and curvatures were also detailed and it was stipulated that when the interface between the growing oxide and the metal show a wavy geometry, then compressive stresses at right angles to the interface will lead to local stresses that could lead to both elastic or plastic scale deformations.[310]

Fracture toughness (K_{Ic}) of some common oxides growing on different substrates were measured when the defect size giving rise to the crack as long as the critical strain(ε_c) and oxide elastic modulus(E_{ox}) were known. These are temperature dependant and summarized in Table 4-7.[311]

Table 4-7 Fracture toughness of some oxide scales[311]

Oxide	Substrate	E_{ox} (10^5 MPa)	ε_c (10^{-3})	K_{Ic} (MPa$\sqrt{m}$)
Fe_3O_4	$2\frac{1}{4}$ Cr 1Mo steel	1.4	1	0.2
Cr_2O_3	Alloy 800	2.5	0.9-5	0.4-2.2
Al_2O_3	18 Cr 0.8Al steel	3.4	0.8-1.6	0.3-1.0
NiO	Ni 99.2	3.15	2.5-7.5	2.0-6.0

Methods for measuring and characterizing the damage behaviour in oxide scales were also detailed such as optical techniques, resonance frequency methods and acoustic emission analysis along with methodologies for assessing the adhesive bond between the oxide scale and the metallic substrate. It was concluded that the mechanical damage caused to the protective scales could be caused by extremely small strains when high temperature alloys are tested.[312]

Most of the earlier attempts in determining the mechanical properties of siderite remained more qualitative in nature as with Palacios' work in 1991.[313] Two distinctive $FeCO_3$ layers were identified using XRD and SEM techniques and those showed different porosities and adhesive properties; it was therefore assumed that the breakdown mechanism of such corrosion layers forming on API N-80 steels is mainly due to their brittleness. Both the mechanisms of pitting through the siderite scale and the process of the iron carbonate film removal in itself were detailed in diagrams but with no further quantitative analysis.

The first time when fracture mechanical properties of $FeCO_3$ scales were assessed goes back to 1996 and this was accomplished by Schmitt et al.[314] who compared available fracture mechanical data with experimental results in what was presented as a failure mode diagram. This diagram showed different regimes termed carbonate yield, brittle spalling or elastic breakdown depending on the strain values and scale thicknesses. The main conclusion was again just qualitative and hints to the fact that intrinsic stresses are the primordial cause to the destruction and spalling of the siderite scales.

Similarly, Nešić and Lunde provided a more detailed insight of the iron carbonate film removal in two-phase flow when studies were conducted on carbon steel in a flow loop apparatus. The results were still only qualitative and siderite scales were categorised as both protective or not and that was

deduced from both electrochemical studies and cross-section micrographs of the scale under the SEM.[315]

4.6.2 Quantitative studies

It was only in 1999 and with the work advancement of Schmitt group again that first fracture mechanical data such as the Young's modulus, fracture stress, fracture strain, internal stress, intrinsic stress and adhesion were published.[159]

These studies were carried out on manganese steels with different microstructures and mechanical data was collected via the four-point loading test technique on scales with thicknesses ranging between 2 and 100 µm. The previous failure mode diagram published in 1996 was thus complemented with newly registered fracture strain data plotted against the film thicknesses while pull-off adhesion tests with piston glued to the scales allowed for the adherence computation between the scales and the steel coupons. It was concluded that the theoretically computed fracture mechanical data corresponds well to the experimental values and some of those are summarised in Table 4-8; a critical scale thickness allowing for the fracture stress to initiate was also estimated in the same study.

Table 4-8 Fracture mechanical data of scales from CO_2 corrosion[159]

Parameter	Estimated	Measured
Young's modulus [GPa]	150	125
Fracture stain [10^{-3}]	9.33	1.8 to 5.6
Adhesion [MPa]	----	8.4 to 18.3
Limiting scale thickness [10^{-6} m]	1.46	

The developed failure mode diagram for iron carbonate corrosion products schematised as per Figure 4-15 is based on the developed failure mode diagram for iron carbonate corrosion products with spalling boundaries for effective surface fracture energies of 100%, 50% and 20% of the estimated ideal value as described in Schmitt et al.[314] paper back in 1996 plotted with the measured fracture strain data computed in the paper published in 1999 by the same group.[316]

Schmitt's findings in 1999 confirmed Palacios conclusions back in 1991 since they also showed a direct link between both the $FeCO_3$ adhesive and cohesive

properties and the microstructure of the underlying sample which chemical composition and further heat treatments could greatly affect the $FeCO_3$ mechanical behaviour.

Ongoing research on the manner and degree to which carbon is being stored within the deep earth have allowed the development of studies of some possible solid phases that might sequester carbon at depth such as iron carbonate. As such, by using techniques such as infrared spectroscopy and high-pressure X-ray diffraction, Santillán and Williams found that the crystal structure of $FeCO_3$ is stable up to 50 GPa at room temperature.[317]
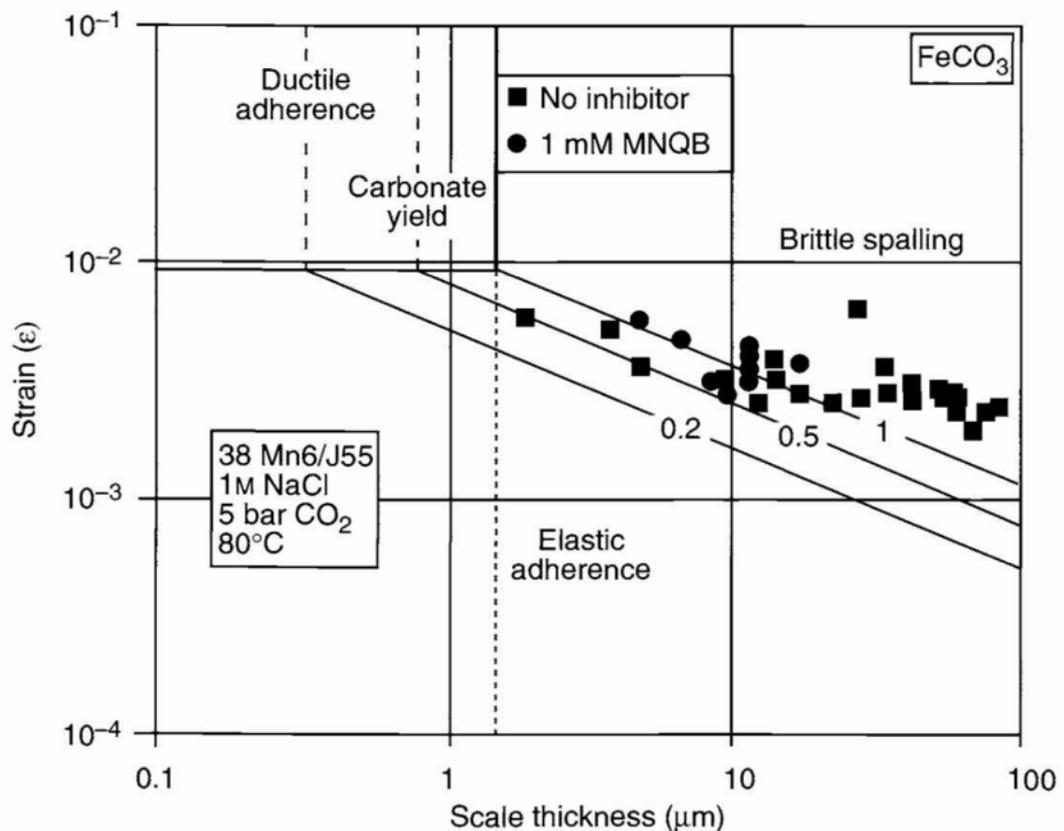
Figure 4-15 Failure mode diagram for $FeCO_3$ scales[159]

4.6.3 Commonly researched mechanical parameters

4.6.3.1 Young's modulus

Young's modulus values for scales commonly encountered in CO_2 corrosion are around 100 GPa on average as per Figure 4-16.

The scale's Young's modulus (E) is expressed in GPa and is extracted from the loading-displacement curve obtained through nano-indentation tests as per Equation 4-13. A_c represents the scale contact area over the steel

substrate and is expressed in m² while S corresponds to the contact stiffness with units of N/m.

Equation 4-13 Equation used for calculating the Young's modulus

$$E = \frac{\sqrt{\pi}}{2\sqrt{A_c}} S$$
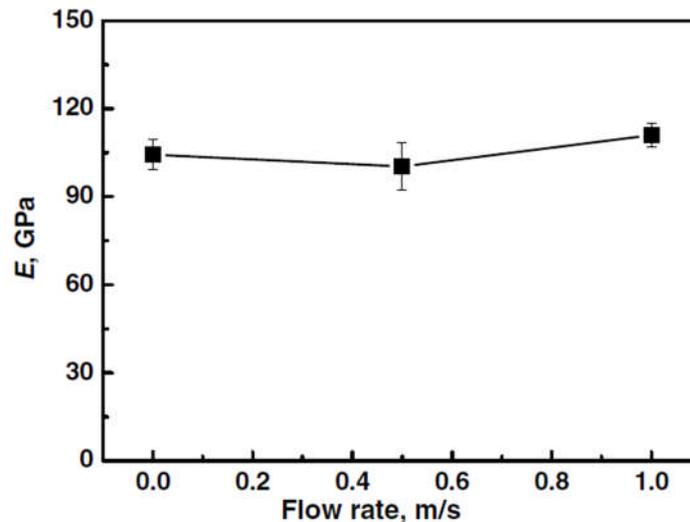
Figure 4-16 Variation of Young's modulus of scale with flow rate.[178]

4.6.3.2 Fracture toughness

This mechanical property can be used in order to determine the resistance of bulk materials to defects such as crack propagations. If the corrosion scales formed during sweet corrosion have low fracture toughness values then it will be easier for scale cracking to develop.[178]

Both nano-indentation and Vickers' indentation techniques are mostly suitable for bulk materials. In order to apply such approaches on a scale surface, the latter should be at least several micrometres thick in order for the plastic deformation of the substrate not to resist the growth of the radial crack; otherwise the observed fracture toughness will be higher than the effective one.

The information available in the literature regarding K_{IC} values for the inter-granular and/or intra-granular brittle fracture of $FeCO_3$ films is limited and inconsistent. In fact, K_{IC} values are not easy to determine due to the micro-

inhomogeneity of their structures; this is explained by the fact that $FeCO_3$ shows polycrystalline single or multilayer structure, porosity, non-uniform flaw distribution, and the presence of non-corroded carbide residues. Paolinelli et al.[318] found that spontaneous fracture can occur in films with porosities as low as 0.1 to 0.2 when the defect length was as small as 10 μm.

Vickers' indentation allows the calculation of the fracture toughness of the corrosion scale (K_{Ic}) following Equation 4-14 if the test is carried out on the film cross-section. E is the Young's modulus as defined in Equation 4-13, F is the applied load in Newton (N), H corresponds to hardness in GPa and c is derived from the total length of the crack expressed as 2c and the coefficient α equals 0.04.

Equation 4-14 Determination of fracture toughness

$$K_{Ic} = \alpha \sqrt{\frac{E}{H} \frac{F}{c^{3/2}}}$$
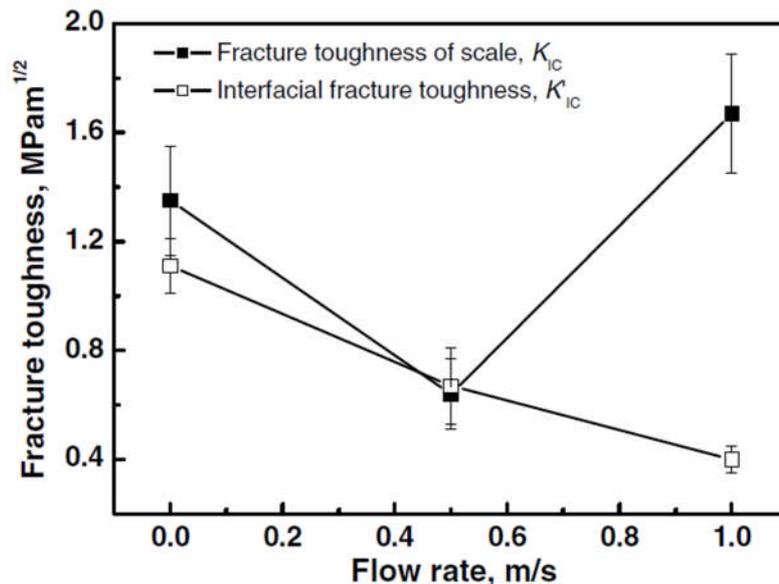
Figure 4-17 Variation of fracture toughness with flow rate.[178]

Fracture toughness values for scales commonly encountered in CO_2 corrosion are around 1.4 MP am$^{0.5}$ on average as seen in Figure 4-17.

4.6.3.3 Interfacial fracture toughness

This is a measurement of crack propagation resistance at the interface and adhesion-strength of the scale to steel. The method and its calculation

equations were based on the properties of soft coatings on hard substrates and they are also measured via basic indentation tests. The interfacial fracture toughness between the scale and the substrate allows the determination of the scale delamination. The drawback of such methods is inherent to the CO_2 corrosion scale products themselves due to their porous and inhomogeneous structure and the zigzag interface between them and the steel substrate which limits both the indentation crack initiation and propagation.

The interfacial fracture toughness K'$_{Ic}$ calculated between the scale and the substrate follows Equation 4-15 and this is done using an edged notched specimen during a tensile test.

Equation 4-15 Interfacial fracture toughness relation

$$K'_{Ic} = f \, \frac{P}{B \, b} \, \sqrt{a \, \pi}$$

Where $f = 1.12 - 0.23 \frac{a}{b} + 10.6 \left(\frac{a}{b}\right)^2 - 21.7 \left(\frac{a}{b}\right)^3 + 30.4 \left(\frac{a}{b}\right)^4$ and P represents the applied load in Newton (N). The length of a single edge notch is given by the parameter a expressed in metres (m) while b corresponds to the width of the used sample also expressed in metres. Finally B is the specimen thickness with in metres too.

4.6.3.4 Adhesion strength

Corrosion scales usually have an adhesion to the underlying steel averaged to 2 MPa as shown in Figure 4-18. The adherence and thickness of the siderite scale is mainly affected by the microstructure of the underlying metal. Uniaxial tension tests allow the determination of the adhesion strength between the scale and the steel surface by following Equation 4-16 where $\overline{\sigma_{bi}}$ represents the valid adhesion strength, F$_i$ the fracture load and A correspond to the surface of the $FeCO_3$ scale which is covering the underlying steel.

When the thickness and density of the iron carbonate scale increases, it becomes prone to amplified inner stress. This stress varies slowly during the early stages of scale formation but rises much more quickly after the first 40 hours. This is why experiments should be held for long periods such as 240 hours in order to assess how easy it is to crack the scale with the increased inner stresses induced. It should be noted that the protectiveness from corrosion attack does not depend on the siderite film thickness but on its structure and morphology.
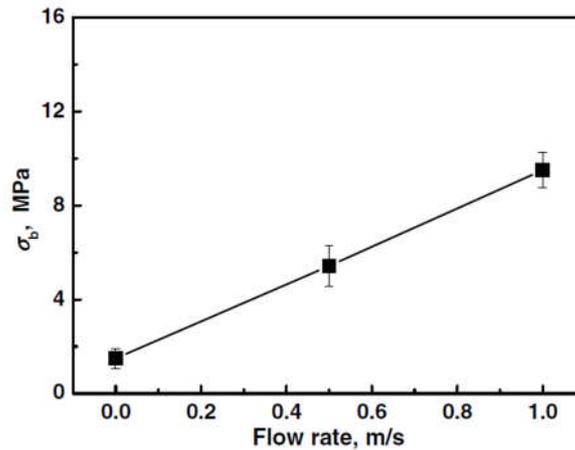
Figure 4-18 Variation of adhesive strength between scale and substrate with flow rate.[178]

Equation 4-16 Adhesion strength determination

$$\overline{\sigma_{b\iota}} = \frac{F_i}{A}$$

Lopez et al.[319] publication in 2003 remains the most detailed review paper on the effect that the specimen microstructure could have on the adhesion force between the growing $FeCO_3$ corrosion film and the top surface of the steel sample. Two main contradictory studies are highlighted where the presence of the pearlitic structure seems to favour the growth of well-adherent $FeCO_3$ films as shown by Palacios et al.[313] in 1991 and confirmed by Schmitt et al.[314] in 1996.

However, it was also shown that a martensitic-bainitic microstructure obtained via quenching and tempering results in a better adherent corrosion products as suggested by Dugstad et al.[320] in 2001. The microstructure of the steel, not only influences the adhesion of the growing films, but it also affects their morphology and the proportion of the various chemical compounds present such as iron oxide passivating formations.

4.6.4 Film breakdown mechanisms

It is well recognised that complete or partial removal of protective films can cause severe uniform or localised corrosion, respectively and thus a better understanding of such mechanism could prove vital for a better corrosion mitigation.[198, 321] Two independent mechanisms can be responsible for $FeCO_3$ film disruption in an undisturbed single-phase flow: mechanical removal by hydrodynamic forces and chemical removal by dissolution but it was also shown that a synergistic effect can be occurring between both.[322]

Chemical dissolution is mainly related to a higher acidity or drop in pH; it was shown that this mechanism was mass transfer controlled when tests were carried out in turbulent single phase flow cells where the pH was changed between 3 and 6.1.[323] The severity of the dissolution was directly correlated to the solution acidity.

The morphology of such change was only partial and selective film removal was observed showing a multitude of open pores. These appear first on the top film layer which is crystalline and dissolution-resistant, which inevitably leads to a more porous, dissolution-susceptible inner layer and severe further dissolution.

When mechanical removals are of order, it is still debated whether, in turbulent flow, the hydrodynamic wall-shear stress can mechanically remove a protective iron carbonate layer formed on mild steel in a carbon dioxide corrosion environment.

Schmitt et al.[324] introduced the terminology of "freak waves" which develop in the near wall region of a flow system and assumed that these could possibly contain large enough energy to remove $FeCO_3$ layers. Recently, a single-phase water flow and a wide range of gas-liquid flow regimes have been studied in order to accurately measure wall shear stress and the effect that this could have on the delamination of iron carbonate films.

With the highest value of the stresses not exceeding 10^2 Pa in an atmospheric pressure flow systems and required forces of the order of 10^7 Pa to remove an iron carbonate precipitate from its steel surface, it could be concluded that wall shear stress in multiphase flow lines is not sufficient to damage $FeCO_3$ layers.[325]

This can be described as a step forward in this research field since the use of the lateral force from the AFM tip (Figure 4-19) seems to replicate the field conditions better than the tensile tests developed in earlier publications.[227]

Another property which could prove vital for the protectiveness of the iron carbonate film is its resistivity to erosion. Using a direct impingement geometry flow loop, it was shown that iron carbonates formed at 65°C were thicker and more resistant to erosion wear when compared to their scale counterpart grown at 88°C.[228]
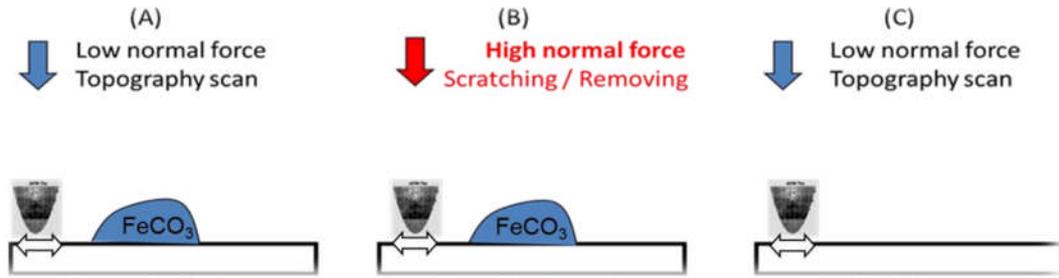
Figure 4-19 A three-step procedure for imaging and removing $FeCO_3$ crystals from the steel surface.[325]

4.7 Iron carbonate film interactions

One possible outcome of this research would be the possibility of providing a viable and economical alternative to the excessive use of corrosion inhibitors in the oilfield industries by enhancing the naturally grown iron carbonate corrosion layers via the addition of silicon-based nanofillers. But in case these nanofillers and flow-assurance additives are to be used concomitantly, a basic understanding of the behaviour of the iron carbonate film when both corrosion and/or scale inhibitors are present seems vital.

4.7.1 Interactions with corrosion inhibitors

Many studies have tried to show whether or not a pre-existing corrosion scale such as iron carbonate film is required for the corrosion inhibitors to adsorb to the specimen surface. Depending on the testing conditions, the presence of such corrosion by-products could be beneficial sometimes and detrimental in others.[231] The fact that the addition of some corrosion inhibitors hinders the iron carbonate film growth is thus obvious as depicted in Figure 4-20.

In order to adsorb onto the iron carbonate layer, any inhibitor should displace a water molecule from its surface first. Thus the inhibitor will bind preferentially to the surface and prevent the corrosive species from being transported to the underlying steel surface. The majority of the CO_2 corrosion inhibitors are amphiphilic surface active molecules branched with hydrocarbon chains twelve to eighteen carbon long (C_{12}-C_{18}).

Common quantum mechanics methodologies, in combination with molecular modelling studies, have shown the importance of the alkyl chain length of imidazoline corrosion inhibitors with $FeCO_3$ films.[242] It was also established

that the energy of bilayer film formation becomes more exothermic with increasing alkyl chain length.[247]

(a)   (b)
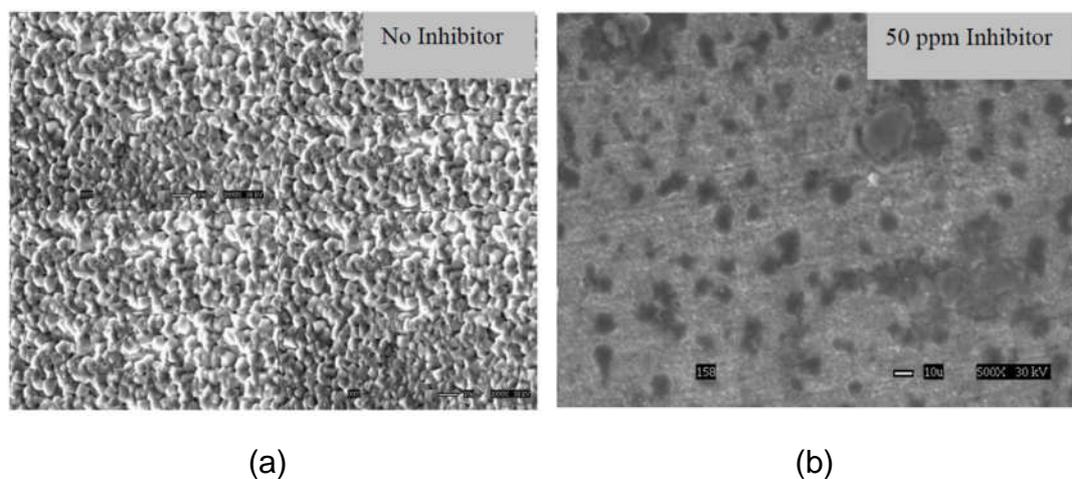
Figure 4-20 Top view showing 10µm scale bar for specimen (a) without inhibitor and (b) with 50 ppm inhibitor A at pH 6.6, Fe^{2+} = 50 ppm, SS = 150, T = 80°C , stagnant conditions adapted from Sun et al.[231]

One major characteristic of these inhibitors is their adsorption and self-assembly tendency which is related to the created hydrophobic interaction. In fact, this formed structure influences the corrosion rate by acting on the mass transfer of the species involved in the corrosion reaction or by simply blocking part of the reacting active surface area.[302] As such, the interaction between oleic imidazoline, a corrosion inhibitor commonly used in carbon dioxide corrosion mitigation, and iron carbonate can be asserted by following the $FeCO_3$ zeta potential fluctuations as shown in Figure 4-21.

Some corrosion inhibitors such as trimethyl n-octadecyl ammonium bromide were shown to increase the Young's modulus of the $FeCO_3$; in a study by Ramachandran et al.[326] it was stipulated that this will strengthen the corrosion product film and enhance its protectiveness.

Molecular mechanics allowed the calculation of the $FeCO_3$ Young's modulus and this information was used with existing theory for the fracture mechanics of corrosion product scales to understand the destruction of corrosion by-product layers under conditions of high shear.

In summary, the interaction of different corrosion inhibitors with the iron carbonate scale could lead to opposing effects of enhancing or inhibiting the corrosion process depending on the corrosion inhibitor types and the environmental conditions, mainly the presence of oil.[327]
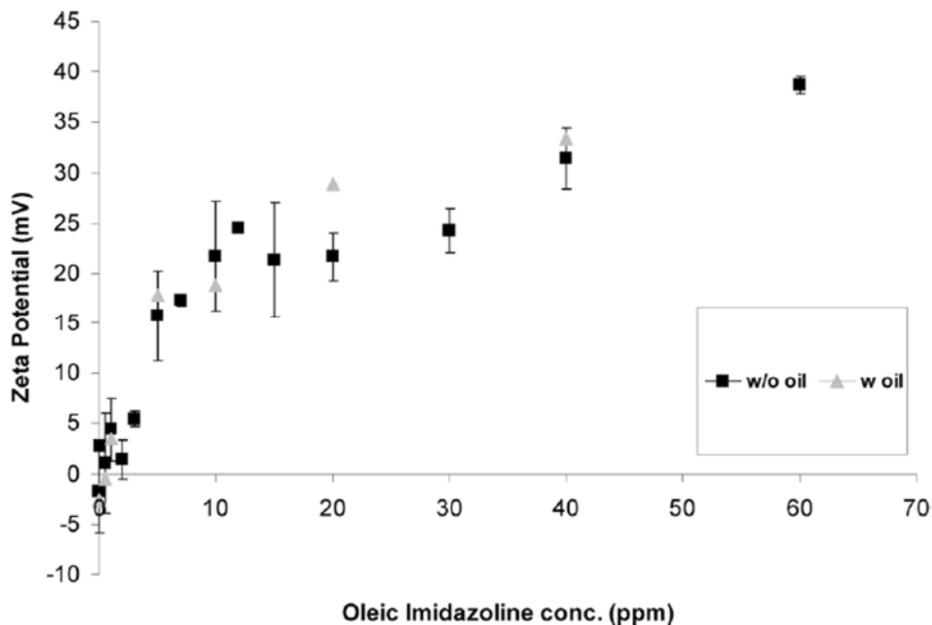
Figure 4-21 Zeta potential of $FeCO_3$ versus total added concentration of oleic imidazoline product. Experimental conditions: 22°C, 1 bar CO_2, pH=6, 0.1 wt% NaCl brine, oil content 2 volume %, adapted from Foss et al.[302]

4.7.2 Interactions with scale inhibitors

The effects of scale inhibitors on corrosion rates have been studied for both phosphate based and polycarboxylic acid types and results have shown that they both hinder the growth of a dense and protective iron carbonate layer thus lowering the corrosion resistance of the carbon steel system in CO_2 saturated environments as shown in Figure 4-22.[230] For instance, the kinetics of iron carbonate nucleation and precipitation have been studied in the absence and presence of sulphonated polycarboxylic acid, polyvinyl sulphonate, carboxymethyl inulin and sodium citrate and results showed that a pseudo scale was formed while all tested scale inhibitors were not able to alter the iron carbonate nucleation and growth.[328]

Many other chemicals are used recurrently in the oilfield to mitigate various flow assurances issues as is the case for glycols which are used in the treatment of hydrates. It was shown that the effects of such additives on the iron carbonate film growth could be contradictory since a mitigating effect was established from some tests, while other data showed some synergy and additional tests showed on the contrary an antagonistic behaviour.[329] MEG was shown to affect both the polymorphic abundance, the morphology of the

particles and the transformation rates for calcium carbonate and it is suspected that similar behaviour will occur with iron carbonate since they are both isostructural by nature.
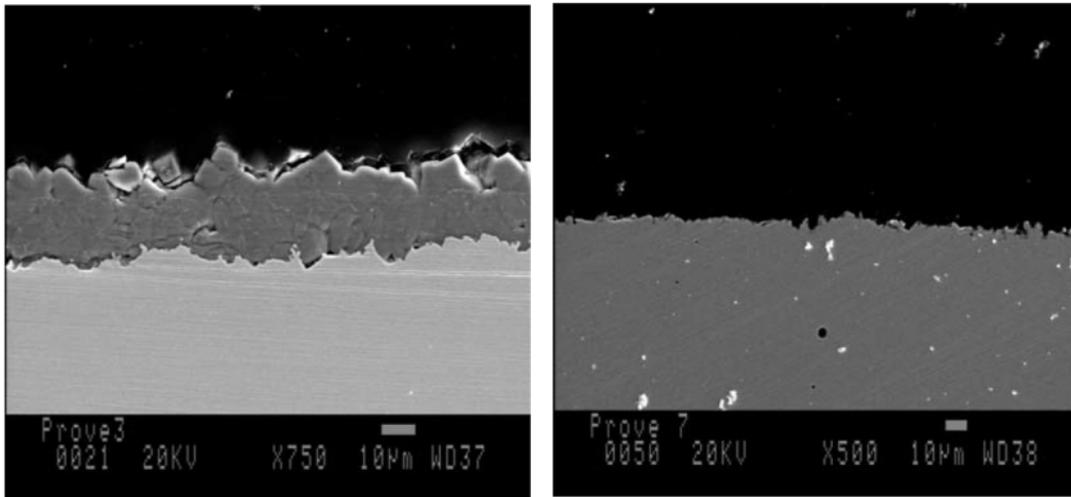
Figure 4-22 Cross-sections of the surface of specimens corroded (a) without scale inhibitor at pH=6.5 and (b) with a generic scale inhibitor for 300 hours adapted from Foss et al.[230]

4.8 Rationale and key role of FeCO$_3$ as a corrosion mitigator

When iron carbonate films are well adherent to the underlying steel and compact, they offer a corrosion protection which is similar to the one achieved by applying common carbon dioxide corrosion inhibitors as shown in Figure 4-23. As such, corrosion rates as low as 0.3mmpy are observed when 50ppm of the CI is added or a protective FeCO$_3$ has grown as represented by the dotted line.
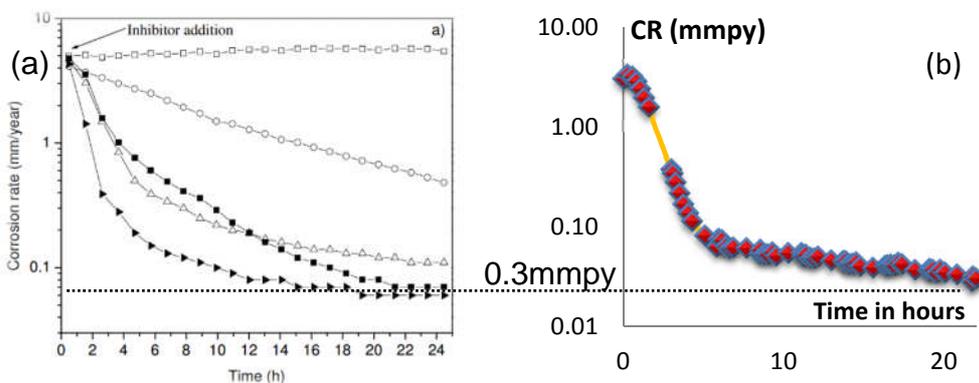
Figure 4-23 Comparison between the CR variation when (a) bis-imidazoline CI is added[40] and when (b) an iron carbonate corrosion layer has developed.

108

Moreover, a thorough examination of the literature shows that in general, corrosion inhibitors achieve a corrosion rate drop up to 0.1 mmpy while a protective iron carbonate layer brings the corrosion rate to values ten times lower as shown in Table 4-9.

Table 4-9 Corrosion rate for a film forming corrosion inhibitor covered surface in CO_2 saturated conditions over mild steels showing that in general iron carbonate is more protective by almost an order of magnitude

Conditions	Structure name	CR (mmpy)	Reference
55°C, pH=5.5 3% NaCl	200 ppm of 1-[(2-hydroxyethyl) amino]-2-(salicylideneamino) ethane	0.16	Ahovan et al.[330]
66°C, pH=6.3 1.7% NaCl	4 ppm of stearic imidazoline	0.05	Jovancicevic et al.[247]
25°C 3% NaCl	100mg/L of dendric derivative with tetra-imidazoline	0.099	He et al.[331]
25°C, pH=3.8 3.5% NaCl	15 ppm of Itraconazole	0.282	Ibraheem et al.[332]
65°C, pH=7.5 3.5% NaCl	Iron carbonate	0.055	Yaro et al.[333]
60°C, 0.1% NaCl $1.8 < P_{CO_2} < 2.6$ $5.5 < pH < 6$	Iron carbonate	<0.01	Dugstad et al.[334]
25°C, 1% NaCl 88 mmol/L of HCO_3^-	Iron carbonate	0.004	Berntsen et al.[289]
75°C, pH=6.5 P_{CO_2} = 10 bars	Iron carbonate	0.00665	Gao et al.[244]

Step 1: Semi in situ coating of $FeCO_3$ on carbon steel by flushing with a $FeCO_3$-forming solution such as $NaHCO_3$

Step 2: CO_2 capture process with solvents being highly corrosive after absorbing CO_2

Equipment downtime

Step 3: Removal of non-uniform corrosion layer by flushing chemical solutions and semi in-situ recovery of $FeCO_3$ coating by re-flushing
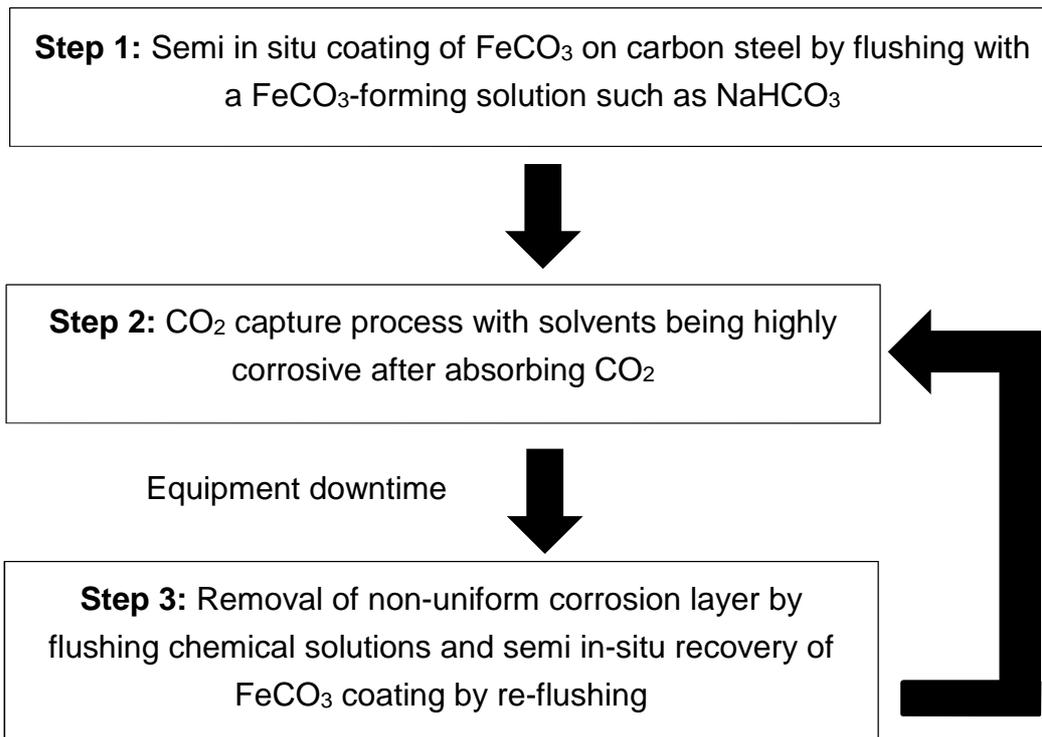
Figure 4-24 Proposed flushing procedure to protect process units in a post-combustion CO_2 capture system[335]

This protective property of the iron carbonate has seen recently some implementation in carbon capture and storage environments where a $FeCO_3$ coating process toward the corrosion protection of carbon steel in a post-combustion CO_2 capture system has been implemented as per Figure 4-24. As such, Zheng et al.[335] showed that a sodium bicarbonate ($NaHCO_3$) solution is a practical flushing solution in a real capture system because its fast implementation as a coating process in order to build a protective $FeCO_3$ layer, environmentally friendly nature, lower cost, and easy process control.

This research focuses on the protective barrier properties of iron carbonate and the approach concentrates on enhancing the nucleation of the $FeCO_3$ crystals and creating a more robust but less brittle corrosion layers extrapolating on commonly available nanocomposite procedure by inserting hybrid organic-inorganic nanofillers in the system of choice. This methodology is explained in the next chapter which summarizes the use of nanocomposites in the oil and gas industry.

4.9 Summary of literature review

Carbon steel remains the material of choice in many oil and gas sectors such as production and transmission pipelines. This is mostly due to its low cost and adequate mechanical properties. The major drawback is that it can be subjected in specific conditions to extensive chemical degradation as is the case when environments containing dissolved carbon dioxide or hydrogen sulphide are dominant.

Carbon dioxide is believed to exist in most oil and gas resources especially with the implementation of the EOR techniques. Section 3.6.2 highlighted the various approaches commonly implemented in order to reduce the corrosion degradation. While suitable corrosion inhibitors perform adequately by reducing the corrosion rate by a factor of ten, this approach remains costly due to its recurrence and environmentally not friendly due to the use of hazardous materials.

It was shown in section 4.4 that in a well-defined matrix of environmental conditions, mainly pH and temperature, a naturally developing corrosion layer known as iron carbonate is found to be even more protective if well-adherent and compact and usually corrosion rates are seen to drop towards values even lower than 0.001 mmpy.

The objective of this research as described in section 1.7 and schematised in Figure 1-11 aims at taking advantage of the addition of a hybrid nanofiller known as OA-POSS to accomplish two deeds: first it is thought to accelerate the nucleation of iron carbonate crystals in specific conditions that are detailed in the results chapter along with its capability to incorporate within the corrosion film and improve some of its mechanical properties such as reducing its brittleness due to the organic side-chains of the incorporated nanofillers.

The next part tries to describe in more detail the chosen working electrode which is carbon steel X65 and the reasons behind selecting a specific nanofiller that is octaammonium-POSS. It also covers the major surface analysis and electrochemical techniques implemented to achieve the desired experiments and uncover the described mode of action of the combined iron carbonate-nanofiller system.

Part III. Materials and methods

Chapter 5 Materials used in this study

5.1 Working electrode

5.1.1 General properties

The working electrode terminology is used in relation to the electrochemical test setup used which is the three-electrode cell as described in section 4.5.1. X65 (UNS K03014) is the material used in this research as the corroding specimen. The value showing after the X such as 65 denotes the yield strength of the specimen e.g. 65,000 psi for the selected X65 mild steel.

Table 5-1 details the nominal composition and as any carbon steel alloy, X65 shows iron as the principal element while the carbon content is below 2.5 wt% and is known to control the percentage of the pearlitic-ferritic composition affecting the nucleation and growth of $FeCO_3$.

Table 5-1 X-65 carbon steel elemental composition in weight percentage

C	Si	P	S	Mo	Ni	Nb	V	Mn	Fe
0.15	0.22	0.025	0.002	0.17	0.09	0.054	0.057	1.422	97.81

5.1.2 Microstructure

The steel is in a normalised form and consequently possesses a ferritic/pearlitic microstructure as shown in Figure 5-1 where the pearlite and the proeutectoid ferrite are in dark and light colour respectively; the pearlite consists of alternating layers of cementite and ferrite.

Etching was conducted using Nital which is 98% propan-2-ol and 2% nitric acid. Prior to that, the sample was cast into resin then polished to a very fine surface finish of 3 micrometres. The etching was repeated 3 times for a duration of 20-30 seconds until the microstructure borders were evident.

The presence of vanadium (V) and niobium (Nb) suggests that the specimen is a microalloyed steel so some of the carbon should be tied up in alloy carbides. But assuming that all the carbon is free and using the lever rule, the mass fraction of ferrite/pearlite could be estimated as per Equation 5-1 and

the maximum solid solubility in ferrite, eutectoid composition and temperature from the phase diagram in Figure 5-3.[336] A, E and B are defined as the hypo-eutectoid, the eutectoid and the hyper-eutectoid regions respectively.

Equation 5-1 Lever rule to compute phase fractions of pearlite and ferrite

$$W_f^p = \frac{wt\% \, C - 0.025}{0.83 - 0.025} x100$$

$$W_f^\alpha = \frac{0.93 - wt\% \, C}{0.83 - 0.025} x100$$

b

a

50 μm
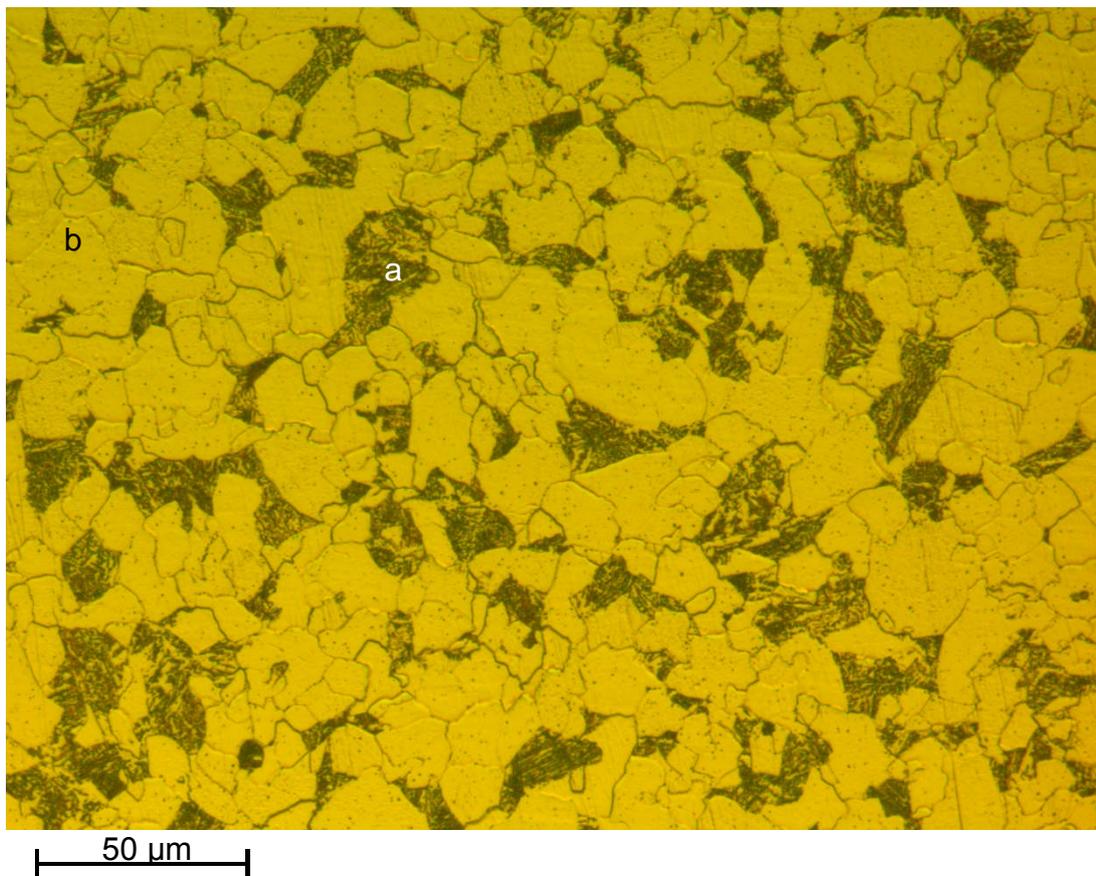
Figure 5-1 Microstructure of X65 after light etching showing (a) the dark pearlitic regions and (b) light ferritic areas

The pearlite W_f^p and proeutectoid ferrite W_f^α fractions are thus equal to 16 and 84% respectively if the temperature is assumed to be 1333 °F. The α-ferrite is a solid solution of carbon in α-iron and has a body centre cubic crystal structure and low solubility of carbon up to 0.025% at 1333 ºF. At 0.83%C, the transformation is eutectoid, called pearlite where gamma austenite changes

113

into alpha ferrite and Fe_3C cementite. The pearlite fraction is directly dependant on the carbon weight percentage and is known to increase with it.

As seen in Figure 5-1, ferrite is the major constituent (proeutectoid ferrite and α ferrite) showing epitaxial morphology while being soft and easily deformed. On the other hand, cementite or the iron carbide phase is hard, brittle and detrimental to the formability of the carbon steel, so the less the better. The microstructure also shows the transformed austenite hot rolled crystal structure into proeutectoid ferrite (α) and pearlite which is a combination of pearlitic ferrite and cementite. This percentage was correlated with a MATLAB simulation which showed roughly a 21 to 79 percentage of pearlite to ferrite respectively as shown in Figure 5-2.
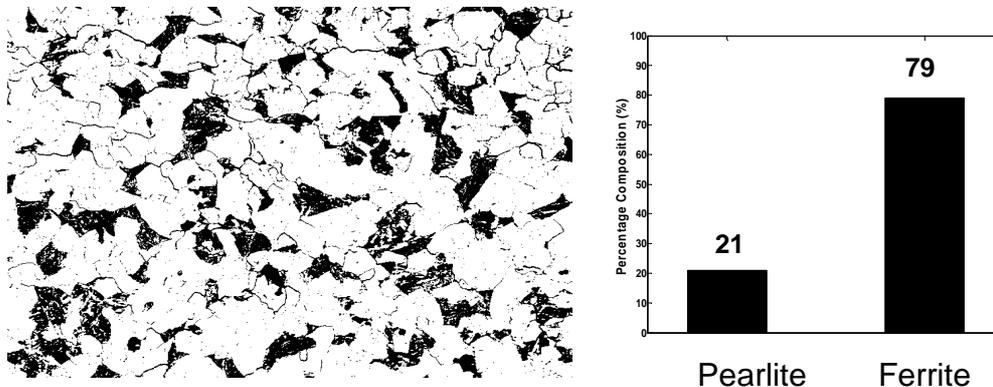
Figure 5-2 X65 Microstructure analysed as dark/white regions using MATLAB

Generally, microstructures that promote anchoring of the corrosion film products will lead to the formation of protective well-adherent films, thus decreasing the corrosion rate. An example of that is the normalized carbon steel as opposed to the quenched tempered microstructure as described earlier in section 3.5.5. Pearlite increases the anchoring of the corrosion layer while both ferrite and cementite increases the galvanic corrosion effect.

In fact, after the corrosion mechanism initiates and pearlite is formed in the shape of adjacent platelets, it is assumed that the localized increase in ferrous iron concentration in these cavities promotes the formation of iron carbonate films. On the contrary, when the corroding element is α-ferrite microstructure, this will leave cementite which is a conductor favouring the galvanic coupling between the carbon steel surface and the Fe_3C layer; in other terms increasing the corrosion rate and limiting the $FeCO_3$ film formation.
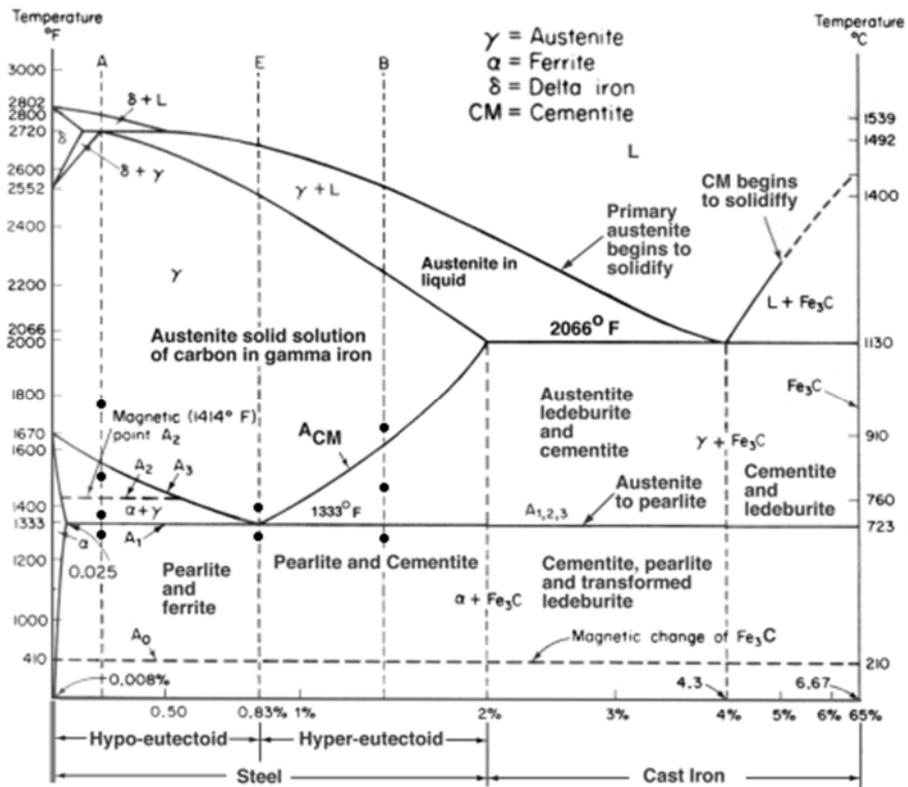
Figure 5-3 Iron-Iron Carbide Phase Diagram[336]
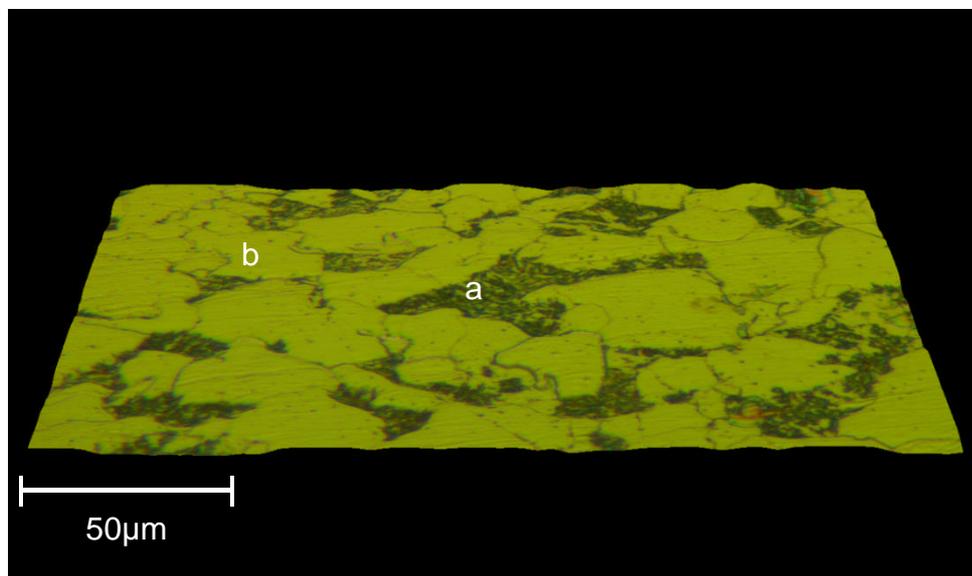
Figure 5-4 3D simulation of the X65 surface extracted from optical microscopy visualisation showing the dark pearlite (a) and clear ferrite (b) regions

Hence, the knowledge of the working electrode microstructure can give preliminary or expected behaviour of the steel once in contact with the carbon dioxide saturated brine environment and the extent of protective $FeCO_3$

formation could be anticipated. Figure 5-4 shows the pearlite in the valleys as the anchoring sites for the start of the $FeCO_3$ crystallisation process while the ferrite is on the hills.

5.1.3 Blank X65 carbon steel Energy-dispersive X-ray (EDX) mapping

A X65 carbon steel sample was polished to a surface finish of 1200 Silicon Carbide (SiC), and analysed in order to provide a baseline for the future comparison between the blank steel mapping results (Figure 5-5) and when the corrosion layers are able to develop and cover the underlying steel surface. The main elements on the freshly polished carbon steel are iron, manganese, carbon, fluorine and silicon which is in accordance with the X65 carbon steel elemental composition in weight percentage given in Table 5-1.
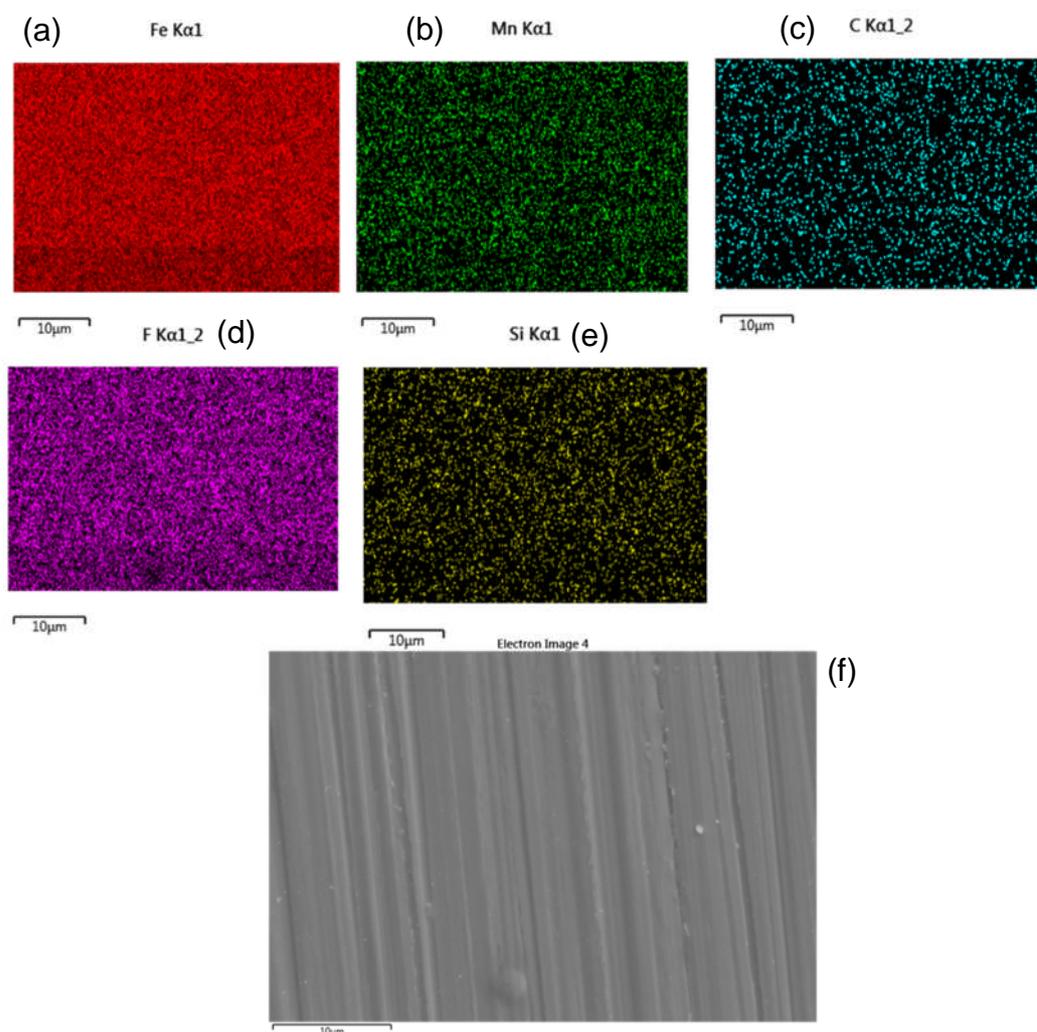
Figure 5-5 EDX map of 1200 SiC finished X65 carbon steel showing (a) Iron-Fe, (b) Manganese-Mn, (c) Carbon-C, (d) Fluorine-F and (e) Silicon-Si and (f) the corresponding SEM micrograph

5.1.4 Sample preparation

Sample preparation for electrochemical corrosion testing requires cutting the samples to the desired dimension, mounting them into resin before polishing and cleaning. The carbon steel samples were sectioned to a dimension of 15 mm x 15 mm x 5 mm in order to expose a surface area of 2.25 cm^2. Wires were soldered to the back of each test sample before embedding them in a non-conducting resin (Varidur10 from Buehler).

Prior to each test, the samples were wet-ground progressively using P120, P320 and P600 Metprep metallographic silicon carbide abrasive paper unless otherwise specified. These ground surfaces were then degreased with acetone, rinsed with distilled water and dried with compressed air before immersion into the test solution. Each test was ran with two samples thus exposing a total surface area equal to 4.5 cm^2 which is important to note with regard to the quantity of ferrous iron diffusing in one litre of brine.

5.2 Nanofillers

A discrete structurally well-defined cage-like molecule known as OctaAmmonium POSS or OA-POSS (Figure 5-6)[337] was selected with the aim of blending within the growing iron carbonate film thus filling some voids inside the porous growing corrosion layer in order to improve its mechanical properties and increase its barrier activity.
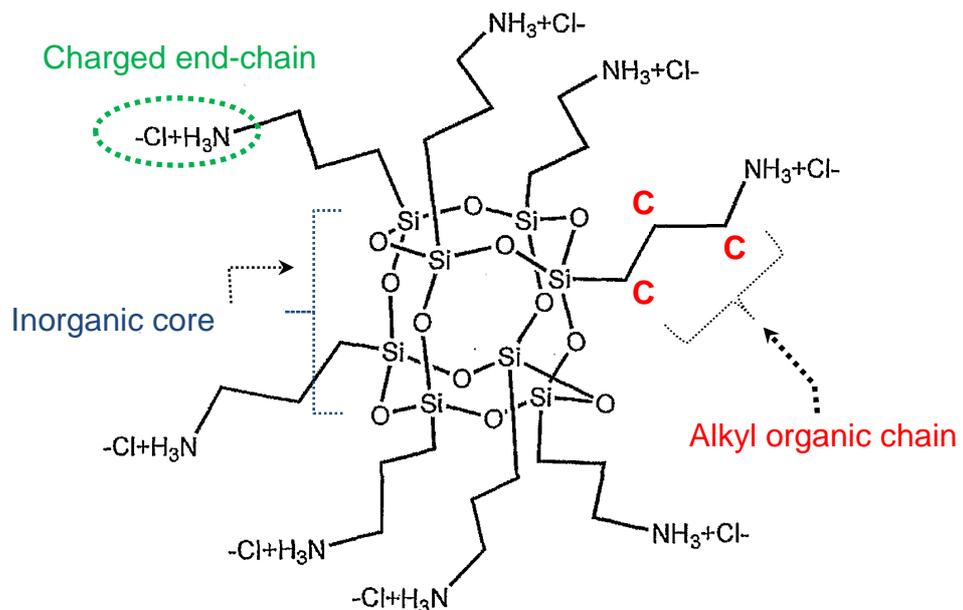
Figure 5-6 OctaAmmonium POSS chemical formula[337]

117

Octa(3-aminopropyl)octasilsesquioxane octahydrochloride also known as OA-POSS has its organic side chains part of the amine group attached to an aminopropyl alkyl chain composed of 3 carbon atoms as shown on one branching. The organic side-chains are believed to introduce more malleability through the generally brittle $FeCO_3$ corrosion product. A detailed description behind the reasons that led to choose this product is described in section 5.2.1.

5.2.1 Choice of nanofiller

The nanofiller should have a hybrid characteristic that is an inorganic part able to enhance the mechanical properties and an organic counterpart to limit the increase in brittleness. OA-POSS provides such a duality with the internal inorganic core made of silicon and the organic side chains being an ammonium functionalised short carbon chain.

Since most processed wells show an oil-in-water phase, a compound which is water soluble for ease of administration was sought. OA-POSS is a silsesquioxane derivative that is readily soluble in water which is explained by its eight hydrophilic positively charged ammonium groups ($-NH2$) which are protonated to form ($-NH3^+$) once dissolved in the brine solution.

Up to date, only two POSS derivatives have been tested as water soluble, the other being a poly-ethylene oxide POSS moiety.[338] The water miscibility should greatly ease the experimental trials because they will not be any need to add any surfactant-like chemical in order to stabilize and keep the POSS molecules away from each other in order to hinder their natural agglomeration tendency.

The researched nanofiller should adhere to the steel surface and OA-POSS nitrogen atoms are known to be part of the anchoring groups as proved by the use of organic corrosion inhibitors with similar chemical reactive sites such as quaternary ammoniums;[339] this is expected to enhance the bonding affinity between the nanofiller and the carbon steel surface being incorporated through the gradually developing $FeCO_3$ matrix.

It was shown in section 4.5.2 that the zeta potential of $FeCO_3$ is negative above a pH of six and that is also valid for carbon steel due to its potential of zero charge;[340] the researched nanofiller should be positively charged in order for electrostatic attraction to initiate and OA-POSS is also such a compound.

Another possible advantage of using such side chains with quaternized amines is that they have been shown to improve the already protective ability of the siderite passivation layer when used as part of a corrosion inhibitor.[341] Also the sorption of silicon on three different corrosion products magnetite, goethite and siderite, was shown to increase when the pH was raised from 3 to 7 and OA-POSS is a silicon-rich compound.[342]

Lastly, the presence of oxygen atoms in the molecule core and hence the expected siderite film enrichment with these atoms could also be considered as beneficial to both stability and adhesion of the nanocomposite as described by Kermani et al.[117]

5.2.2 OA-POSS physico-chemical properties

Some of the OA-POSS readily published properties are summarized in Table 5-2.[343] The compound was purchased from hybrid plastics and is designated as AM0285.

Table 5-2 OctaAmmonium POSS known properties

Commercial name	AM0285 Hybrid Plastics
Chemical formula	$C_{24}H_{72}Cl_8N_8O_{12}Si_8$
Molecule volume ($Å^3$)	1100
Maximum distance ($Å$)	16.47
Molecular weight (Dalton)	1173.18
Thermal gravimetric analysis	Stable up to 300°C

The high thermal stability is in accordance with the temperature range usually encountered in oil and gas transport pipeline which rarely exceeds 150°C. The thermogravimetric analysis (TGA) shows that OA-POSS will not decompose even for temperature as high as 300°C as depicted by the dotted line in Figure 5-7.[344]

Titration of OA-POSS showed that no conversion of ammonium groups into primary amines shall occur at a pH below 7 as seen in Figure 5-8. Hence, the polyamide counterpart will only form at pH values higher than 7 which are higher than the pH range used in this study so the chemistry of the OA-POSS should be stable and its charge maintained.

The method used for titration as per Figure 5-8 was the dynamic equivalence-point titration where the consumed amount of hydroxyl per POSS was calculated from the difference between the hydroxyl added and the measured hydroxyl, divided by the amount of POSS present in the solution.
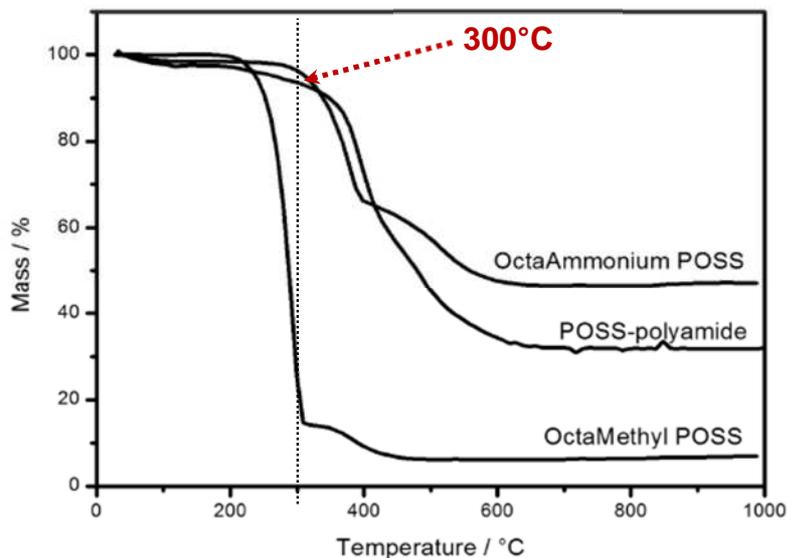
Figure 5-7 Thermogravimetric analysis of OA-POSS[344]
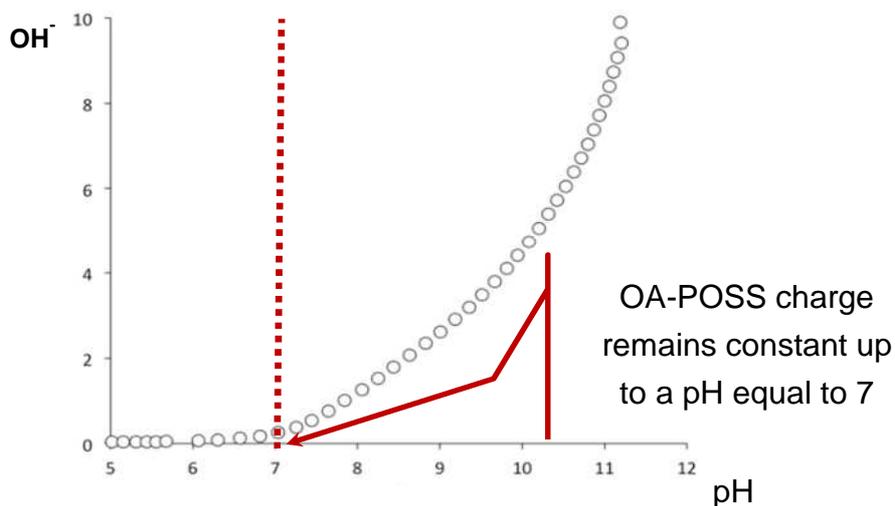
Figure 5-8 Titration of aqueous POSS with NaOH solution showing the number of hydroxyl molecules consumed per POSS molecule at various pH [344]

Table 5-3 Element concentration and element ratio of OA-POSS

Compound	Element ratio			
	C/N	O/Si	O/N	Cl/N
OA-POSS (experimental)	3.35	1.64	1.56	0.91
OA-POSS (theoretical)	3.00	1.50	1.50	1

X-ray Photoelectron Spectroscopy (XPS) measurements were also performed and they show that the element concentrations and element ratios of OA-POSS are in reasonable agreement with its molecular formula: $C_{24}H_{72}Cl_8N_8O_{12}Si_8$. The chlorides will create ionic bonds with the positively charged ammonium on the functionalized silicon groups (Table 5-3).[345]

5.2.3 OA-POSS structure

POSS nanoparticles have very small sizes ranging from 1 to 3 nm thus they cannot be directly observed via SEM techniques.[346] The XRD pattern of OA-POSS was also referenced in the literature and corresponds to compound A in Figure 5-9.[347] It shows a sharp reflection at 2θ= 6.9 and 7.5 that is arising most likely from crystalline POSS aggregates.
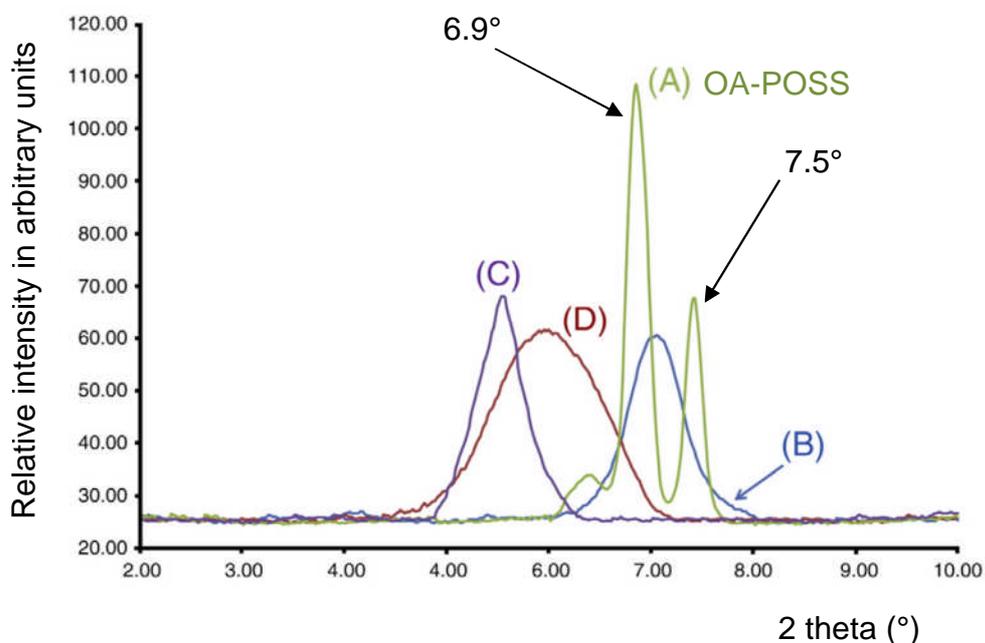
Figure 5-9 XRD pattern of OA-POSS (A) adapted from Perrin et al.[347]

The diffraction pattern of the OA-POSS used in this research showed two distinct behaviours since both crystalline and amorphous silsesquioxanes moieties were depicted. This effect could be related to water vapour contamination but since these are dissolved in water during the tests, it was estimated that the crystalline configuration did not have an effect on the molecule activity. As seen in Figure 5-10, it appears that there is a band between 2θ values of 6 and 8 but no distinct peaks. Moreover the lower compactness of the OA-POSS molecules in the powder and its low density could affect the diffraction peaks quality.
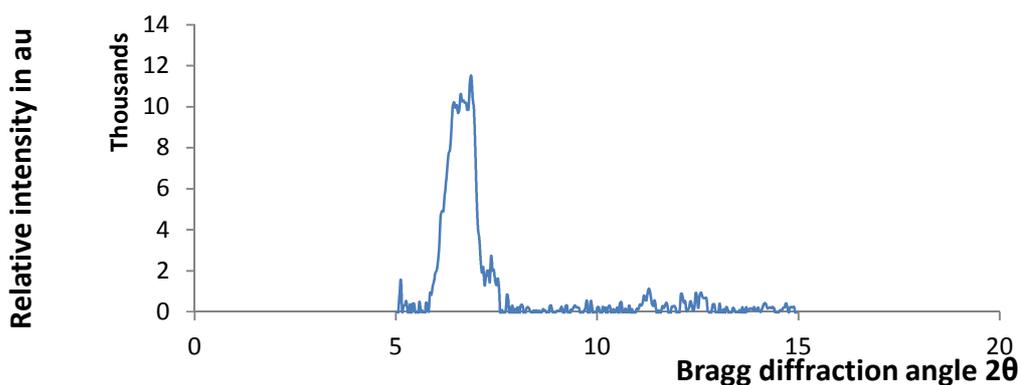
Figure 5-10 XRD pattern of OA-POSS used in this study (batch 2)

The non-crystallinity of the purchased product was further confirmed by TEM micrographs and the absence of diffraction pattern as seen in Figure 5-11 after being precipitated in hexane.

(a)   (b)
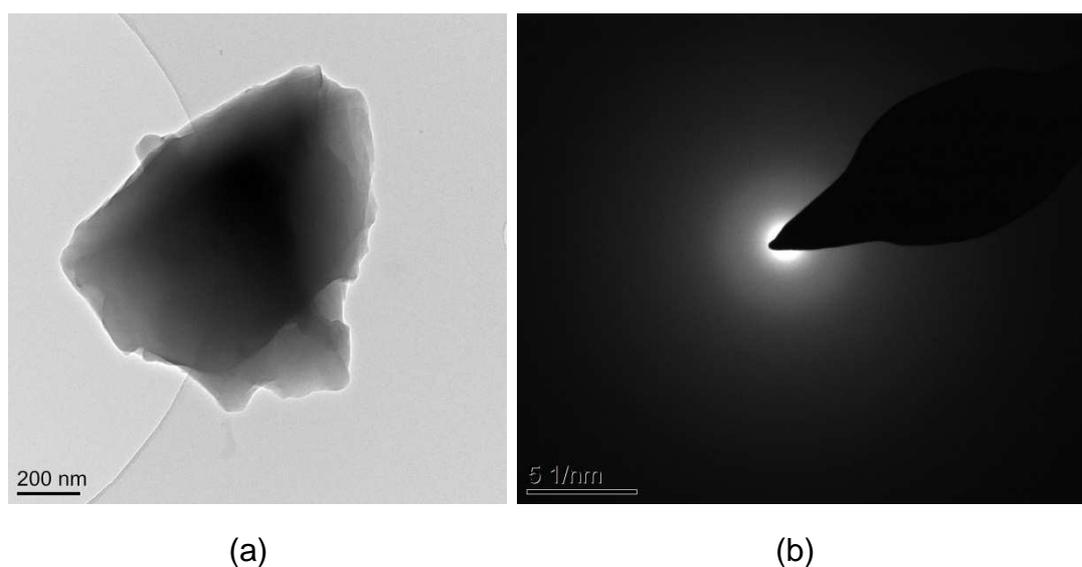
Figure 5-11 TEM micrograph (a) and diffraction pattern (b) of OA-POSS

122

The two batches of OA-POSS and their respective XRD patterns are shown in Figure 5-12 where the broad diffraction peak at about $2\theta = 18.7°$ is attributed to the amorphous structure of POSS moieties.[348]
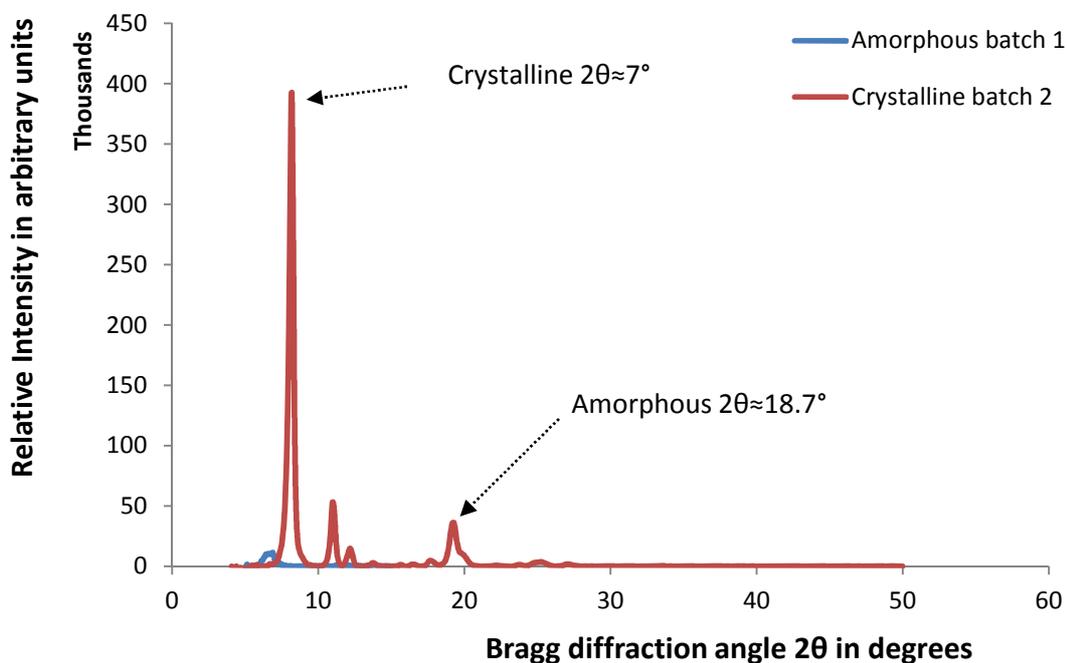
Figure 5-12 XRD pattern of two OA-POSS batches

Another parameter of interest which has also been already determined for the OA-POSS molecule is the pore size distribution and relative pore concentration when OA-POSS form a self-assembled hybrid network as described in Table 5-4.

Table 5-4 Pore size within the POSS hybrid network

pH	Lifetime (ns)	Pore diameter (nm)	Intensity (%)
7	0.99 ± 0.07	0.39 ± 0.03	8.3 ±1.2
	2.05 ± 0.02	0.65 ± 0.01	
9.46	0.60 ± 0.05	0.21 ± 0.06	17.4 ± 6.2
	2.22 ± 0.08	0.68 ± 0.02	2.6 ± 0.2
10.90	1.56 ± 0.12	0.55 ± 0.03	5.5 ±0.2
	3.40 ± 0.62	0.86 ± 0.06	1.6 ±0.3

Pore size determination was accomplished by Dalwani et al.[345] using a spectroscopic technique known as positron annihilation lifetime spectroscopy. The samples were measured at room temperature under vacuum and the lifetimes are converted to pores' sizes from semi-empirical formulas which are not detailed herein.

5.3 Synthetic iron carbonate

Iron (II) carbonate powder CAS# [563-71-3] was purchased from Strem Chemicals in order to mimic an $FeCO_3$/OA-POSS interaction by carrying out nitrogen adsorption BET tests. The chosen product was tested under X-ray for diffraction pattern and showed symmetrical geometry which is stackable with the iron carbonate grown in the corrosion tests as shown in Figure 5-13.
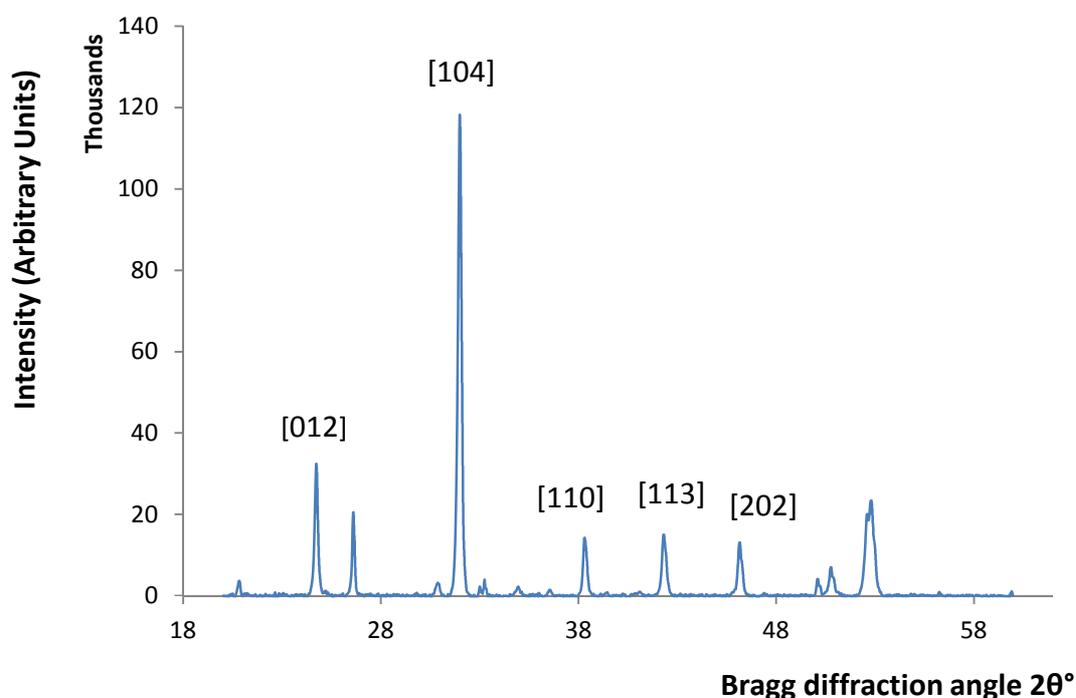
Figure 5-13 Synthetic iron carbonate diffraction pattern

All 5 peaks corresponding for the h,k,l Miller indices [012], [104], [110], [113] and [202] were found to overlap with the diffraction angle 24.76°, 32.76°, 38.32°, 42.29° and 46.14° respectively

Chapter 6 Experimental conditions and methods

6.1 Environmental conditions

6.1.1 Temperature

After screening through a well-defined matrix of temperature (50 to 80°C) and pH (3.75 to 7), it was decided to run all tests at a pH of 6.6 and a temperature of 60°C for reasons described in Chapter 7. This is mainly due to the fact that these environmental conditions represent the lower border for the formation of crystalline iron carbonate and upcoming results detail how the OA-POSS encourages the $FeCO_3$ crystal nucleation in thermodynamic conditions where they should normally not appear as shown in the potential-pH diagram in Figure 6-1 which was computed at a ferrous iron concentration of 1 ppm and a CO_2 partial pressure of 1 bar.[349] In fact, depending on the surface roughness and other parameters, it is unlikely to form $FeCO_3$ crystals without enriching the system with ferrous ions such as adding ferrous chloride for instance.
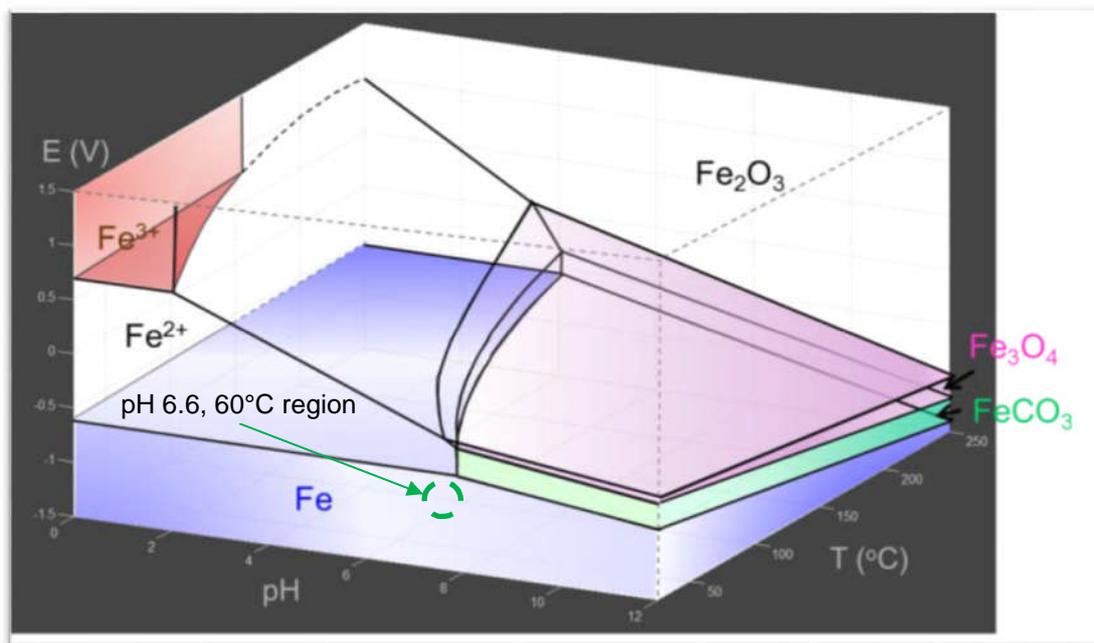
Figure 6-1 Potential-pH-temperature diagram for Fe-CO_2-H_2O systems[187]

6.1.2 Acidity and choice of pH

The pH probe is known to undergo slight shifts between tests after calibration, as such, it was decided to run all tests at a specific mass of sodium bicarbonate used as a buffer thus allowing for a pH of 6.6 to be attained. This

is based on the equilibrium of carbon dioxide in water which could be summarised as per Equation 6-1.

Equation 6-1 Schematic of CO2 successive dissolution in water

$$CO_{2(g)} \leftrightarrow CO_{2(l)} \leftrightarrow H_2CO_3 \leftrightarrow HCO_3^- + H_3O^+ \leftrightarrow CO_3^{2-} + H_3O^+$$
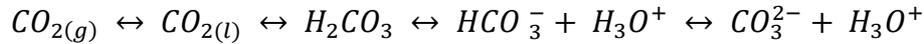
It is known that carbonic acid is a weak acid which dissociates in two steps as per Equation 6-2 and Equation 6-3 with the respective dissociation constants pK_{a1} and pK_{a2}.

Equation 6-2 Carbonic acid dissolution

$$H_2CO_3 + H_2O \leftrightarrow HCO_3^- + H_3O^+$$

Equation 6-3 Bicarbonate dissolution

$$HCO_3^- + H_2O \leftrightarrow CO_3^{2-} + H_3O^+$$
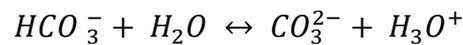
Equation 6-4 Protolysis constant K_{a1}

$$K_{a1} = \frac{[HCO_3^-][H_3O^+]}{[H_2CO_3]} \approx \frac{[HCO_3^-][H_3O^+]}{[CO_2 + H_2CO_3]} \approx \frac{[HCO_3^-][H_3O^+]}{[CO_{2\,l}]}$$

Equation 6-5 Protolysis constant K_{a2}

$$K_{a2} = \frac{[CO_3^{2-}][H_3O^+]}{[HCO_3^-]}$$

The other two dissociation constants involved in the CO2 dissolution in water correspond to the dissociation of sodium bicarbonate described as per Equation 6-6 and the other is the water equilibrium constant highlighted in Equation 6-7.

Equation 6-6 Equilibrium constant for sodium bicarbonate dissociation

$$Na^+_{(aq)} + HCO^-_{3(aq)} \leftrightarrow NaHCO_{3(aq)}$$

$$K_{NaHCO_3} = [Na^+][HCO_3^-]$$
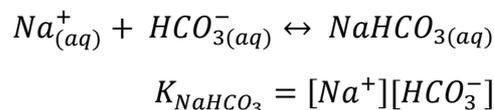
Equation 6-7 Water dissociation and equilibrium constant

$$2H_2O_{(l)} \leftrightarrow H_3O^+_{(aq)} + OH^-_{(aq)}$$

$$K_{water} = [H_3O^+_{(aq)}][OH^-_{(aq)}]$$
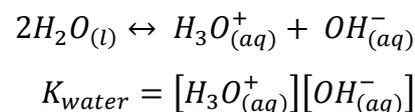
There are many ways of solving these equations in order to get the molarity of sodium bicarbonate needed to achieve a pH of 6.6; the water dissociation constant will be discarded since the pH is close to neutral. By using Le Chatelier principle, we can compute the sodium concentration as described in Equation 6-8 where the dissolved HCO_3^- before the acid-base reactions is equal to the sodium quantity but also to the sum of all acid-base couples present.

Equation 6-8 Le Chatelier principle applied to CO_2 equilibrium in water

$$[Na^+] = [CO_{2(l)}] + [HCO_3^-] + [CO_3^{2-}]$$

$$\text{or } [Na^+] = \frac{[H_3O^+][HCO_3^-]}{K_{a1}} + \frac{[H_3O^+][CO_3^{2-}]}{K_{a2}} + \frac{K_{NaHCO_3}}{[Na^+]}$$

$$\text{Which leads to } [Na^+] = \sqrt{K_{NaHCO_3}\left(\frac{[H_3O^+]^2}{K_{a1}\,K_{a2}} + \frac{[H_3O^+]}{K_{a2}} + 1\right)}$$

The concentration of H_3O^+ is directly computed from the pH as per Equation 6-9.

Equation 6-9 pH relationship

$$pH = -log[H_3O^+]$$

$$\text{or } [H_3O^+] = 10^{-pH}$$

The other dissociation constants were calculated at 60°C from polynomial fits as shown in Table 6-1 with T being the temperature in Kelvin.

Table 6-1 Polynomial fit to the equilibrium constants[350]

Equilibrium constant	$log\ K = a + b.T + c.T^{-1} + d.T^2$			
	a	b	c	d
log K_{a1}	13.8845	-0.03763	-3072.590	$1.4273.10^{-5}$
log K_{a2}	17.4200	-0.05797	-4080.582	$3.6045.10^{-5}$
log $KNaHCO_3$	1.8528		-606.240	

The above assumptions lead to log K_{a1}, log K_{a2} and log K_{NaHCO_3} respectively equal to -6.31, -10.15 and 0.03 as determined by potentiometric titration; this corresponds to a concentration of sodium ions approximately equal to 0.044 moles which is equivalent to a weight of sodium bicarbonate around 3.68 grams. These calculations are purely theoretical and it appears from laboratory trials that an extra 3.1 grams are needed to reach an equilibrium pH of 6.6 thus the bicarbonate mass added throughout all tests was equal to 6.78 grams.

It should also be noted that these constants were computed at a NaCl concentration of 0.1 Mol/L while laboratory tests were ran at approximately 0.6 Mol/L.

6.1.3 Salinity and choice of brine composition

Unless specified otherwise, all tests were ran at a NaCl loading of 3.5%. The salinity is known to affect the solution resistance but also the solubility of gases such as CO_2. This value was chosen because it is the nearest to the sea water composition and the most widely abundant in the literature. It is also stated in ASTM G31 - 72(2004) entitled "Standard Practice for Laboratory Immersion Corrosion Testing of Metals" that the typical test solution to carry corrosion experiments corresponds to 0.6 mol/L of NaCl.

Table 6-2 Forties brine composition[351]

Salt	g/L
$BaCl,2H_2O$	0.44
$NaHCO_3$	0.68
KCl	0.7
$SrCl,6H_2O$	1.44
$MgCl_2,6H_2O$	4.21
$CaCl_2,6H_2O$	17.19
NaCl	74.7

Some tests were ran in Forties brine with its composition as shown in Table 6-2. This solution simulates the aggressive saline environment existing in oil and gas wells and is considered an aggressive solution due to the presence of high concentrations of chloride and bicarbonate ions.

6.1.4 CO_2 partial pressure and solubility

At atmospheric pressure, the CO_2 partial pressure is averaged to 0.8 bar since at 60°C the water vapour pressure is equal to 19.948kPa or approximately 0.2 bar. Also in a 3.5% NaCl, the CO_2 solubility will be around 0.0116 mole/Kg of water as depicted in Figure 6-2.[352] Both unbuffered and buffered CO_2 tests were undertaken as described in the next two sub-sections.

Equation	$y = exp(a+b*x+c*x^2)$		
Adj. R-Square	0.99415		
		Value	Standard Error
0.67m NaCl	a	-2.67346	0.03607
0.67m NaCl	b	-0.03873	0.00381
0.67m NaCl	c	1.49158E-4	7.14332E-5
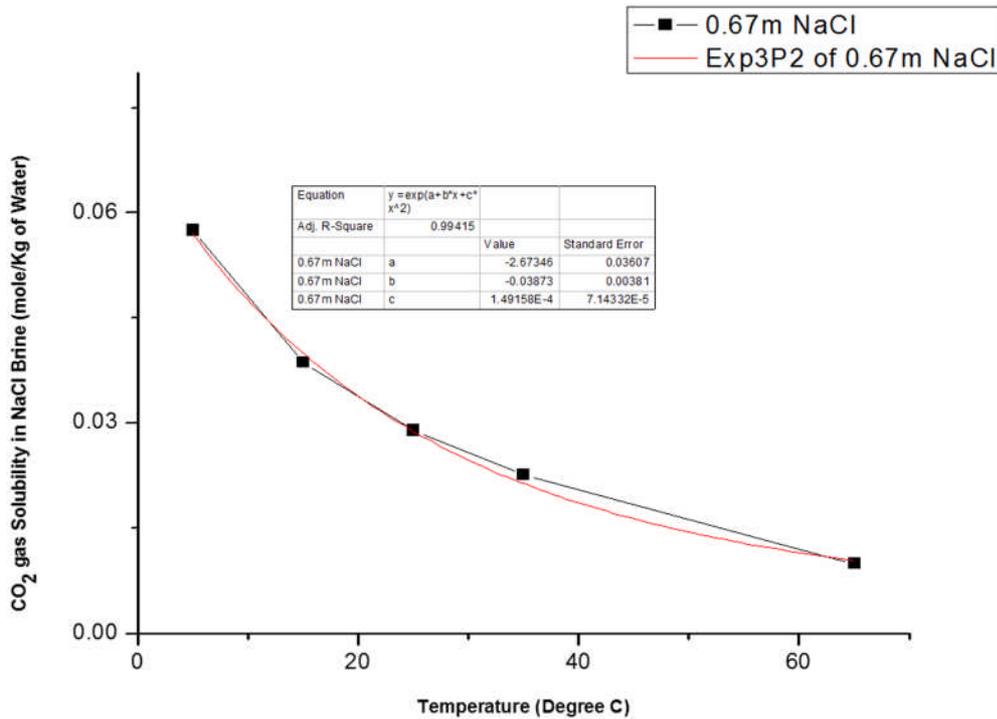
Figure 6-2 Raw solubility data for CO_2 gas sourced from literature[352]

6.1.4.1 Unbuffered tests

All tests were ran using standard bubble tests as described by Wang et al.[353] In order to deaerate the test solution to values below 20ppb of dioxygen gas and saturate it with CO_2 gas, the electrolyte was sparged with CO_2 gas overnight for a minimum of 12 hours. A CO_2 saturated solution of 3.5 wt% NaCl at 60°C was shown to have a pH stabilising around 3.85. This value seems in accordance with other published data at slightly lower concentration of NaCl.[354] Two working electrodes were immersed into the test cell after being polished, degreased with acetone, rinsed with distilled water and dried with compressed air, allowing for ferrous iron to be released from a surface area equal to 4.5 cm^2 in total.

6.1.4.2 Buffered CO$_2$ corrosion tests

Similarly to 6.1.4.1, the only difference in these tests was the addition of the required weight of sodium bicarbonate at the start of the sparging in order to limit the potential oxygen ingress to the sole introduction of the working electrodes. The amount of added $NaHCO_3$ is described in section 6.1.2.

Upon test completion, the samples are washed with distilled water, air dried, and carefully stored in a desiccator plastic bag left in a deaerated chamber; this reduces the probability of oxidation of corrosion products prior to any planned surface analysis. When light interferometry was implemented, the corrosion products were removed by using Clarke's solution prior to pitting corrosion analysis. Moreover, these corrosion products were progressively dissolved in 15% acetic acid when ICP was implemented.

It should be noted that the non-uniformity of test duration was mainly due to the fact that running long term tests was hindered by uncontrolled main CO$_2$ shortages.

6.1.5 Flow conditions

All tests were ran in static conditions in a glass beaker having a volume equal to one litre. The only disturbances involved are the magnetic stirrers running at 250 rpm and the continual CO$_2$ bubbling at a flow rate of 0.1 litre per minute.

6.2 Electrochemical techniques

Three different techniques were implemented to record electrochemical responses in this study; linear polarisation, Tafel polarisation and electrochemical impedance spectroscopy. The three-electrode cell used in this work also comprised of a silver-silver chloride InLab® Reference electrode; the reference system is an ARGENTHALTM with a silver ion tap bathing in a 3 mol/L potassium chloride solution. Corrosion rate and solution resistance measurements were conducted using both DC and AC measurements with an ACM GILL12 potentiostat. Most electrochemical experiments were repeated at least three times to ensure the reproducibility.

6.2.1 Linear Polarisation Resistance (LPR)

Linear polarisation resistance measurements were performed by polarising the working electrode from -15 mV below the open circuit potential to +15 mV above the open circuit potential at a scan rate of 0.25 mV/s to obtain a

polarisation resistance measurement from which the corrosion rate was computed as described in section 2.4.5.

6.2.2 Tafel extrapolation

Tafel polarisation measurements were performed on freshly polished samples in separate tests at each condition after a stable OCP and corrosion rate was achieved to determine anodic and cathodic Tafel constants and ultimately the Stern-Geary coefficient. Tafel plots were obtained by performing anodic and cathodic sweeps ± 300 mV around the OCP at a sweep rate of 10 mV/min. Both anodic and cathodic sweeps were performed on the same sample by starting with the cathodic test first since it is known to be non-destructive as detailed in section 2.4.4.

6.2.3 Sensitivity in the corrosion rate calculations

Although the real Stern-Geary coefficients are computed as shown in Table 7-3, the corrosion rates quoted in subsequent sections are subject to errors associated with uncertainties in analysing the potential versus log current plots which are used in order to yield the Stern-Geary constant (B). However, the associated errors in the corrosion rates are minor in comparison with the influence of the changes in the polarisation resistance values. Hence, the main message regarding the influence of the investigated parameters on the corrosion rates are essentially unchanged.

6.2.4 Electrochemical Impedance Spectroscopy (EIS)

EIS experiments were ran with an AC sinusoidal excitation of 10 mV for a frequency range starting at 10kHz and ending at 1mHz while registering 40 points per decade.

6.3 Surface analysis techniques

6.3.1 Scanning Electron Microscopy (SEM)

The instrument used for this study is the Zeiss EVO MA15 which irradiates the surface of interest with finely focused electron beam corresponding to high energy electrons; these electrons interact with the surface and produce an array of scattered signals which are then analysed. These could span a wide range of secondary electrons, backscattered electrons, characteristics X-rays and other photons. The technique requires vacuum to be in place for both chemical corrosion and thermal stability control of the filament used as the

gun firing the electrons. This is also of importance for a non-affected secondary electrons when back travelling to the detector.

The SEM has the capacity of obtaining 3D images of surfaces and is mainly implemented as a topographic imaging tool with magnifications ranging from ten to tens of thousands.[355] SEM micrographs from an experiment ran at 60°C in CO_2 saturated environment at a pH of 6.8 after 10 days of static immersion in 3.5% sodium chloride brine are presented hereafter. The topographic image shown in Figure 6-3 was acquired from the back-scattered electrons (CZ BSD) at a magnification of 3,000 and a working distance (WD) of 10mm. The scale bar of 10μm allows for the comparison of the $FeCO_3$ crystal sizes which range between 5 and 10 μm in average in these environmental conditions.
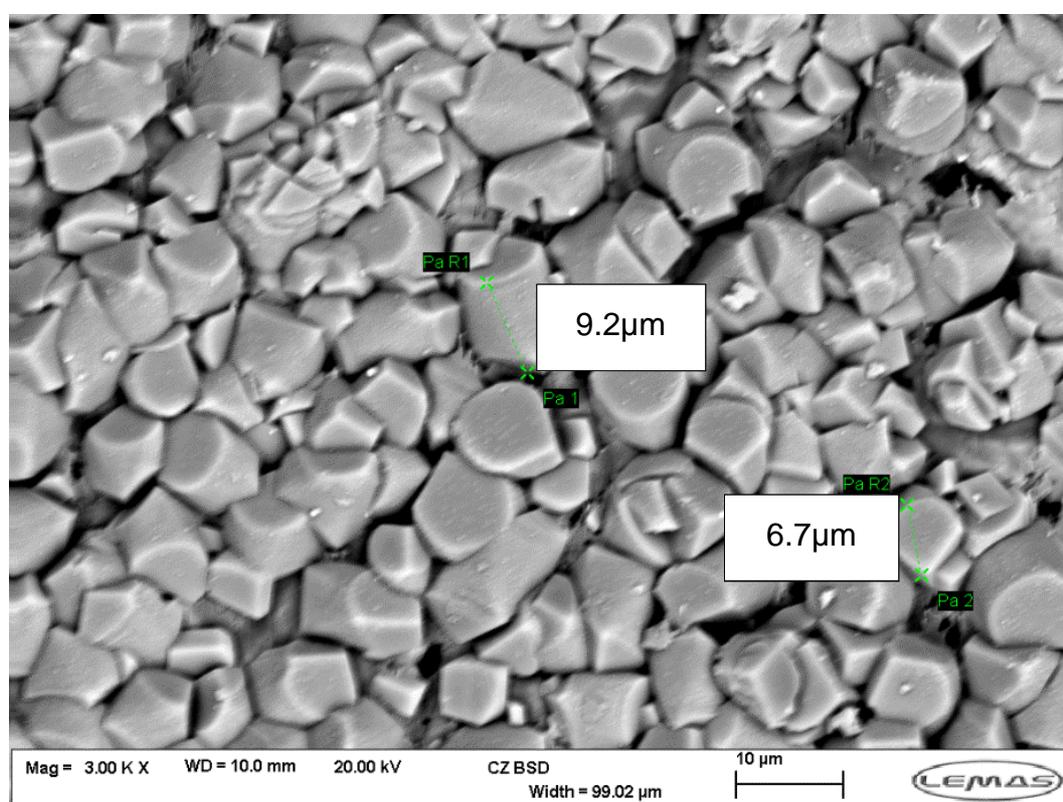
Figure 6-3 SEM top view scan of $FeCO_3$ corrosion layer at 60°C

Thus, the registered signals provide characteristic features of the surface, such as surface topography, crystallography and sometimes the elemental composition. It is known that SEM micrographs rely on surface processes, hence it is able to image bulk samples up to many centimetres in size and its depth of field depend on the instrument design and settings; it can therefore produce images that are good representations of the 3D shape of the studied sample.

The use of square samples allow for a quick characterisation of average thicknesses of the corrosion products by just flipping the samples and casting them in resin. Thus the SEM technique can be an indirect way of assessing the corrosion layer thickness from a cross-section scan of the studied specimen.

Figure 6-4 shows such results at a pH of 6.6, a temperature of 60°C and a constant supply of required ferrous iron to achieve the supersaturation for iron carbonate precipitation. The average thickness was found to be 40 micrometres after a test duration of 10 days. It should be noted that prior to each scan, the sample was attached to an aluminium stub using a carbon sticker and carbon paint then sputter coated in gold for higher resolution micrographs and reduction of sample charging.
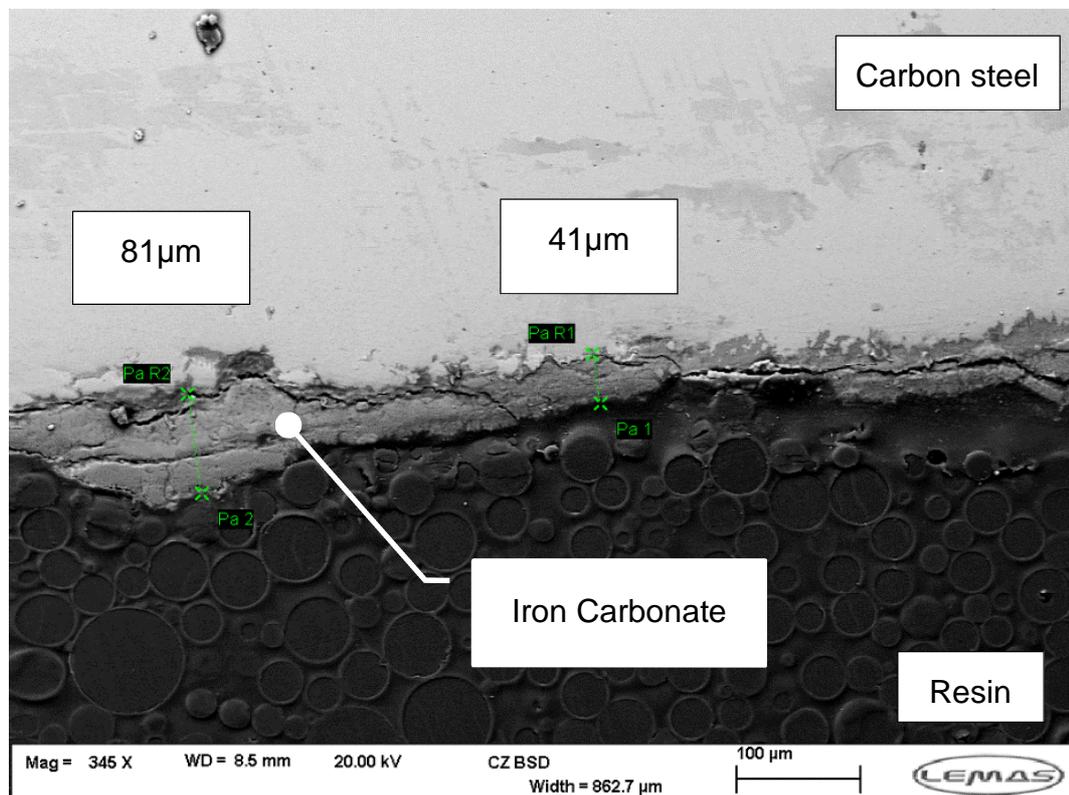
Figure 6-4 SEM cross-section scan of FeCO$_3$ at 60°C

6.3.2 Transmission Electron Microscopy (TEM)

Transmission electron microscopy is an elastic scattering spectroscopy imaging technique which could be done at the sub-nanometre scale with the right choice of the probe forming source. TEM analysis can be used as a direct

133

visualization technique to determine both the morphology and dispersion of the nanoparticles or platelets within the polymer matrix of choice.

SEM was used in conjunction with the Focused Ion Beam (FIB) system (FEI NOVA200 Dual-beam SEM/FIB). It utilizes a gallium ion beam to probe over the surface of a sample; the generated secondary electrons or ions from the interaction of the ion beam with the surface of the studied specimen can be used to obtain high-spatial-resolution micrographs.

The ion beam allows etching of the sample at sites of interest in order to produce cross-sectional images. Thus the FIB/SEM was used as a micro-machining tool in order to analyse the cross-section of the $FeCO_3$ corrosion product layers as shown in Figure 6-5a. This can be coupled to a high resolution EDX analysis as shown in Figure 6-5b.
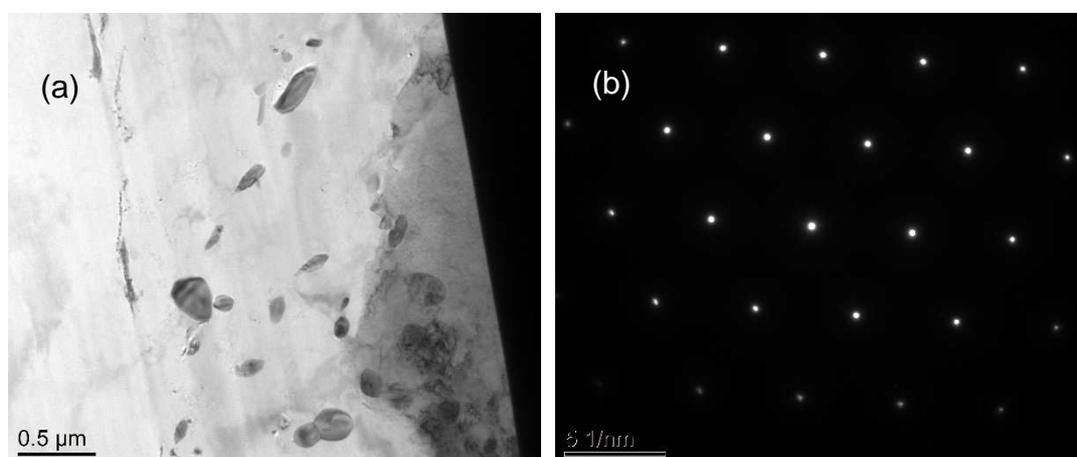
Figure 6-5 TEM micrograph of (a) POSS modified $FeCO_3$ and (b) iron EDX scattering pattern

6.3.3 X-Ray Diffraction (XRD)

X-ray diffraction is a non-destructive analytical technique widely used in order to identify unknown minerals, solid solutions, mixture of minerals, clays, zeolites in addition to more advanced applications as its crystallographic applications in material science. Crystalline substances consisting of parallel rows of atoms separated by unique distances can be studied; $FeCO_3$ in its crystalline form is such a compound. The sample is illuminated with X-rays of a fixed wavelength and the intensity of the reflected radiation is recorded using a goniometer. The data is then analysed for the reflection angle to calculate the inter-atomic spacing and the intensity is measured to discriminate between various d-spacing. Data banks are available and the results are compared in order to identify possible matches of the studied compounds.

6.3.3.1 Multipurpose diffractometers

Measurements were performed on a panalytical X'pert multipurpose diffractometers (MPD) with a voltage of 40 kV and an intensity of 40 mA using dual copper Cu Kα1+2 radiations with 10x10 mm programmable divergence slits. The diffractograms were generally registered on iron carbonate films in the angular region of 2θ=20° to 80° at room temperature and all scans were carried out in continuous mode. Phase identification was accomplished using Panalytical HighScore plus program.

All diffraction pattern were treated using the software HighScore plus by determining, subtracting and replacing the background but also by converting the divergence slits from Automatic Divergence Slit (ADS) to Fixed Divergence Slit (FDS).

It is assumed that, when performed directly over the specimen, XRD tests will allow for an indirect estimation of the $FeCO_3$ film thickness and porosity. When the peak is sharp and of high intensity, it is supposed that the scale is thick, uniform and dense whereas a large low intensity peak will be associated with porous, non-uniform and thin corrosion layer films.

6.3.3.2 Synchrotron tests

The *in situ* synchrotron X-ray diffraction experiments were undertaken using of the powder diffraction beam line (I15) at the Diamond Light source in Oxfordshire. The beam line provides high-energy, high-flux synchrotron XRD in combination with a small beam size. Energies higher or equal to 40keV are required to penetrate through the water (15 mm path length) in the flow cell and beam sizes lower or equal to 70 microns allowed scanning of the samples with good spatial resolution. The X-ray beam energy in these experiments was set up to 40 keV (i.e. λ = 0.3099 Å) and the beam size was 70 μm x 70 μm (vertical x horizontal). The sample exposure time was 30 seconds.

The flux available at I15, together with the fast data collection times which is lower or equal to just one second of the Perkin Elmer flat panel detector allowed for the intermediate phases to be measured and data collection was performed at high resolution rapidly. Diffraction images were recorded using a Perkin Elmer flat panel detector located 975 mm from the sample. Conventional 2-theta diffraction pattern were generated by radial integration of the Debye rings using the programme Fit2D with subsequent data analysis performed by profile fitting and Rietveld analysis.

The designed electrochemical synchrotron x-ray diffraction (SXRD) flow cell integrated with *in situ* electrochemistry is capable of generating flow velocities up to 2 m/s at temperatures in excess of 80°C whilst also possessing the ability to facilitate diffraction measurements through water, enabling high flow velocities to be maintained over the course of the experiment while diffraction pattern are being collected in real time which can correlate with electrochemical measurements.

The developed flow system is integrated with a 3-electrode cell consisting of a combined reference and counter electrode and an X65 steel coupon. A formulated saline solution circulates within a closed loop between the flow cell and a locally heated 1 litre vessel via the use of a centrifugal micro-pump to provide precise flow rate control. The 1 litre vessel is also continuously sparged with CO_2 throughout the experiment to ensure the temperature is maintained and the solution is fully de-aerated, thus mimicking the oil and gas production environments. Once flow is started in the cell, electrochemical measurements and X-ray diffraction measurements commence. The main variables within the test solution included the flow rate, the temperature and the pH.

The conversion of the diffraction angles between the dual copper Cu Kα1+2 radiations is shown in Table 6-3. It should be noted that the 2θ values are in degrees while the θ values are in radians. As such, the XRD results shown in Figure 8-21 are relying on a [104] Miller indices that shows a 40 kV (Kα1+2) diffraction angle of 32° which corresponds to a 35 KeV diffraction angle of 7.266°.

Table 6-3 Conversion between 40 kV (Kα1+2) and 35 KeV Cu for FeCO$_3$ diffraction angles.[356]

2θ (°)	λ$_{Cu}$ (Å)	θ$_{Cu}$ (rad)	d-spacing (Å)	λ$_{35KeV}$ (Å)	θ$_{35KeV}$ (rad)	2θ$_{35KeV}$ (°)
24	1.5406	0.2094	3.7049	0.3542	0.0478	5.4797
32	1.5406	0.2792	2.7946	0.3542	0.0634	**7.2668**
38	1.5406	0.3316	2.3660	0.3542	0.0749	8.5854
42	1.5406	0.3665	2.1495	0.3542	0.0825	9.4522
46	1.5406	0.4014	1.9714	0.3542	0.0900	10.3080
50.5	1.5406	0.4407	1.8058	0.3542	0.0982	11.2564
52.5	1.5406	0.4581	1.7416	0.3542	0.1019	11.6726
52.8	1.5406	0.4608	1.7324	0.3542	0.0896	10.2629
61	1.5406	0.5323	1.5177	0.3542	0.1170	13.4020

Similarly when tests were ran at 40KeV, the representative diffraction angle for the [104] Miller indices was computed to be equal to 6.35° as shown in Table 6-4; these values are used in Figure 10-19.

Table 6-4 Conversion between 40 kV (Kα1+2) and 40 KeV Cu for $FeCO_3$ diffraction angles.[356]

2θ (°)	λ_{Cu} (Å)	θ_{Cu} (rad)	d-spacing (Å)	λ_{40KeV} (Å)	θ_{40KeV} (rad)	$2\theta_{40KeV}$ (°)
24	1.5406	0.2094	3.7049	0.3099	0.0418	4.7939
32	1.5406	0.2793	2.7946	0.3099	0.0555	**6.3569**
38	1.5406	0.3316	2.366	0.3099	0.0655	7.51
42	1.5406	0.3665	2.1495	0.3099	0.0722	8.2678
46	1.5406	0.4014	1.9714	0.3099	0.0787	9.0159
50.5	1.5406	0.4407	1.8058	0.3099	0.0859	9.8448
52.5	1.5406	0.4581	1.7416	0.3099	0.0891	10.2086
52.8	1.5406	0.4608	1.7324	0.3099	0.0896	10.2629
61	1.5406	0.5323	1.5177	0.3099	0.1023	11.7195

The wavelength corresponding to 35KeV or 40 KeV was converted by using the Plank-Einstein relation shown in Equation 6-10 where h is the Plank's constant equal to $4.135667662(25) \times 10^{-15}$ eV.s and c is the speed of light approximately equal to 3.00×10^8 m/s.

Equation 6-10 Plank-Einstein relation

$$E = \frac{h.c}{\lambda}$$

6.3.4 Surface profilometry

White light interferometry was used to investigate localised corrosion behaviour. As any other surface interferometry, it is a spectroscopic technique which employs the interference between wave fronts of light beams exiting the same source and allowing the measurement of small surface irregularities.

The available NPFLEX 3D interferometer acts as an optical device that divides a beam of white light exiting a single source into two beams and then recombines them in order to extract information about the original state of the source waves and to create an interference pattern. The pitting corrosion extent was thus estimated indirectly via the study of the maximum pit depth and average of the 10 deepest pits as per ASTM G46-94.

The corrosion layers obtained during the bubble tests carried out in CO_2 saturated environment are removed by cleaning the surface with a Clarke's solution which composition is detailed in Table 6-5 at room temperature. This corresponds actually to the ASTM G 1-90 solution recommended for cleaning of corrosion products that are formed on iron and steels. The sample surface in then cleaned with acetone and air dried prior to the light interferometry analysis.

Table 6-5 Clarke's solution composition

Compound	Quantity
Hydrochloric acid solution with SG=1.19	1 Litre
Antimony trioxide (Sb_2O_3)	20g
Stannous chloride ($SnCl_2$)	50g

6.4 Chemical and mechanical analysis

6.4.1 Energy-Dispersive X-ray analysis (EDX)

EDX is a micro-analytical technique often used in conjunction with the SEM in order to provide elemental analysis or chemical characterisation of the studied specimen. Usually, the elemental compositions are automatically normalised to yield a sum equal to 100% and this leads to potentially unreliable assessments of the accuracy of the individual elemental compositions. As such, conclusions should not be drawn from EDX on its own but rather on all the complementary analysis techniques described in this chapter.

6.4.2 Brunauer–Emmett–Teller (BET) porosity tests

Adsorption isotherm graphs are usually used to study the process of adsorption; these are graphs showing the relation between the amounts of adsorbate which are adsorbed on the surface of the studied adsorbent on one side and the pressure at constant temperature on the other side. Different adsorption isotherms have been established during the past years such as Freundlich, Langmuir and BET theory.

BET theory stated that the true picture of physical adsorption is not a single layer as described by Langmuir at low pressure but rather a multilayer formation in a general rule; when high pressure and low temperature are of order, thermal energy of gaseous molecules decreases and more and more

gaseous molecules are available per unit surface area, thus multilayer adsorption ensues.

The BET relation is given as per Equation 6-11 along with the BET constant.

Equation 6-11 BET equation and BET constant

$$V_{total} = \frac{V_{mono}.C.\left(\frac{P}{P_0}\right)}{(1 - \frac{P}{P_0})(1 + C\left(\frac{P}{P_0}\right) - \frac{P}{P_0})}$$

$$\text{with } C = e^{\frac{E_1 - E_L}{R.T}}$$

The pressures P and P_0 are the equilibrium and the saturation pressure of adsorbates at the temperature of adsorption respectively. V_{total} is the adsorbed gas quantity; the V_{mono} is defined as the adsorbed volume of gas at high pressure conditions allowing the coverage of the surface with a unique layer of gaseous molecules. C is a the BET constant which is a coefficient relating the two equilibrium constants; E_1 is the heat of adsorption for the first layer, and E_L is that for the second and higher layers and is equal to the heat of liquefaction.

In this study, TriStar 3000 automated gas adsorption analyser and TriStar 3000 analysis program were used in order to assess the porosity of powdered iron carbonate, OA-POSS and the mixture in order to check for any interactions between the selected nanofiller and inorganic powder. Application of the BET method allows for the determination of surface area, pore volume and pore size of the studied specimen by collecting a whole isotherm for the sample.

In order to accomplish that, solid samples are pre-treated by applying some combination of heat, vacuum, and/or flowing gas to remove adsorbed contaminants acquired (typically water and carbon-dioxide) from atmospheric exposure. The solid is then cooled, under vacuum, usually to cryogenic temperature (77 K or -195°C) and the quantity of nitrogen gas needed to give a monolayer coverage of the available surface is determined by the TriStar 3000. This is made possible by collecting the isotherm and following how the pressure over the sample varies with the amount of nitrogen gas taken up by the sample.

A nitrogen adsorptive is actually dosed to the solid in controlled increments; after each dose of adsorptive, the pressure is allowed to equilibrate and the

quantity adsorbed is calculated. The quantity adsorbed at each pressure and temperature defines an adsorption isotherm, from which the quantity of gas required to form a monolayer over the external surface of the solid is determined. With the area covered by each adsorbed gas molecule known, the surface area can be calculated. In order for the registered values to be acceptable, a correlation coefficient ≥0.999 should be obtained.

6.4.3 Inductively Coupled Plasma Optical Emission Spectrometry (ICP-OES)

The ICP-OES is used for the detection of trace metals. It is a spectrometric technique which relies on the inductively coupled plasma to produce excited atoms and ions that emit electromagnetic radiation at wavelengths characteristic of a particular element. It is implemented in order to assess for the silicon atom incorporation within the $FeCO_3$ corrosion products. The matrix was an $FeCO_3$ grown at 60°C by adding 50ppm $FeCl_2$ while the tested specimen were obtained by dissolving the naturally growing $FeCO_3$ corrosion films in the presence of various amounts of OA-POSS in 15% acetic acid.

Since it was not possible to analyse 15% acetic acid directly, each sample was diluted tenfold in 1% nitric acid. First, a rough analysis was carried out to estimate the concentration of Si present in the samples; with this data, the instrument was calibrated between 0.1 and 0.5 ppm Si using the above mentioned specimen as standards. The detection limit was determined from the instrument calibration curve and the precision of the analysis was determined by analysing one sample (2 mg OA-POSS) six times and calculating the 95% uncertainty interval. The accuracy of the analysis was determined by spiking the same sample with a known amount of Si, analysing if six times and calculating the recovery.

6.4.4 Raman/FTIR spectroscopy

Both RAMAN and FTIR were used as an additional complimentary technique mainly to ascertain the presence of the $FeCO_3$ corrosion layers but also the SI-O bonds which are representative of the administered nanofiller.

6.4.4.1 Raman spectroscopy

Raman spectroscopy is another technique which could give insight with regards to the chemical characterisation of the sample surface. It can detect both organic and inorganic species which is the case of the hybrid nanofiller used. The excitation radiation source in Raman is monochromatic thus it is

more energetic when compared with standard infrared sources. Two laser wavelengths of 488 nm and 785 nm are available for the InVia Renishaw Raman Spectroscopy instrument. This study uses the 488 nm laser in transmission mode for all the experiments to make sure the results are always comparable.

6.4.4.2 FTIR spectroscopy

FTIR is carried out to obtain an infrared spectrum which could identify different chemical bonds of samples. The principle of this technique is to shine a beam of various infrared light wavelengths and measure how much of that beam is absorbed by the sample. Therefore, the chemical bonding on the surface can be discovered. The FTIR facility Perkin Elmer Spectrum 100 can perform both solid and liquid state analysis and the former was applied for the purpose of this research.

6.4.5 Nanoindentation

Nanoindentation tests were performed using the Nano Test (Micro Materials Limited, UK), with a Berkovich diamond indenter. For the purpose of statistics and reliability, 60 loading/unloading curves were made in each experiment to find the average results. All experiments were performed at a constant loading and unloading rate equal to 0.2mN/s and to a maximum load of 1 mN (controlled maximum load). The hold time at maximum load was 20 s, and thermal drift correction was set at 60 s of holding period at 80% unloading. The unloading curves were used to derive the hardness and modulus values by analytical technique developed by Loiver and Pharr.[357]

The raw nanoindentation data provides only the reduced modulus values E_r and these need to be corrected according to Equation 6-12 in order to obtain the Young's modulus E_s.

Equation 6-12 Conversion from the reduced to Young's modulus

$$\frac{1}{E_r} = \frac{(1 - v_i^2)}{E_i} + \frac{(1 - v_s^2)}{E_s}$$

Here, E_i is the indenter modulus equal to 1140 (diamond), v_i is the indenter Poisson's ratio equal to 0.07, v_s is the iron carbonate Poisson's ratio assumed to be equal to 0.3.

Part IV. Results, discussion and future work

Chapter 7 Choice of test conditions and OA-POSS early stage interactions

In order to observe the effect that OA-POSS has on the iron carbonate film, long term tests were carried out to follow any enhancement of the grown iron carbonate film from the addition of the silsesquioxane moieties, whether of a mechanical or an electrochemical nature. This chapter highlights why a temperature equal to 60°C and a pH equal to 6.6 were chosen to run the experiments and how the OA-POSS affects the electrochemistry of the system and modifies the morphology of the grown corrosion layers.

7.1 Free drift experiments and choice of temperature and pH

Long term tests for a period of ten days were undertaken at a fixed pH of 6.8 and gradually increasing the temperature by 10°C from 50°C up to 80°C in order to assess the experimental set up repeatability by comparing results to published data. Both electrochemical AC and DC techniques along with surface analysis methods, mainly XRD and SEM were implemented. Due to local laboratory restrictions during the 3 months when these tests were carried out, it was not possible to undertake repeats since the test duration was as long as ten days.

7.1.1 General trend and pseudo-passivation issues

The corrosion rates variation in mmpy for a period of 240 hours in conditions of variable temperature and a fixed pH are plotted in Figure 7-1. Tests ran at 50°C showed a corrosion rate stabilising around 0.05 mmpy while tests ran at higher temperatures of 60, 70 and 80°C had their corrosion rate stabilising at steady states values lower than 0.001mmpy.

It appears that the higher the temperature, the more the pseudo-passivation state is prone to appear as validated by the much lower current densities and OCP ennoblement to more positive potentials observed in Figure 7-2. When such pseudo-passivating behaviour is in order, the corrosion rates drop to even lower values and the small currents render the follow-up of the electrochemical evolution quite challenging and subject to heavy fluctuations.
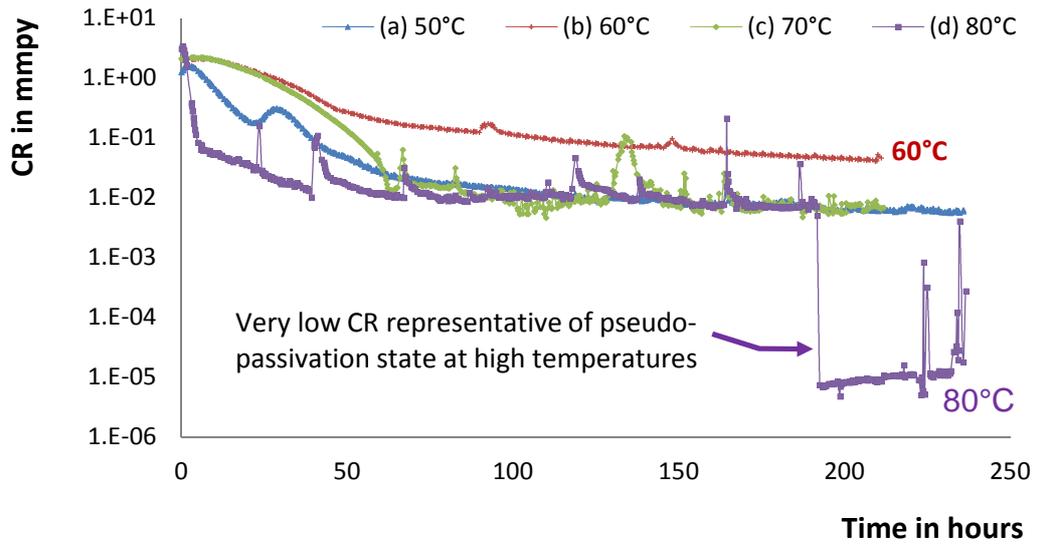
Figure 7-1 CR variation of X65 carbon steel sample in a CO_2 saturated environment at a pH of 6.8 and 3.5% NaCl at (a) 50°C (b) 60°C (c) 70°C and (d) 80°C for a duration of 10 days
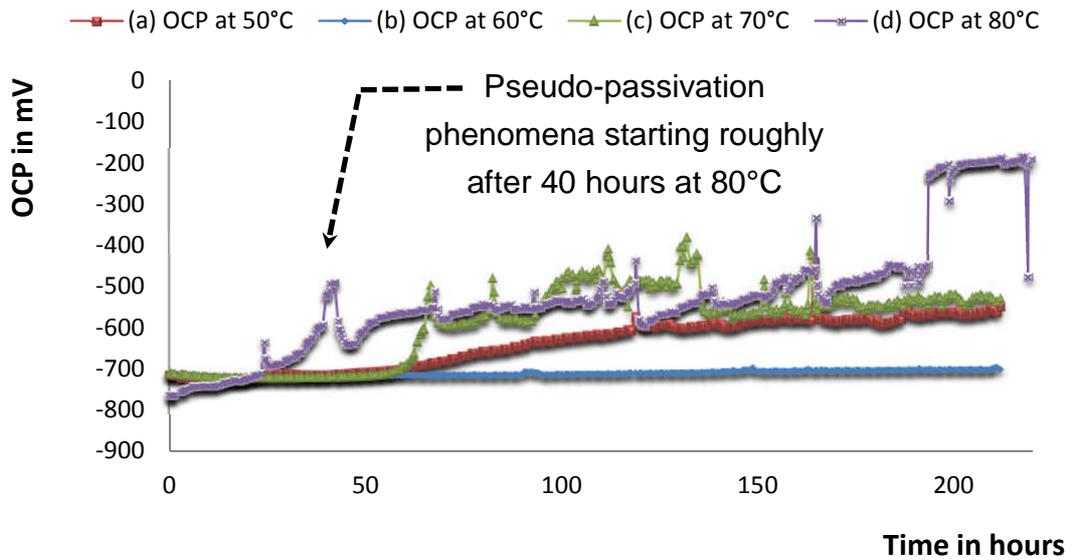
Figure 7-2 OCP variation of carbon steel X65 carbon steel sample in a CO_2 saturated environment at a pH of 6.8 and 3.5% NaCl at (a) 50°C (b) 60°C (c) 70°C and (d) 80°C for a duration of 10 days

This is the reason why only tests where pseudo passivating conditions did not occur were taken into account and compared in this study in order to disregard effects from corrosion products other than the $FeCO_3$ and to simplify the interpretation.

This trend is more obvious at a temperature of 80°C with the OCP reaching more positive values as high as -200mV while the OCP at 60°C is very stable with values around -695mV for the whole test duration.

At all studied temperatures, iron carbonate was found to be the main crystalline phase that grew on the X65 carbon steel as shown in Figure 7-3 summarizing the various XRD diffraction patterns registered after the 10 days test duration. By comparing the intensities of the iron carbonate [104] to the iron [110] Miller indices, the abundance of the $FeCO_3$ phase can be indirectly assessed as shown in Table 7-1.

The complete list of Miller indices were previously detailed in Table 4-1 but since the intensity is known to be the highest for hkl values corresponding to the [104] Miller index, the comparisons are made using this particular peak.

It is important to note in Figure 7-3 that the Bragg diffraction angle corresponding to the [104] Miller index appears at slightly different values for each temperature which could be explained by the evolution of diverse intrinsic stresses that evolve due to the altered morphology and size of the grown iron carbonate crystal. The blank term is used to describe a test where the nanofiller has not been added.
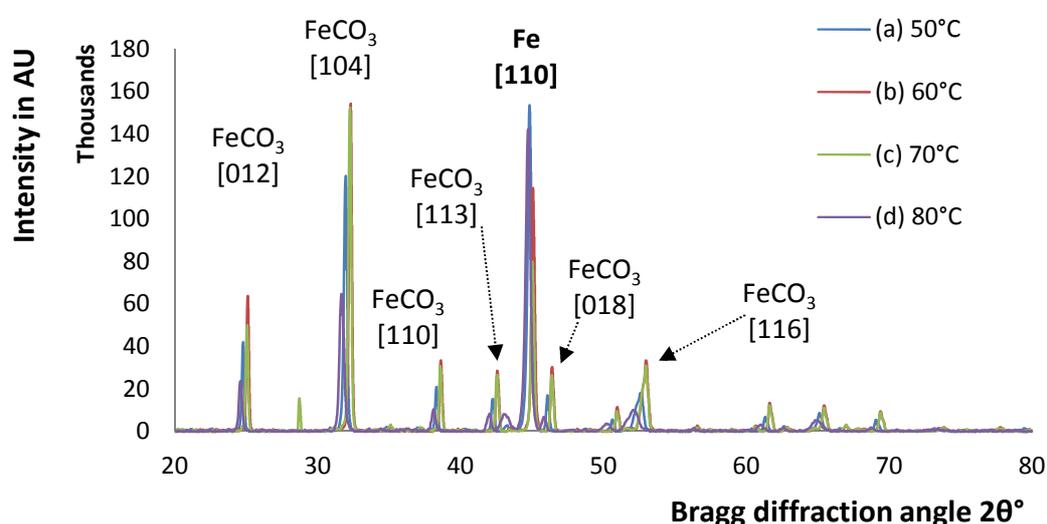
Figure 7-3 XRD diffraction pattern for (a) 50°C (b) 60°C, (c) 70°C and 80°C [pH 6.8, 3.5% NaCl, 240 hours]

These relative intensities can be indirectly linked to the crystalline phase abundance such as surface coverage and film thickness. As such, the iron

carbonate film thickness seems to be the lowest at 80°C and this is known to be due to the formation of a thinner, more compact and more protective corrosion films at a fixed pressure when the temperature is increased as previously described in section 4.4.1.

Table 7-1 XRD $FeCO_3$ to Fe ratio calculation at 50, 60, 70 and 80°C

2θ	Component	Intensity Value	Ratio [FeCO$_3$/Fe]
31.96°	Blank FeCO$_3$ (50°C)	120,034	0.78
44.81°	Blank Fe (50°C)	153,450	
32.31°	Blank FeCO$_3$ (60°C)	153,970	1.34
45.06°	Blank Fe (60°C)	114,617	
32.26°	Blank FeCO$_3$ (70°C)	152,409	1.90
45.01°	Blank Fe (70°C)	79,879	
31.66°	Blank FeCO$_3$ (80°C)	64,737	0.45
44.71°	Blank Fe (80°C)	142,192	

The computed ratios between the intensities of the $FeCO_3$ [104] Miller index and the peak corresponding to the X65 steel sample show that when raising the temperature from 50 to 80°C, the iron carbonate abundance evolves in the following increasing order: 80, 50, 60 then 70°C as suggested by the corresponding $FeCO_3$/Fe ratios computed in Table 7-1. This shows that running tests for a duration as long as 240 hours can provide contradictory results with the available data from the literature discussing similar set of conditions but for only 10 hours.[358]

The main observation from such values is the fact that the degree of $FeCO_3$ protectiveness is not directly linked to the corrosion layer abundance but rather to its degree of adhesion and compactness. While electrochemical techniques help describe the corrosion rate variation and surface layer growth over the working electrode, surface analysis techniques such as cross-section micrographs can help with the analysis of the scale adhesion to the substrate and the iron carbonate crystal distribution within the corrosion layer.

7.1.2 Detailed behaviour and system evolution at a pH of 6.8 and a temperature of 50°C for 240 hours

The Nyquist EIS data for the tests ran at 50°C is summarised in Figure 7-4 and Figure 7-5 which is a zoom on the dotted area to expand the first 24 hours impedance values.
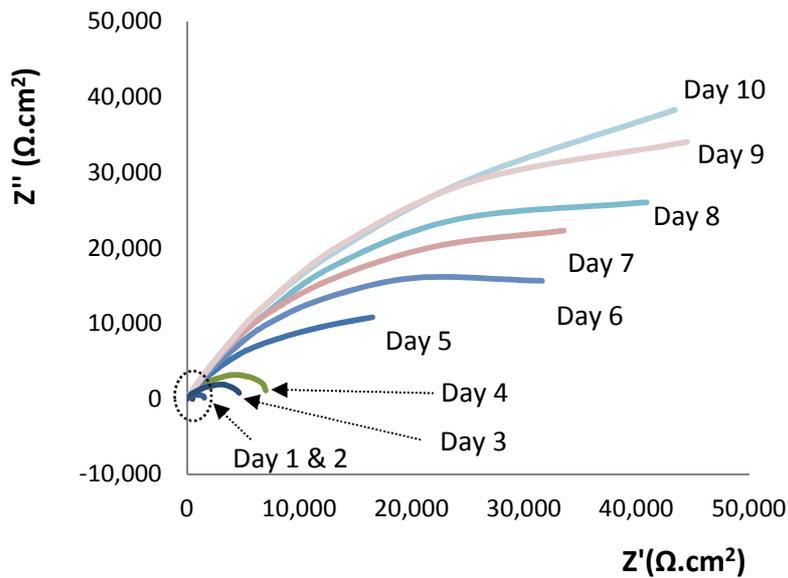
Figure 7-4 Nyquist plot of a X65 carbon steel sample in a CO_2 saturated environment at a pH of 6.8 and 3.5% NaCl at 50°C for a test duration of 10 days showing 1 data acquisition per day for ease of reading
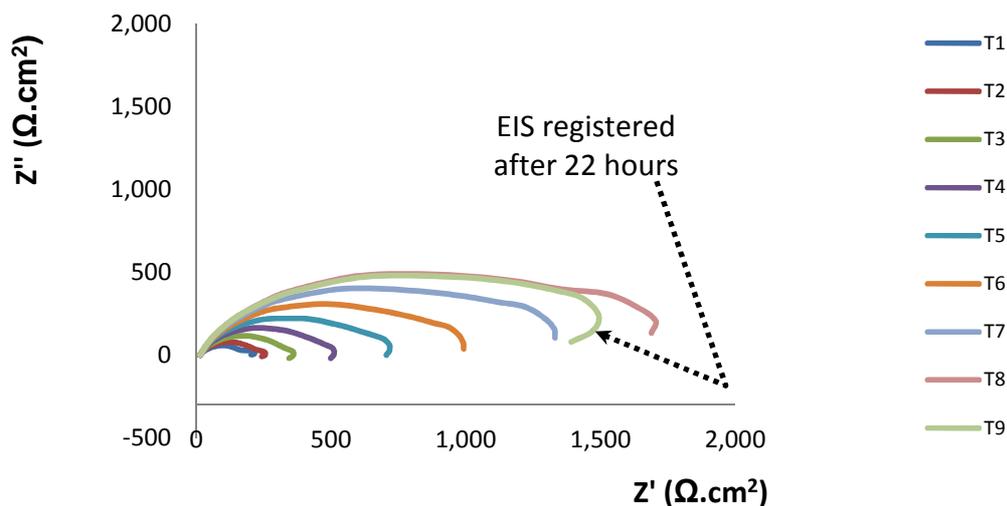
Figure 7-5 Nyquist plot of a X65 carbon steel sample in a CO_2 saturated environment at a pH of 6.8 and 3.5% NaCl at 50°C for the first 24 hours (every T is equal to 2.6 hours)

The real impedances exceed 10,000 $\Omega.cm^2$ after day 4 while the imaginary impedances reach the same value after 5 days. The system appears to evolve from a capacitive regime in the first few days to a sort of diffusion-limited behaviour which is obvious from the expanded loops replacing the ideal semi-circles which usually require the introduction of the Warburg resistances in order to build adequate equivalent circuits.

The Bode plot shows the establishment of a second time constant (T_{FeCO3}) after almost three days as seen in Figure 7-6 with the EDL time constant (T_{EDL}) showing in the first day around 10 Hz while the second time constant relating to the formation of the protective iron carbonate layer appears at lower frequencies in the 10 to 100 mHz zone.
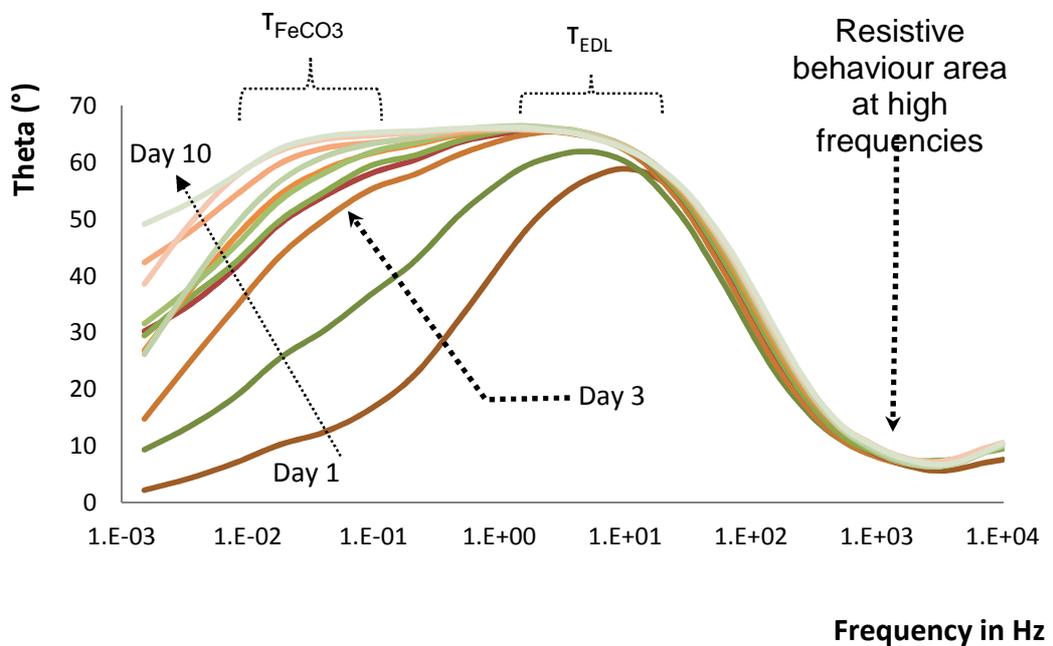
Figure 7-6 EIS Bode phase shift plot of a X65 carbon steel sample in a CO_2 saturated environment at a pH of 6.8 and 3.5% NaCl at 50°C for a test duration of 10 days showing 1 data acquisition per day (T is the time constant)

Thus the impedance responses appear to be resistive at the high frequencies as indicated by the absence of any phase shifts while they are mostly capacitive at intermediate frequencies with the value of the phase shift (Theta) increasing towards 65° by day ten.

With all major iron carbonate Miller indices present, Figure 7-7 shows that $FeCO_3$ is the main detected phase in the corrosion layer growing in these conditions. The corrosion film is not dense as inferred from the [104] $FeCO_3$ to [110] Fe Miller indices ratio which is lower than unity and this can be indirectly linked to the CR variation as per Figure 7-1.
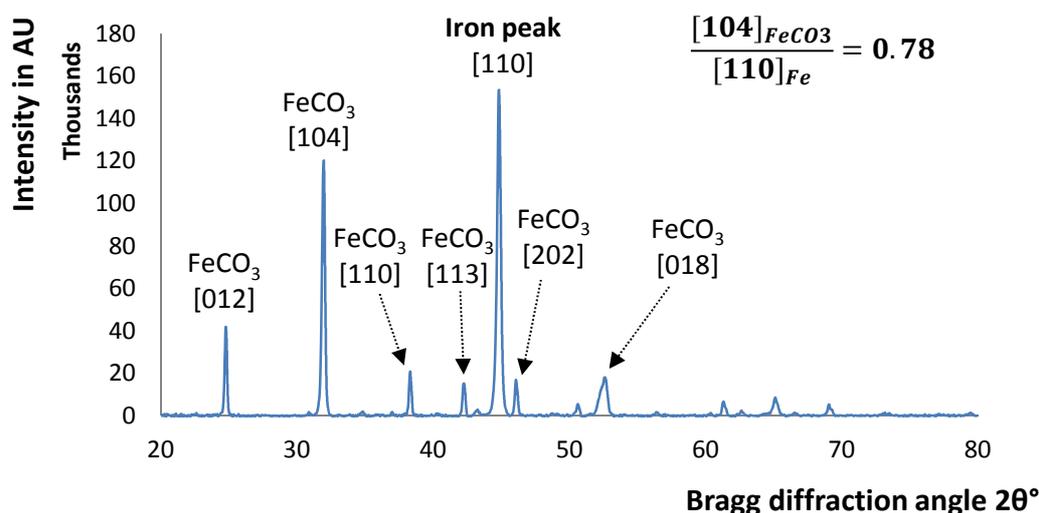
Figure 7-7 XRD diffraction pattern of a corrosion layer grown over an X65 carbon steel in CO_2 saturated environment at 50°C [pH 6.8, 3.5% NaCl, 240 hours]

Top view micrographs and cross-sections showing the average $FeCO_3$ film thickness for tests ran at 50°C and a pH of 6.8 are shown in Figure 7-8 and Figure 7-9 respectively. The iron carbonate films do not seem to be homogeneous and the crystals formed in these conditions appear to have different sizes and shapes, mainly prismatic and cubic (Figure 7-8b). This could be linked to different kinetic regimes of both nucleation and growth mechanisms; it appears as though new crystal layers with smaller crystal sizes around 3µm are forming within bigger already grown crystals with width reaching values higher than 10µm. Some areas showing a partially detached corrosion layer are visible (Figure 7-8a).

The cross-section view shows a dis-bonded corrosion film layer which could be due to the heat induced by casting the resin during the sample preparation. Nonetheless, the average film thickness at this running temperature appears to be in the range of 15µm. The increase in resolution in Figure 7-9 (a, b) shows two crystal layers that have detached and the average sum of both layers should be considered to assess for the scale thickness. This layer is

located in between the biggest areas comprised of the carbon steel and the resin.

30µm wide detached FeCO$_3$ area

(a)

Mag = 1.00 K X   WD = 7.0 mm   20.00 kV   SE1   10 µm
Width = 297.0 µm

LEMAS

Cubic FeCO$_3$

Prismatic FeCO$_3$

(b)

Mag = 4.00 K X   WD = 7.0 mm   20.00 kV   SE1   10 µm
Width = 74.26 µm

LEMAS
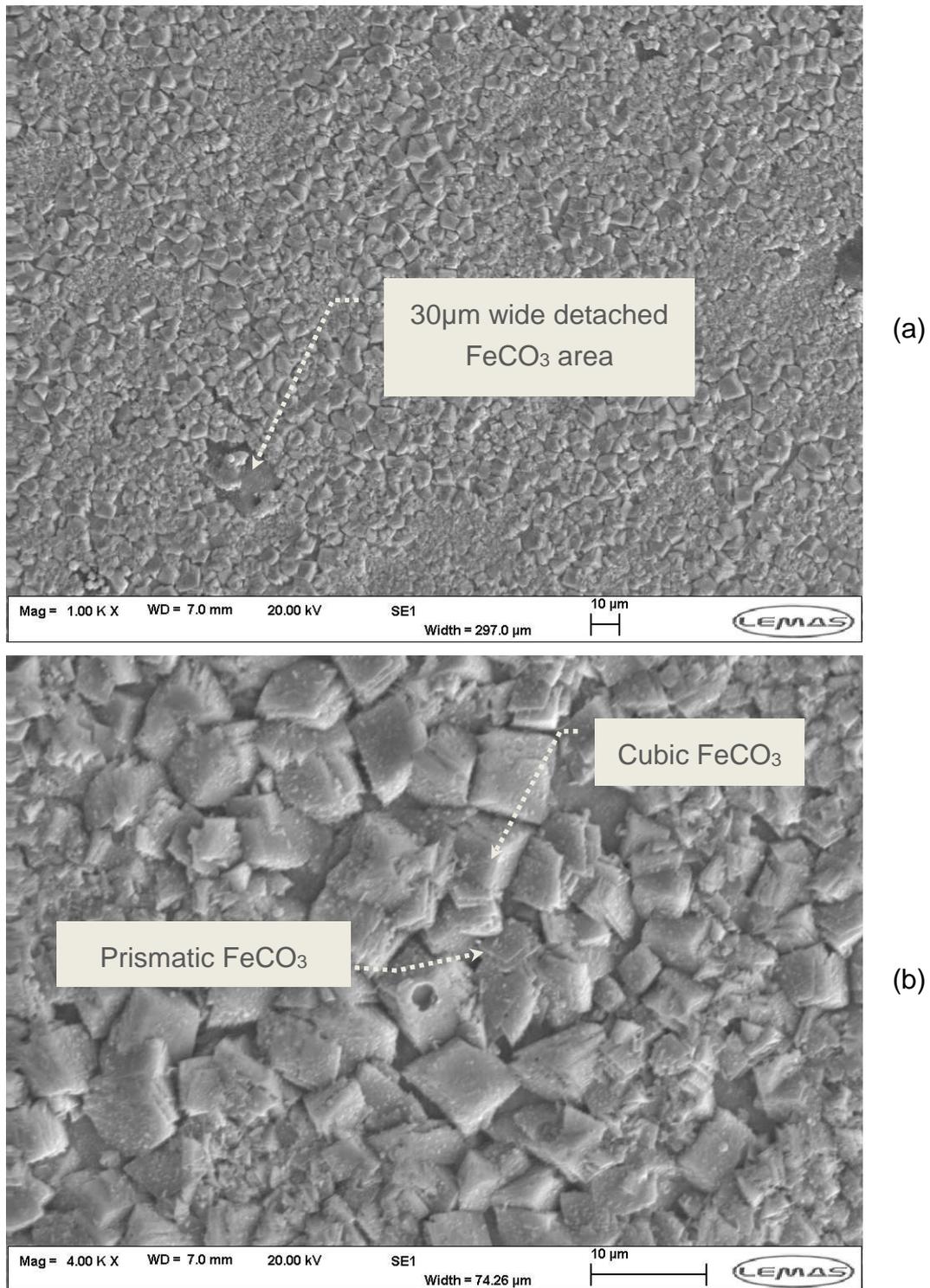
Figure 7-8 SEM micrographs topography view of X65 samples at various magnifications as shown by the corresponding scale bars [pH=6.8, 50°C, 3.5% NaCl, 10 days] showing (a) FeCO$_3$ crystals uniformly covering steel surface and (b) differential FeCO$_3$ crystal growth
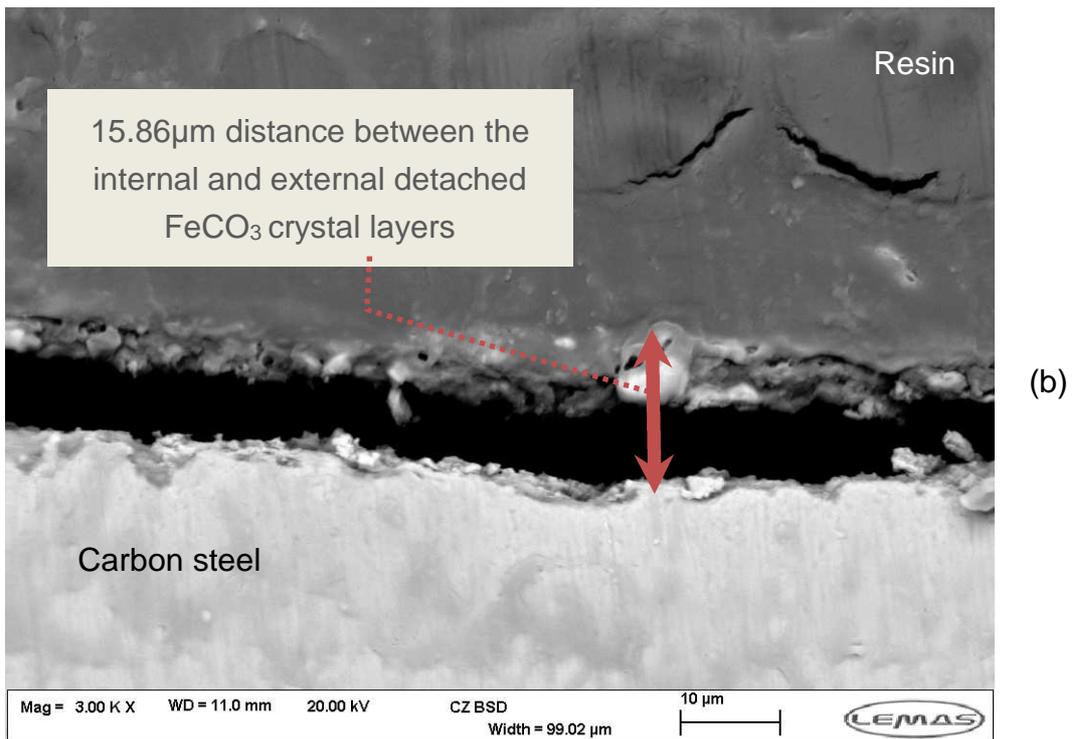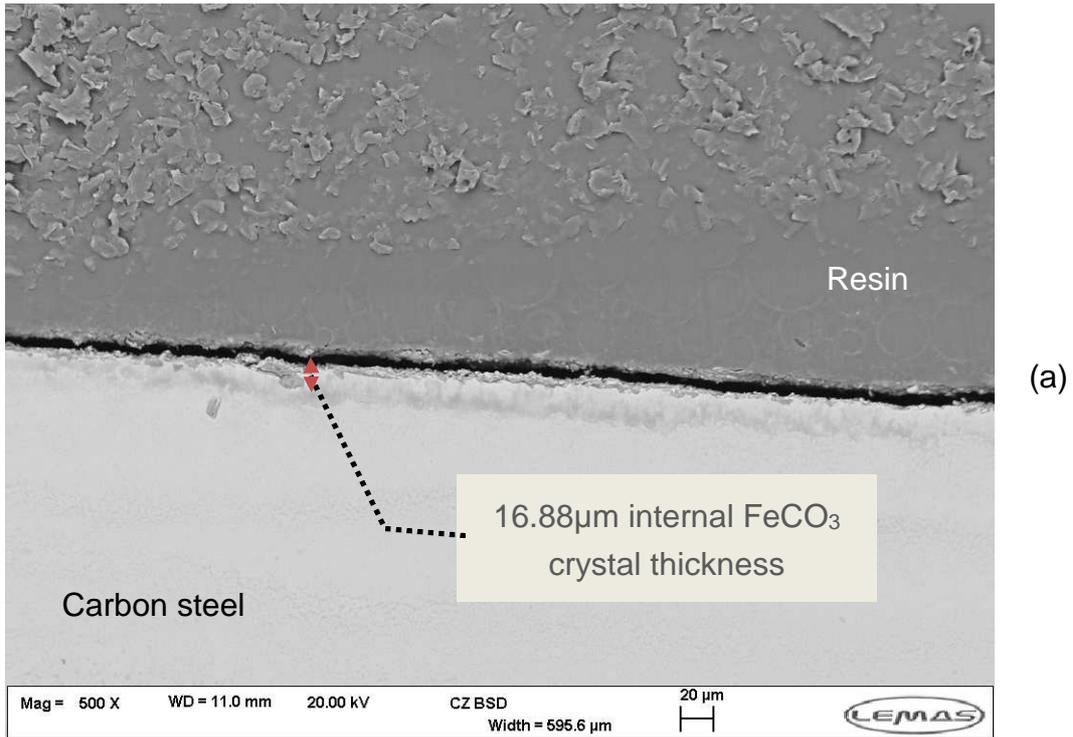
Figure 7-9 Cross-section SEM micrographs of FeCO₃ growing over X65 samples at various magnifications as shown by the corresponding scale bars [pH=6.8, 50°C, 3.5% NaCl, 10 days] showing (a) the delaminated FeCO₃ layer all along the steel surface area of contact and (b) a zoom showing a distance of 15μm between the FeCO₃ crystals attached to both the resin (up) and the carbon steel (bottom).

7.1.3 System evolution at a pH6.8, 60°C for 240 hours

When experiments are carried out at 60°C, the capacitive behaviour appears to be more pronounced for the whole test duration while both imaginary and real impedance values are more constrained as seen in Figure 7-10; the respective corrosion rate drops are mainly due to the iron carbonate film build-up and not any other corrosion layer such as the pseudo-passivation layers that are known to provide a higher degree of protection as seen from the corrosion rate drops in Figure 7-1 at both 70 and 80°C.
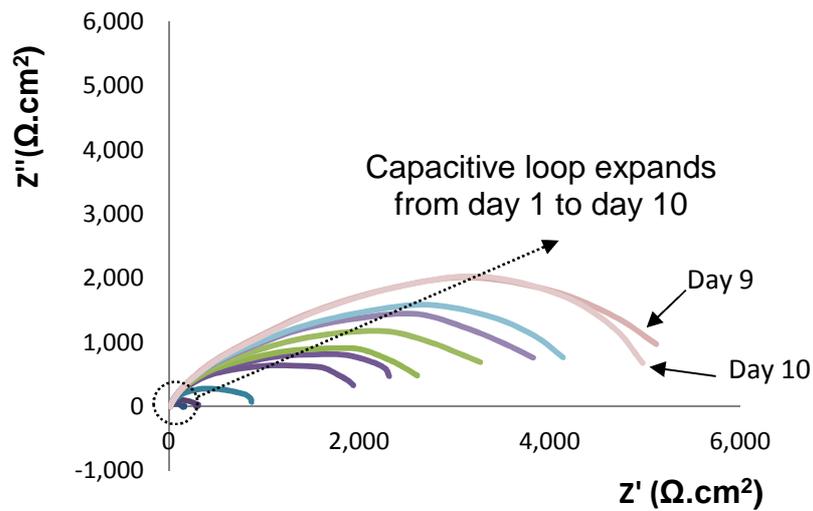
Figure 7-10 Nyquist plot of a X65 carbon steel sample in a CO_2 saturated environment at a pH of 6.8 and 3.5% NaCl at 60°C for a test duration of 10 days showing 1 data acquisition per day for ease of reading
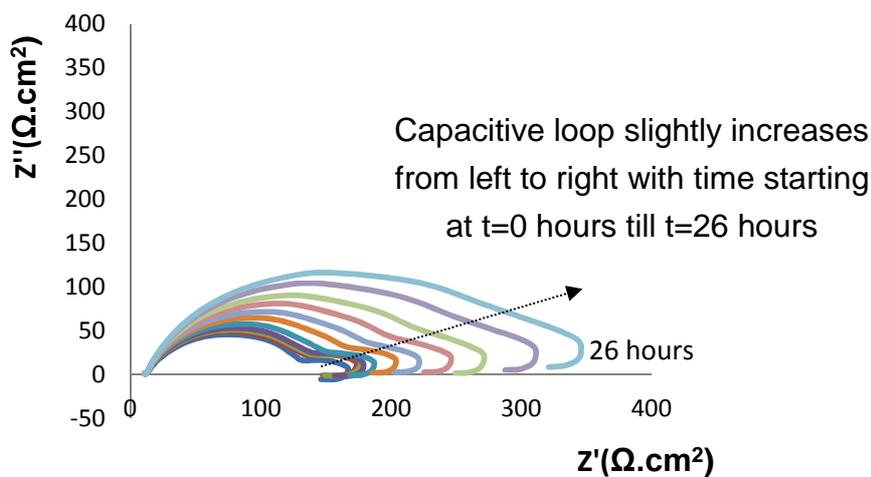
Figure 7-11 Nyquist plot of a X65 carbon steel sample in a CO_2 saturated environment at a pH of 6.8 and 3.5% NaCl at 60°C for the first day (every measurement is separated by 2.6 hours lap)

The kinetics of iron carbonate film formation seem slower at 60°C as seen by the expansion of the impedance values during the first 26 hours. As such Figure 7-11 shows the evolution of inductive loops the first 6 hours which are linked to the adsorption of salts and the establishment of the EDL layer but the capacitive loop growth is not as accentuated as at 50°C. When comparing both EIS and CR variations from LPR, the iron carbonate layers appear to be growing faster at 50°C but they are less protective.

Moreover, the time constant which is usually associated with the iron carbonate film growth between 0.1 and 0.01 Hz is not easily discernible on the EIS Bode plot at 60°C as could be observed in Figure 7-12 where the phase shift angle reached only 40° after 9 days as compared to the 65° phase shift registered for the tests ran at 50°C. The lower phase shift angle indicates a lesser capacitive behaviour which is related to the lower CR drop.
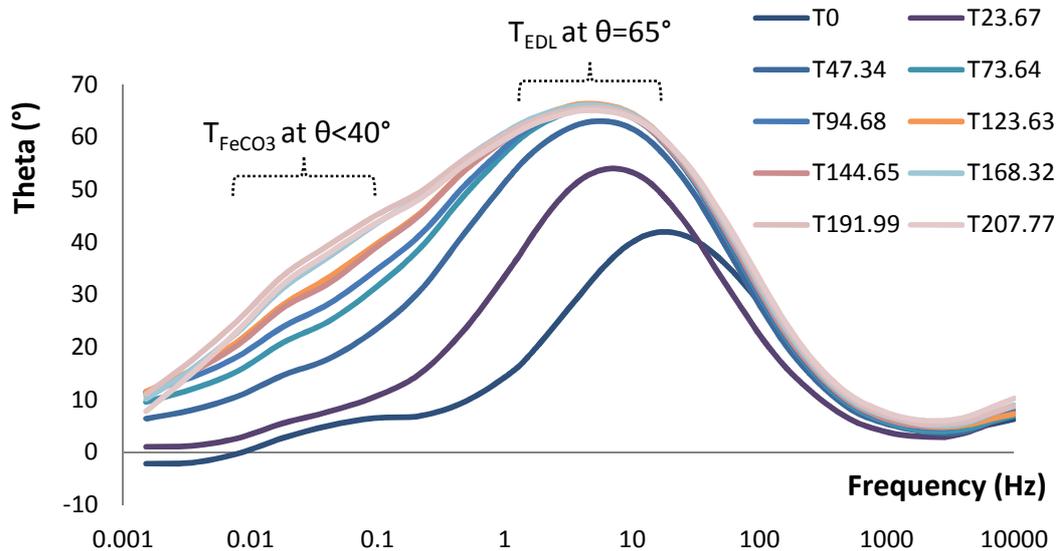
Figure 7-12 EIS Bode phase shift plot of a X65 carbon steel sample in a CO_2 saturated environment at a pH of 6.8 and 3.5% NaCl at 60°C for a test duration of 10 days showing 1 data acquisition per day

Similarly to the tests ran at 50°C, the XRD diffraction pattern registered at 60°C shows that iron carbonate is again the dominant crystalline phase as seen by the high intensity peaks at all respective Bragg angles in Figure 7-13. This hints to the fact that although the kinetics are slower, after 10 days, the corrosion film obtained is thicker since the [104] $FeCO_3$ to [110] Fe Miller indices ratio is higher than unity.
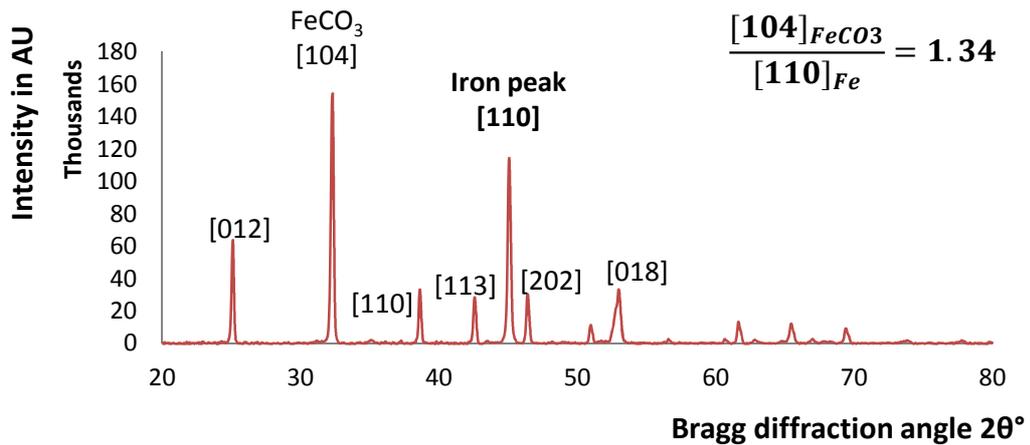
Figure 7-13 XRD diffraction pattern of a corrosion layer grown over an X65 carbon steel in CO_2 saturated environment at 60°C [pH 6.8, 3.5% NaCl, 98 hours]

When looking at the cross-section, the dis-bonded scale layer has an average thickness roughly equal to 20µm if crystals on both sides of the carbon steel and resin are accounted for as depicted in Figure 7-14. The fact that the layer is subject to a cohesive failure suggests its weaker mechanical resistance when compared to the layer grown at 70°C for example.
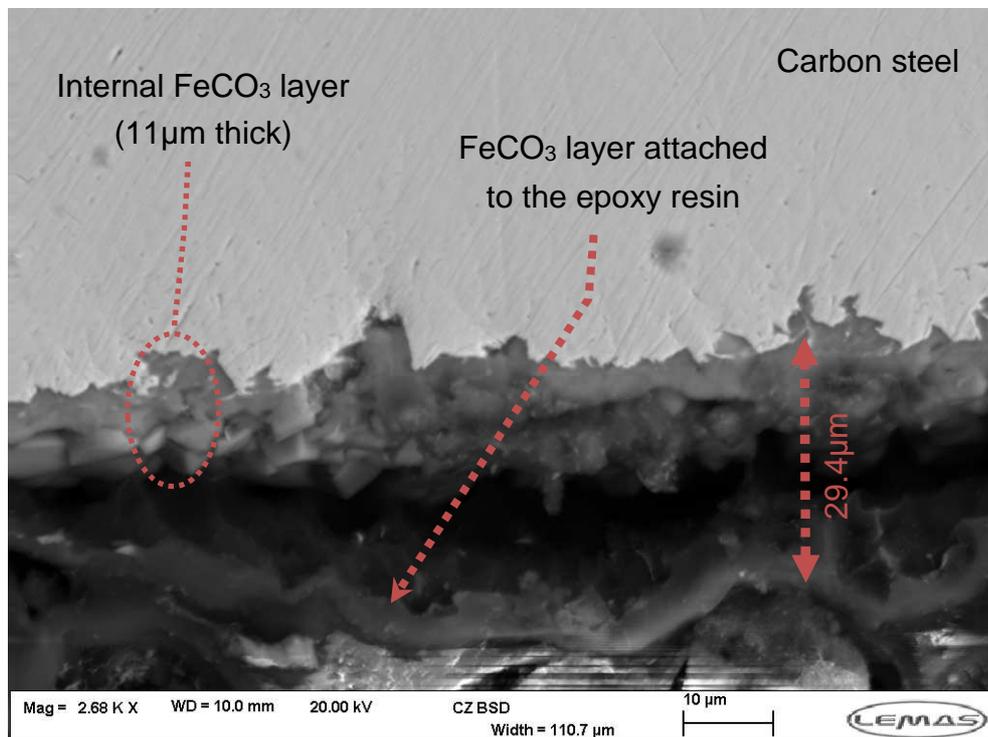
Figure 7-14 Cross-section SEM micrograph of X65 sample with the scale bar of 10µm [pH=6.8, 60°C, 3.5% NaCl, 10 days]

Regions without FeCO₃ crystals

20 µm

Mag = 1.00 K X   WD = 16.5 mm   20.00 kV   SE1   Width = 297.0 µm

(a)

9.2µm cubic FeCO₃ crystal

Smaller FeCO₃ crystals nucleating on top of pre-grown FeCO₃ crystal

10 µm

Mag = 3.00 K X   WD = 10.0 mm   20.00 kV   CZ BSD   Width = 99.02 µm
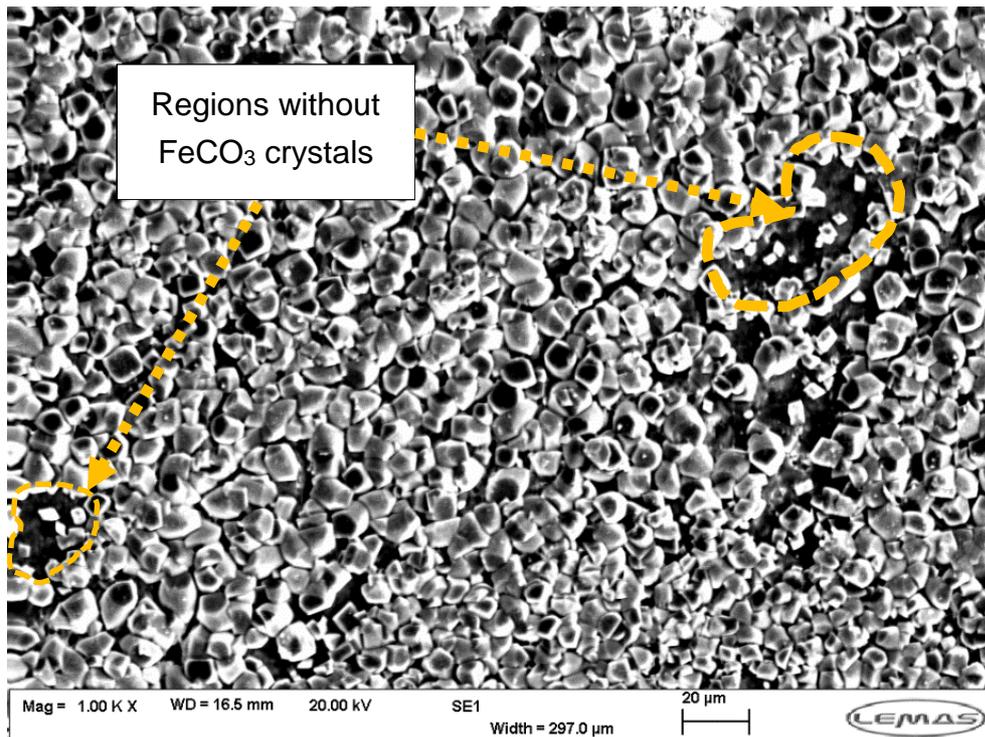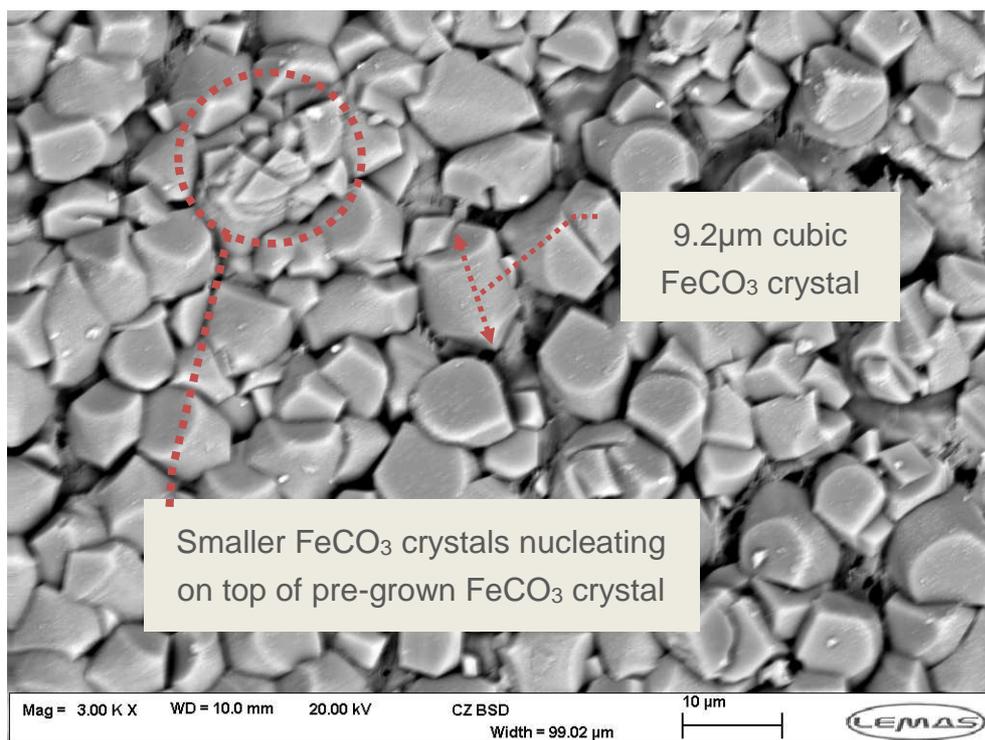
(b)

Figure 7-15 SEM micrographs topography view of X65 samples at various magnifications as shown by the corresponding scale bars [pH=6.8, 60°C, 3.5% NaCl, 10 days] with (a) lower magnification showing some areas deprived of FeCO₃ crystals and (b) a higher magnification depicting the FeCO₃ crystal size and spaces in between

The top view micrographs obtained at 60°C show a more homogeneous corrosion layer with smaller iron carbonate crystals averaging 5 to 10 μm in width as observed in Figure 7-15. These appear to be mainly cubic when compared to the leaflet or platelet like $FeCO_3$ crystals developing at 50°C.

Although uniformly covering the underlying carbon steel surface in most of the scanned area, some spaces between the $FeCO_3$ crystals are still evident as seen in Figure 7-15a. These holes highlighted with the dotted area are almost a micrometre wide which is more than enough for water molecules and other corrosion reactants to diffuse through.

7.1.4 Detailed behaviour at 70°C

At 70°C, the X65 carbon steel evolution during the first 2 days seems very similar to the tests ran at 60°C as per Figure 7-16; salt cations and anions from the 3.5% NaCl brine adsorb on the substrate surface in the first 6 hours; this behaviour is deduced from the negative values of the imaginary impedances and the establishment of adsorptive inductive loops. The solution resistance deduced from the real impedance values crossing the axis at the highest frequencies is around $11\Omega.cm^2$. An increase in the polarization resistance at low frequencies indicates that a protective film was formed and a lower corrosion rate was observed. In Figure 7-16, the larger diameter for the first day was obtained at the 25th hour indicates that the corrosion rate decreased more rapidly at the end of 25th hour of EIS measurement.
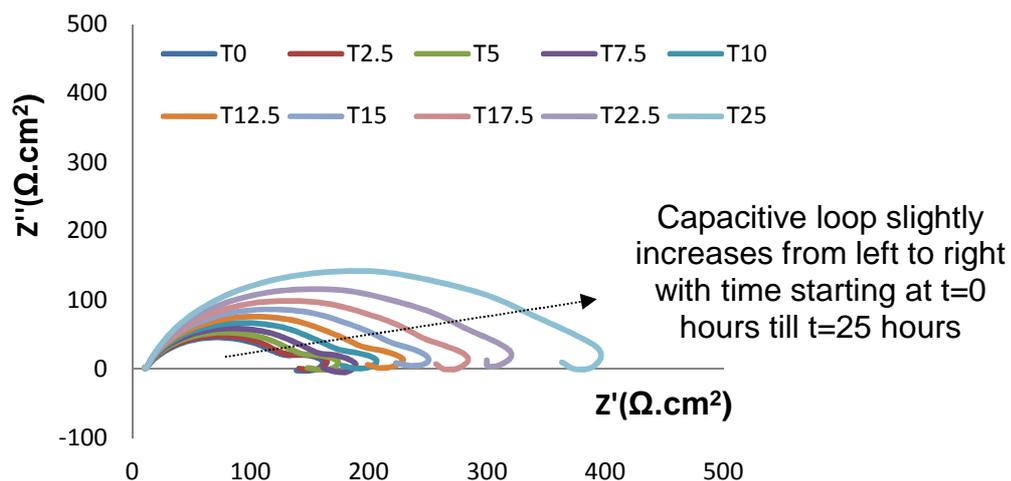
Figure 7-16 Nyquist plot of a X65 carbon steel sample in a CO_2 saturated environment at a pH of 6.8 and 3.5% NaCl at 70°C for the first day. The legend shows the acquisition time in hours and every measurement is separated by 2.6 hours lap

This monotonous trend is disrupted after 3 days' time, and the establishment of a pseudo-passivation layer and more complex corrosion films renders the interpretation of the EIS data quite challenging. Nonetheless, the switch from the typical Nyquist plot of CO_2 corrosion depicted by the semi-circular loop as per the Randal circuit to a diffusion controlled reaction is obvious after 49 hours as seen in Figure 7-17.
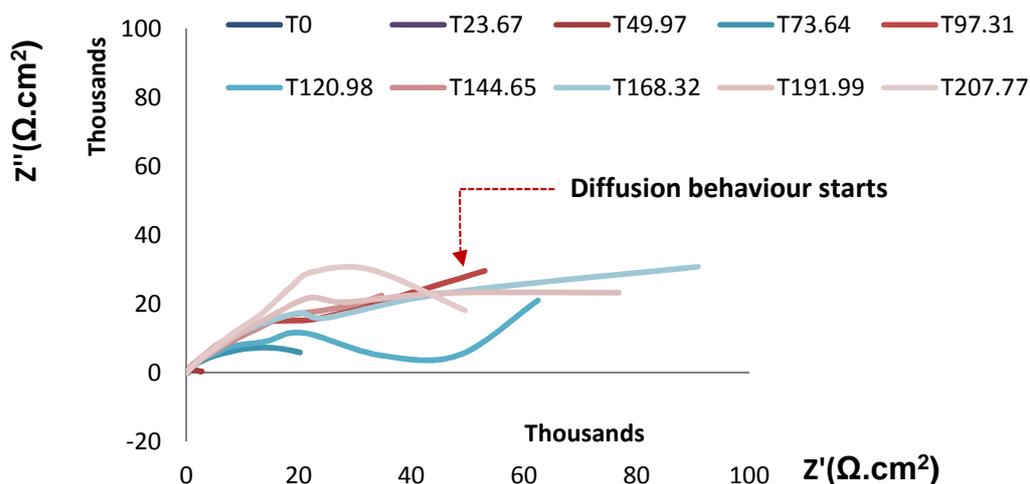
Figure 7-17 Nyquist plot of a X65 carbon steel sample in a CO_2 saturated environment at a pH of 6.8 and 3.5% NaCl at 70°C for a test duration of 10 days showing 1 data acquisition per day for ease of reading. The legend shows the acquisition time in hours.
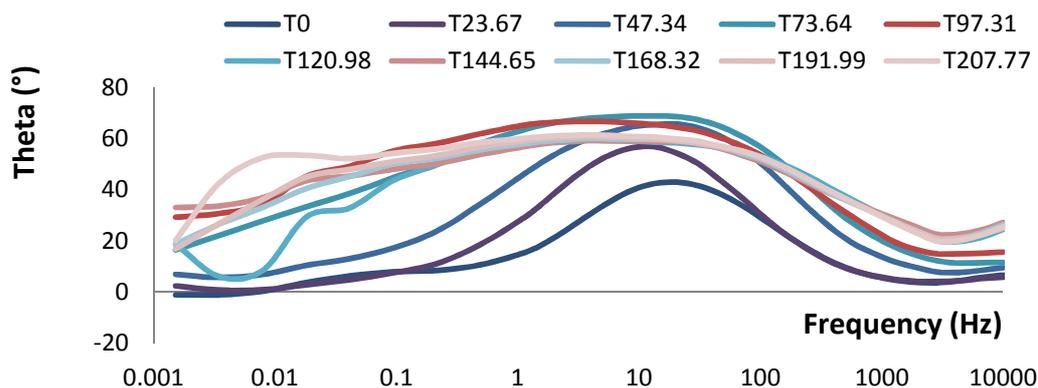
Figure 7-18 EIS Bode phase shift plot of a X65 carbon steel sample in a CO_2 saturated environment at a pH of 6.8 and 3.5% NaCl at 70°C for a test duration of 10 days showing 1 data acquisition per day. The legend shows the acquisition time in hours

The impedance values are twice as big when compared to the ones obtained at 50°C which corresponds to the formation of much more protective corrosion layers (Figure 7-17). Similarly the interpretation of the Bode plot is no simple task with the multitude of time constants appearing around 10 Hz, 0.1 Hz and even below 0.01Hz (Figure 7-18).

The iron carbonate crystalline structure is still easy to depict on the XRD diffraction pattern as shown in Figure 7-19. Moreover the $FeCO_3$ [104] Miller index intensity is almost double the Fe [110] Miller index which hints to the growth of a rather thick corrosion layer.

$$\frac{[104]_{FeCO3}}{[110]_{Fe}} = 1.9$$
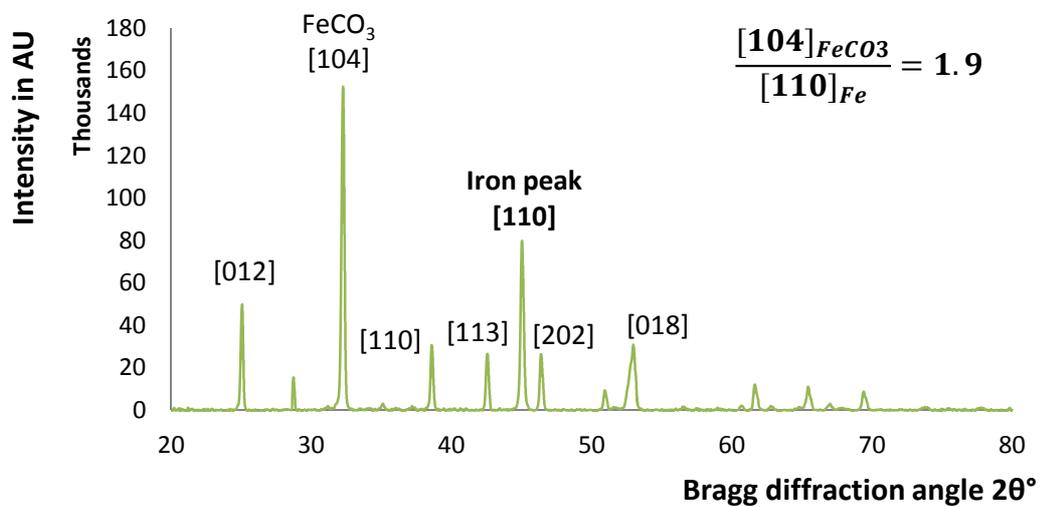
Figure 7-19 XRD diffraction pattern of a corrosion layer grown over an X65 carbon steel in CO_2 saturated environment at 70°C [pH 6.8, 3.5% NaCl, 98 hours]

The top view micrographs and cross-sections showing the average $FeCO_3$ film thickness are presented in Figure 7-20. The crystal size distribution looks even more uniform than tests ran at 60°C with width averaging 10 to 15µm; Even though the crystals are bigger, the average iron carbonate corrosion film thickness seems in the order of 12µm which hints to a preferential unidirectional growth of the iron carbonate crystals.

Moreover, the crystals do not look lamellar or built up of sheets as for crystals grown at 50°C but rather like a complete bigger single semi-circular crystal. The system does not seem very compact since some voids and apparent non-covered areas are visible on the top view micrograph showing dark black porous zones (Figure 7-20a). The whitish formations are most likely some crystalline salts from the brine.
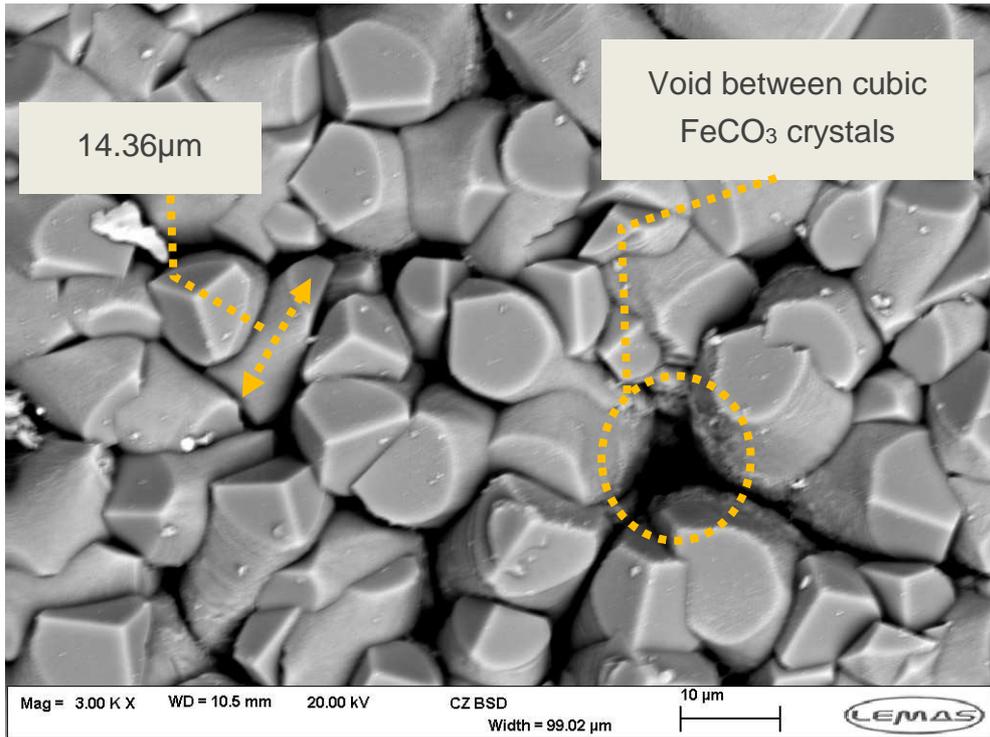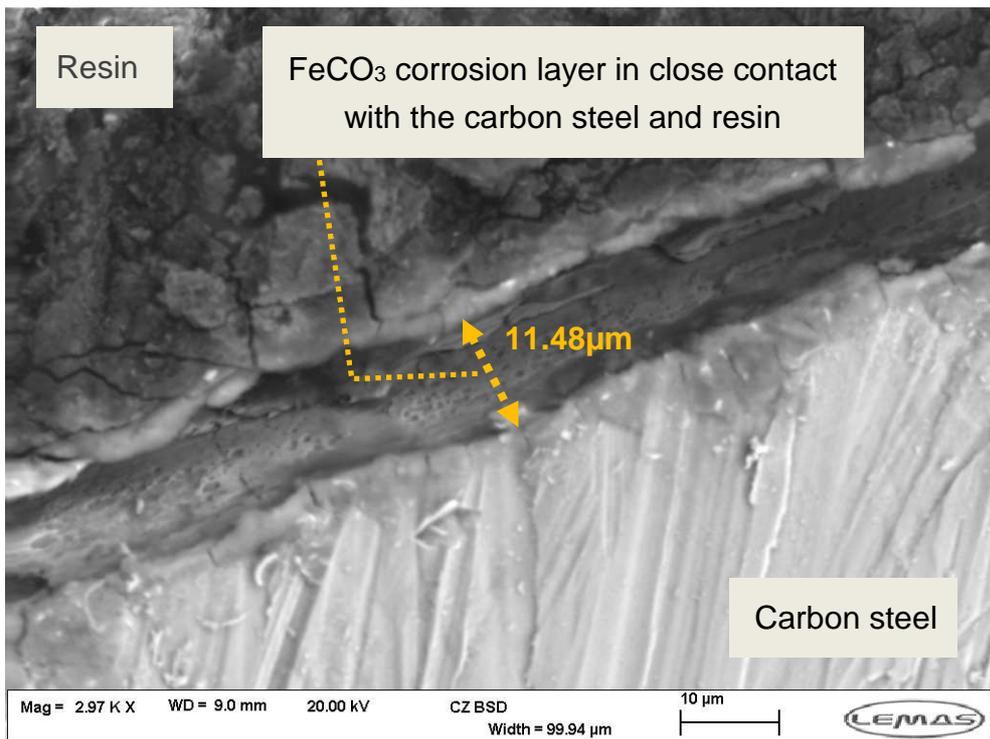
Figure 7-20 SEM top view micrograph (a) and cross-section micrograph (b) of X65 carbon steel sample with the scale bar of 10μm [pH=6.8, 70°C, 3.5% NaCl, 10 days]

The fact that the grown film at this temperature did not show a cohesive delamination due to the surface preparation of resin casting could suggest higher mechanical properties of the iron carbonate films grown at higher temperatures. This observation proves that it is very hard to correlate the XRD intensities and the iron carbonate film thicknesses since the tests ran at 70°C show the biggest intensities registered for the [104] iron carbonate Miller index but the film thickness was smaller than both films grown at 50 and 60°C.

7.1.5 Detailed behaviour at 80°C

At 80°C, the system is even more complex when the data is registered for a 10 days duration and is mainly characterised by a very quick corrosion rate drop starting at day 1 due to the formation of a very protective iron carbonate layer (Figure 7-21). There seems to be little timeframe allowed for adsorptive effects to be spotted such as the EDL equilibrium since corrosion layers starts evolving quite early at this high temperature accelerating the kinetics of the corrosion reactions.
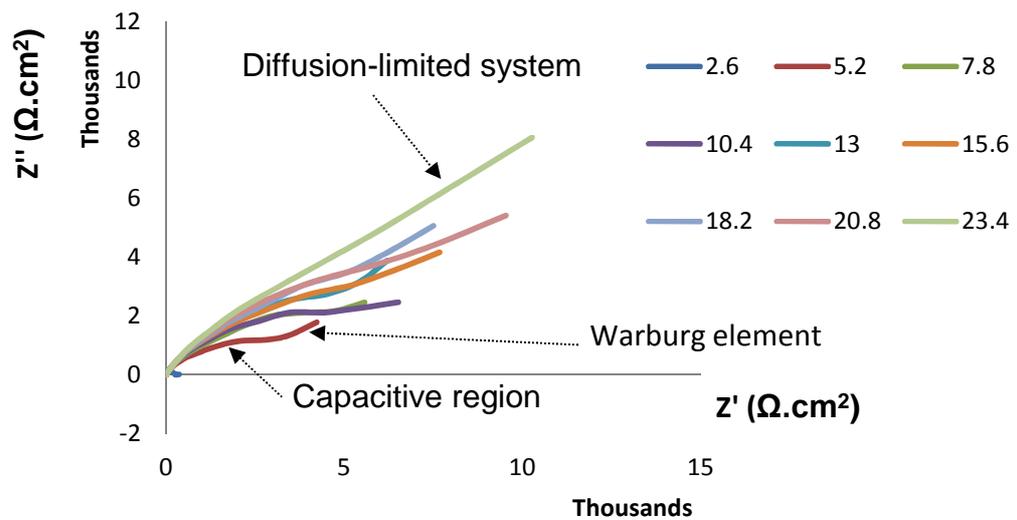
Figure 7-21 Nyquist plot of a X65 carbon steel sample in a CO_2 saturated environment at a pH of 6.8 and 3.5% NaCl at 80°C for the first day (The legend shows the time in hours)

In fact, the previously described capacitive behaviour is quickly replaced by a diffusion-limited system after just 2.5 hours and the apparition of the Warburg impedance. Such switch is explained by a very fast nucleation and growth of protective iron carbonate crystals.

After 8 days, the impedance values increase exponentially to exceed tens of millions of $\Omega.cm^2$. For that reason, Figure 7-22 only shows the evolution up to 190 hours. At some points, the Warburg impedance disappears and the

systems seems to shift back to a more capacitive behaviour thus depicting the complexity and the continual change in the on-growing corrosion scale layers at such temperature.
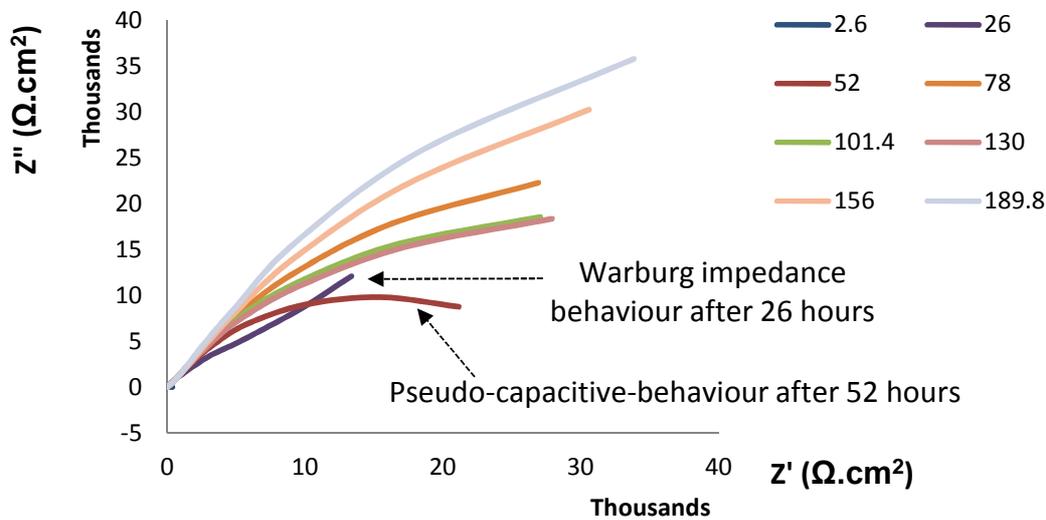
Figure 7-22 Nyquist plot of a X65 carbon steel sample in a CO_2 saturated environment at a pH of 6.8 and 3.5% NaCl at 80°C for a test duration of 10 days showing only the first 8 days for clarity; the legend shows the time in hours

As such, the Warburg impedance is present at the acquisition point corresponding to 26 hours and this is replaced by a more capacitive trend for the data acquired later after 52 hours from the start of the test.
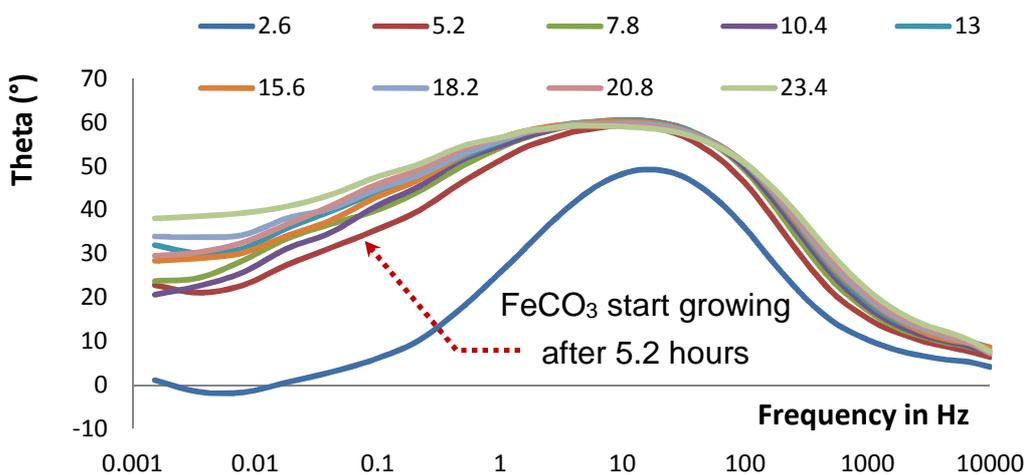
Figure 7-23 EIS Bode phase shift plot of a X65 carbon steel sample in a CO_2 saturated environment at a pH of 6.8 and 3.5% NaCl at 80°C for a test duration of 10 days showing the data acquired during the first 24 hours. The legend represents the time in hours.

This data is complemented with the corresponding phase versus frequency shift where it appears clearly that the second time constant linked to the iron carbonate development is clearly evident just after 5 hours as can be seen in Figure 7-23.

Although the XRD diffraction peaks in Figure 7-24 showed the lowest intensity ratios between the iron carbonate [104] and iron [110] Miller indices, the corrosion layer appear the most protective as per the corrosion rate drop in Figure 7-1.

$$\frac{[104]_{FeCO3}}{[110]_{Fe}} = 0.45$$
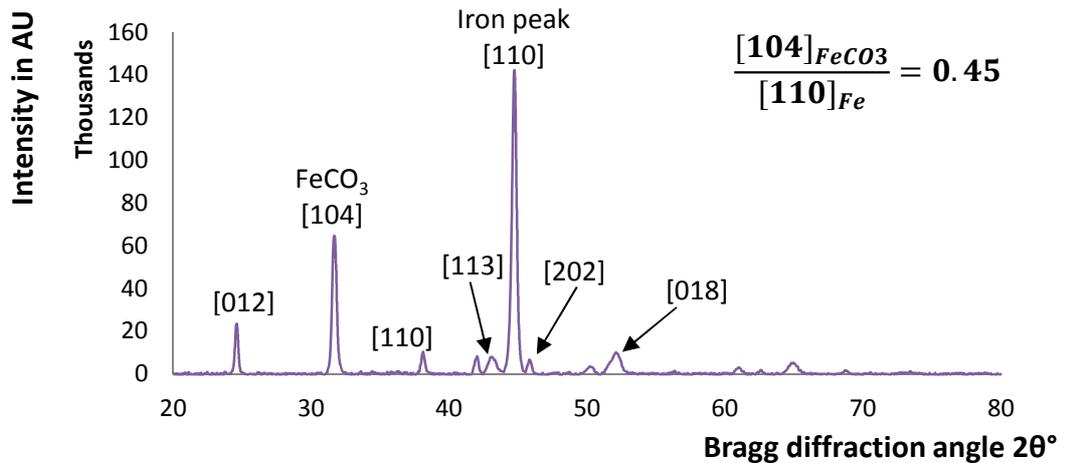
Figure 7-24 XRD diffraction pattern of a corrosion layer grown over an X65 carbon steel in CO_2 saturated environment at 70°C [pH 6.8, 3.5% NaCl, 98 hours]

The top view micrographs and cross-sections showing the average $FeCO_3$ film thickness for tests ran at 80°C and a pH of 6.8 are presented in Figure 7-25 and Figure 7-26 respectively. While the crystals are smaller in size as would be expected and varying between 2 to 5µm, many areas have some gaps and thus the underlying carbon steel surface is not fully covered with the $FeCO_3$ corrosion scale layer as would be expected at such high temperature.

This might explain the low ratio of [104] $FeCO_3$ to [110] Fe Miller indices even when compared to the tests ran at 50°C. This means that the corrosion protection is not mainly due to the iron carbonate film but rather to a basal thinner layer that is expected to have formed when the OCP showed a pseudo-passivation response only few hours after the test has started.

Similarly to the corrosion layers formed at 50 and 60 °C, the resin casting provoked a cohesive delamination of the scale layer which showed average thicknesses in the range of 10µm.
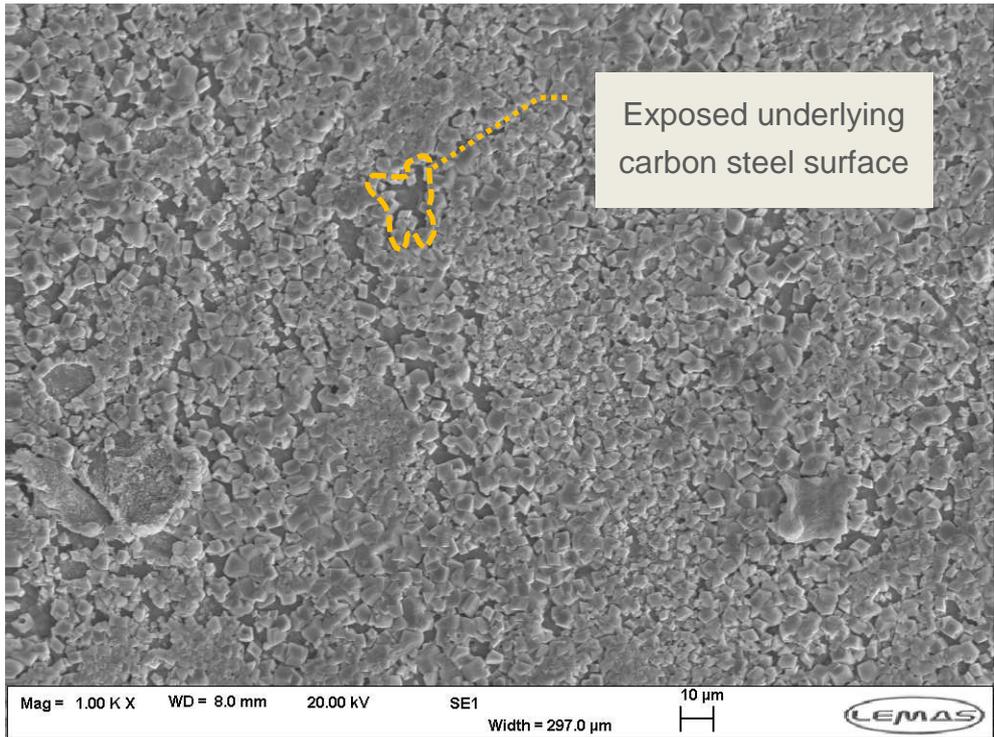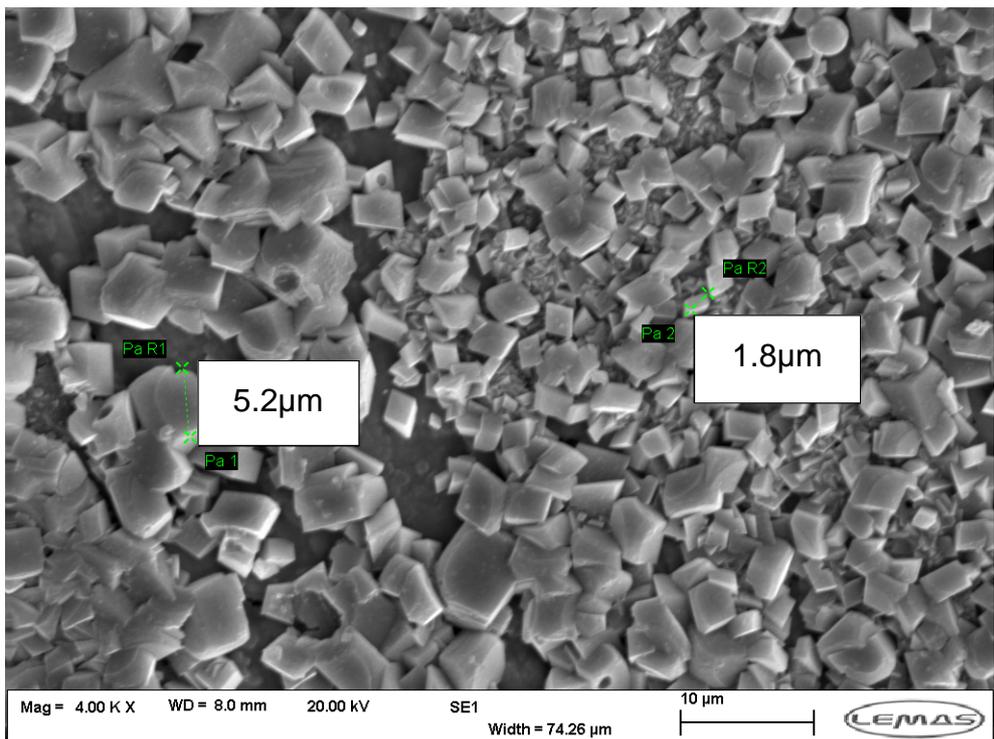
Figure 7-25 SEM micrographs topography view of X65 samples at various magnifications (a) showing various areas not covered with $FeCO_3$ and (b) $FeCO_3$ crystal of various dimensions representative of a delayed crystal nucleation and growth phenomena [pH=6.8,80°C,3.5% NaCl, 10 days]

(a)

(b)
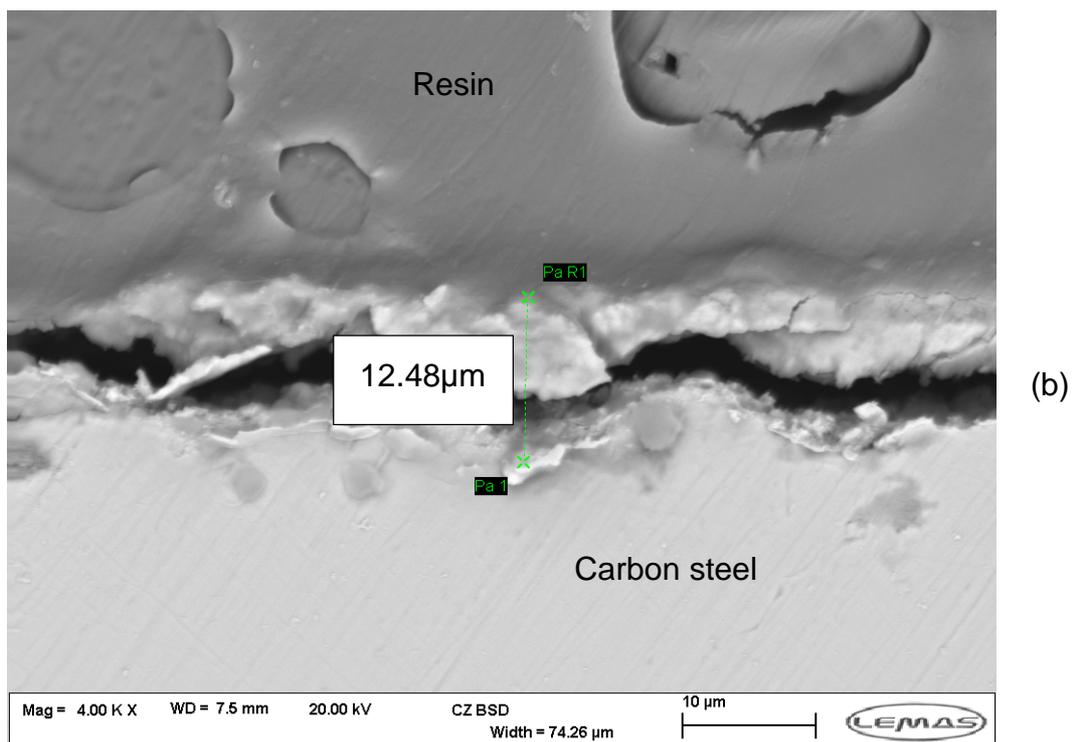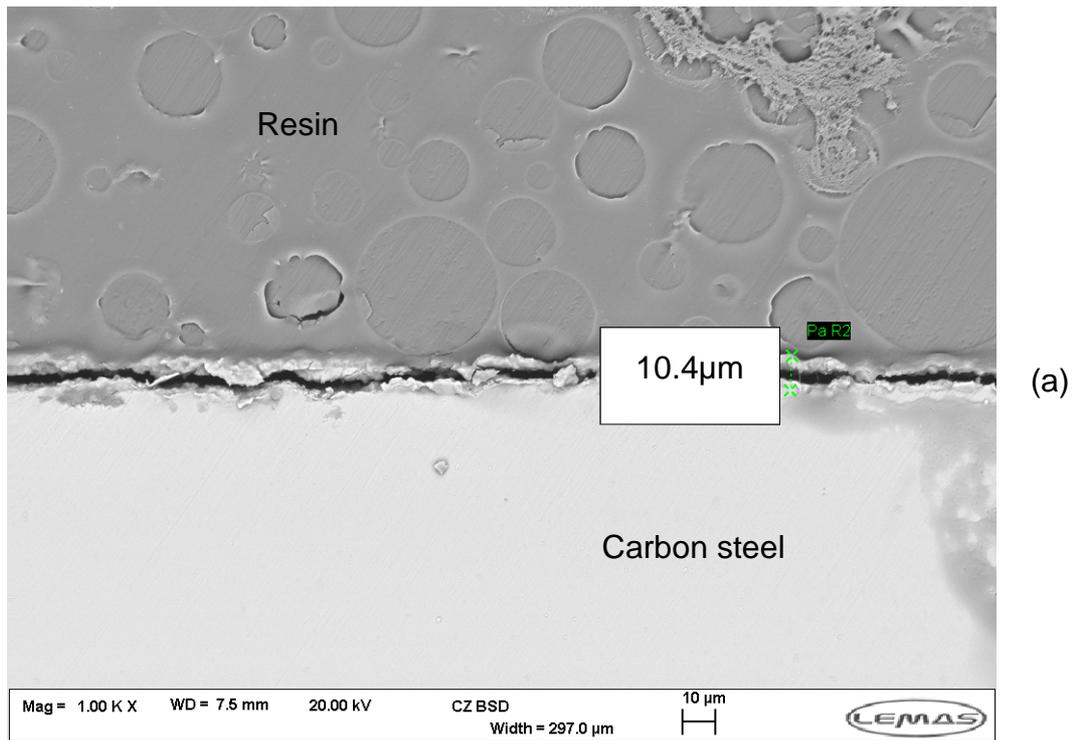
Figure 7-26 Cross-section SEM micrographs of X65 samples at various magnifications [pH=6.8, 80°C, 3.5% NaCl, 10 days] showing (a) the slightly dis-bonded corrosion layer along the underlying steel surface and (b) a zoom on an area where the $FeCO_3$ scale layer seems to have resisted such delamination

Although the quickest corrosion rate drop and best corrosion mitigation was registered at 80°C as depicted in Figure 7-1, the compiled data from both the SEM micrographs and the XRD diffraction patterns do not seem in total accordance with such CR variations. This could be explained by the fact that $FeCO_3$ crystal growth and film coverage are not the only factors that should be taken into account when describing the corrosion layer protectiveness level. In fact, an underlying amorphous and pseudo-passivating sublayer that is supposed to grow in conditions where local pH values are shifted to pseudo-passivation conditions could explain the higher degree of protection.

In summary, due to the simplicity of the registered electrochemistry as depicted by the EIS data and the stability of the OCP for a duration as long as 10 days, it was concluded that running tests at 60°C would allow a better follow-up of changes incurred when the OA-POSS hybrid nanofillers are administered to the brine chemistry especially that the corrosion rate is the lowest so any enhancement is expected to be more pronounced and easier to detect.

7.1.6 Setting up the highest pH at which no protective iron carbonate films form

Sections 7.1.6.1 and 7.1.6.2 highlight how the administration of the nanofiller help easily distinguish between two systems at the chosen pH of 6.6. In the absence of the nanofiller, no iron carbonate forms while the simple addition of the nanofiller is shown to promote iron carbonate crystal growth.

7.1.6.1 Electrochemical evolution when no nanofiller is added

In another set of experiments, the pH effect was studied by dropping it progressively by 0.1 digit starting from a pH equal to 7 since it is mostly likely to form iron carbonate scale even at low temperature when the pH is higher than 7 as depicted in the potential-pH diagram in Figure 6-1. It was observed that at a pH of 6.6 and a temperature of 60°C no protective iron carbonate was able to develop. This was previously highlighted in the literature where additional ferrous iron is needed in order to accelerate the kinetics of iron carbonate growth.[271]

In fact, a slight increase in the pH to a value as high as 6.75 shows a big increase in the charge transfer resistance as registered in EIS tests as shown in Figure 7-27. The real impedance values Z' exceed 6,000 $\Omega.cm^2$ by the tenth day while the imaginary impedance Z" reach values as high as 3,500 $\Omega.cm^2$; the growth in the semi-circle diameter is equivalent to a corrosion rate drop

and such high impedance values are characteristic of the formation of protective corrosion layers.
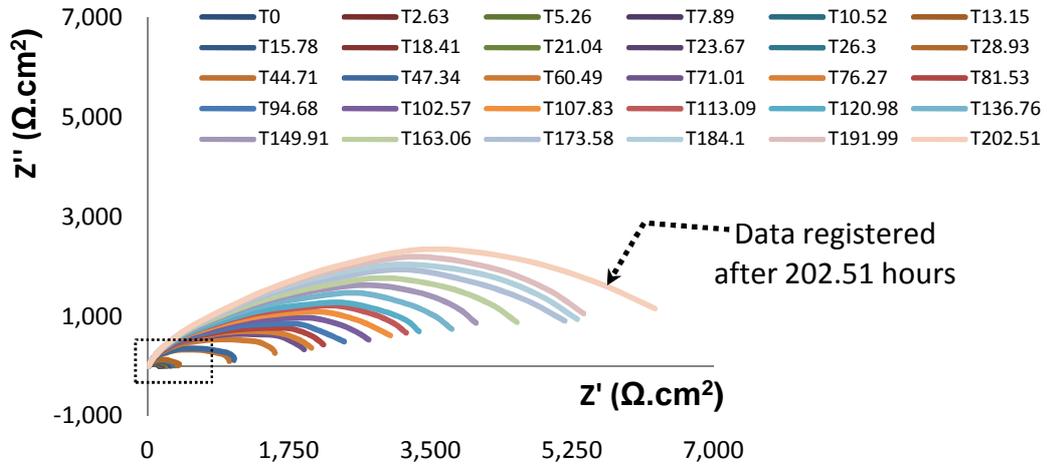
Figure 7-27 Nyquist plot of a X65 carbon steel sample in a CO_2 saturated environment at a pH of 6.75 and 3.5% NaCl at 60°C for a test duration of 10 days; T represent the time of EIS acquisition time in hours

Details of the dotted area are shown in Figure 7-28 and should be compared to the impedance values from Figure 7-29 in order to assess the effect of decreasing the pH from 6.75 to 6.6.
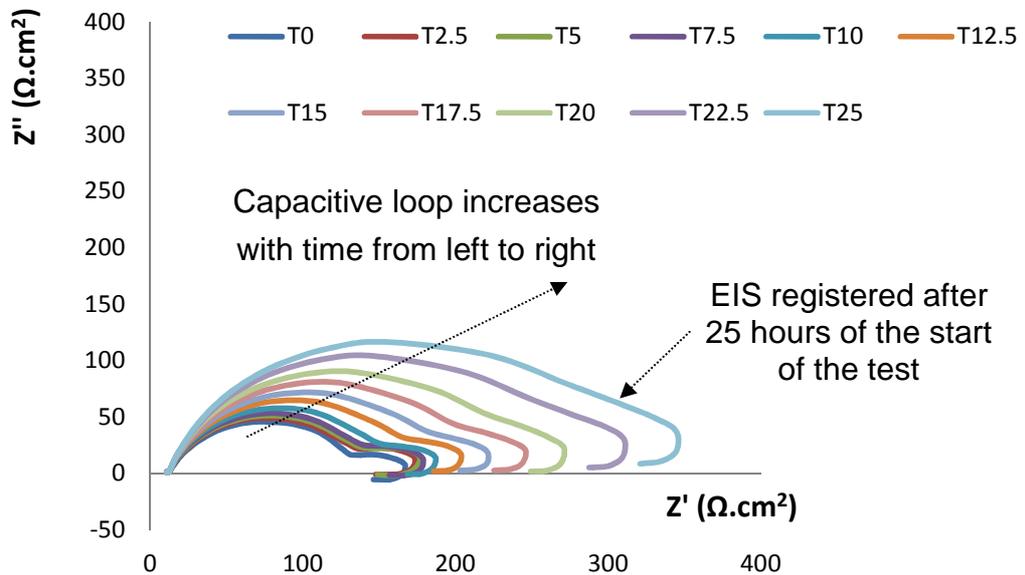
Figure 7-28 Nyquist plot at 60°C, pH 6.75, 3.5% NaCl, 0.8 bar CO_2 (first 24 hours data)

While the imaginary impedances are almost twice bigger at a pH of 6.75, the real impedance increases progressively from starting values as low as 150

$\Omega.cm^2$ to reach 350 $\Omega.cm^2$ in just 24 hours while these stay stagnant around 120 $\Omega.cm^2$ when the pH is buffered at lower values equal to 6.6 for a period as long as 5 days.
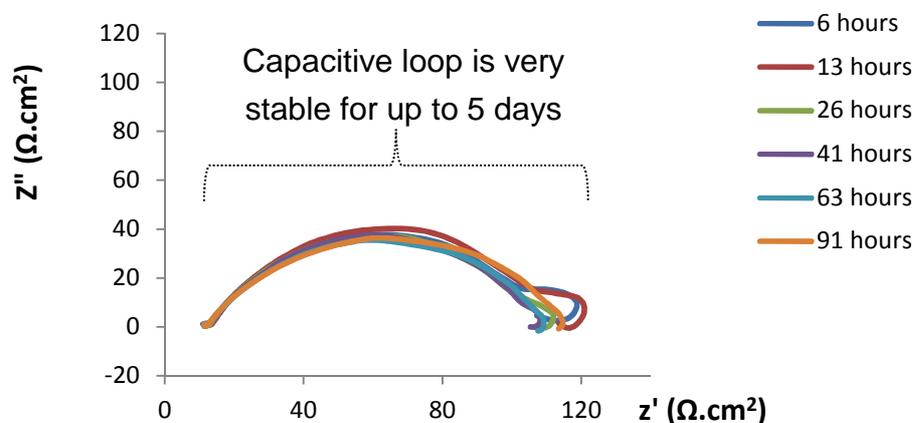
Figure 7-29 Nyquist plot of a X65 carbon steel sample in a CO_2 saturated environment at a pH of 6.6 and 3.5% NaCl at 60°C for a test duration of 5 days

7.1.6.2 Electrochemical evolution with the presence of the nanofiller

In order to easily assess any modification to the system when OA-POSS is added to the brine mixture, the pH of 6.6 looks promising for two main reasons; first the system's electrochemistry seems stable with no real change in the CRs as proven by the fixed size of the registered capacitive loops and second no protective layer seems to be forming. These assumptions could prove useful to compare values when the experimental set-up is disturbed via the introduction of a new reactant which corresponds to the silsesquioxane based nanofiller.

Moreover, when the pH is only 0.1 digit higher than 6.6, polarisation resistance data for both OA-POSS treated samples and blank tests are difficult to compare. In fact, both setups show values higher than thousands of $\Omega.cm^2$ thus rendering it challenging to judge from a surface topography point of view the effect of the nanofiller since both systems are creating covering and protective $FeCO_3$ films as suggested by the R_p values in Figure 7-30. Actually, when both R_p are increasing and both systems are forming protective iron carbonate layers, it is harder to distinguish any enhancing effect of the added chemical if only electrochemical techniques are implemented.
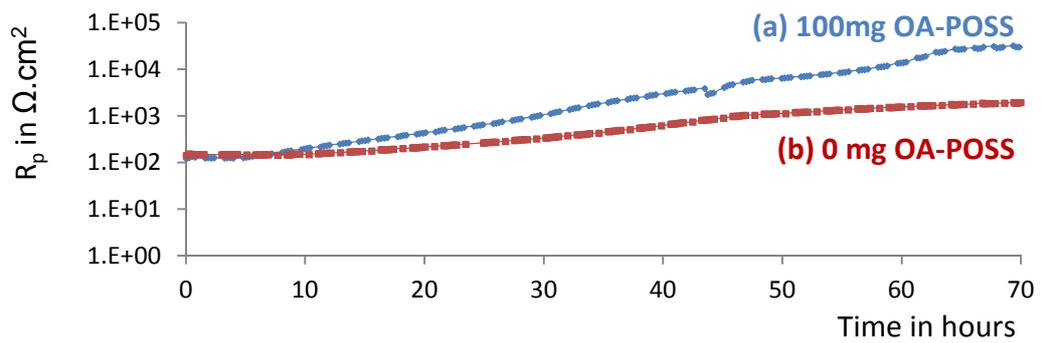
Figure 7-30 R_p variations for X65 carbon steel samples (a) when 100mg OA-POSS was added and (b) blank tests ran at pH 6.7, 60°C, 3.5% NaCl, 0.8 bar CO_2

In fact, electrochemically speaking, adding 100mg of OA-POSS at a pH of 6.6 shows a system which evolves as a test running at a slightly higher pH of 6.75 at the same temperature of 60°C as seen in Figure 7-31. Both corrosion rates start at values close to 2.5 mmpy before dropping below 1mmpy after the first 15 hours or so.
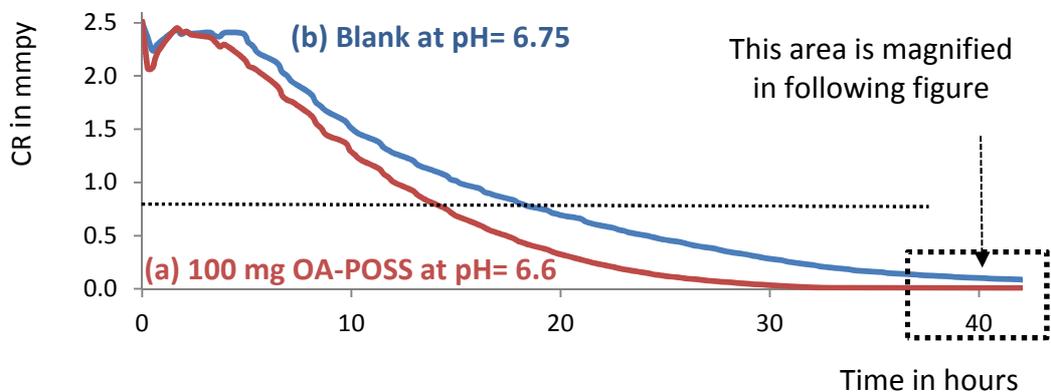
Figure 7-31 CR variation of X65 sample (a) subjected to 100 mg OA-POSS at a pH of 6.6 and (b) a blank sample at pH 6.75 [60°C, 3.5% NaCl, 0.8 bar CO_2]

Similarly, both systems reach a steady state after roughly two days with corrosion rates lower than 0.1 mmpy and 0.01 mmpy for the tests ran at pH 6.75 and 6.6 with 100mg OA-POSS respectively as shown in the expanded area in Figure 7-32. This is one of the major advantages of protecting a system with $FeCO_3$ rather than corrosion inhibitors since the CR drop to values which are tenfold lower. It also appears as though the iron carbonate layers grown

in the presence of OA-POSS induce a corrosion rate drop which is more accentuated than when naturally growing corrosion films are allowed to develop. The $FeCO_3$ grown in the presence of OA-POSS also seems to reach the steady state region at an earlier time.
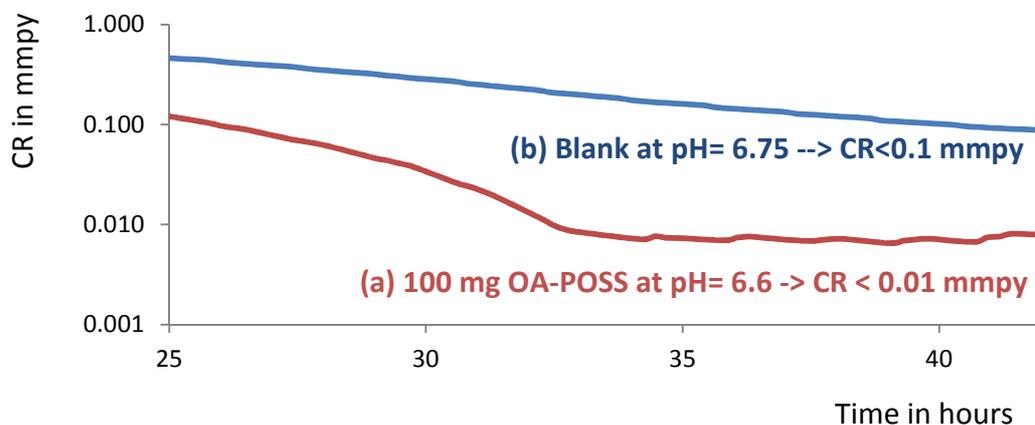
Figure 7-32 Focus on the steady state region of Figure 7-31 [60°C, 3.5% NaCl, 0.8 bar CO_2]

In summary, the choice of running tests at a pH equal to 6.6 and a temperature equal to 60°C was made in order to have a system which provides an electrochemical and surface topography that could be easily analysed. This should help to spot the nanofiller beneficial effects such as facilitating the growth of iron carbonate and thus reducing the corrosion rate.

The previous tests were shown in order to explain the rationale behind carrying out the corrosion experiments at a temperature of 60°C and a pH equal to 6.6 in order to evaluate the effect that the OA-POSS nanofiller has on iron carbonate film such as its precipitation kinetics. Since the OCP variation for a ten day was the most stable at a temperature of 60°C and no iron carbonate was able to nucleate and grow at a pH of 6.6, these environmental parameters were carried out in the next sections.

7.2 Assessment of the OA-POSS early stage interactions

7.2.1 OA-POSS administration time is crucial

Knowing that at a pH of 6.6 and a temperature of 60°C, no protective $FeCO_3$ layer forms for five days at least, the next question that was addressed was whether adding OA-POSS at the start of the test could help grow an iron

carbonate protective layer. It appears as described hereafter that the probability of obtaining a protective iron carbonate layer is much higher if a pre-corrosion time is set prior to administering the hybrid POSS moieties.

7.2.1.1 OA-POSS dissolved at the start

When the OA-POSS was added directly at the start of the experiment, it had no clear effect on the system electrochemistry which seems to remain stable in the chosen running conditions. As such, Figure 7-33 shows that a system that does not contain OA-POSS and another where 100 OA-POSS were added at the start of the test show corrosion rates that are comparable and roughly stable around a value of 2.75 mmpy and 2.5 mmpy respectively for a test duration up to 108 hours.
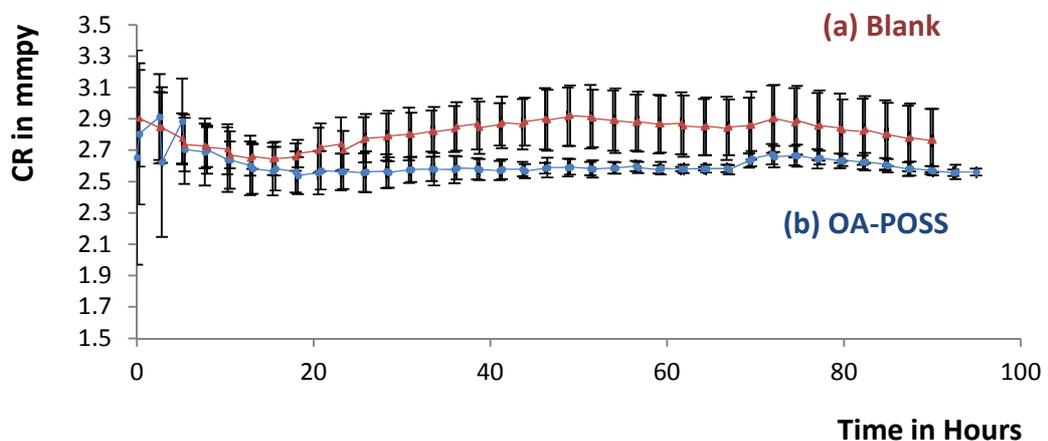
Figure 7-33 CR variations of tests ran at 60°C, pH 6.6, 3.5% NaCl, 0.8bar CO_2 (a) without adding OA-POSS and (b) after dosage of 100mg OA-POSS at the start of the test

This is a slight drop of 0.25 mmpy which is far below what is expected when a corrosion product layer is protective. It should be noted that these corrosion rates were extracted from LPR results as per Equation 2-31 without taking into account the real Tafel constants since the final aim is to compare the blank and OA-POSS electrochemical variations and not the absolute values in themselves.

The tests where OA-POSS was dissolved in the brine solution show much lower standard deviations as seen from the error bars in Figure 7-33b, which suggests that the adsorption of the OA-POSS tend to stabilise both the anodic and cathodic reactions occurring on the carbon steel surface. In fact, tests ran without OA-POSS have the CR fluctuate between 2.7mmpy and 3.1 mmpy

while these only evolve between 2.4mmpy and 2.6mmpy when the nanofiller is dissolved at the start of the test.
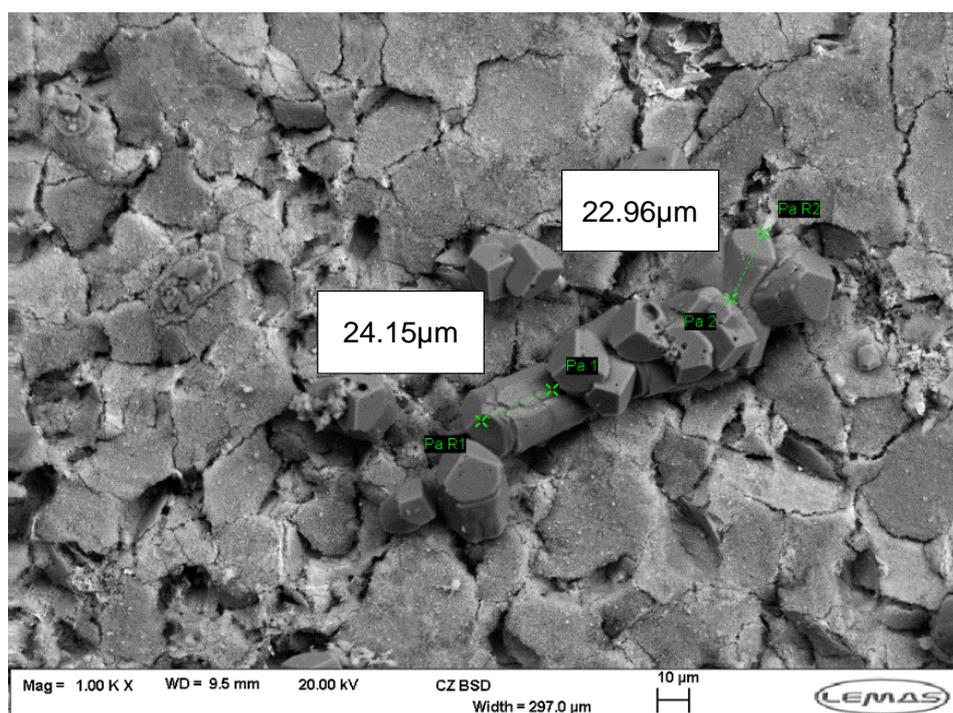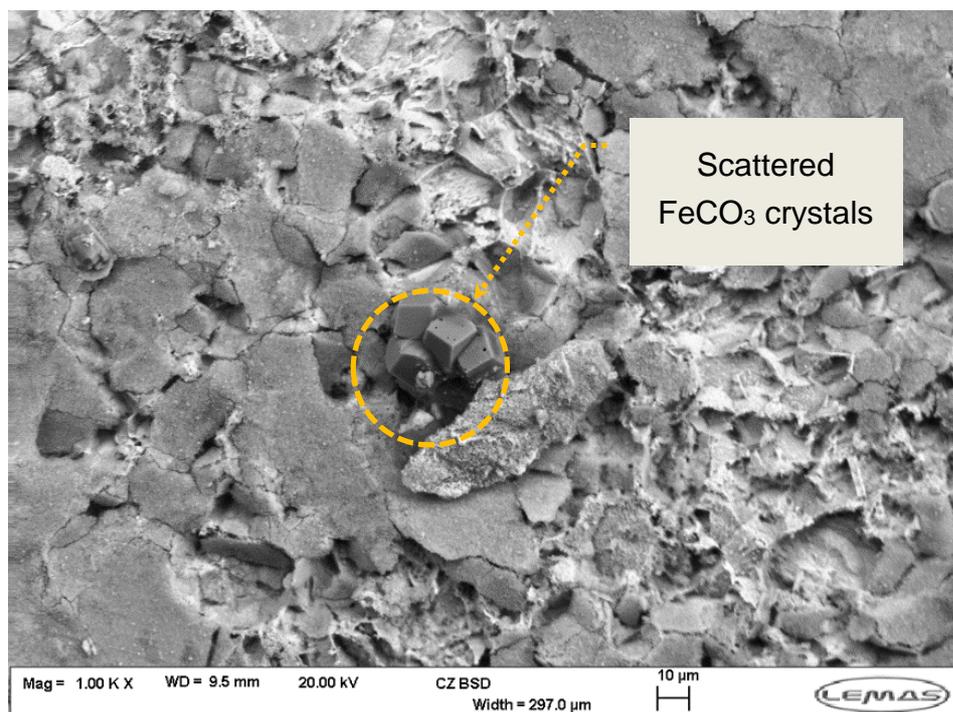
Figure 7-34 SEM micrographs topography view of X65 samples when no OA-POSS is administered at various magnifications shown by the respective scale bars [pH=6.6, 60°C, 3.5% NaCl, 0mg OA-POSS, 98 hours] with (a) corrosion layers showing isolated $FeCO_3$ crystals as shown in the dotted area and (b) dimensions of the few grown $FeCO_3$ crystal islands

The surface composition in both cases looked very similar and comprised an amorphous layer as suggested by the XRD results in Figure 7-35. There appear to only be very few scattered iron carbonate crystals as shown inside the dotted area in Figure 7-34a. The amorphous corrosion products seem very complex and made up of a multitude of interlacing layers showing various roughness levels. The $FeCO_3$ crystals appear large and average 20µm in their longest direction. These have a cubic shape with some pores appearing all over their surface.
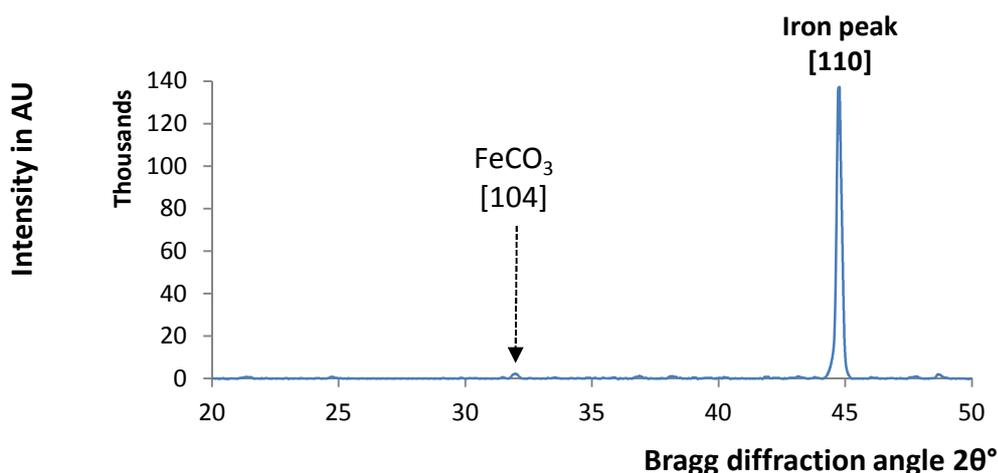
Figure 7-35 XRD diffraction pattern for a blank test when 0mg OA-POSS was added [pH 6.6, 60°C, 3.5% NaCl, 0.8bar CO_2, 98 hours] with [104] and [110] corresponding to $FeCO_3$ and Fe Miller indices respectively

The ratio of the relative intensities between the [104] $FeCO_3$ and [110] Fe Miller indices was equal to 0.0167 as extracted from the XRD diffraction pattern shown in Figure 7-35. The other iron carbonate representative Miller indices showed very low intensities which is consistent with the absence of the $FeCO_3$ protective corrosion layer on the steel surface in these conditions.

EIS data registered in these conditions show also identical trends for both systems as shown in Figure 7-36 and Figure 7-37. Nyquist plots show one time constant (τ) around 5 Hz for the 98 hour test with a solution resistance around 12 $\Omega.cm^2$ and Resistance Charge Transfer (R_{CT}) near the value of 112 $\Omega.cm^2$ for both systems. The main difference is that tests ran while adding OA-POSS to the brine seem to have a more apparent inductive loop behaviour at the lower frequencies as seen in Figure 7-37 which should correspond to the adsorption of the silicon enriched silsesquioxane chemicals in a similar way to the described adsorption of some electrosorbed intermediates as described by Bai et al.[359]

171
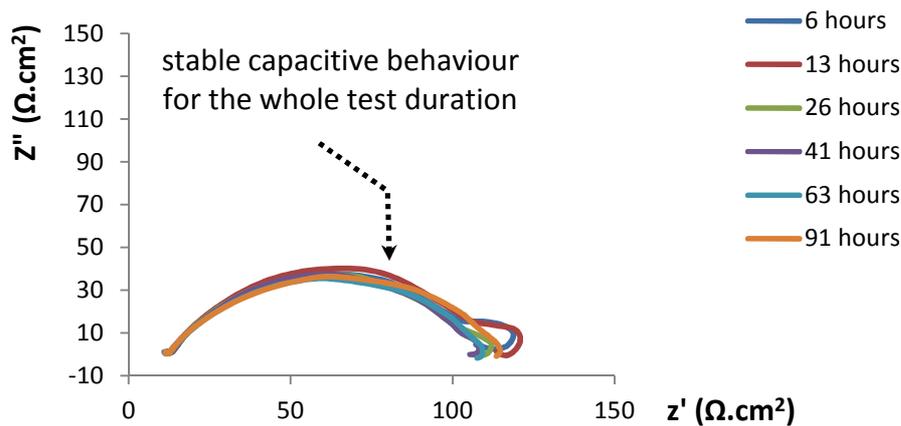
Figure 7-36 Nyquist plot for blank tests at 60°C, pH 6.6, 3.5% NaCl, 0.8bar CO_2
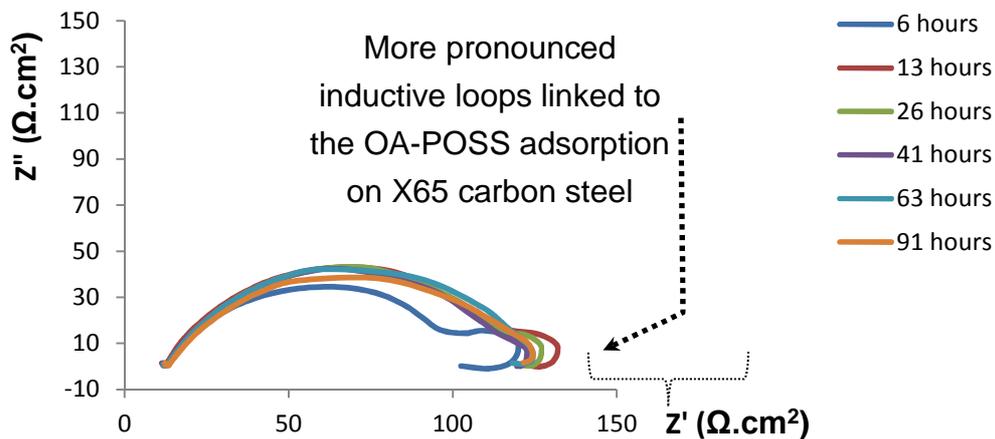
Figure 7-37 Nyquist plot when 100mg OA-POSS is added at the start at 60°C, pH 6.6, 3.5% NaCl, 0.8bar CO_2

The Bode plots confirm that there exists one time constant around 10Hz corresponding to the EDL for the blank test (Figure 7-38) while a time constant shifted towards 1 Hz is predominant for the OA-POSS modified systems respectively as shown in Figure 7-39. Both blank and OA-POSS modified systems show similar phase angles of the order of 40° which is commonly seen on carbon steel in similar conditions; this capacitive behaviour and the impedance values describe a system where no protective layer is forming since no diffusion effects are observed.
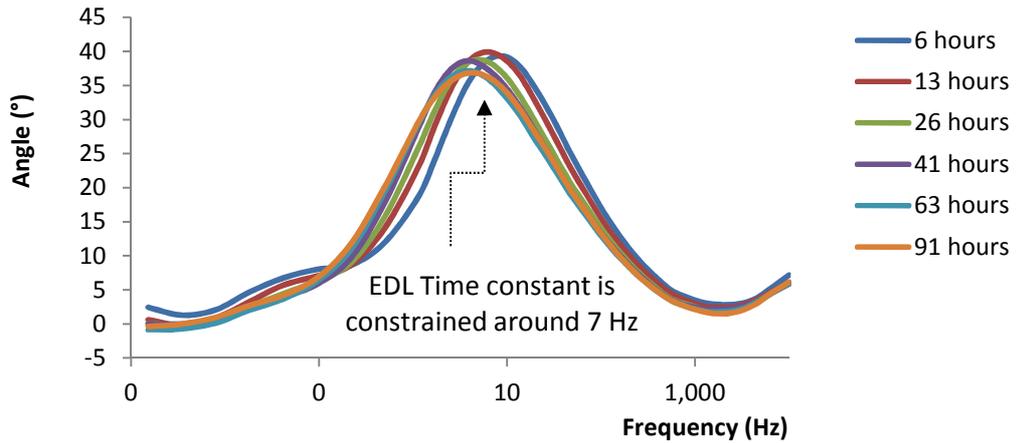
Figure 7-38 Bode plot (phase shift versus frequency) for blank tests at 60°C, pH 6.6, 3.5% NaCl, 0.8bar CO_2
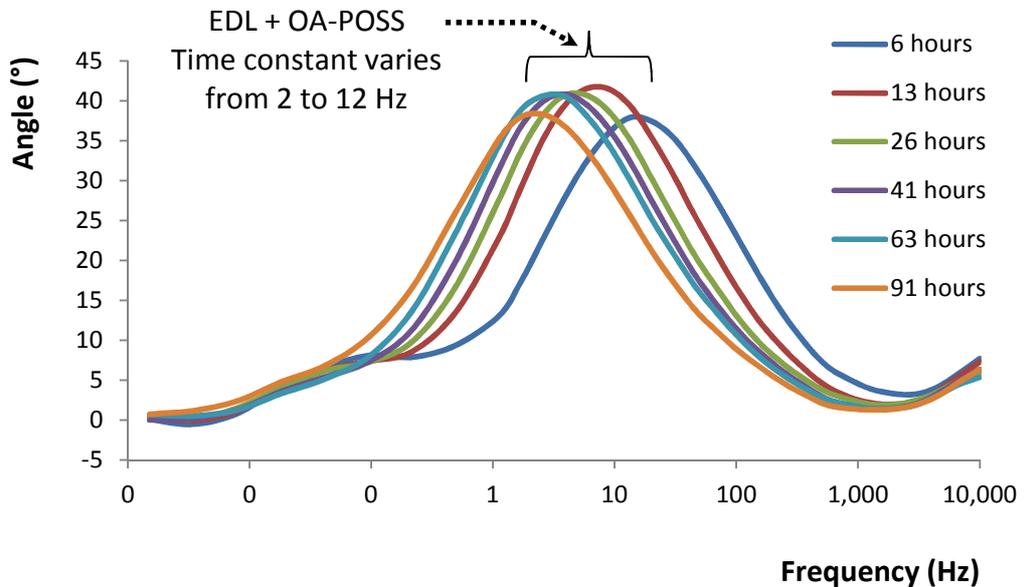
Figure 7-39 Bode plot (Phase shift versus frequency) when 100 mg OA-POSS is added at 60°C, pH 6.6, 3.5% NaCl, 0.8bar CO_2

7.2.1.2 Pre-corrosion time effect

From the numerous tests undertaken, it appeared that the best repeatable results occur if the system is allowed to evolve for a period of 2 hours before OA-POSS is added to the mixture as shown in the CR variations in Figure 7-40 where 20mg of OA-POSS are administered after a 2 hour pre-corrosion time. In general, it was observed that working under a pre-corrosion status is actually better than working on a clean surface.

In fact, when a pre-corrosion time is allowed, a lower concentration of OA-POSS is required in order to enhance the $FeCO_3$ crystal growth and protective film formation. Meanwhile, in this scenario, the OCP steadily increases toward more anodic values as shown in Figure 7-41 while if no pre-corrosion is allowed, both OCP variation of an OA-POSS and blank tests seem almost identical as depicted in Figure 7-42.
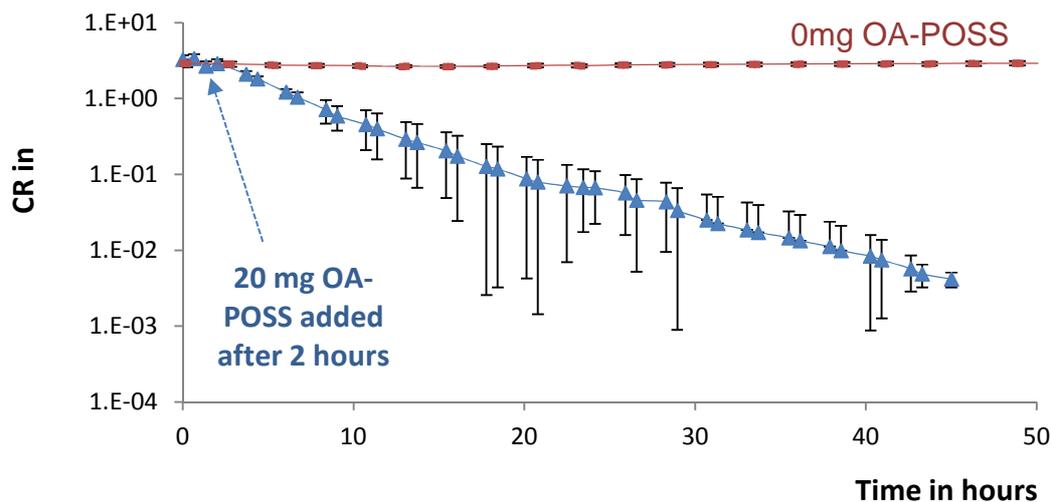
Figure 7-40 CR variation of (a) 20 mg OA-POSS modified samples versus (b) blank specimen [pH 6.6, 60°C, 3.5% NaCl, 0.8bar CO_2]
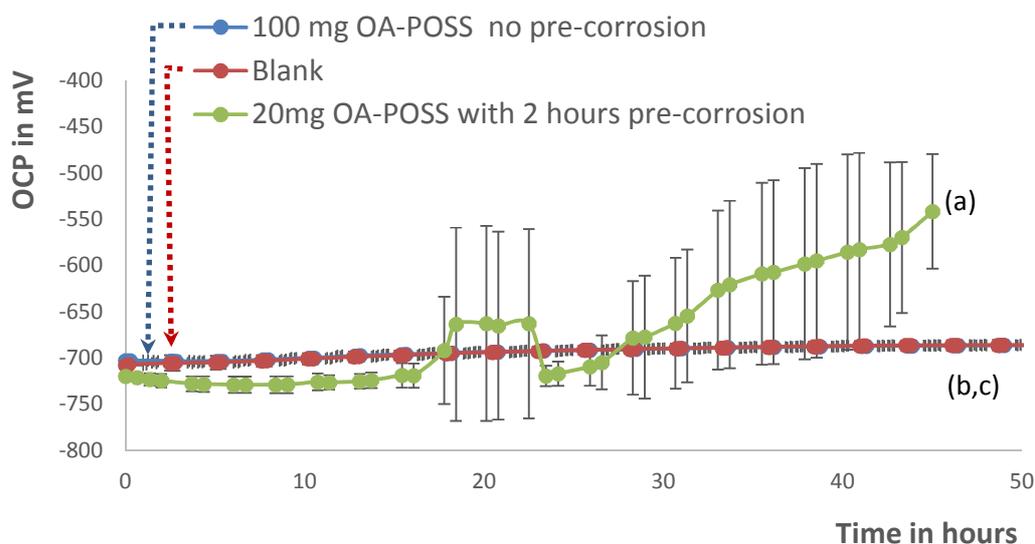
Figure 7-41 OCP variation when tests are ran (a) with 20 mg OA-POSS after 2 hours pre-corrosion, (b) in blank conditions and (c) when 100mg OA-POSS are dissolved at the start [pH 6.6, 60°C, 3.5% NaCl, 0.8bar CO_2]
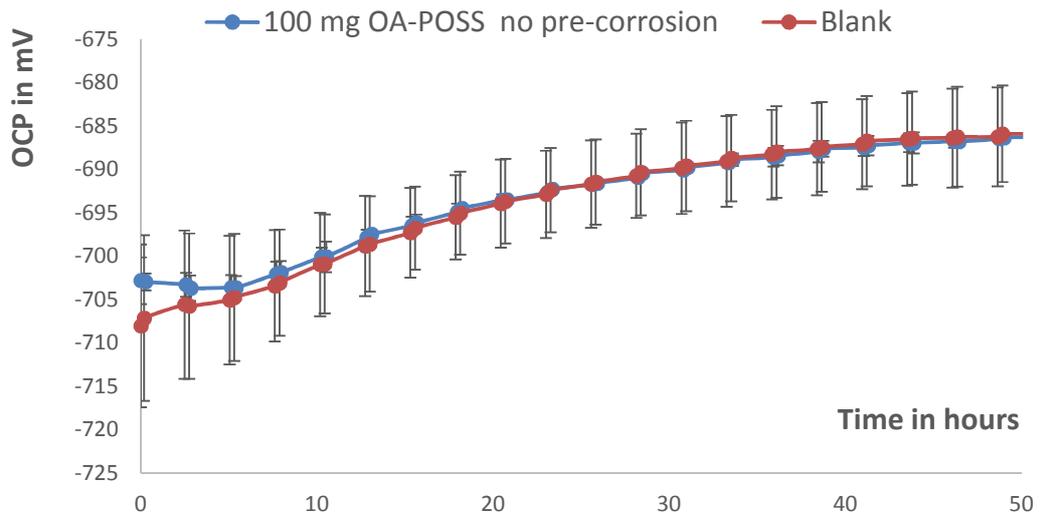
Figure 7-42 OCP variation comparison when tests are ran with 100 mg OA-POSS with no pre-corrosion or blank [pH 6.6, 60°C, 3.5% NaCl, 0.8bar CO_2]

When compared to the effect of ferrous iron via additives such as ferrous chloride, the OA-POSS effect seems to be more potent than even adding 50 ppm $FeCl_2$ as seen in Figure 7-43. While it takes roughly 40 hours for the CR to drop below 1mmpy when $FeCl_2$ is added, it already decreased as low as 0.01mmpy for the same duration when 20 mg OA-POSS were added.
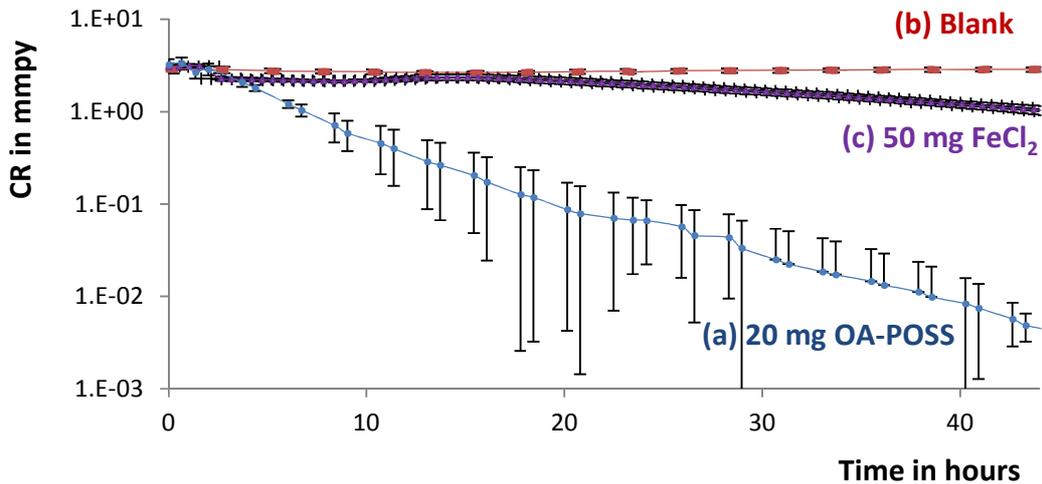
Figure 7-43 CR variation of (a) 20 mg OA-POSS modified samples versus (b) blank specimen and (c) 50mg $FeCl_2$ interacting tests [pH 6.6, 60°C, 3.5% NaCl, 0.8bar CO_2]

7.2.1.3 Steel wool versus FeCl$_2$

At the chosen conditions of temperature (60°C) and pH (6.6), no iron carbonate film is seen to develop during the first 5 days. When such a film was required to grow in the absence of the nanofiller, either a direct dosage of FeCl$_2$ or a continuous ferrous iron provided from the dissolution of steel wool in the test solution could be provided.

When steel wool is the ferrous iron source, the FeCO$_3$ appears to be more compact than when FeCl$_2$ single addition at the start of the test is achieved as seen in both the top view and cross-section of X65 samples ran at 60°C for 10 days at a pH of 6.6 in Figure 7-44. This could be explained by the fact that the continual presence of the excessive higher ferrous iron concentration could help the nucleation and growth process which is time-dependant and progressive with the corrosion layer growing in thickness for up to days before suffering from internal stresses as depicted in Table 4-6.

When relying on the continuous ferrous iron pumping from the steel wool in the solution, the surface coverage (Figure 7-44a) and film thickness (Figure 7-44b) of the FeCO$_3$ were very high, with a corrosion layer thickness averaging 40µm. Nonetheless, the repeatability of the electrochemical tests proved very challenging and such administration pathway of the ferrous chloride has not been implemented for the remainder of the tests. Instead 50ppm of FeCl$_2$ is administered in order to prepare iron carbonate films when deemed necessary to overcome supersaturation limitations; such is the case when a blank FeCO$_3$ was grown for the purpose of comparing mechanical properties between OA-POSS enriched and naturally grown FeCO$_3$ corrosion layers as described in section 8.5.

Chemical analysis relying on EDX was undertaken mainly in order to assess the content percentage in carbon, iron and oxygen and compare with iron carbonate elemental proportions; as such Figure 7-45 shows a cross-section map analysis based on a secondary electron emission micrograph where additional chloride from the brine was also present.

The most abundant elements iron, carbon and oxygen present herein are compatible with the assumed grown iron carbonate layer since the mapping was done inside this corrosion film. A localised point EDX identification on the same sample is shown in Figure 7-46 with the corresponding elemental weight percentage distribution as summarised in Table 7-2 where the weight

percentage sigma values are to be correlated with the standard deviation of each registered peak count.

(a)

(b)
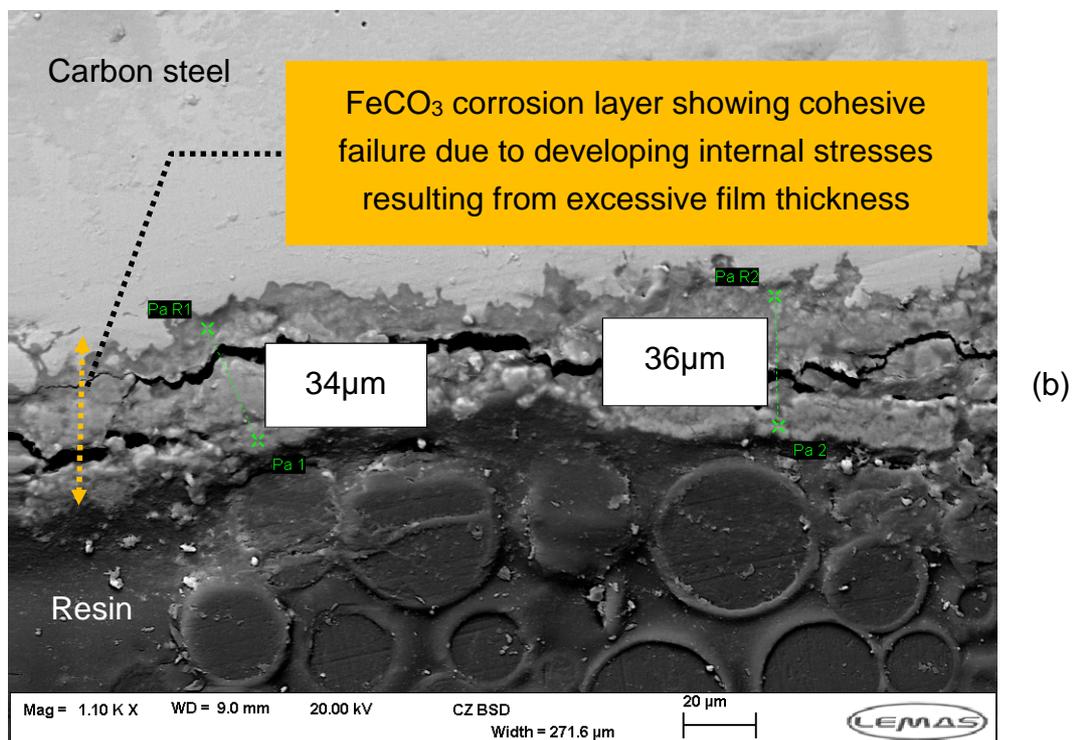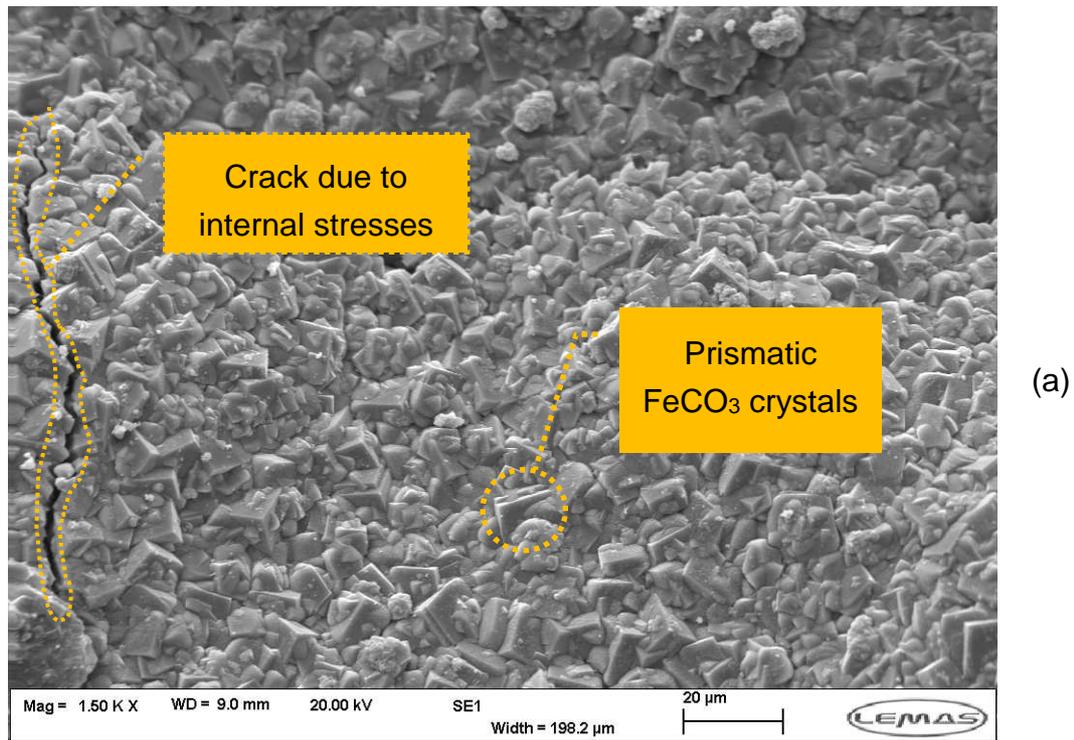
Figure 7-44 SEM micrographs (a) topography view and (b) cross-section of X65 samples with scale bar of 20μm at a pH=6.6, 60°C, 3.5% NaCl, 0.8bar CO_2 100mg steel wool, 10 days

(a)

(b) Fe Kα1

(c) C Kα1_2

(d) O Kα1

(e) Cl Kα1
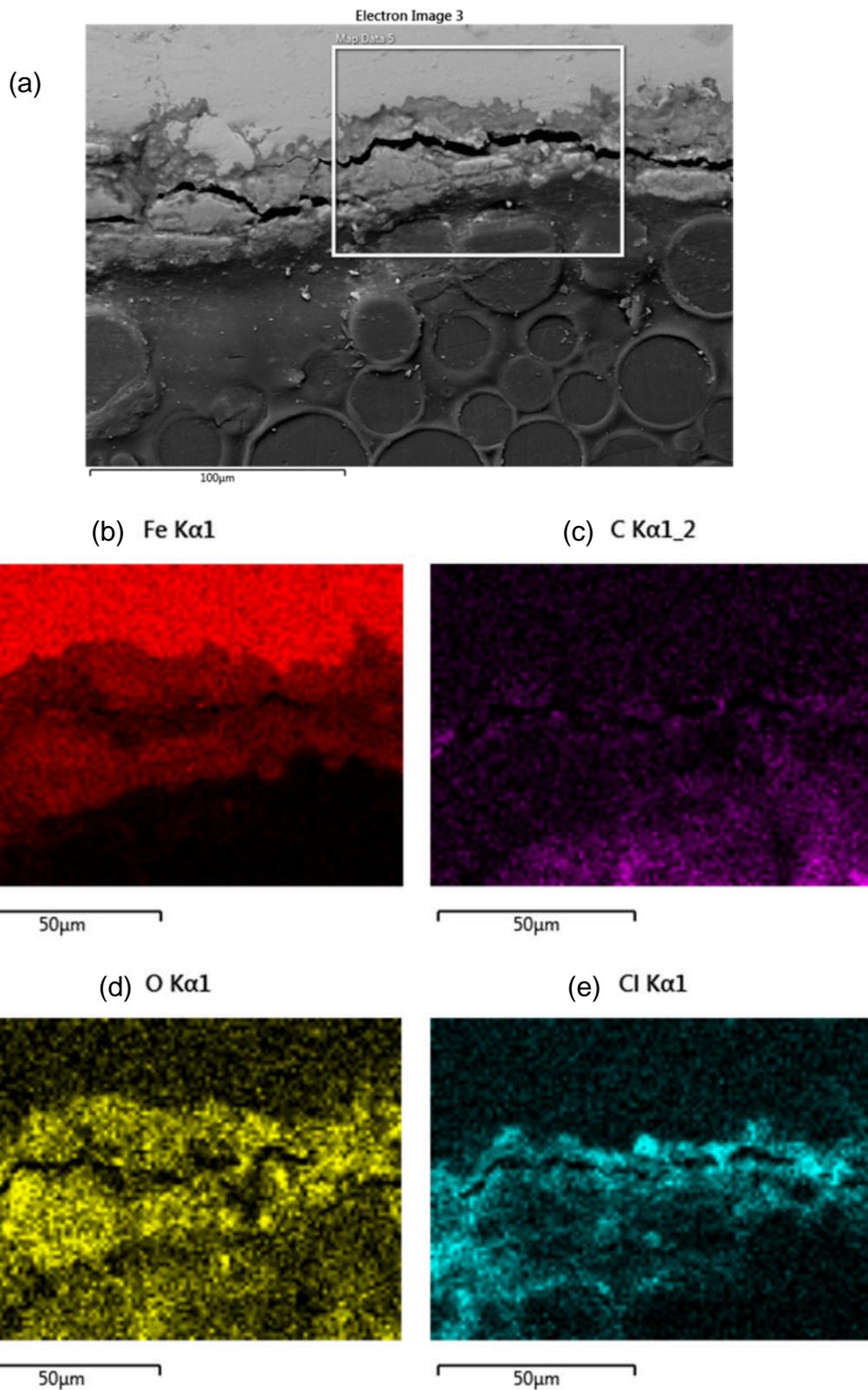
Figure 7-45 EDX map of corrosion layer grown at 60°C, pH 6.6, 3.5% NaCl, 100mg steel wool, 0.8bar CO_2, with (a) SE micrograph (b) Iron-Fe (c) Carbon-C (d) Oxygen-O and (e) Chloride-Cl

(a)

Electron Image 4

100μm

(b)
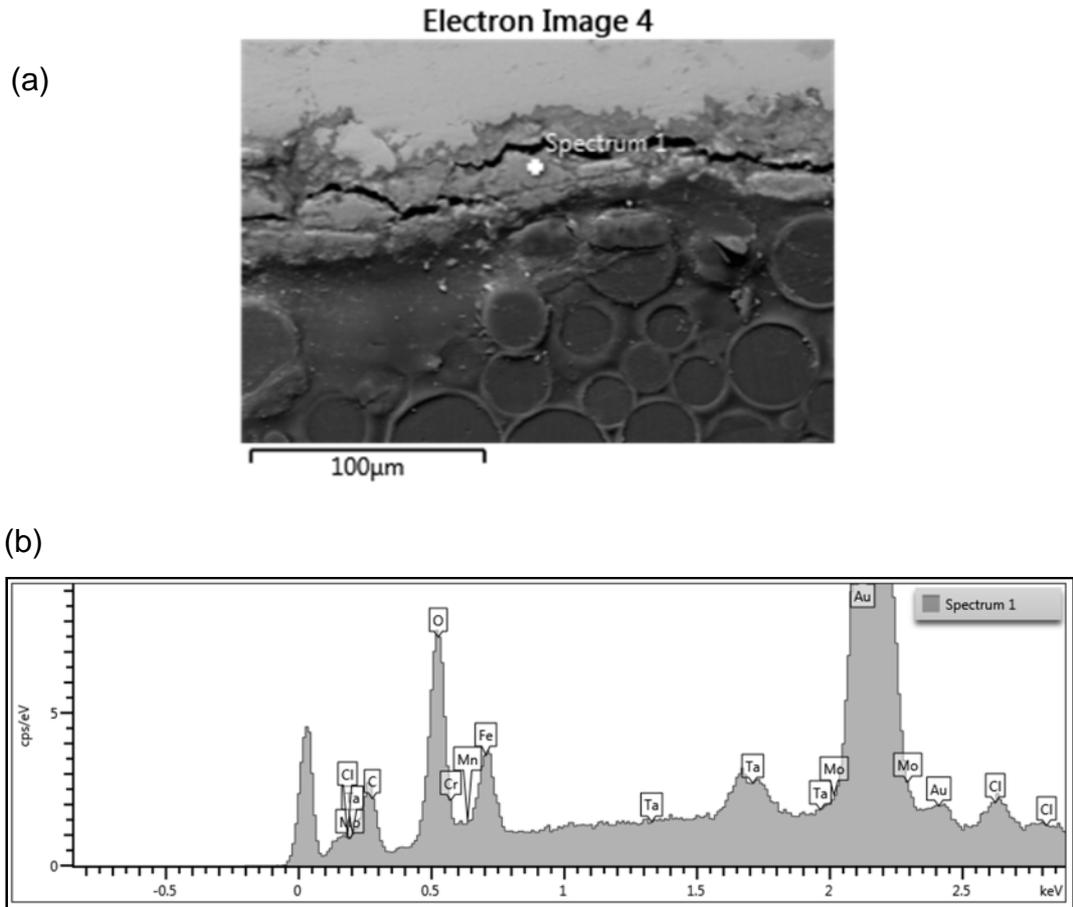
Figure 7-46 Single point EDX of corrosion layer grown at 60°C, pH 6.6, 3.5% NaCl, 100mg steel wool with (a) SE micrograph (b) EDX single point spectre

Table 7-2 Single point weight percentage elemental distribution of corrosion layer grown at 60°C, pH 6.6, 3.5% NaCl, 100mg steel wool

Element	wt%	wt% Sigma
C	15.28	0.81
O	14.17	0.31
Cl	0.80	0.07
Cr	0.28	0.08
Mn	1.11	0.11
Fe	64.64	0.74
Mo	1.95	0.41
Ta	1.78	0.26
Total:	100.00	

7.2.2 Effect of the nanofiller addition on the OCP and Tafel constant in the first hours

7.2.2.1 OCP and OA-POSS

The OA-POSS seems to induce a more cathodic potential when administered to the experimental solution as shown in Figure 7-47. The OCP starts to shift from values around -723mV to potentials equal to -730mV and this behaviour lasts for approximately 40 minutes before the OCP stabilises at a value around -728mV.

Moreover, the data shows a slight decline in the CR from a value around 3.5 mmpy to 2.2 mmpy before stabilising back around 3 mmpy. These two observations are most likely linked to the adsorption of the silsesquioxane moieties on the carbon steel X65 surface as observed previously with the EIS Bode plots as in Figure 7-37. This is attributed to a slight cathodic shift since polarisation tests show that the nanofiller acts mainly on perturbing the cathodic counterpart of the Tafel graph as shown later in Figure 7-48.
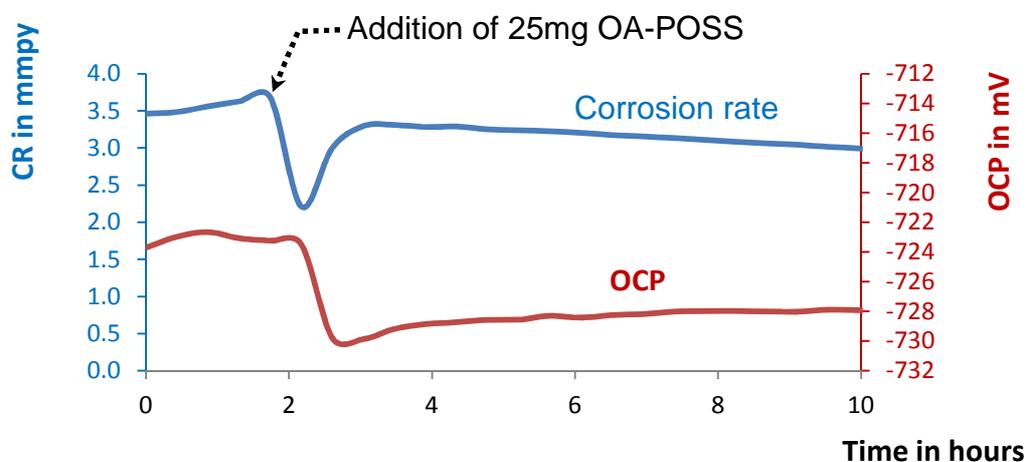
Figure 7-47 CR and OCP variation after adding 25 mg OA-POSS at 60°C, pH 6.6, 3.5% NaCl, 0.8bar CO_2

Otherwise the OCP is quite stable for a day before shifting to more positive values as seen in Figure 7-41. It should be noted that these tests were carried out with a nanofiller loading of 25mg since as it is shown in section Chapter 8 and section 8.4, these loadings, qualified as medium loadings, were responsible for the best $FeCO_3$ crystal nucleation and localised corrosion mitigation.

180

7.2.2.2 Stern-Geary coefficient and OA-POSS

Polarisation tests were undertaken in order to assess the behaviour of the carbon steel surface in the presence of the silsesquioxane moieties. This is expected to allow for the computation of the Tafel constants in both conditions but also to check whether OA-POSS behaves in a similar way to other film-forming CO_2 corrosion inhibitors which are known to mainly affect the cathodic polarisation curve. The polarisation characteristics of carbon steel with the presence of OA-POSS are shown in Figure 7-48 for that purpose.
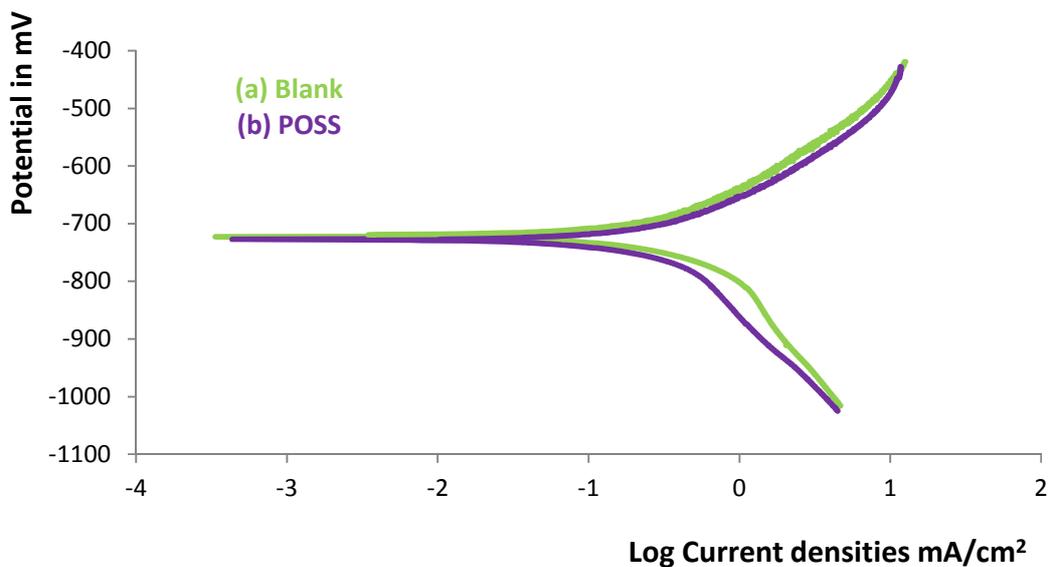
Figure 7-48 Tafel Extrapolation of (a) a blank and (b) an OA-POSS enriched X65 carbon steel polished to 600 SiC surface finish at 60°C, pH of 6.6 3.5%NaCl and 0.8bar CO_2 registered at the start of the test

Details of the Tafel constants are shown separately in Figure 7-49 and Figure 7-50 and numerical values are summarised in Table 7-3. The methodology followed to compute the anodic Tafel constant βa is shown in Figure 7-49 where tangents are drawn at values higher than ±100mV from OCP and crossing over it at the corrosion current value. The Tafel constant is then just read by checking the Y-axis values of the potential (-680mV and -490mV in the case of βa when no OA-POSS is added as per Figure 7-49) over a decade (Log current density between 0 and 1). After just 2 hours, the Stern-Geary constants are around 54.6 and 45.7mV/decade for the blank and OA-POSS treated samples respectively.

In summary, it looks as if OA-POSS is switching the OCP to more noble values (10mV shift) and that it affects mainly the cathodic slope but not considerably as in the case of a film-forming imidazoline based corrosion inhibitor.
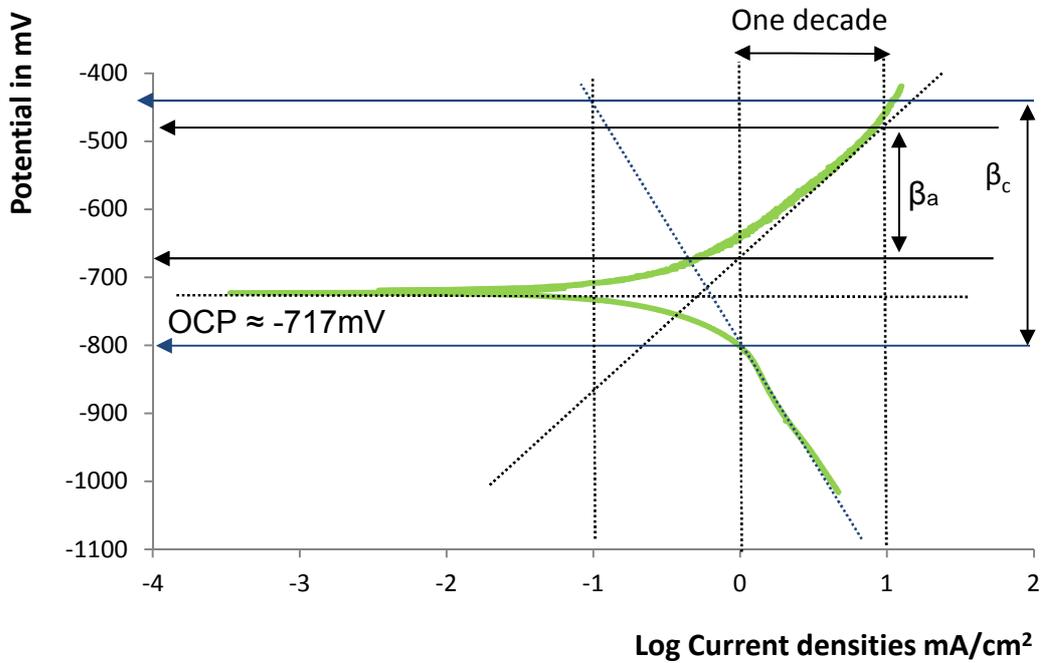
Figure 7-49 Tafel constants calculations for a blank test at 60°C, pH of 6.6 3.5%NaCl and 0.8bar CO_2
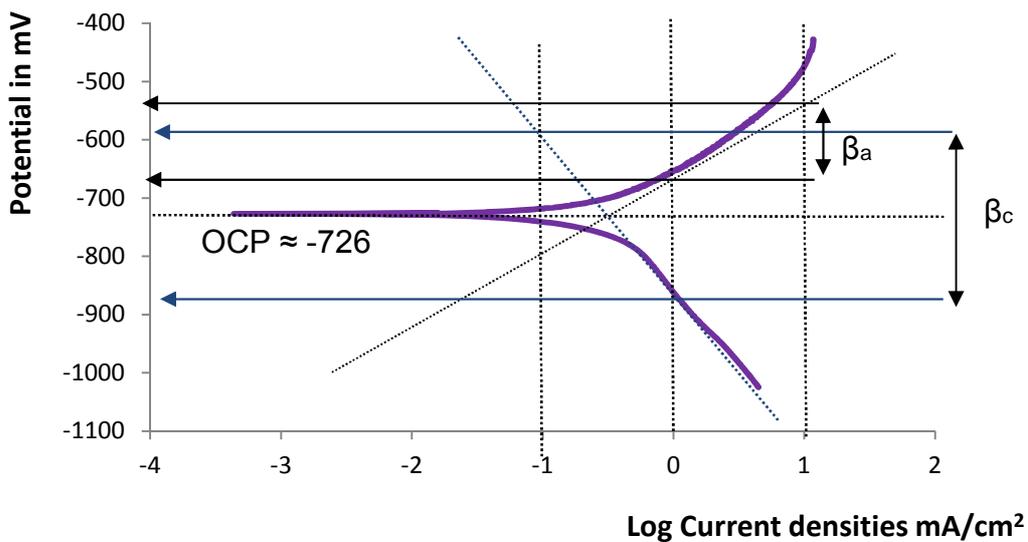
Figure 7-50 Tafel constants calculations for an OA-POSS treated sample at 60°C, pH of 6.6 3.5%NaCl and 0.8bar CO_2

Table 7-3 Summary of results for the polarisation test

Material	API-5L-X65 carbon steel
Surface area	2.25 cm^2
Surface finish	600 SiC
Brine volume	1 litre
Brine composition	3.5% NaCl
Temperature	60°C
pH	6.6
Added buffer	7.8g NaHCO$_3$
LPR Sweep	±300 mV
Sweep Rate	10 mV/minute
Procedure	Tangents plotted in the linear region ± 100 mV or higher respective OCP
OCP blank cathodic	-716 mV
OCP blank anodic	-719 mV
OCP POSS cathodic	-725 mV
OCP POSS anodic	-727 mV
Blank β$_a$	190 mV/decade
Blank β$_c$	370 mV/decade
Blank Stern-Geary constant	54.6 mV/decade
POSS β$_a$	165 mV/decade
POSS β$_c$	290 mV/decade
POSS Stern-Geary constant	45.7 mV/decade

It should be noted though that these values were collected 2 hours after the test starts; if undertaken directly, they appear as per Figure 7-51 and the Stern-Geary constant is around to 55.8mV/decade. The implications of the Stern-Geary constant on the CR values remain limited as discussed previously in section 6.2.3 due to the R_p values which are orders of magnitude higher.
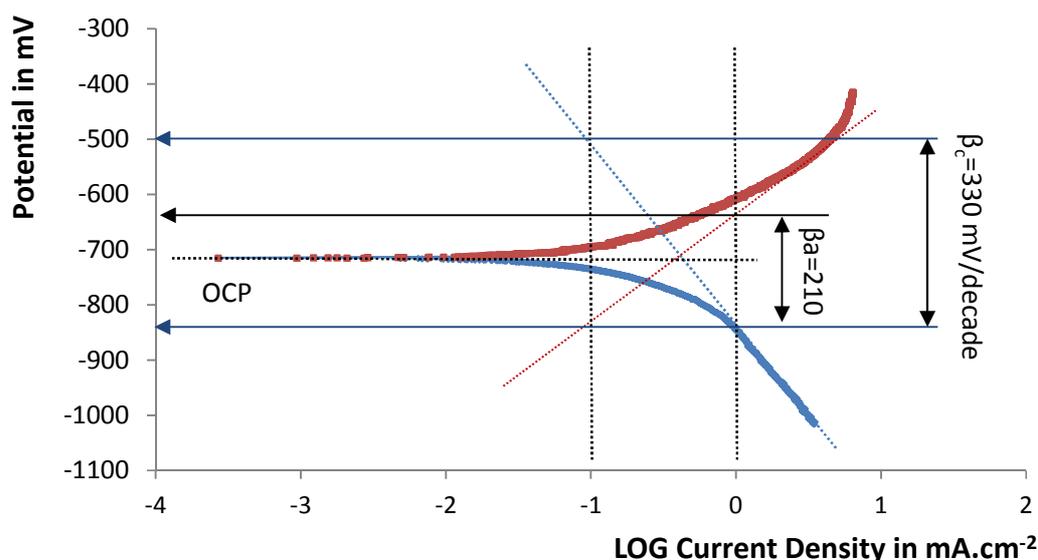
Figure 7-51 Tafel Extrapolation of X65 carbon steel polished to 600 SiC surface finish at 60°C, pH of 6.6 3.5%NaCl and 0.8bar CO_2 after 98 hours

The Tafel extrapolation shown in Figure 7-51 corresponds to both cases where OA-POSS was administered at the start of the test or not as per the corrosion rate variations shown in Figure 7-33 where the OA-POSS effect seems negligible.

In summary, the CR drop observed when OA-POSS is added is not due to the fact that the silsesquioxane moieties are forming a protective film by themselves; rather, they are enhancing the iron carbonate crystal growth at a fixed pH which is providing later the required protection. So the mode of action of CO_2 corrosion inhibitors and OA-POSS is totally different and should not be compared.

7.2.3 The effect of OA-POSS administration method

Adding the OA-POSS as a powder or dissolved beforehand, dissolved totally in one time addition or sequentially on a daily basis forces the corroding system to behave differently as seen in Figure 7-52. It was actually

established that pre-dissolving the OA-POSS powder in a CO_2 saturated brine from the test solution itself prior to pipetting the mixed volume back in the setup contributed to a better availability of the nanofiller to interact with the X65 steel surface and thus explains the electrochemical results.
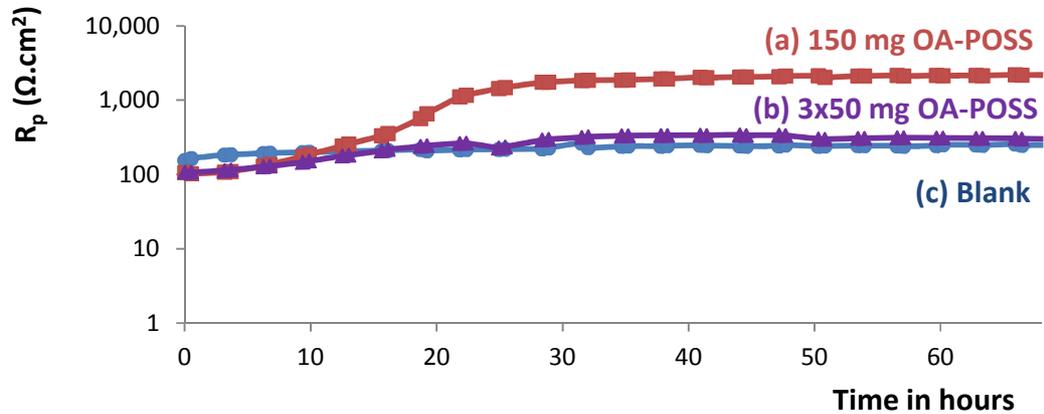
Figure 7-52 Polarisation resistance from DC LPR tests ran at 60°C, 3.5% NaCl, pH 6.6 and 0.8bar CO_2 with (a) 150 mg OA-POSS added at the start (b) 50 mg added thrice at 20 hours interval and (c) 0mg OA-POSS termed as blank test

Both the quantity and administration time have an effect on the potency of the OA-POSS. The diffraction pattern of corrosion films that developed in such conditions are shown in Figure 7-53 and the respective ratios of the [104] $FeCO_3$ Miller index when compared to the carbon steel iron [110] Miller index peak are computed in Table 7-4.
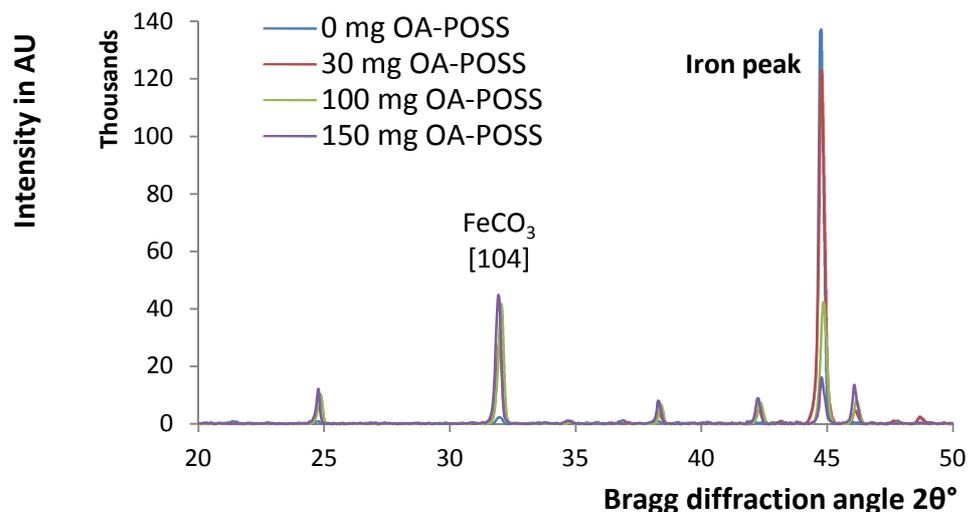
Figure 7-53 XRD diffraction pattern for (a) blank (b) 30mg (c) 100 and (d) 150 OA-POSS enriched solution [pH 6.6, 60°C, 3.5% NaCl, 0.8bar CO_2, 98 hours]

It appears as though the iron carbonate density increases with the concentration of the nanofiller added since the $FeCO_3$ to iron ratio increases from 0.0167 to 0.2282 then 0.9885 and 2.8006 when the OA-POSS loading varies from 0 to 30 to 100 and 150 mg in that order. Nonetheless, the $FeCO_3$ abundance as extracted from the Miller indices ratio is not directly related to the degree of protectiveness since the $FeCO_3$ crystals obtained by sequentially adding 3x50mg OA-POSS show the highest $FeCO_3$/Fe ratio as per Table 7-4 but the corrosion rate drop as shown in Figure 7-52c is almost identical to a blank test with an R_p around 300 $\Omega.cm^2$.

Table 7-4 XRD $FeCO_3$ to Fe ratio calculations at pH 6.6 for various OA-POSS loadings

2θ	Component	Intensity Value	Ratio [FeCO₃/Fe]
31.97°	Blank $FeCO_3$	2,298	0.0167
44.77°	Blank Fe	137,087	
31.97°	$FeCO_3$ - 30 mg POSS	28,018	0.2282
44.77°	Fe - 30 mg POSS	122,757	
32.04°	$FeCO_3$ - 100 mg POSS	41,769	0.9885
44.84°	Fe – 100 mg POSS	42,253	
31.92°	$FeCO_3$ - 150 mg POSS	44,796	2.8006
44.77°	Fe - 150 mg POSS	15,995	

When the electrochemical results are compared to the micrographs, it seems that adding the total weight of OA-POSS directly or sequentially affect the iron carbonate crystal nucleation and growth since the crystals have big differences in size and shape.

As such, the crystals formed by running the test as per the conditions described in Figure 7-52a provide crystals smaller than 10µm in dimension as seen in Figure 7-54.

Thus it can be assumed that the administration method enhances the crystal nucleation stages since more crystals are formed than when the OA-POSS is added sequentially every 24 hours as seen in the bigger crystals shown in Figure 7-55. The latter is explained by a more dominant crystal growth aspect and not crystal nucleation as described previously.

When running the electrochemical bubble tests as per the conditions described in Figure 7-52b, crystals as big as 40µm are obtained and the corresponding degree of protectiveness is much lower than the corrosion films obtained when all the hybrid nanofiller is dissolved directly at the start of the experiment as seen by the polarisation resistance values depicted in Figure 7-52.

This is in agreement with the known behaviour of iron carbonate scale degree of protectiveness since it was already detailed in section 3.5.3 where it was stated that bigger iron carbonate crystals forming a thicker layer will be less protective as compared to smaller $FeCO_3$ crystals and thinner films.

As such, the OA-POSS has a better effect in creating a more protective layer if administered in batch in the first hours when most of the X65 surface is still available for it to adsorb to. It was decided to always carry out the addition of the studied nanofiller in batch after two hours pre-corrosion for the remainder of the discussed results.

It should also be highlighted that when only 30 mg OA-POSS is administered directly at the start of the test, nucleation of the iron carbonate is assisted as seen by the highly scattered iron carbonate crystals (Figure 7-56). In fact, more iron carbonate crystals were able to grow when compared to a blank test which is in accordance with the higher [104] Miller index observed in Figure 7-53b.

These crystals are shown at various magnifications in Figure 7-56 and it could be estimated that the porosity of the film is very high since the corrosion layer is not fully covering the surface; it was thus estimated that the ratio of the intensities between the [104] $FeCO_3$ to [110] Fe Miller indices is slightly higher than the blank test and averaging a value close to 0.22 as computed in Table 7-4.
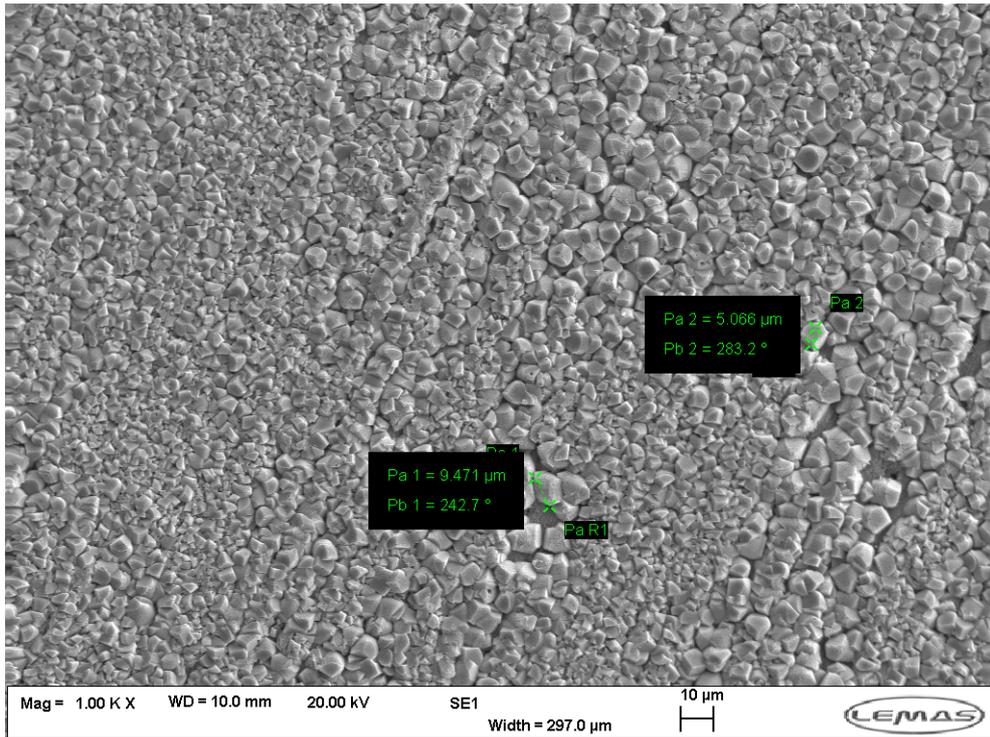
(a)
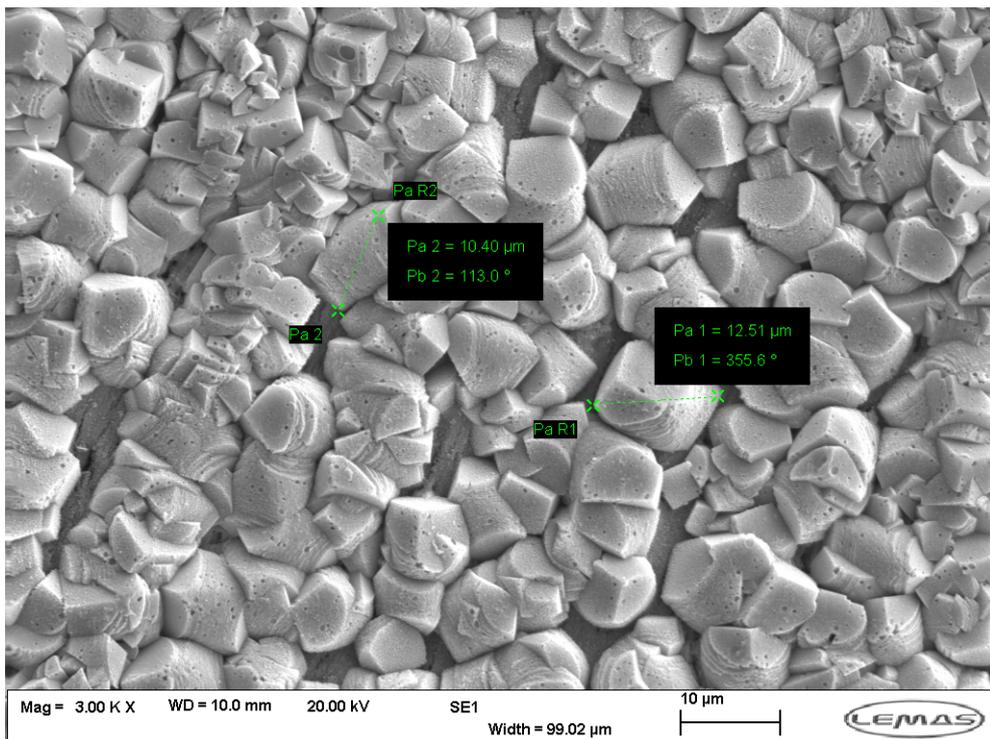
(b)

Figure 7-54 SEM micrographs topography view of X65 samples when 150mg OA-POSS are added to the test solution at increasing magnifications shown by the scale bars [pH=6.6, 60°C,3.5% NaCl, 0.8bar CO_2, observed after 98 hours] (a) X65 fully covered surface with gradually growing $FeCO_3$ crystals (b) focus on the $FeCO_3$ crystals with leaflet-like shape and interlacing properties
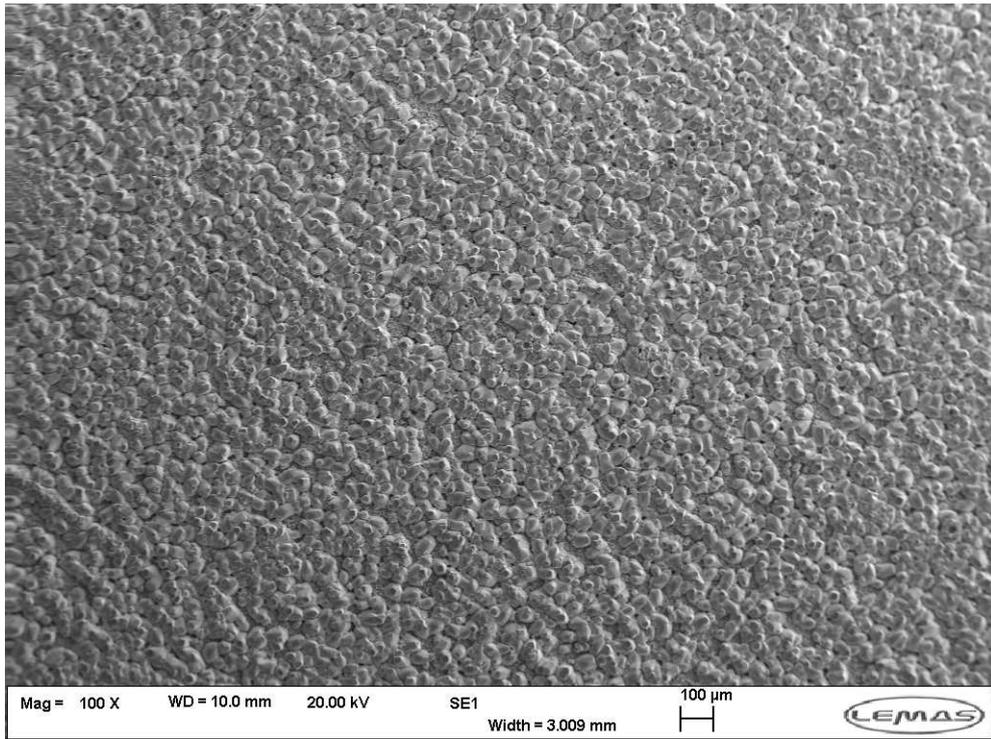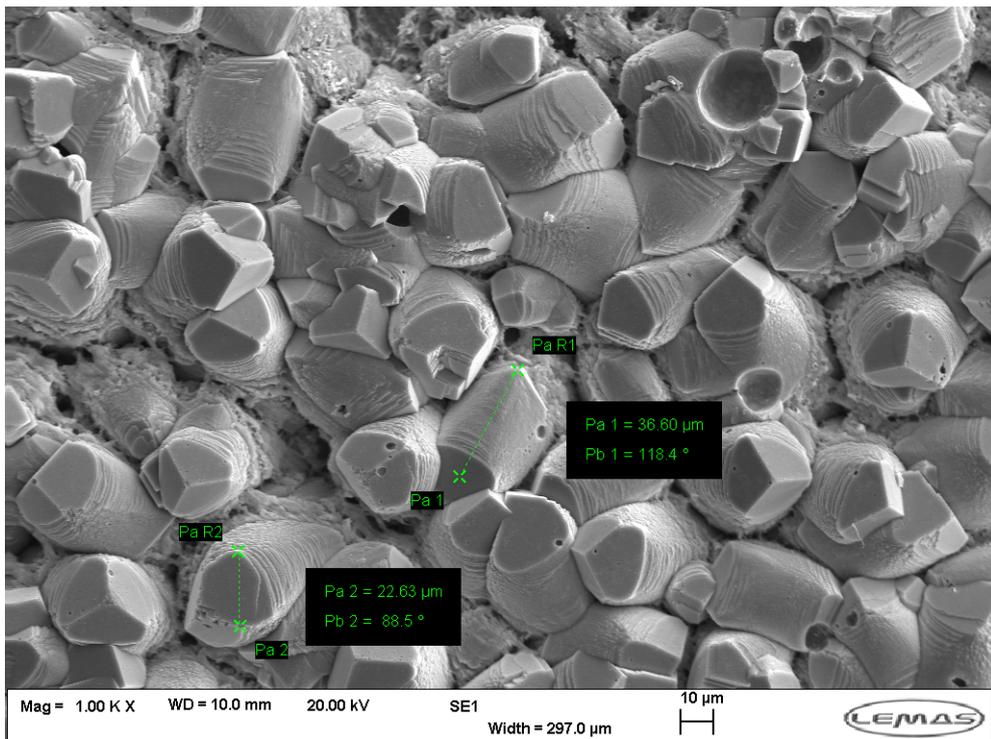
Figure 7-55 SEM micrographs topography view of X65 samples when 150mg OA-POSS are added sequentially as 50mg loading during the first 3 days at a 24 hours interval to the test solution at increasing magnifications shown by the scale bars [pH=6.6, 60°C,3.5% NaCl, 0.8bar CO_2, observed after 98 hours] (a) compact and fully covering $FeCO_3$ film over X65 sample (b) focus on the $FeCO_3$ crystals with leaflet-like shape and depicting crystal sizes averaging 30 microns
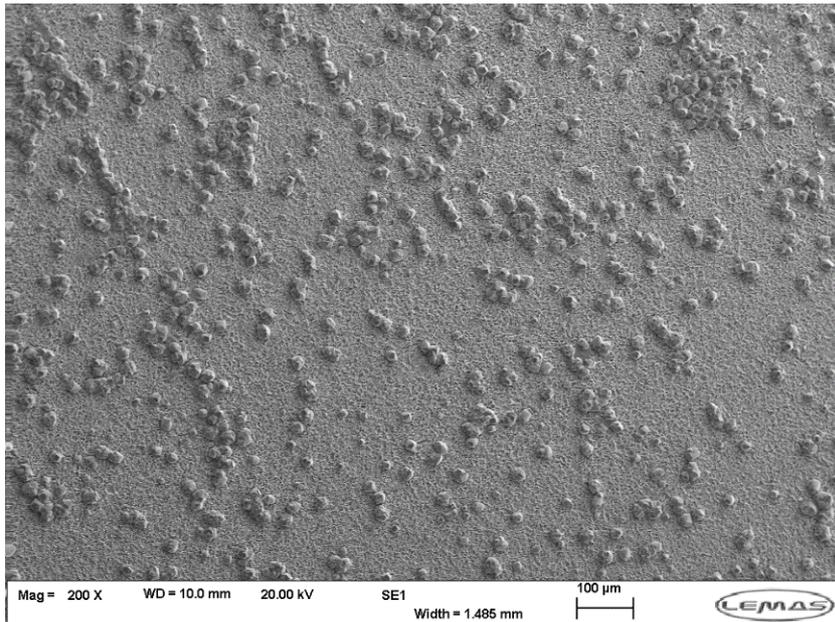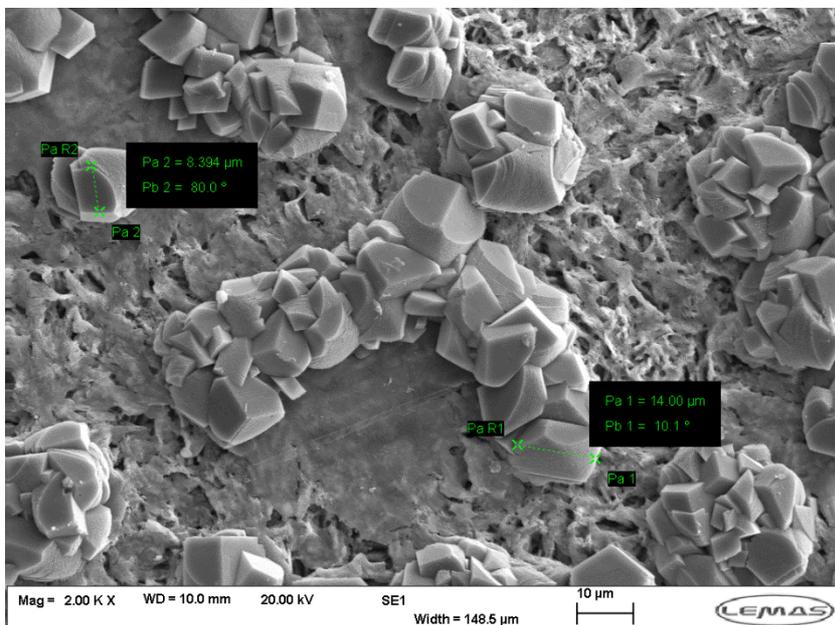
Figure 7-56 SEM micrographs topography view of X65 samples when 30mg OA-POSS are added to the test solution at various magnifications as shown on the scale bar [pH=6.6, 60°C,3.5% NaCl, 30mg OA-POSS, 98 hours] depicting (a) a mostly amorphous corrosion layer with some $FeCO_3$ crystal islands covering the steel and (b) a zoom on the $FeCO_3$ crystal showing their size and shape

As discussed previously in section 4.3.1, the iron carbonate precipitation follows a two-step process known as nucleation and growth. Whenever a solid steel surface such as carbon steel X65 is present, the nucleation phase is over relatively quickly and can be disregarded due to the numerous substrate imperfections being good candidates for nuclei formation. It is assumed that

the addition of OA-POSS at the start of the test seems to increase the duration of the nucleation phase since smaller crystals are obtained at the end of the test duration (Figure 7-54).

Generally crystals grow from a large number of discrete nuclei into larger structures which may or may not join, forming a porous film and this is exactly what was observed when only 30 mg OA-POSS were added at the start of the test as seen in Figure 7-56 with cube-like and rhombohedra of $FeCO_3$ crystals agglomerating on various areas of the corroding carbon steel.

Even though the $FeCO_3$ crystals are mostly cubic in shape regardless of the OA-POSS loading the fact that this can affect the crystal growth phase should not be regarded lightly as most publications agree on the fact that in the case of iron carbonate formation on a heterogeneous mild steel substrate, the net precipitation rate is governed by crystal growth mechanism as the rate determining step. Thus as described in Chapter 8, monitoring the concentration of the added nanofiller controls the kinetics of the $FeCO_3$ crystal growth and consequently the corrosion rate evolution.

7.3 Summary of environmental conditions matrix and kinetic activity of the silsesquioxane nanofiller

It was shown in section 7.1 how important the effect of temperature on the iron carbonate growth at a fixed pH can be. While SEM micrographs allow the corrosion layer surface coverage to be quantified, the diffraction pattern gathered from XRD tests gave more insight with regard to the density of these corrosion layers. It could be concluded that relying solely on the surface coverage and the thickness of the developed corrosion film is not enough to predict the extent of corrosion mitigation since it was shown that electrochemical results and surface analysis data do not always evolve in the same way.

Moreover, it was established that a pH of 6.6 and a temperature of 60°C seemed reasonable to assess for the researched nanofiller effect. Indeed, it was observed that the electrochemical and surface analysis results differ greatly since protective iron carbonate layers only start to appear when the silsesquioxane moieties are dissolved in the brine solution. The following chapter tries to detail the effect that various OA-POSS concentrations have on the electrochemistry of the corroding system, the morphology of the grown crystals and the corresponding mechanical enhancement registered.

Chapter 8 OA-POSS as a physico-mechanical enhancer

This section aims to establish whether there exists an optimum OA-POSS level which will densify the iron carbonate thus improving the physico-mechanical properties of the corrosion layer. Published work highlights that when enhancing various properties of a designated polymer via the addition of numerous silsesquioxane derivatives, an effective POSS loading between 3 and 10% seemed prevalent. Thus below and above these values, no apparent mechanical properties' enhancement is visible.

This was used as an initial guide and as a starting point in order to compute reasonable OA-POSS concentration effects to be studied. As such, and by assimilating the iron carbonate layer to be 100 µm thick or lower, the required wt% of OA-POSS with respect to such a $FeCO_3$ film was computed to be lower than 100mg in order to obtain similar weight percentage between the nanofiller and the developing corrosion layer.

When OA-POSS is added after the system is allowed a two hours pre-corrosion time, two kinetic regimes have been observed depending on the nanofiller loading; one where the CR drops below 0.01 mmpy in the first 40 hours if tens of milligrams of the silsesquioxane derivative are added as described in 8.1 and another where it takes more than 2 days for the CR to stabilise if less than 10 mg of OA-POSS is administered as discussed in section 8.2.

8.1 Medium OA-POSS loading and general corrosion

8.1.1 Electrochemical behaviour

When the temperature is equal to 60°C and the pH is equal to 6.6 and OA-POSS is added at loadings between 10 and 60 mg, the CR drops below 0.01 mmpy as compared to a blank test where the CR remains stable at around 3 mmpy as shown in Figure 7-33 previously.

As such, Figure 8-1 and Figure 8-2 show the same concentrations of OA-POSS and slightly different times for CR to drop and stabilize. Nonetheless, 20mg and 30 mg of added nanofiller appear to show the quickest drops in CR in the majority of the electrochemical tests. Moreover a concentration of OA-POSS corresponding to 20mg seems to give the most reproducible results with regard to the CR variation but also to the localised corrosion protection as detailed in section 8.4.
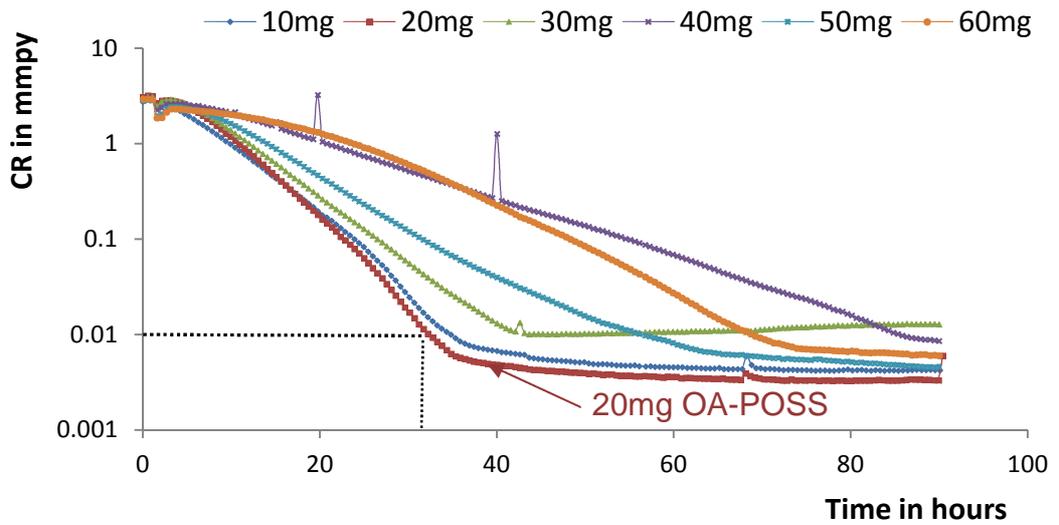
Figure 8-1 CR variations of X65 samples subjected to 10, 20, 30, 40, 50 and 60 mg OA-POSS added after 2 hours [pH 6.6, 60°C, 3.5% NaCl, 0.8bar CO_2]
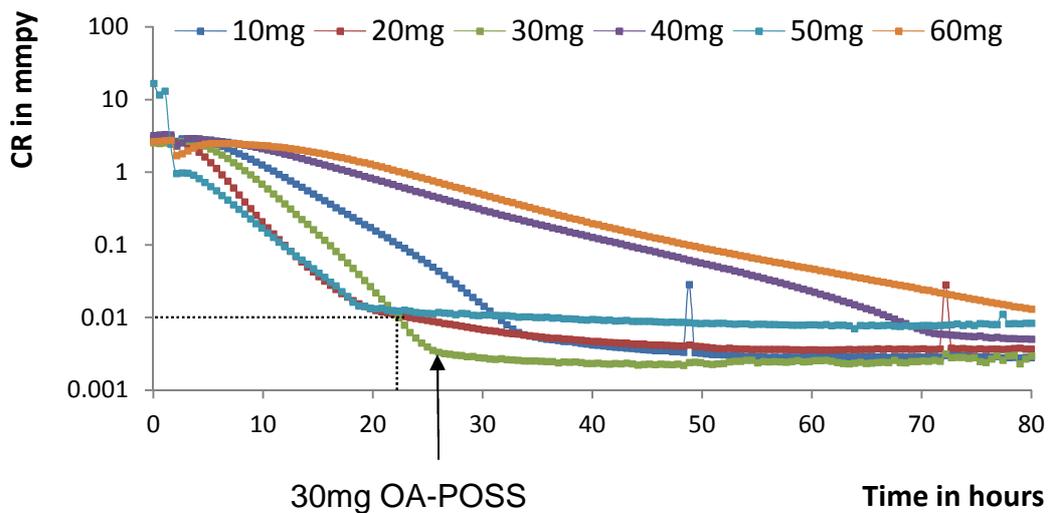
Figure 8-2 CR variations of X65 samples subjected to 10, 20, 30, 40, 50 and 60 mg OA-POSS added after 2 hours [pH 6.6, 60°C, 3.5% NaCl, 0.8bar CO_2]

It could also be noted that overdosing to values as high as 60mg corresponds to the slowest CR drop. The relationship between higher concentrations of OA-POSS and the electrochemical behaviour along with the $FeCO_3$ crystal growth morphology at various pH is detailed in section 9.4.

8.1.2 XRD diffraction pattern corresponding to the OA-POSS medium loading tests

The XRD diffraction patterns when 20mg of OA-POSS is added is shown in Figure 8-3 with an $FeCO_3$ [104] to carbon steel X65 iron [110] Miller indices peak ratio slightly higher than unity. This was deemed representative for the diffraction patterns corresponding to the tests where the nanofiller is added between values ranging from 10 to 60mg.
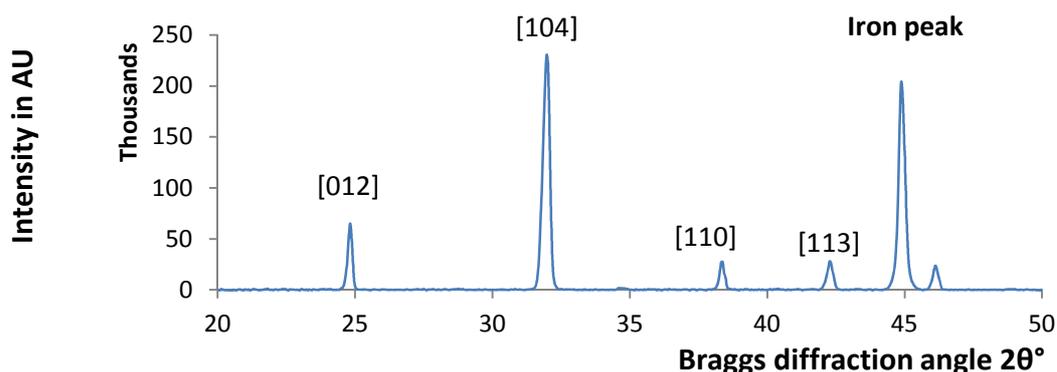
Figure 8-3 XRD diffraction pattern for a test where 20 mg OA-POSS have been added [pH 6.6, 60°C, 3.5% NaCl, 0.8bar CO_2, 98 hours]

8.1.3 SEM results for tests carried out by adding 10 to 60mg OA-POSS

8.1.3.1 Micrographs for test ran with 10mg OA-POSS

Both top-view and cross-section micrographs at 10mg OA-POSS loading are shown in Figure 8-4 and Figure 8-5 respectively. The crystals seem to have a dimension ranging from 5 to 10 microns while the average film thickness is lower than 10 microns as determined by checking the thickness of the corrosion layer through various areas on the cross-section micrograph. Moreover, at very high resolution as per Figure 8-4b, the crystal show a lamellar or leaflet-like composition where pinholes are randomly scattered over the surface and showing an average diameter smaller than 500 nanometres.

The scattered pinholes or porosities are randomly present at various OA-POSS loadings but also in fewer blank tests. The cause behind such defects is discussed in section 10.1.3. They appear to only develop on the surface and not extend though the whole $FeCO_3$ crystal length. In fact, the CR dropping to values as low as 0.001mmpy corroborate the assumption that the corrosion reactants do not reach the steel surface due to the $FeCO_3$ layer.

(a)

(b)

11.8µm

Pinholes almost
0.5 µm thick
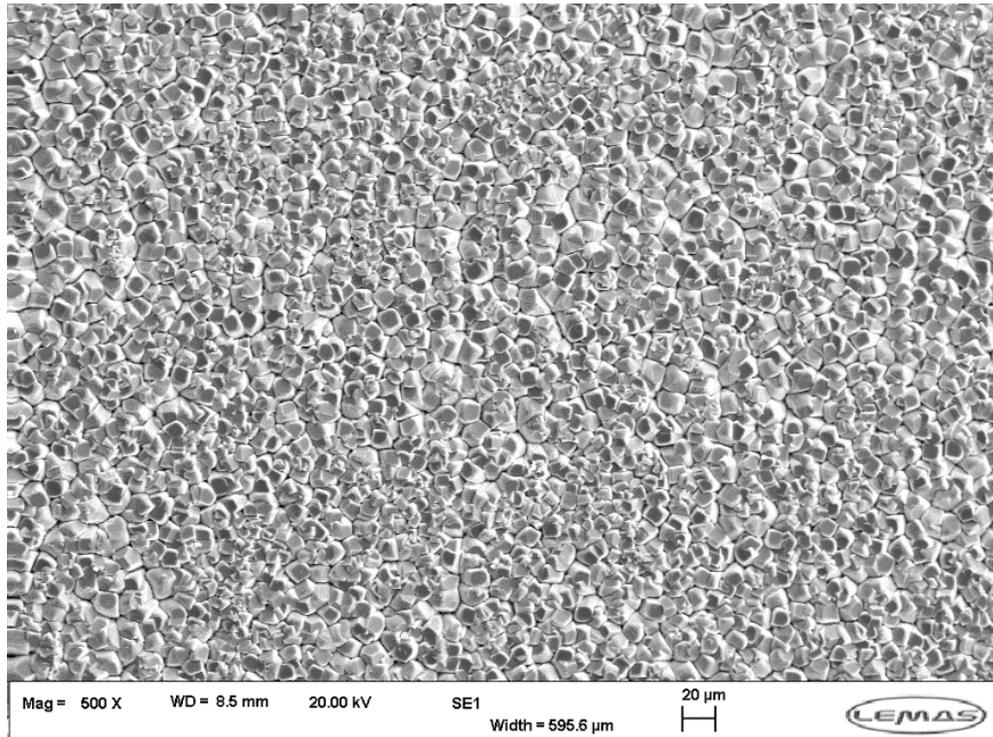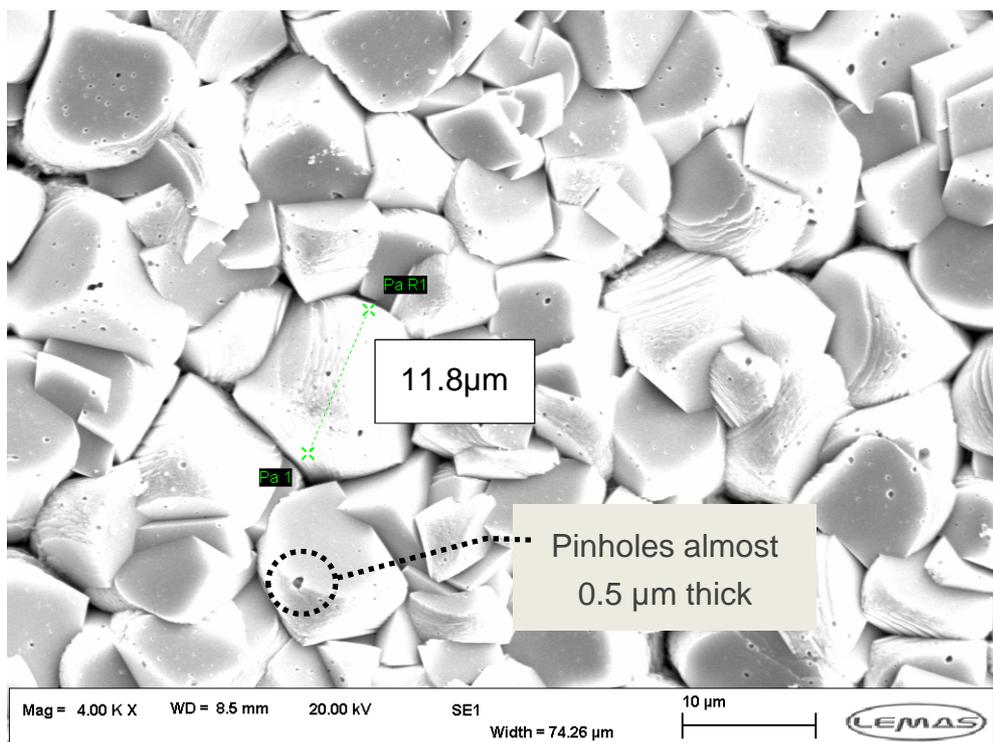
Figure 8-4 SEM micrographs topography view of X65 samples when 10mg
OA-POSS are added to the test solution at various magnifications as
seen from the scale bars [pH=6.6, 60°C,3.5% NaCl, 0.8bar CO_2, 108
hours] with (a) fully covering iron carbonate corrosion layer and (b) focus
on $FeCO_3$ crystal shape and size and presence of pinholes
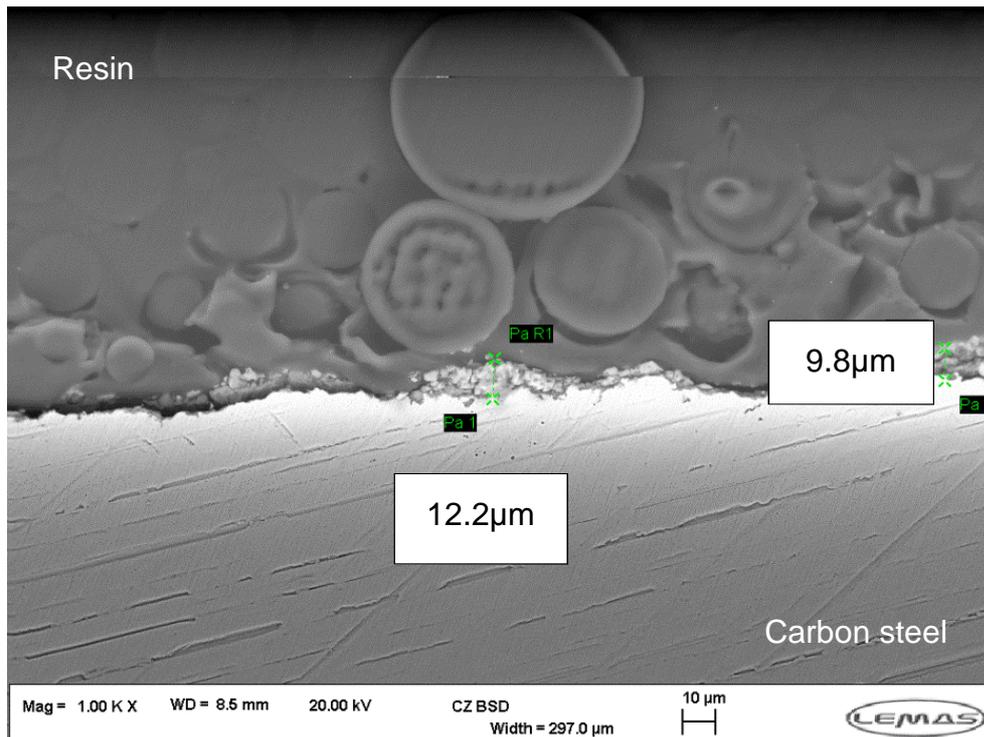
Figure 8-5 Cross-section SEM micrographs of X65 samples when 10mg OA-POSS are added to the test solution showing a scale bar of 10µm [pH=6.6, 60°C, 3.5% NaCl, 0.8bar CO_2, 108 hours]

8.1.3.2 Micrographs for tests ran with 20mg OA-POSS

Similarly, tests at 20mg OA-POSS were undertaken at the same pH of 6.6 and temperature of 60°C and both top view and cross-section micrographs are presented in Figure 8-6 and Figure 8-7. The main difference between these and the tests where only 10mg of the nanofiller was administered is that the grown $FeCO_3$ crystals are slightly smaller in size. Their average dimension is 8µm as shown at high magnification in Figure 8-6b. Moreover, the pinholes observed when 10mg OA-POSS are added are highly reduced, almost inexistent. The cubic and rhombohedral iron carbonate crystals look to be growing as leaflets and are very compact while the average film thickness is less than 5 microns.

The corrosion film appears to be very compact and it is known that a very thin corrosion layer provides better general corrosion resistance. In fact, published papers relating to iron carbonate corrosion products usually describe the iron carbonate layers grown at higher temperatures to be thinner and more protective and the corrosion layers grown with 20mg OA-POSS seem to behave in a similar way.

196

(a)

Pa 2   Pa R1

7.8μm   7.9μm

Pa R2
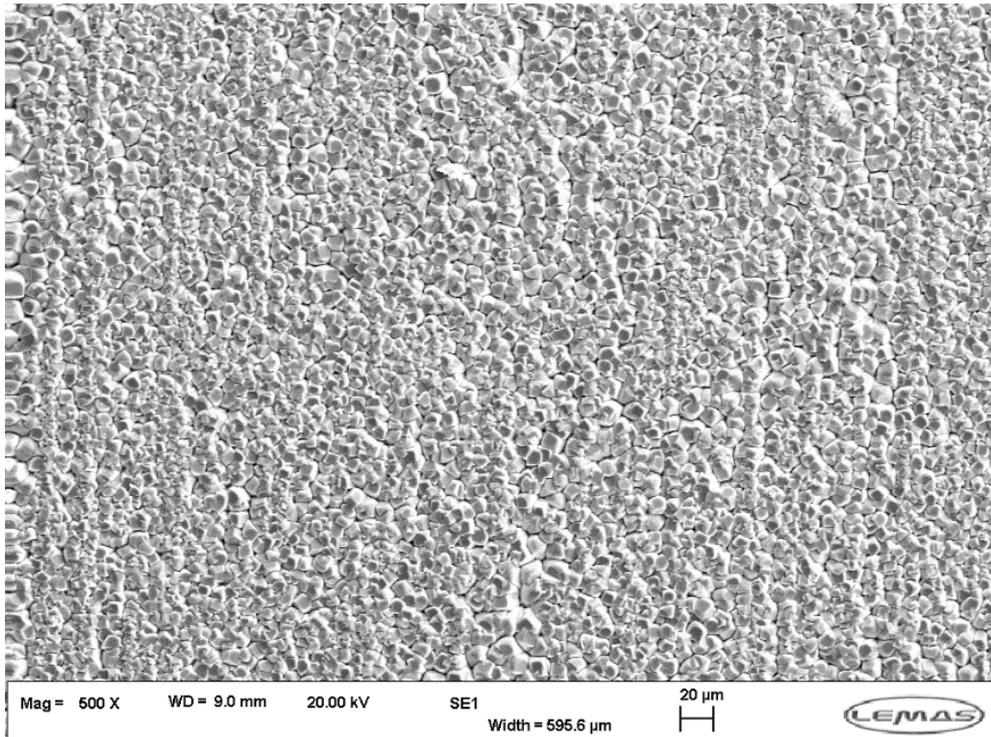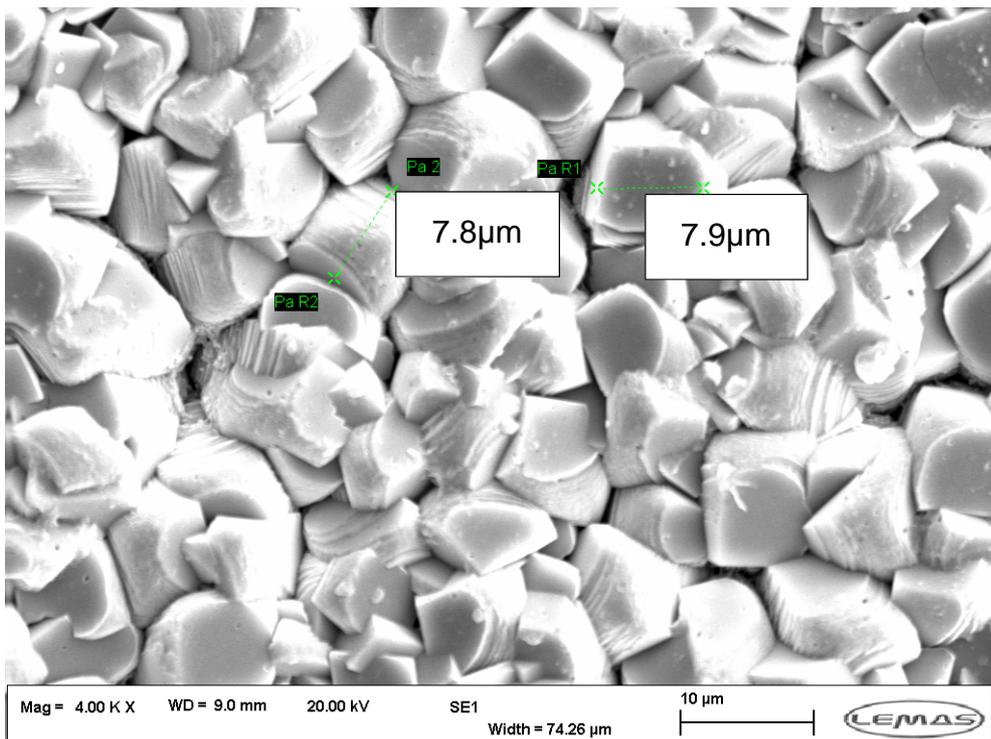
(b)

Figure 8-6 SEM micrographs topography view of X65 samples when 20mg OA-POSS are added to the test solution at various magnifications as shown by the scale bars [pH=6.6, 60°C,3.5% NaCl, 0.8bar CO_2, 108 hours] with (a) fully covering iron carbonate corrosion layer and (b) focus on $FeCO_3$ crystal shape and size and absence of pinholes
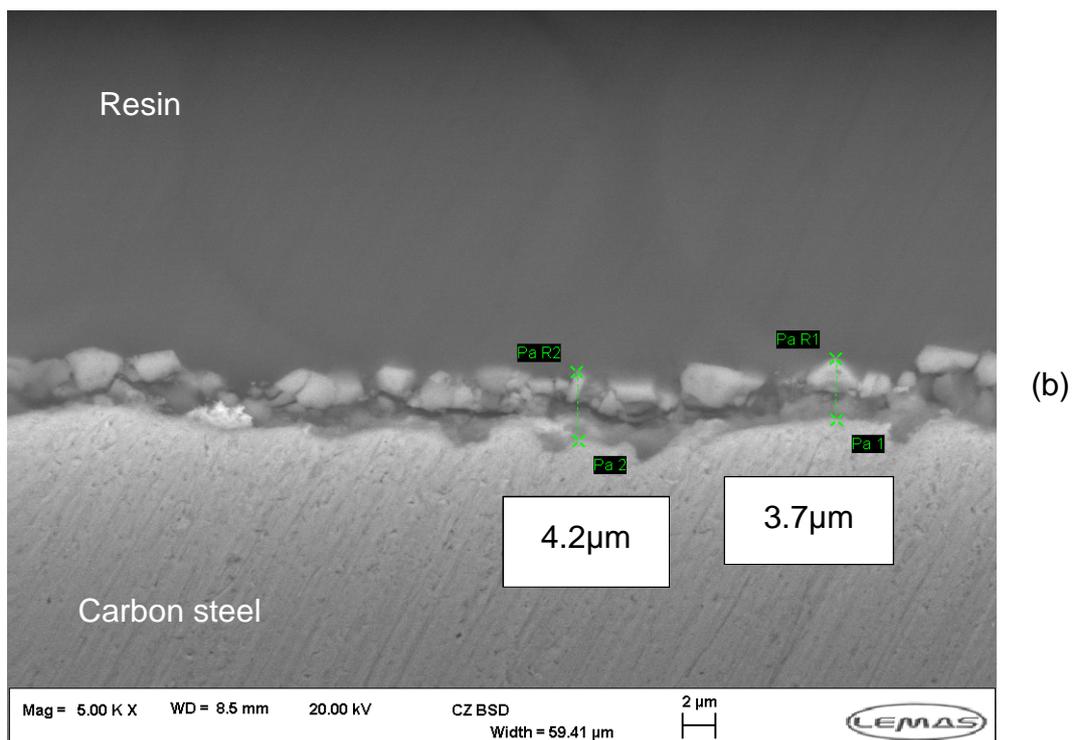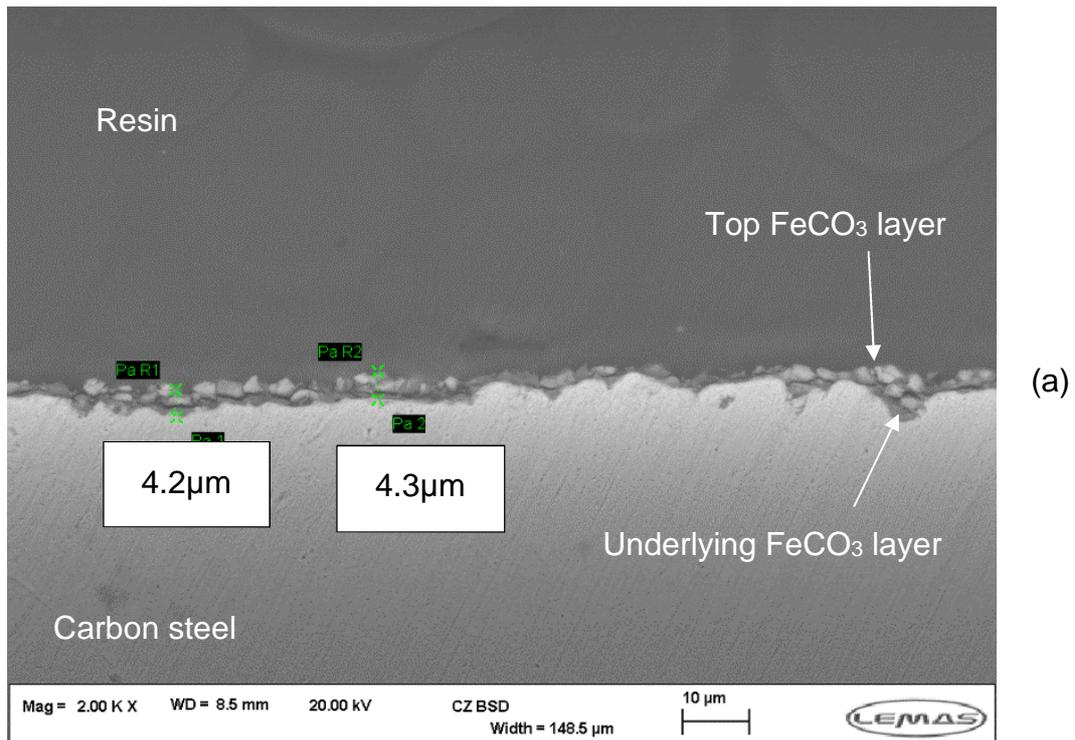
Figure 8-7 Cross-section SEM micrographs of X65 samples when 20mg OA-POSS are added to the test solution at various magnifications as shown by the scale bars [pH=6.6, 60°C,3.5% NaCl, 0.8bar CO_2, 108 hours] showing (a) $FeCO_3$ film with a uniform thickness and (b) a zoom on the corrosion layer showing what appears to be a two-layered crystal growth

The corrosion layer seems to be very uniform in thickness along the various regions as observed in Figure 8-7. It is also very compact and well-adherent with no apparent adhesive or cohesive delamination from the underlying carbon steel sample thus providing adequate protection. The film is organised in two distinct $FeCO_3$ crystal layers. Moreover, the fact that the corrosion layer total thickness is very thin suggests that these crystals are growing mainly in the longitudinal direction along the carbon steel surface axis.

8.1.3.3 Micrographs for tests ran with 30 mg OA-POSS

These micrographs show very close crystal microstructure and film thicknesses as when 20 mg OA-POSS were added as seen on the top-view and cross-section images in Figure 8-8 and Figure 8-9 respectively. The $FeCO_3$ crystals exhibit numerous leaflet layers and a high porosity level mainly on the crystal vertices as seen in the highest magnified micrograph in Figure 8-8b. No evident change in the $FeCO_3$ morphology is observed as the crystals appear cubic in shape and lamellar. In general, the corrosion film is divided mainly between relatively discrete crystals but also some fewer dense and inter-grown crystals.

The thickness of the corrosion layer varies between 4 and 6 micrometres thus it is slightly thicker than the scale film formed when only 20mg OA-POSS is administered. While the formation of a double corrosion layer is evident, there also seems to be a limited cohesive delamination in between the two crystal layers forming the iron carbonate corrosion product. The first internal crystal layer in contact with the carbon steel substrate denoted as (IL) seems to uphold smaller crystalline structures if compared to the bigger crystals found in the slightly delaminated outer layer denoted (OL) in contact with the brine solution as shown in the back-scattered electron micrographs in Figure 8-9.

These results correlate with the published work from Ruzic et al.[360] where the top layer was described as a dense crystalline material primarily formed during the second stage of film formation. It is described as a spontaneous film growth phase when relative supersaturation is low and when the particle growth-mode predominates. In contrast, the inner layer develops during the first rapid precipitation stage of film formation at high supersaturation values under conditions where the nucleation mode prevails, and the $FeCO_3$ film is thought to form by coagulation of crystal nuclei from a colloidal solution close to the metal surface.
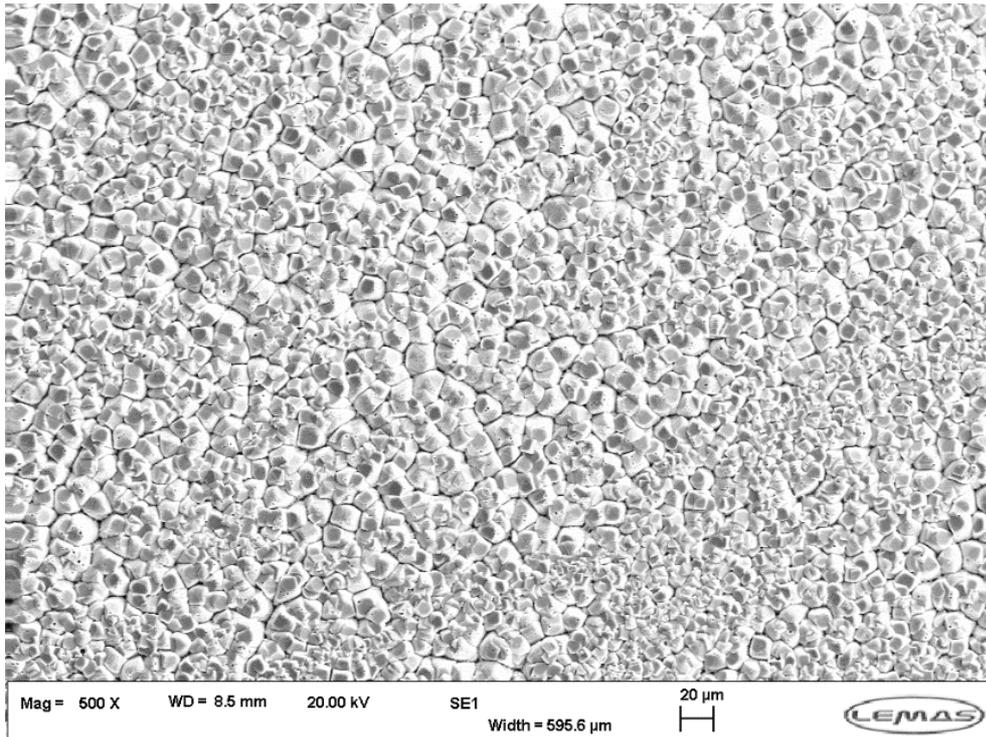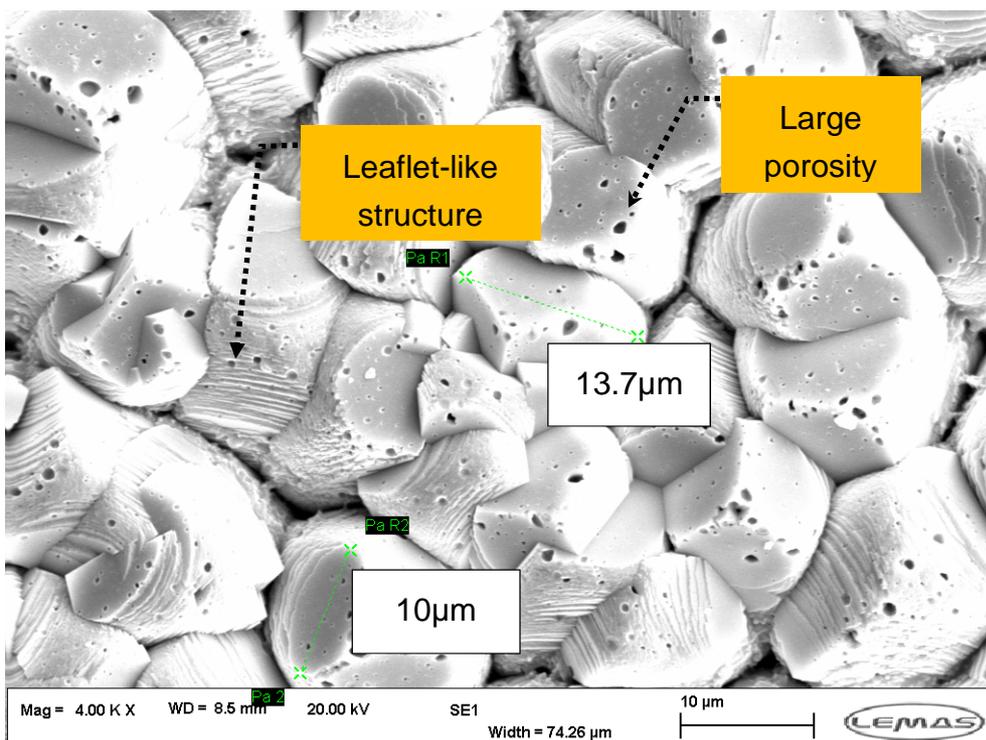
Figure 8-8 SEM micrographs topography view of X65 samples when 30mg OA-POSS are added to the test solution at various magnifications as shown by the scale bars [pH=6.6, 60°C,3.5% NaCl, 0.8bar CO_2, 108 hours] with (a) fully covering iron carbonate corrosion layer and (b) focus on $FeCO_3$ crystal shape and size and excessive presence of pinholes
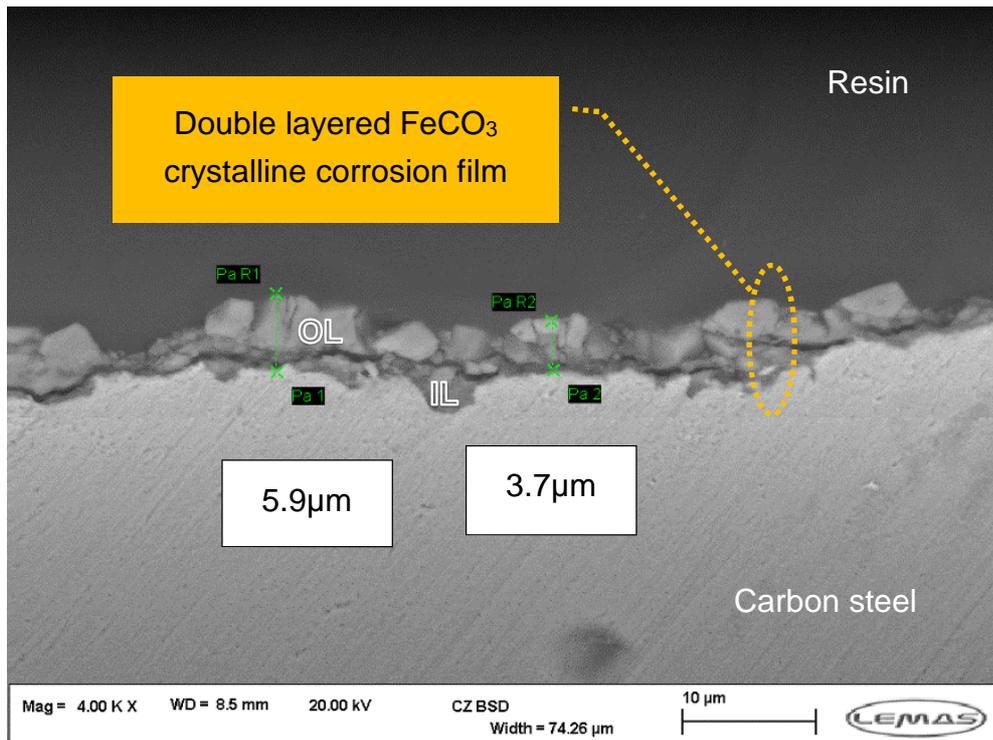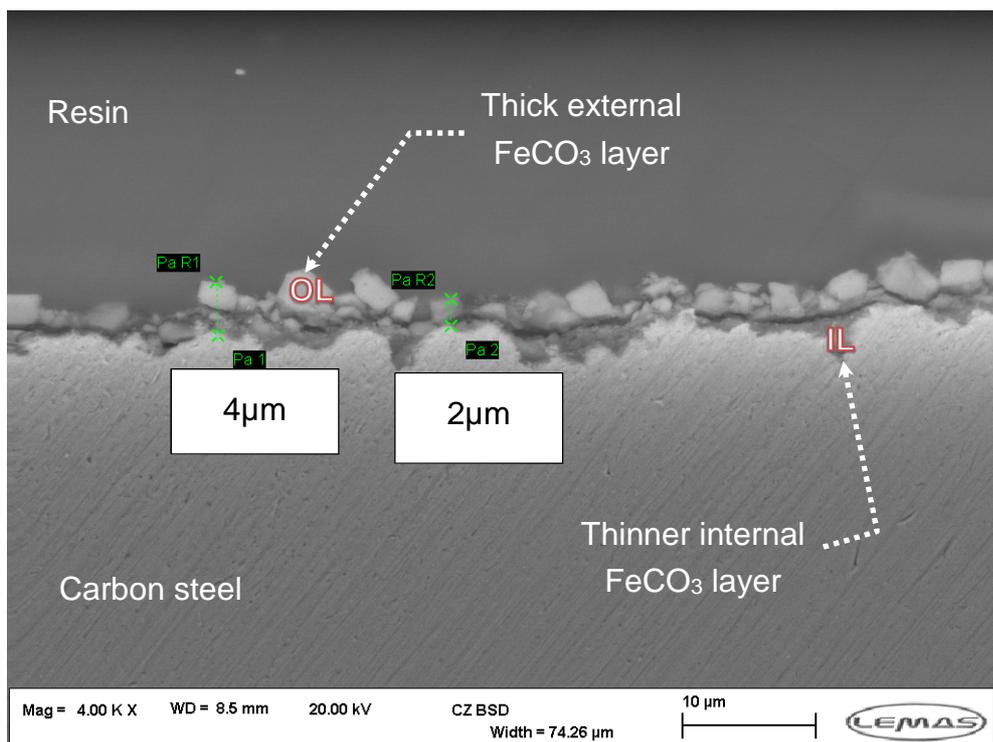
Figure 8-9 Cross-section SEM micrographs of X65 samples when 30mg OA-POSS are added to the test solution showing a 10µm scale bar [pH=6.6, 60°C,3.5% NaCl, 0.8bar CO_2, 108 hours] and a slightly uniform $FeCO_3$ layer with (a) 3 to 5 microns thickness and (b) 2 to 3 microns thickness at various locations

8.1.3.4 Micrographs for tests ran with 40 mg OA-POSS

A set of top view and cross-sectional micrographs are depicted respectively in Figure 8-10 and Figure 8-11 when 40mg OA-POSS are dissolved after 2 hours pre-corrosion time.
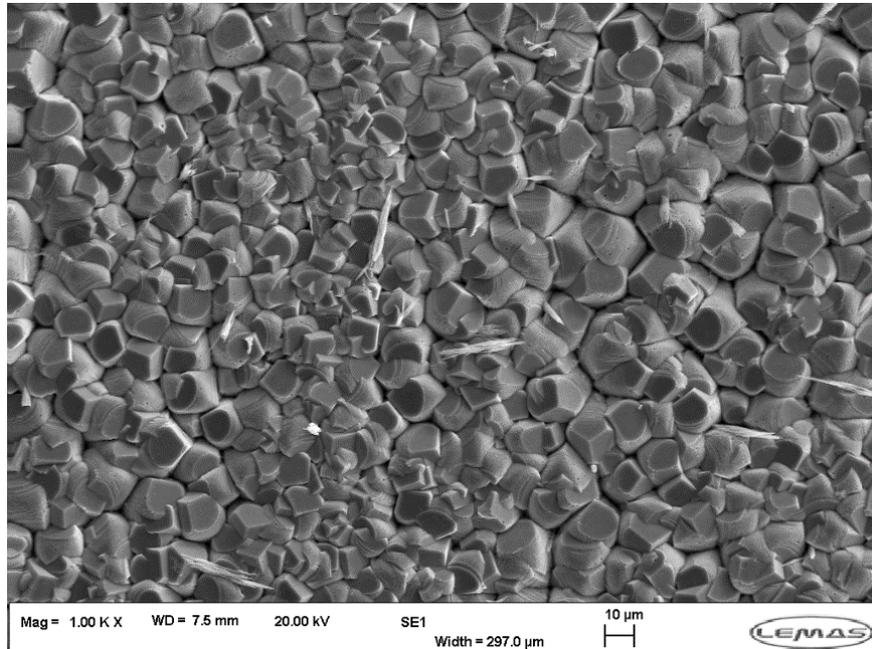
(a)
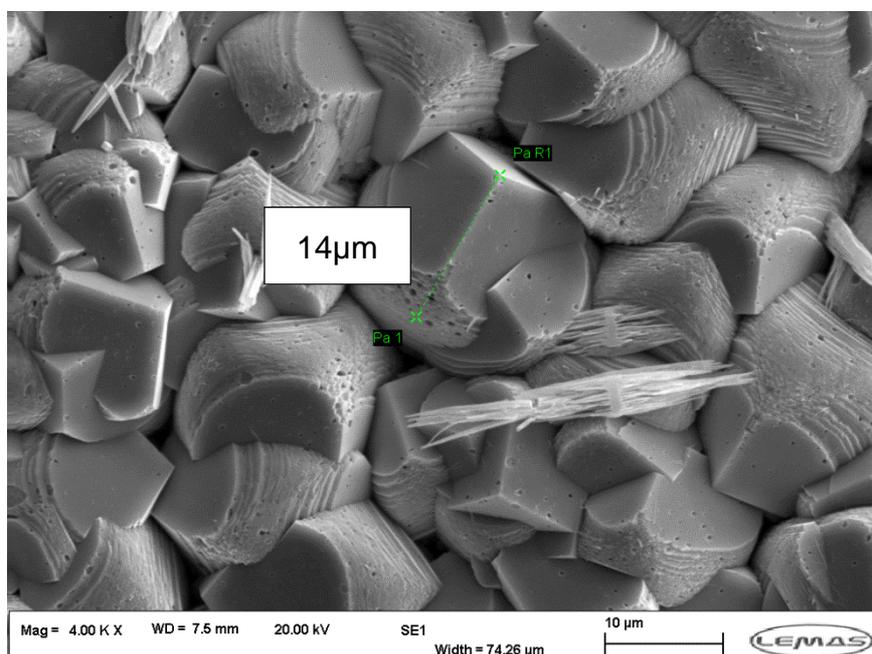
(b)

Figure 8-10 SEM micrographs topography view of X65 samples when 40mg OA-POSS are added to the test solution with 10µm scale bar shown [pH=6.6, 60°C,3.5% NaCl, 0.8bar CO_2, 108 hours]   (a) fully covering $FeCO_3$ corrosion layer formed of smooth and cubic $FeCO_3$ crystals and (b) focus on $FeCO_3$ crystal shape and size and few scattered pinholes
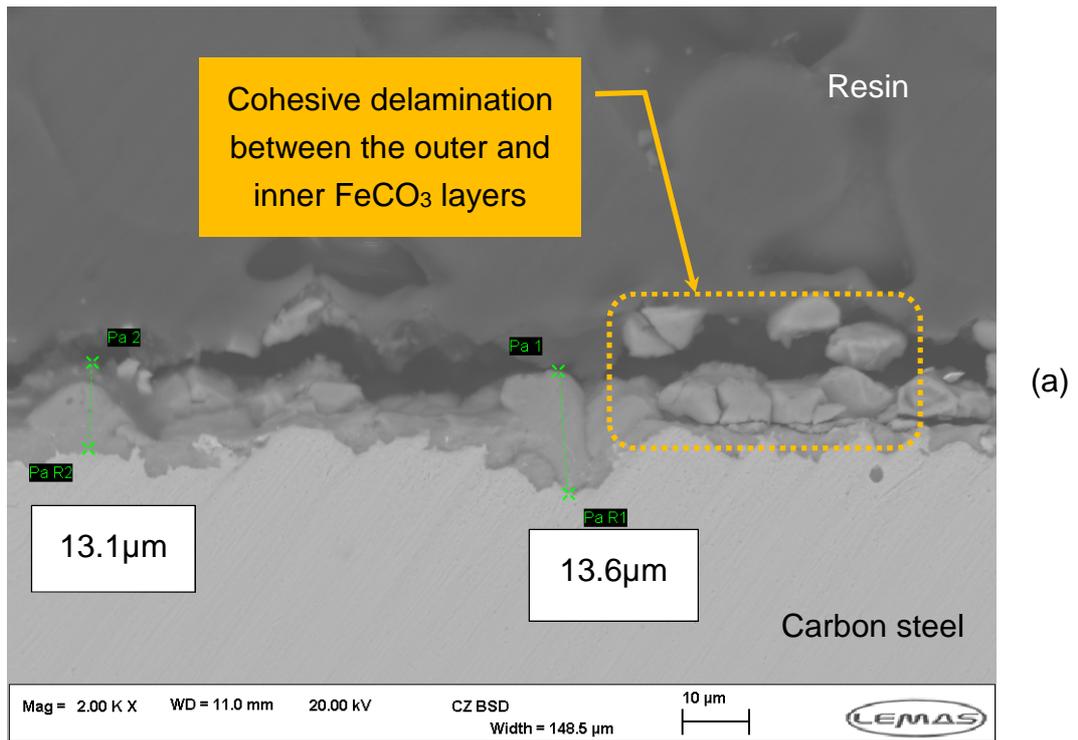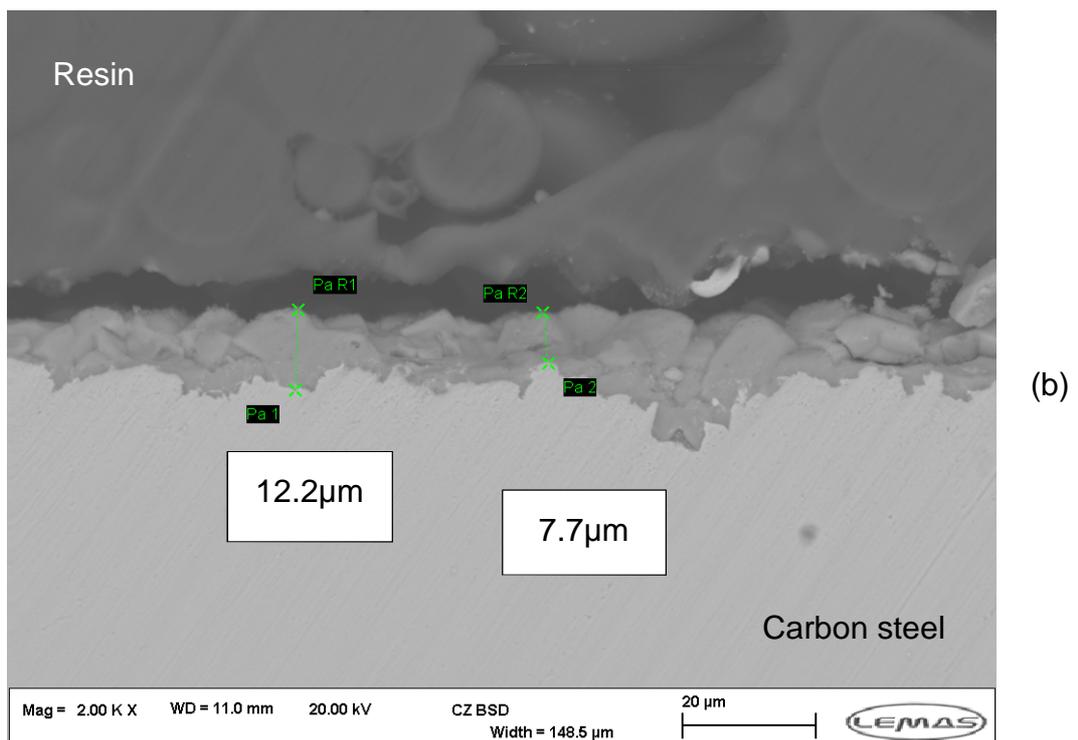
Figure 8-11 Cross-section SEM micrographs of X65 samples when 40mg OA-POSS are added to the test solution at various magnifications as seen by the corresponding scale bars [pH=6.6, 60°C, 3.5% NaCl, 0.8bar CO_2, 108 hours] and depicting two distinct locations with a thickness average around (a) 15μm and (b) 10μm

When 40 mg OA-POSS is added after 2 hours of pre-corrosion, the $FeCO_3$ crystals are closely packed and show a dominant cubic structure (Figure 8-10a) but slightly bigger in size (Figure 8-10b). On the other hand the average film thickness varies between 8 and 12 microns as seen in Figure 8-11.

The cohesive delamination seen in the SEM cross-sections could be linked to a higher internal stress due to the film thickness and the crystals growing vertically but also a heat from the exothermic resin casting procedure should not be ruled out. This breakdown of the corrosion film leaves a thicker internal layer adhering to the carbon steel surface and a thinner outer layer detached with the thermosetting resin.

8.1.3.5 Micrographs for tests ran with 50 mg OA-POSS

The crystals that develop at this OA-POSS concentration are slightly smaller in size and are approximately 10 microns wide as per the added dimension in Figure 8-12b. The average film thickness does not seem very uniform as shown from Figure 8-13 on the various cross-sections and varies from as low as 3 microns to as high as 13 microns on average.

Porosities are also apparent on the higher magnification and are clearly visible in Figure 8-12b. These are scattered mainly on the vertices of the cubic $FeCO_3$ crystals and the largest are almost 500 nanometres wide.

The corrosion layers are very compact and constituted of two crystal layers. The main difference between the iron carbonate crystals grown under these conditions is to be correlated with their morphology. In fact as opposed to the dominant cubic structures previously described, these $FeCO_3$ crystals look more like an equivalent mixture of both semi-circular and cubic crystals.

Since the OA-POSS loading is the only variable in all tests, it seems logical to assume that it is the main reason for such evolution in the $FeCO_3$ crystal shape. It also suggests that the growth of the $FeCO_3$ crystals is enhanced and thus most crystals are similar in size and interlace.

Although the iron carbonate film appears to be compact and the $FeCO_3$ crystals interlocked, the corrosion rate reduction is not as sharp as when 20 mg OA-POSS is added. This lower degree of protectiveness could be linked to the non-uniform thickness of the grown corrosion film and the presence of gaps between the external and internal $FeCO_3$ layers as seen in Figure 8-13b.
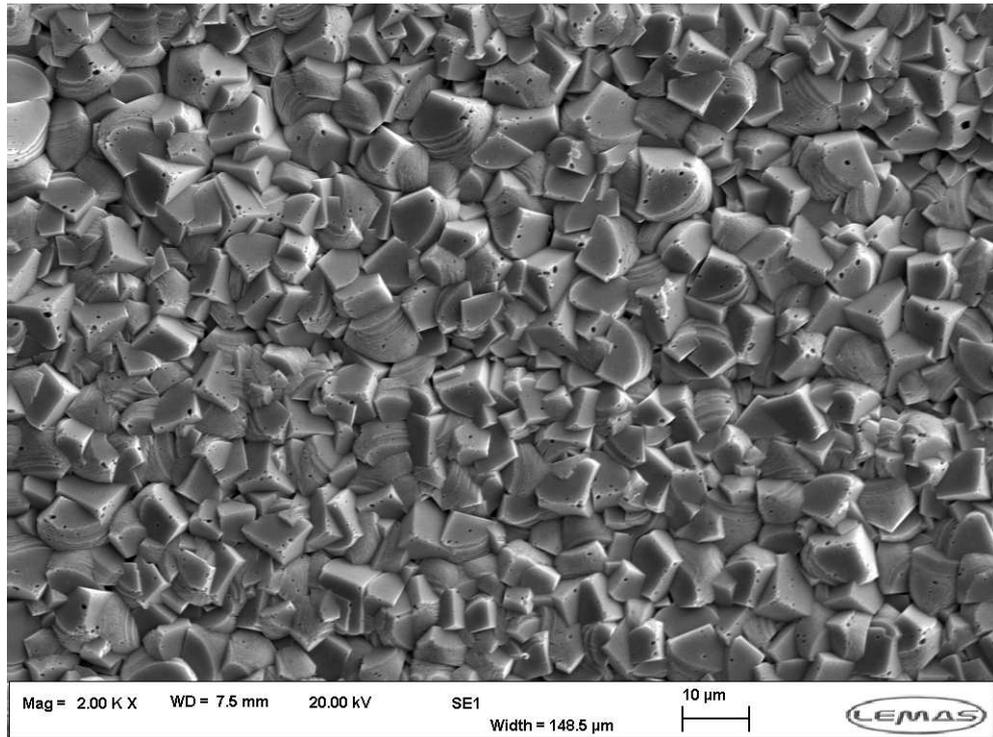
(a)
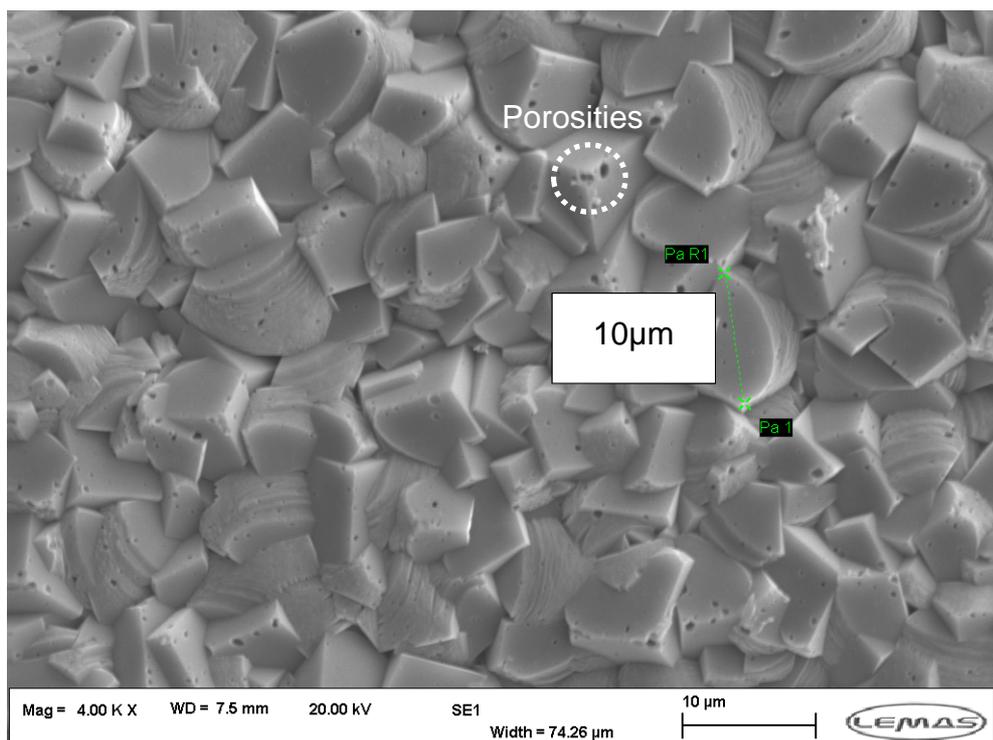
(b)

Figure 8-12 SEM micrographs topography view of X65 samples when 50mg OA-POSS are added to the test solution at various magnifications as seen by the corresponding scale bars [pH=6.6, 60°C,3.5% NaCl, 0.8bar CO_2, 108 hours] (a) focusing on the highly interlaced $FeCO_3$ crystals and (b) depicting an average size of 10µm
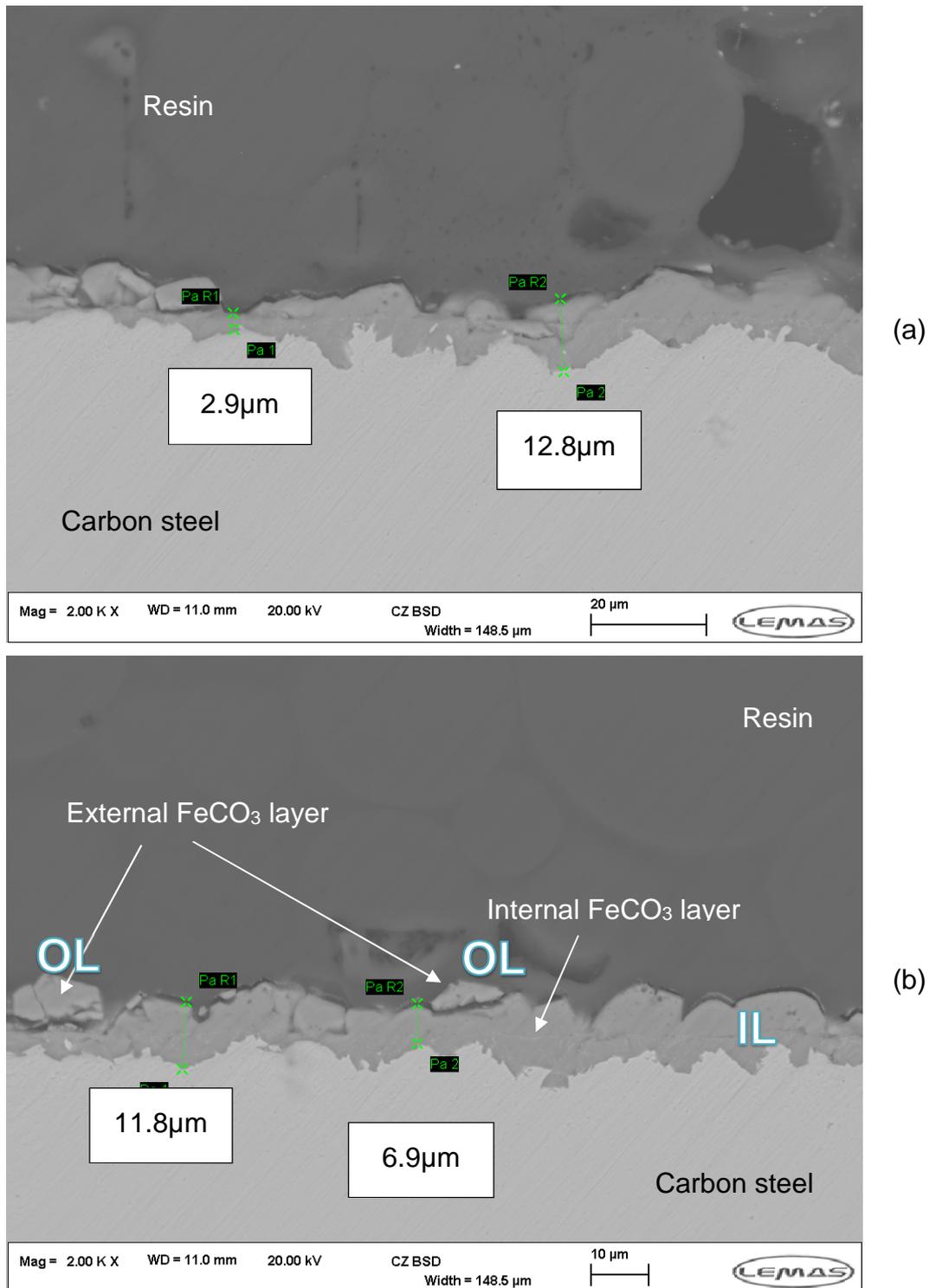
Figure 8-13 Cross-section SEM micrographs of X65 samples when 50mg OA-POSS are added to the test solution at various magnifications as shown by the scale bars [pH=6.6, 60°C, 3.5% NaCl, 0.8bar CO_2, 108 hours] with two locations showing (a) big thickness discrepancies between 3 and 12 microns thickness and (b) a more uniform corrosion film thickness in other areas around 9 microns (OL) depicts the outer layer while (IL) corresponds to the inner $FeCO_3$ layer

8.1.3.6 Micrographs for tests ran with 60 mg OA-POSS

Sixty milligrams of OA-POSS was the highest chosen concentration of the nanofiller in the range termed as medium OA-POSS loadings. The $FeCO_3$ crystals grown in these conditions are 6 to 8µm wide as shown in Figure 8-14 and the average film thickness is similarly around 8µm as per Figure 8-15.

A lower instance of pinholes is observed when running tests with 60mg of the nanofiller and the scale film appears to be composed of two to three iron carbonate layers as per the different locations depicted with a uniform evolution over the whole covered surface as seen in Figure 8-15.

From all the above, it seems as though a single or multiple-layered iron carbonate corrosion film is developing after 118 hours. These fast-growing iron carbonate layers are very protective suggesting that they are very compact and well-adherent to the underlying carbon steel. The fact that the corrosion rate variations follow a similar trend but can swap between the various OA-POSS loading could be explained by the observed discrepancies in the morphology of the corrosion layers formed. In fact, the grown $FeCO_3$ scales show cubic, prismatic and semi-circular crystals with dimensions ranging from 5 to 15 micrometres while the film thickness varies from as low as 3 micrometres to as high as 18 micrometres depending on the film uniformity and stability of the external $FeCO_3$ sub-layer.

Usually the average porosity of the iron carbonate corrosion layers is known to slightly decrease with the increase of the reaction time. In this section, it has been found that although the iron carbonate layer is protective under the test conditions (pH 6.6, 60°C,118 hours), dominant porosities as large as 500 nanometres were scattered on the crystal surface and greatly reduced when 20 mg OA-POSS were added.

It is usually believed that at a temperature as low as 60°C, the iron carbonate starts to grow at the outer surface and inwards, and these films are considered to be poorly protective as elaborated by Farelas et al.[193] But when OA-POSS is added this behaviour seem to be replaced by a more compact and better protective $FeCO_3$ scale acting as diffusion barrier and the limiting factor in the degree of protectiveness at various OA-POSS loadings appear to be the uniformity of the film, the number of layers it is formed of and the morphology of the crystals but also the degree of porosities that are present. In fact, at 60°C, Sun et al.[358] computed a porosity in the $FeCO_3$ corrosion layer ranging between 0.59 and 0.71.
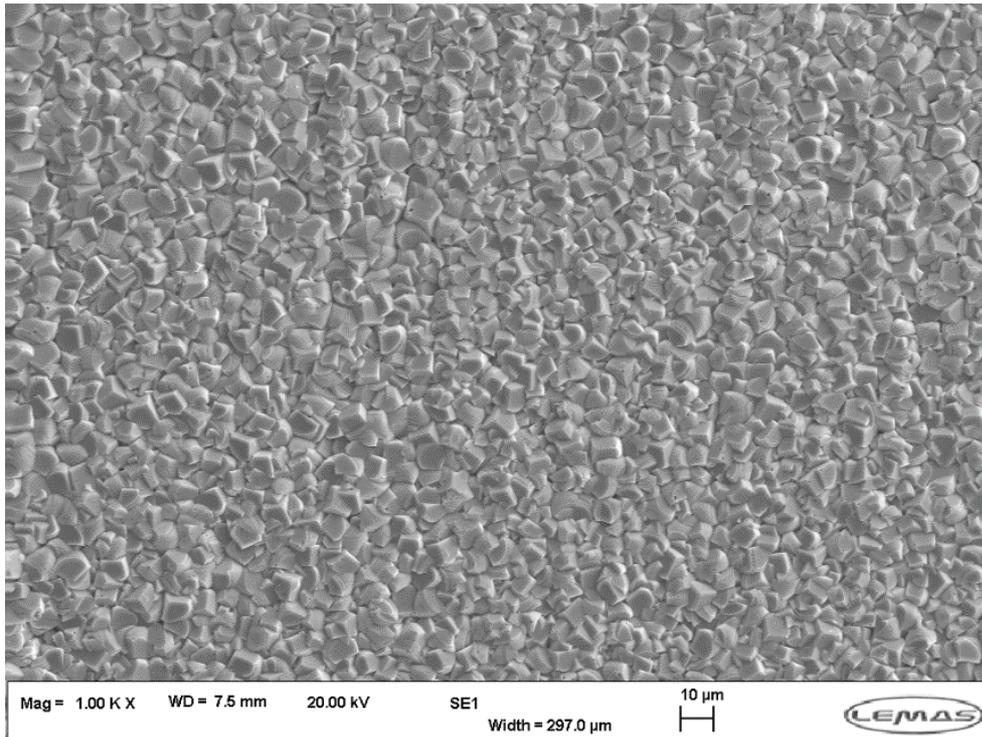
(a)
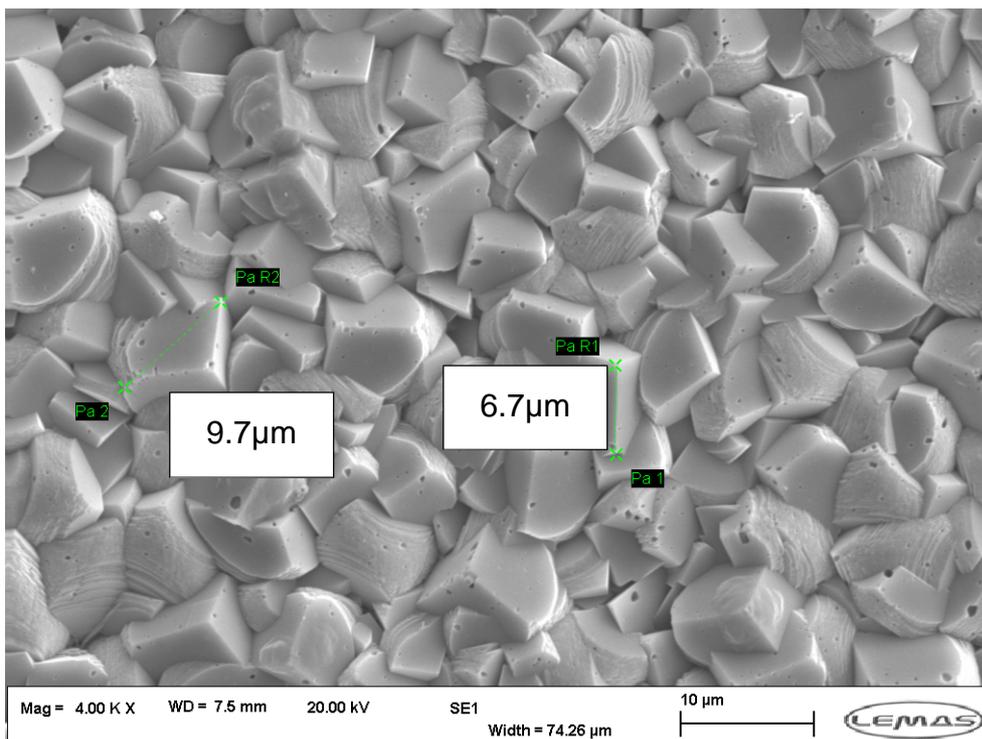
(b)

Figure 8-14 SEM micrographs topography view of X65 samples when 60mg OA-POSS are added to the test solution at various magnifications as shown by the scale bars [pH=6.6, 60°C, 3.5% NaCl, 0.8bar CO_2, 108 hours] (a) showing a very compact and fully covering $FeCO_3$ layer and (b) a focus on the $FeCO_3$ morphology and average size
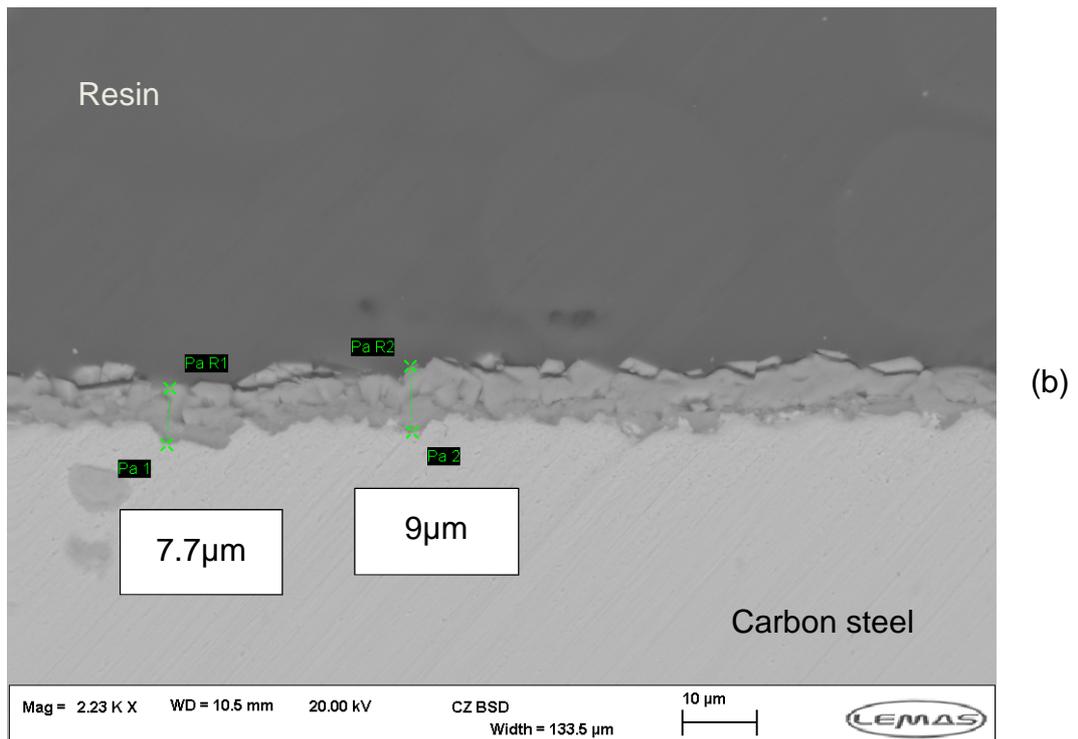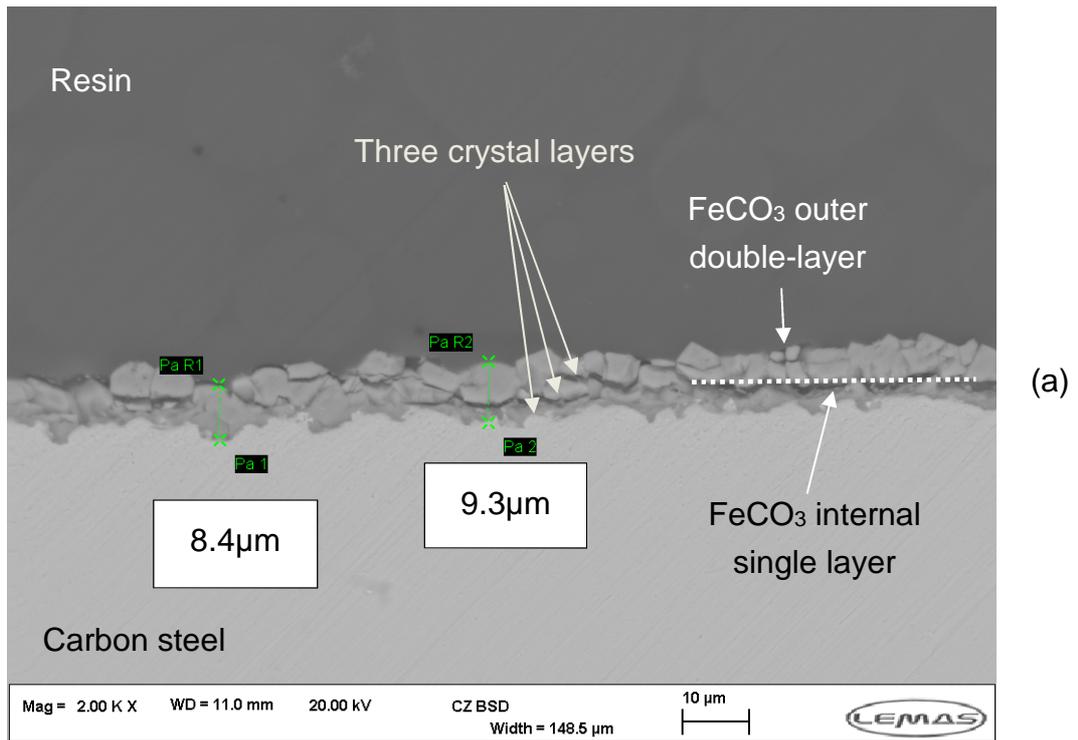
Figure 8-15 Cross-section SEM micrographs of X65 samples when 60mg OA-POSS are added to the test solution at various magnifications as shown by the scale bars [pH=6.6, 60°C, 3.5% NaCl, 0.8bar CO_2, 108 hours] (a) focus on the multi-layered $FeCO_3$ film and (b) focus on the film thickness

8.1.4 EDX analysis

Two areas of an FeCO$_3$ layer grown in the presence of 20mg OA-POSS were analysed via EDX as per Figure 8-16 and Figure 8-17.
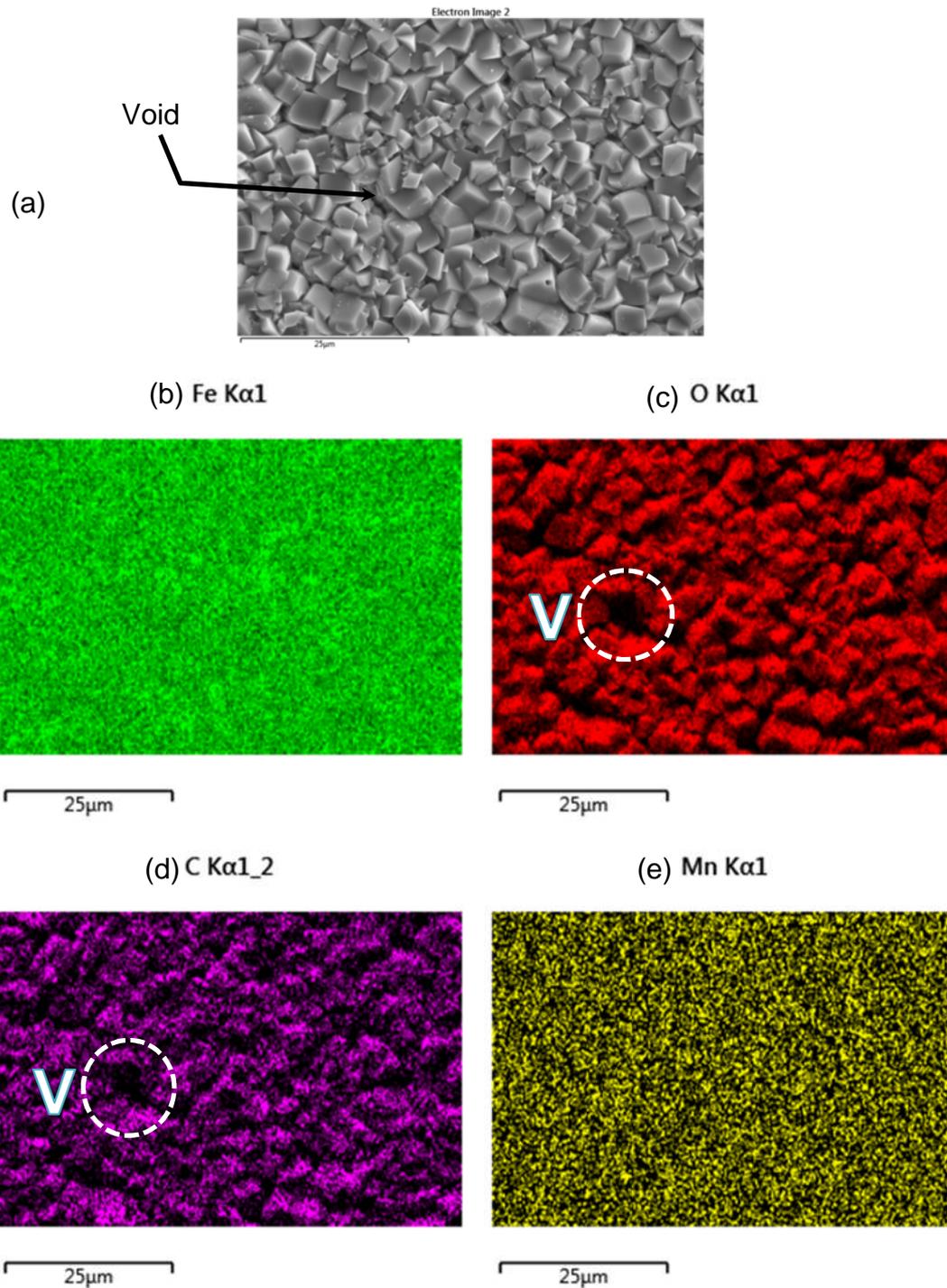
Figure 8-16 EDX map 1 of corrosion layer grown at 60°C, pH 6.6, 3.5% NaCl, 0.8bar CO$_2$ with 20mg OA-POSS added showing the (a) corresponding SE micrograph, (b) Iron-Fe, (c) Oxygen-O, (d) Carbon-C, (e) Manganese-Mn (V) voids

(a) Fe Kα1

(b) O Kα1

V

25μm

25μm

(c) C Kα1_2

(d) Mn Kα1

V

25μm

25μm

(e) Ag Lα1

(f)

Electron Image 3

25μm

25μm
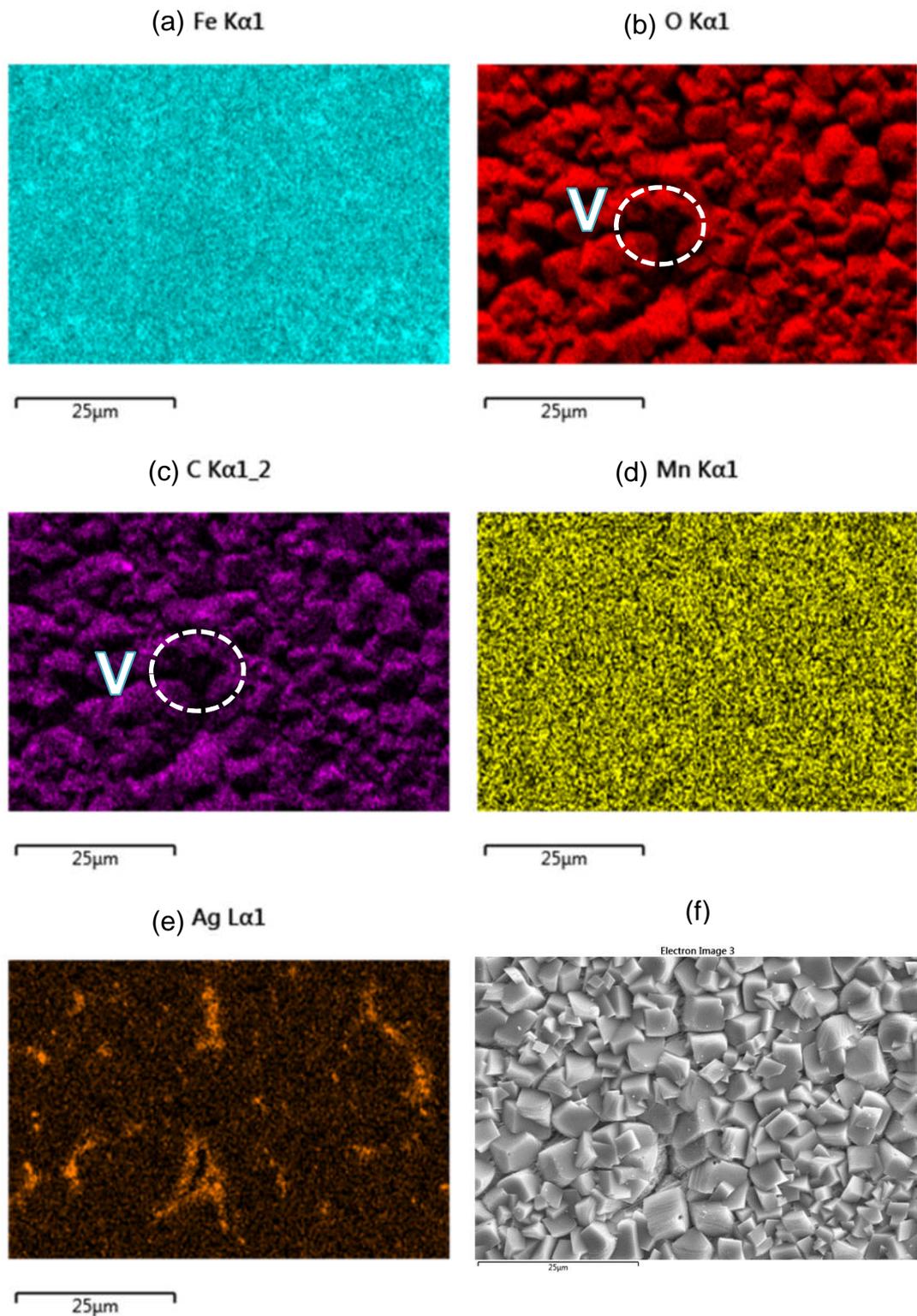
Figure 8-17 EDX map 1 of corrosion layer grown at 60°C, pH 6.6, 3.5% NaCl, with 20mg OA-POSS added (a) Iron-Fe, (b) Oxygen-O, (c) Carbon, (d) Manganese-Mn (e) Silver-Ag and (f) SE micrograph (V) voids

Chemical composition of the corrosion product was recorded by EDX with the aim of complementing the data acquired from the SEM and XRD surface analysis techniques with regard to the chemical composition of the developing corrosion layer. The OA-POSS loading of 20mg was considered to be representative for the corrosion tests ran at 60°C and pH of 6.6.

After careful examination, some voids (V) between the crystals are spotted and these only show iron to be present, which means that the bare steel surface is most probably exposed in these areas as showed with the dotted circle in Figure 8-16 (c, d); while missing both the oxygen and the carbon elements in these slots, it can be deduced that no protective iron carbonate film is covering this specific region.

Another EDX was carried out on a similar sample coated with silver (Figure 8-17) and both show that the iron, carbon and oxygen elements are the dominant phases which is in accordance with the visible $FeCO_3$ crystals covering the underlying carbon steel surface (Figure 8-16a). Similarly, some voids relating to the absence of both oxygen and carbon are observed in Figure 8-17 (b, c) with only the iron element covering all the surface map (Figure 8-17a) which suggests that some areas are not fully covered with an iron carbonate protective layer. The manganese (Mn), present on both scans is an element that is part of the chemical composition of the X65 steel as detailed in Table 5-1 previously.

8.2 Low OA-POSS loading and general corrosion

8.2.1 Electrochemistry

Enhancing the physico-mechanical properties of the corrosion layer is thought of as a one-time modification for an appropriate corrosion mitigation approach. In contrast, film-forming corrosion inhibitors are added recurrently in order for their protective effect to endure. Since CI are added at loadings as low as 1ppm, it was decided to check the potency of the researched nanofiller at such low concentrations too. Thus, six OA-POSS loadings (1, 2, 3, 4, 5 and 6mg) are shown to be responsible for a decrease in the corrosion rates to values lower than 0.01 mmpy too but the longer test durations are required in order to reach a steady state if compared to the experiments undertaken with tens of mg of OA-POSS.

These findings are presented in Figure 8-18 which shows that it takes approximately 60 hours for the corrosion rate to drop below the 0.01 threshold when 1 to 6mg OA-POSS are tested. The lower concentrations of OA-POSS corresponding to 1, 2 and 3 mg seem to provide the quickest CR drop.
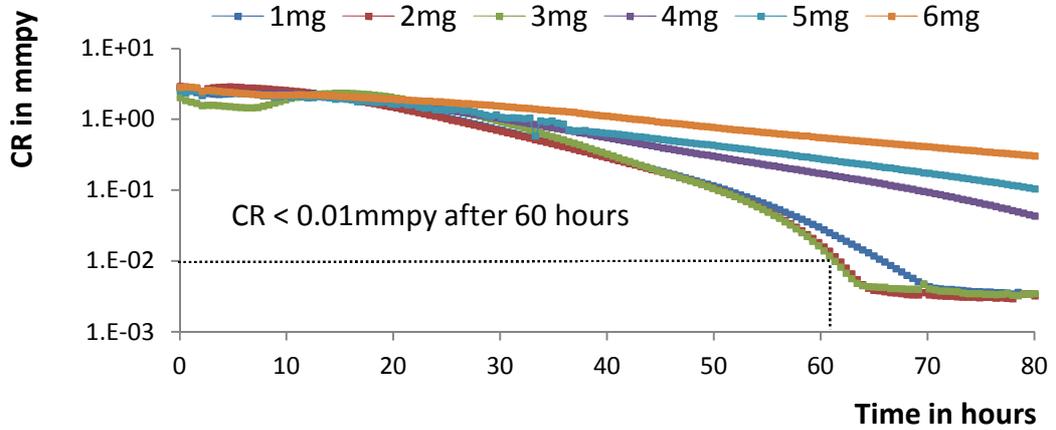
Figure 8-18 CR variations of X65 samples subjected to 1, 2, 3, 4, 5 and 6 mg OA-POSS added after 2 hours [pH 6.6, 60°C, 3.5% NaCl, 0.8bar CO_2]

Similar to the higher loading tests, adding only 1 to 6 mg of OA-POSS induces a drop in the corrosion rates to values lower than 0.01 mmpy if compared to a blank test where the CR remains stable for the whole test duration or 120 hours. As such, the kinetics of the corrosion protective layer formation can vary between 30 and 60 hours (Figure 8-19).
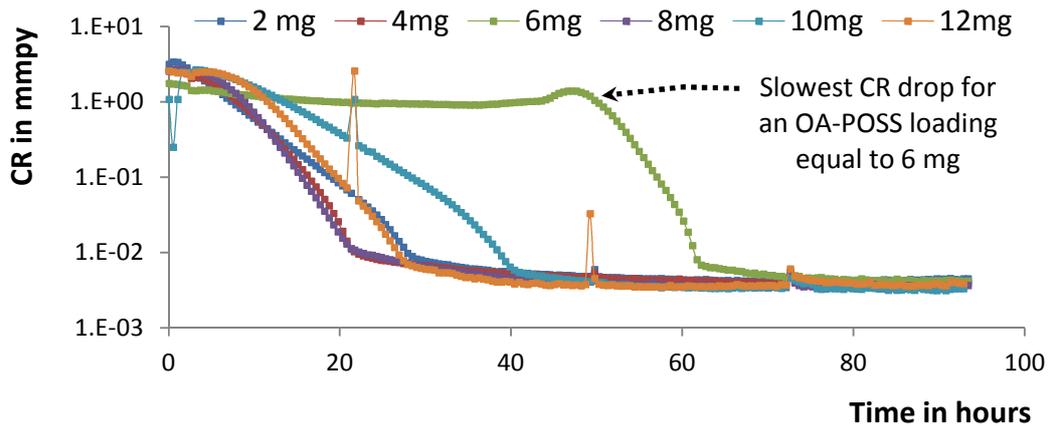
Figure 8-19 CR variations of X65 samples subjected to 2, 4, 6, 8, 10 and 12 mg OA-POSS added after 2 hours [pH 6.6, 60°C, 3.5% NaCl, 0.8bar CO_2]

213

The electrochemical results are shown separately since the swapping in trends described earlier renders the establishment of error bars and standard deviation difficult for the separate concentrations of OA-POSS that were tested. The experiment which showed the minimum standard deviation corresponds to the trial ran at 1 mg OA-POSS as observed in Figure 8-20 where it takes approximately 50 hours for the CR to drop below 0.1 mmpy; this is usually the corrosion rate value established after treatment with most of the commonly used film forming corrosion inhibitors.
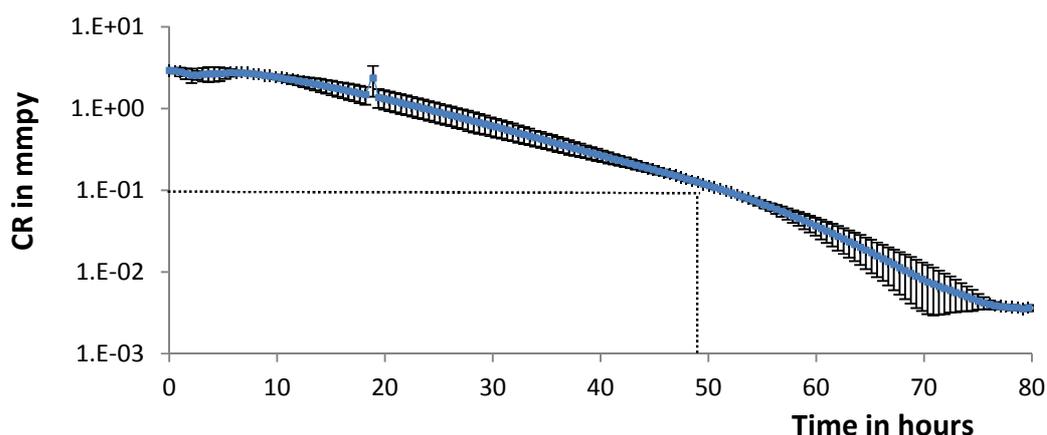
Figure 8-20 CR standard deviation with 1 mg OA-POSS added after 2 hours [pH 6.6, 60°C, 3.5% NaCl, 0.8bar CO_2]

8.2.2 Ex-situ synchrotron diffraction analysis for low OA-POSS loading experiments

The tests ran at OA-POSS concentrations corresponding to loadings lower than 12mg were analysed at the synchrotron facility and the corresponding diffraction patterns are shown in Figure 8-21. The iron carbonate Miller indices are highlighted above the respective diffraction angles. These are related to the corrosion rates variations presented in Figure 8-19. The main observation is that the iron carbonate corrosion layers seem to grow denser with the higher loading of the nanofiller used as suggested indirectly by the respective ratios of the Miller indices (Figure 8-28).

Nonetheless, the CR variations do not vary in the same order. In fact, using 2, 4, 6, 8, 10 or 12mg of OA-POSS allowed the system to evolve to one where the corrosion rate decreased to a steady state value averaging 0.005mmpy but the main difference is the time at which this occurred. This observation can be explained by the fact that the establishment of the fully protective iron carbonate layer is delayed or that some additional sublayer is responsible for

the protective behaviour regardless of the iron carbonate morphology and compactness.
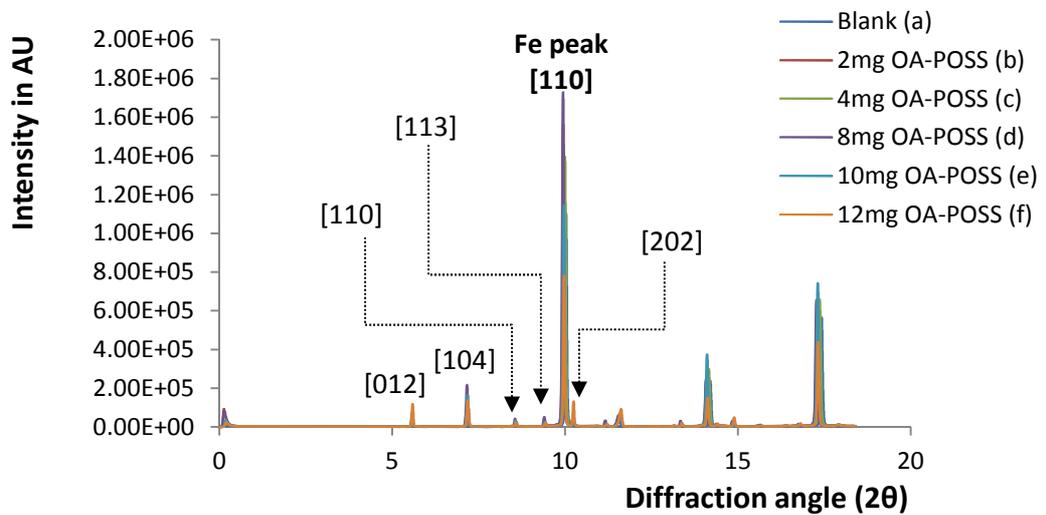
Figure 8-21 Synchrotron diffraction patterns for (a) blank and OA-POSS altered samples (b) 2mg (c) 4mg (d) 8mg (e) 10mg and (f) 12mg [pH 6.6, 60°C, 3.5% NaCl, 0.8bar CO_2, 98 hours]

The conversion between the respective diffraction angles of the synchrotron and CuK_α is based on Table 6-3 for the tests ran at 35KeV. The tests are scattered in their respective diffraction plots for ease of observation (Figure 8-22 to Figure 8-27).
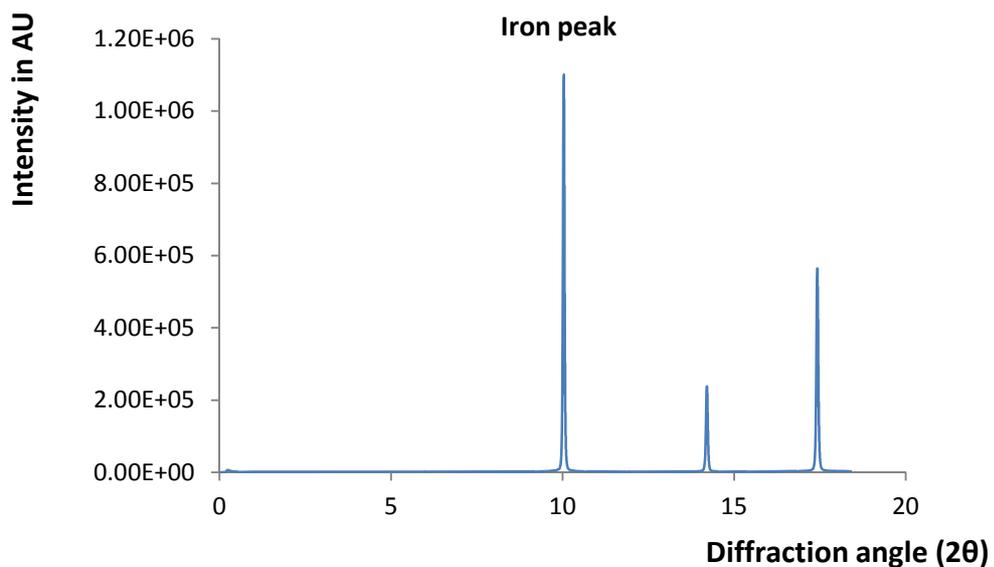
Figure 8-22 Synchrotron diffraction patterns of a an X65 carbon steel polished to 600SiC surface finish
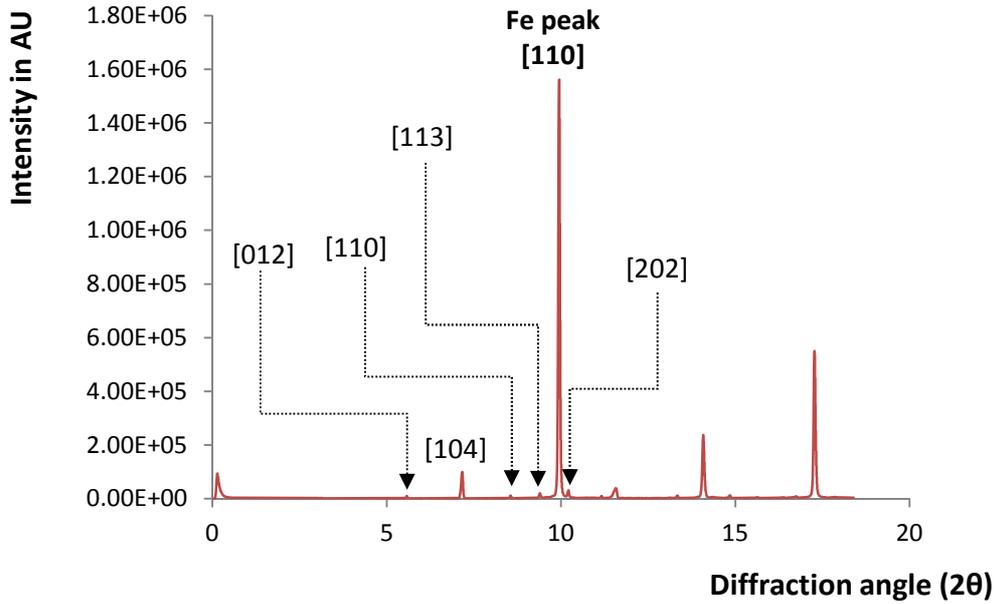
Figure 8-23 Synchrotron diffraction patterns of a corrosion film grown over X65 carbon steel in a CO_2 saturated environment when 2mg OA-POSS are added at pH 6.6, 60°C, 3.5% NaCl, 0.8bar CO_2 for 98 hours
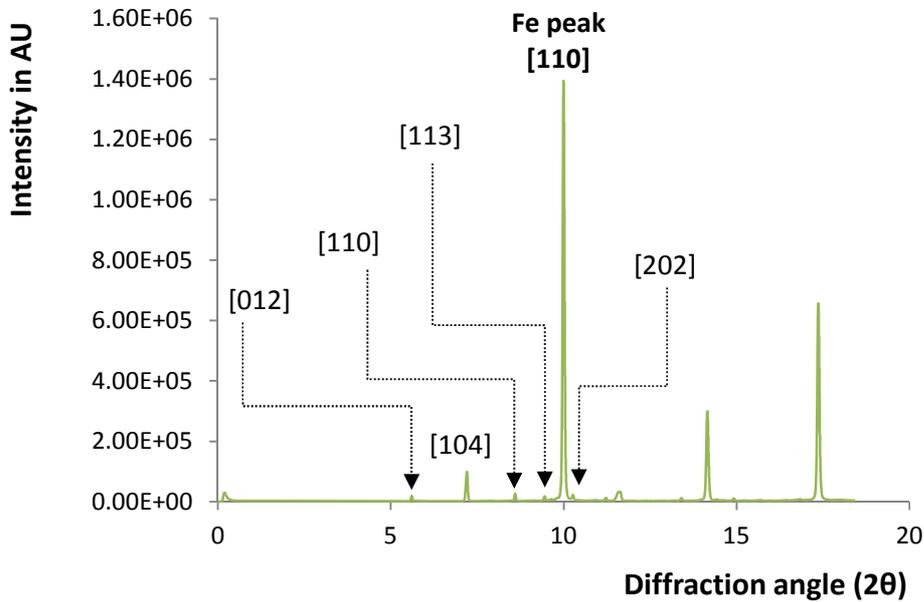
Figure 8-24 Synchrotron diffraction patterns of a corrosion film grown over X65 carbon steel in a CO_2 saturated environment when 4mg OA-POSS are added at pH 6.6, 60°C, 3.5% NaCl, 0.8bar CO_2 for 98 hours
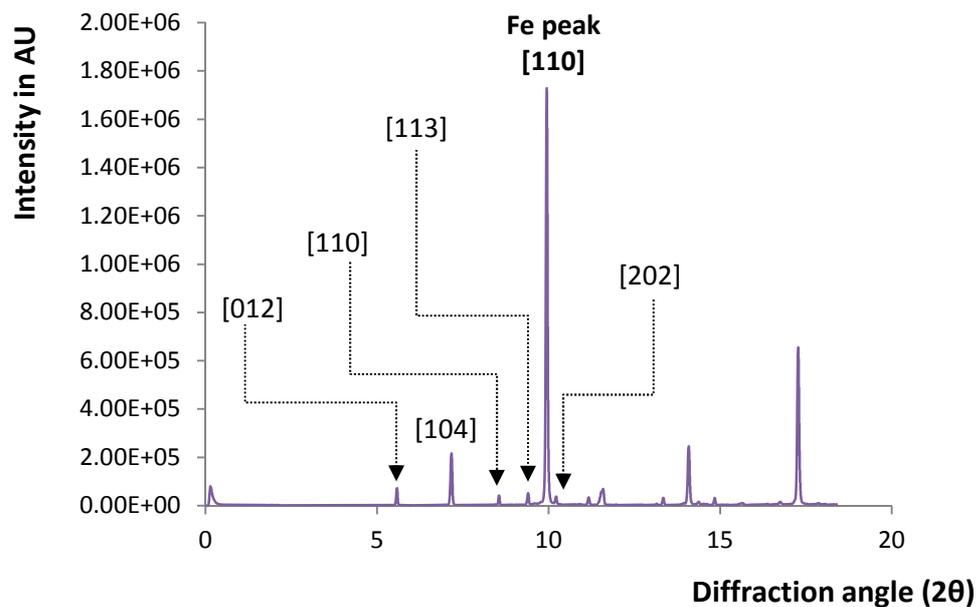
Figure 8-25 Synchrotron diffraction patterns of a corrosion film grown over X65 carbon steel in a CO_2 saturated environment when 8mg OA-POSS are added at pH 6.6, 60°C, 3.5% NaCl, 0.8bar CO_2 for 98 hours
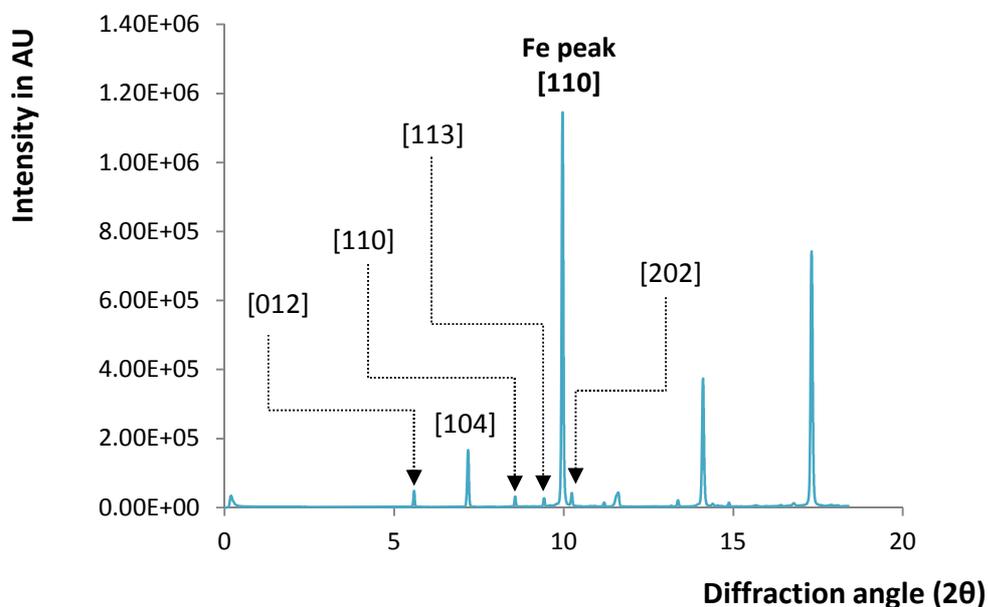
Figure 8-26 Synchrotron diffraction patterns of a corrosion film grown over X65 carbon steel in a CO_2 saturated environment when 10mg OA-POSS are added at pH 6.6, 60°C, 3.5% NaCl, 0.8bar CO_2 for 98 hours
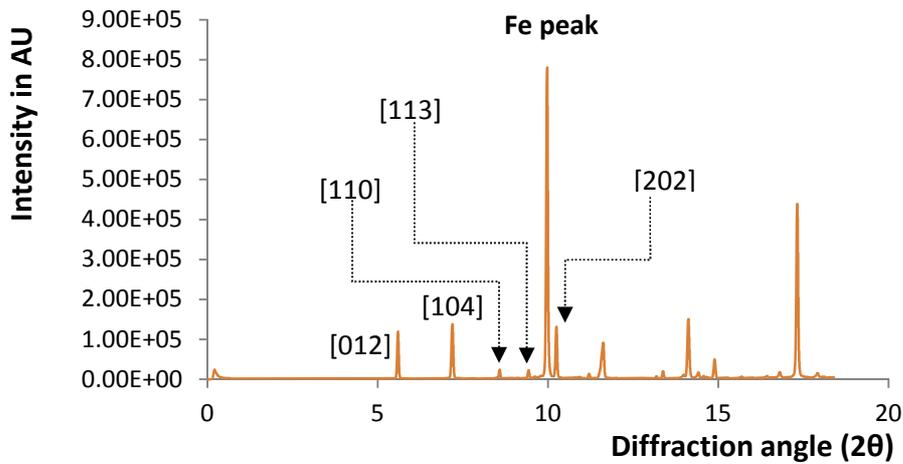
Figure 8-27 Synchrotron diffraction patterns of a corrosion film grown over X65 carbon steel in a CO_2 saturated environment when 12mg OA-POSS are added at pH 6.6, 60°C, 3.5% NaCl, 0.8bar CO_2 for 98 hours

As before the ratios between the registered relative intensities relating to the [104] iron carbonate Miller index were compared to the iron [110] Miller index and the findings are summarised in Table 8-1 and Figure 8-28.

Table 8-1 Relative intensities used from Synchrotron-XRD to compute $FeCO_3$ to Fe ratio calculations at pH 6.6

2θ	Component	Intensity Value	OA-POSS loading
7.16°	FeCO₃	99,700	2mg
9.95°	Fe	1,560,000	
7.20°	FeCO₃	99,000	4mg
9.99°	Fe	1,390,000	
7.16°	FeCO₃	217,000	8mg
9.94°	Fe	1,730,000	
7.18°	FeCO₃	166,000	10mg
9.97°	Fe	1,140,000	
7.19°	FeCO₃	139,000	12mg
9.98°	Fe	780,000	

218
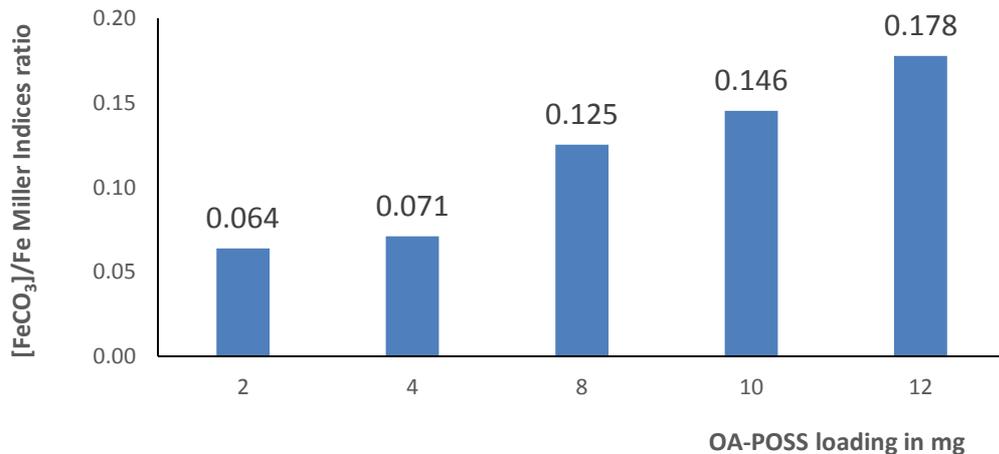
Figure 8-28 $FeCO_3$ to Fe Miller indices ratio calculations at pH 6.6

Again, it appears that the ratio increases with OA-POSS loading meaning that adding more POSS in the selected range induces a denser iron carbonate film; thus $FeCO_3$/Fe ratios led to values of 0.0639, 0.0712, 0.1254, 0.1456 and 0.1782 when 2, 4, 8, 10 and 12 mg OA-POSS were added respectively.

While the Miller indices ratios increase with the OA-POSS increase, the CR is not seen to drop in the same order. Moreover, they are 10 times smaller than the ratios obtained when higher loadings of $FeCO_3$ are administered as per Figure 8-3 and this is explained by the two different techniques and energy levels which are much higher and penetrate deeper into the X65 carbon steel sample in the case of the synchrotron which renders the iron peak much more intense than the $FeCO_3$ counterparts.

8.2.3   Micrographs corresponding to the tests carried out with the lower OA-POSS concentrations

As suggested by the slow decrease of the corrosion rate in Figure 8-18, a fully protective iron carbonate corrosion layer takes a longer time to form when OA-POSS is added at loadings lower than tens of milligrams per litre. The $FeCO_3$ crystals appear bigger in size when compared to their counterparts grown at higher OA-POSS concentration. This finding puts forward the assumption that the crystal growth stage rather than the crystal nucleation stage is favoured in these specific conditions. Moreover, the average film thickness values evolve from as low as 3μm to as high as 16μm and this should be linked to their degree of protectiveness.

219

8.2.3.1 Micrographs for tests ran with 1 and 2 mg of OA-POSS

When adding only 1 and 2mg OA-POSS, $FeCO_3$ crystals appear to be 18µm in width on average as seen by the scale bar and added dimension in Figure 8-29 and Figure 8-30. The scattered surface porosities appear to be bigger in diameter and having a surface opening around 2µm. These are 4 times larger than the 500nm wide pinholes described in section 8.1.3 where 10 to 60 mg OA-POSS is added.

The grown corrosion layers do not appear to be very homogeneous in thickness as deduced from the cross-sections shown in Figure 8-31. In fact, when 2 mg OA-POSS is administered, the $FeCO_3$ film thickness ranges from as low as 2µm to as high as 10µm.

Usually the system consists of two iron carbonate crystal layers with the crystals growing further from the steel showing a thinner morphology. This observation could be linked to the fact that the ferrous iron required to achieve the necessary supersaturation for the crystal nucleation and growth process is scarce due to the diffusion limitation established by the first set of iron carbonate crystals.

In the case of 2mg OA-POSS the surface morphology consists of cubic, prismatic and semi-circular $FeCO_3$ crystals with various sizes corresponding to different growth kinetics and spatial constraints (Figure 8-30a). There appears to be an underlying layer over which the top crystal structure is deposited as highlighted by the dotted area in Figure 8-30b.

Moreover, the fact that the width of the $FeCO_3$ crystals is bigger than the corresponding film thickness suggests that the crystals are growing mostly in one longitudinal direction.

The correlation between the crystal morphology and general corrosion mitigation should be established with regard to the CR variations plotted in Figure 8-18 and Figure 8-19. In fact, while it requires 60 hours for the corrosion rate to reach 0.01mmpy with 1mg OA-POSS addition, the kinetics are much faster with 2mg OA-POSS where only 30 hours are necessary to reach the same degree of protection.

Both the absence of pinholes when 2mg OA-POSS is administered and the good adherence of the bottom $FeCO_3$ layer to the steel could be responsible for such difference in corrosion mitigation.
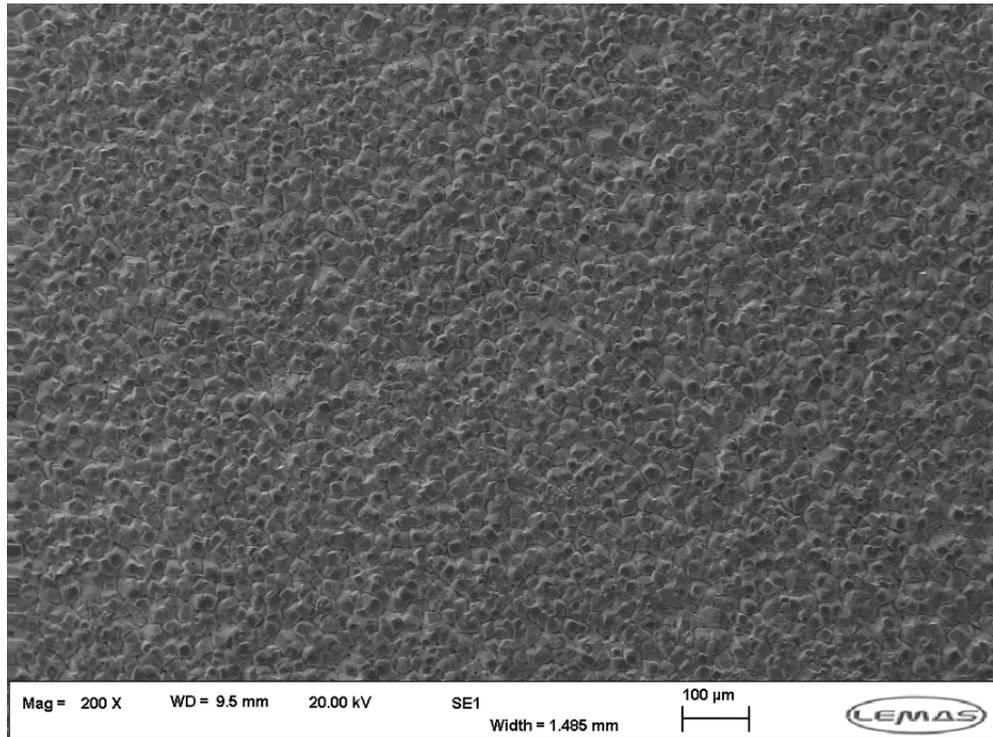
(a)
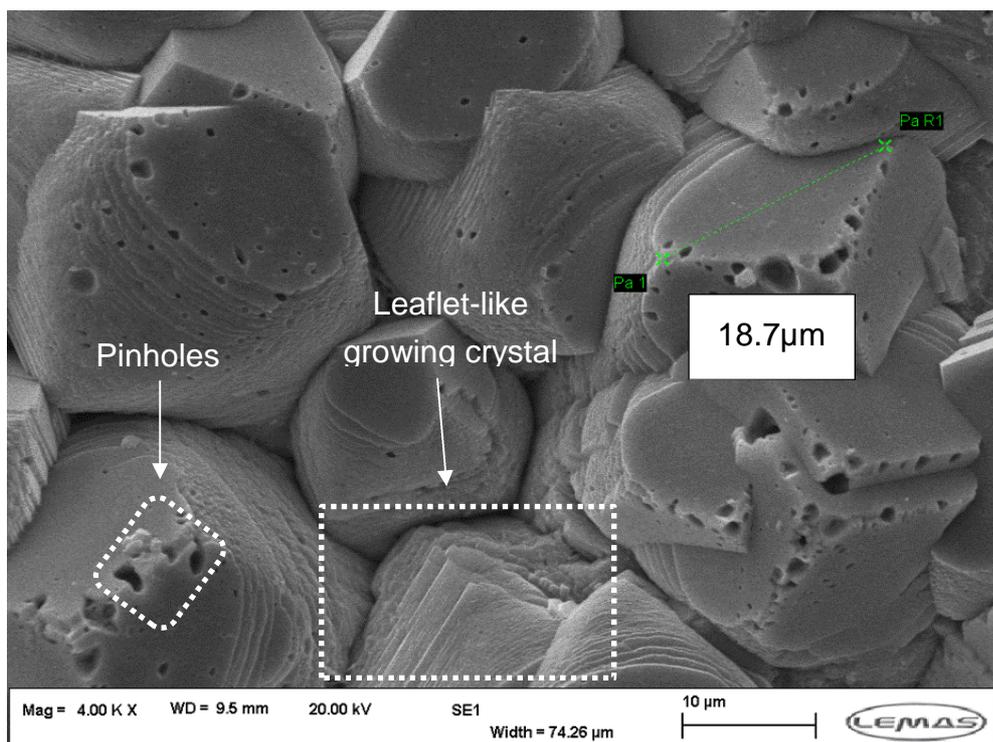
(b)

Figure 8-29 SEM micrographs topography view of X65 samples when 1mg OA-POSS are added to the test solution at various magnifications as shown by the corresponding scale bars [pH=6.6, 60°C, 3.5% NaCl, 0.8bar CO_2, 108 hours] showing (a) the compact and fully-covering $FeCO_3$ corrosion layer and (b) a zoom on the developed crystal morphology and size

221
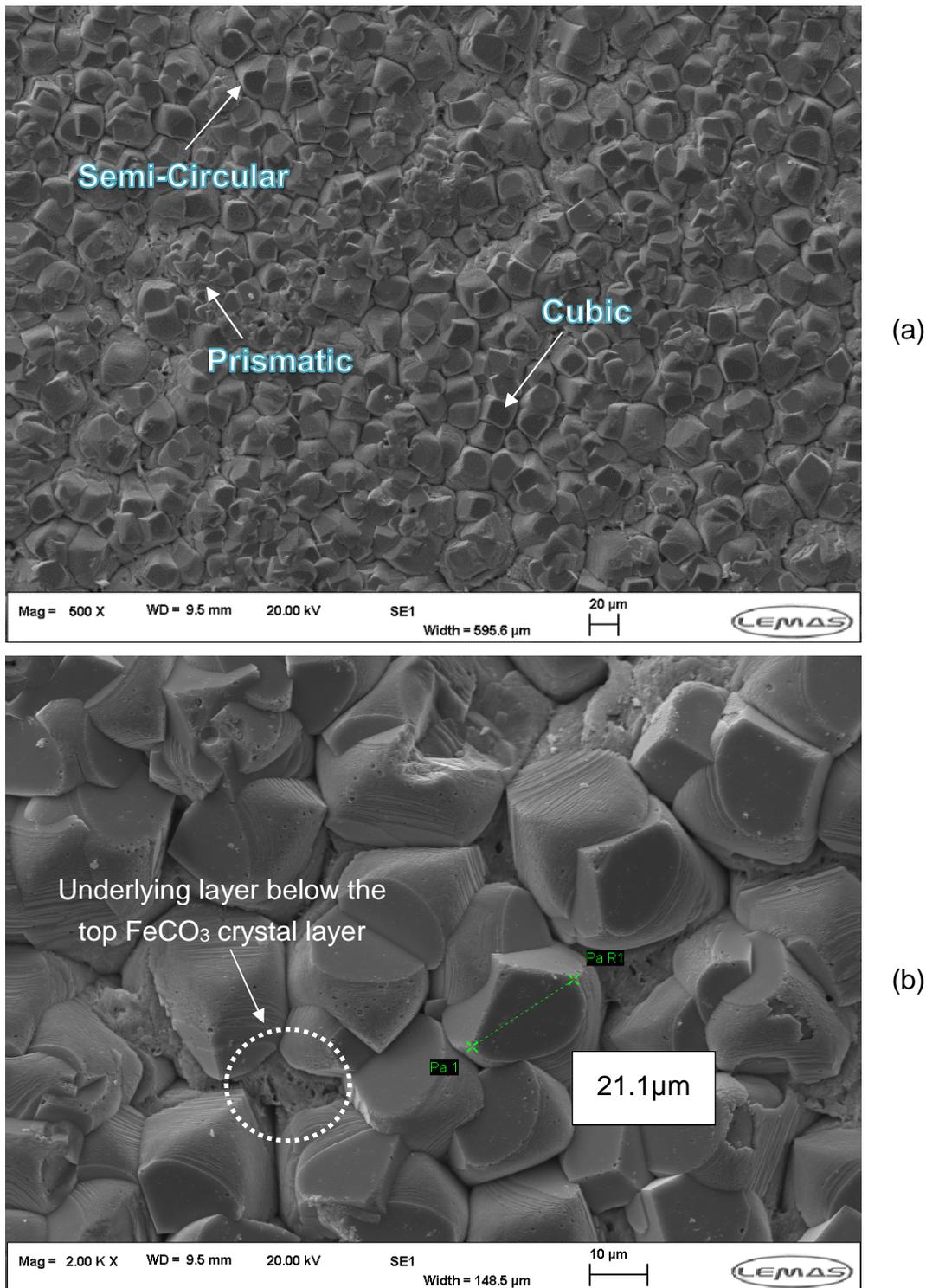
Figure 8-30 SEM micrographs topography view of X65 samples when 2mg OA-POSS are added to the test solution at various magnifications as shown by the corresponding scale bars [pH=6.6, 60°C,3.5% NaCl, 0.8bar CO_2, 108 hours] showing (a) the compact and fully-covering $FeCO_3$ corrosion layer composed of semi-circular, cubic and prismatic types of crystals and (b) a zoom on the developed crystal morphology and size showing no apparent pinholes.
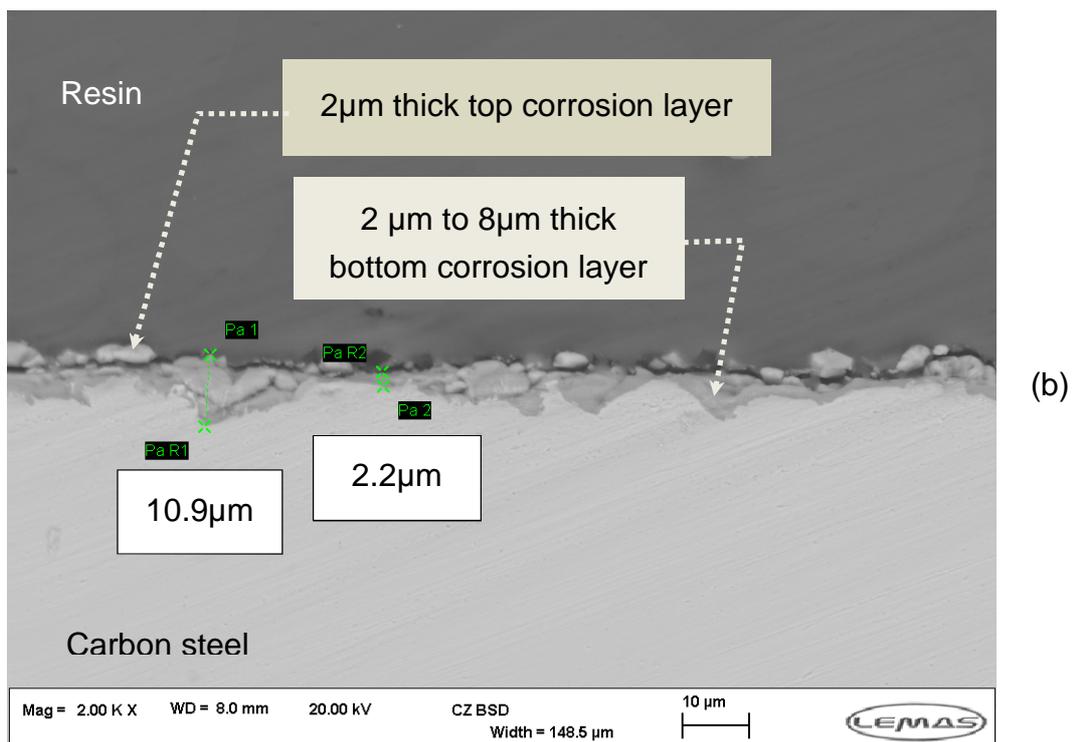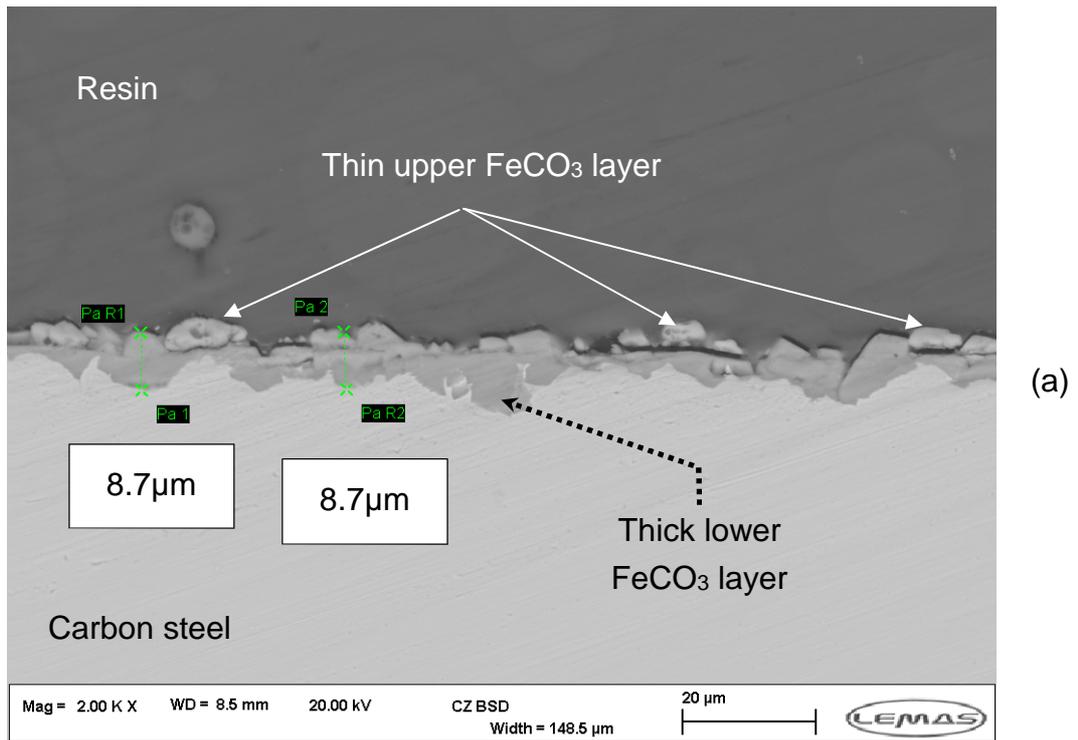
Figure 8-31 Cross-section SEM micrographs of X65 samples when 2mg OA-POSS are added to the test solution at various magnifications as shown on the respective scale bars [pH=6.6, 60°C,3.5% NaCl, 108 hours] showing (a) the double-layered growing iron carbonate corrosion film and (b) variations in the corrosion film thickness

8.2.3.2 Micrographs for tests ran with 3 and 4 mg of OA-POSS

The iron carbonate crystal size at these low loadings of OA-POSS appear to be twice as big as the crystals described in section 8.1.3 where concentrations of the nanofiller ten times higher were injected. As such, the SEM micrograph in Figure 8-32b show that the formed $FeCO_3$ crystals have an average size of 20 microns when 3mg of OA-POSS is administered.

Some pinholes are still scattered around the crystal vertices which appear to be rougher than the iron carbonate crystals obtained in blank conditions when no nanofiller is added. Such morphological instabilities could be explained by a higher localised supersaturation which increases the driving force for the crystal growth to higher levels and leads to a rough $FeCO_3$ crystal surface.

Moreover, two main morphologies of the iron carbonate crystals are found and these are the dominant "plate-like" $FeCO_3$ and the less scattered "prism-like" $FeCO_3$. Usually, the pH is the main driving force for the growth of different crystal morphologies. As such, the main assumption is that various localised pH is of order on the vicinity of the first grown $FeCO_3$ layer. The stability of various $FeCO_3$ morphologies is covered in section 9.4.2.

At 4mg OA-POSS loading, the $FeCO_3$ average crystal size is slightly smaller (15 microns) as seen in Figure 8-33b and it also shows a lower pinhole distribution on its edges. This enhanced trend is further complemented with the apparent high degree of the film compactness (Figure 8-33a) which could explain the quick corrosion drop observed in Figure 8-19. In fact, the CR drops below 0.01mmpy after only 20 hours before stabilizing at a CR of 0.005mmpy.

This assumption is backed up also by the fact that very thin corrosion layers develop at 4mg OA-POSS loading since the average $FeCO_3$ film thickness is around 3 micrometres at various locations as depicted in Figure 8-34a and b. Thinner corrosion layers are known to provide better general corrosion mitigation.

Since the $FeCO_3$ crystals are much bigger in one dimension than the other (15 micrometres in length versus 3 micrometres in height), a preferential growth in the longitudinal direction and the establishment of what seems to be a single layer of a highly protective and thin $FeCO_3$ film is assumed. Further details on the preferential crystal growth is given in section 10.4.2.
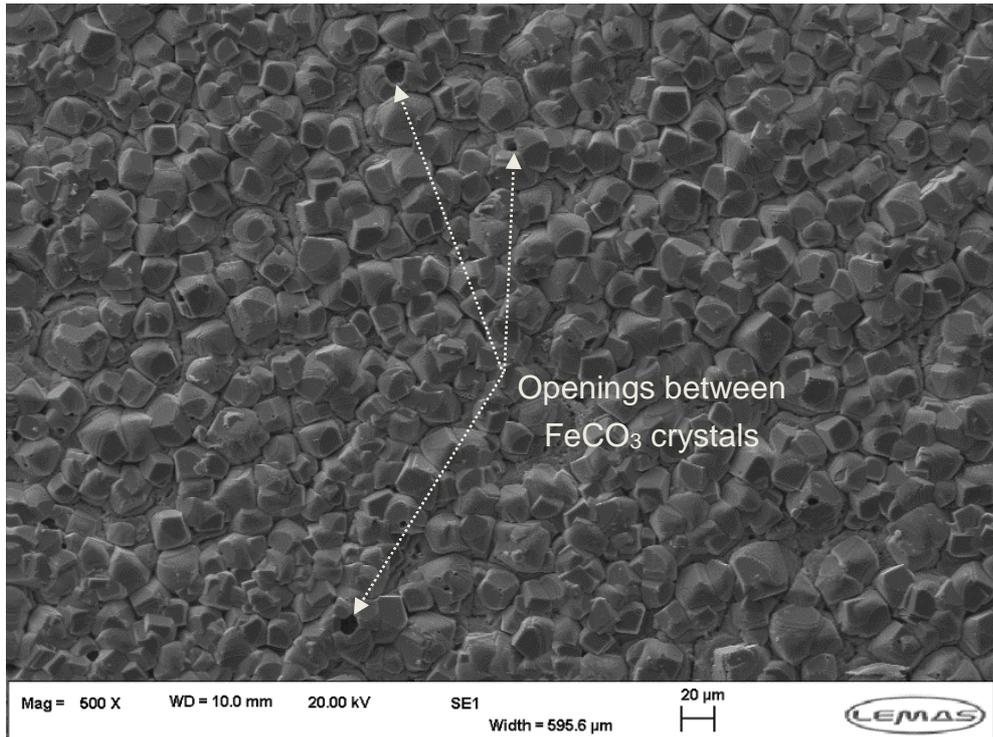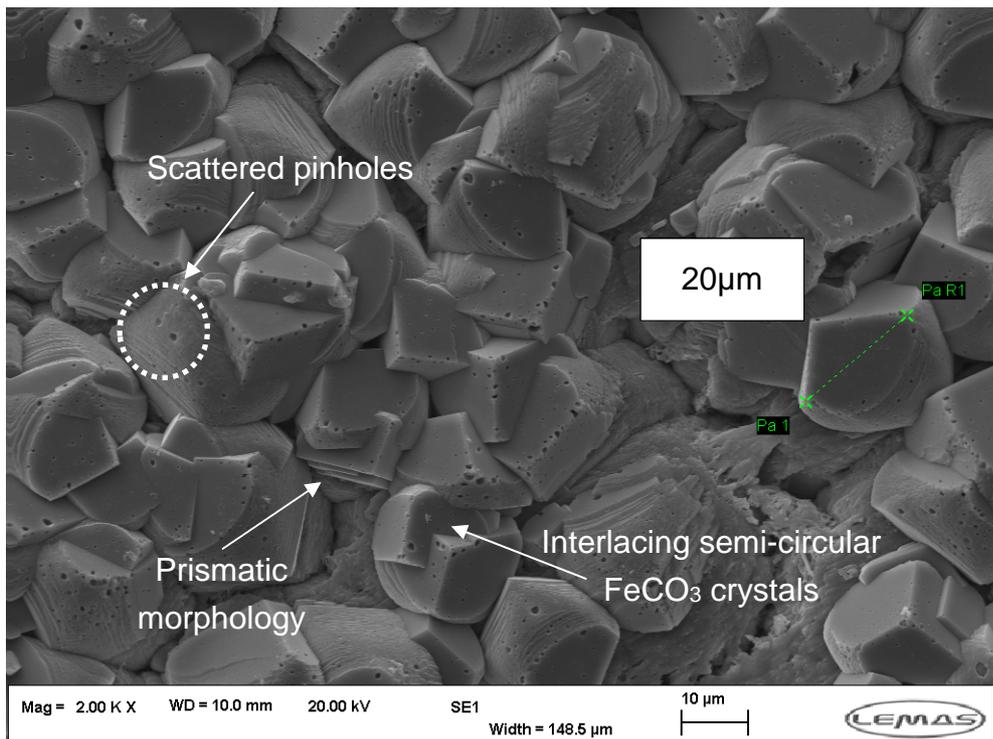
Figure 8-32 SEM micrographs topography view of X65 samples when 3mg OA-POSS are added to the test solution at various magnifications as shown by the respective scale bars [pH=6.6, 60°C,3.5% NaCl, 0.8bar CO_2, 108 hours] showing (a) $FeCO_3$ corrosion layer showing some opening between the crystals and (b) a zoom on the developed crystal morphology and size with pinholes scattered mainly on the edge vertices

(a)

Pinholes are present but are smaller in diameter

13.3µm
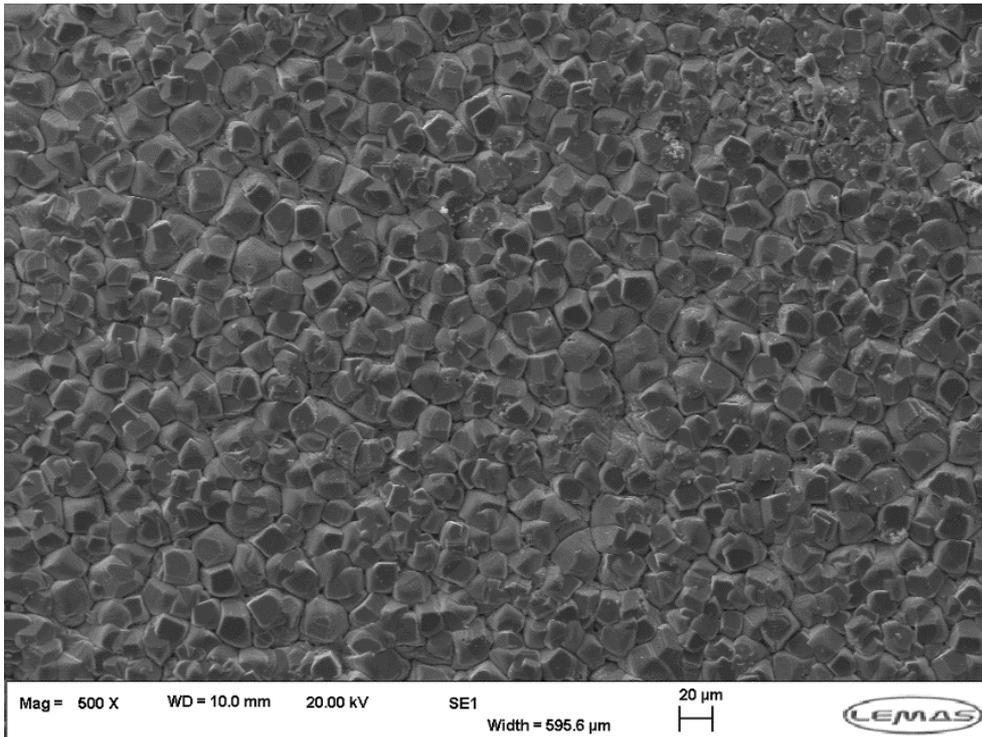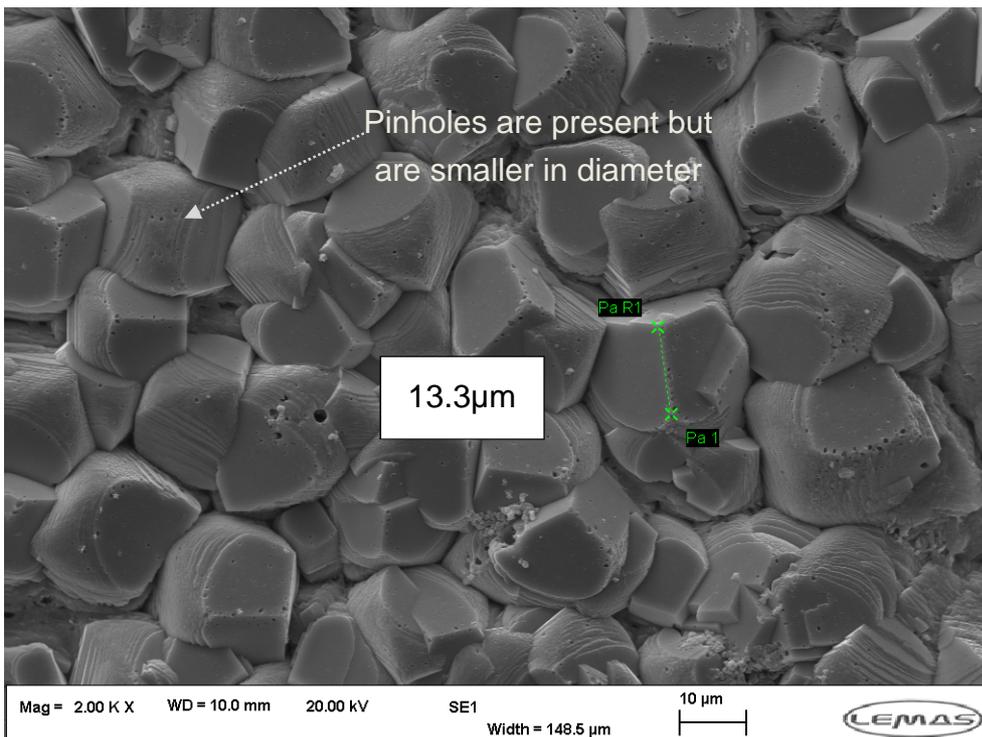
(b)

Figure 8-33 SEM micrographs topography view of X65 samples when 4mg OA-POSS are added to the test solution at various magnifications as shown by the corresponding scale bars [pH=6.6, 60°C,3.5% NaCl, 0.8bar CO_2, 108 hours] showing (a) the compact and fully-covering $FeCO_3$ corrosion layer and (b) a zoom on the developed crystal morphology and size
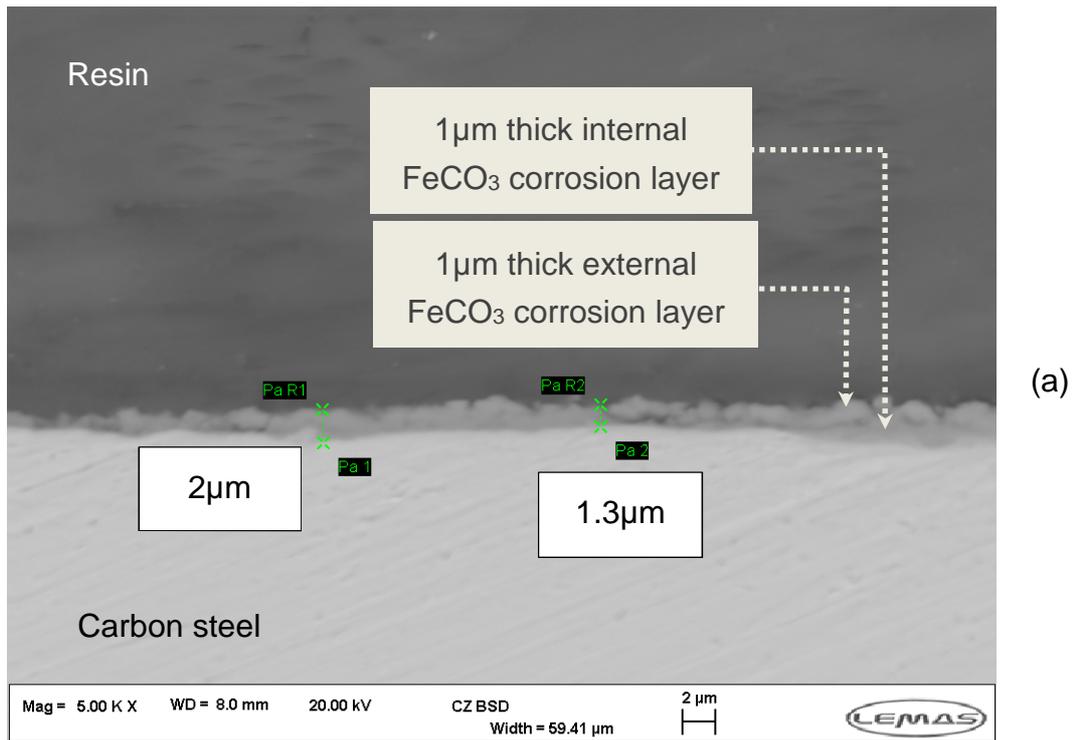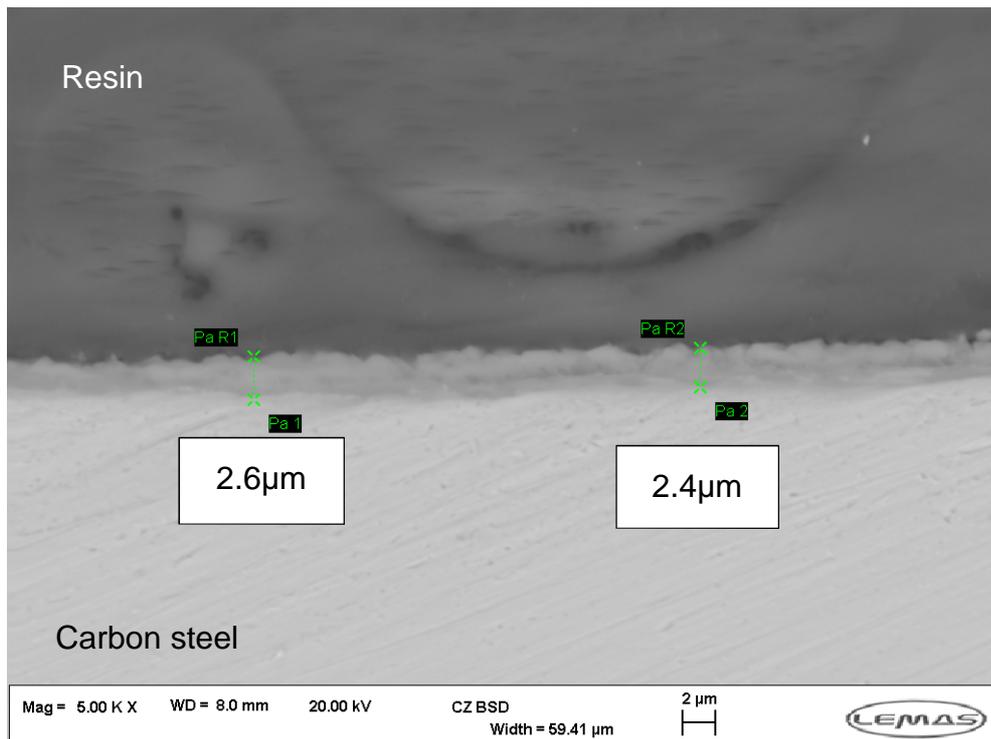
Figure 8-34 Cross-section SEM micrographs of X65 samples when 4mg OA-POSS are added to the test solution at various magnifications as indicated by the respective scale bars [pH=6.6, 60°C,3.5% NaCl, 0.8bar CO_2, 108 hours] showing (a) $FeCO_3$ corrosion layer thinner than 2 micrometres and (b) same $FeCO_3$ corrosion layer thinner than 3 micrometres in different locations

8.2.3.3 Tests at 5, 6 and 8mg OA-POSS

Topographic micrographs of iron carbonate crystals show that these have an average width around 20 microns whether 5 or 6 mg OA-POSS is added as shown by the corresponding scale bar and added dimension on the magnified $FeCO_3$ crystals in Figure 8-35b and Figure 8-36b respectively.

The degree of reduction in the general corrosion rate seems to be mainly related to the iron carbonate film thickness and bonding stability and not to the $FeCO_3$ crystal shape and size. In fact, the higher CR values observed when 6mg OA-POSS is added can be explained by the weak bonding strength between the external and internal iron carbonate corrosion layers.

The obvious cohesive failure observed in Figure 8-37(a, b) and the high average total film thickness exceeding 15 micrometres if both layers are accounted for could be responsible for the long delay needed for the corrosion rate to drop as observed in Figure 8-19 when 6mg OA-POSS are administered. As such, it takes almost 60 hours for the underlying iron carbonate layer to become compact and tight in order for the corrosion rate to drop below 0.01 mmpy and stabilises at 0.005mmpy thereafter.

Although the iron carbonate crystals appear to be tight together and interlacing, some gaps are evident and the underlying corrosion layer as highlighted in the dotted area in Figure 8-36b shows also some porosities. While the morphology of the exposed area does not look crystalline, it is possible that the scale directly covering the steel surface is an agglomeration of nanocrystals. If such, the sizes of the inter-grown nanocrystals are of the order of 100nanometres and these may resemble an amorphous phase when observed at higher magnifications as stated by Fajardo et al.[361] who tried to characterize the corrosion product layer formed on mild steel after exposure to acetic acid.

On the other hand, a more adherent and thinner corrosion product develops when 8mg OA-POSS is added and performs much better with regard to general corrosion mitigation. In fact the iron carbonate corrosion film depicted in Figure 8-38 (a, b) which has an average film thickness around 6 micrometres appears to be well-adherent to the underlying steel substrate. This could explain the corrosion rate dropping to values below 0.01mmpy in just 20 hours as observed in Figure 8-19.
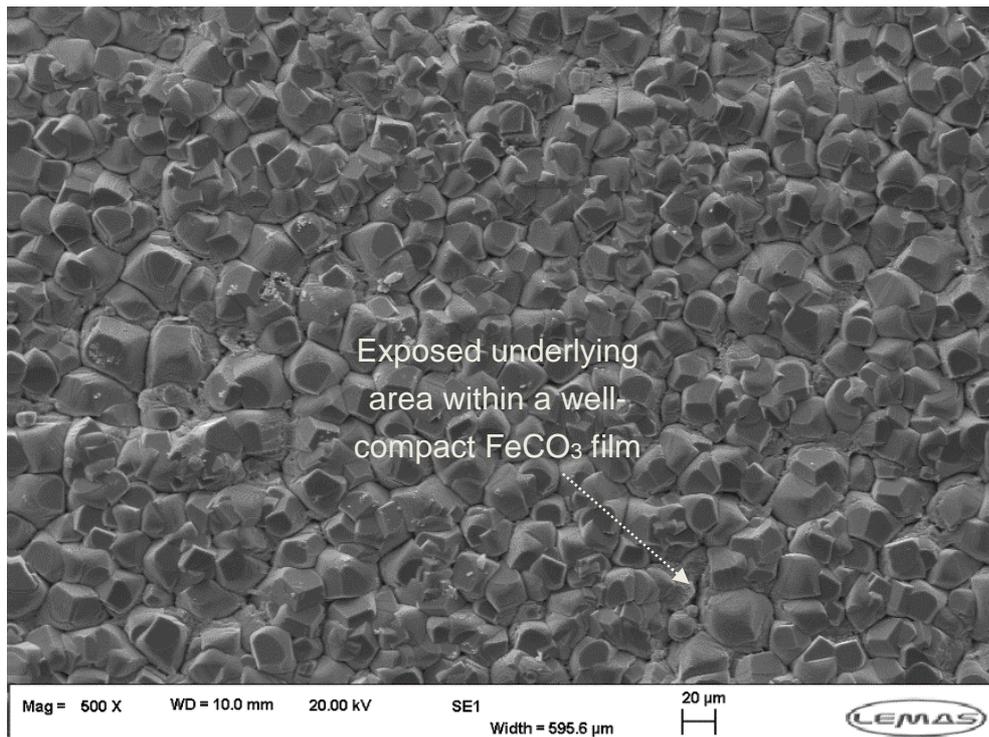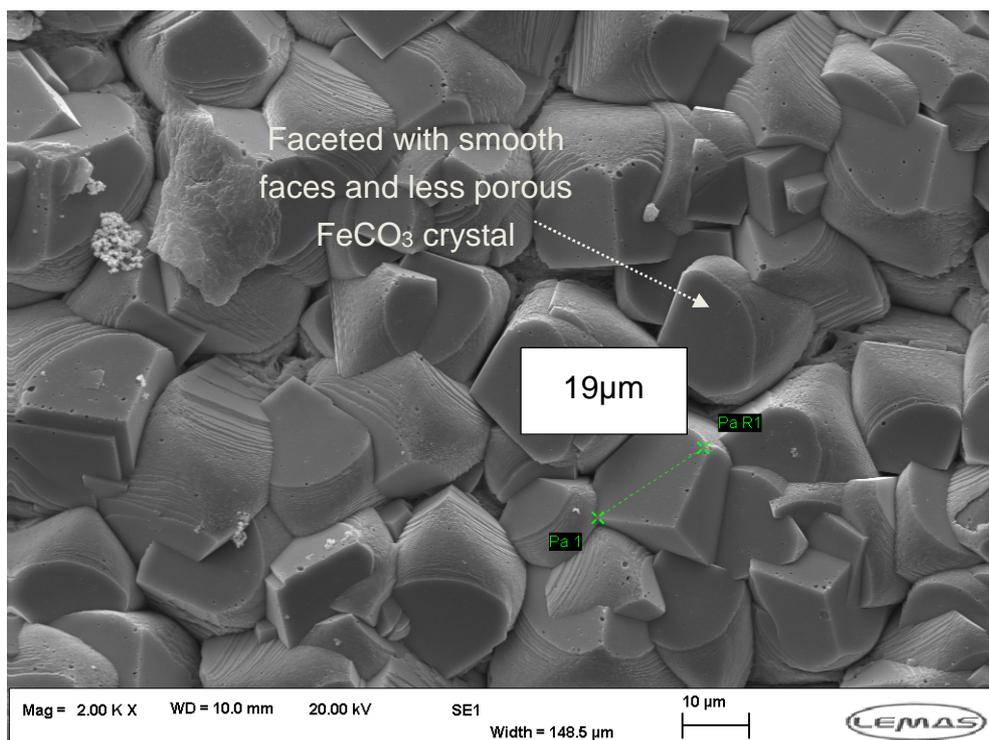
Figure 8-35 SEM micrographs topography view of X65 samples when 5mg OA-POSS are added to the test solution at various magnifications as seen by the respective scale bars [pH=6.6, 60°C,3.5% NaCl, 0.8bar CO_2, 108 hours] showing (a) the compact and fully-covering $FeCO_3$ corrosion layer and (b) a zoom on the developed crystal morphology and size showing highly interlacing of various size $FeCO_3$ crystals
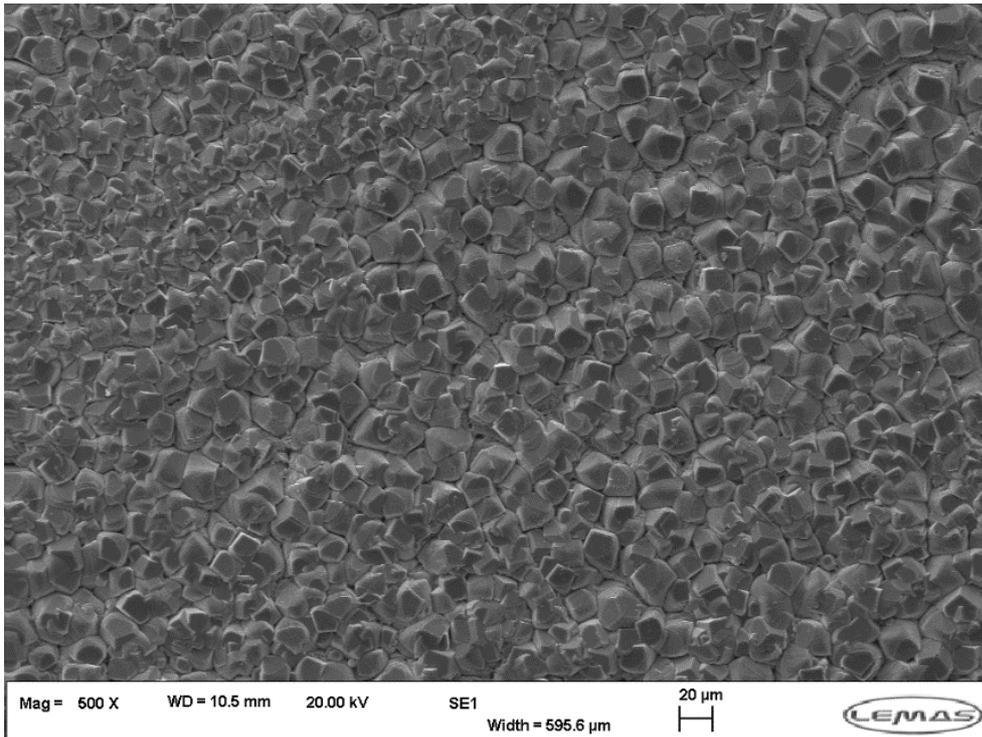
(a)
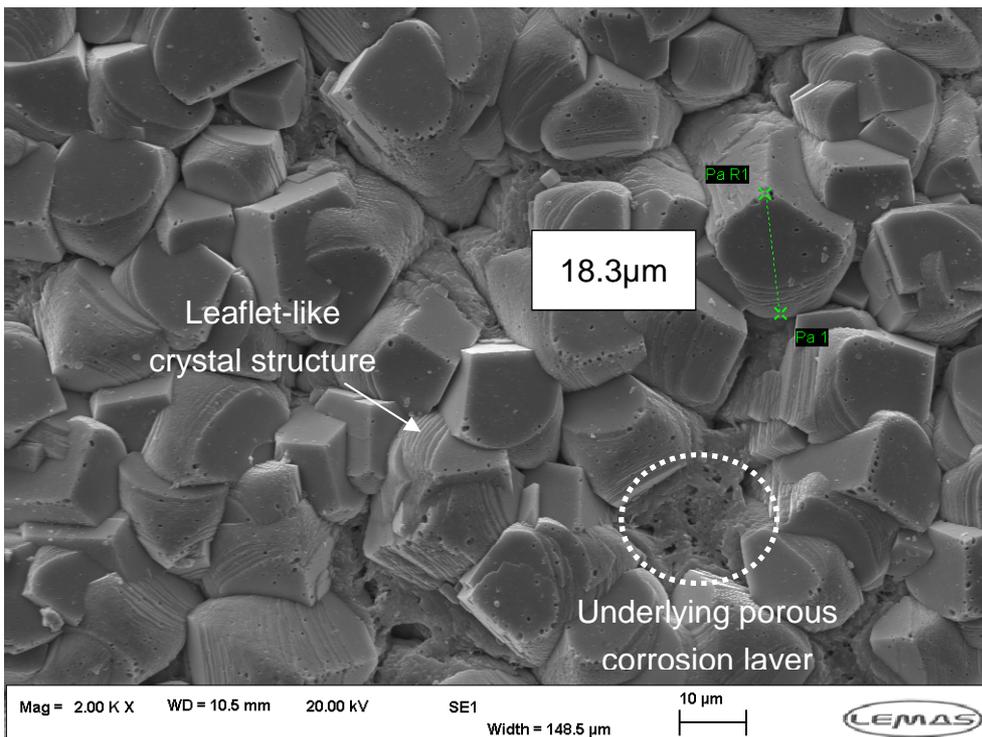
(b)

Figure 8-36 SEM micrographs topography view of X65 samples when 6mg OA-POSS are added to the test solution at various magnifications as seen by the corresponding scale bars [pH=6.6, 60°C,3.5% NaCl, 0.8bar CO_2, 108 hours] showing (a) the compact and fully-covering $FeCO_3$ corrosion layer and (b) a zoom on the developed crystal morphology and size
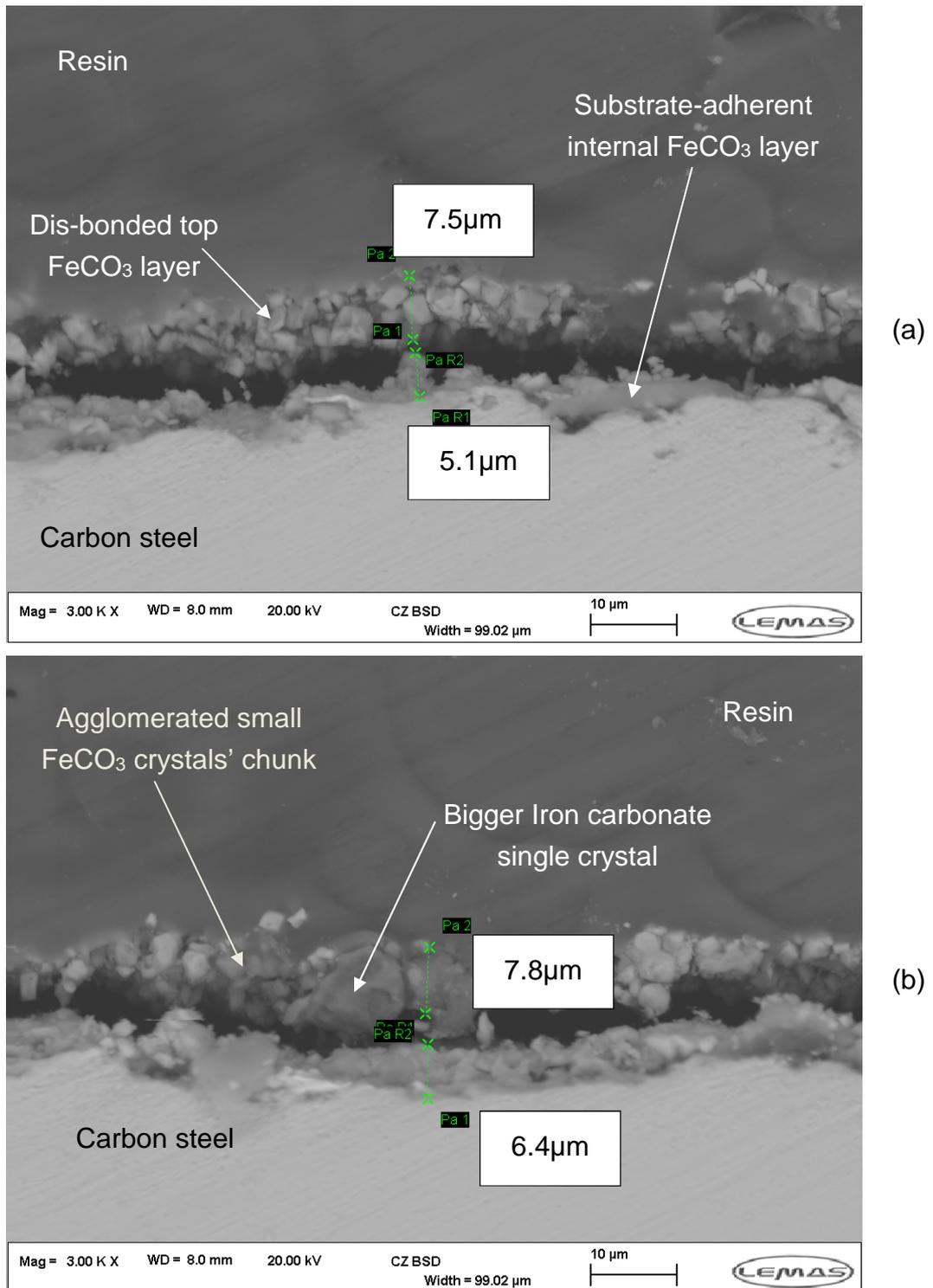
Figure 8-37 Cross-section SEM micrographs of X65 samples when 6mg OA-POSS are added to the test solution at various magnifications as shown on the scale bars [pH=6.6, 60°C,3.5% NaCl, 0.8bar CO_2, 108 hours] showing a disbonded iron carbonate top-layer and an adherent $FeCO_3$ bottom layer in two different regions of the same corrosion film showing (a) a top-layer made of small $FeCO_3$ crystals and (b) a top layer made of bigger $FeCO_3$ crystals
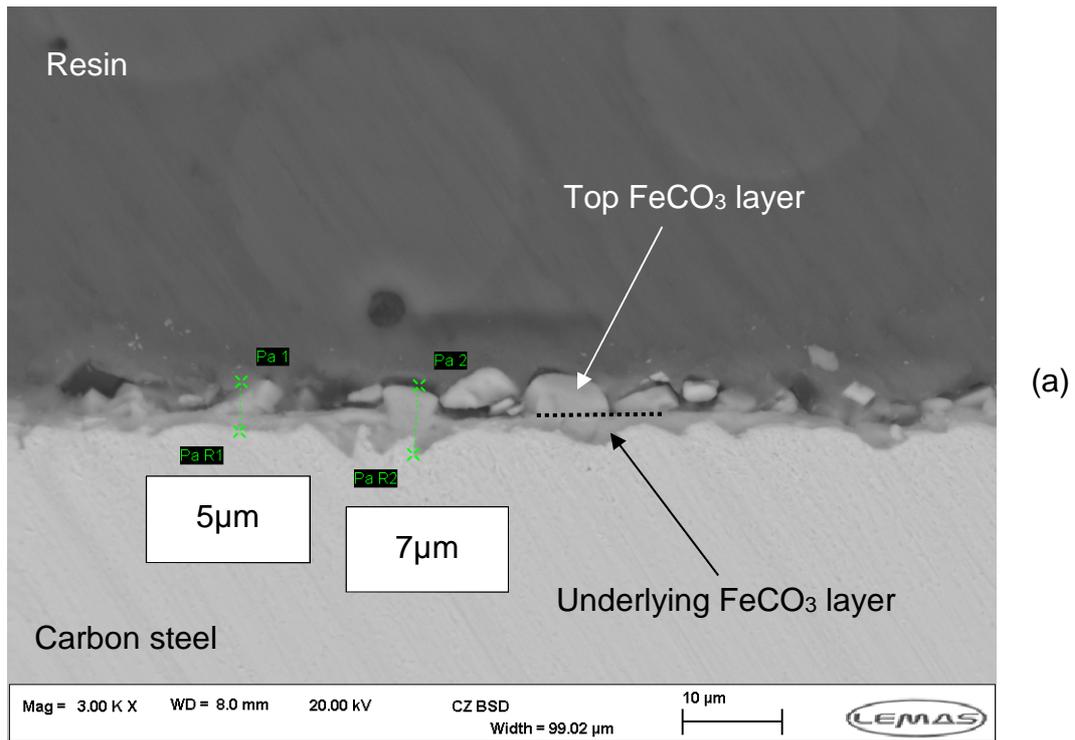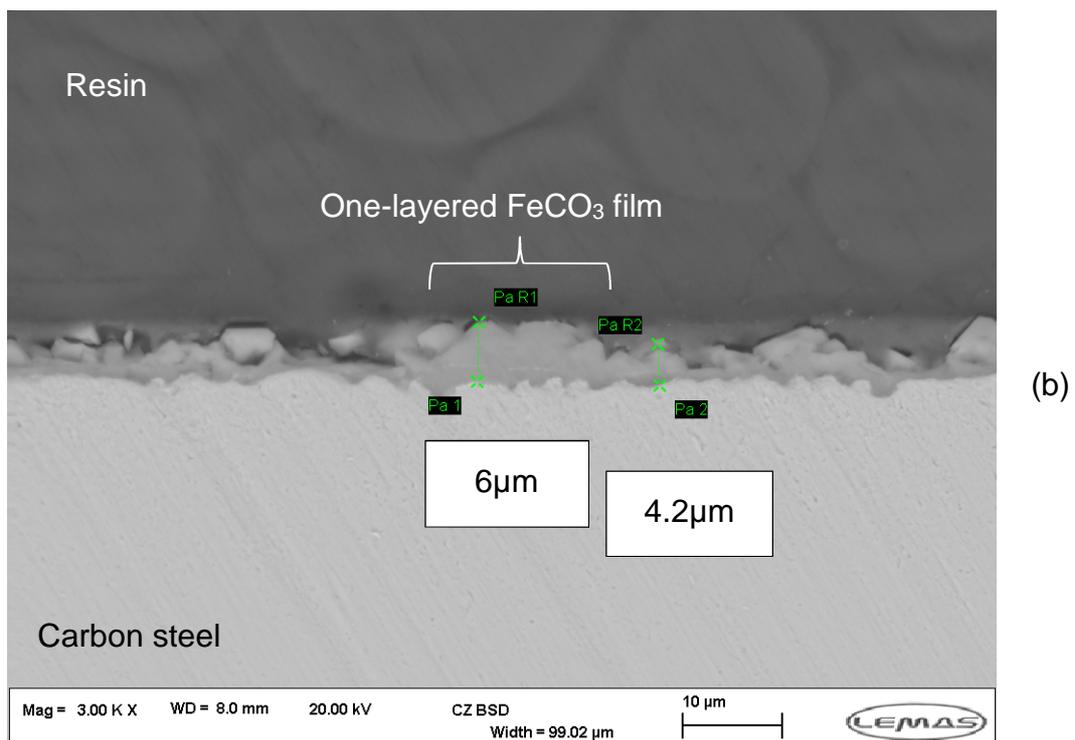
Figure 8-38 Cross-section SEM micrographs of X65 samples when 8mg OA-POSS are added to the test solution at various locations and respective scale bars [pH=6.6, 60°C,3.5% NaCl, 0.8bar CO_2, 108 hours] showing the same iron carbonate film at two different locations (a) double-layered iron carbonate region and (b) some areas with a single iron carbonate layer

Consequently, when considering the tests ran with lower loadings of OA-POSS, it appears as though 4mg OA-POSS is the only loading studied below 10mg at which small sized $FeCO_3$ crystals (10 micrometres on average) have been observed while all the other OA-POSS loadings led to bigger crystals with an average width of 20 micrometres. It should also be noted that the pinholes are less apparent when 4mg OA-POSS is added.

8.3 Summary of general corrosion mitigation

Combining the registered data from both the electrochemical behaviour and the SEM micrographs detailed in sections 8.1 and 8.2 relating to the $FeCO_3$ grown in the presence of OA-POSS, it can be postulated that the corrosion film thickness and $FeCO_3$ sublayer adherence to the steel substrate are the two major characteristics which dictate the degree of protectiveness of the iron carbonate film rather than the crystal morphology, size or degree compactness. As such, thinner developing iron carbonate corrosion layers such as the ones grown in the presence of 4 and 20mg OA-POSS are correlated to the fastest general corrosion rate drops as seen in Figure 8-39. These also correspond to the $FeCO_3$ crystals which are the smallest in size.
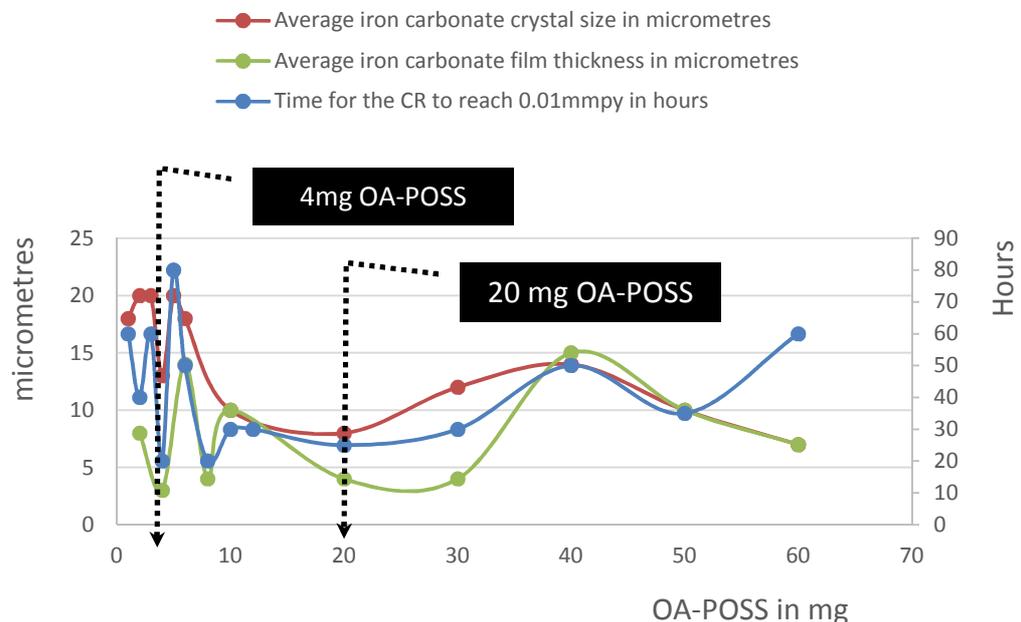
Figure 8-39 Summary of the relationship between $FeCO_3$ crystal morphology, size and film thickness and general corrosion mitigation at various OA-POSS loadings showing in blue the time required to reach the 0.01mmpy corrosion rate threshold in hours, in red the average $FeCO_3$ crystal size in micrometres and in green the average $FeCO_3$ film thickness.

The electrochemical data is depicted in Figure 8-39 as the time required to reach 0.01mmpy which is ten times lower than the value expected for a corrosion inhibitor to be assessed as effective, that is 0.1 mmpy. The importance of such advantage and relying on the degree of protectiveness provided by the $FeCO_3$ corrosion layers was detailed in Table 4-9.

8.4 Localised corrosion mitigation

While implemented electrochemical techniques such as linear polarisation resistance only permits the follow-up of the general corrosion rate and assumes the degradation mechanism to be uniform on all the studied carbon steel surface, light interferometry allows to portray the extent of localised corrosion.

After careful removal of the iron carbonate corrosion layer by using Clarke's solution, the corresponding underlying surface showed better localised corrosion protection when this layer was allowed to develop in the presence of OA-POSS as seen in Figure 8-40 to Figure 8-43. This is concluded from the lower values of the highest peaks registered on the corresponding interferometry profiles with the dark blue coloured regions corresponding to the deepest localised attacks. It should be noted that the deepest pit is shown relative to the corroded area.

The tests ran with 20 mg OA-POSS showed the best localised corrosion protection as seen in Figure 8-42 by the absence of eminent pits. The deepest pits found in the presence of OA-POSS were registered for a concentration of 10 mg as seen in Figure 8-43. The 3D profiles summarised in Figure 8-44 show clearly that the carbon steel surface covered by an iron carbonate film grown in the presence of 20mg OA-POSS is almost inert to any localised attack as observed by the absence of dark blue areas in Figure 8-44c.

It should be noted that the general corrosion influence on the pit depths was not taken into account. As such the pit depths registered in the absence of added OA-POSS (Figure 8-40) should be considered even deeper since the general corrosion rate was shown to be stable around 3mmpy for the duration of the test or 118 hours (Figure 7-33a). The higher localised corrosion attack observed at an OA-POSS loading of 10mg could be linked to the scattered porosities randomly appearing over the $FeCO_3$ crystal vertices. The width of these defects are judged large enough to allow water molecules and other corrosion reactants to diffuse to the underlying steel substrate.
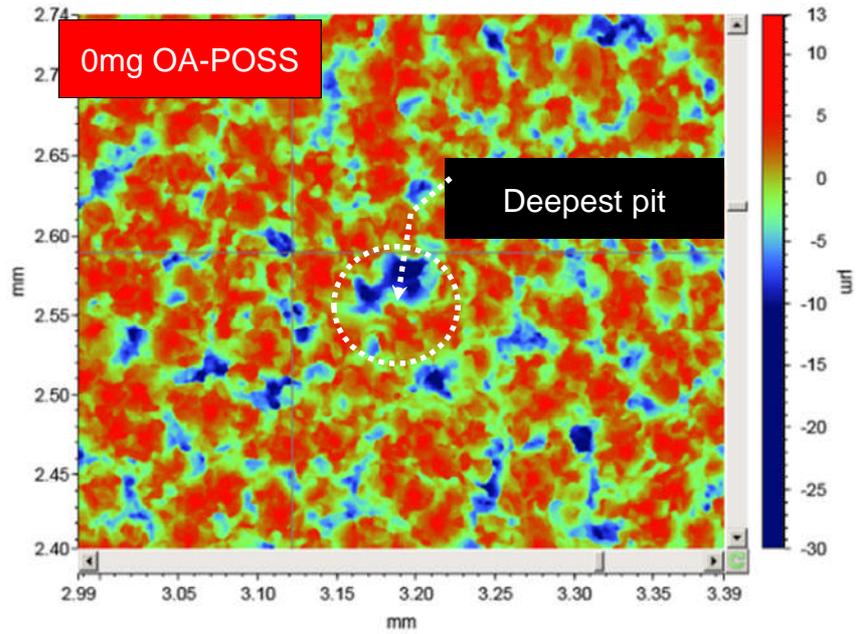
(a)
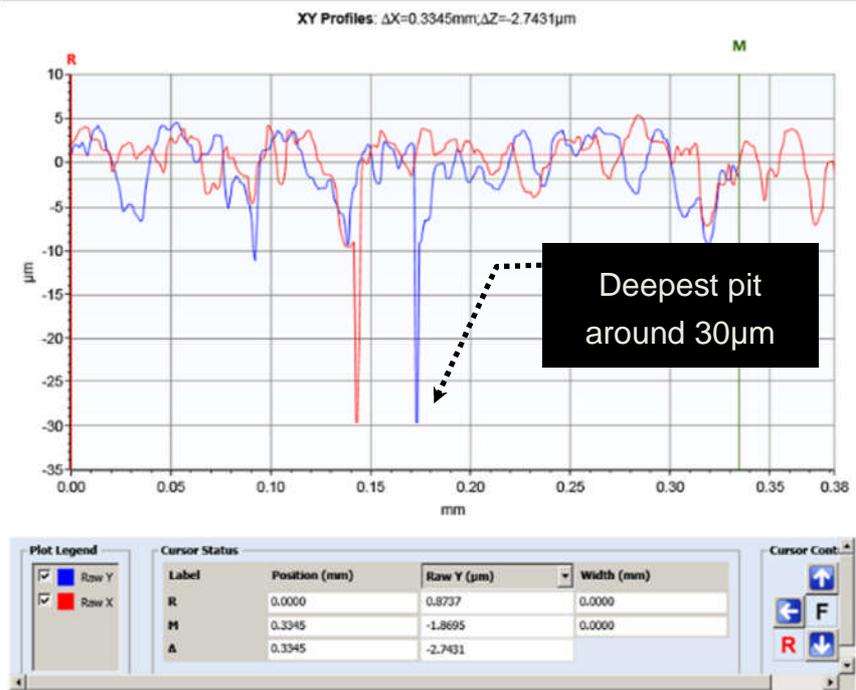
(b)

Figure 8-40 Vertical light interferometry 2D images of the deepest pits obtained for the surface beneath a FeCl$_2$ grown iron carbonate film showing (a) the horizontal profile with the sample dimensions in mm and the topographic height variation in micrometres, (b) the coordinates of a designated deepest pit. Analysis was carried out on samples after being subjected to the corrosive environment for 98 hours at pH6.6, 60°C, 0.8bar CO$_2$ and 3.5% NaCl.
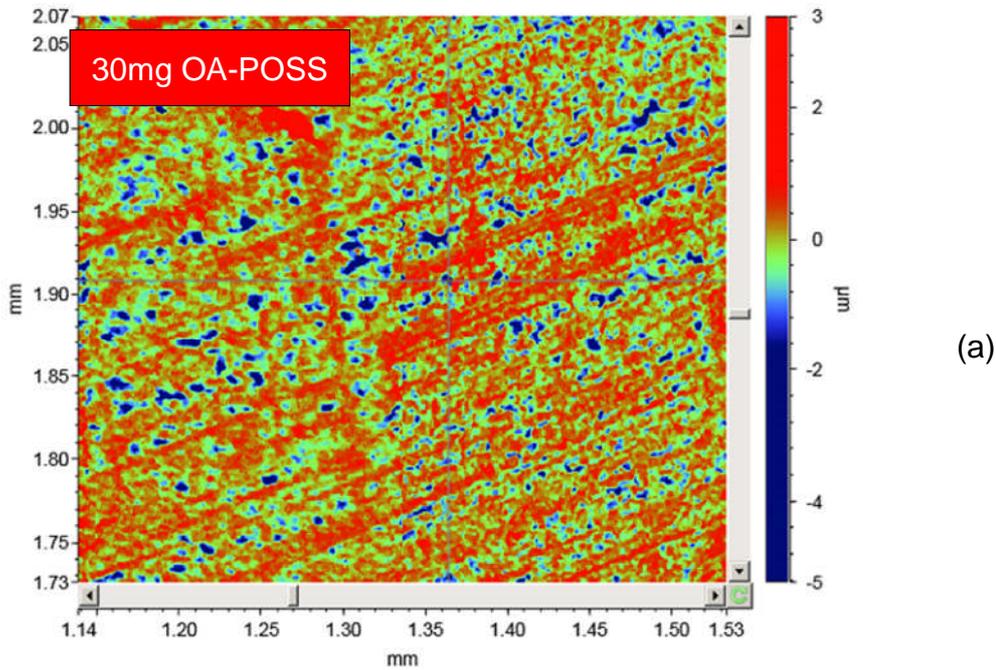
(a)
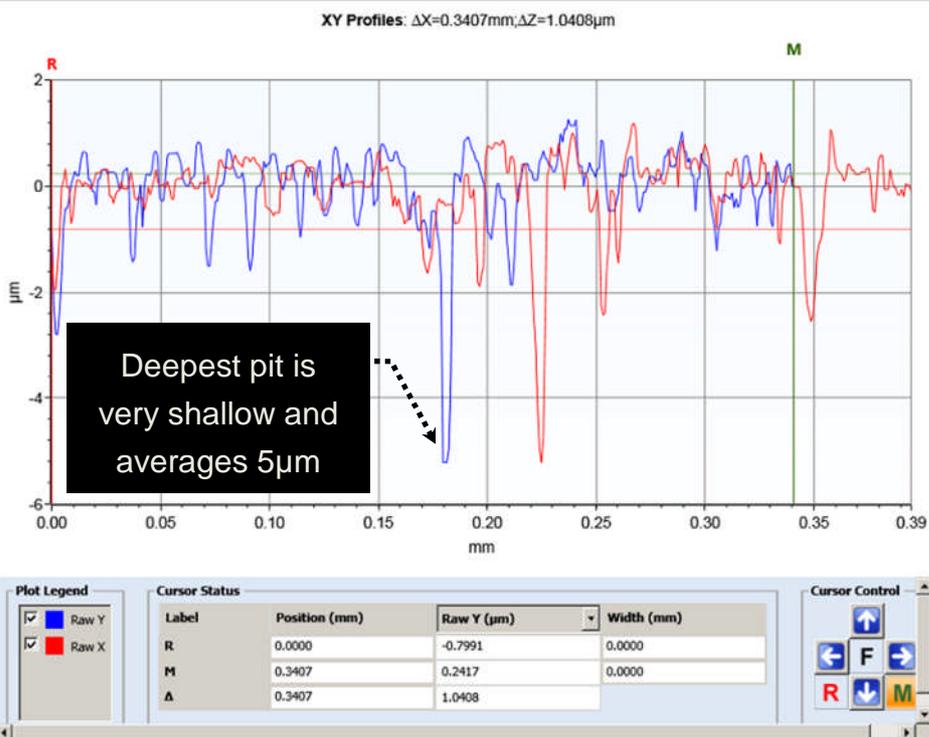
(b)

Figure 8-41 Vertical light interferometry 2D images of the deepest pits obtained for the surface beneath an iron carbonate film grown by adding 30mg OA-POSS showing (a) the horizontal profile with the sample dimensions in mm and the topographic height variation in micrometres, (b) the coordinates of a designated deepest pit. Analysis was carried out on samples after being subjected to the corrosive environment for 98 hours at pH6.6, 60°C, 0.8bar CO_2 and 3.5% NaCl.

(a)

(b)
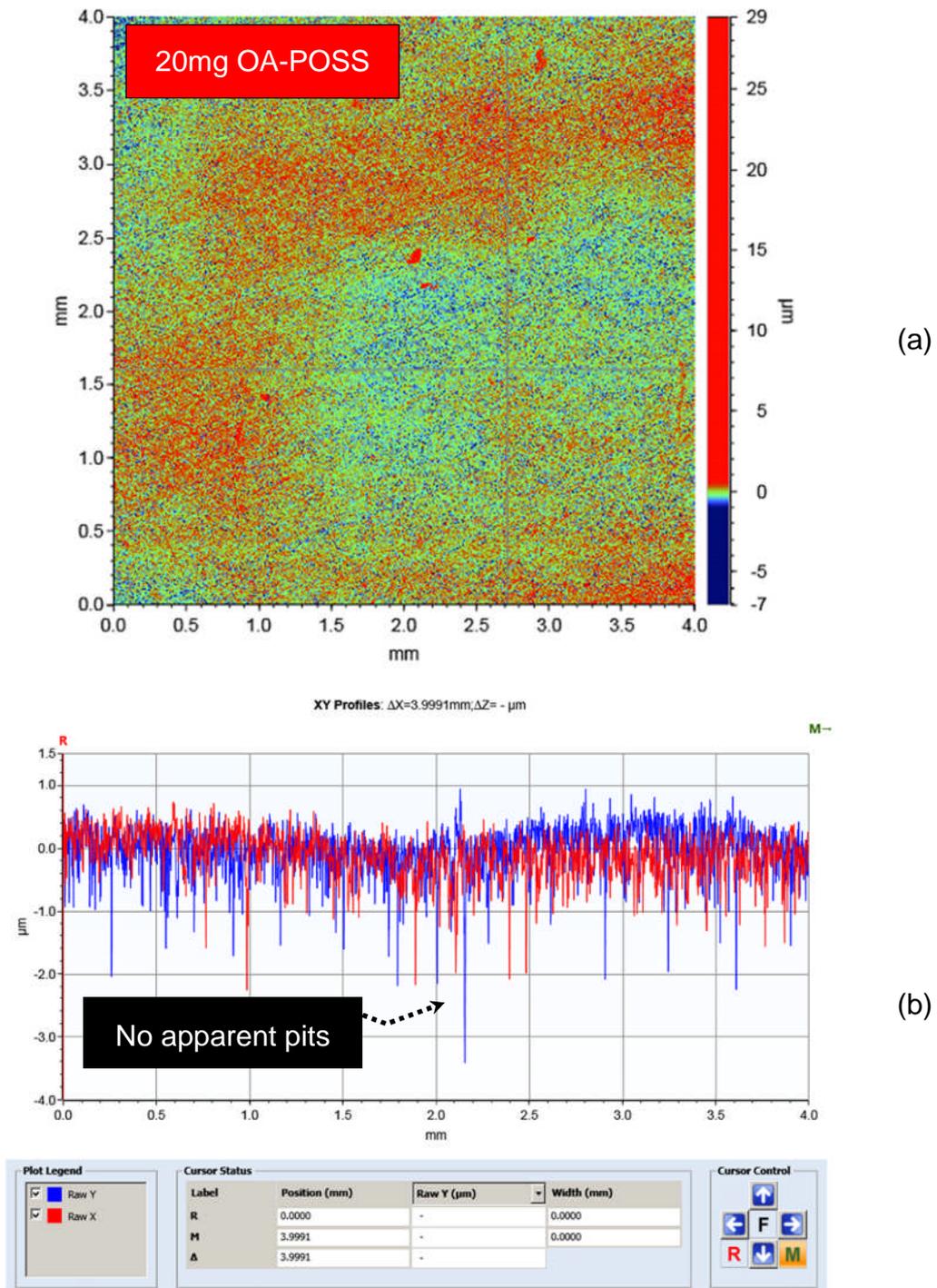
Figure 8-42 Vertical light interferometry 2D images of the deepest pits obtained for the surface beneath an iron carbonate film grown by adding 20mg OA-POSS showing (a) the horizontal profile with the sample dimensions in mm and the topographic height variation in micrometres, (b) the coordinates of a designated deepest pit. Analysis was carried out on samples after being subjected to the corrosive environment for 98 hours at pH6.6, 60°C, 0.8bar CO_2 and 3.5% NaCl.
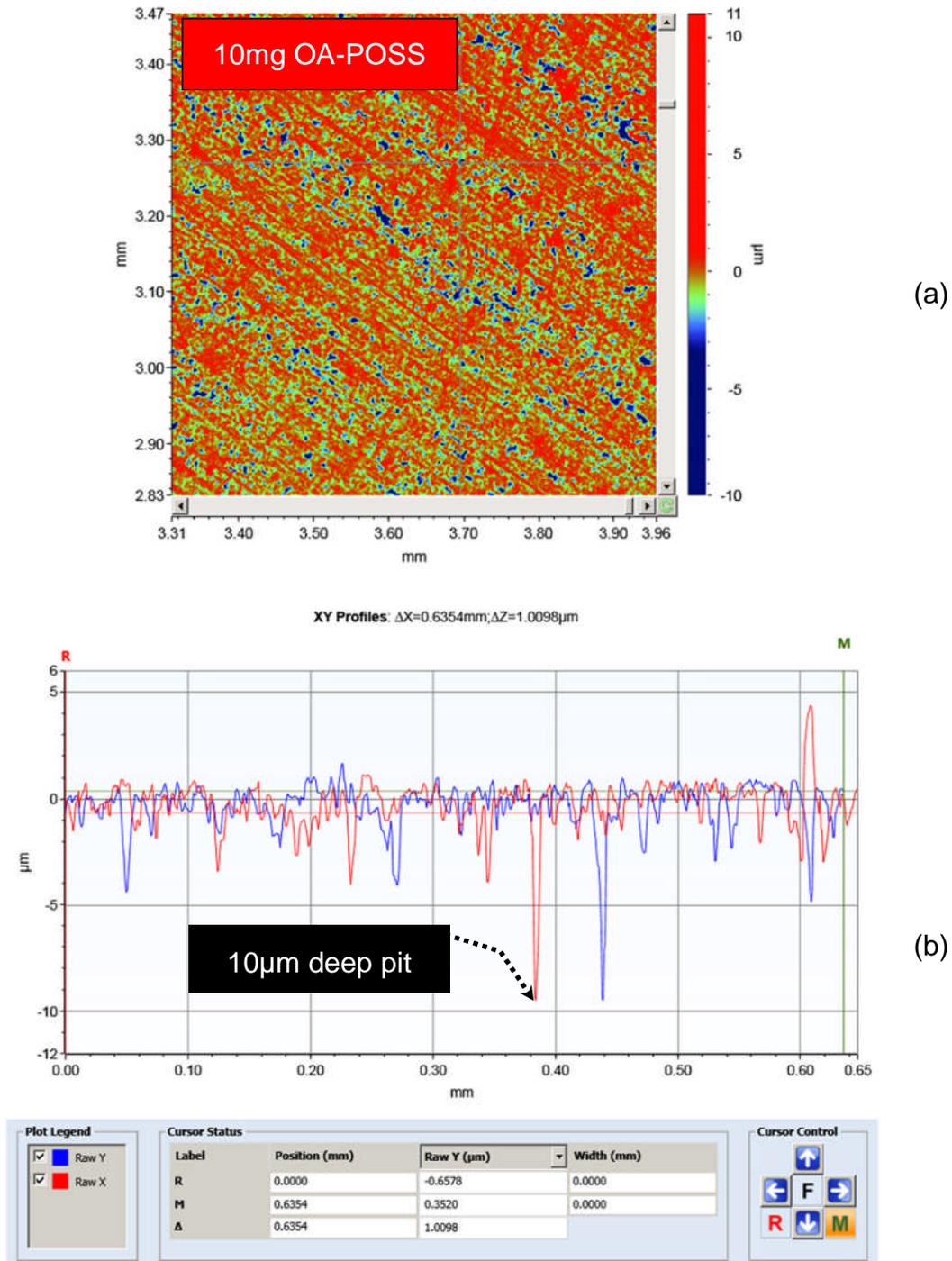
Figure 8-43 Vertical light interferometry 2D images of the deepest pits obtained for the surface beneath an iron carbonate film grown by adding 10mg OA-POSS showing (a) the horizontal profile with the sample dimensions in mm and the topographic height variation in micrometres, (b) the coordinates of a designated deepest pit. Analysis was carried out on samples after being subjected to the corrosive environment for 98 hours at pH6.6, 60°C, 0.8bar CO_2 and 3.5% NaCl.

50mg FeCl₂

(a)

10mg OA-POSS

(b)

20mg OA-POSS

No pitting

(c)
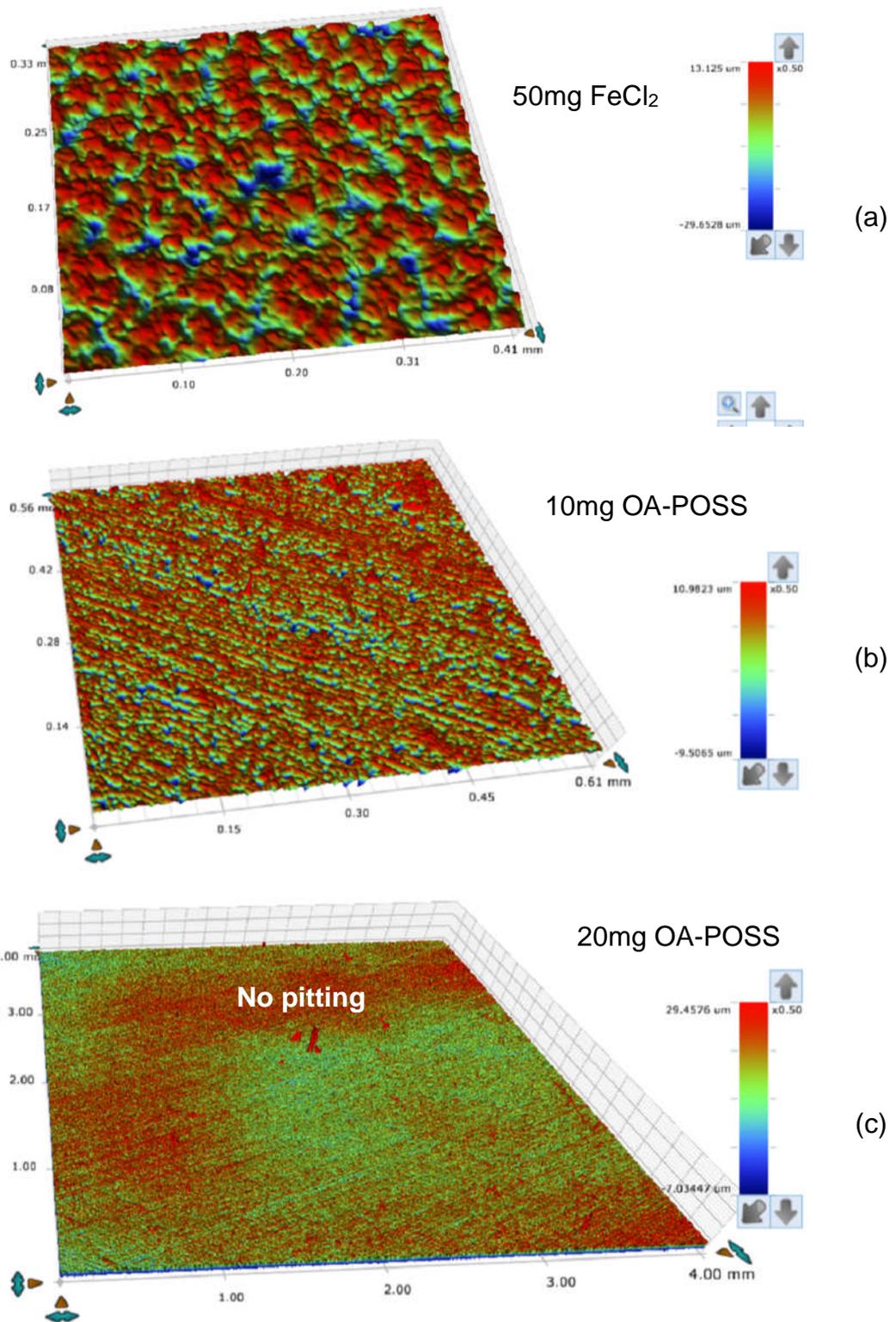
Figure 8-44 Vertical light interferometry 3D scheme of a designated area for the surface beneath an iron carbonate film grown (a) with 50ppm FeCl$_2$ (b) by adding 10mg OA-POSS (c) by adding 20mg OA-POSS. Analysis was carried out on samples after being subjected to the corrosive environment for 98 hours at pH6.6, 60°C, 0.8bar CO$_2$ and 3.5% NaCl.

One main explanation for the observed resilience to heavy localised corrosion attack when 20 mg OA-POSS is added can be related to the crystal morphology as seen in the corresponding SEM micrographs. In fact, the iron carbonate crystals growing at pH6.6 in the presence of 20 mg OA-POSS are very small and compacted together while the developed $FeCO_3$ corrosion layers cover well the entire surface of the underlying carbon steel as seen in Figure 8-45.
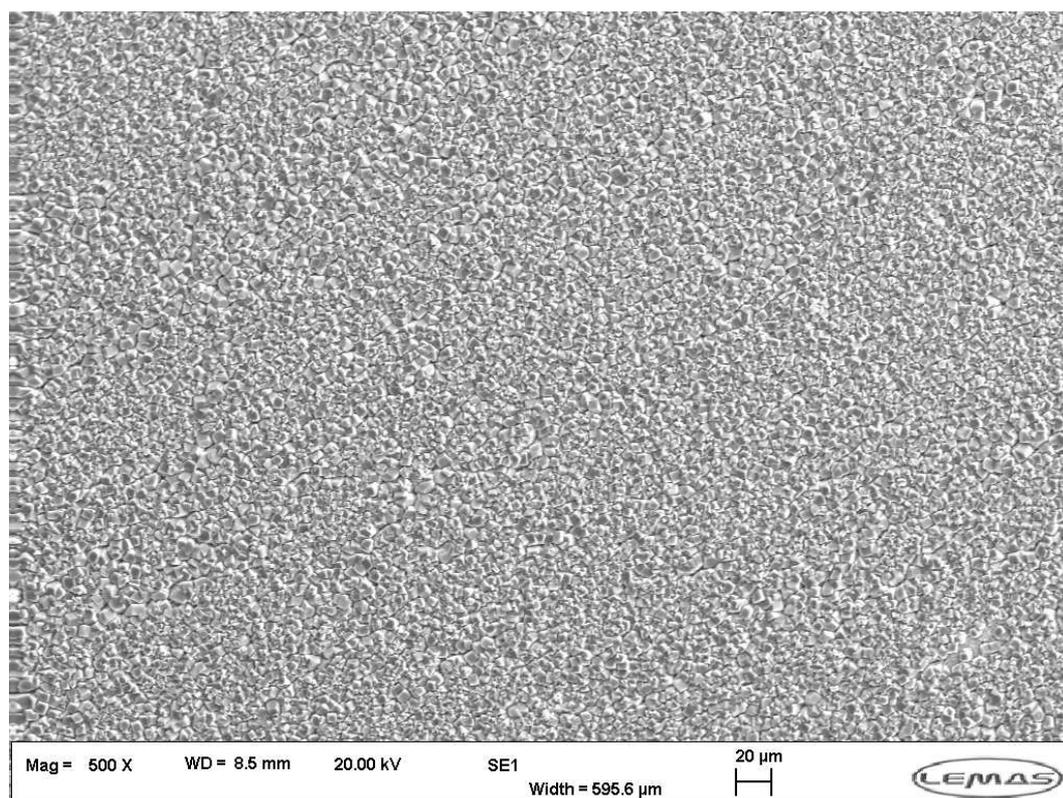
Figure 8-45 SEM micrograph topography view of X65 samples when 20mg OA-POSS are added to the test solution showing a highly compact and well-covering $FeCO_3$ corrosion layer and a scale bar of 20 micrometres [pH=6.6, 60°C,3.5% NaCl, 108 hours]

The $FeCO_3$ crystals have a cubic morphology with few of them constituting agglomerates and growing as leaflets with an average crystal size of 5µm (Figure 8-46a) while the thickness of the corrosion layer does not exceed 4 micrometres (Figure 8-46b). These two observations are usually affiliated with such high protective capabilities of the grown scale since published papers usually describe the iron carbonate layers grown at higher temperatures to be thinner and more protective and the corrosion film grown with 20mg OA-POSS seem to behave similarly.
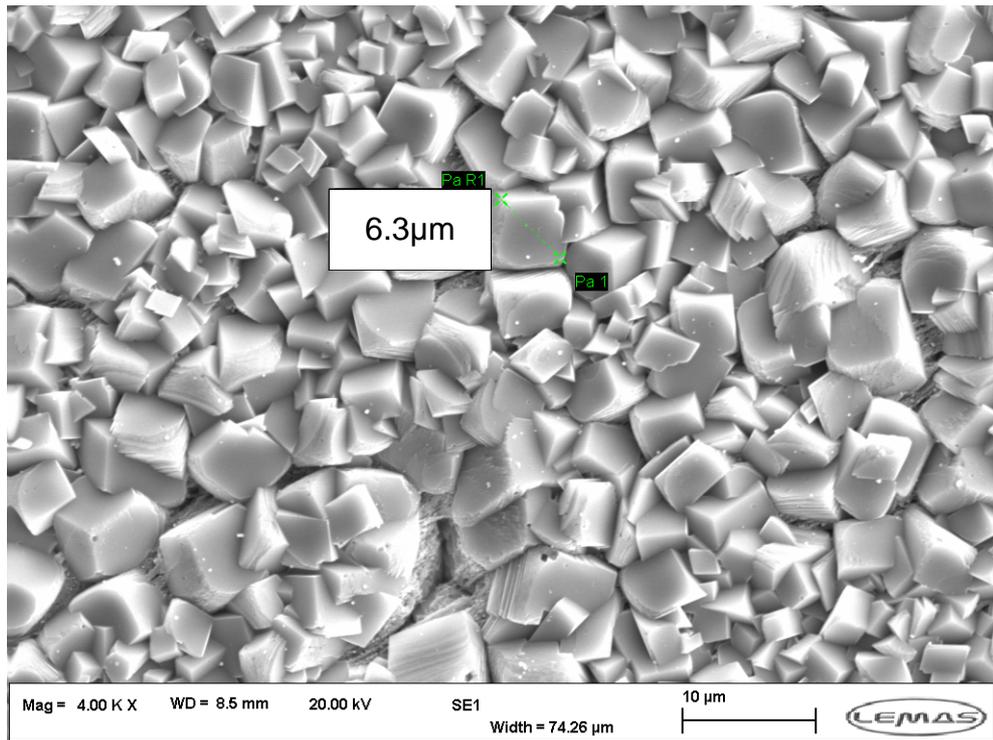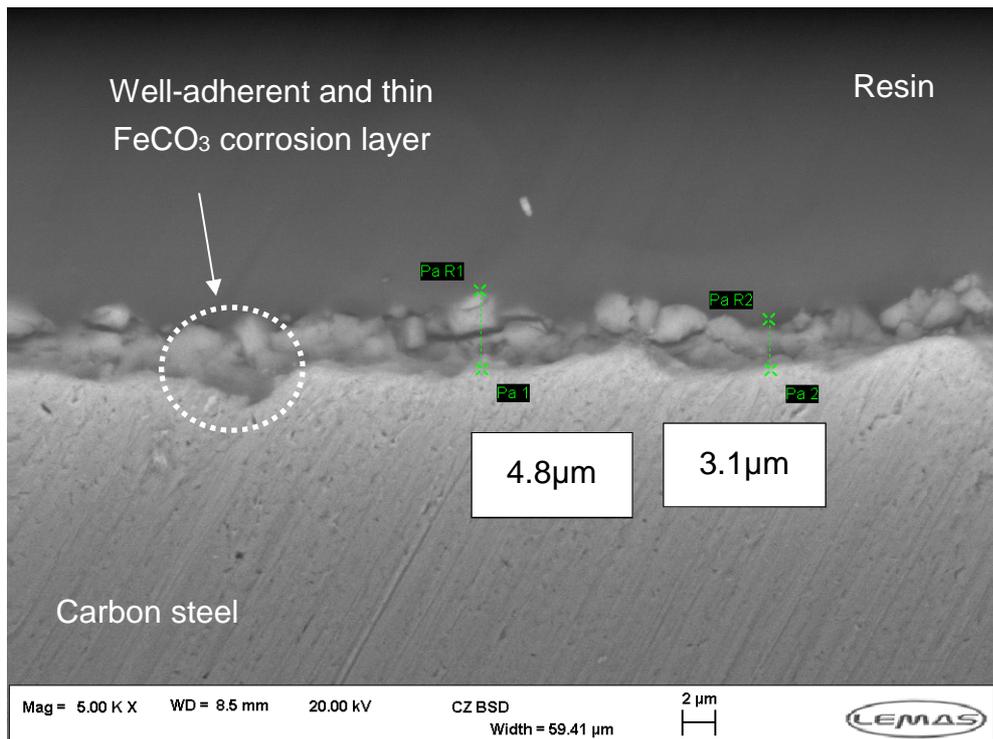
Figure 8-46 SEM micrographs topography view of X65 samples when 20mg OA-POSS are added to the test solution at various magnifications as shown by the scale bar [pH=6.6, 60°C,3.5% NaCl, 108 hours] focusing on (a) the dimension and morphology of the prismatic and leaflet-like $FeCO_3$ crystals and (b) the thickness of a corresponding $FeCO_3$ layer

8.5 Mechanical properties enhancement

8.5.1 Nanoindentation

The registered data show that the loading and unloading curves, in the case of the tests where iron carbonate was grown by adding 50ppm $FeCl_2$, are more scattered than the ones where OA-POSS was added as shown in Figure 8-47a and Figure 8-47b respectively.
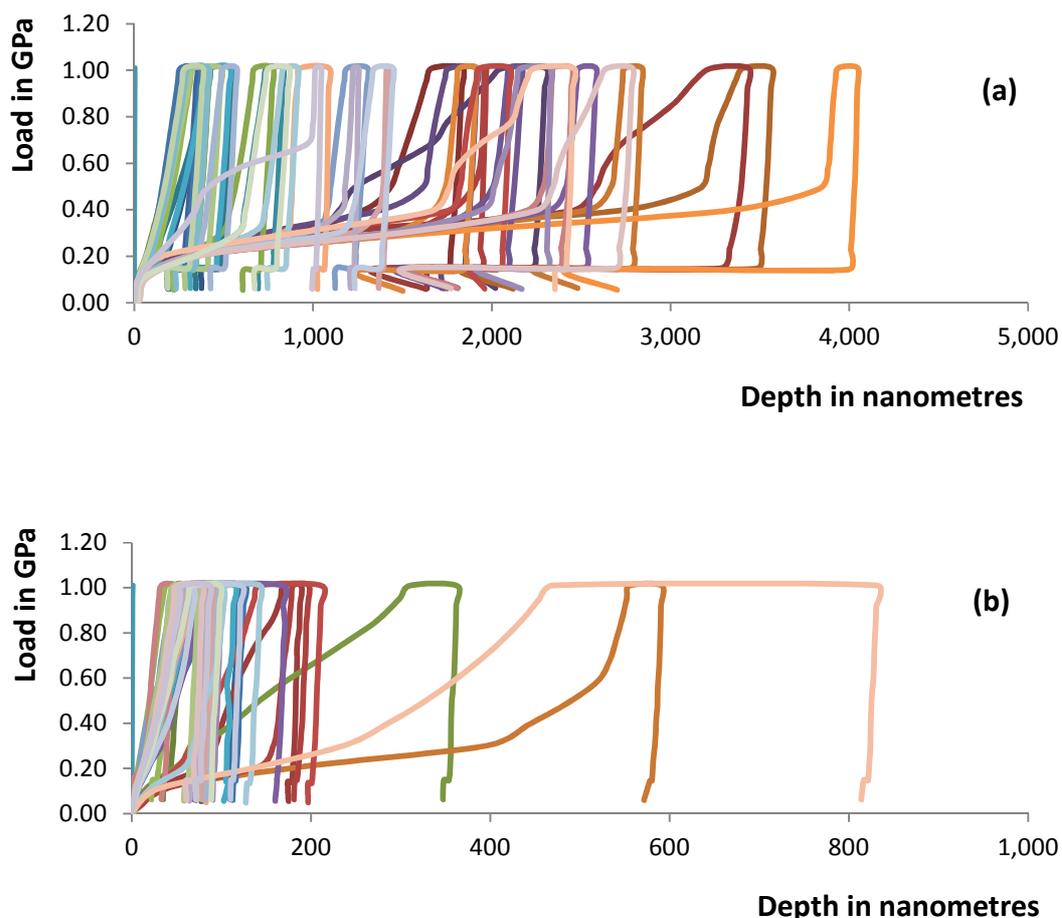
Figure 8-47 40 cycles of loading and unloading nanoindentation curves done on $FeCO_3$ corrosion films grown with (a) 0mg OA-POSS, 50ppm $FeCl_2$ and (b) 100 mg OA-POSS. [pH=6.6, 60°C,3.5% NaCl, 108 hours]

This is correlated to the fact that the maximum depth attained when indenting a $FeCO_3$ not treated with OA-POSS is much bigger than when the nanofiller is added as seen in Figure 8-48. The indent travels ten times deeper in the corrosion layer, at the same loading value, when the iron carbonate is not subjected to any nanofiller additions.
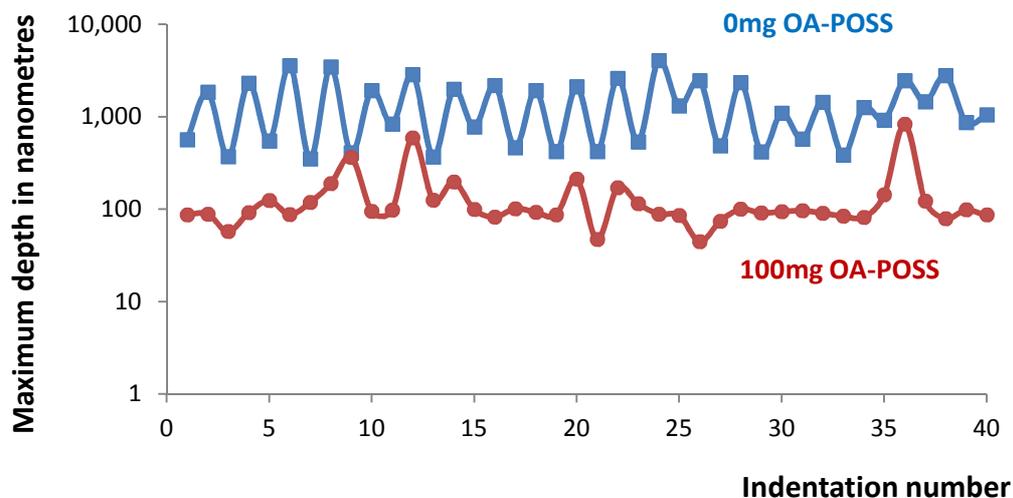
Figure 8-48 Maximum indent depth of a blank and OA-POSS modified $FeCO_3$

A summary of the hardness and modulus data obtained on three different loading of OA-POSS modified iron carbonate layers is shown in Figure 8-49.
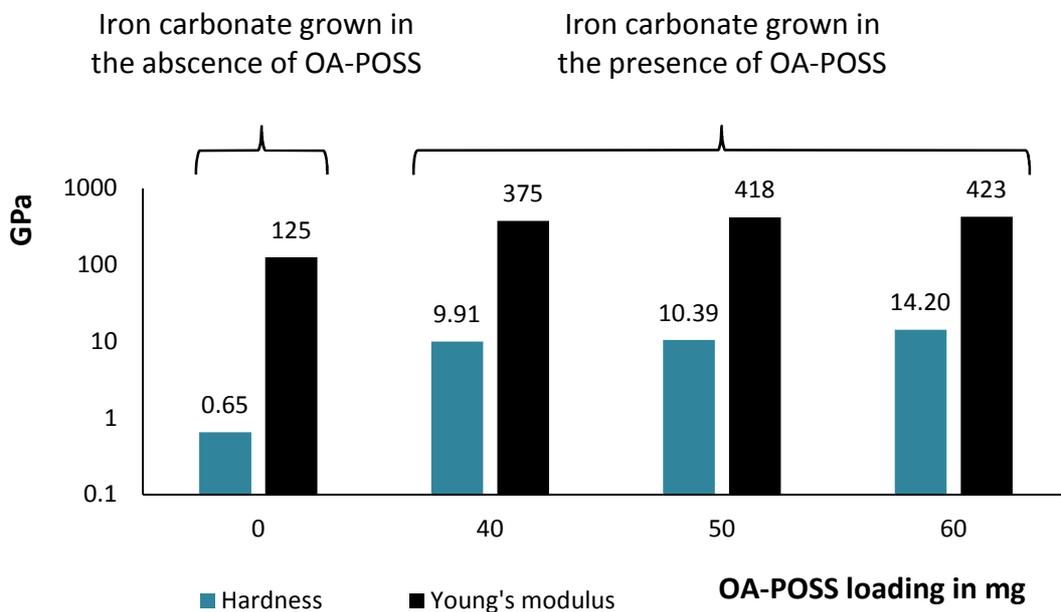
Figure 8-49 Mechanical properties obtained from ferrous enriched (50ppm FeCl$_2$ and 0mg OA-POSS) and OA-POSS enriched (40, 50 and 60 mg OA-POSS) FeCO$_3$ corrosion layers [pH=6.6, 60°C, 3.5% NaCl, 108 hours]

The hardness is seen to increase tenfold while the Young's modulus is enhanced by a factor of three; these improvements are comparable to literature values where other POSS derivatives have been added to different polymers in the 3 to 5% loading range as previously detailed in section 1.8.

8.5.2 Inductively Coupled Plasma Optical Emission (ICP-OES) analysis

After careful dissolution of the iron carbonate corrosion layers in 15% acetic acid, the ICP-OES showed that the $FeCO_3$ film which grows in the presence of the hybrid nanofiller OA-POSS contains higher levels of silicon ranging between 1.5ppm and 2 ppm. On the other hand, the iron carbonate corrosion layer grown when only $FeCl_2$ is administered in order to increase the ferrous iron supersaturation showed a lower silicon content of the order of 0.2 ppm as shown in Figure 8-50.
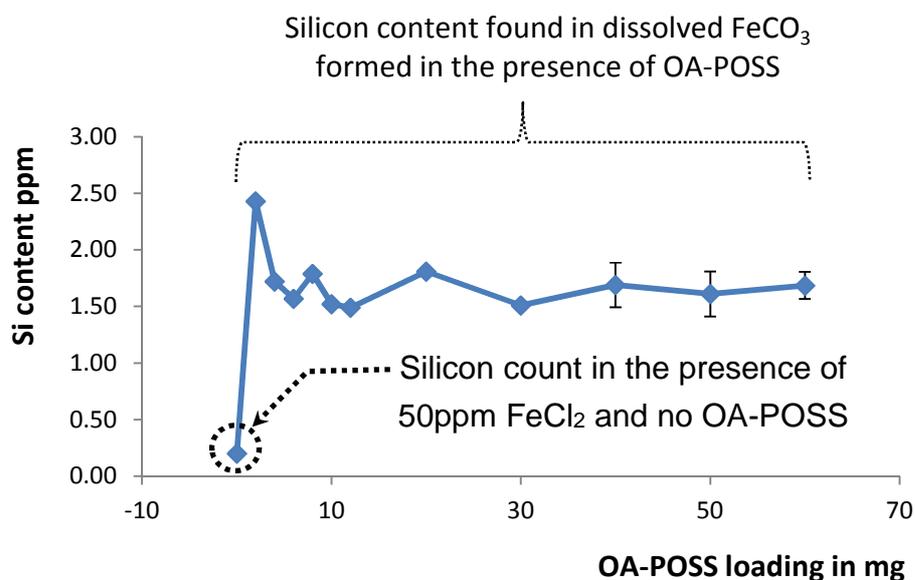
Figure 8-50 Silicon uptake as computed from the ICP-OES analysis

It is estimated that the silicon content as computed from the ICP-OES results are equivalent to an average OA-POSS to $FeCO_3$ volume ratio equal to 3% which is very comparable to the weight percentage range of nanofiller added to various polymers in what is called the effective region of 3 to 10%. Such conclusion is reached by following the facts and assumptions provided in Figure 8-51.

244

Facts

*Every OA-POSS molecules contains 8 silicon atoms

*The volume of one OA-POSS molecule is equal to 1.1 nm3

*Molecular weight of silicon is equal to 28g/mol

*Avogadro number equal to 6.022×1023

Assumptions

*The silicon content in ppm is equivalent to the silicon content in mg

*All the silicon content detected originates from the OA-POSS molecule

*The $FeCO_3$ average film thickness is 10μm

Figure 8-51 Facts and assumptions for Silicon content calculations

8.5.3 Transmission Electron Microscopy (TEM) analysis

The aim of using the TEM technique is twofold; first it was assumed that the higher resolution could allow for the nanofiller inclusion detection if OA-POSS was re-agglomerating in any way since these hybrid nanofillers are known to do so in specific conditions. In fact, TEM characterizations are commonly employed to investigate the dispersion quality and the morphology of nanocomposite films. Also, a higher resolution could help detect the degree of porosity and surface integrity of single iron carbonate crystal grown with or without the addition of the nanofiller.

A blank and an OA-POSS enriched samples were analysed under high resolution with the TEM after SEM/FIB treatment where the iron carbonate was cut from the sample cross-section in order to uncover any morphological features that could explain such enhancements. On a TEM micrograph, brighter areas correspond to increased scattering of the electrons. As such, Figure 8-52a shows platinum protective layer (PCL) on top of the sample. Because of its average atomic number, the carbonate layer (CL) is lighter than the iron substrate (BM).
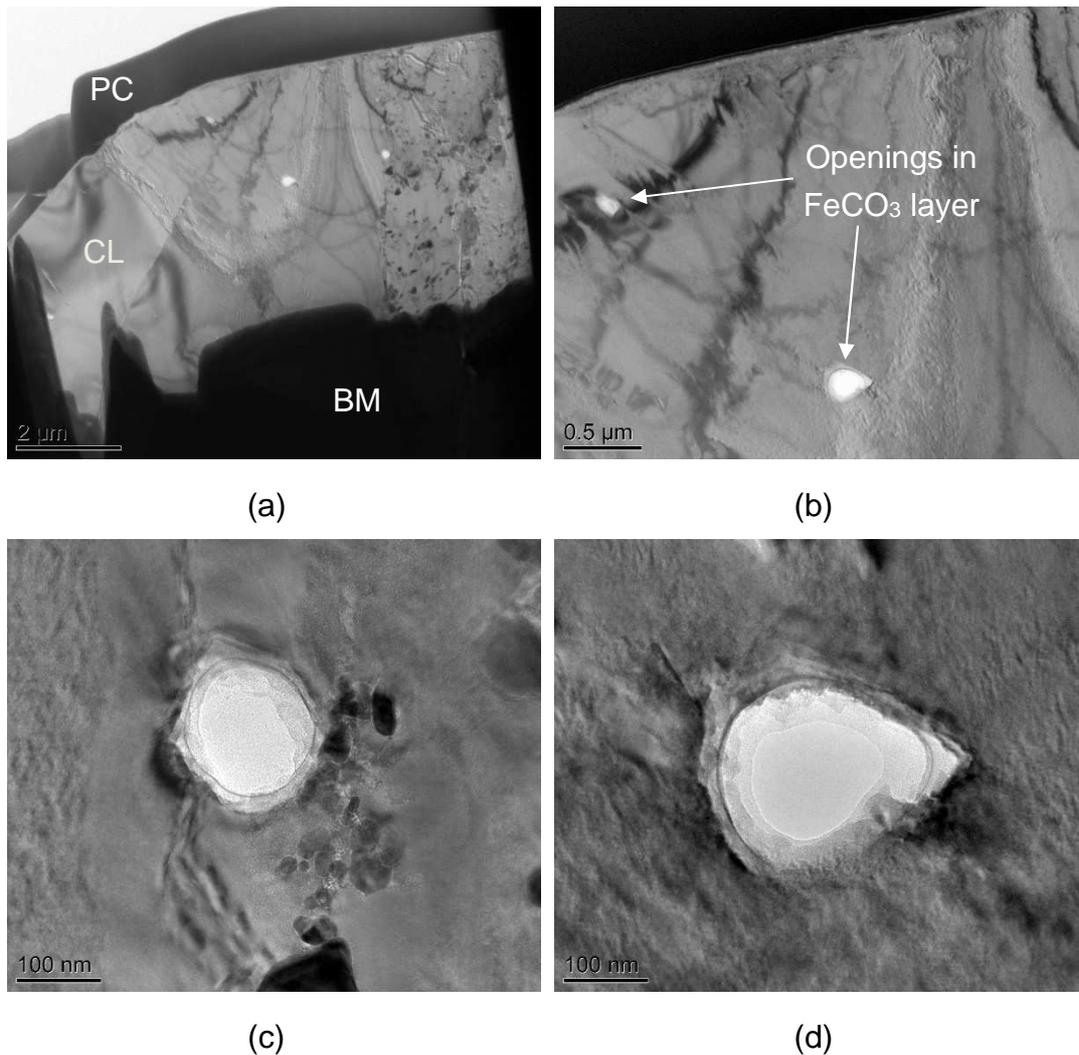
Figure 8-52 TEM image of a cross-section of corrosion product on X65 steel at 60°C, pH6.6, 3.5% NaCl, 0.8bar CO_2, for 98 hours exposed to 100mg of OA-POSS dissolved in the brine chemistry showing (a) the $FeCO_3$ corrosion layer (CL) localised in between the platinum coated layer (PCL) and the base metal (BM) (b) openings on the $FeCO_3$ layer (c, d) zoom on the pinholes

It appears as though the iron carbonate crystal grown in the presence of OA-POSS is showing some pores as seen in Figure 8-52 (c) and (d). These show the same average dimensions (100nm) as the pinholes frequently referenced on the iron carbonate edge vertices such as the ones depicted in Figure 8-4. On the other hand, the $FeCO_3$ corrosion layer obtained under the same conditions but when only 50ppm ferrous chloride were added show a more homogeneous surface as seen in Figure 8-53.
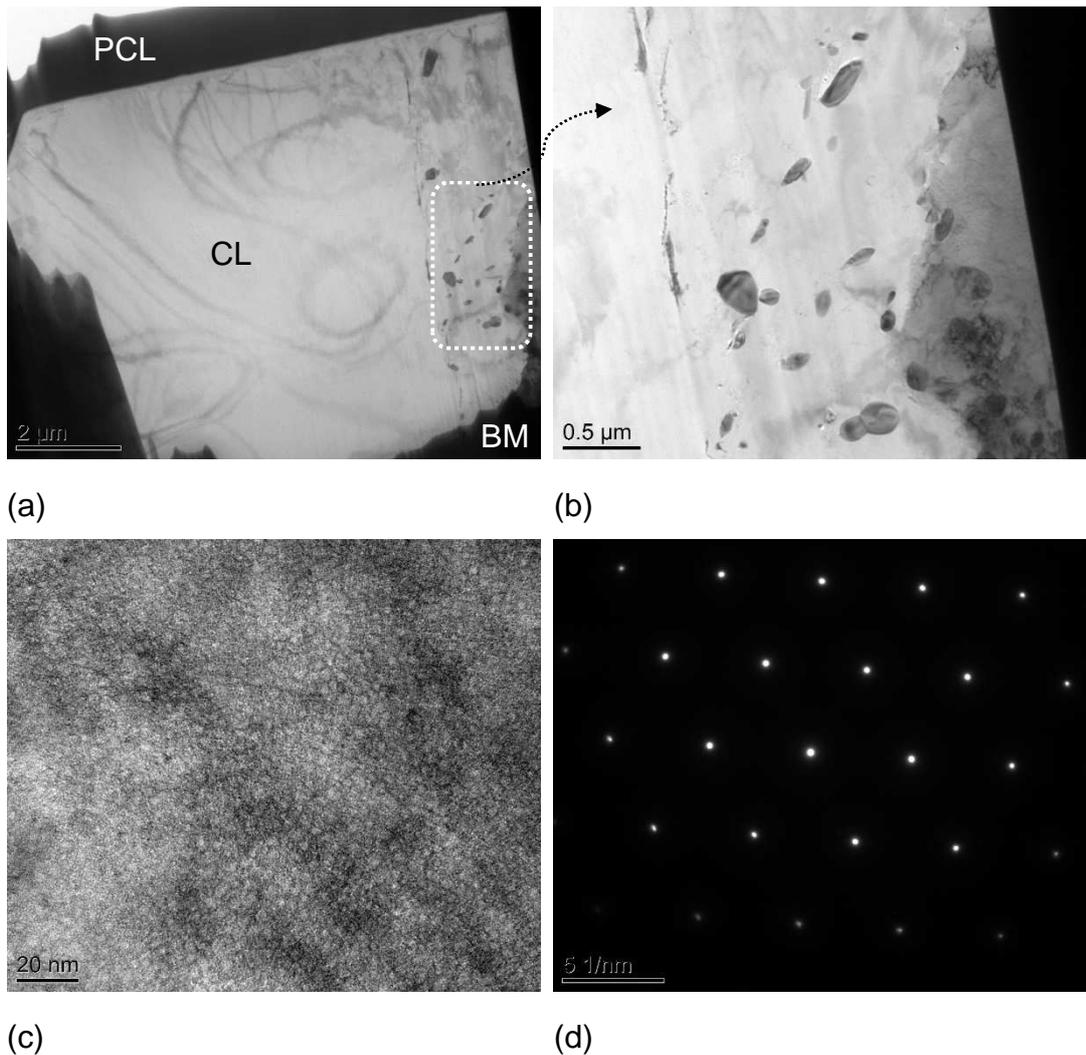
Figure 8-53 TEM micrographs of $FeCO_3$ grown at 60°C, pH6.6, 3.5% NaCl, 50ppm $FeCl_2$, 0.8bar CO_2, 98 hours showing (a) the $FeCO_3$ corrosion layer (CL) localised in between the platinum coated layer (PCL) and the base metal (BM), (b) a zoom on the dotted area and showing some rough locations on the $FeCO_3$ cross-section, (a) a flocculated-like $FeCO_3$ layer when higher magnification is applied and (d) the iron corresponding diffraction pattern

8.5.4 TEM – EDX analysis

Energy-dispersive X-ray spectroscopy was undertaken on the TEM and both blank and OA-POSS enriched samples were checked for chemical composition mapping as shown in Figure 8-54 and Figure 8-55 respectively. The platinum is the protective material used prior to the FIB sample cutting and always appear on the sample treated borders.

247
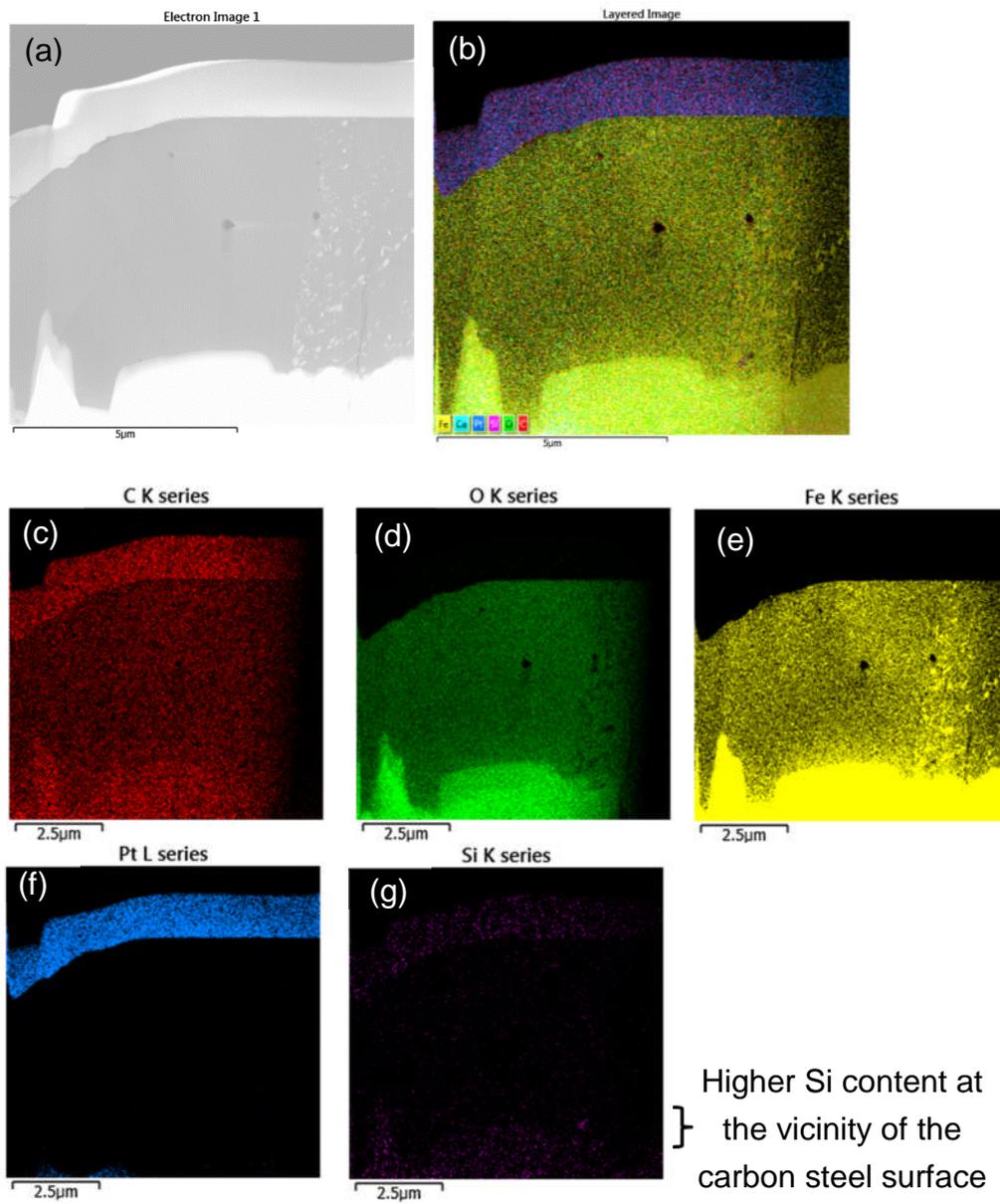
Figure 8-54 EDX map analysis of a $FeCO_3$ corrosion layer grown at 60°C, pH6.6, 3.5% NaCl, 0.8bar CO_2, 98 hours with the addition of 100mg OA-POSS into the brine chemistry showing the (a) SE micrograph, (b) layered map image, (c) Carbon-C (d) Oxygen-O (e) Iron-Fe (f) Platinum-Pt and (g) Silicon-Si elements

The silicon content in Figure 8-54(g) when OA-POSS is dissolved within the brine chemistry seems higher near the carbon steel edge when compared to the abundance of the same element appearing in Figure 8-55(g) where no nanofiller was used.

This corroborates the general assumption that silicon from OA-POSS is being incorporated in the growing iron carbonate crystal. Silicon being the inorganic element which is suspected to be the main generator of the mechanical properties' enhancement described in section 8.5.
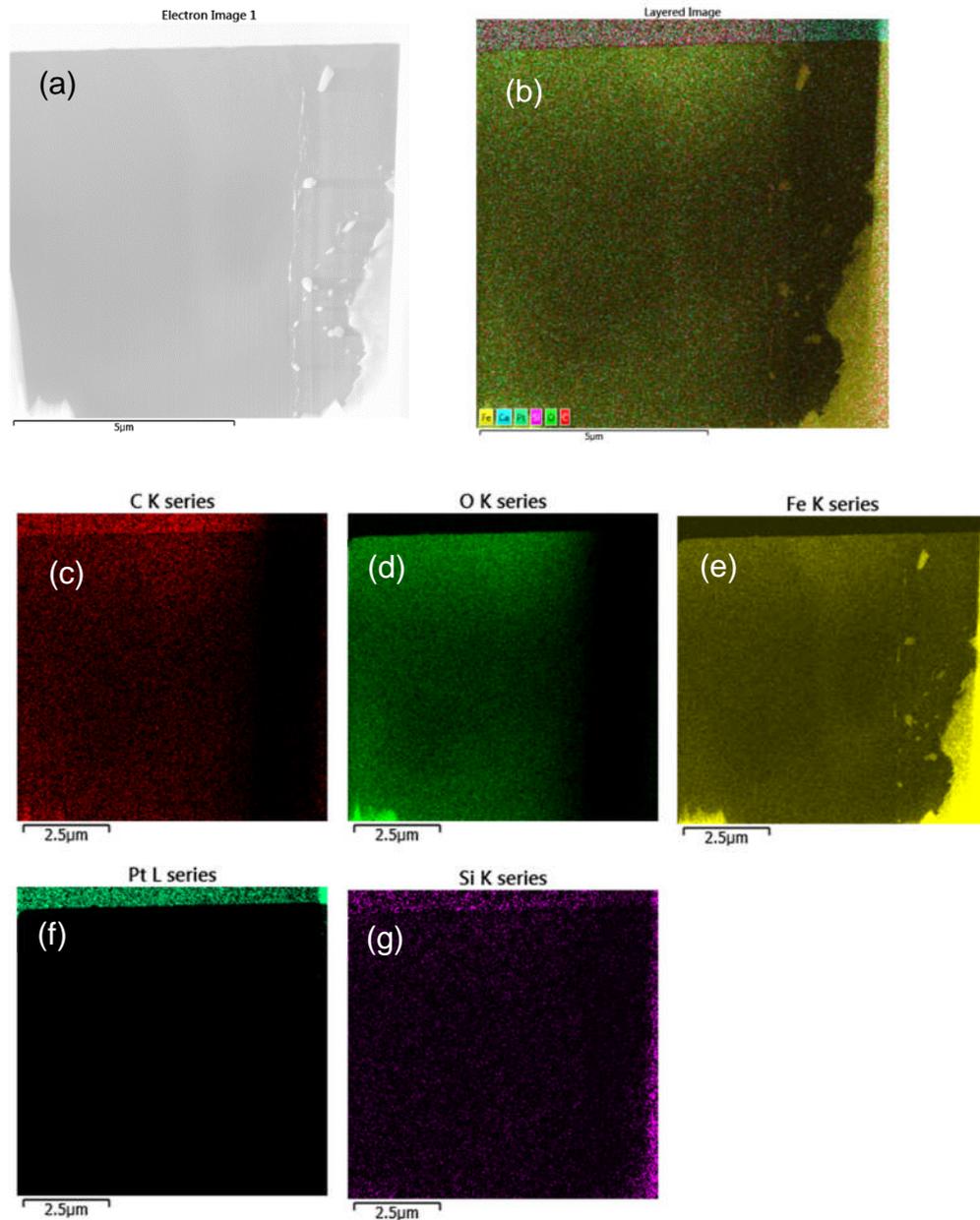
Figure 8-55 EDX map analysis of a $FeCO_3$ corrosion layer grown at 60°C, pH6.6, 3.5% NaCl, 50ppm $FeCl_2$, 0.8bar CO_2, 98 hours with the addition of 50ppm $FeCl_2$ showing (a) SE micrograph, (b) layered map image, (c) Carbon-C (d) Oxygen-O (e) Iron-Fe (f) Platinum-Pt and (g) Silicon-Si elements

8.5.5 BET porosity

The nitrogen adsorption porosity tests were registered for three compounds: Synthetic iron carbonate powder mimicking the grown iron carbonate corrosion layers, OA-POSS in its as purchased dry powder form, and the synthetic $FeCO_3$ premixed with OA-POSS then dried to powder.

As an example, Figure 8-56 show the isotherm logarithmic plot for synthetic iron carbonate which appears to follow an isotherm type III; these are characterised by heats of adsorption less than the adsorbate heat of liquification, that is N_2. The adsorption proceeds following that shape since the adsorbate interaction with an adsorbed layer is greater than the interaction with the adsorbent surface.
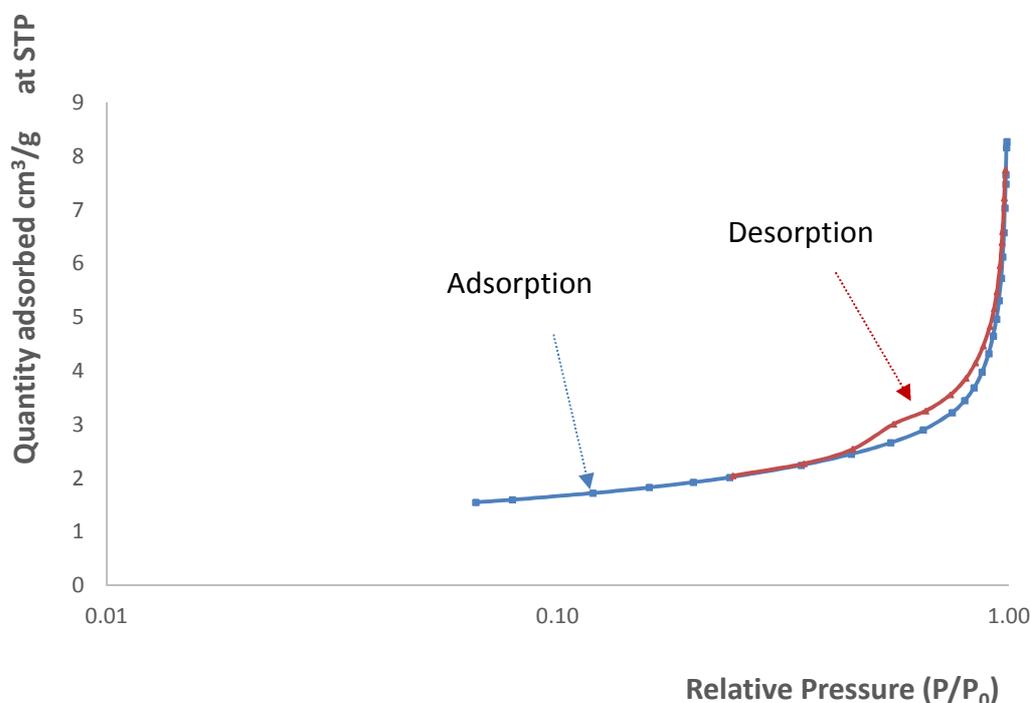
Figure 8-56 Synthetic $FeCO_3$ isotherm log plot

The BET surface area extracted from this plot give a value of 6.8078 ± 0.0492 m²/g corresponding to the studied synthetic iron carbonate compound with a correlation coefficient as high as 0.9998972. The type III isotherm hints to the formation of multilayer while the absence of a flattish portion in the curve indicates that the monolayer formation is missing.

Similarly BET surface area for OA-POSS was found to be equal to 2.5353 m²/g with a correlation coefficient as high as 0.9999425 and the combined OA-POSS with the synthetic iron carbonate gave a BET surface area equal to 0.6015 m²/g with a correlation coefficient as high as 0.9997992.

The reduction in the BET surface area between the synthetic $FeCO_3$ and the iron carbonate combined to OA-POSS suggest that the silsesquioxane moieties are interacting with the iron carbonate or adsorbing to it. This assumption could be extrapolated to the *in situ* grown iron carbonate layer which is growing and assimilating OA-POSS moieties when those are administered to the brine composition.

8.5.6 Raman/FTIR

Both FTIR and RAMAN spectroscopic techniques were implemented as an additional chemical analysis technique to validate the presence of silicon-rich moieties within the produced iron carbonate. It was difficult to differentiate the O-Si adsorption peaks from others especially in the case of the RAMAN tests as shown in Figure 8-57 and Figure 8-58.
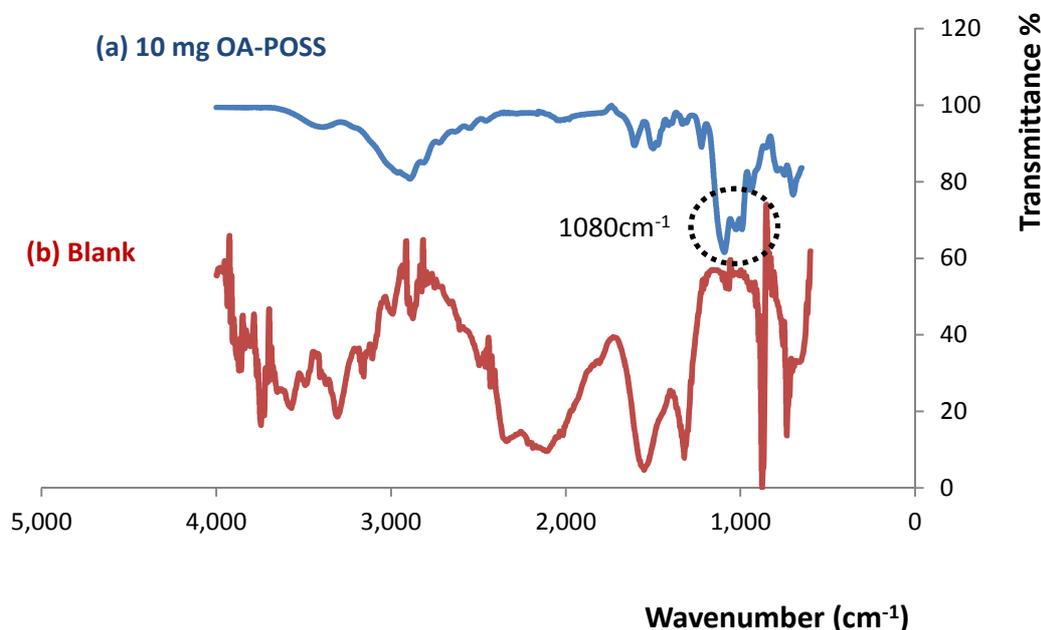
Figure 8-57 FTIR transmittance spectra for X65 carbon steel covered with $FeCO_3$ layer formed at 60°C, pH6.6, 3.5% NaCl, (a) with 10mg OA-POSS or without (b)

The shift of the sharp band near 1080 cm^{-1} is evident in Figure 8-57a in the dotted area; it represents the POSS modified iron carbonate spectra and is attributed to Si-O-Si stretching vibrations, a characteristic stretching value of the silsesquioxane cage. Since it was observed in the nanocomposite, it indicates the presence of filler (OA-POSS)-polymer($FeCO_3$) interactions especially with the lack of symmetry due to its lower concentration in the nanocomposite.[362]
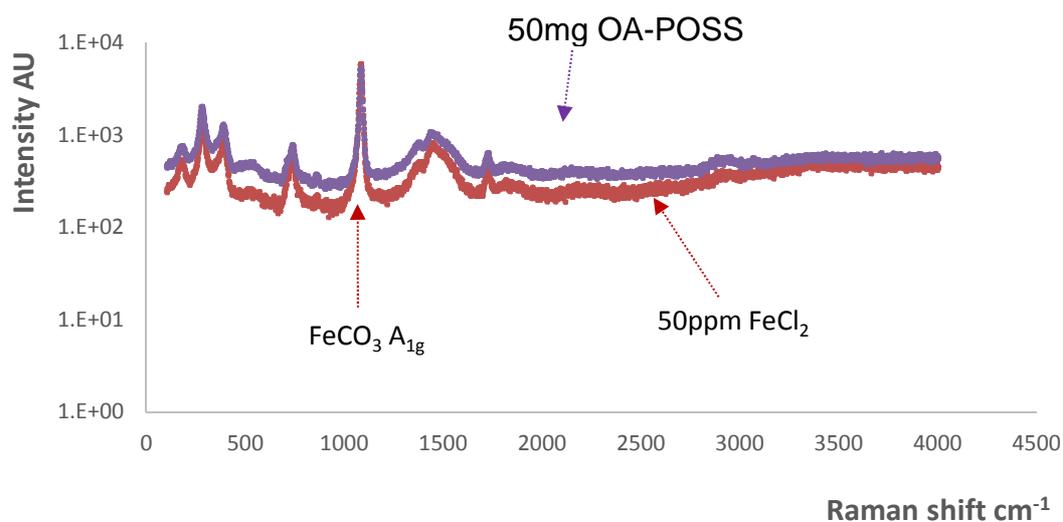
Figure 8-58 RAMAN shifts for blank $FeCO_3$ and 50mg OA-POSS enriched $FeCO_3$ [60°C, pH6.6, 3.5% NaCl, 0.8bar CO_2, 98hours]

The representative RAMAN iron carbonate peak at 1100cm^{-1} also known as the A1g shift is well identified in both POSS rich and blank samples as seen in Figure 8-58. This is at the same time the area where the RAMAN peaks corresponding to the siloxane Si-O-Si group should appear; in fact the known asymmetric stretch for these is located between 1100 and 1000 cm^{-1}.

Chapter 9 OA-POSS behaviour at various pH values and interactions with various ionic species

Previous results have shown that the OA-POSS is able to enhance the iron carbonate crystal growth and the obtained corrosion film mechanical properties at one set of temperature and pH values. This section tries to uncover the potential of the nanofiller when the pH is varied to more acidic conditions.

As detailed in section 3.3, carbonic acid, the driver for sweet corrosion, is a weak acid. The pH of the formation water depends on the CO_2 partial pressure, temperature, and alkalinity. Figure 9-1 shows that for the common case of carbonate-containing reservoirs and moderate temperatures, produced waters should have pH values of 6 or greater. On the other hand, waters exposed to greater amounts of CO_2 in non-carbonate-containing reservoirs can have pH values of 4 or less which validates the rationale behind studying the nanofiller at such lower pH values.[363]
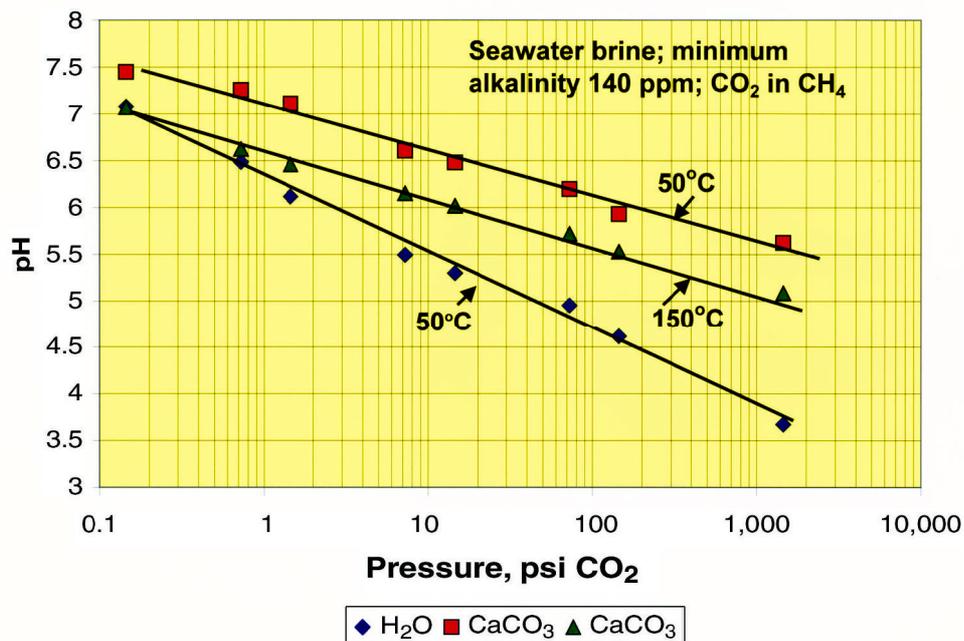
Figure 9-1 Computed pH vs. pressure for a seawater brine exposed to a gas phase containing CO_2; data are shown for seawater alone at 50°C and for calcite-saturated seawater at 50 and 150°C.[363]

It also tries to spot any corrosion mitigation improvement when the pH is increased to a neutral value of 7. In fact conventional reservoir environments are known to have a pH ranging between values as low as 6.5 and as high as 8.5 while the pH is known to reach 12.5 in some hydraulic fracturing jobs.[364]

9.1 Tests ran at very low pH

When carbon dioxide is left bubbling overnight at 60°C in a brine solution at 3.5% NaCl, the pH stabilises around a value as low as 3.75. The silsesquioxane based nanofiller does not seem to have any effect on the electrochemical evolution at this low pH probably due to the lysis of the siloxane group (O-Si-O). The corrosion rates seem stable in both cases at values around 5 mmpy after the first 100 hours of the test duration as seen in Figure 9-2. The first 20 hours show a slightly better protection though when 100mg OA-POSS is added with a CR value at 7mmpy as compared to 8mmpy for a blank test.
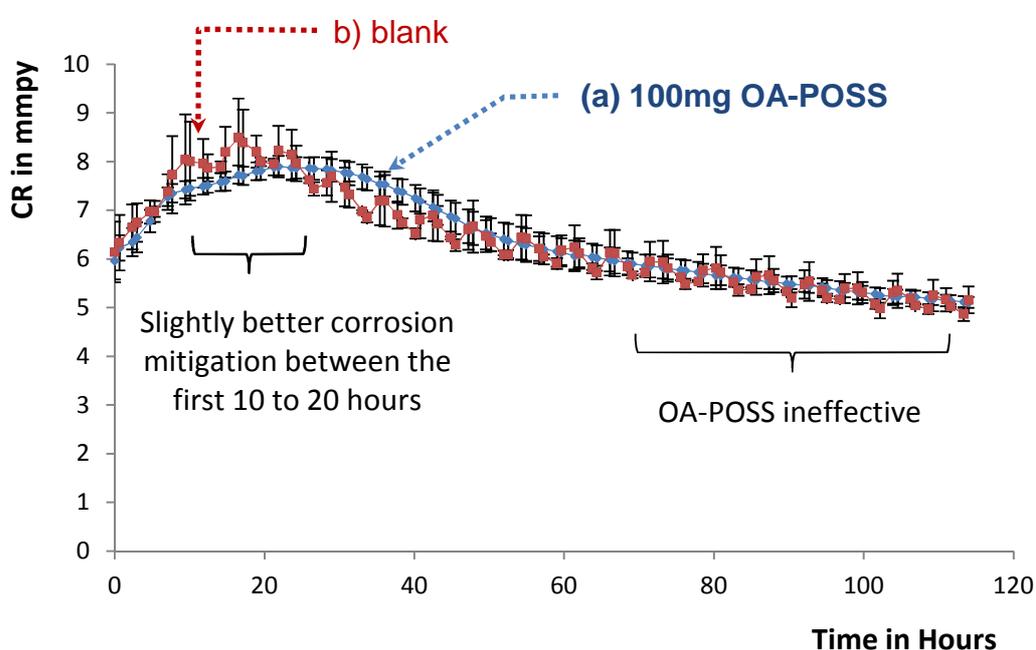
Figure 9-2 CR variation of (a) 100 mg OA-POSS modified system and (b) blank sample both in non-buffered conditions at 60°C, 3.5% NaCl, pH=3.75 and 0.8bar CO_2

The EIS Nyquist plot for the blank test shows a decrease followed by an increase in both the real and imaginary components as seen by following the dotted arrows following the numerical order in Figure 9-3. The real impedance values remained contained below the 70 $\Omega.cm^2$ which explains the very high corrosion rates $\geq$ 5mmpy. The system remains capacitive in nature for the total test duration.
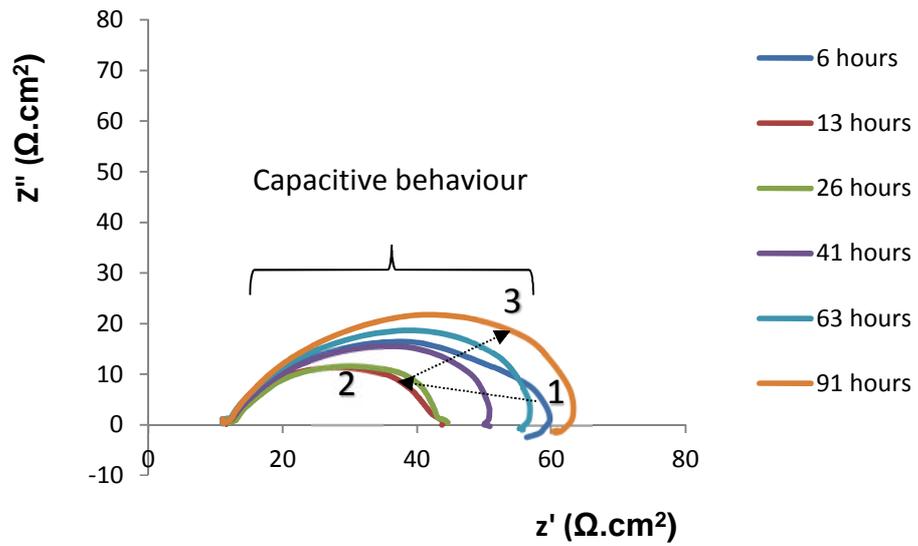
Figure 9-3 Nyquist plot for blank tests at 60°C, 3.5% NaCl, pH=3.75 and 0.8bar CO_2 constituted mainly of capacitive loops

When 100 mg OA-POSS is added, the resulting behaviour of the real impedance appear to be slightly more scattered as shown in Figure 9-4, especially with the higher values registered during the first 12 hours and the more exacerbated inductive loop which are more pronounced in the first day and corresponding to the OA-POSS adsorption over the carbon steel.
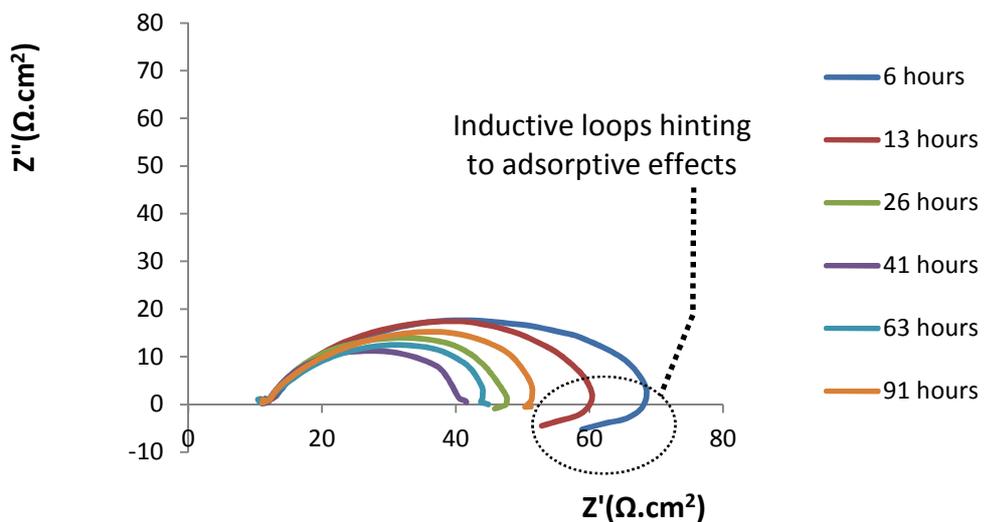
Figure 9-4 Nyquist with 100mg OA-POSS at 60°C, 3.5% NaCl, pH=3.75 and 0.8bar CO_2 showing inductive loops in the dotted area

The blank and OA-POSS modified systems show time constants that are constrained between 10 to 20 Hz and corresponding to the EDL establishment and OA-POSS adsorption as seen on the Bode plot in Figure 9-5. While the specimen grown in blank conditions show a time constant closer to 10 Hz, the X65 samples in contact with OA-POSS treated solutions show a time constant which is more shifted towards slightly higher values reaching 20 Hz at times.

(a) Blank
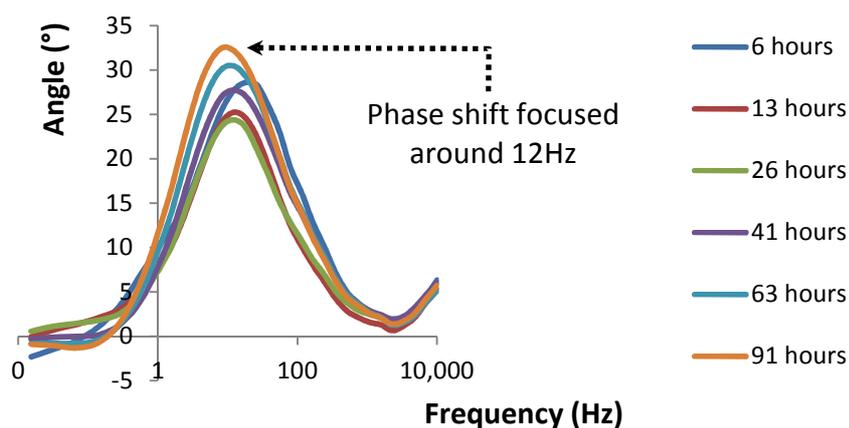
(b) 100 mg OA-POSS
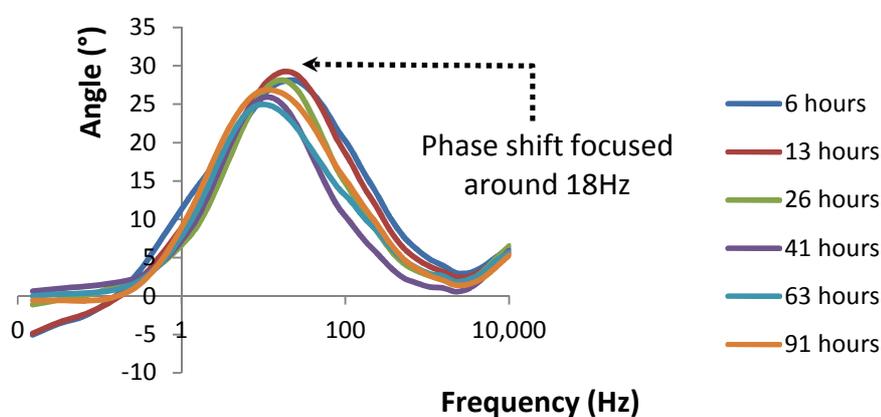
Figure 9-5 Bode plot for (a) blank and (b) OA-POSS modified systems at 60°C, 3.5% NaCl, pH=3.75 and 0.8bar CO_2 showing current phase shifts centred around 12 Hz and 18Hz respectively

9.2 Tests ran in mild acidic conditions at a pH of 5

9.2.1 Electrochemical behaviour at pH5

The effect of OA-POSS on the corrosion rates seems a little more apparent at a pH of 5 as seen in Figure 9-6, especially during the first 20 hours where the blank tests show a corrosion rate higher than 6 mmpy while the OA-POSS treated brine lead to X65 samples having corrosion rates lower than 5mmpy. Both systems seem to be converging towards a steady state where the corrosion rates are averaging 4mmpy after 100 hours of test duration.
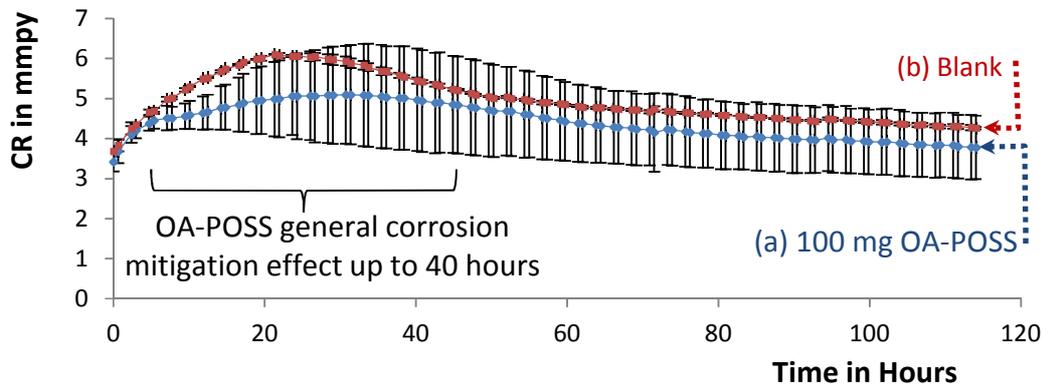
Figure 9-6 CR variation of (a) 100 mg OA-POSS modified sample and (b) blank sample at 60°C, 3.5% NaCl, pH=5 and 0.8bar CO_2

EIS Nyquist data shows no progressive evolution in the real impedance values as seen in Figure 9-7. The imaginary absolute values are 10 $\Omega.cm^2$ higher when compared to an unbuffered test at pH 3.75 and reach 30 $\Omega.cm^2$.
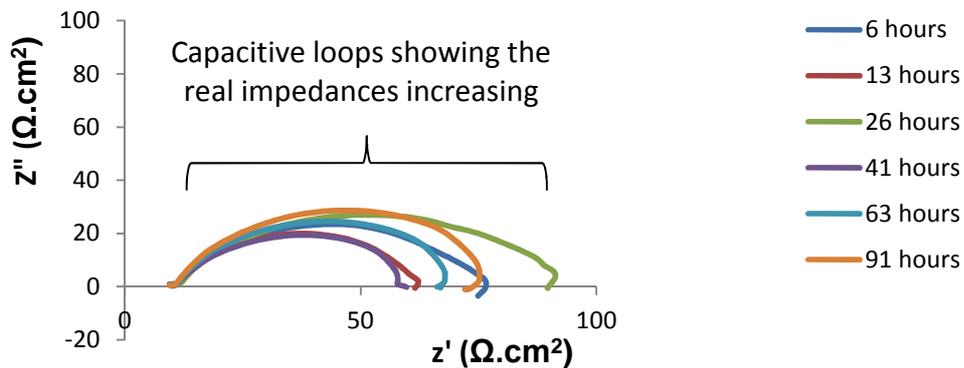
Figure 9-7 Nyquist plot for blank tests at 60°C, 3.5% NaCl, pH=5 and 0.8bar CO_2 showing mainly a capacitive evolution for the test duration

Similar results are extracted from the Nyquist graph at a pH of 5 even when 100mg of OA-POSS are added as per Figure 9-8. As usual the first impedance registered show higher values when OA-POSS is added and reaches 85 $\Omega.cm^2$ versus 60 $\Omega.cm^2$ for the test ran in blank conditions.
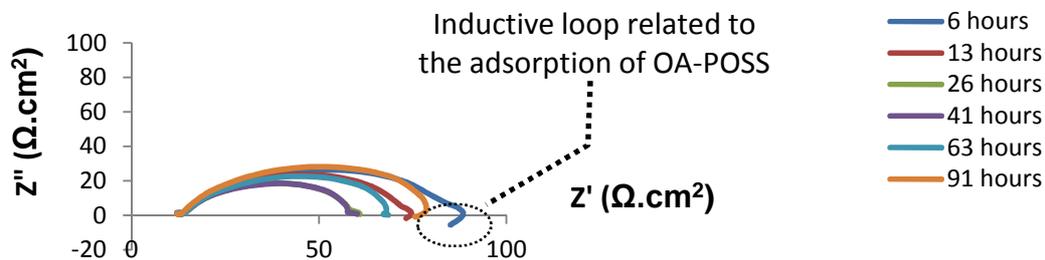
Figure 9-8 Nyquist plot with 100mg OA-POSS at 60°C, 3.5% NaCl, pH=5 and 0.8bar CO_2 showing adsorption of OA-POSS during the first hours

The phase shifts or angle values registered at pH 5 are higher than the ones computed at pH 3.75 which means that the capacitive behaviour is more exacerbated in these conditions as seen in Figure 9-9.

(a) Blank
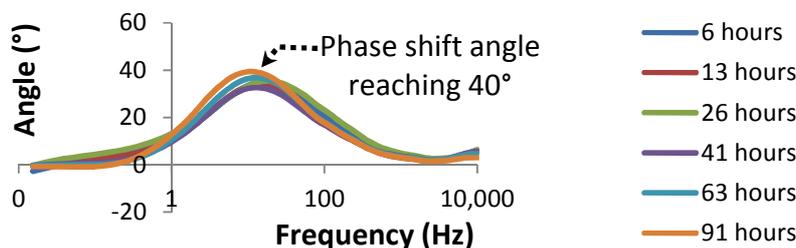
(b) 100 mg OA-POSS
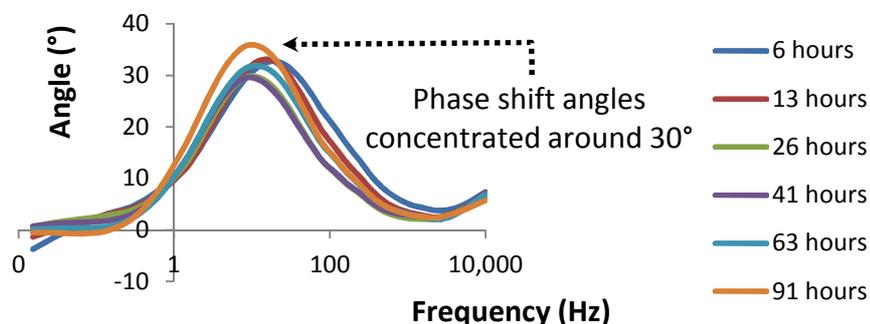
Figure 9-9 Bode plot for (a) tests ran without OA-POSS showing a more capacitive behaviour due to the higher value in the phase shift and (b) tests ran with OA-POSS added to the brine at 60°C, 3.5% NaCl, pH=5 and 0.8bar CO_2

As discussed in section 9.1, there seems to be solely one time constant in both blank and OA-POSS modified systems at pH 5 which means that the formation of any iron carbonate layer is not dominant.

9.2.2 XRD diffraction pattern for tests ran at pH5

When the pH was dropped to a value around 5, it appears that it was very hard to form iron carbonate crystals even though some of the $FeCO_3$ representative Miller indices [110] and [113] were slightly apparent when 100 mg OA-POSS was added to the test solution as seen in Figure 9-10.
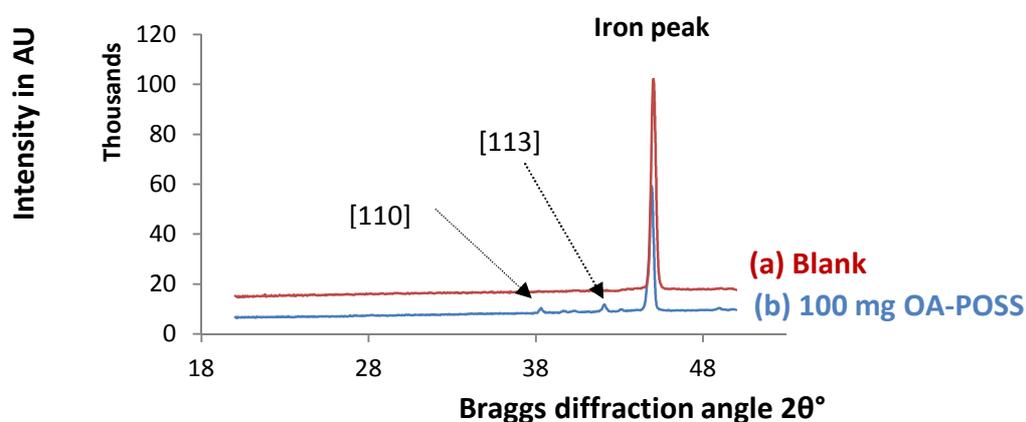
Figure 9-10 XRD diffraction pattern for a test with (a) blank and (b) 100 mg OA-POSS enriched solution [pH 5, 60°C, 3.5% NaCl, 0.8bar CO_2, 98 hours]

The two plots with 0 and 100mg OA-POSS were also separated for more clarity where the background have been subtracted and replaced as per Figure 9-11 and Figure 9-12.
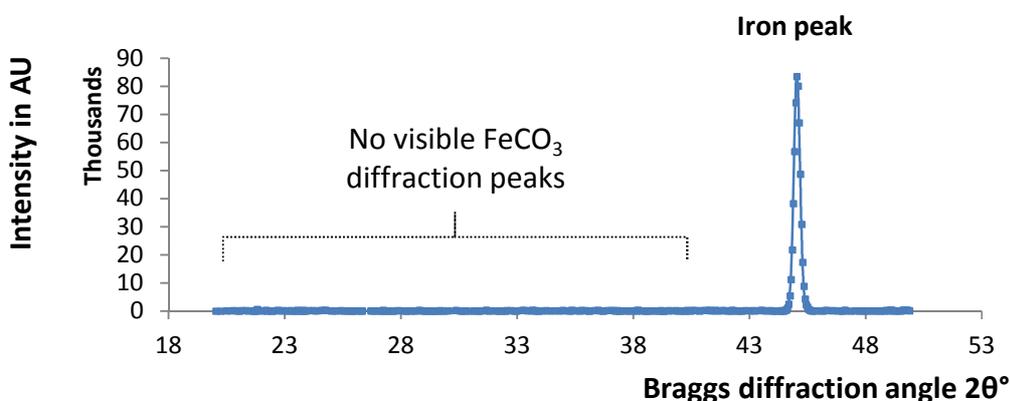
Figure 9-11 XRD diffraction pattern for a blank test [pH 5, 60°C, 3.5% NaCl, 0.8bar CO_2, 98 hours]
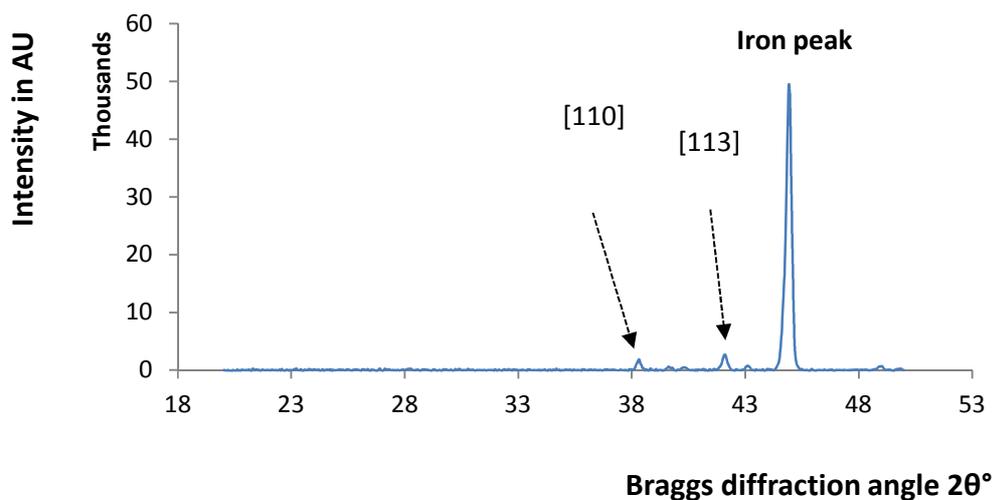
Figure 9-12 XRD diffraction pattern for a X65 sample subjected to 100 mg OA-POSS [pH 5, 60°C, 3.5% NaCl, 0.8bar CO_2, 98 hours]

The fact that the usually dominant [104] Miller index did not show could hint to the fact that in these particular conditions, the nanofiller is enhancing a unidirectional growth of the iron carbonate layer in the less abundant conformations. Moreover when compared to the corresponding corrosion rates variations depicted in Figure 9-6, it seems that these peaks could correspond to crystals that started forming in the first 20 hours before the OA-POSS siloxane O-Si-O group lysis occurred as expected at such low pH values.

9.2.3 SEM showing the corrosion layers grown at pH5

9.2.3.1 Micrographs for blank tests done at a pH equal to 5

When enough sodium hydrogen bicarbonate is added to the test solution in order to increase the pH from its unbuffered value of 3.75 to a higher value equal to 5, the micrographs as depicted in Figure 9-13 show an amorphous 3D layered structure which is non-protective and with a total absence of any iron carbonate as corroborated earlier by the XRD diffraction pattern in Figure 9-11 and the electrochemistry corrosion rate variation corresponding to the blank sample and shown in Figure 9-6.

The film appears to be very porous with pore diameters in the micrometre scale which explains the lack of protection and ease of access of water and other corrosion reactants to the steel surface.

(a)

5μm wide pores
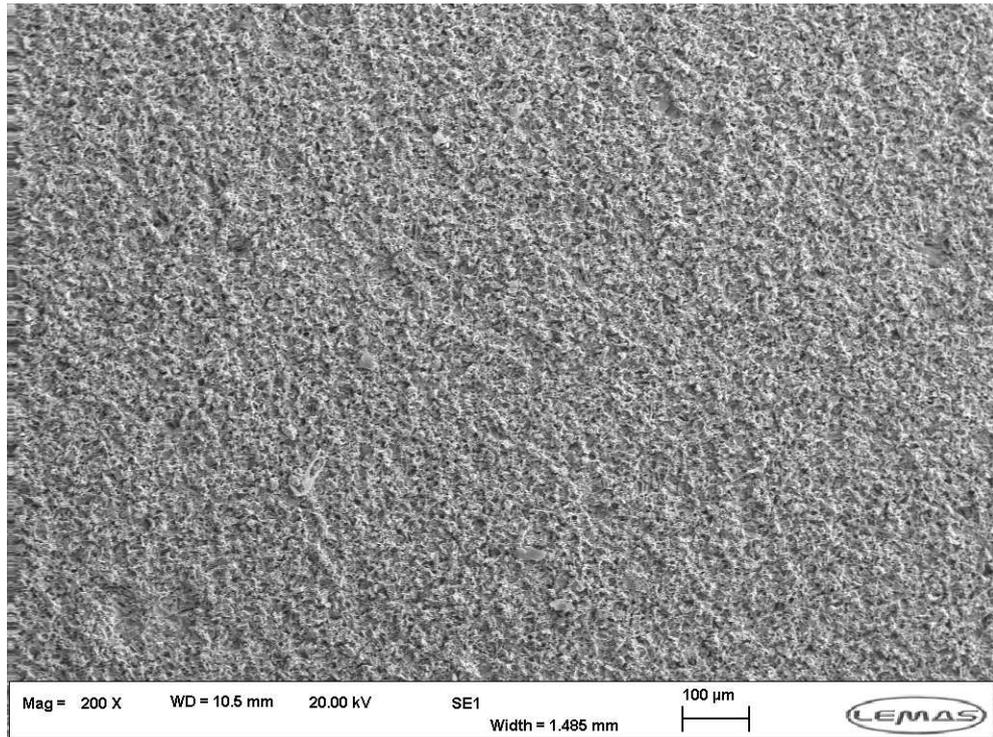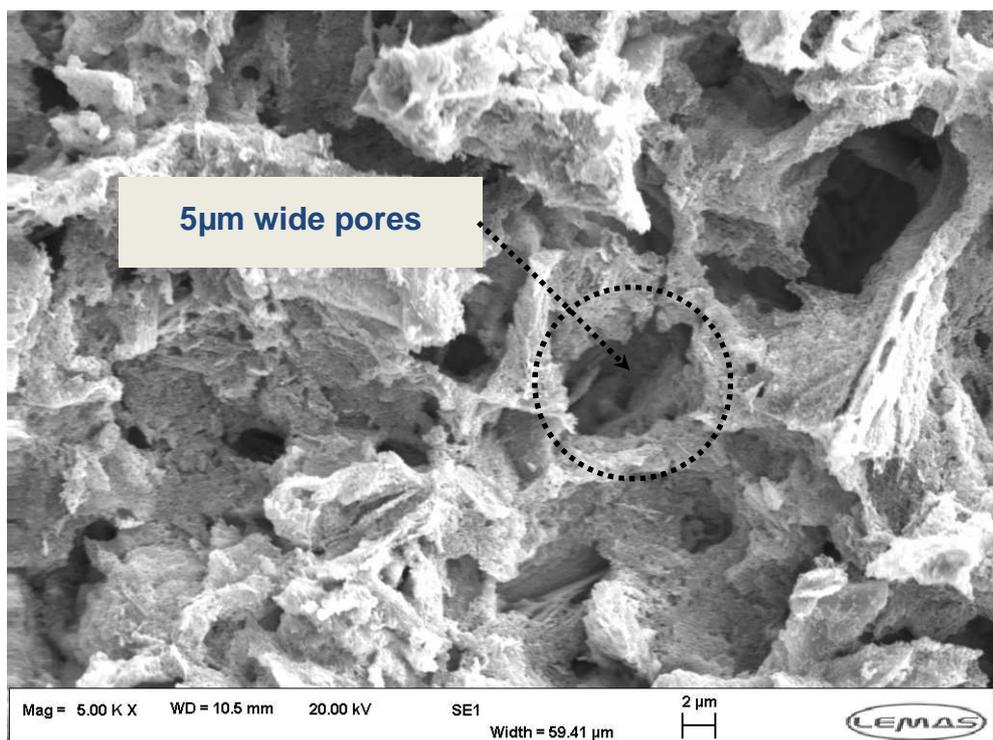
(b)

Figure 9-13 SEM micrographs topography view of X65 samples when 0mg OA-POSS are added to the test solution at various magnifications as seen on the corresponding scale bars [pH=5, 60°C, 3.5% NaCl, 0.8bar CO_2, 118 hours] showing (a) the general surface coverage of the amorphous and porous corrosion layer and (b) a zoom on the corrosion layer openings

9.2.3.2 Effect of 100mg OA-POSS at pH equal to 5

Even though the corrosion rate does not show a drastic drop in these running conditions as seen in Figure 9-6, the XRD pattern shown in Figure 9-12 hint to a start of iron carbonate formation with both peaks corresponding to $FeCO_3$ Miller indices [110] and [113] starting to originate. In conjunction, the micrographs corresponding to these tests shown in Figure 9-14 appear with a totally different topography to the tests ran in the same conditions but without the addition of the silsesquioxane based nanofillers.

The registered micrographs show a corrosion layer which looks like a cracked mud that could be linked to a chemical dehydration. As such Figure 9-14b shows locations that have been subjected to a cohesive delamination of a part of the corrosion layer showing some potentially hidden iron carbonate crystals highlighted in red. The outer layer cracking due to dehydration is a common observation and Sun et al.[365] have made similar comments while studying corrosion layers formed in a mixture of CO_2 and H_2S corrosive environment.

The assumption is that at the start of the test, the OA-POSS was able to help nucleate a certain quantity of iron carbonate crystals but after its lysis due to the pH conditions, an overlapping amorphous layer covered the underlying dispersed crystalline entities and ended up being the dominant phase. Such non-crystalline or even amorphous iron carbonate corrosion layers are referenced in the literature.[253] These corrosion layers are often referred to as "amorphous" and shown to establish on the steel surface and potentially within the voids of the iron carbide layer as discussed by Xia et al.[366] while studying the pitting corrosion of carbon steel in CO_2-containing NaCl brine.

Further EDX analysis is required to confirm if the amorphous surface layer could be assumed to be amorphous ferrous carbonate and these are discussed in section 9.2.4.

Additional XRD diffraction patterns can be used to confirm the presence of iron carbonate. Recent studies have confirmed the possibility of iron carbonate crystal nucleation within an amorphous surface layer as the work published by Ingham et al.[367] with relation to the early stages of $FeCO_3$ crystal nucleation and other carbonates from amorphous precursors. Hence, precipitation of other carbonates such as $CaCO_3$ is known to involve polymer like pre-nucleation clusters and the formation of amorphous phases in solution as precursors to crystalline formation.

(a)

Potential FeCO₃ crystals in sublayer
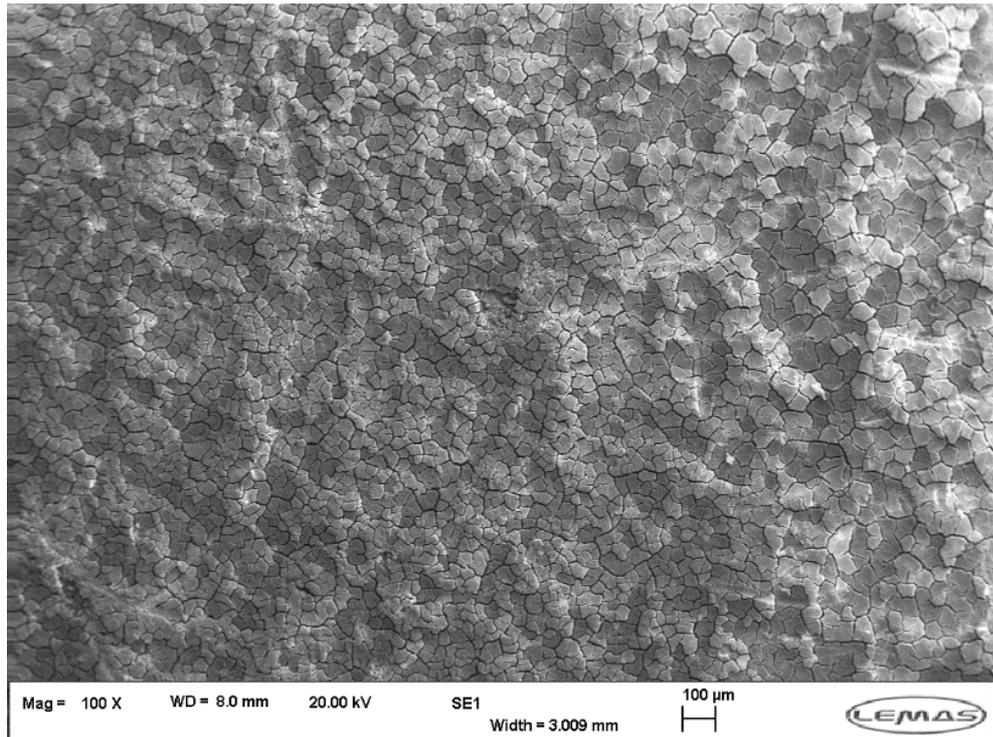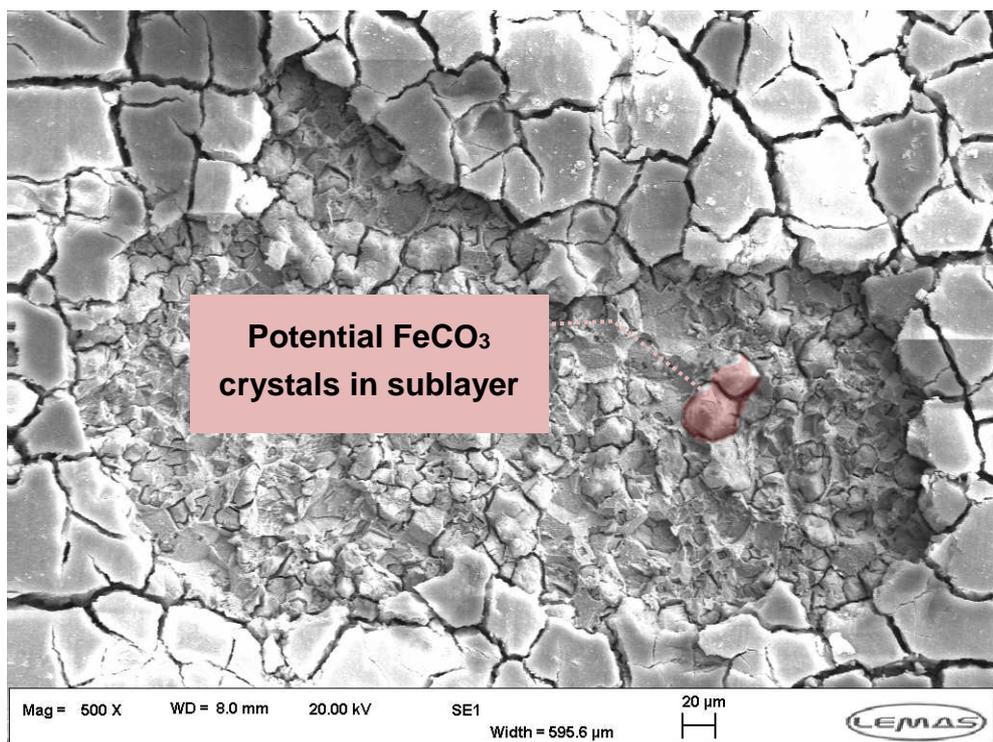
(b)

Figure 9-14 SEM micrographs topography view of X65 samples when 100mg OA-POSS are added to the test solution at various magnifications at as seen on the corresponding scale bars [pH=5, 60°C,3.5% NaCl, 118 hours] showing (a) the general corrosion layer as a mud-cracked covering surface and (b) a zoom on a cohesive delaminated area with what appears to be FeCO₃ scattered crystals highlighted in red

9.2.4 EDX analysis on corrosion layers grown at a pH equal to 5

9.2.4.1 Blank samples at pH equal to 5

EDX ran on samples tested at a pH equal to 5 showed mainly iron, manganese and carbon from the K electron shell and the gold used for coating the sample from the M shell. The oxygen element was not spotted which suppose that no oxygen containing corrosion layers were present over the steel surface as per Figure 9-15 and Figure 9-16.

(a)

(b)

(c)

(d)

(e)
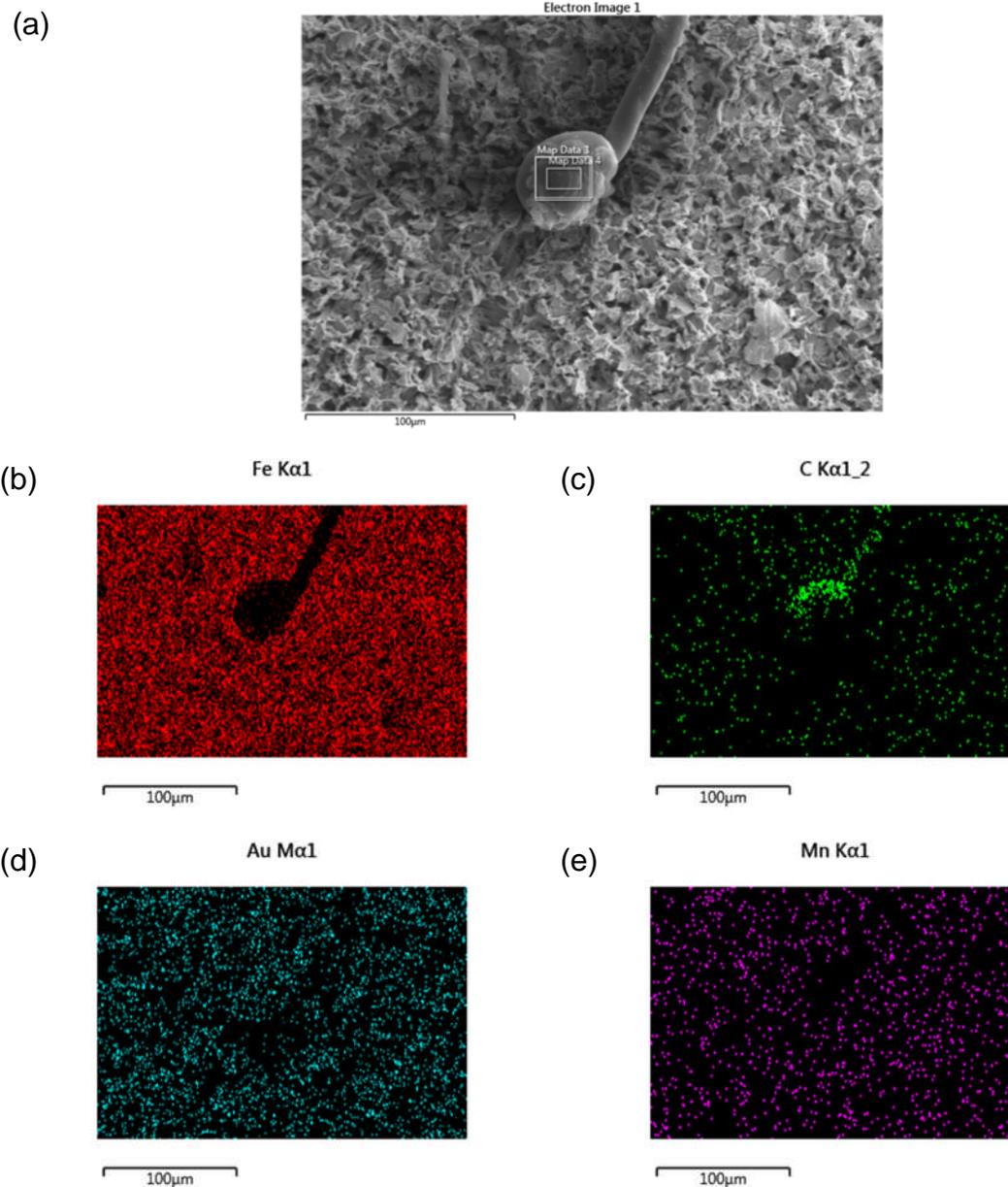
Figure 9-15 EDX map of corrosion layer grown at 60°C, pH 5, 3.5% NaCl, 0.8bar CO_2, 0mg OA-POSS with (a) SE micrograph (b) Iron-Fe (c) Carbon-C (d) Gold-Au and (e) Manganese-Mn

(a)

(b)

(c)
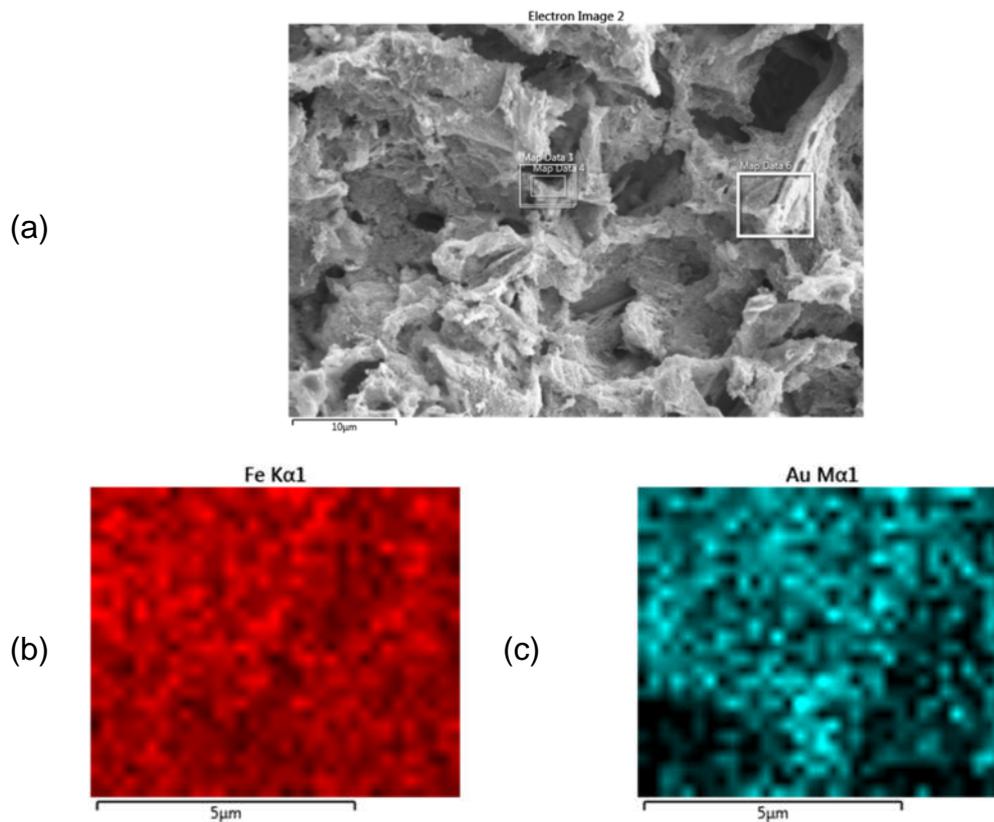
Figure 9-16 EDX map of corrosion layer grown at 60°C, pH 5, 3.5% NaCl, 0.8bar CO_2, 0mg OA-POSS with (a) Higher magnification SE micrograph (b) Iron-Fe and (c) Gold-Au

Thus, at a pH of 5, the EDX mapping results showed mainly iron with some scattered carbon in the corrosion film as depicted in Figure 9-15 while only the iron and gold elements were detected when zooming on the amorphous layer as per Figure 9-16. These results suggest the absence of iron carbonate films due to a minimum content in this amorphous corrosion layer of both carbon and oxygen elements. The artefact in the middle of Figure 9-15 is just due to the presence of a surface contaminant that has most-likely adsorbed during the surface analysis sample preparation step.

9.2.4.2 Samples subjected to 100mg OA-POSS at pH equal to 5

With regard to the corrosion layers that grew over the carbon steel when 100mg OA-POSS were added within the brine chemistry, a single point EDX analysis of the area termed spectrum 1 shown in Figure 9-17 highlights the presence of both iron, carbon and oxygen with their respective weight percentage summarised in Table 9-1. These elements were also spotted when an EDX mapping undertaken at the same conditions over the mud-like corrosion top layer was undertaken and the results are shown in Figure 9-18.
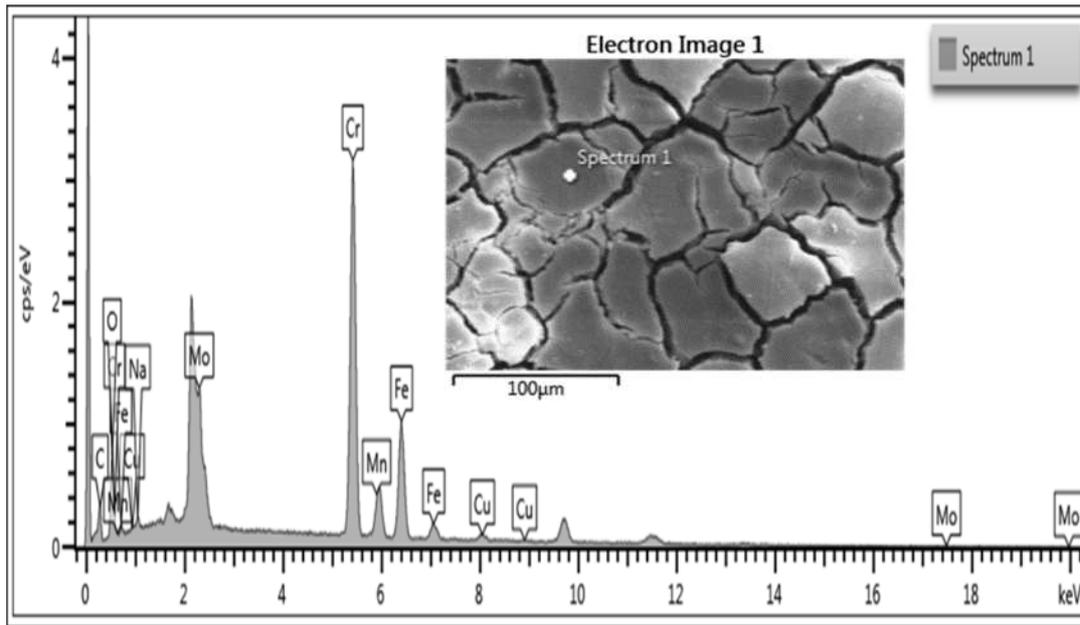
Figure 9-17 Single point EDX 1 of corrosion layer grown at 60°C, pH 5, 3.5% NaCl, 100mg OA-POSS showing the SE micrograph within the EDX single point spectre

Table 9-1 Single point spot 1 weight percentage elemental distribution of corrosion layer grown at 60°C, pH 5, 3.5% NaCl,0.8bar CO_2, 100mg OA-POSS

Element	Atomic %	wt%	wt% sigma
C (Carbon)	**40.39**	**16.01**	0.69
O (Oxygen)	**20.89**	**11.04**	0.30
Na	1.12	0.85	0.14
Cr	22.40	38.45	0.43
Mn	0.43	0.78	0.16
Fe (Iron)	**9.87**	**18.20**	0.27
Cu	0.79	1.66	0.18
Mo	4.11	13.00	0.40
Total:	100.00	100.00	

As described in section 6.4.1, the EDX data should be treated with utmost care and the values such as the chromium content which exceeds the chemical composition of the material studied as shown in Table 5-1 should be disregarded.
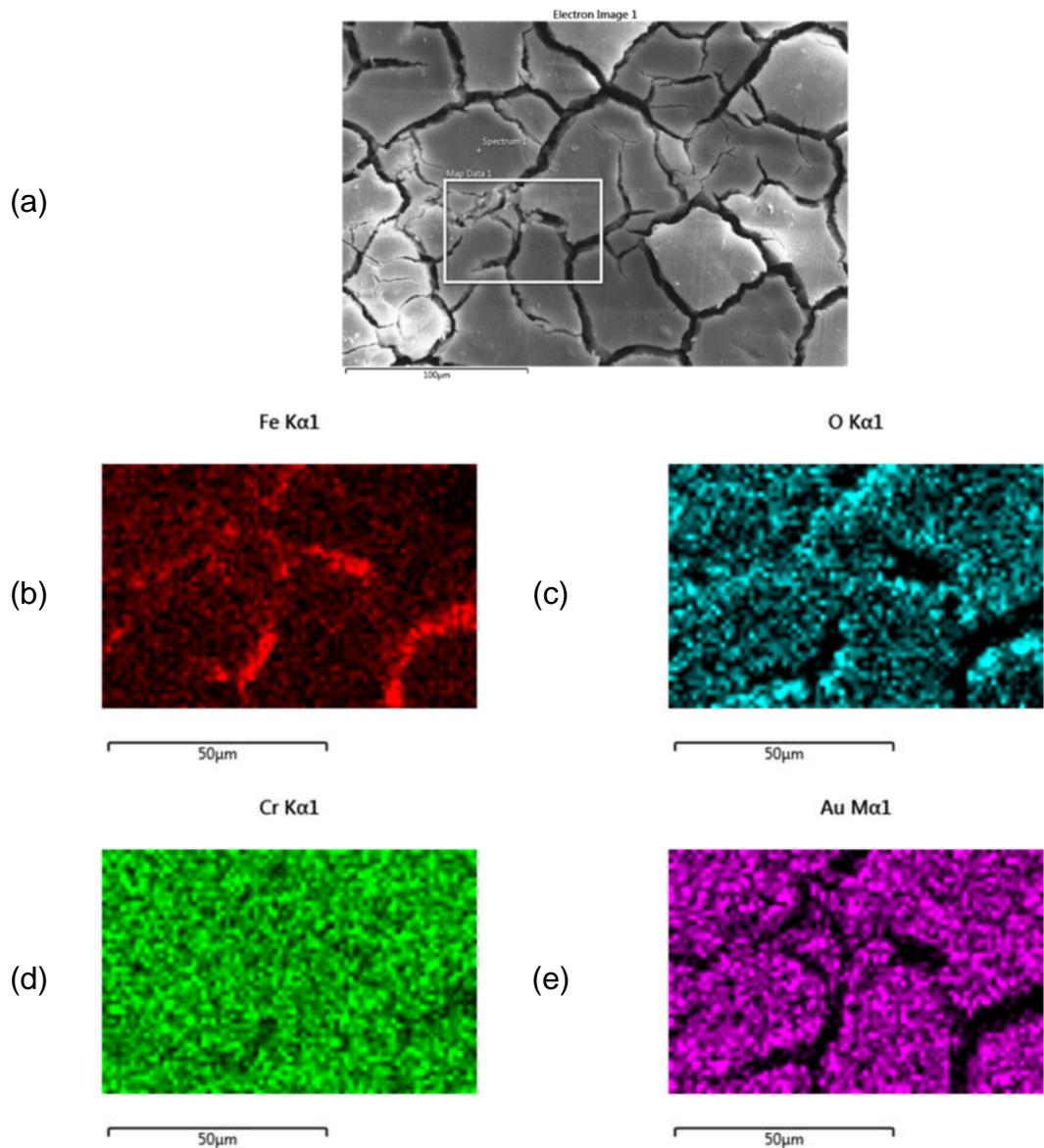
Figure 9-18 EDX map of corrosion layer grown at 60°C, pH 5, 3.5% NaCl, with 100mg OA-POSS added within the brine solution showing (a) SE micrograph, (b) Iron-Fe, (c) Oxygen-O, (d) Chromium (Cr) and (e) Gold-Au

Results from Figure 9-18 suggest the absence of carbon in some parts of the porous corrosion layers which rules out the presence of both iron carbonate and iron carbide in some regions. It is not clear why electrons returning to the K chromium electron shell were dominant and not the ones corresponding to the manganese element when OA-POSS was added.

An additional single point EDX was attempted in an area where the corrosion film showed cohesive delamination and results are shown on two locations: spectrum 4 in Figure 9-19 and Figure 9-20.
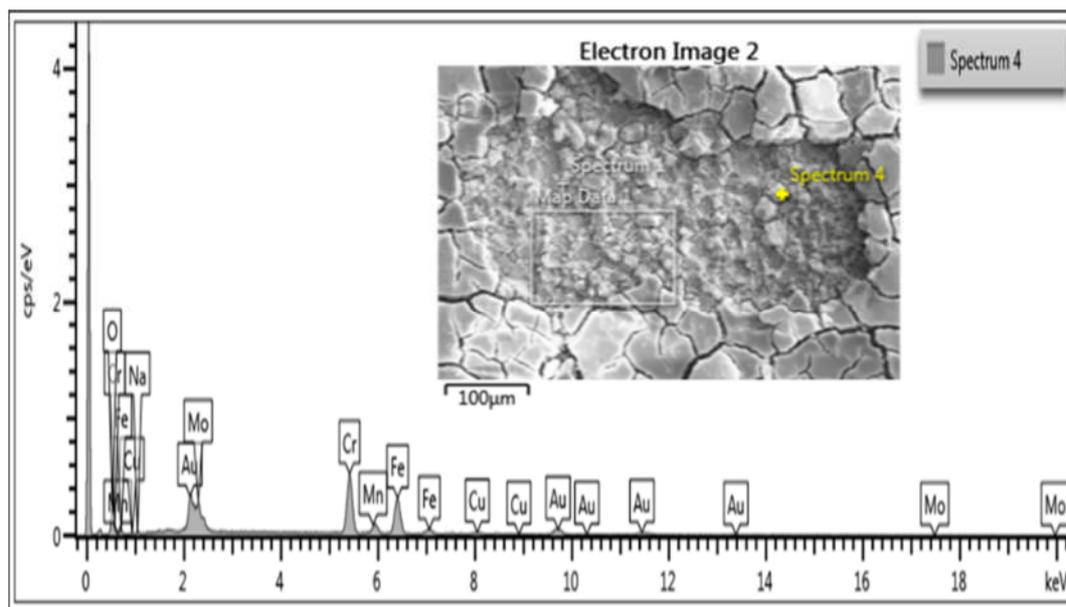
Figure 9-19 Single point EDX 1 of a cohesively failed corrosion layer grown at 60°C, pH 5, 3.5% NaCl, 100mg OA-POSS showing the SE micrograph within the EDX single point spectre

Table 9-2 Single point spot 1 weight % elemental distribution of a cohesively failed corrosion layer grown at 60°C, pH 5, 3.5% NaCl, 100mg OA-POSS

Element	wt%	wt% Sigma
O	**14.61**	**0.57**
Fe	**30.83**	**0.63**
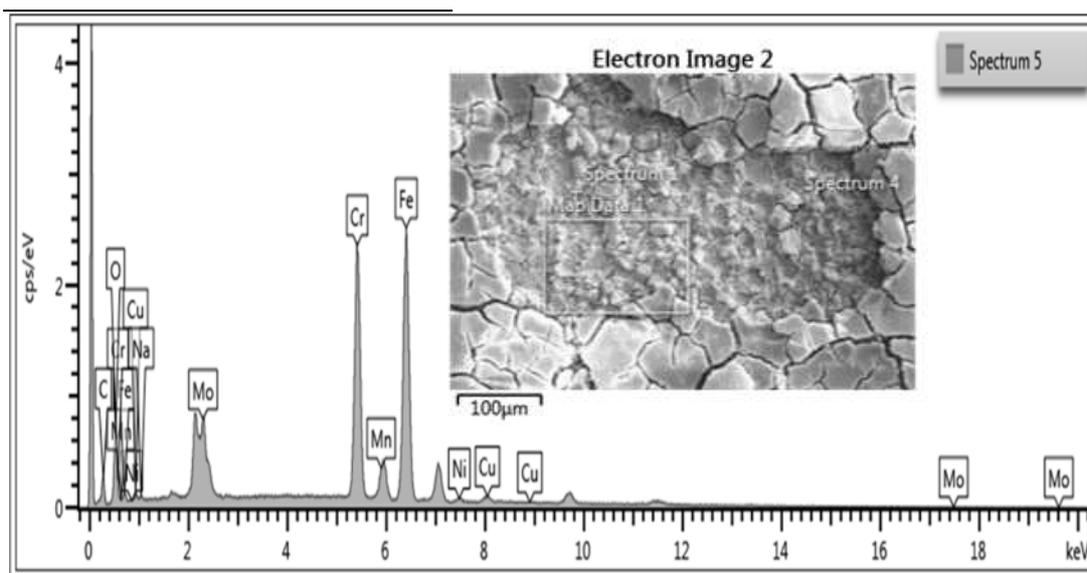
Figure 9-20 Single point EDX 2 of a cohesively failed corrosion layer grown at 60°C, pH 5, 3.5% NaCl, 100mg OA-POSS showing the SE micrograph within the EDX single point spectre

268

Table 9-3 Single point spot 2 weight percentage elemental distribution of a cohesively failed corrosion layer grown at 60°C, pH 5, 3.5% NaCl, 100mg OA-POSS

Element	Atomic %
C	35.54
O	18.26
Fe	24.64

It was assumed earlier from the XRD data in section 9.2.2, that the initial stages of $FeCO_3$ growth were established; combining the results from both Table 9-2 and Table 9-3, it can be postulated that the iron, carbon and oxygen atoms that form the iron carbonate are present. The data collected on a higher magnification micrograph as per Figure 9-21 and Table 9-4 consolidate such assumption.
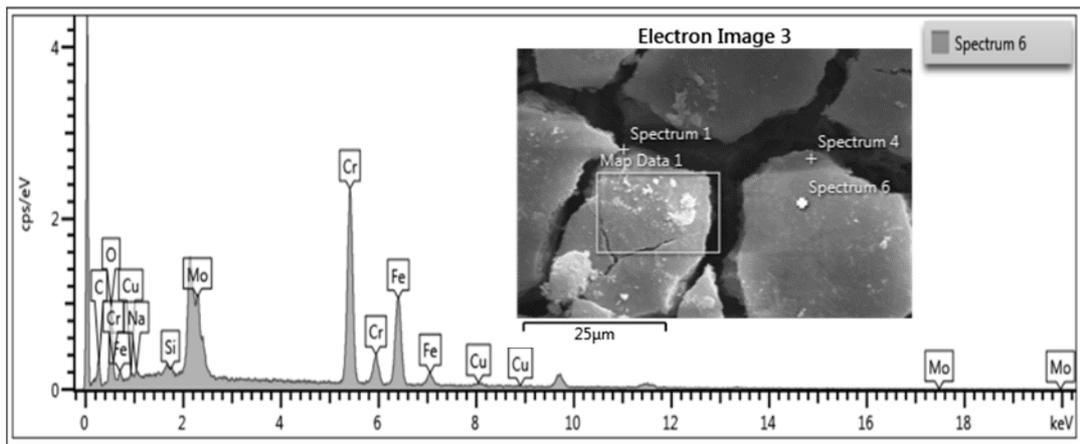
Figure 9-21 Single point EDX (spectrum 6) of a highly magnified area of the corrosion layer grown at 60°C, pH 5, 3.5% NaCl, 100mg OA-POSS showing the SE micrograph within the EDX single point spectre

Table 9-4 Single point weight percentage elemental distribution of a highly magnified area of the corrosion layer grown at 60°C, pH 5, 3.5% NaCl, 100mg OA-POSS

Element	Atomic %
C	39.75
O	27.19
Fe	10.88

9.3 Tests ran in basic conditions at a pH of 7

9.3.1 Electrochemical behaviour at pH7

Both systems where OA-POSS was administered or not show a very quick decrease in the CR even though the tests where the nanofiller has been added show a slightly earlier shift towards lower corrosion rates as seen in Figure 9-22 between the first 10 to 15 hours.
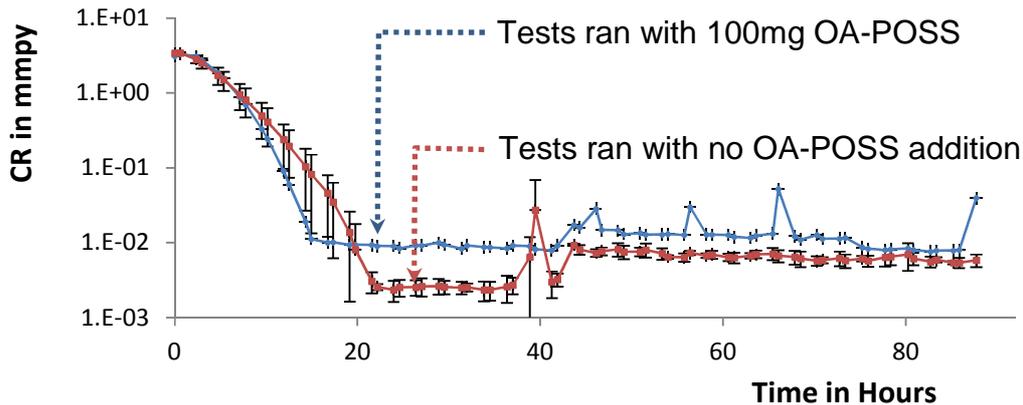
Figure 9-22 CR variation of (a) 100 mg OA-POSS modified sample and (b) blank sample at 60°C, 3.5% NaCl, pH=7 and 0.8bar CO_2

The EIS data show a very fast increase in both the real (Z') and imaginary (Z") parts which is explained by the formation of the $FeCO_3$ protective layer which increases the charge transfer resistance of the system as seen in Figure 9-23. The capacitive behaviour is seen to be evolving towards a diffusion barrier system since the semi-circles are quickly replaced by non-closed arcs which are closer to equivalent circuits where a Warburg resistance can be introduced and representative of such diffusion-limited systems characterised by the establishment of corrosion layers.
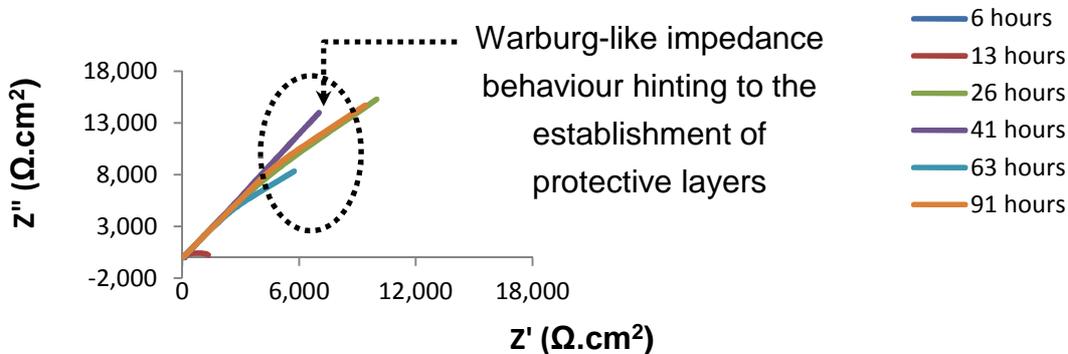
Figure 9-23 Nyquist plot for blank tests at 60°C, 3.5% NaCl, pH=7 and 0.8bar CO_2

Similar trend is observed when 100mg OA-POSS are added as per Figure 9-24; the inductive loop in this scenario is more eminent in the blank conditions in opposition to the previously studied unbuffered and mildly acidic systems. Both real and imaginary components are slightly smaller when OA-POSS is present as compared to a naturally growing $FeCO_3$ corrosion layer.
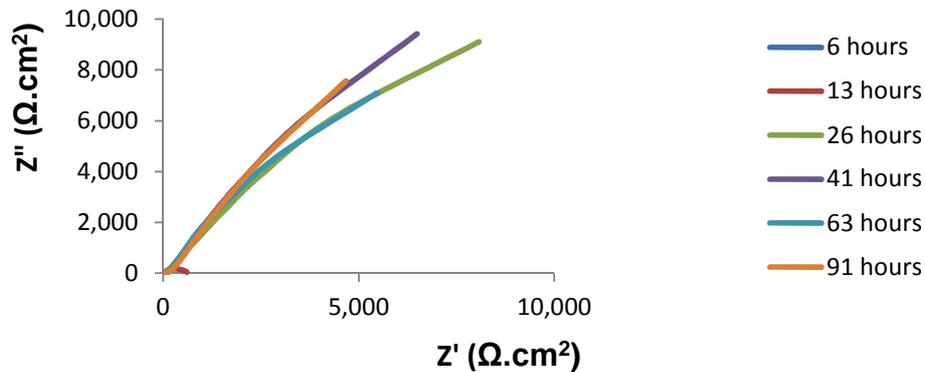
Figure 9-24 Nyquist with 100mg OA-POSS dissolved in the brine chemistry at 60°C, 3.5% NaCl, pH=7 and 0.8bar CO_2

Both blank and OA-POSS modified systems depicted in Figure 9-25 show a second time constant between 10 mHz and 100 mHz on the Bode plot which is characteristic of the evolution of the iron carbonate film.

(a) Blank
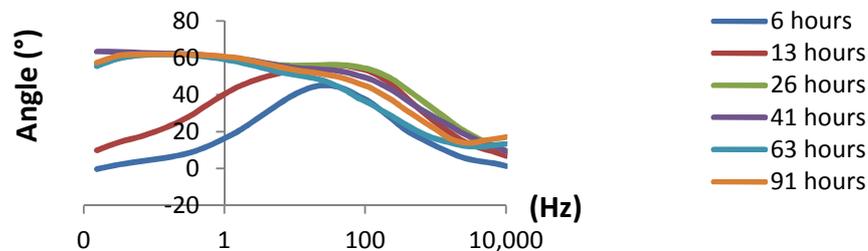
(b) 100 mg OA-POSS
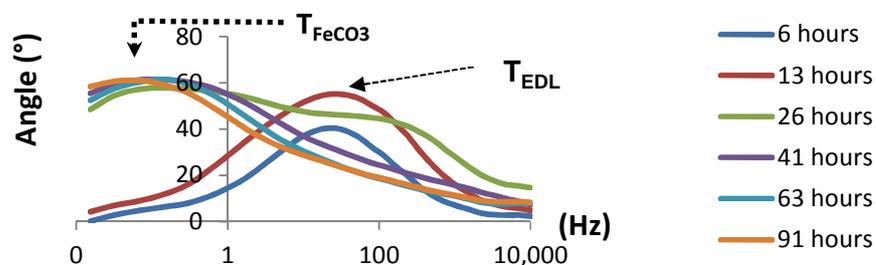
Figure 9-25 Bode plot for (a) blank and (b) OA-POSS modified systems 60°C, 3.5% NaCl, pH=7 and 0.8bar CO_2

The other time constant observed above 1 Hz is representative of adsorbed species such as anions and cations constituting the EDL or the OA-POSS interacting with the steel surface.

9.3.2 XRD diffraction pattern for tests ran at pH7

When the solution pH was buffered to a value of 7, it appeared that an OA-POSS loading as high as 100 mg has no major effect on the film density in these basic conditions. In fact, when extracted from the diffraction pattern shown in Figure 9-26, the ratio between the $FeCO_3$ [104] Miller index and the iron [110] Miller index seems 50% higher for OA-POSS enriched tests ($FeCO_3$/Fe = 1.46) versus the blank experiments ($FeCO_3$/Fe = 1.04).
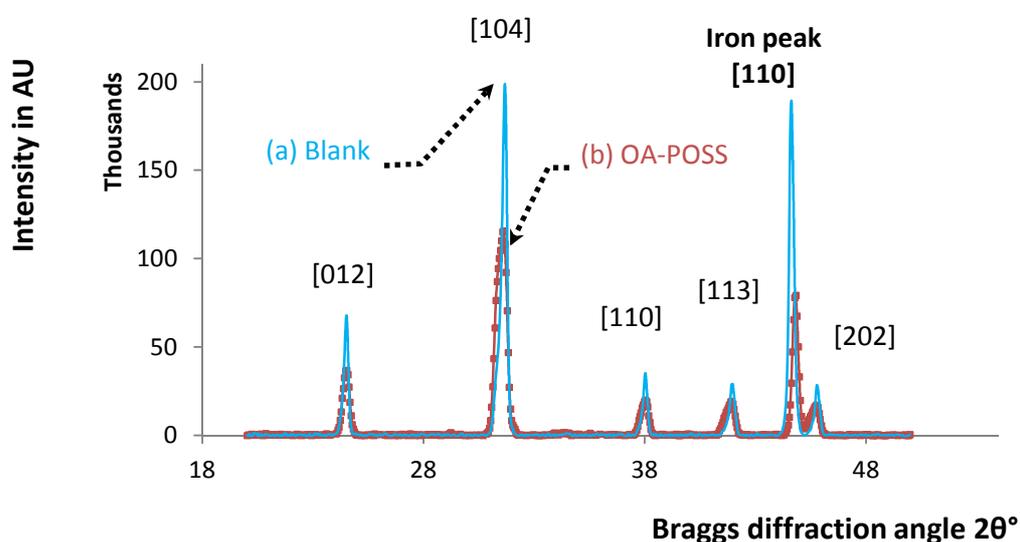
Figure 9-26 XRD diffraction pattern for (a) blank (b) 100mg OA-POSS enriched solution [pH 7, 60°C, 3.5% NaCl, 0.8bar CO_2 98 hours]

As such, even though these CR decreased in a similar way, there appears to be higher $FeCO_3$ density in the coupons which have been subjected to the additional silsesquioxane moieties and the micrographs attached in section 9.3.3 confirm this finding.

Although the iron carbonate protective crystals seem to be more abundant when 100mg OA-POSS are dissolved within the brine chemistry, the corrosion rates variations plotted in Figure 9-22 suggest that these additional layers of $FeCO_3$ are not providing any supplementary general corrosion mitigation.

9.3.3 Micrographs for corrosion films grown at pH7

9.3.3.1 Tests at pH of 7 without OA-POSS
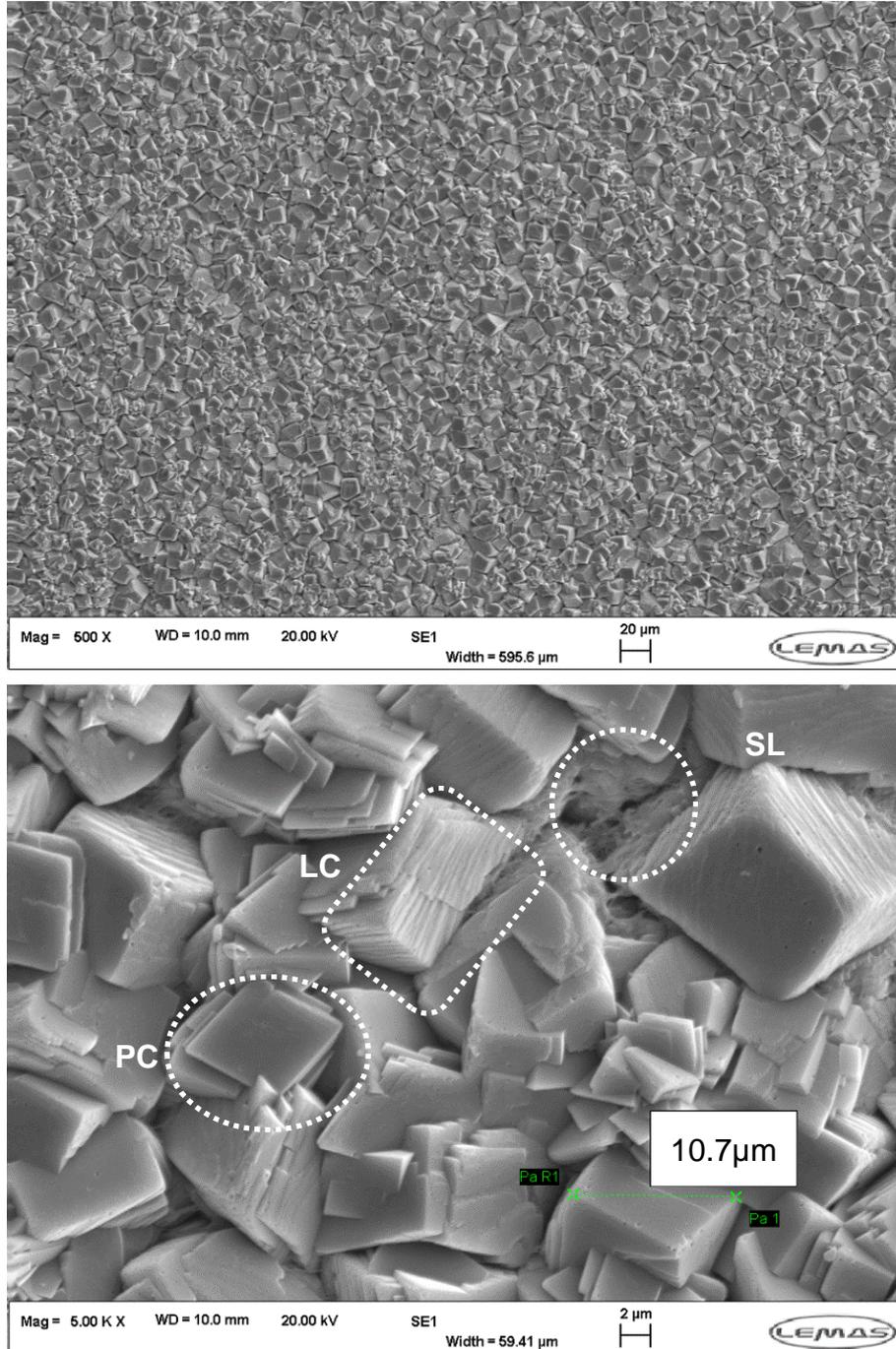
Figure 9-27 SEM micrographs topography view of X65 samples when 0mg OA-POSS are added to the test solution at various magnifications as seen by the corresponding scale bars [pH=7, 60°C,3.5% NaCl,0.8bar CO_2, 98 hours] showing (a) the highly compact and fully-covering $FeCO_3$ crystalline corrosion layer and (b) a zoom on the $FeCO_3$ crystal morphology and dimensions. The dotted areas highlight an underlying sub-layer (SL), interlacing prismatic $FeCO_3$ crystals (PC), and platelet or leaflet-like $FeCO_3$ crystals (LC)

The various top view SEM micrographs shown in Figure 9-27 correspond to the electrochemical data registered in Figure 9-22 and the XRD diffraction pattern shown in Figure 9-26. The scale layer seems to be fully covering the underlying X65 carbon steel substrate with iron carbonate crystals showing small and bigger formations with a platelet like distribution as clearly visible in the higher magnified micrograph in Figure 9-27b.

Thus, crystals as small as 2 μm appears to be growing and protruding from bigger crystals which average width could be estimated to be roughly equal to 10 μm. In general, the majority of the $FeCO_3$ crystals can be qualified as having a cubic or prismatic shape.

The main observation when the pH is raised to a value as high as 7, is that the iron carbonate corrosion layer seems very compact as an exfoliated nanocomposite with leaflet-like $FeCO_3$ crystals almost completely covering the underlying steel. When compared to iron carbonate crystals formed at lower pH values, these crystals seem to be composed of much thinner leaflets which could be assessed from Figure 9-27b to be 20 leaflets per one $FeCO_3$ crystal thus every leaflet is almost 250 nanometres thick.

9.3.3.2 Tests at pH of 7 with OA-POSS

When tests were carried out at the same pH by dissolving 100mg OA-POSS in the brine chemistry, SEM micrographs showed the growth of gigantic iron carbonate crystalline islands protruding above the well-covering crystalline $FeCO_3$ layer as shown in Figure 9-28. These islands were absent when no OA-POSS was added as observed in Figure 9-27 which suggest that the silsesquioxane based nanofiller help the iron carbonate crystal growth.

When looking with higher magnification at the $FeCO_3$ protruding islands as per Figure 9-28b, these appear to be around 150μm in width and formed of an agglomeration of smaller crystals. Although the SEM micrographs only provide 2D information, it appears as though these islands are also around 50 micrometres high if their constituent crystals are accounted for and the size is averaged from the corresponding 20μm scale bar.

One explanation of such statement is that the OA-POSS administered in high quantity (100mg) is readily available at a pH of 7 and keeps adsorbing on the on-growing iron carbonate corrosion layer thus affecting the local chemistry near the buffer area separating the $FeCO_3$ and the brine in a way that it enhances the conditions required for its growth mainly due to surface contact effects and possibly lowering the activation energy.
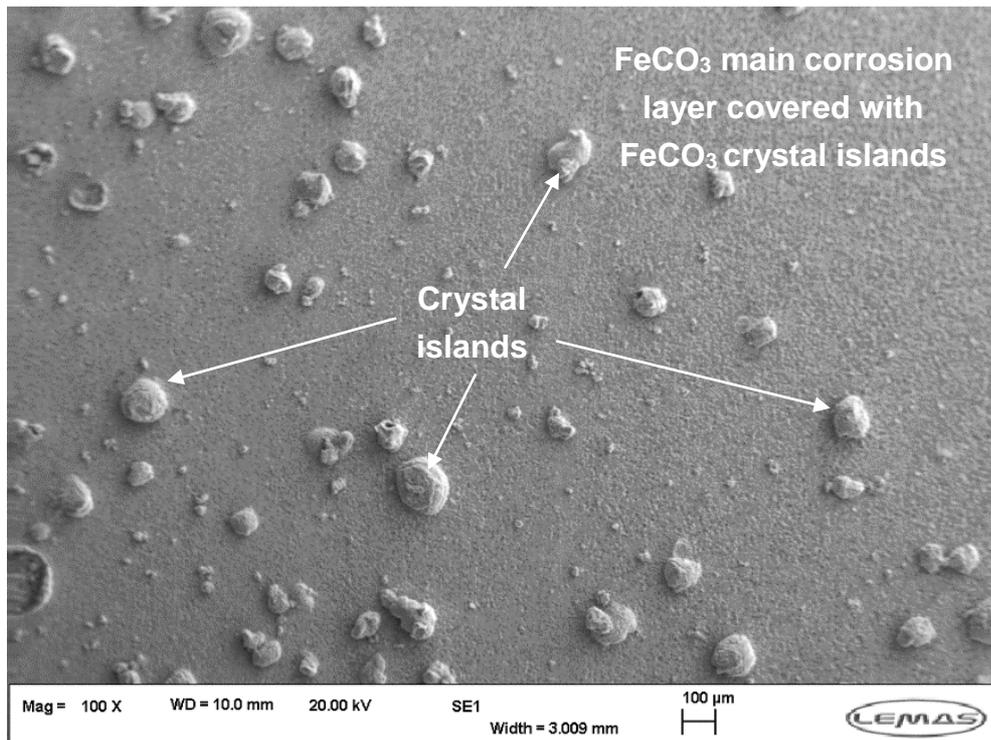
(a)
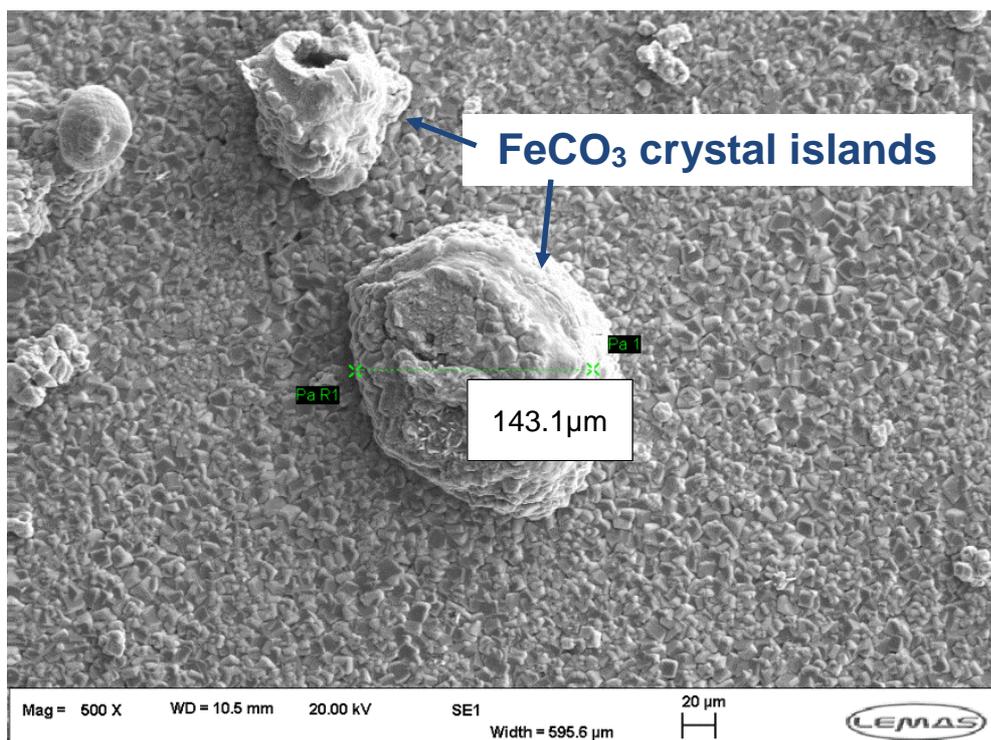
(b)

Figure 9-28 SEM micrographs topography view of X65 samples when 100mg OA-POSS are added to the test solution at various magnifications as seen by the respective scale bars [pH=7, 60°C,3.5% NaCl, 98 hours] showing (a) $FeCO_3$ crystal islands scattered over the $FeCO_3$ main corrosion layer and (b) a zoom on one of these islands showing the excessive crystal growth and dimensions
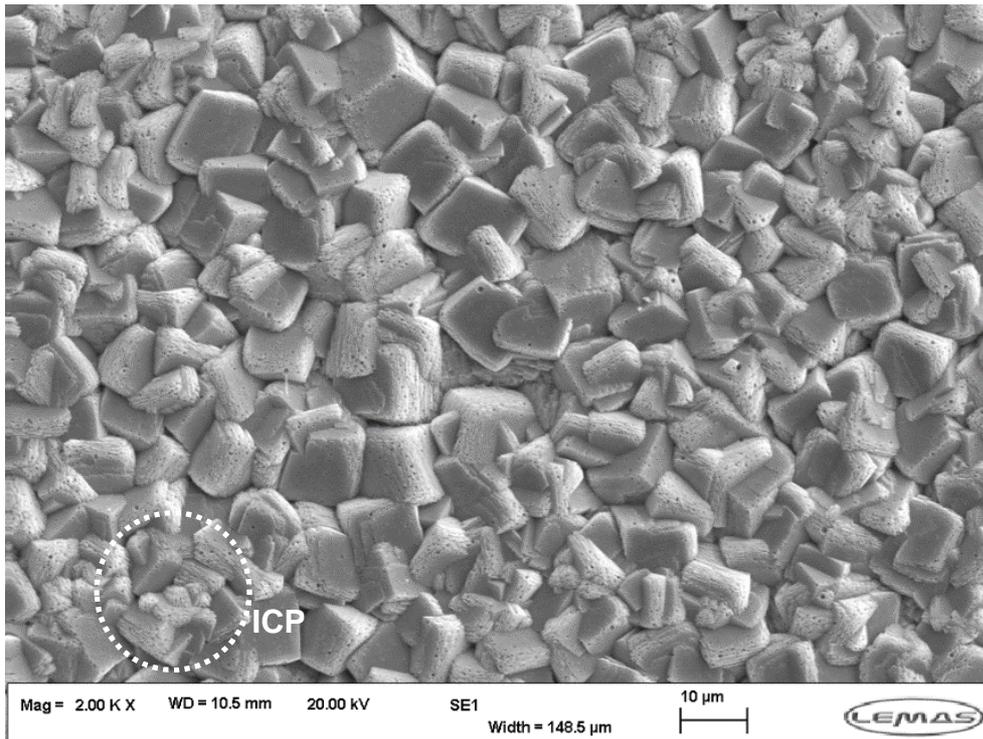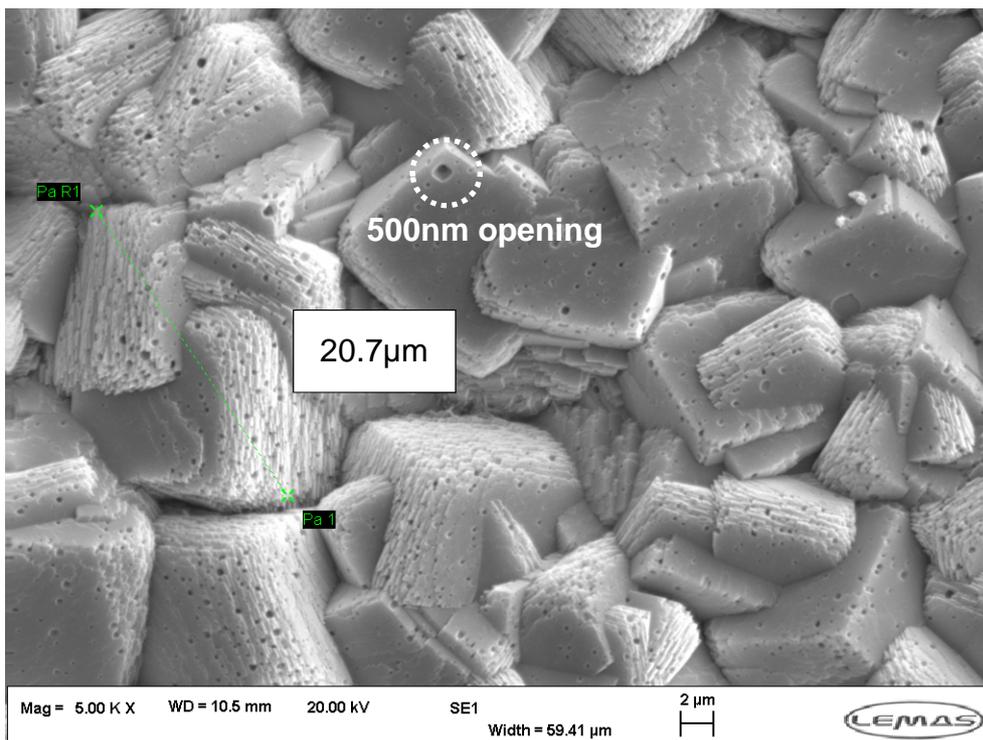
Figure 9-29 SEM micrographs topography view of X65 samples when 100mg OA-POSS are added to the test solution at various magnifications as seen by the respective scale bars [pH=7, 60°C,3.5% NaCl, 98 hours] with a focus on (a) the highly interlaced cubic and prismatic $FeCO_3$ crystals (ICP) and (b) a zoom on the pinholes and rough surface of some $FeCO_3$ crystals showing dimensions

The FeCO$_3$ crystals looked more interlaced and forming a sort of linked chain as seen in Figure 9-29a which hints to a multi-directionality in the iron carbonate growth behaviour. Both prismatic and cubic iron carbonate crystals are present and their dimensions vary from as low as 1 micrometre to as high as 20 micrometres thus being slightly larger than the crystals grown in the same conditions but without adding the nanofiller.

These crystals look rougher and show many randomly generated pinholes around their surface as clearly observed in Figure 9-29b with the biggest opening reaching 500 nanometres in diameter as seen in the dotted area.

The repeated presence of these pinholes when OA-POSS is present suggests that while the nanofiller does enhance the crystal growth of iron carbonate, the morphology of the formed crystalline compound is different that the crystals which form in the absence of OA-POSS. The main differences being to the degree of roughness and the pinhole distribution which seems to be mainly localised around the FeCO$_3$ edge vertices.

Both EDX maps shown in Figure 9-30 and Figure 9-31 confirm the iron carbonate composition with iron-Fe, oxygen-O and carbon-C present.

It should be noted that the crystal islands described in this section look very similar to some calcium carbonate counterparts that grow when ter-polymers CaCO$_3$ inhibitors are added to the solution as discussed by Amjad et al.[368] as shown in the below micrograph.

9.3.4 EDX at pH equal to 7

EDX ran on samples tested at a pH value equal to 7 were registered on two locations as shown in Figure 9-30 and Figure 9-31. The three elements required for the establishment of an iron carbonate layer are all accounted for in both cases as iron, carbon and oxygen are abundantly present. It should be noted that the dark areas present on the gold, oxygen and iron maps are related to the presence of small iron carbonate crystal islands as seen on the SEM micrograph in Figure 9-30a.

In comparison, both chemical analysis show the same elements but when OA-POSS is added the intensity of these elements is higher especially in the case of carbon. It should also be noted that the crystal islands observed in the presence of the nanofiller are much larger and more abundant than when a test is ran without OA-POSS addition.
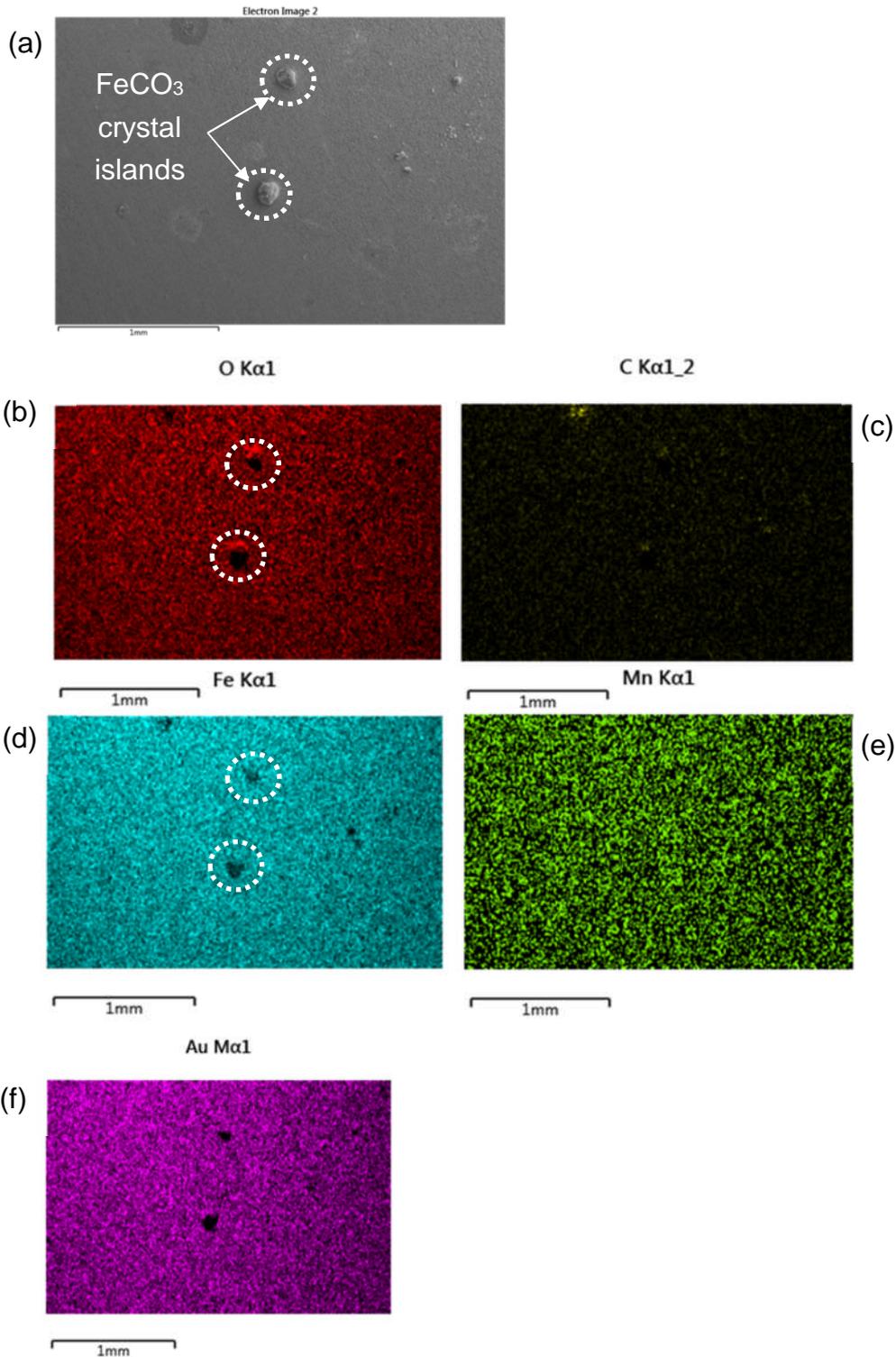
Figure 9-30 EDX map 1 of corrosion layer grown at 60°C, pH 7, 3.5% NaCl, with 0mg OA-POSS added to the brine chemistry (a) SE micrograph, (b) Oxygen-O, (c) Carbon-C, (d) Iron-Fe, (e) Manganese-Mn and (f) Gold-Au. The dotted areas correspond to the small $FeCO_3$ protruding crystal islands
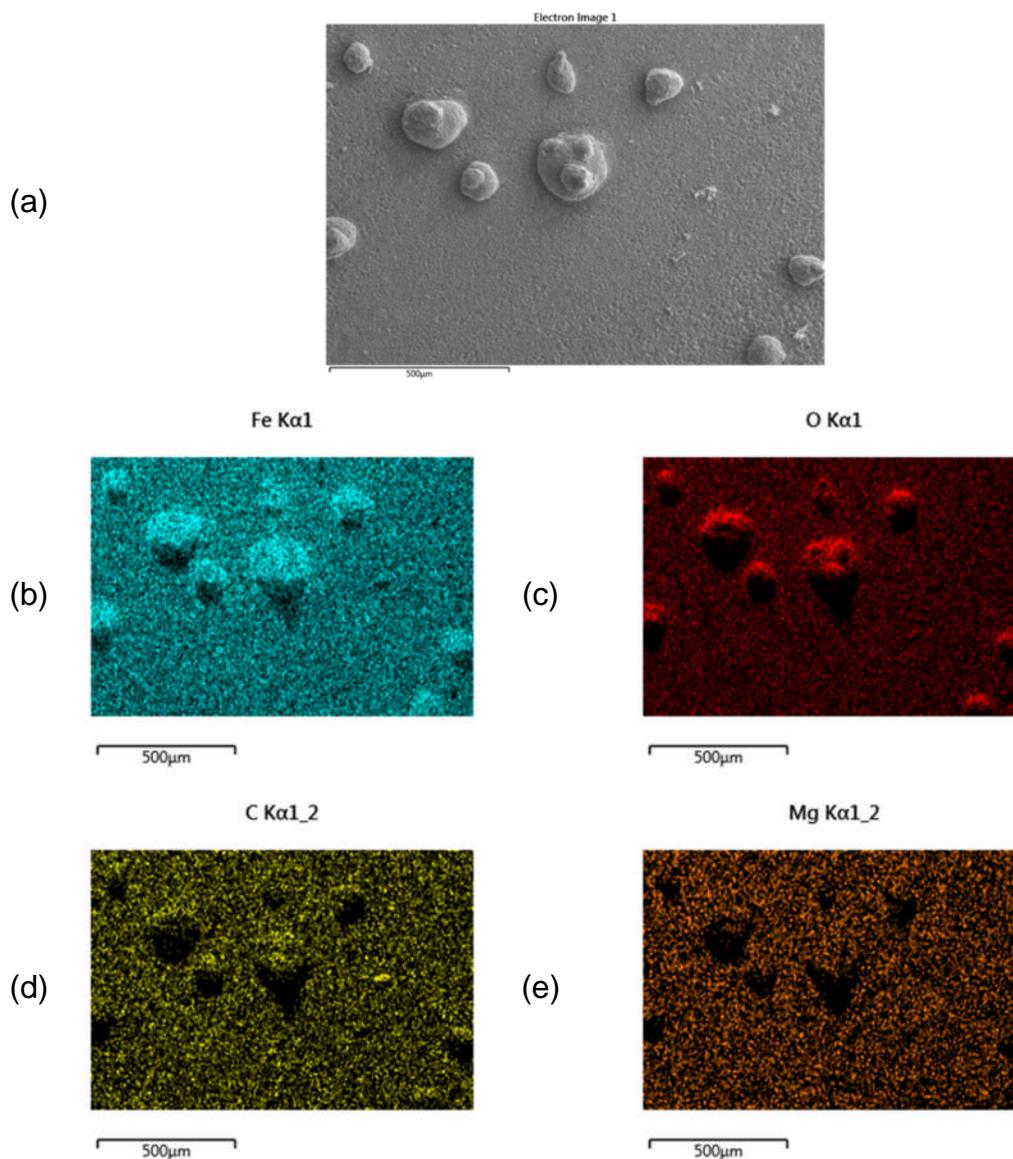
Figure 9-31 EDX map 2 of corrosion layer grown at 60°C, pH 7, 3.5% NaCl, with 100mg OA-POSS added (a) SE micrograph, (b) Iron-Fe, (c) Oxygen-O, (d) Carbon-C, and (e) Magnesium-Mg

9.4 OA-POSS loading effect

Advances in polymer technologies show that in the case of POSS moieties there appears to be a critical concentration above which the molecule is not effective; it can even show anti-synergistic results. This section describes the attempt of overloading the test solution with higher concentrations of OA-POSS in order to assess the possibility of overcoming the lower pH restrictive potency.

Since previous tests at a pH equal to 5 showed that OA-POSS helped slightly decrease the CR during the first few hours, it was thought that adding more of the nanofiller could enhance this trend.

9.4.1 Electrochemical behaviour at pH5 and pH6 with high OA-POSS concentrations

When OA-POSS concentrations corresponding to loadings as high as 600mg are administered at low pH, the CR variation remains stable for as long as 120 hours. In fact, Figure 9-32 shows that adding more OA-POSS does not improve its potency or help form $FeCO_3$ crystals since the CR at both pH5 and pH6 are quite stable at values of 6 mmpy and 3.5 mmpy respectively.
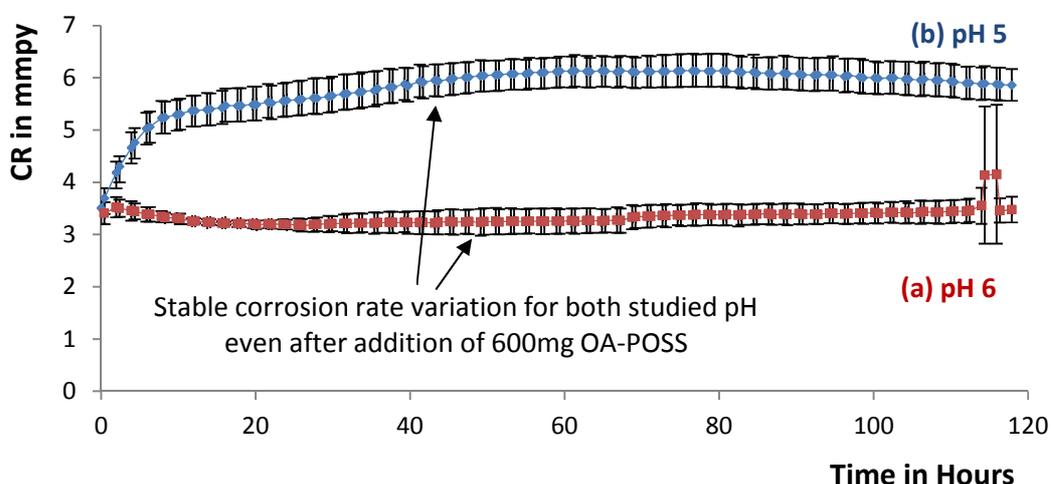
Figure 9-32 CR variation of 600 mg OA-POSS modified samples at (a) pH 6 and (b) pH 5 [60°C, 3.5% NaCl, 0.8bar CO_2] showing that a higher loading of OA-POSS is not able to reduce the general corrosion rate

Moreover, EIS data at pH5 shows similar results for both 100 mg OA-POSS and 600mg OA-POSS as shown in Figure 9-33. The Bode plot at pH5 and 600mg OA-POSS show a more scattered time constant which fluctuates below and above 10 Hz as seen in Figure 9-34. Thus, it appears that 100mg OA-POSS helped reduced the pH to slightly lower values than when 600mg OA-POSS is added (Figure 9-6).

Even at higher pH equal to 6, adding 600 mg OA-POSS did not allow for the CR evolution to be disturbed and a stable value of charge transfer resistance was registered as seen in Figure 9-35; although the single time constant was more secluded around a value of 10 Hz as shown in Figure 9-36.
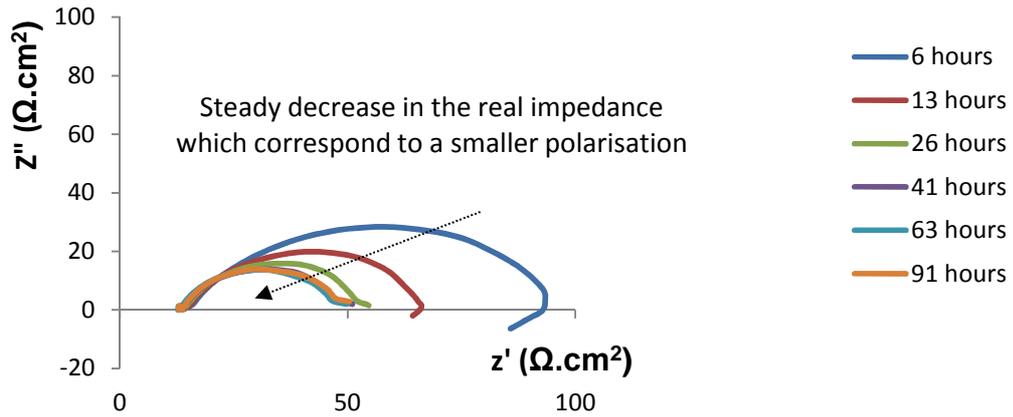
Figure 9-33 Nyquist plot with 600mg OA-POSS [60°C, 3.5% NaCl, pH=5, 0.8bar CO_2] showing a decrease in the real impedance with time
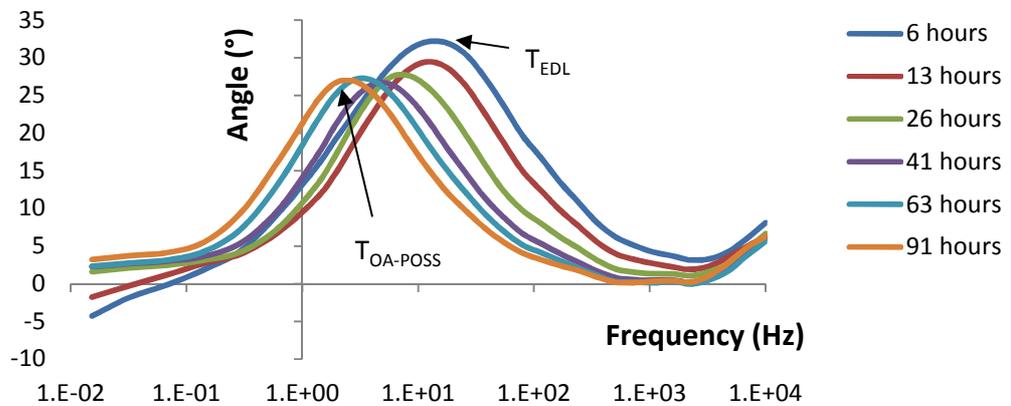
Figure 9-34 Bode plot for 600mg OA-POSS modified systems [60°C, 3.5% NaCl, pH=5, 0.8bar CO_2] showing a shift in the time-constants corresponding to the EDL and OA-POSS adsorption
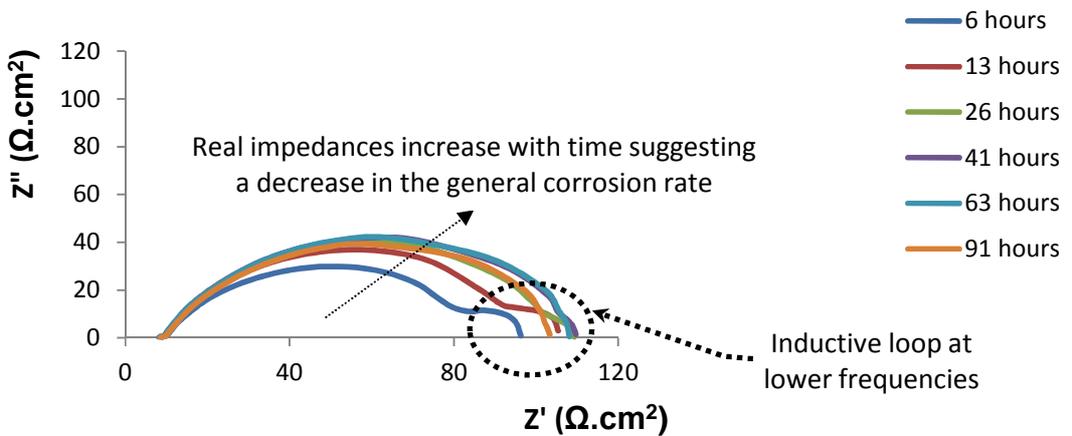
Figure 9-35 Nyquist with 600mg OA-POSS [60°C, 3.5% NaCl, pH=6, 0.8bar CO_2] with a more apparent inductive loop like behaviour at the lower frequencies as seen in the dotted area
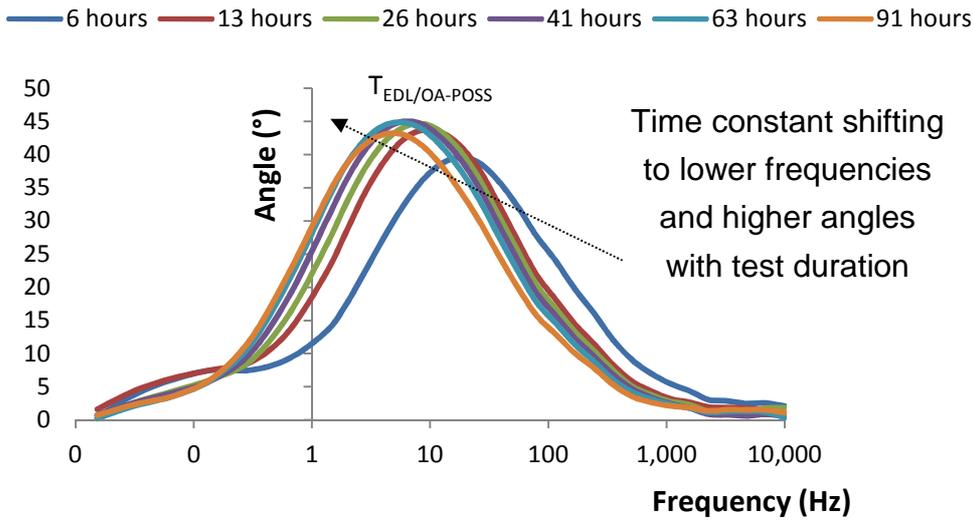
Figure 9-36 Bode plot for 600mg OA-POSS modified systems [60°C, 3.5% NaCl, pH=6, 0.8bar CO_2]

Similarly, adding higher concentrations of OA-POSS at pH 6.6 seems to slow down the kinetics of the declining corrosion rate trend as seen in Figure 9-37 where 300mg OA-POSS were administered instead of the 100 mg previously added amount as the start of the corrosion experiment with no pre-corrosion time allowed.
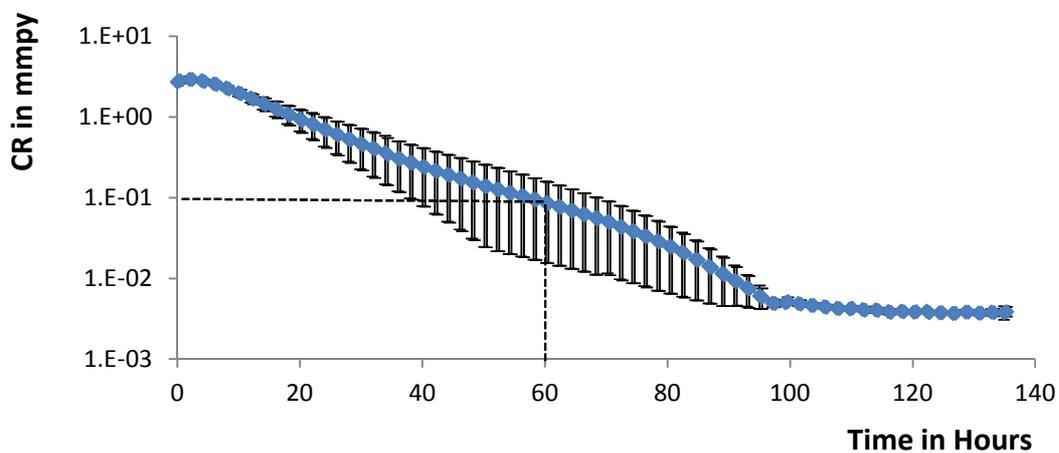
Figure 9-37 CR variation of 300 mg OA-POSS modified samples pH 6.6 60°C, 3.5% NaCl and 0.8bar CO_2

Thus, the higher OA-POSS concentrations seem to induce an anti-synergic effect where the corrosion rate is seen to drop gradually and reaches values lower than 0.1 mmpy only after 56 hours.

9.4.2 Micrographs of the obtained corrosion layers at pH5 and pH6 with high OA-POSS loadings

Tests with loadings of OA-POSS as high as 600 mg were not able to overcome the energy barrier which permits the nucleation and growth of iron carbonate crystals as can be seen in the micrographs in Figure 9-38 and Figure 9-39 corresponding to tests ran at pH5 and pH6 respectively. These tests were carried out by dissolving the nanofiller in the brine solution directly at the start of the test before registering the first electrochemical signal.

These micrographs corroborate with the corrosion rates variations observed in Figure 9-32 where the electrochemical stability hint to the absence of any protective layer formation for the whole test duration which is 120 hours. In fact, the corrosion films observed at the test end are very porous with pore diameters in the range of 10 micrometres and 5 micrometres for the test carried out at a pH of 5 and 6 respectively. These porosities are highlighted with a dotted area in both Figure 9-38b and Figure 9-39b.

Nonetheless, the corrosion layer formed at a pH of 5 when 600mg OA-POSS were added seemed formed of more structured globules as when compared to the randomly arranged lattice observed in Figure 9-13 with pores covering a limited surface area. As such, the corrosion layer seems to be slightly more compact but only when comparing with its counterpart ran without OA-POSS at the same pH and detailed in section 9.2.3.

The scale layer formed at a slightly higher pH of 6 also seemed to develop an amorphous layer even with the addition of higher concentrations of the nanofiller and the micrographs detailed in Figure 9-39 look very similar to the ones registered at a pH equal to 5. The main difference is in the porosity level and the average dimension of the openings which seem twice smaller. These smaller orifices could be responsible for the general corrosion rate evolution observed in Figure 9-32 since the general morphology of the corrosion layer is similar in any other aspect.

Both set of micrographs show no iron carbonate crystal formations but rather an amorphous corrosion layer which was proven to be non-protective as seen by the stability of the registered corrosion rate from the start of the electrochemical test to its end. No further surface analysis techniques were carried out in these conditions since both the general corrosion rate variation and corrosion film morphology assert with no doubt that the grown corrosion layer in not protective at both pH5 and 6.

Amorphous and highly porous corrosion layer

(a)

Mag = 500 X   WD = 12.5 mm   20.00 kV   SE1   20 µm   Width = 595.6 µm   LEMAS

10µm long porosity

(b)

Mag = 3.00 K X   WD = 12.5 mm   20.00 kV   SE1   10 µm   Width = 99.02 µm   LEMAS
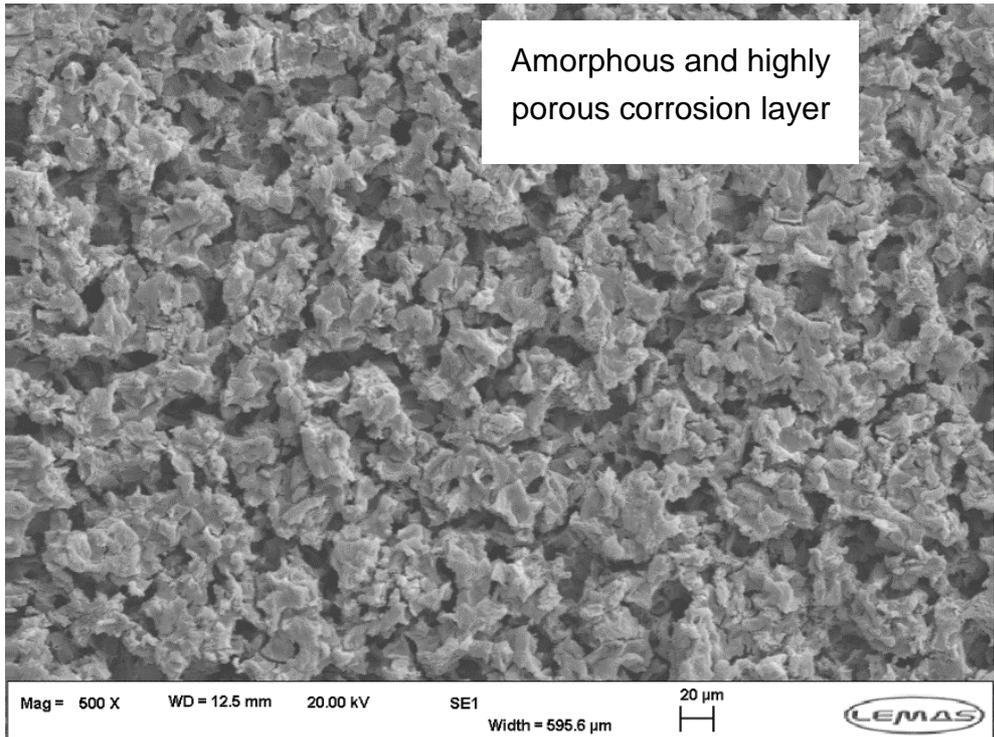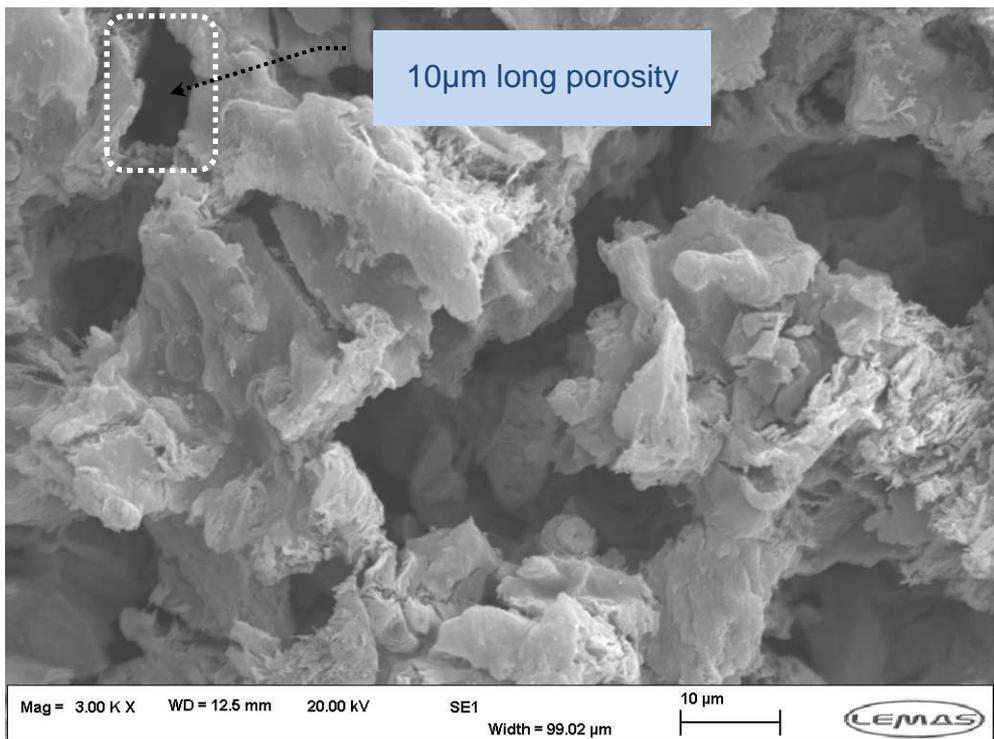
Figure 9-38 SEM micrographs topography view of X65 samples when 600mg OA-POSS are added to the test solution at various magnifications as per the respective scale bars [pH=5, 60°C, 3.5% NaCl, 0.8bar CO_2, 118 hours] showing (a) highly porous and amorphous corrosion layer and (b) a magnification of the openings exceeding ten of micrometres

Highly porous corrosion layers

(a)

Mag = 500 X   WD = 13.5 mm   20.00 kV   SE1   20 µm
Width = 595.6 µm

3 µm diameter opening

(b)

Mag = 3.00 K X   WD = 13.0 mm   20.00 kV   SE1   10 µm
Width = 99.02 µm
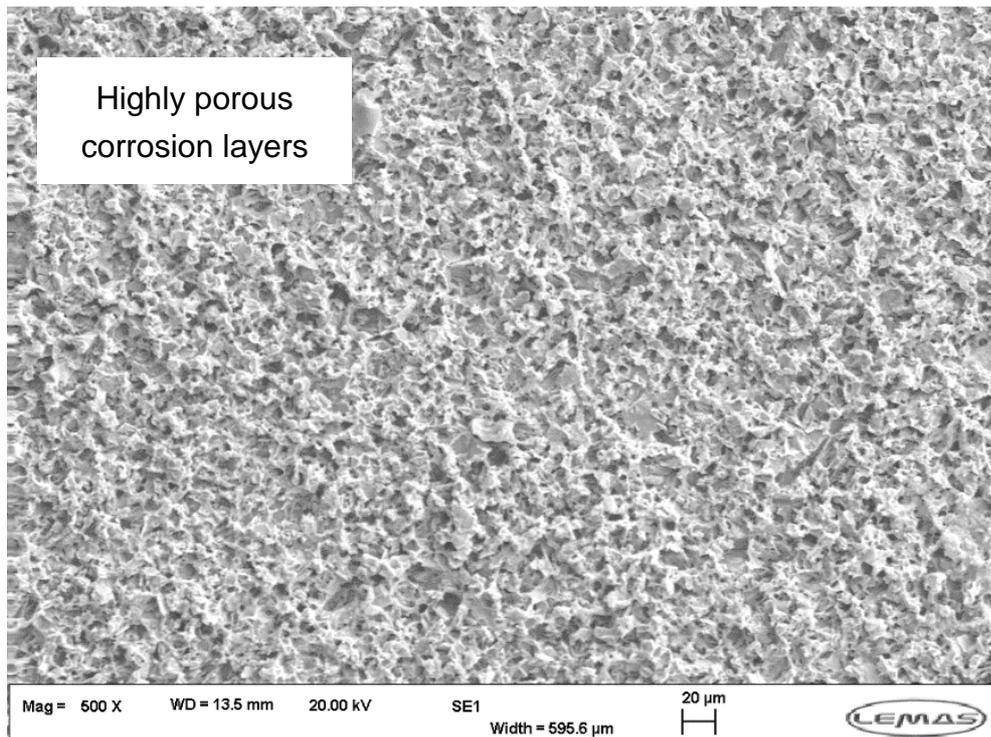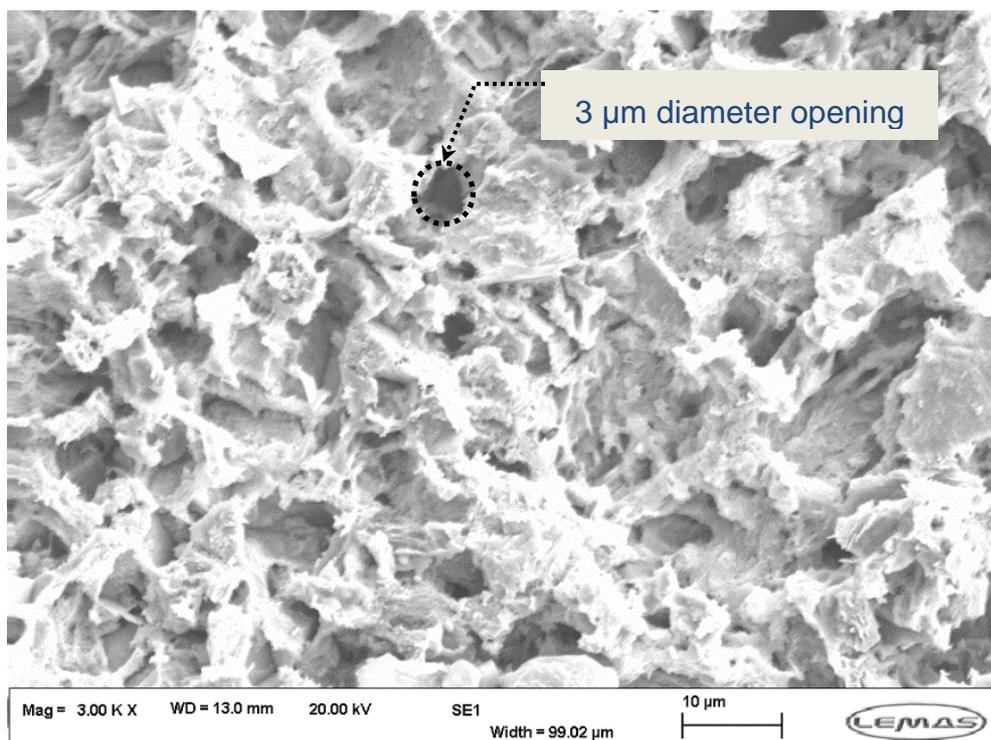
Figure 9-39 SEM micrographs topography view of X65 samples when 600mg OA-POSS are added to the test solution at various magnifications as per the respective scale bars [pH=6, 60°C,3.5% NaCl, 0.8bar CO_2, 118 hours] focusing on (a) the randomly interlaced but porous and amorphous corrosion layer and (b) the magnification on some openings which have a diameter smaller than 5 micrometres

285

9.5 OA-POSS interactions with various cations

9.5.1 OA-POSS and FeCl$_2$ combined effect?

It was observed that no iron carbonate film grows at the chosen environmental conditions unless ferrous supersaturation is increased via the addition of FeCl$_2$. Thus, it was thought of interest to study the interaction between the chosen nanofiller and the ferrous chloride additive to analyse any positive or negative interaction. As such, FeCl$_2$ and OA-POSS are added simultaneously to the brine directly at the start of the test, there appears to be an inhibitory effect which could be explained by a competition to access the X65 steel surface between the two chemicals.

Per se, Figure 9-40 shows no significant difference in the CR drop when OA-POSS is added when FeCl$_2$ was already present in the experimental solution. The final CR registered when 50ppm FeCl$_2$ are added is around 0.45 mmpy while the test ran with the joint addition of 20mg OA-POSS stabilises at 0.35mmpy. The High CR rate value after 2 hours is to be considered as a RE setup biased error that was fixed for the reminder of the test duration by swapping reference electrodes.
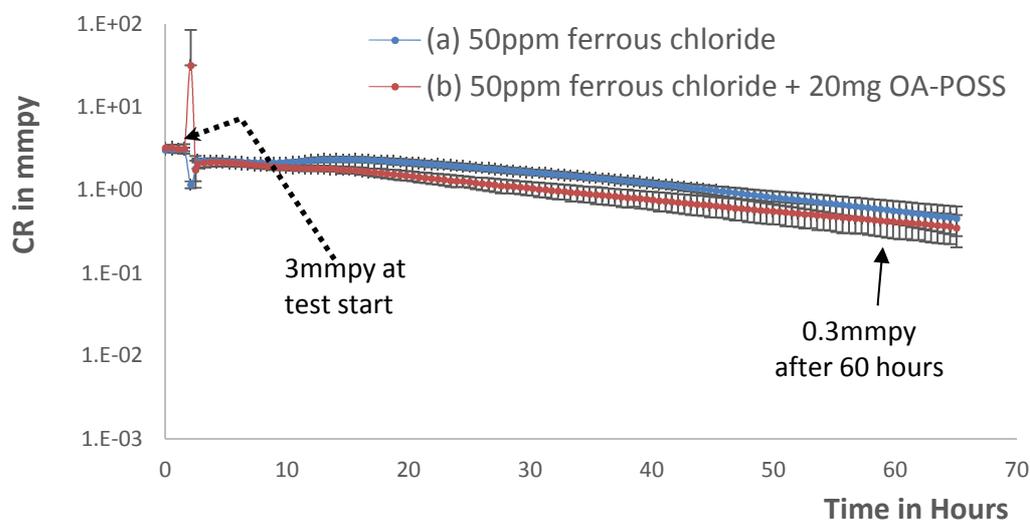
Figure 9-40 CR variation of 50 mg FeCl$_2$ added in conjunction with 20 mg OA-POSS [pH 6.6, 60°C, 3.5% NaCl, 0.8bar CO$_2$] showing similar trends with the (a) test ran with only ferrous chloride showing a slightly higher general corrosion rate evolution than (b) the test carried out with the joint presence of OA-POSS

On the contrary, when both FeCl$_2$ and OA-POSS are added after a pre-corrosion period, then the OA-POSS activity seems to be re-established as shown in Figure 9-41.
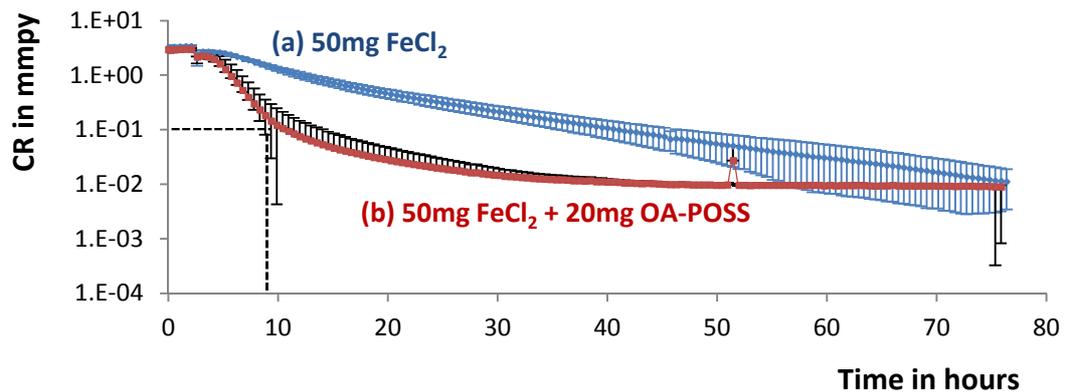
Figure 9-41 CR variation with (a) 50 mg FeCl$_2$ and (b) 50 mg FeCl$_2$ and 20 mg OA-POSS when both are added after 2 hours pre-corrosion [pH 6.6, 60°C, 3.5% NaCl, 0.8bar CO$_2$]

It is clear that the corrosion rate is dropping below 0.1 mmpy in just 8 hours while it takes almost 40 hours to reach the same CR if relying solely on ferrous iron ions addition via FeCl$_2$. The steady state of the 0.01 corrosion rate is visible when both chemicals are mixed while the CR seems not to have reached such equilibrium when only ferrous chloride was added.

9.5.2 OA-POSS behaviour in a complex brine composition

When OA-POSS is added into a salt composed of many cations and anions such as the Forties Brine which composition was given previously in Table 6-2, then it appears as though the effect of OA-POSS is hindered as shown in Figure 9-42.
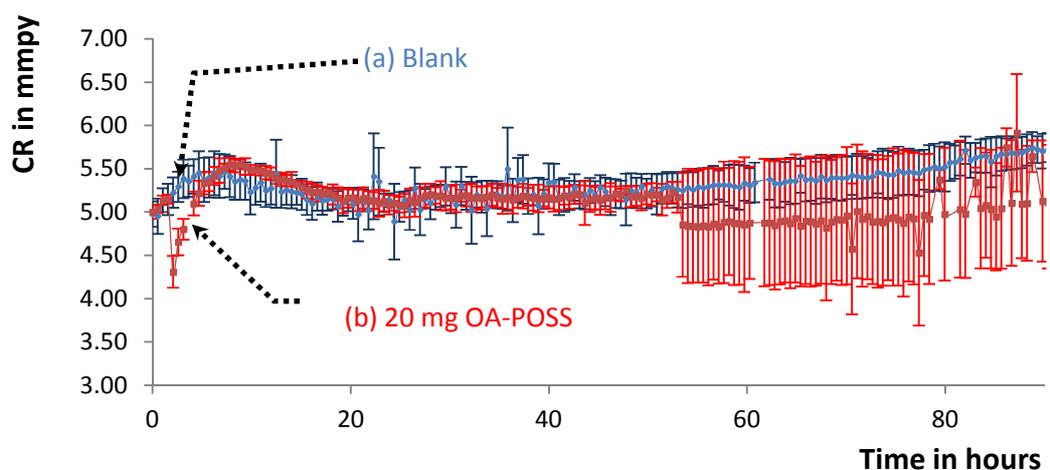
Figure 9-42 CR variation of CO$_2$ corrosion test carried out in Forties brine in an unbuffered solution (a) without OA-POSS and (b) with OA-POSS at pH 5.1, 60°C, and 0.8bar CO$_2$

The CR drop when OA-POSS is administered seem scarce in a complex brine solution which could be explained by less active surface availability for the OA-POSS to adsorb to possibly due to a thicker and more complex EDL layer. The main interesting observation is the OA-POSS activity in the first few hours following its administration where lower CR are observed when compared to the blank test; one assumption is that the nanofiller is not allowed to persist and is most likely washed away by other cations present in the specified brine.

9.5.3 Interactions with other cations

The behaviour of OA-POSS was studied in the presence of 0.134 moles of potassium chloride (KCl) and 0.2 moles of strontium chloride ($SrCl_2$) to see how it affects the $FeCO_3$ formation prior to adding OA-POSS. As observed in Figure 9-43, strontium divalent cations seem to have an anti-synergic effect with regard to corrosion rate reduction while the potassium monovalent cations showed corrosion rates similar to the addition of 50 ppm $FeCl_2$. Since none of the administered salts seemed to have a positive effect on the corrosion rate decrease, further interactions with OA-POSS was not studied.
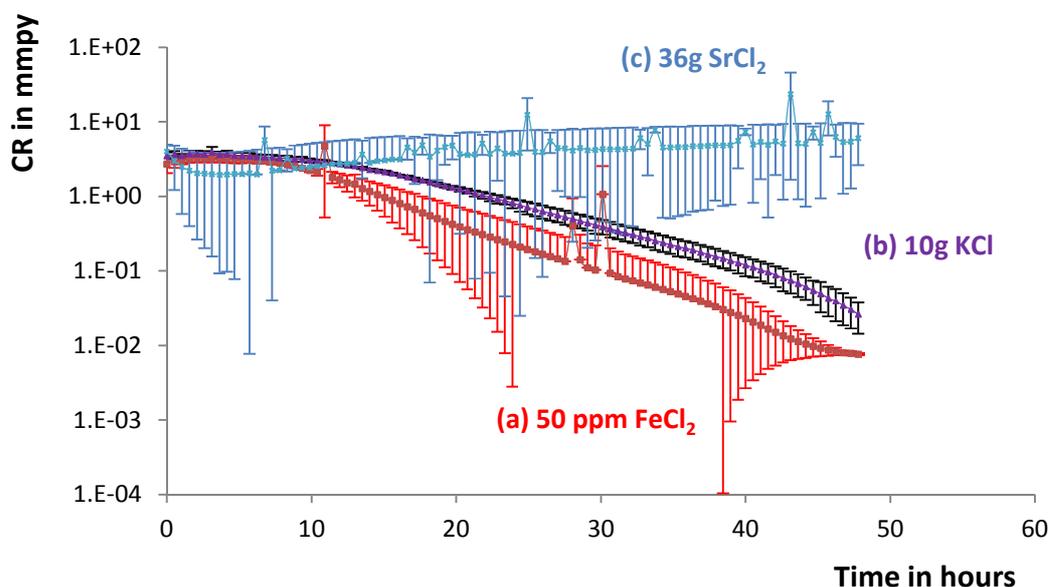
Figure 9-43 CR variation of X65 with (a) 50 ppm $FeCl_2$, (b) 10 g KCl and (c) 36g $SrCl_2$ at pH 6.6, 60°C, 3.5% NaCl, and 0.8bar CO_2

9.6 Summary of OA-POSS potential as an iron carbonate enhancer

While it was observed that OA-POSS is able to help increase the nucleation rate of iron carbonate crystals at a pH equal to 6.6 and a temperature of 60°C, the nanofiller also showed a synergistic effect when added in combination to an excess of ferrous chloride ions.

When the pH was increased to a neutral value, although the corrosion rate variation did not appear to be modified, the morphology of the developed iron carbonate films showed excessive protuberance of crystalline islands similar to some calcium carbonate counterparts as depicted in Figure 9-44.
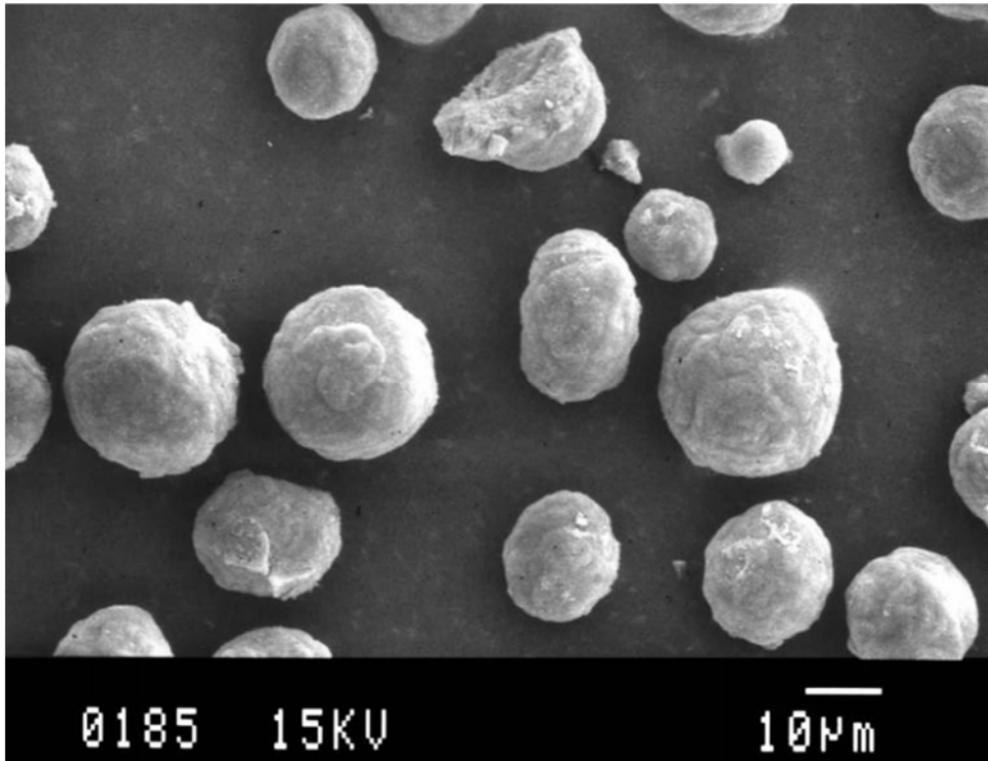
Figure 9-44 SEM picture of $CaCO_3$ crystals grown in the presence of commonly used phosphonates/polymer blends inhibitors[368]

Although the low pH appeared to hinder the OA-POSS activity after few hours probably due to the lysis of the Si-O-Si bonds, the fact that the iron carbonate Miller indices [110] and [113] were detected at a pH of 5 proves that the silsesquioxane moieties encouraged the establishment of $FeCO_3$ crystals at an earlier stage. The OA-POSS molecule could be later modified in order to withstand these harsher conditions in an approach similar to the molecular dynamic simulations carried out by Meng et al.[369] and this is detailed in section 10.1.2.

Chapter 10 Discussion and suggestions for future work

This research was set with the main belief that a nanofiller possessing organic sidechains in its chemical structure could help reduce the brittleness of the corrosion iron carbonate layer once integrated within it. The incorporated silicon-enriched nanofiller should also make the hybrid iron carbonate more resistant to various factors that could limit its potential protective ability such as shear stress, erosive wear, chemical dissolution or interaction with other flow assurance additives such as corrosion or scale inhibitors. In fact, higher hardness is known to help mitigate erosive wear as discussed in previous publications such as the one by Divakar et al.[370]

While hardness and modulus of the hybrid iron carbonate were achieved with a slight improvement in the elastic recovery parameter, the major nanofiller side effect was its ability to influence the nucleation and growth of the iron carbonate crystals. This was manifested through the electrochemical results which could be related to a kinetic acceleration of the $FeCO_3$ crystal film evolution. The main outcome led to both a localised and a general CO_2 corrosion mitigation. A list of the major findings related to the silsesquioxane-based nanofiller addition along the techniques implemented to reach such conclusions is summarised in Table 10-1.

Table 10-1 OA-POSS achieved effect and technique used for such assertion

Achieved goal	Assertion technique
Creation of a hybrid FeCO₃ and silicon incorporating within the growing iron carbonate film	• ICP-OES (Figure 8-50) • BET (section 8.5.5) • TEM/EDX (Figure 8-54) • FTIR (Figure 8-57) • XRD (Table 7-4)
OA-POSS acting as a nucleating agent	• LPR (Figure 8-1) • In-situ XRD (Figure 10-20)
General corrosion mitigation	• Electrochemistry and surface morphology (Figure 8-39)
Localised corrosion mitigation	• VSI (section 8.4)
Mechanical properties enhancement	• Nanoindentation (Figure 8-49)

10.1 Creation of a hybrid iron carbonate

In order to link the enhancement in some of the mechanical properties to the OA-POSS addition, the presence of the silicon atom in the iron carbonate corrosion layer was validated via various approaches such as ICP analysis, BET porosity tests, Raman spectra and TEM/EDX silicon mapping. It is assumed that any augmentation in the concentration of this element can solely be provided via the nanofiller silicon inorganic core.

10.1.1 Hunt for the excess silicon within the grown $FeCO_3$

The ICP results detailed in section 8.5.2 showed a tenfold higher silicon content in the studied iron carbonate layer when various loadings of OA-POSS were administered as opposed to the corrosion layer grown solely by adding 50ppm $FeCl_2$. The average silicon concentration was around 0.2ppm when no nanofiller was dissolved at the start of the test while this value increased when tens of milligrams of OA-POSS were added with values ranging between 2.5 and 3.5 ppm on average (Figure 8-50). These results suggest that the iron carbonate corrosion layer growing with dissolved OA-POSS in the brine chemistry contains more silicon and thus the iron carbonate film growing in these conditions was termed a hybrid iron carbonate.

While it was impossible to directly spot the OA-POSS as a molecule with the high resolution TEM, an EDX analysis showed that a higher level of the silicon element was accumulating in the vicinity of the underlying carbon steel as shown in OA-POSS enriched environments and blank tests specimen from Figure 8-54g and Figure 8-55g respectively. This could suggest that the OA-POSS is incorporating only in the area near the carbon steel surface after adsorbing to it and does not incorporate through the thickness of the iron carbonate film.

Moreover, both the BET tests (section 8.5.5) and the FTIR analysis (Figure 8-57) complemented the theory of the silicon excess in the hybrid $FeCO_3$. The first via the obvious change in the BET surface area when OA-POSS and synthetic iron carbonate were intermixed. The latter by showing the shift of the sharp band near 1080 cm^{-1} which is attributed to Si-O-Si stretching vibrations and thus corresponds to OA-POSS within the studied corrosion layer.

The ratios calculated between the iron carbonate [104] Miller index to the iron [110] Miller index constitutes an additional solid proof of the silicon-rich nanofiller within the corrosion film. In fact, all the registered data from the

291

powder XRD or the synchrotron XRD showed that this ratio increases with the increasing concentration of the OA-POSS added.

Thus, the current research shows results confirming the incorporation of OA-POSS with the growing iron carbonate corrosion layers and the beneficial effects this have on both corrosion mitigation and mechanical properties' enhancement although the detailed steps for such an incorporation mechanism require further investigation.

Similarly, Figure 10-1 shows images of other silsesquioxane based nanofillers incorporating in epoxy nanocomposites; the nanofillers appear as uniformly dispersed discrete spherical POSS-rich particles with a diameter smaller than 0.5 μm within the continuous epoxy matrix.

Thus, the epoxy plays the role of the bulk matrix and the POSS the nanofiller via a solvent-intercalation route such as the one described by Korucu et al.[371] in order to produce Poly-ethylene oxide/clay nanocomposites by a solution intercalation method using chloroform as a solvent. This confirms that relying on the solvent intercalation route to produce a nanocomposite can be successful in specific conditions and produce mechanical enhancements although melt intercalation routes remain dominant.
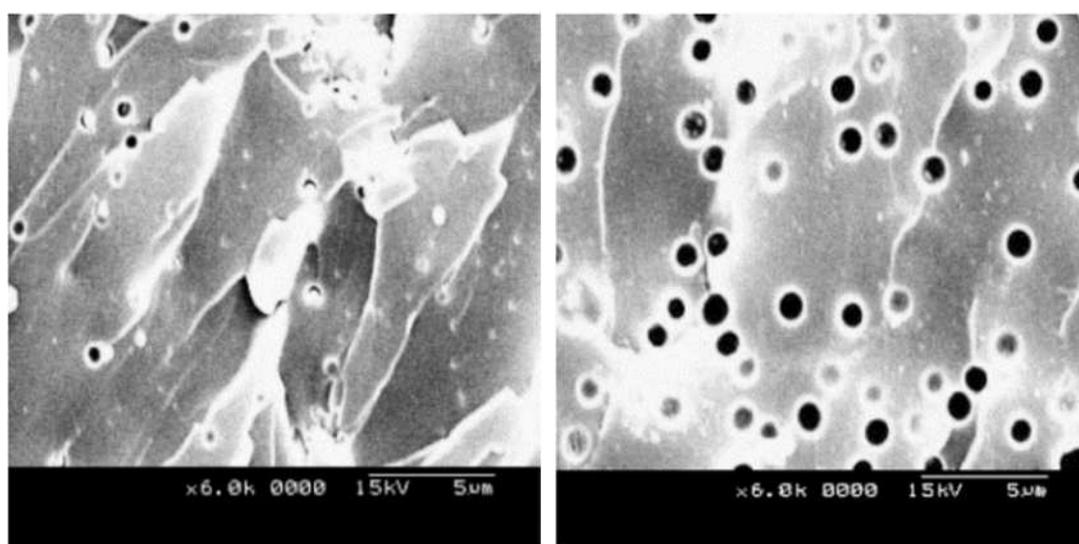
(a)   (b)

Figure 10-1 SEM images of epoxy nanocomposites containing (a) 5 wt.% of octanitrophenyl-POSS and (b) 15 wt.% of octanitrophenyl-POSS[372]

Although iron carbonate is not a polymer, both $FeCO_3$ and polymer structures can share the crystallinity feature. In fact, crystallinity in polymers is more complex than in metals and polymer molecules are often partially crystalline, with crystalline regions dispersed within amorphous material. Crystallinity occurs when linear polymer chains are structurally oriented in a uniform three-dimensional matrix. When looking at a polymer in which crystallization has occurred, it looks very similar in regard to a polycrystalline material as described with respect to metallic materials. That is, individual grains are present and the crystallization process begins at the centre of these grains via a chain-folding process.[373] Figure 10-2 reveals a space-filling spherulitic superstructure, with the size of spherulites being of the order of magnitude of 5–20 µm.

$$T_c = 130\,°C$$
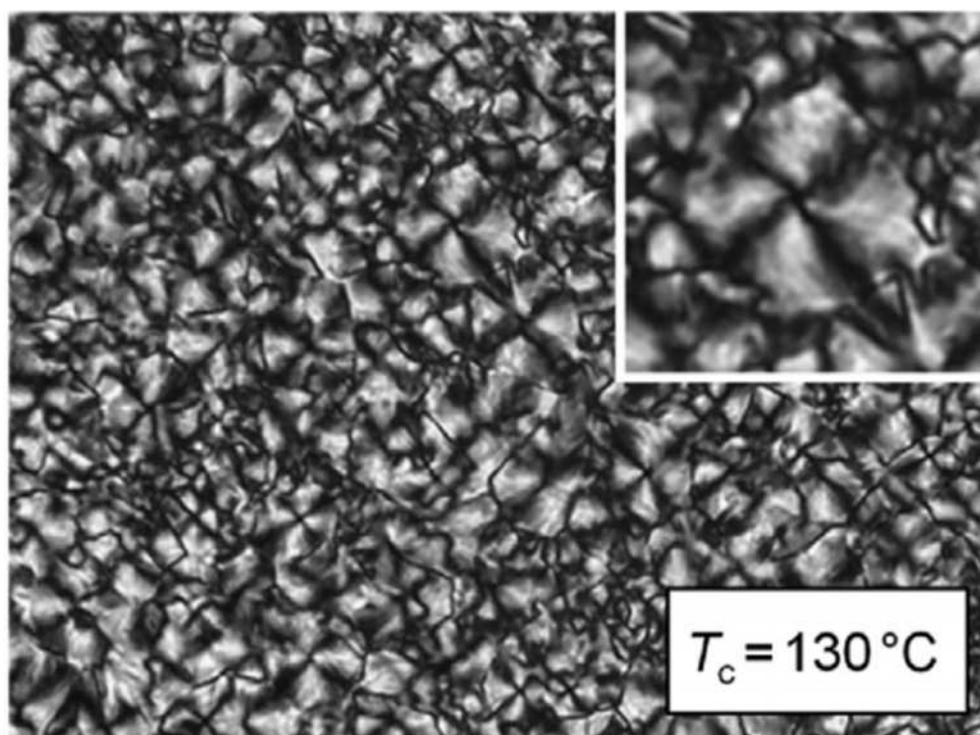
Figure 10-2 Polarized light microscopy micrographs of samples of the polymer poly-butylene terephthalate which has been isothermally melt-crystallized at 130°C , that is, at the temperature of maximum rate of high-temperature crystallization processes. The inset in the right image is a soft zoom of a spherulite illustrating the rotation of the Maltese cross 45° off the polarizer axes which are parallel to the image borders.[374]

10.1.2   Other nanofiller options?

OA-POSS was the nanofiller of choice for being readily available, water soluble and containing both organic and inorganic chemistry. Nonetheless, other nanofillers have also been tested such as nanoclays. For example,

bentonite was added directly in the brine chemistry or dissolved in acetonitrile beforehand in order to assess for any beneficial electrochemical or mechanical effects within the on-growing iron carbonate corrosion layer. Figure 10-3 shows that the corrosion rate reduces when bentonite is added to the test solution but not as sharply as when OA-POSS was administered. The main difference was the surface effect due to the adsorption of these silicon moieties to the carbon steel surface which shifted the starting corrosion rate to lower values averaging 2mmpy.
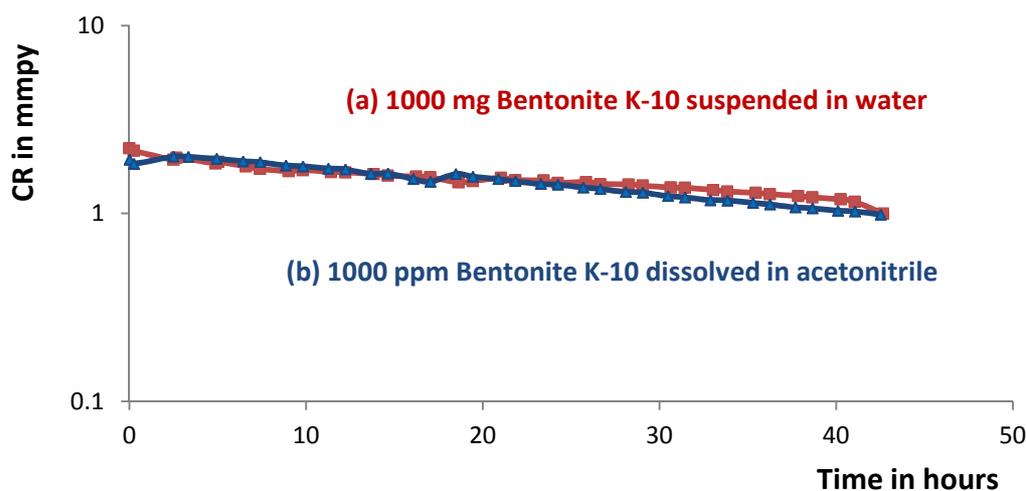
Figure 10-3 CR of X65 carbon steel specimen when Bentonite K-10 is administered (a) suspended in water or (b) dissolved in acetonitrile [pH 6.6, 3.5% NaCl, 60°C, 0.8bar CO_2]

Recent studies related to nanocomposite technologies are focusing on running molecular dynamic simulations in order to assess for the solubility parameter of a target polymer such as Polydimethylsiloxane (PDMS) then designing target silsesquioxane-based nanofillers via the modification of the organic side chains in a way that will render the POSS molecules' solubility parameter close to their target polymer before blending.

As such, octaisobutyl-POSS and allylisobutyl-POSS with solubility parameters equal to 15.46 and 15.52 $(J/cm^3)^{1/2}$ as compared to the solubility parameter of PDMS equal to 14.7$(J/cm^3)^{1/2}$ were used in a study carried out by Meng et al.[369] It is estimated that running similar calculations in order to define the solubility parameter of the iron carbonate then undertaking a simulation of the most appropriate side chains on an POSS moiety which will bring its solubility parameter to values close to the one calculated for the iron carbonate will help them intermix better.

These molecules could be hydrophilic or hydrophobic or amphiphilic and depending on that, the best blending technique; melt, *in situ* or solvent intercalation should be implemented in order to attain an exfoliated nanofiller fully dispersed in the iron carbonate for the best mechanical and physical properties enhancement.

10.1.3   Porosity and FeCO$_3$ crystal roughness analysis

One of the main observations in this research is linked to the scattered porosities and surface roughness visible on many grown iron carbonate crystals as seen on the SEM micrographs. Thus, although a hybrid silicon-enriched FeCO$_3$ corrosion product was grown, the morphology of some of the obtained crystals remain to be assessed and any link between the OA-POSS addition and the porosity emergence to be elucidated.

In order to better analyse the reason behind such morphology, literature focusing on calcium carbonate crystal nucleation and growth is required. An example of such pinholes is shown in Figure 10-4 but it should be noted that tests ran with or without OA-POSS showed a certain degree of roughness and porosities that randomly cover the FeCO$_3$ crystal vertices.
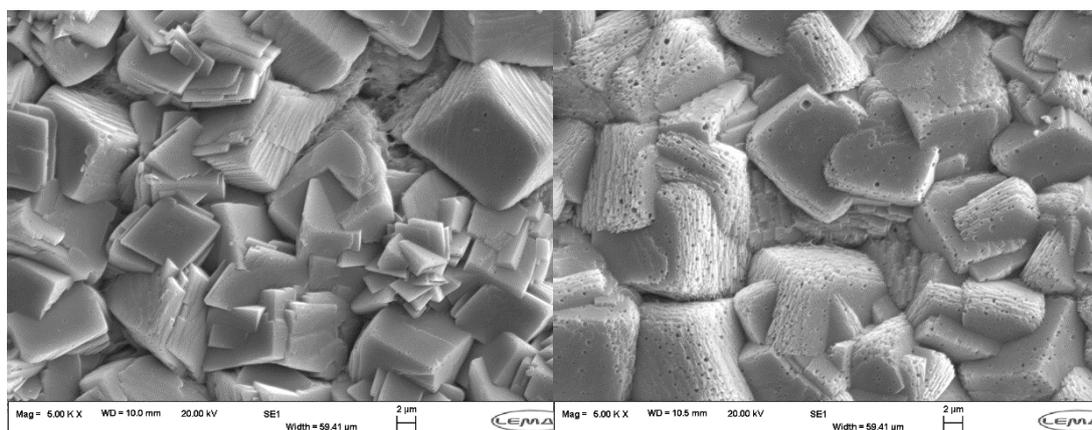
(a)   (b)

Figure 10-4 SEM micrographs of FeCO$_3$ crystals grown at pH 7, 35g NaCl, 60°C, 118 hours, 600SiC showing (a) smooth FeCO$_3$ crystal faces with 0mg OA-POSS and (b) rough FeCO$_3$ crystal faces with100mg OA-POSS showing addition porosities on the vertices

In order to assess the effect of flow and salinity on the extent of such defects, additional experiments were carried out and corresponding micrographs are depicted in Figure 10-5 and Figure 10-6 respectively. The first two assumptions are that a higher stirring degree reduces the size of the porosities while a higher salinity reduces the porosities' number.

(a)   (b)
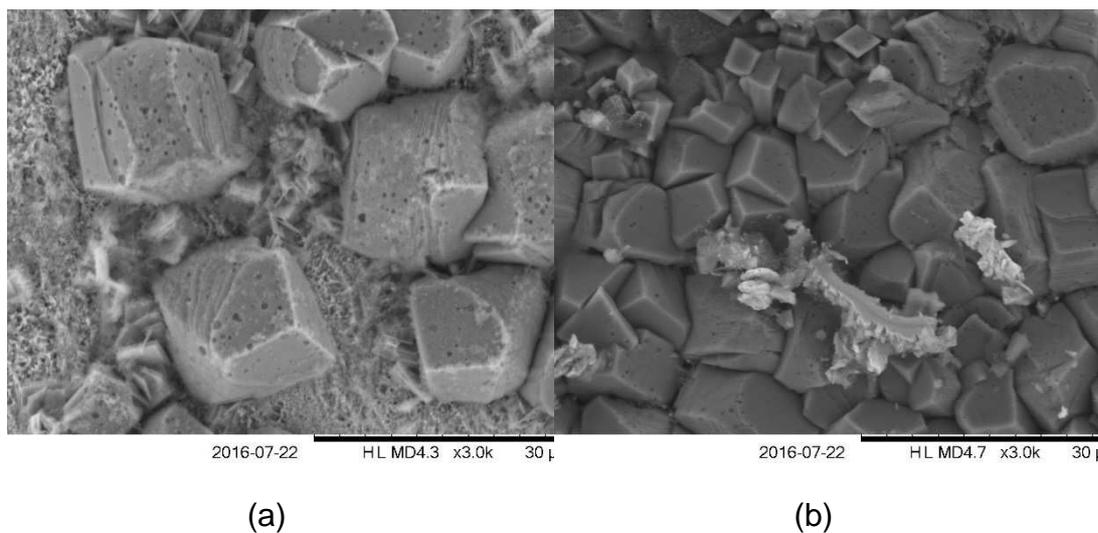
Figure 10-5 SEM micrographs of FeCO$_3$ crystals grown with 35g NaCl, 7.5g NaHCO$_3$, 80°C, 24hours, 1200SiC at a magnetic stirrer speed of (a) 0 RPM and (b) 750 RPM

(a)   (b)
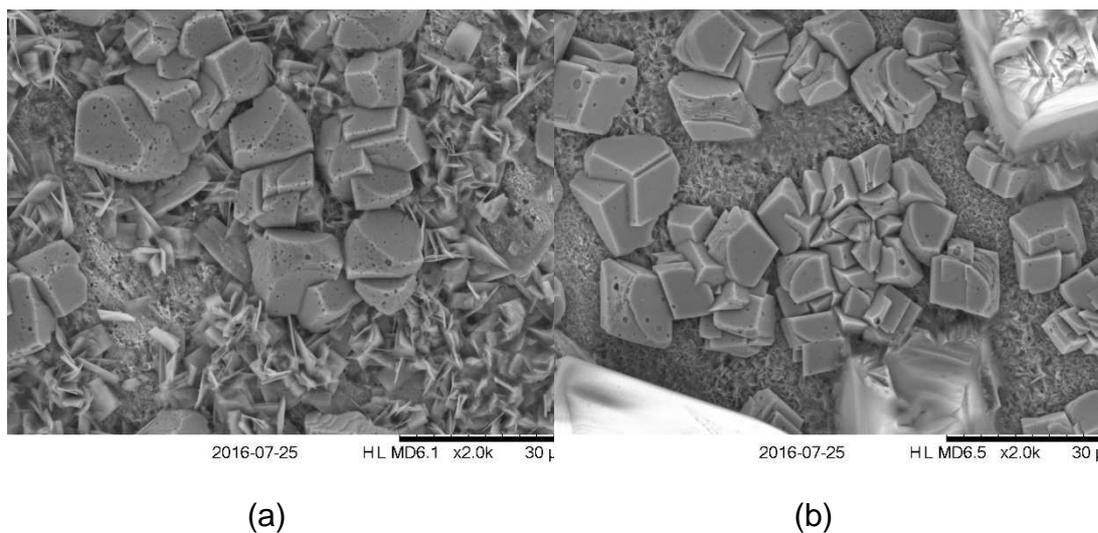
Figure 10-6 SEM micrographs of FeCO$_3$ crystals grown with 7.5g NaHCO$_3$, 80°C, 24hours, 250RPM,1200SiC with (a) 10g NaCl and (b) 100g NaCl

The closest morphologies found in the literature with relation to such defects is the work done by Guo et al.[375] where some obvious imperfections are located on the edges or corners of the calcite crystal surfaces, together with slightly shallow grooves distributed on the interface between two crystal faces as observed in Figure 10-7. The proposed theory is that the porosity or specific surface area of CaCO$_3$ crystals can be tuned by altering the volume ratio of N,N-dimethylformamide/cyclohexanol which is a polypeptide-type-block copolymer in a mixed solvent solution.

296
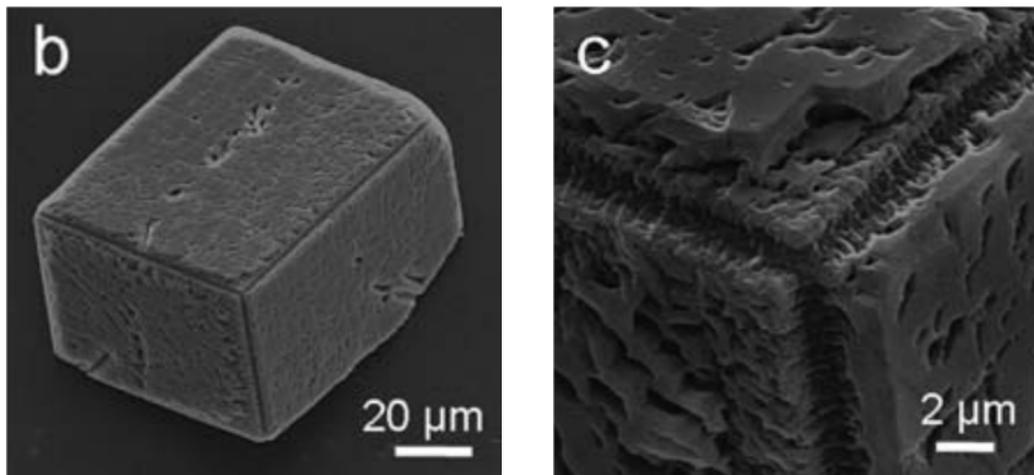
Figure 10-7 SEM images of calcium carbonate crystals obtained in aqueous solution and showing a high degree of porosities and surface roughness. The initial concentration of calcium chloride and polymer were 10mM and 1 g/L, respectively.[375]

It is assumed that the formation of specific $CaCO_3$ crystals with hierarchical and porous structures could be ascribed to the colloidal aggregation transition and self-assembly of calcium carbonate precursor in a desirable mixed solvent. This suggests that further work with the aim of detecting the presence of a similar $FeCO_3$ precursor could prove vital for better understanding the $FeCO_3$ nucleation and growth process. It is proposed that *in situ* techniques where electrochemical and AFM tests are coupled or *in situ* synchrotron tomography could help achieve such aims.

Other work by Beck et al.[376] emphasised that some specific $CaCO_3$ growth such as the dendritic ramifications is governed by mass transfer in the sense that diffusion is the slowest step in the cascade of processes involved in the formation of the crystal, and that diffusion controls the overall crystal growth rate. Thus calcite crystals growing in a regime of morphological stability become faceted with smooth faces as a result of a spiral growth mechanism at lower supersaturation and a two dimensional nucleation mechanism at higher supersaturation. While increasing the driving force to even higher levels leads to a rough crystal surface, and to morphological instabilities. As such, running further tests in order to assess local supersaturations effects on the $FeCO_3$ growth mechanism could prove advantageous in understanding $FeCO_3$ crystal growth mechanisms.

10.2 Carbon dioxide corrosion mitigation and OA-POSS

10.2.1 General corrosion rate reduction

The results collected in this research hint to a direct alteration of the X65 surface electrochemical behaviour when the nanofiller is present; this is seen in both the OCP swap and the general corrosion rate modification for the first minutes after the OA-POSS is added to the brine solution. As such, both blank and nanofiller enriched systems show totally different behaviour and this is apparent when analysing the data plotted in Figure 7-47 which relate to static tests undertaken in a bubble test setup but also in Figure 10-18 corresponding to *in situ* flow tests ran at the synchrotron facility.

For all tests ran at 60°C, pH 6.6, 3.5% NaCl, 0.8bar CO_2, 600 SiC surface finish in a total volume of one litre and a continuous CO_2 bubbling, the corrosion rate is stable for a period as long as 98 hours as seen in Figure 7-33.

This steady state is only slightly perturbed when 50ppm $FeCl_2$ are added to the brine mixture as per Figure 7-43 or greatly modified when various OA-POSS loadings are transfused into the system as shown in Figure 8-1 for example.

The addition of these silsesquioxane based nanofillers appear to behave as though the pH value is shifted by 0.2 units to higher values while being actually maintained as seen in Figure 7-31. When the time required to reach a corrosion rate value as low as 0.3mmpy is plotted for the various OA-POSS concentrations tested, the trend appears as per Figure 10-8.
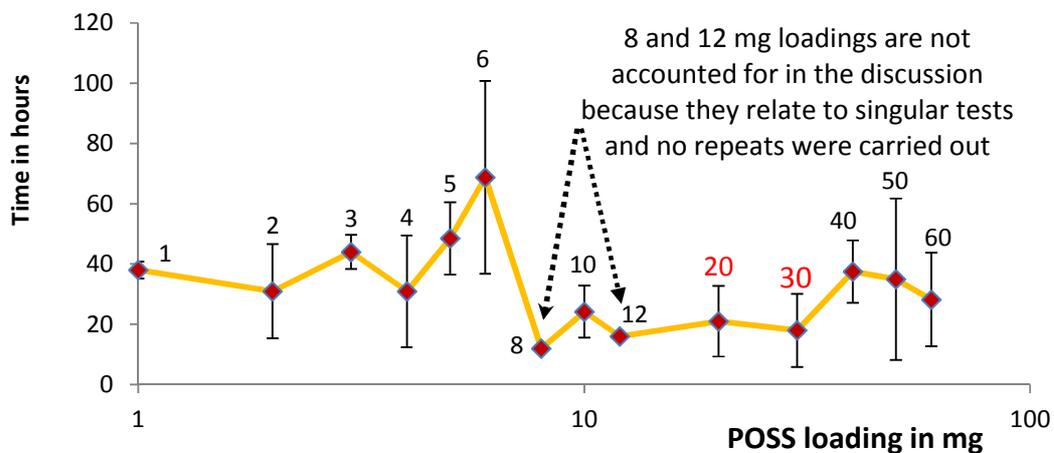
Figure 10-8 Time required to reach 0.3mmpy at various OA-POSS loadings as per the added labels from 1 to 60 mg

298

Two of these loadings which were repeated more than 3 times and showed the fastest corrosion rate drop and later the lowest steady state are 20 and 30 mg OA-POSS. In fact, both loadings show the quickest steady state stabilisation at corrosion rate values lower than 0.01 mmpy as seen from Figure 8-1 to Figure 10-22. When these values are coupled to the corresponding average film thicknesses deduced from the cross-sections depicted in section 8.1.3 and section 8.2.3, the two loadings of 20 and 30mg OA-POSS are again to be highlighted since they show a very thin iron carbonate layer than could be linked to the good corrosion mitigation registered. As such, Figure 10-9 shows that both loadings of 20 and 30mg allow the growth of iron carbonate films thinner than 5 µm and it is a common knowledge that such thin films are more compact and provide higher corrosion protection.
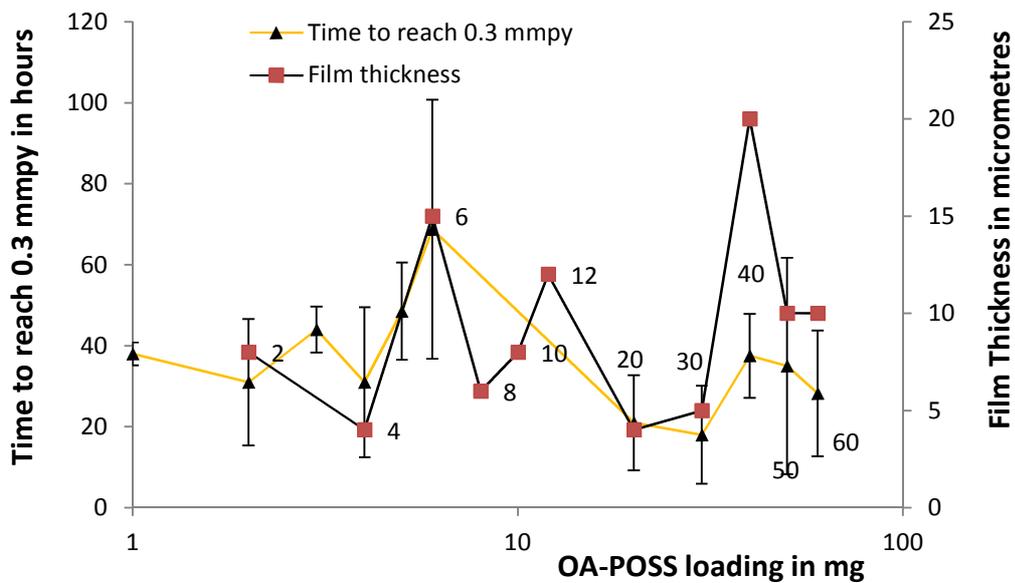
Figure 10-9 Comparison between electrochemical and film thickness results showing the OA-POSS loadings labels from 2 to 60 mg

Another important aspect of the electrochemical effect of the selected silsesquioxane nanofiller is its ability to drop the corrosion rates below an 0.01 mmpy threshold while most commonly used corrosion inhibitors only provide in general a drop in corrosion rates to values around 0.1 mmpy making the reliance on iron carbonate as a corrosion mitigating method a better alternative. Moreover, it is estimated that if adapted to various acidity levels this approach could ultimately reduce operational expenditures by replacing the costly recurrent corrosion inhibitors batch treatments.

10.2.2 Localised corrosion rate reduction

Occurrences of pitting corrosion in CO_2-containing environments have grown to become a major concern to the oil and gas industry in recent years. Pitting corrosion of carbon steel can be complex and is unpredictable in nature with significant challenges that are usually associated with inhibiting pit propagation once it has initiated. The actual mechanism of pitting corrosion in carbon steel materials is still not clear, especially when compared to the current understanding of pitting corrosion of passive alloys such as stainless steel materials. In the latter, the mechanisms of corrosion, passivation and pitting corrosion are relatively well understood and largely revolve around the localised breakdown of the passive film leading to propagation of pitting attack.

All the electrochemical results detailed in this thesis whether undertaken in DC or AC setups assume that the corrosion is uniform which provides only estimates of the general degradation mechanism. By removing the corrosion layers with suitable solvents such as Clarke's solution, it is possible to use profilometry techniques to assess for the depth of the pinholes on the X65 carbon steel surface and these are directly linked to the extent of the localised corrosion phenomenon.

Although significant reduction in the uniform corrosion rate when an iron carbonate corrosion layer is formed is normal, pitting corrosion was observed with pits as deep as 30 micrometres. Only when the surface is covered by the hybrid iron carbonate, did the localised corrosion and deepest pits reduce. As such, Figure 10-10 shows the various maximum pits on the surface of X65 carbon steel at 60°C and a pH of 6.6 after 98 hours exposed to a 3.5 wt. % NaCl solution saturated with CO_2. It also details the number of pits per squared millimetre computed when a threshold of 1 µm is assumed. It should be noted that the conditions described as containing 0mg OA-POSS required adding 50ppm $FeCl_2$ in order to grow the $FeCO_3$ layer prior to removing it with Clarke's solution.

Even though an iron carbonate compact and fully covering layer has grown over the carbon steel surface and the general corrosion rates have dropped to values lower than 0.01 mmpy, localised corrosion remains an issue as shown by the deepest pits obtained when the nanofiller was absent thus allowing deepest pits of 30µm to develop after 98 hours.

Naturally growing iron carbonate crystals as the ones described in section 4.2 are not able to hinder such localised attack and it appears that only when silsesquioxane based moieties are blended within the corrosion layer that these pits are minimised and almost inexistent when an OA-POSS loading equal to 20mg is added.
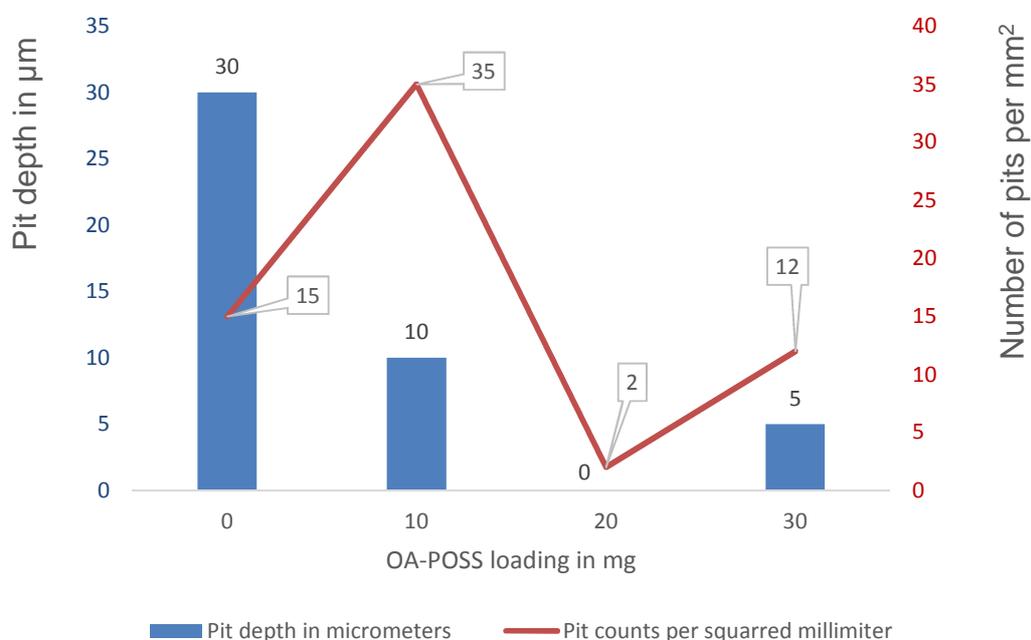
Figure 10-10 Maximum pit depths and pit count at various OA-POSS concentrations

Although it was difficult to locate pits under conditions where 20mg OA-POSS were added, additional tests to ensure that the entire steel surface is scanned in order to accurately determine the true susceptibility of the surface to pitting corrosion should be undertaken. Moreover, while the number of pits on the surface was observed to significantly reduce by adding OA-POSS, no quantitative pit count was conducted in this study and it should be considered in future investigations along with the computation of respective pit factors at various OA-POSS concentrations.

10.3 Mechanical properties enhancement

10.3.1 Hardness enhancement

When a compressive force is applied over a solid material such as the studied iron carbonate corrosion layer, hardness gives a measure of how resistant this compound is to different kinds of permanent shape changes. In the case of the implementation of the nanoindentation tests described in section 8.5, the

measured hardness is actually the resistance of the cross-sectioned $FeCO_3$ to material deformation due to a constant compression load from a sharp object which is the indenter. It was shown that when iron carbonate is grown at 60°C and a pH of 6.6 by adding 50mg $FeCl_2$ in a CO_2 saturated environment and a 3.5 wt% NaCl, then the registered hardness is averaging a value near 1 GPa while this is almost multiplied by a factor of 10 when 40, 50 or 60mg of OA-POSS was added to the brine solution thus reaching hardness values as high as 10 GPa.

Since spaces exist between atoms in a crystal lattice and $FeCO_3$ crystal lattice is not an exception, two types of defects can be created by the incorporation of the silsesquioxane moieties within any plane of the iron carbonate structure as depicted in section 5.2.3. First a substitutional defect is created when a different type of atom is formed at the lattice site that should normally be occupied by a metal atom; silicon instead of iron for that matter. Also, another type of defect termed interstitial defect can be of order if there exists an atom in a site where there should normally not be.

As the silicon radii is lower than the one for iron, 11.1nm versus 15.6nm respectively, these defects could be a plausible explanation for the increased hardness if point defects are considered. A scheme comparing the volumes of both silicon and iron elements is drawn in Figure 10-11.

Silicon (R=111 Å)   Iron (R=156 Å)
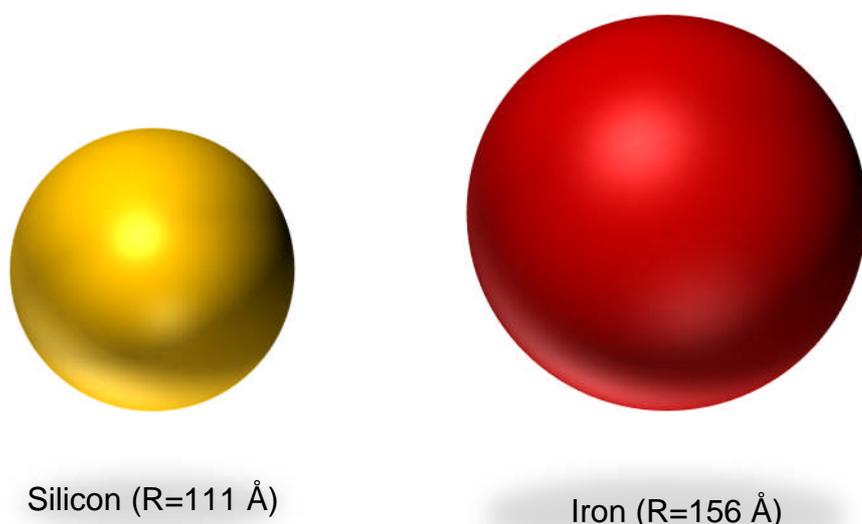
Figure 10-11 Silicon versus iron elements atomic radii compared (not to scale)

It should be noted though that any OA-POSS molecule that incorporates within the iron carbonate corrosion layer will be replacing roughly four molecules of FeCO$_3$ since the volumes of each are 1100 Å^3 and 330 Å^3 respectively. As such Figure 10-12 gives an idea of how much space a single OA-POSS molecule will take within the iron carbonate grown corrosion layer.
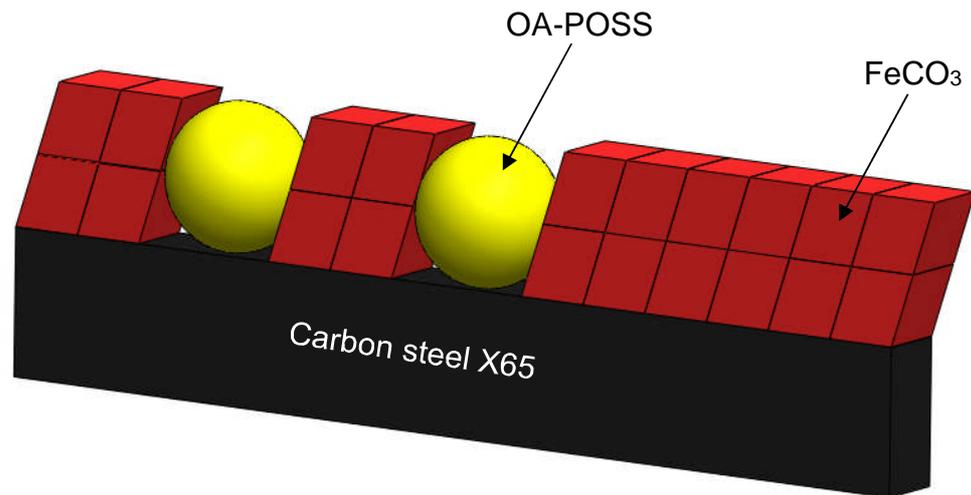
Figure 10-12 Schematic of potential OA-POSS insertion within the iron carbonate crystal lattice

10.3.2   Young's modulus improvement

The registered nanoindentation values not only depict an increase in the hardness but also in the Young's modulus which sees a surge from values around 100 GPa to values three times higher reaching 300 GPa. The Young's modulus also known as the elastic modulus is a mechanical property of linear elastic solid materials and since adding the OA-POSS is increasing this parameter, it can be assumed that the elasticity of the modified iron carbonate is enhanced. Thus the aim of using a hybrid nanofiller with a silicon-rich core to increase the mechanical properties such as the hardness discussed in section 10.3.1, but maintain the elasticity has been achieved.

The Young's Modulus computed from nanoindentation tests predicts how much the iron carbonate sample shortens under compression and the values generated are very close to the ones displayed by molybdenum which are around 330 GPa too as a matter of comparison.

10.3.3   Elastic Recovery Parameter (ERP) evolution

The Elastic recovery parameter is defined as per Equation 10-1 where h_{max} is the depth beneath the specimen free surface at maximum load or P_{max} and h_f is the non-recovered depth of the indenter inside the aerogel sample.

Equation 10-1 Elastic recovery parameter

$$ERP = \frac{h_{max} - h_f}{h_{max}}$$

One of the aims of this research focused on incorporating a nanofiller comprising an organic sidechain with the hope of improving its malleability. The ERP values registered at various OA-POSS loading show that bigger depth interval (h_f, h_{max}) are registered at medium OA-POSS loading and thus a better elastic recovery is actually found by assimilating such hybrid nanofiller to the growing iron carbonate scale.

Therefore, it could be deduced that medium OA-POSS additions can lead to an increase of the ERP by roughly doubling its value while excessive additions of the nanofiller induce a fall back to the ERP registered for iron carbonate film grown in the absence of the nanofiller as seen in Figure 10-13.
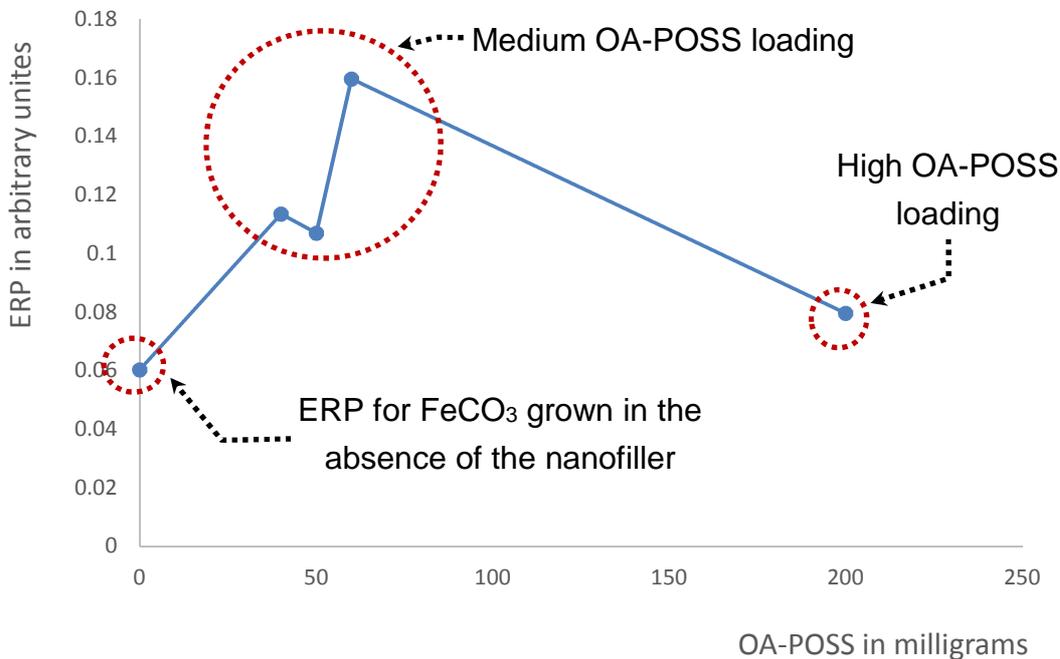
Figure 10-13 ERP at different OA-POSS concentrations

The schematic plotted in Figure 10-14 shows how an iron carbonate film grown in the presence of OA-POSS has more recovery as seen by the depth of the left indent after retraction. It should be noted that the fracture toughness should be calculated in future work in order to better assess the elasticity of the hybrid corrosion layers but this was deemed not feasible in this work because the cracks left after the indentation tests were not assessed in due time.

(a) Iron carbonate grown in the presence of OA-POSS

(b) Iron carbonate grown in blank conditions with no hybrid nanofiller additions
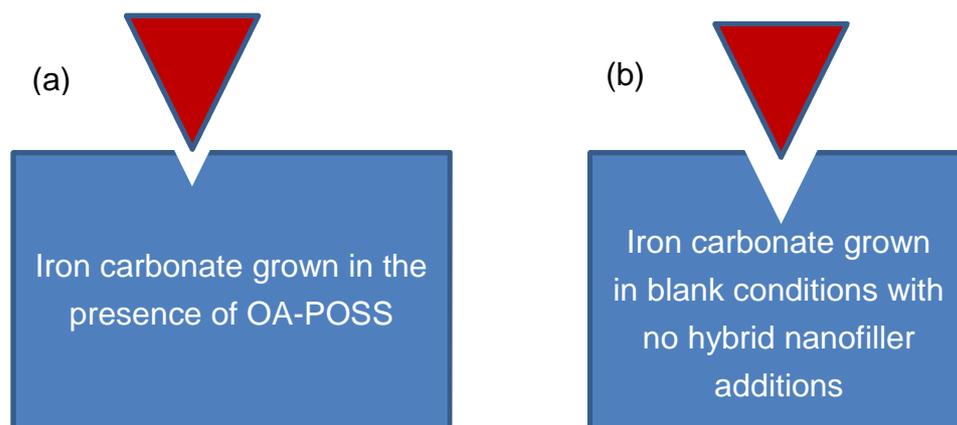
Figure 10-14 Schematic of elastic recovery in the case of $FeCO_3$ growing (a) in the presence or (b) absence of the hybrid nanofiller

10.3.4 Summary of mechanical properties

The extent of both hardness and modulus enhancement is in accord with literature values where these were seen to be increased to a maximum of 10. Moreover, the critical active POSS moieties concentration to achieve such mechanical improvements was found to be in the range of 3 to 10 wt% of the studied matrix. It was established in section 8.5.2 that the steady uptake of OA-POSS in the dissolved iron carbonate layer was around 2ppm on average which corresponds to 3% in volume of a 10μm thick and uniformly grown $FeCO_3$ corrosion layer.

All techniques used to validate the presence of Silicon in the corrosion by-product showed positive results besides the RAMAN spectra. As such, the change in BET surface area suggests that OA-POSS powder was interacting and adsorbing on the free active sites of the tested synthetic iron carbonate. The Energy-Dispersive X-Ray undertaken at high resolution using the TEM also showed a much higher silicon content when a blank and an OA-POSS enriched scale layer was tested.

10.4 OA-POSS supposed mode of action

10.4.1   OA-POSS as a nucleating agent

10.4.1.1   Metastable iron carbonate precursor theory

Recently, many published papers try to link the crystal nucleation and growth of iron carbonate with the pre-formation of its potential precursor. Although very little is known about $FeCO_3$ precursor phases and possible formation pathways, similarities with the more studied calcite counterpart are being investigated since it was shown that an amorphous calcium carbonate (ACC) precursor exists as a biomineral.

Thus, it was shown by Didericksen et al.[294] that the identified iron carbonate precursor may potentially form during anaerobic corrosion or bacterial iron reduction. The assumption in this research is that if such a metastable precursor is forming that OA-POSS might be interacting with it and decreasing the activation energy that must be overcome prior to the nucleation process start.

The assumed precursor which is defined as being "not truly amorphous "could therefore undergo a faster amorphous to crystalline transition in the presence of the OA-POSS moieties. Similarly this theory can also prove logical if the newly discovered chukanovite as described by Pandarinathan et al.[377] is the candidate precursor for the fully grown iron carbonate crystals.

Moreover, chromium Cr^{3+} excess was shown to increase the precipitation rate of the gel-like or amorphous carbonate precursor layer which leads to the fully crystalline rhombohedral $FeCO_3$.[367] Similarities with the calcite amorphous precursor and the effect that any reactants can have on such intermediate formation should thus be investigated further.

The above assumption seems plausible since at the experimental conditions of choice which are a temperature of 60°C and a pH of 6.6, it was found very difficult to nucleate and grow iron carbonate unless OA-POSS was dissolved also in the 3.5 wt% NaCl brine solution in CO_2 saturated atmospheric pressure. The sketch drawn in Figure 10-15 can explain how the described plausible mechanism of OA-POSS affecting the precipitation rate of the intermediate thermodynamic amorphous structures.
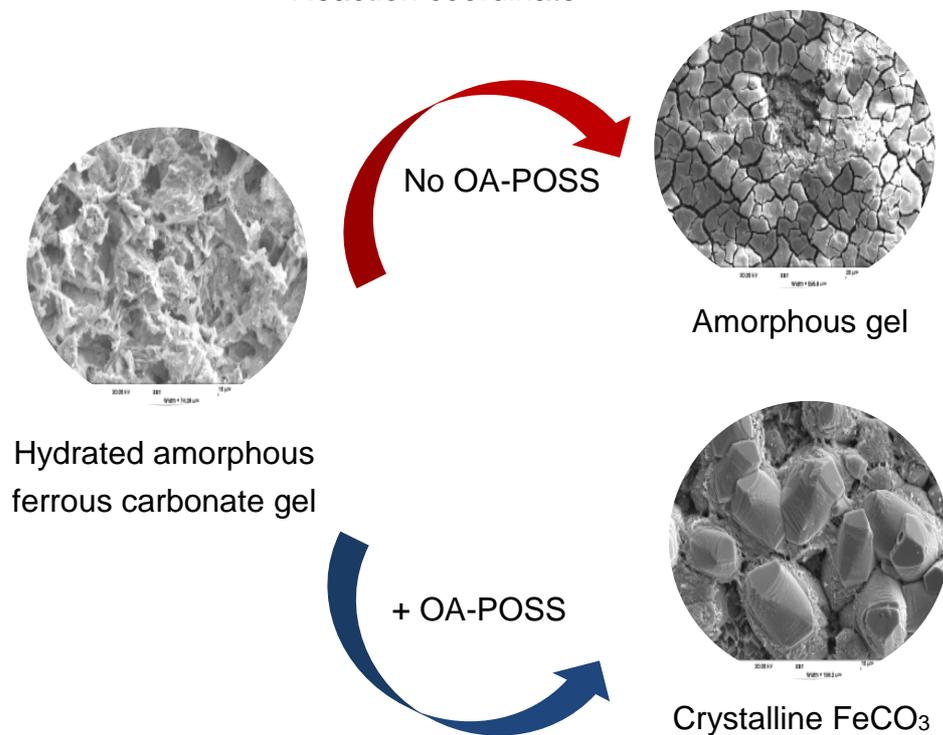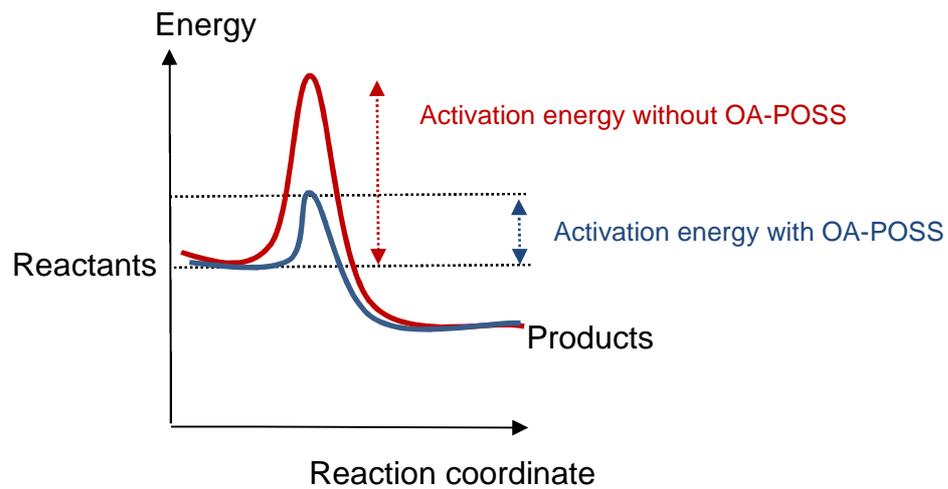
Figure 10-15 Representation of possible OA-POSS mode of action at pH 6.6, 60°C, 3.5 wt% NaCl, 0.8bar CO_2 and 600 SiC surface finish

The reactants represent the chemistry of the carbon dioxide corrosion reaction while the products represent the crystalline iron carbonate obtained when the activation energy barrier can be overcome.

Such theory is backed up by recent findings where octaisobutyl POSS, another silsesquioxane derivative studied with the silicone polymer show that the POSS is acting as a nucleating agent. Similar results were also found when another POSS derivative was mixed with a polypropylene polymer; it

was actually established that the POSS molecules exhibited nucleation activity only at 10 wt% loading in high-density polyethylene, but were not effective nuclei at lower loadings.[378] The mechanism was explained by the fact that the POSS molecules significantly increased the crystallisation rate, possibly by acting as a weak cross-linker.

10.4.1.2 OA-POSS adsorption and surface roughness

Since OA-POSS seems to operate better and drops more acutely the corrosion rate when a pre-corrosion time is permitted, it was thought that this phenomenon could be linked to a roughness effect in the corroding X65 carbon steel surface which was investigated herein but running tests at two different surface finishes in the presence of the silsesquioxane moieties.

There seems to be a higher decrease in corrosion rate on a rougher surface as shown in Figure 10-16 and this behaviour could help understand better the enhanced activity of OA-POSS when a pre-corrosion period is allowed as a longer pre-corrosion time is expected to roughen the surface and leave more exposed pearlitic regions.
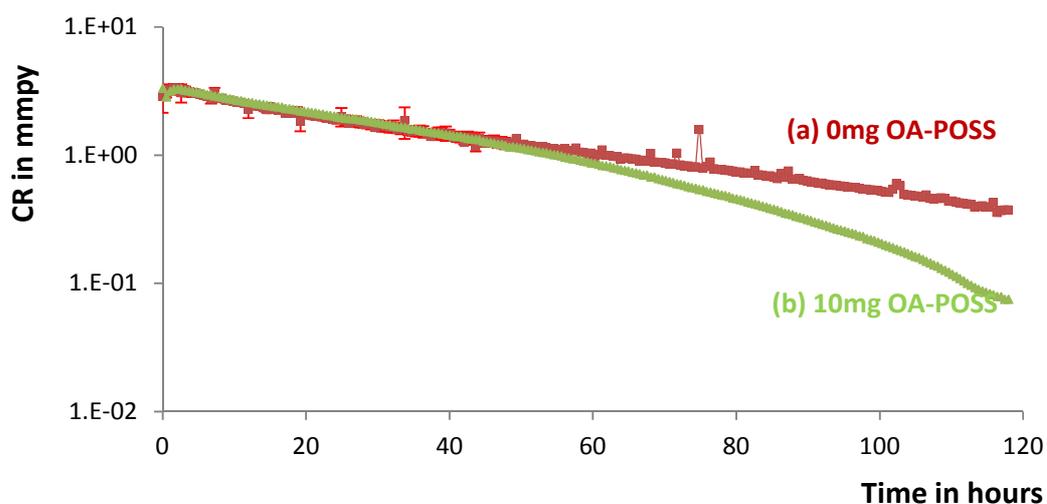
Figure 10-16 CR of (a) X65 sample polished to a 120 SiC surface (a) without OA-POSS and (b) with 10mg OA-POSS [pH 6.6, 60°C, 3.5% NaCl, 0.8bar CO_2]

When short term tests were undertaken with or without OA-POSS addition on a rougher carbon steel surface which has been polished to a 120 SiC surface finish, it appears as though the solution containing 30mg OA-POSS lead to a faster growth of the iron carbonate crystals as seen in Figure 10-17. These micrographs can be correlated with the electrochemical evolution shown in Figure 10-16.

Blank **30mg OA-POSS**

Denser FeCO$_3$ crystals when OA-POSS and surface roughness effects are present jointly
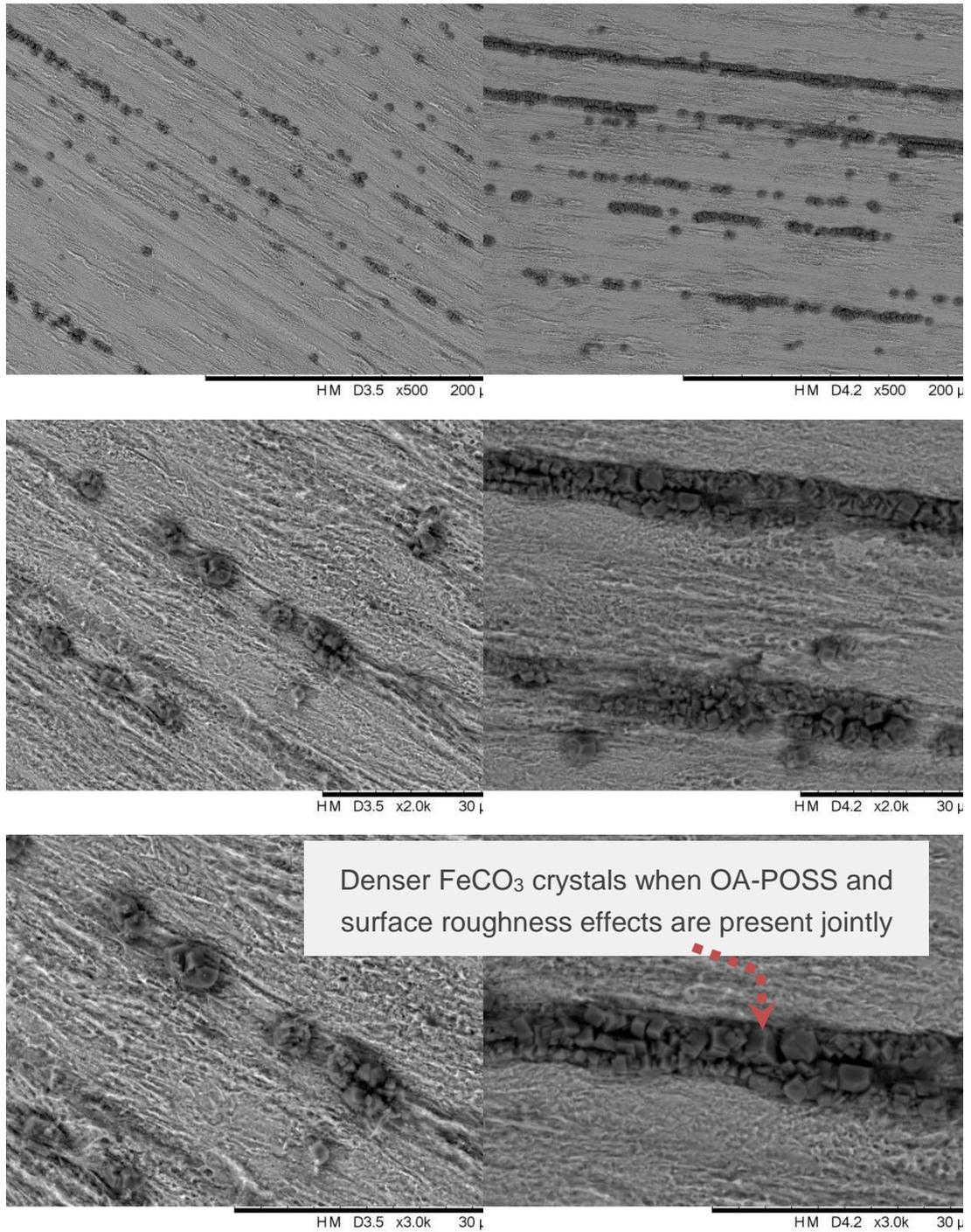
Figure 10-17 SEM micrographs topography view of X65 samples when 0mg OA-POSS (left side) and 30mg OA-POSS (right side) are added to the test solution at various magnifications [pH=6.6, 60°C,3.5% NaCl, 0.8bar CO$_2$, 6 hours and 120 SiC finish]

10.4.1.3 Synchrotron XRD flow cell tests

A short *in situ* synchrotron test was also carried out in order to spot at what time the first $FeCO_3$ crystal appears and the electrochemical results for this test are shown in Figure 10-18.
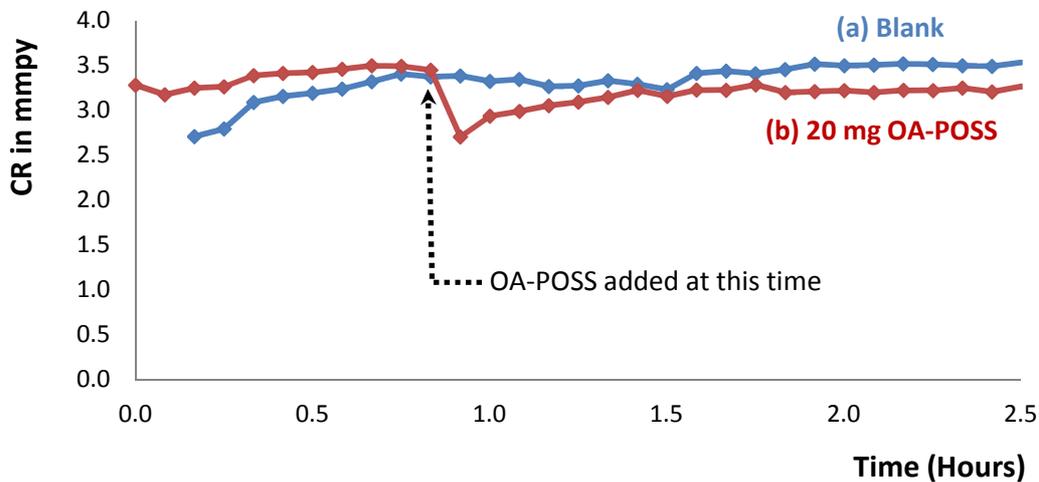
Figure 10-18 CR variation for a blank test (a) versus an experiment where 20mg OA-POSS were added (b) [pH 6.3, 80°C, 3.5% NaCl, 0.52 bar CO_2pp, 0.1m/s]

The XRD diffraction pattern collected for the test which electrochemistry is plotted in Figure 10-18 are shown for only the latest 5 peaks registered for the test duration of 2,5 hours as seen in Figure 10-19 with a zoom on the area where the $FeCO_3$ major Miller index is expected as per Figure 10-20.
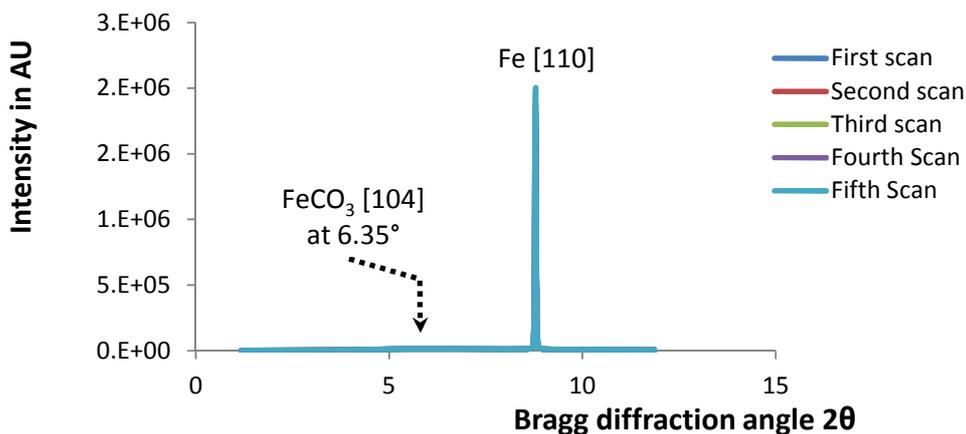
Figure 10-19 Synchrotron diffraction pattern for an experiment where 20mg OA-POSS were added *in situ* [pH 6.3, 80°C, 3.5% NaCl, 0.52 bar CO_2pp, 0.1m/s]

The OA-POSS was added 42 minutes after a period of pre-corrosion then the first $FeCO_3$ peak appeared on the 77th minute. It is interesting to note that

while the FeCO$_3$ peak appeared earlier in the tests where OA-POSS was added, it grew at a much slower rate than in the blank test done in the same conditions.
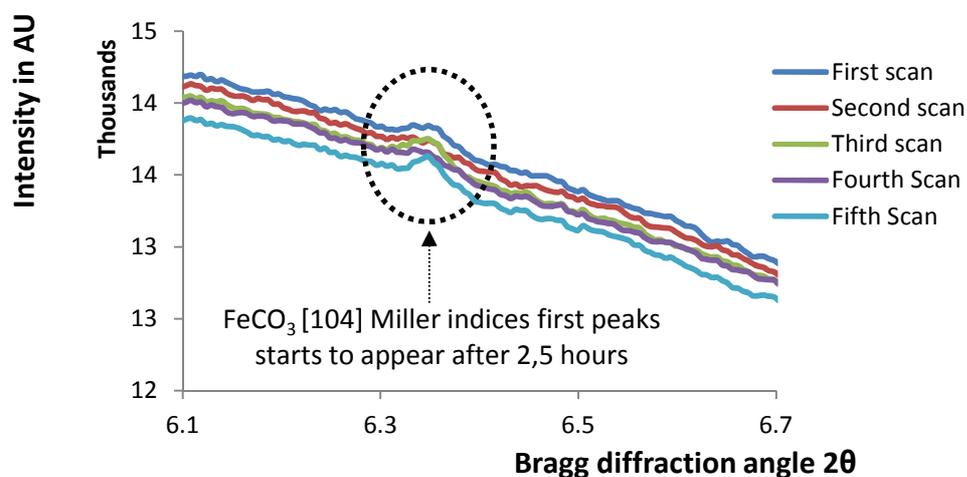
Figure 10-20 Zoom on the synchrotron diffraction pattern for an experiment where 20mg OA-POSS were added *in situ* [pH 6.3, 80°C, 3.5% NaCl, 0.52 bar CO$_2$pp, 0.1m/s]

The diffraction angle in this test should be extracted from the values detailed in Table 6-4 where the FeCO$_3$ [104] Miller index appears at $2\theta = 6.3569°$ and these peaks could be the representation of the first iron carbonate crystal seeds. It should be noted that a flow was applied in these *in situ* synchrotron tests equal to 0.1m/s which was not the case in all static tests undertaken at the corrosion laboratories of the University of Leeds.

10.4.2   OA-POSS as a preferential growth initiator

Another major observation from this research is the fact that in most cases, the iron carbonate crystals grew preferentially alongside the carbon steel surface (epitaxial growth) since the crystal size from the cross sections was much less than the size of the top view crystals. Shindo et al.[379] have studied the chemical environment of the CaCO$_3$ crystal growth by AFM observation of polyhedral micro-etch pits during dissolution and the effects of some ionic species have on the preferential growth of some Miller indices.

Whether OA-POSS is having similar effects by minimising the total surface Gibbs energy for the iron carbonate to grow preferentially in one direction is possible but further analysis is needed.

It is known that the relative stabilities of polar and neutral surfaces strongly depend on pH, since protonation of the carbonate ions changes distributions

of positive and negative electric charges at the surfaces. The equilibrium crystal form of $FeCO_3$ at pH6.6 needs to be established in order to confirm or not if a specific Miller plane could be stabilized with OA-POSS adsorbing at the crystal during the growth stage.

Another observation was the numerous morphologies obtained for the grown $FeCO_3$ crystals regardless of their size at various OA-POSS loadings. These can lead to various applications since cubes, prisms and rhombohedra shapes have different physical properties such as surface area and oil absorption. The numerous morphologies occur usually at various pH values as discussed by Fajardo et al.[361] when studying the solubility of $FeCO_3$ in the presence of acetic acid using an electrochemical quartz crystal microbalance and the fact that these occur at a single bulk pH when OA-POSS is added sustains the theory of several localised pH values in the vicinity of the on-growing crystals.

10.4.3 OA-POSS and cation vacancy doping theory

Another potential theory about the OA-POSS mode of action could be linked to its positive charge which exists at the operational pH of 6.6 with the ammonium groups being charged since no conversion of ammonium groups into primary amines occurs at a pH below 7 as shown in Figure 5-8. This allows for chloride ions which are negative to electrostatically interact with the ammonium groups and later adsorb to the pre-formed iron carbonate layer. In fact Guo et al.[380] believed that $FeCO_3$ had strong adsorption to anions via Coulombic as well as Lewis acid–base interactions.

Recent studies relying on Mott-Schottky electrochemical technique have shown that some ions could allow the formed iron carbonate to swap between an n-type or a p-type semiconducting behaviour.[260] The $FeCO_3$ shows dense microstructure and lower interstitial cation or anion vacancy doping allowing a strong corrosion resistance of the film in the first case scenario. On the contrary, higher cation vacancy doping was found and the integrity of the $FeCO_3$ microstructure was damaged, which decreased the transfer resistance of electron and mass, ultimately reducing the protective ability of the corrosion film.[260]

It is postulated that the higher protectiveness of the formed iron carbonate layers with regard to the localised corrosion mitigation described in section 10.2.2 can be explained by the fact that the OA-POSS molecules are enhancing the creation of an n-type semi-conductor behaviour of the $FeCO_3$ corrosion layer. When looking at Figure 10-21, seven most commonly seen

reactions that occur on the steel, film and solution system interfaces are depicted and labelled in Roman numeric from I to VII.

Inside the figure:

X65 Carbon steel

Solution

$J_{V_{Fe}^{2-}}$

$Fe + V_{Fe}^{2-} \rightarrow V_{Fe} + 2e^- \ (II)$

$Fe_{Fe} + X^{x-}.nH_2O \rightarrow Fe(H_2O)_n^{2+} + V_{Fe}^{2-} + X^{x-} \ (I)$

$Fe \rightarrow Fe_i^{2+} + V_{Fe} + 2e^- \ (III)$

$Fe_i^{2+} + X^{x-}.nH_2O \rightarrow Fe(H_2O)_n^{2+} + X^{x-} \ (IV)$

$J_{Fe_i^{2+}} \ and \ J_{V_O^{2+}}$

$Fe \rightarrow Fe_{Fe} + V_O^{2+} + 2e^- \ (V)$

$V_O^{2+} + H_2[O].nH_2O \rightarrow [O]_O + 2H^+ \ (VIa)$

$\frac{1}{x} V_O^{2+} + X^{x-}.nH_2O \rightarrow X_O^{2-x}.nH_2O \ (VIb)$

$Fe[O] + 2H^+ + \frac{n}{2} H_2O \rightarrow Fe(H_2O)_n^{2+} + H_2[O] \ (VII)$
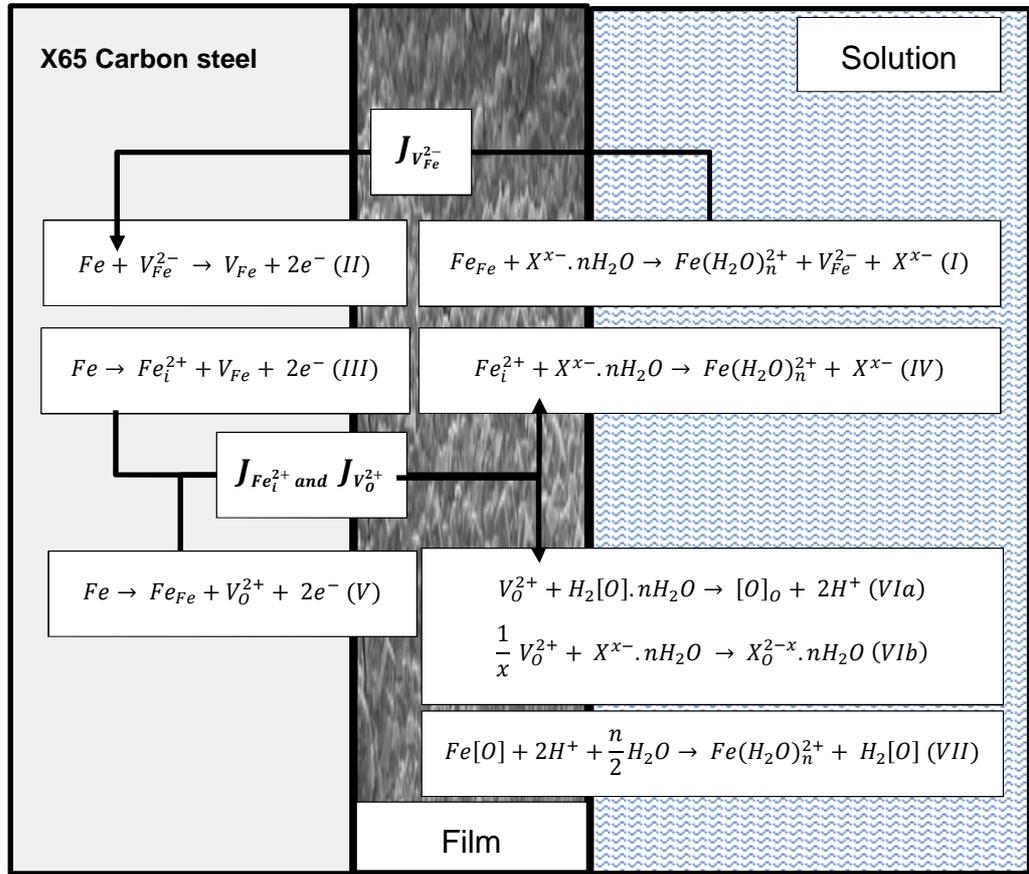
Film

V_{Fe}^{2-} = cation vacancy

$X^{x-}.nH_2O$ = Hydration anion

V_O^{2+} = anion vacancy

$[O]$ = film forming anion

Fe_i^{2+} = interstitial cation

$Fe(H_2O)_n^{2+}$ = aqueous ferrous ion

V_{Fe} = neutral vacancy

$Fe[O]$ = film compound

Fe_{Fe} = ferrous ion in a cation site

$[O]_O$ = anion in an anion site

Figure 10-21 Physicochemical mechanism for the semiconductor type of FeCO₃ films adapted from Ren et al.[260]

These can be divided between reactions that occur on the outer layer of the iron carbonate (I, IV, VI and VII) while the reminder evolve on the internal FeCO₃ side (II, III and V).

In summary, the cation vacancy is generated according to reaction (I) by adsorption of a hydration anion on the active ferrous ion present in a cation site on the formed iron carbonate layer; this is assimilated to the catalysis of adsorbed species. The next step is the diffusion of the cation vacancy from the film/solution interface to the film/steel interface as per reaction (II) which eliminates it. On the other hand, the anion vacancy and interstitial cation release are due to reactions (III) and (V) and these diffuse to the film surface before being consumed as per equations (IV) and (VI). The ultimate reaction (VII) is equivalent to the corrosion layer or film dissolution.

The OA-POSS activity is explained here as a potential kinetic effect which helps favour the establishment of an n-type semiconducting layer known to be more protective.

Equation 10-2 n-type semiconducting flux behaviour

$$J_{V_{Fe}^{2-}} < J_{Fe_i^{2+}} + J_{V_O^{2+}}$$

Equation 10-3 p-type semiconducting flux behaviour

$$J_{V_{Fe}^{2-}} > J_{Fe_i^{2+}} + J_{V_O^{2+}}$$

Thus when the flux of the cation vacancies is higher than the combined flux of the interstitial cations and anion vacancies, then the n-type semiconducting behaviour is of order.

The solvation of the OA-POSS by the chloride ions is possible since by adding 100mg of OA-POSS, this corresponds to a number of moles equal to 85µmol/Litre and the 3.5 wt% of NaCl provides 0.6 mol/Litre of chloride ions; this means that chloride is in excess since every OA-POSS molecule requires only 8 molecules of chloride to be fully solvated or 0.68m mol/Litre. The solvated OA-POSS molecule was previously schematised in Figure 5-6.

10.4.4   OA-POSS potency and effectiveness

In some of the electrochemical tests, the potency of the OA-POSS seems to decrease as observed in Figure 10-22 where only the 30mg loading showed a quick CR decrease. Likewise, Figure 10-23 illustrates tests ran at loadings between 10 and 60mg OA-POSS where longer times were required before the CR actually decreased below the 0.01mmpy threshold.

This observation requires more investigation and Figure 10-24 shows another set of results where the CR values only reached the 0.01 mmpy barrier after 100 hours even when 20mg OA-POSS is added.
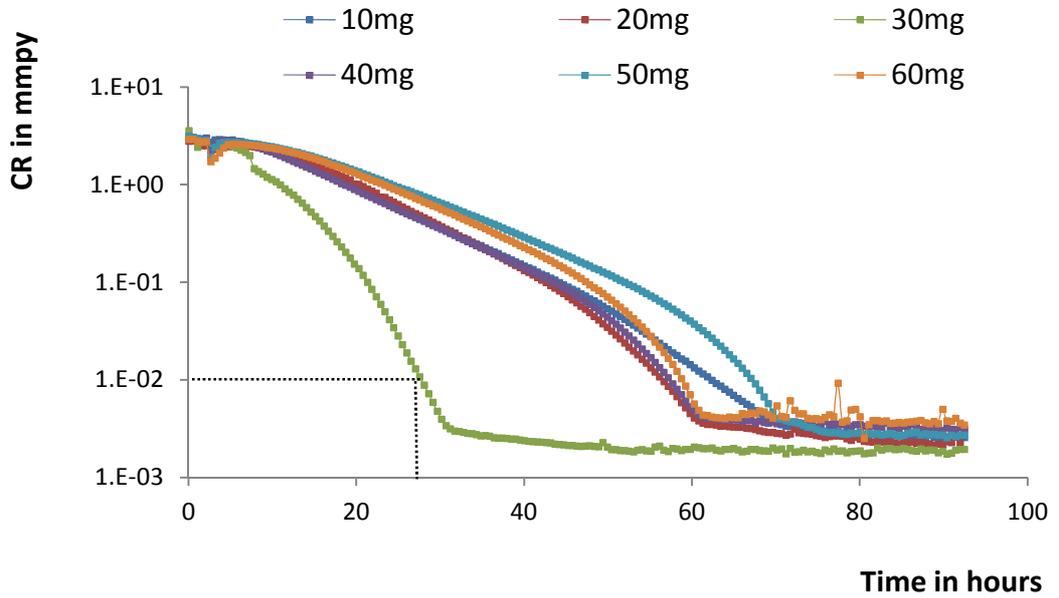
Figure 10-22 CR variations of X65 samples subjected to 10, 20, 30, 40, 50 and 60 mg OA-POSS added after 2 hours [pH 6.6, 60°C, 3.5% NaCl, 0.8bar CO_2]
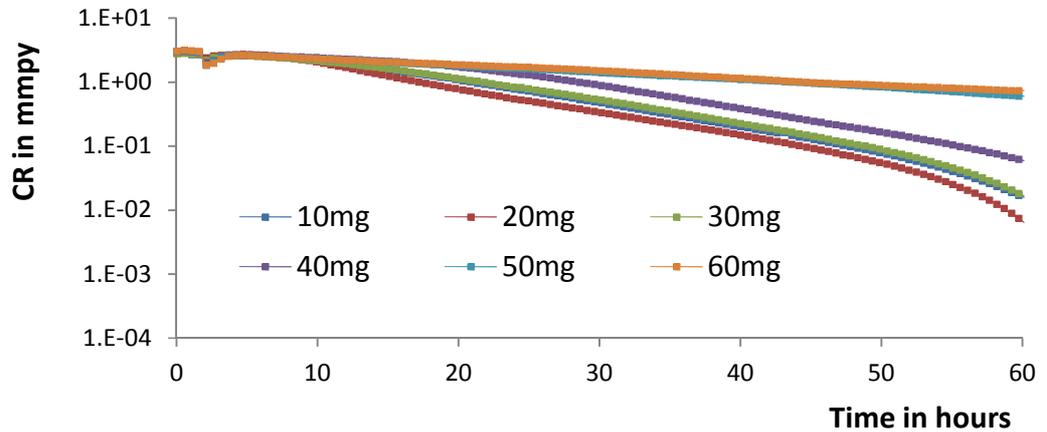
Figure 10-23 CR variations of X65 samples subjected to 10, 20, 30, 40, 50 and 60 mg OA-POSS added after 2 hours [pH 6.6, 60°C, 3.5% NaCl, 0.8bar CO2]
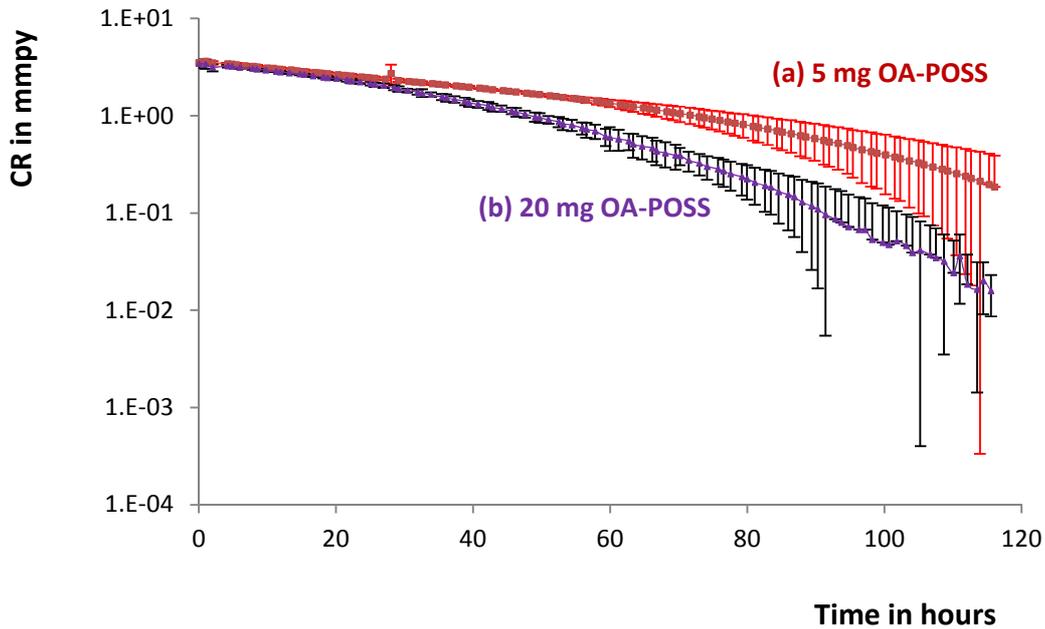
Figure 10-24 CR variations of X65 samples subjected to (a) 5 mg OA-POSS and (b) 20 mg OA-POSS added after 2 hours [pH 6.6, 60°C, 3.5% NaCl, 0.8bar CO2]

Nonetheless, the CR variations depicted in Figure 10-22, Figure 10-23 and Figure 10-24 still display a clear and quick drop in the CR variation from values around 3.5mmpy to values lower than 0.01 mmpy when compared to a totally blank test where the CR remains stable at values around 3.5 mmpy for 120 hours as per Figure 7-33. In fact, even when the OA-POSS potency is reduced, the real impedance values Z' observed when silsesquioxanes moieties are added reach values as high as 1000 $\Omega.cm^2$ as seen in Figure 10-25 when 5mg OA-POSS are administered. These values still exceed 10,000 $\Omega.cm^2$ when 20mg OA-POSS are added as per Figure 10-25 while these remain stagnant around 120 $\Omega.cm^2$ as shown previously in Figure 7-36 if no OA-POSS is added.

In fact, tests ran with 5mg OA-POSS show that the real impedance exceeds the 1000 $\Omega.cm^2$ after 63 hours as depicted in Figure 10-25. Moreover, the test ran with higher concentration of OA-POSS shows higher impedance values at shorter test durations; that is after just 12 hours as seen in Figure 10-26.
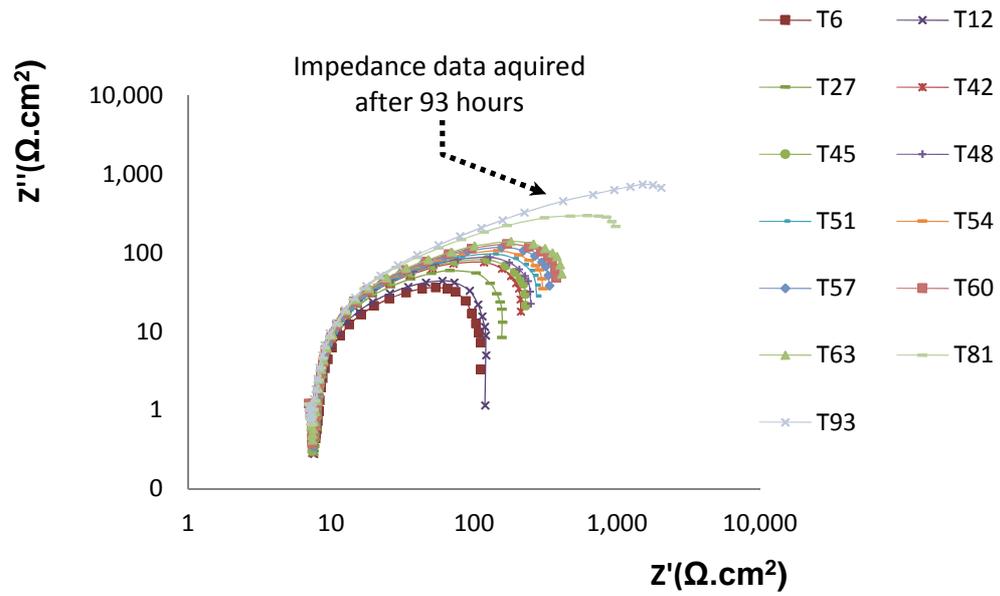
Figure 10-25 Nyquist EIS plot with 5 mg OA-POSS added [60°C, 3.5% NaCl, pH=6.6, 0.8bar CO_2]
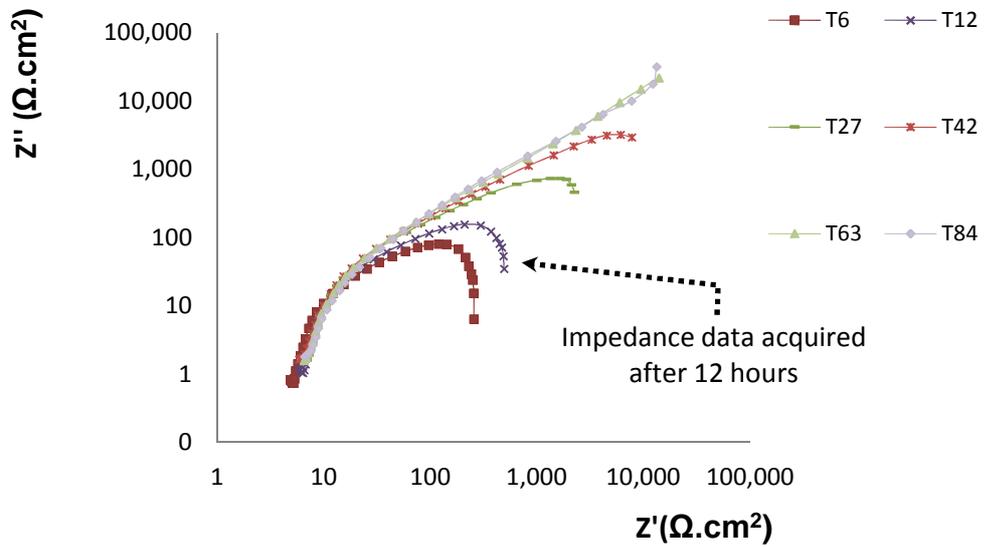
Figure 10-26 Nyquist EIS plot with 20 mg OA-POSS added [60°C, 3.5% NaCl, pH=6.6, 0.8bar CO_2]

Similarly, the potency decrease in the OA-POSS was also seen when tests with lower concentration of the nanofiller were undertaken as seen in Figure 10-27.
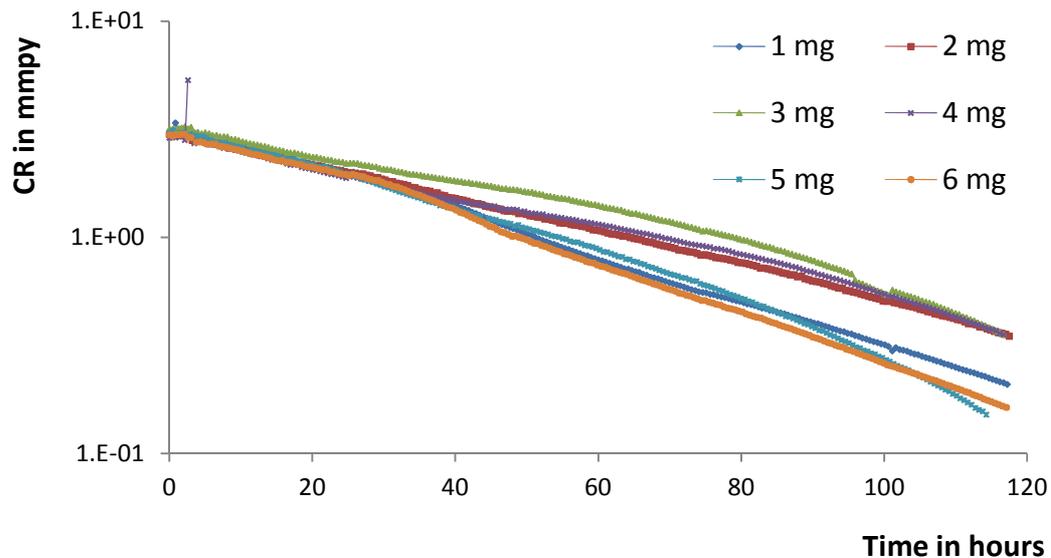
Figure 10-27 CR variations of X65 samples subjected to 1, 2, 3, 4, 5 and 6 mg OA-POSS added after 2 hours [pH 6.6, 60°C, 3.5% NaCl, 0.8bar CO_2]

Again even with this slow but steady corrosion rate decline, the trend is distinctive from the one where no nanofiller is added since the latter show no slight change in its electrochemistry for a period as long as 120 hours (Figure 7-33 and Figure 7-36).

These observations with relation to the delayed growth of protective iron carbonate layers should be further investigated by purchasing new OA-POSS product and comparing results from a freshly produced nanofiller with experiments ran with the same product after it has expired since a shelf life issue could be causing such observations.

10.4.5 Schematic representation of the chain of events that occur over the steel surface when OA-POSS is added

Since the nanofiller was seen to provide better electrochemical results after a pre-corrosion period, it is logical to assume that the created surface roughness will help the OA-POSS adsorb onto the carbon steel exposed surface. Once the hybrid nanofiller is available at the steel surface, it is postulated that it interacts with the iron carbonate precursor, reducing the activation energy which is necessary for the crystal nucleation process to occur. Consequently, once the first set of $FeCO_3$ nuclei start showing, an interlacing hybrid iron carbonate which is rich with OA-POSS on its lower side develops and shows mechanical enhancement and provide a higher general and localised corrosion protection.

318
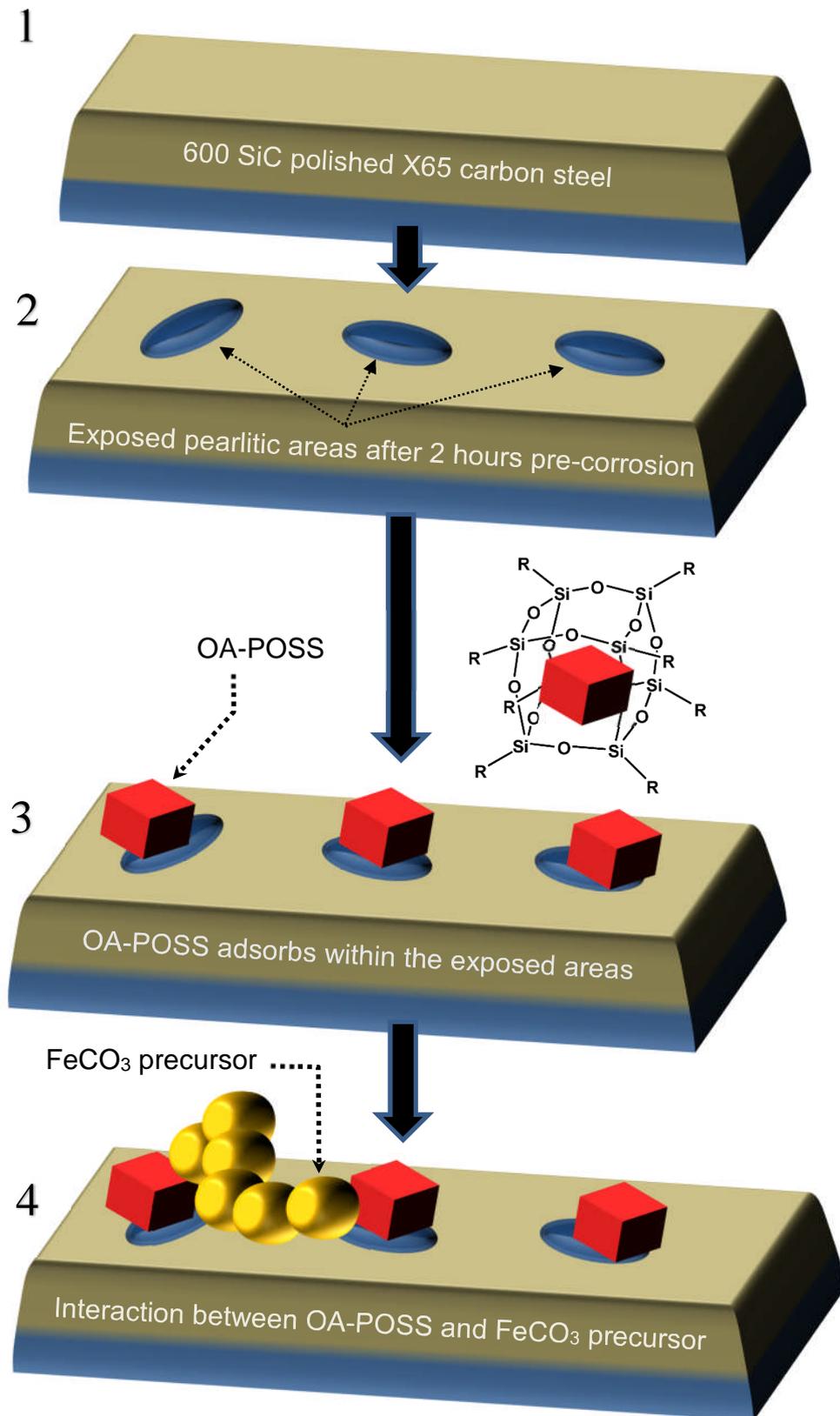
Figure 10-28 Schematic of the assumed OA-POSS mode of action

- In fact, after 2 hours pre-corrosion, there will be an excess of available electrons mainly in the pearlitic regions which will be negatively charged. At a pH of 6.6, the OA-POSS is positively charged and will adsorb to the negatively charged carbon steel. Since the OA-POSS is formed from 8 ammonium side groups, some remaining groups will interact with the chlorides ions and a solvation mechanism will occur.
- It is assumed that the now negatively charged OA-POSS surface in contact with the brine solution will play the role of a ferrous iron sink thus bringing the excess Fe^{2+} in the vicinity of the chloride ions and thus increasing locally the supersaturation of this element which is a required step for the precipitation of iron carbonate.
- Although the detailed mechanism of such intermediate step is not validated, it is assumed that an amorphous carbonate derivative forms firstly over the OA-POSS molecules which aggregation within the pearlitic areas play the role of an anchor that will help later nucleate the iron carbonate crystals.

10.5 Conclusions and summary of research key findings

The following list tries to summarise the main findings that have been detailed through the results chapter.

- The free drift tests were carried out for a period of ten days and while they showed a stable OCP for the experiments ran at 60°C (Figure 7-2), they also highlighted the fact that the iron carbonate films are subjected to chemical dissolution after that long exposure period especially at higher temperature since these tests showed the lowest $FeCO_3$ [113] to iron [110] Miller indices ratio (Table 7-1). This led to the decision of running the tests where the nanofiller is added at 60°C but also for a shorter period of time of 7 days.
- When the pH was decreased from a value of 7 downward, it appeared that pH 6.6 is the acidity at which no iron carbonate protective layer forms at 60°C. In fact only singular and scattered small iron carbonate islands formed from 5 crystals on average do show under the SEM on the top of the underlying carbon steel. All of these $FeCO_3$ crystals are cubic in shape (Figure 7-34).
- The OA-POSS effect on the corrosion rate at a pH of 6.6 and a temperature of 60°C was very similar to the corrosion rate variation of experiments ran at a pH of 6.75 without the OA-POSS addition (Figure

7-32). This suggests that adding the nanofiller helps form the $FeCO_3$ crystals while the pH is constant but at lower pH values.

- Adding the OA-POSS molecule appears to directly affect the OCP and brings it to more negative values by mainly affecting the cathodic reaction (Figure 7-47). The corrosion rate is also affected during the first 30 minutes and this could be attributed to the first stage adsorption of the OA-POSS on the carbon steel sample (Figure 7-36).

- The addition of the OA-POSS appears to induce a protective layer that is responsible for the corrosion rate dropping below values of 0.01 mmpy in less than 24 hours (Figure 7-40). This protective layer is composed of iron carbonate as shown by complementary surface analysis technique, mainly XRD and SEM (Figure 7-53 and Figure 7-54).

- Adding the OA-POSS in one shot achieves better corrosion rates drops as when compared to tests where the same quantity was added sequentially during a 3 days' period (Figure 7-52). This suggests that the nanofiller requires to adsorb on the freshly corroded carbon steel surface before other corrosion layers hinder this process.

- The XRD ratios between the [113] $FeCO_3$ Miller index and the [110] iron Miller index increase with the increasing concentration of the added nanofiller and this was shown on both high (Table 7-4) and low OA-POSS loadings (Figure 8-28). This suggests that the higher the OA-POSS weight added, the denser is the iron carbonate corrosion layer created in these environmental conditions. Similar observations were registered at higher pH values of 7 (Figure 9-26).

- The $FeCO_3$ crystals grown in the presence of the OA-POSS regardless of the nanofiller concentration appear more interlaced and the corrosion films are more compact with both cubic and prismatic $FeCO_3$ crystals present. Most of the $FeCO_3$ crystals also appear to grow via a leaflet-like build up mechanism (Figure 8-30).

- When tens of grams of OA-POSS are added within the brine solution after a 2 hours pre-corrosion time, the iron carbonate crystals and protective layers appear after roughly 24 hours and they help drop the corrosion rate to values lower than 0.01mmpy (Figure 8-2). The corrosion layers are mainly constituted of very small $FeCO_3$ crystals, and the layer appears very compact (Figure 8-4a). The corrosion layers are mainly formed of two superposing $FeCO_3$ crystals and the iron carbonate layer is relatively thin with a value around 5µm (Figure 8-7b).

321

Moreover, the double layered iron carbonate film looks closely tight with no cohesive delamination (Figure 8-13b).

- In the case of OA-POSS loadings lower than 10mg/L, the corrosion rate is also seen to drop below 0.01mmpy but it takes 20 to 60 hours to accomplish such trend (Figure 8-19). This finding could prove vital in case the OA-POSS is to be administered industrially at similar dosage as the administered corrosion inhibitors. The $FeCO_3$ crystals are slightly bigger and average 20µm (Figure 8-32b) although the corrosion layer thickness remains uniform, very thin and below 5 µm (Figure 8-34a).

- Light interferometry results have shown that adding OA-POSS help reduce the localised corrosion attack in the following order with regard to the nanofiller loading in milligrams (20 > 30 > 10 > blank) while the pit count shows slightly higher pits when 10mg OA-POSS are added but these are very small in depth when compared to the pits observed in a blank test (Figure 10-10). This finding is crucial and the apparent morphology change between experiments where a naturally growing iron carbonate and an OA-POSS enriched iron carbonate could be used as a tool to limit localised corrosion or pit growth initiation (Figure 8-44).

- Nanoindentation results showed that the Young's modulus of the hybrid iron carbonate film is 4 times higher than naturally grown iron carbonate corrosion film in the same environmental conditions while its hardness is increased by a factor of ten (Figure 8-49). Moreover, the elastic recovery parameter of the $FeCO_3$ corrosion layers grown with medium loadings of the nanofiller show values which are two to three times higher when compared to those of $FeCO_3$ films grown with the absence of the nanofiller or with excessive concentrations (Figure 10-13). This suggest that the nanofiller is able to improve some of the film mechanical properties that are known to help resist mechanical effects such as erosion, mainly the film hardness, while sustaining or even improving its malleability.

- The mechanical improvement of the hybrid iron carbonate film is linked to the silicon enrichment provided from the OA-POSS inorganic core and this was validated from examinations such as ICP-OES (Figure 8-50), EDX/TEM (Figure 8-54), BET porosity tests (section 8.5.5) and FTIR (Figure 8-57).

- While the OA-POSS activity was hindered in the presence of foreign cations such as calcium (Figure 9-42), it showed a synergistic effect with regard to the corrosion rate mitigation when coupled to ferrous chloride addition (Figure 9-41). Although no corrosion mitigation was observed at pH as low as 3.75 (Figure 9-2), the OA-POSS was able to reduce the corrosion rate during the first 50 hours by a value averaging 1.5mmpy at a pH of 5 (Figure 9-6). Moreover, XRD scans ran at a pH of 5 showed that both [110] and [113] iron carbonate Miller indices are visible when the nanofiller is added. These results are very promising and it could be hoped that altering the nanofiller side chains in a way that will help resist the acidic environmental hydrolysis could prove very beneficial in order to grow iron carbonate protective films at even lower pH values than the ones tested in this research.

10.6 Proposed additional work

The current research finding can be pushed forward by analysing the OA-POSS under other environmental physical, chemical and mechanical stresses. As such tests at high flow velocities, adhesion and wear resistance of the nanocomposite like iron carbonate can be assessed.

Moreover a totally new hybrid POSS moiety can be designed by relying on molecular dynamic solubility parameter assessment. Recently focus on bacterial grown iron carbonate is increasing and some findings could help establish bacterial colonies which are known to alter the localised pH. As such, these bacteria can help synthesise a protective iron carbonate at lower pH thus providing protective levels where siloxane moieties would be hydrolysed.

10.6.1   Wider range of environmental parameters

While repeats for the long term tests shown in section 7.1 are required in order to validate the assertions corresponding to the relationship between the degree of protection of the iron carbonate corrosion layer and its abundance as indirectly assessed from the XRD relative intensities, more experiments should also be undertaken in order to evaluate the effect of a wider range of velocity and acidity on the OA-POSS beneficial effects.

10.6.1.1   Velocity

The addition of the silsesquioxane based nanofiller of choice has been able to mitigate both general and localised corrosion but that was done under static

conditions where the only perturbation brought to the system was due to the continuous bubbling of carbon dioxide inside the beaker and the magnetic stirrer evolving at 250 rpm. The only test ran in flow conditions was undertaken in the *in situ* synchrotron flow cell for just 2.5 hours and as such a larger matrix of velocities should be investigated by running tests on the rotating cylinder electrodes for example in laminar and turbulent flow and assess for the iron carbonate film stability.

10.6.1.2   Acidity

It will be interesting to push forward the testing of the OA-POSS to lower pH values progressively starting at 6.6 and going down and checking for the iron carbonate crystal growth extent since some appeared when 100mg OA-POSS were added at a pH of 5 as seen in Figure 9-12. Moreover it was shown that dissolving the iron carbonate films in 15% acetic acid which is a necessary step for the ICP analysis took almost 24 hours for the OA-POSS modified scales prior to full film dissolution whereas iron carbonate films formed only by adding 50ppm of $FeCl_2$ dissolved in just 4 to 6 hours. It could be of interest to run a series of tests where the solution is buffered to high pH values in order to grow corrosion films with and without the presence of OA-POSS then try and dissolve these formed scaled by reducing the pH to more acidic values.

10.6.1.3   Test duration

The free draft experiments detailed in section 7.1 showed that after ten days, the iron carbonate corrosion layer appear to start dissolving even at temperatures as high as 80°C. It is proposed that repeating these tests while adding OA-POSS could provide insight whether the nanofiller has any beneficial effect on limiting this chemical dissolution and trying to uncover such underlying mechanisms.

10.6.2   Additional mechanical tests

10.6.2.1   Adhesion testing

Carrying out adhesion tensile tests in order to assess the bond strength between the formed iron carbonate corrosion layer and the underlying steel could be of paramount importance since it is one of the most important characteristic required for an efficient protective scale layer. It was referenced in previous studies that such parameter increases when the a compact inner scale with few defects, especially near the interface between the scale and steel is formed due to the fact that under-deposit corrosion was promoted by

the corrosion product scale and the precipitation of $FeCO_3$ at the points on the scale-steel interface filled in the corrosion layer.[178]

Stating the obvious, good protective properties of the iron carbonate films are supposed to be conditional on the good bonding between the film and the corroding metal as opposed to detached films whose protective capability is seriously reduced even when they are very dense. There seems to be a confirmed link between the film adhesive or cohesive properties and steel microstructure which is determined by chemical composition of the steel and heat treatment and it could prove useful to check if the initial stages of OA-POSS adsorption on the X65 carbon steel alter the bonding of the growing corrosion layer.

10.6.2.2   Porosity

The porosity of the synthetic iron carbonate was determine via the BET nitrogen adsorption isotherms but it could prove useful to attempt a systematic determination of all iron carbonate layers formed in CO_2 saturated environments using techniques such as nano X-ray computed tomography. This technique is known to have lower resolution than FIB/SEM but is non-destructive and does not require impregnation and vacuum. It allows for the determination of many parameters such as the scale porosity, its pore connectivity, tortuosity, structural diffusivity coefficient and the mean pore size.[381]

10.6.2.3   Wear

Since most production pipelines include residual components such as sand in some areas, assessing any improvement in the shear resistance of the iron carbonate modified corrosion layer could prove also useful. These tests can rely on weight loss determination after running tests in recirculating flow rigs or rotating cylinder electrodes in the presence of sand particles with different shapes.[244]

10.6.3   Biomimetic and bacterial iron carbonate

Recently a multitude of published research papers focused on bacterial grown nanoscale iron carbonate. The first clear experimental evidence of bio-geo-chemically formed siderite and ferrihydrite in the natural environment was discovered by Sawicki et al.[382] in 1995. They found very fine particles of siderite, typically 2-3 nm in size, in the anaerobic face at the rock-biofilm boundary. The biofilm occurred shortly after the hole was drilled, and

developed rapidly in just four to six weeks, eventually covering the whole of the wet surface or about 20% of the total area for a thickness up to 10 mm. The idea here could focus on using these sessile bacterial communities to produce siderite biofilms by sorbing produced Fe^{2+} ions and tuning bacterial gene expression to changing environments in order to adapt to various parameters such as harsh temperatures and acidity levels.

Evidence for microbial mediation in the synthesis of iron carbonate in sediment samples from Rio Tinto, a shallow river with very acidic waters, indicate that carbonates are formed in physico-chemical conditions ranging from acid to neutral pH. Acidiphilium sp. PM, an iron-reducing bacterium isolated from Rio Tinto, was actually found to be mediating the precipitation of iron carbonate under acidic conditions and at temperatures as low as 30°C.[235]

Since these bacteria modify the system in a way allowing them to overcome the kinetic barriers to carbonate formation, this can be adapted for the benefit of designing a system relying on such bacteria in order to synthesise and protect pipelines at high acidity and low temperatures. In fact, by locally neutralizing the pH and lowering the Fe^{3+}/Fe^{2+} ratio, these bacteria were able, in a biotic medium, to induce mineral precipitation by modifying the conditions of their surrounding environment and/or concentrating ions in the bacterial cell envelope and by acting as nucleation sites. These could be also experimented for a potential self-healing action on a dissolved or mechanically damaged iron carbonate corrosion layer.

References

1.	Pavlik, Z., *Population and Development.* Acta Universitatis Carolinae, Geographica, 1995. **30**(1-2): p. 43-51.
2.	Chamberlin, R.V., *The Big World of Nanothermodynamics.* Entropy, 2015. **17**(1): p. 52-73.
3.	Brondel, D., et al., *Corrosion in the Oil Industry.* Oilfield Review, 1994. **6**(2): p. 4-18.
4.	Davis, J.R., *The Effects and Economic Impact of Corrosion*, in *Corrosion: Understanding the Basics*, J.R. Davis, Editor. 2003, ASM International. p. 1-20.
5.	Center, P.P.R.M.L. *Silver Bridge after collapse* 1967 25/06/2016]; Available from: http://pprivermuseum.com/SilverBridge/default.html.
6.	Mallinson, L., *Ageing Studies and Lifetime Extension of Materials.* 2012: Springer US.
7.	Schmidt, S. and H. Weigt, *Interdisciplinary Energy Research and Energy Consumption: What, Why, and How?* Energy Research and Social Science, 2015. **10**: p. 206-219.
8.	Smith, L.C., *The New North: The World in 2050.* 2011: Profile Books.
9.	Wang, Z., Y. Xu, and B. Suman, *Research Status and Development Trend of Ultrasonic Oil Production Technique in China.* Ultrasonics Sonochemistry, 2015. **26**: p. 1-8.
10.	Rodrigues Cezário, W., et al., *The Energy Revolution in the USA and the Pre-Salt Reserves in Brazil: Risks and Opportunities for the Brazilian Petrochemical Industry.* Futures, 2015. **73**: p. 1-11.
11.	Nduagu, E.I. and I.D. Gates, *Unconventional Heavy Oil Growth and Global Greenhouse Gas Emissions.* Environmental Science and Technology, 2015. **49**(14): p. 8824-8832.
12.	Plazak. *Natural Gas Production from US Shale.* 2013 25/06/2016]; Available from: https://commons.wikimedia.org/wiki/File:Natural_Gas_Production_from_US_Shales_2000-2013.png.
13.	Centner, T.J. and G. Kostandini, *Local Governments Want Authority to Address Problems: The Case of Horizontal Drilling and Hydraulic Fracturing In the United States.* Land Use Policy, 2015. **49**: p. 227-235.
14.	Badiru, A.B. and S.O. Osisanya, *Project Management for the Oil and Gas Industry: A World System Approach.* 2013: Taylor & Francis.
15.	Papavinasam, S., *Chapter 1 - The Oil and Gas Industry*, in *Corrosion Control in the Oil and Gas Industry*, S. Papavinasam, Editor. 2014, Gulf Professional Publishing: Boston. p. 1-39.
16.	Attanasi, E.D. and P.A. Freeman, *Commercial Possibilities for Stranded Conventional Gas from Alaska's North Slope.* Natural Resources Research, 2014. **23**(1): p. 175-193.
17.	Nguyen, T.V., et al., *Life Performance of Oil and Gas Platforms: Site Integration and Thermodynamic Evaluation.* Energy, 2014. **73**: p. 282-301.
18.	Zou, C., et al., *Types, Characteristics, Genesis and Prospects of Conventional and Unconventional Hydrocarbon Accumulations:*

Taking Tight Oil and Tight Gas in China as an Instance. Shiyou Xuebao/Acta Petrolei Sinica, 2012. **33**(2): p. 173-187.

19. Energy, S.L. *Conventional and unconventional gas sources.* 2006 25/06/2016]; Available from: http://www.sanleonenergy.com/about-us/briefing-note-on-unconventional-exploration-and-production.aspx.

20. Papon, P., *Shale Gas: Myths and Realities The Stakes in This Much-Heralded Revolution and Its Limitations.* Futuribles: Analyse et Prospective, 2014(399): p. 81-98.

21. Holditch, S.A., *Tight Gas Sands.* Journal of Petroleum Technology, 2006. **58**(6): p. 86-93.

22. Heidersbach, R., *Metallurgy and Corrosion Control in Oil and Gas Production.* 2010: Wiley.

23. Ropital, F., Y. Chauvin, and T. Jones, *Corrosion and Degradation of Metallic Materials: Understanding of the Phenomena and Applications in Petroleum and Process Industries*, in *Corrosion and Degradation of Metallic Materials: Understanding of the Phenomena and Applications in Petroleum and Process Industries.* 2010, Editions Technip. p. 1-3.

24. Laumb, J.D., et al., *Wellbore Corrosion And Failure Assessment for CO_2 EOR And Storage: Two Case Studies In The Weyburn Field.* International Journal of Greenhouse Gas Control, 2016.

25. Conference, C. *CO_2-EOR.* 2012 17-06-16]; Available from: http://www.co2conference.com/.

26. Papavinasam, S., *Chapter 5 - Mechanisms*, in *Corrosion Control in the Oil and Gas Industry*, S. Papavinasam, Editor. 2014, Gulf Professional Publishing: Boston. p. 259.

27. Frankel, G., *Coatings for Corrosion Protection.* 2010: Electrochemical Society.

28. von Baeckmann, W., W. Schwenk, and W. Prinz, *Handbook of Cathodic Corrosion Protection.* 1997: Elsevier Science.

29. Ghali, E., V.S. Sastri, and M. Elboujdaini, *Corrosion Prevention and Protection: Practical Solutions.* 2007: Wiley.

30. Philip A. Schweitzer, P.E., *Encyclopedia Of Corrosion Technology.* 2004: CRC Press.

31. Matsumura, M., *Erosion-Corrosion: An Introduction to Flow Induced Macro-Cell Corrosion.* 2012: Bentham Science Publishers.

32. Singh, R., *Pipeline Integrity Handbook - Risk Management and Evaluation.* 2014: Elsevier.

33. Muhlbauer, W.K., *Pipeline Risk Management Manual: Ideas, Techniques, and Resources.* Vol. Chapter 15 - Risk management. 2004: Elsevier.

34. Riggs Jr, O.L., *Theoretical Aspects of Corrosion Inhibitors and Inhibition.* Corrosion inhibitors, 1973: p. 7-27.

35. Dietsche, F., et al., *Organic Corrosion Inhibitors for Interim Corrosion Protection.* 2007, NACE International.

36. Sastri, V.S., *Corrosion Inhibitors: Principles and Applications.* 1998: Wiley-Blackwell.

37. Fink, J.K., *Chapter 6 - Corrosion Inhibitors*, in *Petroleum Engineer's Guide to Oil Field Chemicals and Fluids.* 2012, Gulf Professional Publishing: Boston. p. 219.

38. Sanatkumar, B.S., J. Nayak, and A.N. Shetty, *The Corrosion Inhibition of Maraging Steel Under Weld Aged Condition by 1(2E)-1-(4-Aminophenyl)-3-(2-Thienyl)Prop-2-En-1-One In 1.5 M Hydrochloric Acid Medium.* Journal of Coatings Technology Research, 2012. **9**(4): p. 483-493.

39. Raja, P.B., et al., *Reviews on Corrosion Inhibitors: A Short View.* Chemical Engineering Communications, 2016. **203**(9): p. 1145-1156.

40. Farelas, F. and A. Ramirez, *Carbon Dioxide Corrosion Inhibition of Carbon Steels Through Bis-Imidazoline and Imidazoline Compounds Studied by EIS.* International Journal of Electrochemical Science, 2010. **5**(6): p. 797-814.

41. Education, C.A.C., et al., *Assessment of Corrosion Education.* 2009: National Academies Press.

42. Koch, G.H., *Corrosion Cost and Preventive Strategies in the United States*, NTiS, Editor. 2002: Dublin, OH. p. 786.

43. Papavinasam, S., *Corrosion Control in the Oil and Gas Industry.* 2013: Elsevier Science.

44. (ERCB), U.B., *Pipeline Performance in Alberta.* 2007: 205-5th Street SW, Calgary, Alberta, Canada.

45. Haas, B., *Sinopec Workers Detained after Fatal Pipeline Blast* Hydrocarbon Processing, 2013.

46. M.S. Günter Schmitt, G.F.H., , E.-H.H. Wayne Burns, Antoine Pourbaix,, and a.G. Jacobson, *Global Needs for Knowledge Dissemination, Research, and Development in Materials Deterioration and Corrosion Control.* 2009, The World Corrosion Organization. p. 44.

47. Kapusta, S., L. Balzano, and P.M. Te Riele, *Nanotechnology Applications in Oil and Gas Exploration and Production.* 2011, International Petroleum Technology Conference.

48. Brown, J.M., D. Curliss, and R.A. Vaia, *Thermoset-Layered Silicate Nanocomposites. Quaternary Ammonium Montmorillonite with Primary Diamine Cured Epoxies.* Chemistry of Materials, 2000. **12**(11): p. 3376-3384.

49. Yilmaz, S., et al., *Fracture Toughness Analysis of O-POSS/PLA Composites Assessed by Essential Work of Fracture Method.* Composites Part B: Engineering, 2014. **56**(0): p. 527-535.

50. Grala, M., Z. Bartczak, and M. Pracella, *Morphology and Mechanical Properties of Polypropylene-POSS Hybrid Nanocomposites Obtained by Reactive Blending.* Polymer Composites, 2013. **34**(6): p. 929-941.

51. El Achaby, M., et al., *Mechanically Strong Nanocomposite Films Based On Highly Filled Carboxymethyl Cellulose with Graphene Oxide.* Journal of Applied Polymer Science, 2016. **133**(2).

52. Panwar, A., V. Choudhary, and D.K. Sharma, *Review: A review: Polystyrene/Clay Nanocomposites.* Journal of Reinforced Plastics and Composites, 2011. **30**(5): p. 446-459.

53. Yu, J., et al., *In Situ Development of Self-Reinforced Cellulose Nanocrystals Based Thermoplastic Elastomers by Atom Transfer Radical Polymerization.* Carbohydrate Polymers, 2016. **141**: p. 143-150.

54. Kvarekval, J. and A. Dugstad. *Corrosion Mitigation with pH Stabilization in Slightly Sour Gas/Condensate Pipelines.* in *CORROSION*. 2006. NACE International.
55. Barbucci, R., *Integrated Biomaterials Science*. 2007: Springer US.
56. Kaw, A.K., *Mechanics of Composite Materials, Second Edition*. 2005: CRC Press.
57. Li, Z. and R. Yang, *Synthesis, Characterization, and Properties of a Polyhedral Oligomeric Octadiphenylsulfonylsilsesquioxane.* Journal of Applied Polymer Science, 2014. **131**(20).
58. Tishchenko, G. and M. Bleha, *Diffusion Permeability of Hybrid Chitosan/Polyhedral Oligomeric Silsesquioxanes (POSS™) Membranes to Amino Acids.* Journal of Membrane Science, 2005. **248**(1–2): p. 45-51.
59. Mori, H., *Design and Synthesis of Functional Silsesquioxane-Based Hybrids by Hydrolytic Condensation of Bulky Triethoxysilanes.* International Journal of Polymer Science, 2012. **2012**: p. 17.
60. Wang, X.T., et al., *Photochemistry of Azobenzene Side-Chains Liquid Crystalline Containing Pendant Polyhedral Oligomeric Silsequioxanes (POSS)*, in *Advanced Materials Research*. 2013. p. 316-319.
61. Solouk, A., et al., *Surface Modification of POSS-Nanocomposite Biomaterials Using Reactive Oxygen Plasma Treatment for Cardiovascular Surgical Implant Applications.* Biotechnology and Applied Biochemistry, 2011. **58**(3): p. 147-161.
62. Fabritz, S., et al., *Bioconjugation on Cube-Octameric Silsesquioxanes.* Organic & Biomolecular Chemistry, 2013. **11**(14): p. 2224-2236.
63. Cozza, E.S., et al., *Preparation, Characterization, and Properties of Nanofibers Based on Poly(vinylidene fluoride) and Polyhedral Oligomeric Silsesquioxane.* Polymers for Advanced Technologies, 2012. **23**(9): p. 1252-1257.
64. Ciesielczyk, F., K. Szwarc-Rzepka, and T. Jesionowski, *Evaluation of Physicochemical Properties of a New Group of SiO_2/Silane/POSS Hybrid Materials.* Surface and Interface Analysis, 2013. **45**(6): p. 998-1007.
65. Tanaka, K. and Y. Chujo, *Unique Properties of Amphiphilic POSS and Their Applications.* Polymer Journal, 2013. **45**(3): p. 247-254.
66. Zuckerman, J.J. and A.P. Hagen, *Inorganic Reactions and Methods: Oligomerization and Polymerization ; Formation of Intercalation Compounds. Volume 17*. 1990: VCH Publishers.
67. Zhang, Z., et al., *Curing Behavior and Dielectric Properties of Amino-Functionalized Polyhedral Oligomeric Silsesquioxane/Cyanate Ester Resin Hybrids.* High Performance Polymers, 2013. **25**(4): p. 427-435.
68. Kickelbick, G., *Functional Molecular Silicon Compounds I*. Structure and Bonding. Vol. Vol. 155. 2014: Springer. 233.
69. Dintcheva, N.T., et al., *Interaction in POSS-Poly(Ethylene-Co-Acrylic Acid) Nanocomposites.* Polym J, 2014. **46**(3): p. 160-166.
70. Sanchez, C., et al., *Applications of Hybrid Organic-Inorganic Nanocomposites.* Journal of Materials Chemistry, 2005. **15**(35-36): p. 3559-3592.

71.   Ebunoluwa Ayandele, B.S., Paschalis Alexandridis, *Polyhedral Oligomeric Silsesquioxane (POSS)-Containing Polymer Nanocomposites.* Nanomaterials, 2012. **2**(4): p. 445-475.

72.   Tanaka, K. and Y. Chujo, *Chemicals-Inspired Biomaterials: Developing Biomaterials Inspired by Material Science Based on POSS.* Bulletin of the Chemical Society of Japan, 2013. **86**(11): p. 1231-1239.

73.   Xu, D., L.S. Loo, and K. Wang, *Pervaporation Performance of Novel Chitosan-POSS Hybrid Membranes: Effects of POSS and Operating Conditions.* Journal of Polymer Science, Part B: Polymer Physics, 2010. **48**(21): p. 2185-2192.

74.   Mukhopadhyay, S., *Nanoscale Multifunctional Materials: Science & Applications.* 2011: Wiley.

75.   DeArmitt, C., *Polyhedral Oligomeric Silsesquioxanes in Plastics*, in *Applications of Polyhedral Oligomeric Silsesquioxanes*, C. Hartmann-Thompson, Editor. 2011, Springer Netherlands. p. 209-228.

76.   Lamm, M.H., T. Chen, and S.C. Glotzer, *Simulated Assembly of Nanostructured Organic/Inorganic Networks.* Nano Letters, 2003. **3**(8): p. 989-994.

77.   Ochi, M., Y. Uno, and M. Harada, *Effects of 3D Structure of Silsesquioxane Moieties on the Thermal and Optical Properties of Transparent Epoxy/Silsesquioxane Hybrid Materials.* Journal of Materials Science, 2013: p. 1-8.

78.   An, Y.-C., et al., *Organic-Inorganic Polymer Hybrids of Polystyrene with Ladderlike Polyphenylsilsesquioxanes.* Polym. J, 2008. **40**(6): p. 538-542.

79.   Kim, K.M. and Y. Chujo, *Polymer Hybrids With Functionalized Silsesquioxanes Via Two Physical Interactions In One System.* Journal of Polymer Science, Part A: Polymer Chemistry, 2003. **41**(9): p. 1306-1315.

80.   Hartmann-Thompson, C., *Applications of Polyhedral Oligomeric Silsesquioxanes.* 2011: Springer.

81.   Papavinasam, S., *Chapter 5 - Mechanisms*, in *Corrosion Control in the Oil and Gas Industry*, S. Papavinasam, Editor. 2014, Gulf Professional Publishing: Boston. p. 256.

82.   Stansbury, E.E. and R.A. Buchanan, *Fundamentals of Electrochemical Corrosion.* 2000: A S M International.

83.   McCafferty, E., *Introduction to Corrosion Science.* Introduction to Corrosion Science. 2010. 1-575.

84.   Baboian, R., *Corrosion Tests and Standards.* 1995: ASTM International.

85.   Rakhit, A.K., *The Essentials of Material Science and Technology for Engineers.* 2013: Xlibris Corporation.

86.   Elayaperumal, K. and V.S. Raja, *Corrosion Failures: Theory, Case Studies, and Solutions.* 2015: Wiley.

87.   Pletcher, D. and F.C. Walsh, *Industrial Electrochemistry.* 2012: Springer Netherlands.

88.   Popov, B.N., *Corrosion Engineering: Principles and Solved Problems.* 2015: Elsevier Science.

89. Testing, A.S.f. and Materials, *Annual Book of ASTM Standards*. 2007: ASTM.

90. Cicek, V., *Corrosion Engineering*. Vol. Chapter 6. 2014: Wiley.

91. Levinovitz, A.W. and N. Ringertz, *The Nobel Prize: The First 100 Years*. 2001: Imperial College Press.

92. Kelly, R.G., et al., *Electrochemical Techniques in Corrosion Science and Engineering*. 2002: CRC Press.

93. Ahmad, Z., *Principles of Corrosion Engineering and Corrosion Control*. 2006: Elsevier Science.

94. Tilley, R.J.D., *Understanding Solids: The Science of Materials*. 2004: Wiley.

95. Wikipedia. *Pourbaix diagram*. 2016 17-06-16]; Available from: https://en.wikipedia.org/wiki/Pourbaix_diagram#cite_note-1.

96. Frankel, G.S., et al., *Corrosion Science: A Retrospective and Current Status in Honor of Robert P. Frankenthal : Proceedings of the International Symposium*. 2002: Electrochemical Society.

97. Taylor, C.D. and P. Marcus, *Molecular Modeling of Corrosion Processes: Scientific Development and Engineering Applications*. 2015: Wiley.

98. Barnartt, S., *Primary Current Distribution Around Capillary Tips Used in the Measurement of Electrolytic Polarization.* Journal of The Electrochemical Society, 1952. **99**(12): p. 549-553.

99. Thomas, J.G.N., *The Electrochemistry Of Corrosion*, G. Hinds, Editor. p. 19.

100. Bockris, J.O.M. and A.K.N. Reddy, *Modern Electrochemistry 2B: Electrodics in Chemistry, Engineering, Biology and Environmental Science*. 2001: Springer.

101. Perez, N., *Electrochemistry and Corrosion Science*. 2007: Springer US.

102. Barnes, C.E., *Chemistry of Advanced Materials: An Overview (ed.s Interrante, Leonard V.; Hampden-Smith, Mark J.).* Journal of Chemical Education, 2000. **77**(9): p. 271-316.

103. DoITPoMS. *Kinetics of Aqueous Corrosion*. 2015 24/06/16]; Available from: http://www.doitpoms.ac.uk/tlplib/aqueous_corrosion/printall.php.

104. Bockris, J.O.M., D. Drazic, and A.R. Despic, *The Electrode Kinetics of the Deposition and Dissolution of Iron.* Electrochimica Acta, 1961. **4**(2-4): p. 325-361.

105. Badea, G., et al., *Polarisation Measurements Used for Corrosion Rates Determination.* Journal of Sustenable Energy, 2010. **1**.

106. Reddy, A.K. and M.E. Gamboa-Adelco, *Modern Electrochemistry 2A: Fundamentals of Electrodics*. Vol. 2A. 2000: Springer.

107. McCafferty, E., *Validation of Corrosion Rates Measured by the Tafel Extrapolation Method.* Corrosion Science, 2005. **47**(12): p. 3202-3215.

108. Talbot, D.E.J. and J.D.R. Talbot, *Corrosion Science and Technology*. 2010: CRC Press.

109. Kear, G. and F.C. Walsh, *The Characteristics of a True Tafel Slope.* Corrosion and materials, 2005. **30**(6): p. 51-55.

110. Jenkins, A. *The Challenges Associated With the Development and Application of Oil and Gas Corrosion Inhibitors.* in *Society of Petroleum Engineers - SPE International Conference and Exhibition on Oilfield Corrosion 2014: New Challenges for a New Era.* 2014.
111. Engineers, N.A.o.C., *ANSI/NACE MR0175/ISO 15156.* 2009.
112. Wang, P., et al., *Effect of H_2S/CO_2 Partial Pressure Ratio on theTensile Properties of X80 Pipeline Steel.* International Journal of Hydrogen Energy, 2015. **40**(35): p. 11925-11930.
113. Nešić, S., *Key Issues Related to Modelling of Internal Corrosion of Oil and Gas Pipelines – A Review.* Corrosion Science, 2007. **49**(12): p. 4308-4338.
114. Koch, G.H., et al., *Corrosion cost and preventive strategies in the United States.* 2002: Turner-Fairbank Highway Research Center.
115. Dugstad, A. and M. Halseid, *Internal Corrosion In Dense Phase CO_2 Transport Pipelines - State of the Art And the Need For Further R&D.* 2012, NACE International.
116. Zhu, J.L., et al., *Advances on Research of CO_2 Induced Corrosion and Its Protection.* Corrosion Science and Protection Technology, 2007. **19**(5): p. 350-353.
117. Kermani, M.B. and A. Morshed. *Carbon Dioxide Corrosion in Oil and Gas Production: A Compendium.* in *CORROSION.* 2003. Houston, TX: NACE International.
118. Ghareba, S. and S. Omanovic, *Interaction of 12-Aminododecanoic Acid With a Carbon Steel Surface: Towards the Development of 'Green' Corrosion Inhibitors.* Corrosion Science, 2010. **52**(6): p. 2104-2113.
119. Barker, R., Y. Hua, and A. Neville, *Internal Corrosion of Carbon Steel Pipelines for Dense-Phase CO_2 Transport in Carbon Capture and Storage (CCS) – A Review.* International Materials Reviews, 2017. **62**(1): p. 1-31.
120. Gu, T., et al., *Coupled Effect of CO_2 Attack and Tensile Stress on Well Cement Under CO_2 Storage Conditions.* Construction and Building Materials, 2017. **130**: p. 92-102.
121. Zhang, J., et al., *Chemical Analysis of the Initial Corrosion Layer on Pipeline Steels in simulated CO_2 Enhanced Oil Recovery Brines.* Corrosion Science, 2012. **65**(0): p. 397-404.
122. Gulbrandsen, E., M. Foss, and J. Sjöblom, *Interaction of Carbon Dioxide Corrosion Inhibitors With Corrosion Products Deposit.* 2008, NACE International.
123. Paul, S. and B. Syrek-Gerstenkorn, *Can Thermally Sprayed Aluminum (TSA) Mitigate Corrosion of Carbon Steel in Carbon Capture and Storage (CCS) Environments?* Journal of Thermal Spray Technology, 2017. **26**(1-2): p. 184-194.
124. Yin, Z.F., et al., *Effect of Temperature on CO_2 Corrosion of Carbon Steel.* Surface and Interface Analysis, 2009. **41**(6): p. 517-523.
125. Fajardo, V., et al., *Multipronged Characterization of the Corrosion Product Layer Formed on Mild Steel after Exposure to Acetic Acid.* 2013, NACE International.

126.   Moiseeva, L.S., *Carbon Dioxide Corrosion of Oil and Gas Field Equipment.* Protection of Metals, 2005. **41**(1): p. 76-83.

127.   Prepared by the Working Party on Corrosion in, O., M.B. Gas - Edited by: Kermani, and L.M. Smith, *CO_2 Corrosion Control in Oil and Gas Production - Design Considerations: (EFC 23).* 2011: Maney Publishing.

128.   Heuer, J.K. and J.F. Stubbins, *An XPS Characterization of $FeCO_3$ Films From CO_2 Corrosion.* Corrosion Science, 1999. **41**(7): p. 1231-1243.

129.   Heidari, P., et al., *A Comparison of WAG and SWAG Processes: Laboratory and Simulation Studies.* Energy Sources, Part A: Recovery, Utilization and Environmental Effects, 2013. **35**(23): p. 2225-2232.

130.   Dugstad, A. *Fundamental Aspects of CO_2 Metal Loss Corrosion - Part 1: Mechanism.* in *CORROSION.* 2006. San Diego, CA: NACE International.

131.   Nesic, S., *Effects of Multiphase Flow on Internal CO_2 Corrosion of Mild Steel Pipelines.* Energy and Fuels, 2012. **26**(7): p. 4098-4111.

132.   B.R Linter, G.T.B., *Reactions of Pipeline Steels in Carbon Dioxide Solutions.* Corrosion Science, 1999. **41**(1): p. 117-139.

133.   Nordsveen, M., S.N.R. Nyborg, and A. Stangeland, *A Mechanistic Model for Carbon Dioxide Corrosion of Mild Steel in the Presence of Protective Iron Carbonate FilmsPart 1: Theory and Verification.* Corrosion, 2003. **59**(05).

134.   De Waard, C. and D.E. Milliams, *Carbonic Acid Corrosion Of Steel.* Corrosion, 1975. **31**(5): p. 177-181.

135.   Nesic, S. and J. Postlethwaite, *Modelling of CO_2 Corrosion Mechanisms*, in *Modelling Aqueous Corrosion*, K. Trethewey and P. Roberge, Editors. 1994, Springer Netherlands. p. 317-335.

136.   Hany Mohamed Abd El-Lateef, V.M.A., Leylufer Imran Aliyeva, Teyyub Allahverdi Ismayilov and *Corrosion Protection of Steel Pipelines Against CO_2 Corrosion - A Review.* Chemistry Journal 2012. **02**(02): p. 52-63.

137.   Gopal, M., R. Zhang, and S. Rajappa, *Modeling the Diffusion Effects Through the Iron Carbonate Layer in the Carbon Dioxide Corrosion of Carbon Steel.* 1998, NACE International.

138.   Tanupabrungsun, T., B. Brown, and S. Nesic, *Effect of pH on CO_2 Corrosion of Mild Steel at Elevated Temperatures.* 2013, NACE International.

139.   K. Videm, A.D., *Film Covered Corrosion, Film Breakdown and Pitting Attack of Carbon Steels in aqueous CO_2 Environments*, in *NACE International.* 1988: Houston, TX.

140.   M.Singer, L.C., A.Mohsen, A.Jenkins, *Top Of Line Corrosion - Part 1: Review of the Mechanism and Laboratory Experience*, in *CORROSION 2014.* 2014, NACE, 2014: San Antonio, TX. p. paper no. 4055.

141.   Michelin, A., et al., *Investigation at the Nanometre Scale on the Corrosion Mechanisms of Archaeological Ferrous Artefacts by STXM.* Journal of Analytical Atomic Spectrometry, 2013. **28**(1): p. 59-66.

142. Guo, X.P. and Y. Tomoe, *The Effect of Corrosion Product Layers on the Anodic and Cathodic Reactions of Carbon Steel in CO_2-Saturated MDEA Solutions at 100°C.* Corrosion Science, 1999. **41**(7): p. 1391-1402.
143. de Waard, C., U. Lotz, and D.E. Milliams, *Predictive Model for CO_2 Corrosion Engineering in Wet Natural Gas Pipelines.* Corrosion, 1991. **47**(12): p. 976-985.
144. Tran, T., B. Brown, and S. Nesic, *Corrosion of Mild Steel in an Aqueous CO_2 Environment – Basic Electrochemical Mechanisms Revisited*, in *CORROSION*. 2015, NACE International.
145. (Ed.), T.R., *Shreir's Corrosion* (first ed.) ed, ed. E. Science. 2009.
146. Kapusta, S.D., B.F.M. Pots, and I.J. Rippon, *The Application of Corrosion Prediction Models to the Design and Operation of Pipelines.* NACE International.
147. Kelland, M.A., *Production Chemicals for the Oil and Gas Industry, Second Edition.* 2014: CRC Press.
148. Tomson, M.B. and M.L. Johnson, *How Ferrous Carbonate Kinetics Impacts Oilfield Corrosion.* 1991, Society of Petroleum Engineers.
149. Baylis, J.R., *Factors other than Dissolved Oxygen Influencing the Corrosion of Iron Pipes.* Industrial & Engineering Chemistry, 1926. **18**(4): p. 370-380.
150. Schmitt, G. and M. Horstemeier, *Fundamental Aspects of CO_2 Metal Loss Corrosion - Part II: Influence of Different Parameters on CO_2 Corrosion Mechanisms.* 2006, NACE International.
151. Pessu, M.F., D.R. Barker, and P.A. Neville, *The Influence of pH on Localized Corrosion Behaviour of X65 (UNS K03014) Carbon Steel in CO_2-Saturated Brines.* Corrosion, 2015. **0**(0): p. null.
152. Pessu, F., R. Barker, and A. Neville, *The Influence of pH on Localized Corrosion Behavior of X65 (UNS K03014) Carbon Steel in CO_2-Saturated Brines*, in *NACE - International Corrosion Conference Series*. 2015.
153. Feigel, R.E.H., L. E.; Gomez, G. J., *Manual for Determining the Remaining Strength of Corroded Pipelines*, in *A supplement for the ASME B31 pressure piping*. 2012, ASME. p. 60.
154. A.Dunlop, H.L.H., P.R.Rhodes, *Fundamental Considerations in Sweet Gas Well Corrosion*, in *Advances in CO_2 Corrosion*, R.H.H.a. H.P.Goddard, Editor. 1984, NACE, Houston, 1984. p. 52.
155. Nyborg, R. and A. Dugstad, *Mesa Corrosion Attack in Carbon Steel and 0.5% Chromium Steel.* 1998, NACE International.
156. bin, H.J., et al., *Electrochemical Investigation of Localized CO_2 Corrosion on Mild Steel.* 2007, NACE International.
157. Nyborg, R. and A. Dugstad, *Understanding and Prediction of Mesa Corrosion Attack.* 1998, NACE International.
158. Han, J., et al., *Spontaneous Passivation Observations During Scale Formation on Mild Steel in CO_2 brines.* Electrochimica Acta, 2011. **56**(15): p. 5396-5404.
159. Schmitt, G.A., et al., *Understanding Localized CO_2 Corrosion of Carbon Steel from Physical Properties of Iron Carbonate Scales*, in *CORROSION 99.* 1999, NACE.

160. Fern, et al., *Galvanic Corrosion Following Local Breakdown of a Scale Formed on X-65 in CO_2 Saturated Solutions*. 2015, NACE International.

161. Halvorsen, A.M. and T. Sontvedt, *CO2 Corrosion Model for Carbon Steel Including Wall Shear Stress Model for Multiphase Flow and Limits for Production Rate to Avoid Mesa Attack*. 1999, NACE International.

162. Bruce Brown, D.Y., Srdjan Nešić, *Localized Corrosion in an H_2S / CO_2 Environment*, in *International Corrosion Conference*, I. Curran Associates, Editor. 2008, NACE International: Las Vegas, Nevada.

163. McAllister, E.W., *Pipeline Rules of Thumb Handbook: A Manual of Quick, Accurate Solutions to Everyday Pipeline Engineering Problems*. 2013: Elsevier Science.

164. Schmitt, G., et al., *A Probabilistic Model for Flow Induced Localized Corrosion*. 2000, NACE International.

165. Nešić, S., *Carbon Dioxide Corrosion of Mild Steel*, in *Uhlig's Corrosion Handbook*. 2011, John Wiley & Sons, Inc. p. 229-245.

166. Roberge, P., *Handbook of Corrosion Engineering*. 1999: Mcgraw-hill.

167. A. Ikeda, M.U., S. Mukai, *Advances in CO_2 Corrosion*, in *NACE International,*. 1994: Houston, TX. p. 39-51.

168. Lotz, U., L. van Bodegom, and C. Ouwehand, *Effect of Type of Oil or Gas Condensate on Carbonic Acid Corrosion.* Corrosion, 1991. **47**(8): p. 635-645.

169. Oehler, M.C., et al., *Testing of Generic Volatile Inhibitor Compounds in Different Top-Of-The-Line Corrosion Laboratory Test Methods*, in *NACE - International Corrosion Conference Series*. 2012. p. 3894-3908.

170. Foss, M., E. Gulbrandsen, and J. Sjöblom, *CO_2 Corrosion Inhibition and Oil Wetting of Carbon Steel with Ferric Corrosion Products*, in *NACE - International Corrosion Conference Series*. 2009.

171. Nyborg, R., A. Dugstad, and T.G. Martin, *Top of Line Corrosion With High CO_2 and Traces Of H_2S*. 2009, NACE International.

172. Eliyan, F.F., F. Mohammadi, and A. Alfantazi, *An Electrochemical Investigation on the Effect of the Chloride Content on CO_2 Corrosion of API-X100 Steel.* Corrosion Science, 2012. **64**: p. 37-43.

173. Jiang, X., et al., *Electrochemical Investigation of the Role of Cl^- on Localized Carbon Dioxide Corrosion Behavior of Mild Steel.* Corrosion, 2013. **69**(1): p. 15-24.

174. Gao, X., B. Brown, and S. Nesic, *Effect of Chloride on Localized Corrosion Initiation of Carbon Steel in a CO_2 Aqueous Environment*, in *NACE - International Corrosion Conference Series*. 2014.

175. Esmaeely, S.N., et al., *Effect of Calcium on the Formation and Protectiveness of an Iron Carbonate Layer in CO_2 Corrosion.* Materials Performance, 2014. **53**(5): p. 54-59.

176. Zhang, L., et al., *Effect of Pressure on Wet H_2S / CO_2 Corrosion of Pipeline Steel*. 2009, NACE International.

177. Moraes, F.d., et al., *Characterization of CO_2 Corrosion Product Scales Related to Environmental Conditions*. 2000, NACE International.

178. Gao, K., et al., *Mechanical Properties of CO$_2$ Corrosion Product Scales and Their Relationship to Corrosion Rates.* Corrosion Science, 2008. **50**(10): p. 2796-2803.

179. Li, D., et al., *Effects of Temperature on CO$_2$ Corrosion of Tubing and Casing Steel.* 2013, NACE International.

180. Wang, Y., *Effect of Temperature on CO$_2$/H$_2$S Corrosion of Oil Tube Steels*, in *Advanced Materials Research*. 2014. p. 111-114.

181. Ingham, B., et al., *In Situ Synchrotron X-Ray Diffraction Study of Surface Scale Formation During CO$_2$ Corrosion of Carbon Steel at Temperatures Up to 90 °C.* Corrosion Science, 2010. **52**(9): p. 3052-3061.

182. Sun, W., S. Nešić, and R.C. Woollam, *The Effect of Temperature and Ionic Strength on Iron Carbonate (FeCO$_3$) Solubility Limit.* Corrosion Science, 2009. **51**(6): p. 1273-1276.

183. Ko, M., et al., *In situ synchrotron X-ray diffraction study of the effect of microstructure and boundary layer conditions on CO2 corrosion of pipeline steels.* Corrosion Science, 2015. **90**(0): p. 192-201.

184. Hua, Y., R. Barker, and A. Neville, *Effect of Temperature on the Critical Water Content for General and Localised Corrosion of X65 Carbon Steel in the Transport of Supercritical CO$_2$.* International Journal of Greenhouse Gas Control, 2014. **31**: p. 48-60.

185. Honarvar Nazari, M., S.R. Allahkaram, and M.B. Kermani, *The effects of temperature and pH on the characteristics of corrosion product in CO2 corrosion of grade X70 steel.* Materials and Design, 2010. **31**(7): p. 3559-3563.

186. Kermani, B., et al., *A Working Party Report on CO$_2$ Corrosion Control in Oil and Gas Production: Design Considerations.* 1997: Institute of Materials.

187. Tanupabrungsun, T., B. Brown, and S. Nesic, *Effect of pH on CO$_2$ Corrosion of Mild Steel at Elevated Temperatures*, in *NACE - International Corrosion Conference Series*. 2013.

188. Li, W., et al., *Investigation of pseudo-passivation of mild steel in CO2 corrosion.* Corrosion, 2014. **70**(3): p. 294-302.

189. Tanupabrungsun, T., B. Brown, and S. Nesic. *Effect of pH on CO$_2$ Corrosion of Mild Steel at Elevated Temperatures*. in *CORROSION*. 2013. Orlando, Fl: NACE International.

190. Olsen, S. and A.M.K. Halvorsen, *Corrosion Control by pH Stabilization*, in *NACE - International Corrosion Conference Series*. 2015.

191. Edmonds, et al., *The Effect of Alloying on the Resistance of Carbon Steel for Oilfield Applications to CO$_2$ Corrosion.* Materials Research, 2005.

192. Ochoa, N., et al., *CO$_2$ Corrosion Resistance of Carbon Steel in Relation With Microstructure Changes.* Materials Chemistry and Physics, 2015. **156**: p. 198-205.

193. Farelas, F., B. Brown, and S. Nesic, *Iron Carbide and its Influence on the Formation of Protective Iron Carbonate in CO$_2$ Corrosion of Mild Steel.* 2013, NACE International.

194. Akeer, E., B. Brown, and S. Nesic, *The Influence of Mild Steel Metallurgy on the Initiation of Localized CO_2 Corrosion in Flowing Conditions*, in *NACE - International Corrosion Conference Series*. 2013.

195. Liang, W.E.I., X. Pang, and G.A.O. Kewei, *Effects of Crude Oil on the Corrosion Behavior of Pipeline Steel Under Wet CO_2 Conditions*. Materials Performance, 2015. **54**(5): p. 58-62.

196. Paolinelli, L.D., T. Pérez, and S.N. Simison, *The Effect of Pre-Corrosion and Steel Microstructure on Inhibitor Performance in CO_2 Corrosion*. Corrosion Science, 2008. **50**(9): p. 2456-2464.

197. Clover, D., et al., *The Influence of Microstructure on the Corrosion Rate of Various Carbon Steels*. Journal of Applied Electrochemistry, 2005. **35**(2): p. 139-149.

198. Shadley, J.R., et al., *Erosion-Corrosion of a Carbon Steel Elbow in a Carbon Dioxide Environment*. 1996.

199. Nyborg, R., *CO_2 Corrosion Models For Oil And Gas Production Systems*. 2010, NACE International.

200. Olsen, S., et al., *CO_2 Corrosion Prediction Model - Basic Principles*, in *NACE International*. 2005, NACE International: Houston, Texas.

201. Gatzke, L.K.H., R. H., *The COPRA Correlation. A Quantitative Assessment of Deep, Hot Gas Well and Its Control*, in *NACE*. 1983. p. 1-29.

202. Olsen, S., *CO2 Corrosion Prediction by Use of the NORSOK M-506 Model - Guidelines and Limitations*. 2003, NACE International.

203. Ne, et al., *An Open Source Mechanistic Model For CO_2 / H_2S Corrosion Of Carbon Steel*. 2009, NACE International.

204. DeWaard, C., Lotz, U., *Prediction of CO_2 Corrosion of Carbon Steel*., in *CORROSION*, NACE, Editor. 1993: Houston, TX. p. Paper No. 69.

205. Wang, H., J.Y. Cai, and W.P. Jepson, *CO_2 Corrosion Mechanistic Modeling and Prediction in Horizontal Slug Flow*. 2002, NACE International.

206. Woollam, R.C. and S. Hernandez, *Assessment and Comparison of CO_2 Corrosion Predicition Models*. 2006, Society of Petroleum Engineers.

207. Nesic, S., J. Cai, and K.-L. Lee, *A Multiphase Flow and Internal Corrosion Prediction Model for Mild Steel Pipelines*. 2005, NACE International: Houston, Texas.

208. Dugstad, A., Lunde, L., Videm, K., *Parametric Study of CO2 Corrosion of Carbon Steel*, in *CORROSION*, NACE, Editor. 1994: Houston, TX. . p. Paper No.14.

209. Srinivasan, S. and R.D. Kane, *Prediction of Corrosivity of CO_2/H_2S Production Environments*. NACE International.

210. Nesic, S., J. Postlethwaite, and S. Olsen, *An Electrochemical Model for Prediction of Corrosion of Mild Steel in Aqueous Carbon Dioxide Solutions*. CORROSION, 1996. **52**(4): p. 280-294.

211. Masamura, K., et al., *Estimation Models of Corrosion Rates of 13% Cr Alloys in CO_2 Environments*. NACE International.

212. Nyborg, R., *Overview of CO_2 Corrosion Models for Wells and Pipelines*. NACE International.

213. Li, H., et al., *Predicting Localized CO_2 Corrosion In Carbon Steel Pipelines*. 2011, NACE International: Houston, Texas.
214. Shayegani, M., et al., *Modelling of Carbon Dioxide Corrosion of Steel With Iron Carbonate Precipitation.* Corrosion Engineering Science and Technology, 2009. **44**(2): p. 128-136.
215. Dayalan, E., Vani, G., Shadley, J.R., Shirazi, S.A., Rybicki, E.F., *Modeling CO_2 Corrosion of Carbon Steels in Pipe Flow*, in *NACE*. 1995: Houston, TX. . p. Paper No. 118.
216. Dayalan, E., et al., *CO_2 Corrosion Prediction in Pipe Flow Under $FeCO_3$ Scale-Forming Conditions.* NACE International.
217. Nesic, S., et al., *Advancement in Predictive Modeling of Mild Steel Corrosion in CO_2 and H_2S Containing Environments*, in *NACE - International Corrosion Conference Series*. 2015.
218. Okafor, P.C., X. Liu, and Y.G. Zheng, *Corrosion Inhibition of Mild Steel by Ethylamino Imidazoline Derivative in CO_2-Saturated Solution.* Corrosion Science, 2009. **51**(4): p. 761-768.
219. Sastri, V.S., *Environmentally Friendly Corrosion Inhibitors*, in *Green Corrosion Inhibitors*. 2011, John Wiley & Sons, Inc. p. 257-303.
220. Fendler, J.H., *The Colloidal Domain: Where Physics, Chemistry, Biology, and Technology Meet.* Advanced Materials, 1996. **8**(3): p. 260-260.
221. Zheludkevich, M.L., et al., *Anticorrosion Coatings with Self-Healing Effect Based on Nanocontainers Impregnated with Corrosion Inhibitor.* Chemistry of Materials, 2007. **19**(3): p. 402-411.
222. Palumbo, O., et al., *Anelastic Spectroscopy Study of Iron Carbonate Scales From CO_2 corrosion of steel.* Materials Science and Engineering: A, 2009. **521–522**(0): p. 343-346.
223. Sherik, A.M., et al., *Effect Of Triethylene Glycol on Corrosion of Carbon Steel In H_2S, CO_2, and O_2 Environments*. 2011, NACE International.
224. Yang, G.R., et al., *Corrosion Behavior of 2205 Duplex Stainless Steel in Saturated H_2S/CO_2 Solution Containing Different Cl-Concentration.* Cailiao Rechuli Xuebao/Transactions of Materials and Heat Treatment, 2015. **36**(8): p. 229-236.
225. Paul, S., *Thermally Sprayed Corrosion Resistant Alloy Coatings on Carbon Steel for Use in Supercritical CO_2 Environments*, in *NACE - International Corrosion Conference Series*. 2015.
226. Islam, M.M., T. Pojtanabuntoeng, and R. Gubner, *Condensation corrosion of carbon steel at low to moderate surface temperature and iron carbonate precipitation kinetics.* Corrosion Science, 2016.
227. Yang, Y., et al. *Mechanical Strength and Removal of a Protective Iron Carbonate Layer Formed on Mild Steel in CO_2 Corrosion*. in *CORROSION*. 2010. San Antonio, TX: NACE International.
228. Al-Aithan, G.H., et al., *A Mechanistic Erosion-Corrosion Model for Predicting Iron Carbonate ($FeCO_3$) Scale Thickness in a CO_2 Environment With Sand*, in *NACE - International Corrosion Conference Series*. 2014.

229. Biegler, C. and M.R. Houchin, *Siderite (FeCO$_3$): Its Dissolution and Interaction With Stannic Oxide in Aqueous Suspensions.* Colloids and Surfaces, 1986. **21**(C): p. 267-278.
230. Foss, M.S., M.E. Seiersten, and K. Nisancioglu, *Interaction Between Scale Inhibitors and FeCO$_3$ Precipitation on Carbon Steel*, in *SPE International Oilfield Corrosion Symposium.* 2006, Society of Petroleum Engineers: Aberdeen, UK.
231. Sun, W., K. Chokshi, and S. Nesic, *Iron Carbonate Scale Growth and the Effect of Inhibition in CO$_2$ Corrosion of Mild Steel*, in *CORROSION 2005.* 2005, NACE International.
232. Rodrigues, A.G., et al., *Paleoenvironmental Implications of Early Diagenetic Siderites of The Paraíba Do Sul Deltaic Complex, Eastern Brazil.* Sedimentary Geology, 2015. **323**: p. 15-30.
233. Munoz, M., et al., *Continental Basinal Origin of Ore Fluids From Southwestern Massif Central Fluorite Veins (Albigeois, France): Evidence From Fluid Inclusion and Stable Isotope Analyses.* Applied Geochemistry, 1999. **14**(4): p. 447-458.
234. Loope, D.B. and R.M. Kettler, *The Footprints of Ancient CO$_2$-Driven Flow Systems: Ferrous Carbonate Concretions Below Bleached Sandstone.* Geosphere, 2015. **11**(3): p. 943-957.
235. Sánchez-Román, M., et al., *Microbial Mediated Formation of Fe-Carbonate Minerals Under Extreme Acidic Conditions.* Sci. Rep., 2014. **4**.
236. Bodor, S., et al., *Microbially Mediated Iron Ore Formation, Silicic Superunit, Rudabánya, Hungary.* Ore Geology Reviews, 2016. **72, Part 1**: p. 391-401.
237. Derek Lovley, C.L.Z., Juske Horita, David R. Cole, Jizhong Zhou, and Tommy J. Phelps., *Temperature-Dependent Oxygen and Carbon Isotopes Fractionations of Biogenic Siderite.* Geochimica et Cosmochimica Acta, 2001. **14**: p. 2257-2271.
238. Mortimer, R.J.G. and M.L. Coleman, *Microbial Influence on the Oxygen Isotopic Composition of Diagenetic Siderite.* Geochimica et Cosmochimica Acta, 1997. **61**(8): p. 1705-1711.
239. Pekov, I.V., et al., *Chukanovite, Fe$_2$(CO$_3$)(OH)$_2$, a New Mineral from the Weathered Iron Meteorite Dronino.* European Journal of Mineralogy, 2007. **19**(6): p. 891-898.
240. Keller, L.P., Thomas, K.L., McKay, D.S., *The Nature of Carbon-Bearing Phases in Hydrated Interplanetary Dust Particles.* Meteoritics, 1994. **29**: p. 480–481.
241. A.Dugstad, *The Importance of FeCO$_3$ Super-saturation on CO$_2$ Corrosion of Carbon Steels*

in *CORROSION/1992.* 1992, NACE International, 1992: Houston, TX. p. Paper No.14.
242. Yang, D., O. Rosas, and H. Castaneda, *FeCO$_3$ Layer Evolution for API 5L X52 Steel in Carbon Dioxide-Saturated NaCl Brine in the Presence of 1-Decyl-3-Methylimidazolium Chloride.* Corrosion Science, 2014. **87**(0): p. 40-50.

243. Hua, Y., et al., *Relating Iron Carbonate Morphology To Corrosion Characteristics For Water-Saturated Supercritical CO_2 Systems.* Journal of Supercritical Fluids, 2015. **98**: p. 183-193.

244. Gao, M., X. Pang, and K. Gao, *The Growth Mechanism of CO_2 Corrosion Product Films.* Corrosion Science, 2011. **53**(2): p. 557-568.

245. Hernandez, J., A. Muñoz, and J. Genesca, *Formation of Iron-Carbonate Scale-Layer and Corrosion Mechanism of APIX70 Pipeline Steel in Carbon Dioxide-Saturated 3% Sodium Chloride.* Afinidad, 2012. **69**(560): p. 251-258.

246. Han, J., et al., *Roles Of Passivation And Galvanic Effects In Localized CO_2 Corrosion Of Mild Steel.* 2008, NACE International.

247. Ramachandran, S., V. Jovancicevic, and M.B. Ward. *Understanding Interactions Between Corrosion Inhibitors and Iron Carbonate Films Using Molecular Modeling.* 1999. NACE International.

248. Schultz, L.N., et al., *High Surface Area Calcite.* Journal of Crystal Growth, 2013. **371**(0): p. 34-38.

249. Chai, L. and A. Navrotsky, *Synthesis, Characterization, and Enthalpy of mixing of the $(Fe,Mg)CO_3$ Solid Solution.* Geochimica et Cosmochimica Acta, 1996. **60**(22): p. 4377-4383.

250. Nagai, T., et al., *Pressure-Induced Spin Transition in $FeCO_3$-siderite studied by X-Ray Diffraction Measurements.* Journal of Physics: Conference Series, 2010. **215**.

251. Ming, X., et al., *First-principles study of pressure-induced magnetic transition in siderite FeCO3.* Journal of Alloys and Compounds, 2012. **510**(1): p. L1-L4.

252. Kiss, M.L., et al., *Transition From Single Crystalline $FeCO_3$ to Layered and Ordered Nanostructured $α-Fe_2O_3$.* Materials Letters, 2015. **158**: p. 214-217.

253. Guo, S., et al., *Corrosion of Alloy Steels Containing 2% Chromium in CO_2 Environments.* Corrosion Science, 2012. **63**(0): p. 246-258.

254. Joshi, G.R., *Elucidating Sweet Corrosion Scales*, in *School of Materials - Corrosion and Protection Centre*. 2015, University of Manchester-Faculty of Engineering and Physical Sciences. p. 280.

255. Li, T., et al., *Mechanism of Protective Film Formation During CO_2 Corrosion of X65 Pipeline Steel.* Journal of University of Science and Technology Beijing: Mineral Metallurgy Materials (Eng Ed), 2008. **15**(6): p. 702-706.

256. Yin, Z., et al., *Characteristics of CO_2 Corrosion Scale Formed on P110 Steel in Simulant Solution With Saturated CO_2.* Surface and Interface Analysis, 2008. **40**(9): p. 1231-1236.

257. Ruzic, V., M. Veidt, and S. Nesic, *Protective Iron Carbonate Films Part 1: Mechanical Removal in Single-Phase Aqueous Flow.* 2006.

258. Jasinski, R., *Corrosion of Low Alloy Steel in Crude Oil/Brine/CO_2 Mixtures.* The Electrochemical Society: Surfaces, Inhibition and Passivation, 1986. **86**: p. 139–148.

259. Rosli, N.R., Y.S. Choi, and D. Young, *Impact of oxygen ingress in CO2 corrosion of mild steel*, in *NACE - International Corrosion Conference Series*. 2014.

260. Ren, C., et al., *Physicochemical Performance of FeCO3 Films Influenced by Anions.* RSC Advances, 2015. **5**(26): p. 20302-20308.

261. Anderko, A.M., *Simulation of FeCO$_3$/FeS Scale Formation Using Thermodynamic and Electrochemical Models.* 2000, NACE International.

262. Gabrielli, C., et al., *Nucleation and Growth of Calcium Carbonate by an Electrochemical Scaling Process.* Journal of Crystal Growth, 1999. **200**(1–2): p. 236-250.

263. Sun, W. and S. Nešić, *Kinetics of Corrosion Layer Formation: Part 1—Iron Carbonate Layers in Carbon Dioxide Corrosion.* Corrosion, 2008. **64**(4): p. 334-346.

264. Lasaga, A.C., *Kinetic Theory in the Earth Sciences.* 2014: Princeton University Press.

265. Yang, Y., *Removal Mechanisms of Protective Iron Carbonate Layer in Flowing Solutions*, in *Chemical Engineering (Engineering and Technology)*. 2012, Ohio University.

266. Johnson, M.L., *Ferrous Carbonate Precipitation Kinetics: A Temperature Ramped Approach.* 1991, Rice University.

267. Lister, T. and J. Renshaw, *Understanding Chemistry for Advanced Level.* 2000: Thornes.

268. Fosbøl, P.L., K. Thomsen, and E.H. Stenby, *Review and Recommended Thermodynamic Properties of FeCO$_3$.* Corrosion Engineering, Science and Technology, 2010. **45**(2): p. 115-135.

269. Holland, T.J.B. and R. Powell, *An Enlarged and Updated Internally Consistent Thermodynamic Dataset with Uncertainties and Correlations: The system K2O–Na2O–CaO–MgO–MnO–FeO–Fe2O3–Al2O3–TiO2–SiO2–C–H2–O2.* Journal of Metamorphic Geology, 1990. **8**(1): p. 89-124.

270. Tomson, M.L.J.a.M.B., *Ferrous Carbonate Precipitation Kinetics and its Impact CO$_2$ Corrosion*, in *NACE International,.* 1991: Houston, TX. p. Paper no. 268,.

271. Sun, W., *Kinetics of Iron Carbonate and Iron Sulfide Scale Formation in CO2/H2S Corrosion* in *Faculty of the Russ College of Engineering and Technology* 2006, Ohio University. p. 50-52.

272. Garside, J., *Advances in the Characterization of Crystal Growth.* AIChE Symp. Ser., 1984. **80**: p. 23-38.

273. Gulbrandsen, E., *Acetic Acid And Carbon Dioxide Corrosion Of Carbon Steel Covered With Iron Carbonate.* 2007, NACE International.

274. Palencsár, A., E. Gulbrandsen, and K. Kateřina. *Corrosion Inhibition Under FeCO$_3$-Forming Conditions at Elevated Temperatures.* in *Society of Petroleum Engineers - SPE International Conference and Exhibition on Oilfield Corrosion 2014: New Challenges for a New Era.* 2014.

275. Yang, Y., B. Brown, and S. Nesic. *Study of Protective Iron Carbonate Layer Dissolution in a CO$_2$ Corrosion Environment.* in *CORROSION.* 2013. Orlando, FL: NACE International.

342

276. Bénézeth, P., J.L. Dandurand, and J.C. Harrichoury, *Solubility Product of Siderite (FeCO₃) as a Function of Temperature (25– 250 °C).* Chemical Geology, 2009. **265**(1–2): p. 3-12.

277. Jensen, D.L., et al., *The Solubility of Rhodochrosite (MnCO₃) and Siderite (FeCO₃) in Anaerobic Aquatic Environments.* Applied Geochemistry, 2002. **17**(4): p. 503-511.

278. H.J, S., *On Equilibrium in the System: Ferrous Carbonate, Carbon Dioxide and Water.* J. Amer. Chem. Soc., 1918. **40**: p. 879.

279. Singer, P.C. and W. Stumm, *The Solubility of Ferrous Iron in Carbonate-Bearing Waters.* Journal (American Water Works Association), 1970. **62**(3): p. 198-202.

280. Péré, J.B.a.C., *Détermination Expérimentale du Coefficient de Solubilité du Carbonate Ferreux en Milieux Aqueux.* Trib. CEBEDEAU 1976. **29**(387): p. 75–81.

281. Reiterer, F., W. Johannes, and H. Gamsjäger, *Semimicro Determination of Solubility Constants: Copper(II) Carbonate and Iron(II) Carbonate.* Microchimica Acta, 1981. **75**(1): p. 63-72.

282. Richard A. Robie, H.T.H., Bruce S. Hemingway, *Heat Capacities and Entropies of Rhodochrosite (MnCO₃) and Siderite (FeCO₃) between 5 and 600 K.* American Mineralogist, 1984. **69**(3-4): p. 349-357.

283. Braun, R.D., *Solubility of Iron(II) Carbonate at Temperatures Between 30 and 80°.* Talanta, 1991. **38**(2): p. 205-211.

284. Bruno, J., et al., *On the Influence of Carbonate in Mineral Dissolution: I. The Thermodynamics and Kinetics of Hematite Dissolution in Bicarbonate Solutions at T = 25°C.* Geochimica et Cosmochimica Acta, 1992. **56**(3): p. 1139-1147.

285. Silva, C.A.R., X. Liu, and F.J. Millero, *Solubility of Siderite (FeCO₃) in NaCl Solutions.* Journal of Solution Chemistry, 2002. **31**(2): p. 97-108.

286. Ruzic, V. and U.o. Queensland, *Mechanisms of Protective FeCO₃ Film Removal in Single-phase Flow-accelerated CO₂ Corrosion of Mild Steel.* 2005: University of Queensland.

287. Nesic, S., et al., *Mechanistic Modeling for CO₂ Corrosion with Protective Iron Carbonate Films.* 2001, NACE International.

288. Figueiredo, C.M.S., et al., *Crystal Growth of FeCO₃ in Mixed Monoethylene Glycol and Water Solvent.* Crystal Research and Technology, 2015. **50**(5): p. 354-361.

289. Berntsen, T., M. Seiersten, and T. Hemmingsen, *Effect of FeCO₃ Supersaturation And Carbide Exposure On the CO₂ Corrosion Rate of Carbon Steel.* 2011, NACE International.

290. Johnson, M.L., *Ferrous Carbonate Precipitation Kinetics: A Temperature Ramped Approach.* 1991, Rice University.

291. Artamonova, I.V., I.G. Gorichev, and E.B. Godunov, *Study of Calcium and Iron Carbonate Dissolution Kinetics in Order to Resolve Corrosion Problems in Carbonate Solutions.* Chemical and Petroleum Engineering, 2014.

292. Ferreira, L.R.M., et al., *CO2 Corrosion in the Region Between the Static and Turbulent Flow Regimes.* Materials Research, 2015. **18**(2): p. 245-249.

293. Nyborg, R. and A. Dugstad, *Understanding and Prediction of Mesa Corrosion Attack.* 2003, NACE International.

294. Dideriksen, K., et al., *Formation and Transformation of a Short Range Ordered Iron Carbonate Precursor.* Geochimica et Cosmochimica Acta, 2015. **164**: p. 53-70.

295. Greenberg, J. and M. Tomson, *Precipitation and Dissolution Kinetics and Equilibria of Aqueous Ferrous Carbonate vs Temperature.* Applied Geochemistry, 1992. **7**(2): p. 185-190.

296. Greenberg, J., *High Temperature Kinetics of Precipitation and Dissolution of Ferrous-carbonate.* 1987, Rice University.

297. Marion, G.M., D.C. Catling, and J.S. Kargel, *Modeling Aqueous Ferrous Iron Chemistry at Low Temperatures with Application to Mars.* Geochimica et Cosmochimica Acta, 2003. **67**(22): p. 4251-4266.

298. Bénézeth, P., J.L. Dandurand, and J.C. Harrichoury, *Solubility Product of Siderite ($FeCO_3$) as a Function of Temperature (25-250 °C).* Chemical Geology, 2009. **265**(1-2): p. 3-12.

299. J.S.Jacobs, *Metamagnetism of siderite ($FeCO_3$).* J.Appl.Phys., 1961. **34**: p. 1106-1107.

300. Johnson, J.D., et al., *Enhancing Gas and Oil Production With Zeta Potential Altering System.* 2010, Society of Petroleum Engineers.

301. Moulin, P. and H. Roques, *Zeta Potential Measurement of Calcium Carbonate.* J Colloid Interface Sci, 2003. **261**(1): p. 115-26.

302. Foss, M., E. Gulbrandsen, and J. Sjoeblom, *Adsorption of Corrosion Inhibitors onto Iron Carbonate $FeCO_3$ Studied by Zeta Potential Measurements.* Journal of Dispersion Science and Technology, 2010. **31**(2): p. 200-208.

303. Charlet, L., Wersin, P. & Stumm, W., *Surface charge of carbonate minerals.* Geochimica et Cosmochimica Acta, 1990. **54**: p. 2329-2336.

304. Zhang, C., et al., *One Step Hydrothermal Synthesis of $FeCO_3$ Cubes for High Performance Lithium-ion Battery Anodes.* Electrochimica Acta, 2015. **182**: p. 559-564.

305. Kennell, G.F., K.L. Heppner, and R.W. Evitts, *Modelling Carbon Dioxide Corrosion With Film Crystallization and Erosion.* Canadian Journal of Chemical Engineering, 2007. **85**(3): p. 350-359.

306. Romaine, A., et al., *Corrosion Processes of Carbon Steel in Argillite: Galvanic Effects Associated With the Heterogeneity of the Corrosion Product Layer.* Electrochimica Acta, 2015. **182**: p. 1019-1028.

307. Nesic, S. and K.-L.J. Lee. *A Mechanistic Model for Carbon Dioxide Corrosion of Mild Steel in the Presence of Protective Iron Carbonate Films Part 3: Film Growth Model.* in *Corrosion.* 2003.

308. Chicot, D., et al., *Mechanical Properties of Magnetite (Fe_3O_4), Hematite (α-Fe_2O_3) and Goethite (α-FeO·OH) by Instrumented Indentation and Molecular Dynamics Analysis.* Materials Chemistry and Physics, 2011. **129**(3): p. 862-870.

309. Schütze, M., D.R. Holmes, and I.o. Corrosion, *Protective Oxide Scales and Their Breakdown.* 1997, Wiley. p. 67-87.

310. Suo, Z., *Wrinkling of the Oxide Scale on an Aluminum-Containing Alloy at High Temperatures.* Journal of the Mechanics and Physics of Solids, 1995. **43**(6): p. 829-846.

311. Schütze, M. 1983, RWTH Aachen: Federal Republic of Germany.

312. Hou, P.Y., et al., *Proceedings of the Symposium on High Temperature Corrosion and Materials Chemistry.* 1998: Electrochemical Society.

313. Palacios, C.A. and J.R. Shadley, *Characteristics of Corrosion Scales on Steels in a CO_2-Saturated NaCl Brine.* Corrosion, 1991. **47**(2): p. 122-127.

314. Schmitt, G.A., T. Gudde, and E. Strobel-Effertz. *Fracture Mechanical Properties of CO_2 Corrosion Product Scales and Their Relation to Localized Corrosion.* in *CORROSION 96.* 1996. NACE International.

315. Nesvic´, S. and L. Lunde, *Carbon Dioxide Corrosion of Carbon Steel in Two-Phase Flow.* 1994.

316. Jackman, P.S. and L.M. Smith, *Modelling the Probability of Flow Induced Localised Corrosion from Critical Hydrodynamic Data and Fracture Mechanics Data of Scales from CO_2 Corrosion of Steel*, in *Advances in Corrosion Control and Materials in Oil and Gas Production: (EFC 26).* Maney Publishing.

317. Santillán, J. and Q. Williams, *A High-Pressure Infrared and X-ray Study of $FeCO_3$ and $MnCO_3$: Comparison with $CaMg(CO_3)_2$-Dolomite.* Physics of the Earth and Planetary Interiors, 2004. **143**(1-2): p. 291-304.

318. Paolinelli, L.D. and G.E. Carr, *Mechanical integrity of corrosion product films on rotating cylinder specimens.* Corrosion Science, 2015. **92**: p. 155-161.

319. López, D.A., T. Pérez, and S.N. Simison, *The Influence of Microstructure and Chemical Composition of Carbon and Low Alloy Steels in CO_2 Corrosion. A State-of-the-Art Appraisal.* Materials & Design, 2003. **24**(8): p. 561-575.

320. Dugstad, A., H. Hemmer, and M. Seiersten, *Effect of Steel Microstructure on Corrosion Rate and Protective Iron Carbonate Film Formation.* Corrosion, 2001. **57**(4): p. 369-378.

321. Crolet, J.-L., *Protectiveness of Corrosion Layers*, in *Modelling Aqueous Corrosion*, K. Trethewey and P. Roberge, Editors. 1994, Springer Netherlands. p. 1-28.

322. Ruzic, V., M. Veidt, and S. Nešić, *Protective Iron Carbonate Films— Part 3: Simultaneous Chemo-Mechanical Removal in Single-Phase Aqueous Flow.* Corrosion, 2007. **63**(8): p. 758-769.

323. Ruzic, V., S. Nesic´, and M. Veidt. *Protective Iron Carbonate Films Part 2: Chemical Removal by Dissolution in Single-Phase Aqueous Flow.* in *CORROSION.* 2006. NACE International.

324. Hausler, R.H., C. Consulta, and G. Schmitt, *Hydrodynamic and Flow Effects on Corrosion Inhibition.* 2004, NACE International.

325. Li, W., et al., *Measurement of Wall Shear Stress in Multiphase Flow and Its Effect on Protective $FeCO_3$ Corrosion Product Layer Removal*, in *NACE - International Corrosion Conference Series.* 2015.

326. Ramachandran, S., S. Campbell, and M.B. Ward, *Interactions and Properties of Corrosion Inhibitors with By-Product Layers.* Corrosion, 2001. **57**(6): p. 508-515.

327. Yaakob, S.M. and M.C. Ismail, *Corrosion Inhibitor Performance With Presence of $FeCO_3$ film in CO_2 Corrosion Environment Under Fluid Flow Effect*, in *Advanced Materials Research*. 2013. p. 507-510.

328. Yan, C., et al. *Evaluation of Ferrous Carbonate/Iron Oxides Scaling Risk Under High Temperature in the Absence and Presence of Scale Inhibitors*. in *Proceedings - SPE International Symposium on Oilfield Chemistry*. 2015.

329. Ivonye, I., A. Neville, and C. Wang, *The Corrosion of Carbon Steel In The Presence Of Monoethylene Glycol (MEG) - Assessing the Influence of an Iron Carbonate Scale*, in *NACE - International Corrosion Conference Series*. 2015.

330. Ahovan, M., M. Nasr-Esfahani, and S.A. Umoren, *Inhibitive Effect of 1-[(2-hydroxyethyl) amino]-2-(salicylideneamino)ethane Toward Corrosion of Carbon Steel in CO_2-Saturated 3.0% NaCl Solution.* Journal of Adhesion Science and Technology, 2016. **30**(1): p. 89-103.

331. He, Y., et al., *Imidazoline Derivative With Four Imidazole Reaction Centers as an Efficient Corrosion Inhibitor for Anti-CO_2 Corrosion.* Russian Journal of Applied Chemistry, 2015. **88**(7): p. 1192-1200.

332. Ibraheem, M.A., et al., *Sweet Corrosion Inhibition on API 5L-B Pipeline Steel.* ISRN Metallurgy, 2012. **2012**: p. 15.

333. Yaro, A.S., K.R. Abdul-Khalik, and A.A. Khadom, *Effect of CO_2 Corrosion Behavior of Mild Steel in Oilfield Produced Water*. Journal of Loss Prevention in the Process Industries, 2015. **38**: p. 24-38.

334. Dugstad, A., *Mechanism of Protective Film Formation During CO_2 Corrosion of Carbon Steel*, in *CORROSION 1998*. 1998, NACE International: Houston, TX. p. Paper no.31.

335. Zheng, L., et al., *$FeCO_3$ Coating Process toward the Corrosion Protection of Carbon Steel in a Postcombustion CO_2 Capture System.* Industrial & Engineering Chemistry Research, 2016. **55**(14): p. 3939-3948.

336. Sahu., S.K. *The Iron-Cementite Equilibrium Diagram*. 2013; Available from: https://sengerandu.wordpress.com/tutorials/physical-metallurgy/iron-cementite/.

337. Merrill, N.A., J.E. Garft, and J.D. Clay, *Biocidal Premixtures*. 2007, Google Patents.

338. Han, J., et al., *Water Soluble Octa-Functionalized POSS: All-Click Chemistry Synthesis and Efficient Host-Guest Encapsulation.* Chemical Communications, 2014. **50**(63): p. 8712-8714.

339. Wang, Q., et al., *Synthesis, Characterization and Inhibition Performance of Vanillin-Modified Chitosan Quaternary Ammonium Salts for Q235 Steel Corrosion in HCl Solution.* Journal of Surfactants and Detergents, 2015. **18**(5): p. 825-835.

340. Buchweishaija, J., *Corrosion Inhibition of Carbon Steel by an Amine-Fatty Acid in Acidic Solution.* Tanz. J. Sci., 2003. **29**(1): p. 99-108.

341. Wong, J.E. and N. Park, *Effect of Corrosion Inhibitor Active Components on the Growth of Iron Carbonate Scale Under CO_2 Conditions.* 2008, NACE International.

342. Philippini, V., et al., *Sorption of Silicon on Magnetite and Other Corrosion Products of Iron.* Journal of Nuclear Materials, 2006. **348**(1–2): p. 60-69.

343. Bleha, M., et al., *Effect of POSS™ Functionality on Morphology of Thin Hybrid Chitosan Films.* Designed Monomers and Polymers, 2004. **7**(1-2): p. 25-43.

344. Chemistry, T.R.S.o., *ESI Electronic Supplemetary Material*, in *Journal of materials chemistry.* 2012.

345. Dalwani, M., et al., *Ultra-Thin Hybrid Polyhedral Silsesquioxane-Polyamide Films With Potentially Unlimited 2D Dimensions.* Journal of Materials Chemistry, 2012. **22**(30): p. 14835-14838.

346. Duan, J., E. Litwiller, and I. Pinnau, *Preparation and water desalination properties of POSS-polyamide nanocomposite reverse osmosis membranes.* Journal of Membrane Science, 2015. **473**: p. 157-164.

347. Perrin, F.X., S. Bruzaud, and Y. Grohens, *Structure and Thermal Behaviour of Polyhedral Oligomeric Silsesquioxane Modified Montmorillonite.* Applied Clay Science, 2010. **49**(3): p. 113-119.

348. Zeng, L., et al., *High performance hybrids based on a novel incompletely condensed polyhedral oligomeric silsesquioxane and bismaleimide resin with improved thermal and dielectric properties.* Journal of Materials Science, 2011. **47**(6): p. 2548-2558.

349. Tanupabrungsun, T., *Thermodynamics and Kinetics of Carbon Dioxide Corrosion of Mild Steel at Elevated Temperatures*, in *Faculty of the Russ College of Engineering and Technology.* 2013, Ohio University.

350. Stefánsson, A., P. Bénézeth, and J. Schott, *Carbonic Acid Ionization and the Stability of Sodium Bicarbonate and Carbonate Ion Pairs to 200°C - A Potentiometric and Spectrophotometric Study.* Geochimica et Cosmochimica Acta, 2013. **120**: p. 600-611.

351. Hu, X., et al., *Assessing the Effect of Corrosion Inhibitor on Erosion–Corrosion of API-5L-X65 in Multi-Phase Jet Impingement Conditions.* Wear, 2011. **271**(9–10): p. 1432-1437.

352. Pessu, O.F., *Investigation of Pitting Corrosion of Carbon Steel in Sweet and Sour Oilfield Corrosion Conditions: A Parametric Study*, in *Institute of Functional Surfaces.* 2015, The University of Leeds: Leeds-UK.

353. Wang, J.Q., et al., *Microstructure of X52 and X65 Pipeline Steels.* Journal of Materials Science, 1999. **34**(8): p. 1721-1728.

354. Crolet, J.L. and M.R. Bonis, *pH Measurements in Aqueous CO_2 Solutions Under High Pressure and Temperature.* Corrosion, 1983. **39**(2): p. 39-46.

355. Goldstein, J., *Scanning Electron Microscopy and X-ray Microanalysis: Third Edition.* 2003: Springer US.

356. WolframAlpha. *WolframAlpha computational knowledge engine.* 2016 16/03/2016]; Available from: http://www.wolframalpha.com/.

357. Oliver, W.C. and G.M. Pharr, *An Improved Technique for Determining Hardness and Elastic Modulus Using Load and Displacement Sensing Indentation Experiments.* Journal of Materials Research, 1992. **7**(06): p. 1564-1583.

358. Sun, W. and S. Nesic. *Basics Revisited: Kinetics Of Iron Carbonate Scale Precipitation In CO_2 Corrosion.* in *CORROSION 2006.* 2006.

359. Bai, L. and B.E. Conway, *AC Impedance of Faradaic Reactions Involving Electrosorbed Intermediates: Examination of Conditions Leading to Pseudoinductive Behavior Represented in Three-Dimensional Impedance Spectroscopy Diagrams.* Journal of The Electrochemical Society, 1991. **138**(10): p. 2897-2907.

360. Ruzic, V., M. Veidt, and S. Nesic´. *Protective Iron Carbonate Films Part 2: Chemical Removal by Dissolution in Single-Phase Aqueous Flow.* in *CORROSION 2006.* 2006. NACE International.

361. Fajardo, V., et al. *Study of the Solubility of Iron Carbonate in the Presence of Acetic Acid Using an EQCM.* in *CORROSION 2013.* 2013. Orlando, FL.

362. Akbari, A. and N. Arsalani, *Preparation and Characterization of Novel Hybrid Nanocomposites by Free Radical Copolymerization of Vinyl pyrrolidone with Incompletely Condensed Polyhedral Oligomeric Silsesquioxane.* Journal of Inorganic and Organometallic Polymers and Materials, 2016. **26**(3): p. 536-544.

363. Kriel, B.G., C.A. Lacey, and R.H. Lane, *The Performance of Scale Inhibitors in the Inhibition of Iron Carbonate Scale.* 1994, Society of Petroleum Engineers.

364. Chapman, D. and W. Trybula. *Meeting the Challenges of Oilfield Exploration Using Intelligent Micro and Nano-Scale Sensors.* in *Nanotechnology (IEEE-NANO), 2012 12th IEEE Conference on.* 2012.

365. Sun, J., et al., *Effect of Chromium on Corrosion Behavior of P110 Steels in CO_2-H_2S Environment with High Pressure and High Temperature.* Materials, 2016. **9**(3): p. 200.

366. Xia, Z., K.C. Chou, and Z. Szklarska-Smialowska, *Pitting Corrosion of Carbon Steel in CO_2-Containing NaCl Brine.* CORROSION, 1989. **45**(8): p. 636-642.

367. Ingham, B., et al., *First Stages of Siderite Crystallisation during CO_2 Corrosion of Steel Evaluated Using In Situ Synchrotron Small- and Wide-Angle X-Ray Scattering.* Faraday Discussions, 2015. **180**(0): p. 171-190.

368. Amjad, Z. and R.W. Zuhl, *Kinetic and Morphological Investigation on the Precipitation of Calcium Carbonate in the Presence of Inhibitors.* NACE International.

369. Meng, Y., et al., *Significantly Improving the Thermal Stability and Dispersion Morphology of Polyhedral Oligomeric Silsesquioxane/Polysiloxane Composites by in-situ Grafting Reaction.* Polymer, 2013. **54**(12): p. 3055-3064.

370. Divakar, M., V.K. Agarwal, and S.N. Singh, *Effect of the Material Surface Hardness on the Erosion of AISI316.* Wear, 2005. **259**(1–6): p. 110-117.

371.	Ejder-Korucu, M., A. Gürses, and S. Karaca, *Poly(Ethylene Oxide)/Clay Nanaocomposites: Thermal and Mechanical Properties.* Applied Surface Science, 2016. **378**: p. 1-7.

372.	Ni, Y., S. Zheng, and K. Nie, *Morphology and Thermal Properties of Inorganic-Organic Hybrids Involving Epoxy Resin and Polyhedral Oligomeric Silsesquioxanes.* Polymer, 2004. **45**(16): p. 5557-5568.

373.	Thomas H. Sanders, J., *Factors Affecting Crystallinity in Polymers.* 2016, Georgia Institute of Technology.

374.	Toda, A., R. Androsch, and C. Schick, *Insights Into Polymer Crystallization and Melting from Fast Scanning Chip Calorimetry.* Polymer, 2016. **91**: p. 239-263.

375.	Guo, X., et al., *Controlled crystallization of hierarchical and porous calcium carbonate crystals using polypeptide type block copolymer as crystal growth modifier in a mixed solution.* CrystEngComm, 2011. **13**(6): p. 2054-2061.

376.	Beck, R. and J.P. Andreassen, *The influence of crystallization conditions on the onset of dendritic growth of calcium carbonate.* Crystal Research and Technology, 2012. **47**(4): p. 404-408.

377.	Pandarinathan, V., K. Lepková, and W. van Bronswijk, *Chukanovite ($Fe_2(OH)_2CO_3$) Identified as a Corrosion Product at Sand-Deposited Carbon Steel in CO_2-Saturated Brine.* Corrosion Science, 2014(0).

378.	Liu, L., et al., *Crystallization and Morphology Study of Polyhedral Oligomeric Silsesquioxane POSS/Polysiloxane Elastomer Composites Prepared by Melt Blending.* Polymer, 2007. **48**(11): p. 3201-3212.

379.	Shindo, H. and M. Kwak, *Stabilities of Crystal Faces of Aragonite ($CaCO_3$) Compared by Atomic Force Microscopic Observation of Facet Formation Processes in Aqueous Acetic Acid* Physical Chemistry Chemical Physics, 2005. **7**(4): p. 691-696.

380.	Guo, H., Y. Li, and K. Zhao, *Arsenate removal from aqueous solution using synthetic siderite.* Journal of Hazardous Materials, 2010. **176**(1–3): p. 174-180.

381.	Wargo, E.A., et al., *Comparison of Focused Ion Beam Versus Nano-Scale X-Ray Computed Tomography for Resolving 3-D Microstructures of Porous Fuel Cell Materials.* Journal of Power Sources, 2013. **241**: p. 608-618.

382.	Sawicki, J.A., D.A. Brown, and T.J. Beveridge, *Microbial precipitation of siderite and protoferrihydrite in a biofilm.* Canadian Mineralogist, 1995. **33**(1): p. 1-6.